

Vincent S. Smentkowski *Editor*

# Surface Analysis and Techniques in Biology

 Springer

# Surface Analysis and Techniques in Biology



Vincent S. Smentkowski  
Editor

# Surface Analysis and Techniques in Biology

 Springer

*Editor*

Vincent S. Smentkowski, Ph.D.  
Nanostructures and Surfaces Laboratory  
GE Global Research  
Niskayuna, NY, USA

ISBN 978-3-319-01359-6                      ISBN 978-3-319-01360-2 (eBook)  
DOI 10.1007/978-3-319-01360-2  
Springer Cham Heidelberg New York Dordrecht London

Library of Congress Control Number: 2014931212

© Springer International Publishing Switzerland 2014

This work is subject to copyright. All rights are reserved by the Publisher, whether the whole or part of the material is concerned, specifically the rights of translation, reprinting, reuse of illustrations, recitation, broadcasting, reproduction on microfilms or in any other physical way, and transmission or information storage and retrieval, electronic adaptation, computer software, or by similar or dissimilar methodology now known or hereafter developed. Exempted from this legal reservation are brief excerpts in connection with reviews or scholarly analysis or material supplied specifically for the purpose of being entered and executed on a computer system, for exclusive use by the purchaser of the work. Duplication of this publication or parts thereof is permitted only under the provisions of the Copyright Law of the Publisher's location, in its current version, and permission for use must always be obtained from Springer. Permissions for use may be obtained through RightsLink at the Copyright Clearance Center. Violations are liable to prosecution under the respective Copyright Law.

The use of general descriptive names, registered names, trademarks, service marks, etc. in this publication does not imply, even in the absence of a specific statement, that such names are exempt from the relevant protective laws and regulations and therefore free for general use.

While the advice and information in this book are believed to be true and accurate at the date of publication, neither the authors nor the editors nor the publisher can accept any legal responsibility for any errors or omissions that may be made. The publisher makes no warranty, express or implied, with respect to the material contained herein.

Printed on acid-free paper

Springer is part of Springer Science+Business Media ([www.springer.com](http://www.springer.com))

# Preface

This book came about as a result of a discussion which took place at a Microscopy and Microanalysis meeting. Although the number of research groups working in the field of biological surface chemistry, modification and characterization have increased during the past few decades, a number of advances have been made to standard surface analytical instrumentation, and a number of new instruments have been introduced, only two books on the subject of surface analysis of biological systems have been published (see Refs. [44] and [45] in Chap. 1) and are both now outdated. We felt the time was right for a book which went into more detail on the main surface analysis techniques that are being used to study biological specimens and systems.

The process of editing a book is very rewarding, as you are tasked with identifying best-in-class researchers in their respective fields of study and helping them assemble and refine the content. I very much appreciate that each of the chapter authors took time from their busy schedules to write their chapters. The technical content described in this book is very high. The compilation of chapters will help the biological research community realize the benefits that surface analysis provides. We look forward to seeing a larger number of biologists and medical specialists start using the techniques discussed in this book.

New analysis instruments (such as the QSTAR and the Ionoptika J105 3D Chemical Imager, which are discussed in the future outlook section of Chap. 4) are continuously being developed and introduced to the scientific community; we look forward to seeing what the future has in store. I am also excited to see the next generation of medical devices, which will benefit from surface analysis and will help our society.

Niskayuna, NY, USA

Vincent S. Smentkowski



# Contents

<b>1 Introduction</b> .....	1
Vincent S. Smentkowski	
<b>2 Applications of XPS in Biology and Biointerface Analysis</b> .....	9
Sally L. McArthur, Gautam Mishra, and Christopher D. Easton	
<b>3 Biomolecular Analysis by Time-of-Flight Secondary Ion Mass Spectrometry (ToF-SIMS)</b> .....	37
Daniel Breitenstein, Birgit Hagenhoff, and Albert Schnieiders	
<b>4 Cluster Secondary Ion Mass Spectrometry</b> .....	71
Joseph Kozole and Nicholas Winograd	
<b>5 Biological Tissue Imaging at Different Levels: MALDI and SIMS Imaging Combined</b> .....	99
J. Stauber and Ron M.A. Heeren	
<b>6 Molecular Structure and Identification Through G-SIMS and SMILES</b> .....	141
F.M. Green, I.S. Gilmore, and M.P. Seah	
<b>7 Imaging with the Helium Ion Microscope</b> .....	171
John Notte and Bernhard Goetze	
<b>8 Sum Frequency Generation Vibrational Spectroscopy: A Sensitive Technique for the Study of Biological Molecules at Interfaces</b> .....	195
Andrew P. Boughton and Zhan Chen	
<b>9 Near-Field Scanning Optical Microscopy: A New Tool for Exploring Structure and Function in Biology</b> .....	225
Nicholas E. Dickenson, Olivia L. Mooren, Elizabeth S. Erickson, and Robert C. Dunn	



<b>10 Atomic Force Microscopy: Applications in the Field of Biology</b> .....	255
J.K. Heinrich Hoerber	
<b>11 Multi-technique Characterization of DNA-Modified Surfaces for Biosensing and Diagnostic Applications</b> .....	289
Chi-Ying Lee, Lara J. Gamble, Gregory M. Harbers, Ping Gong, David W. Grainger, and David G. Castner	
<b>Index</b> .....	315

# Contributors

**Andrew P. Boughton** Department of Chemistry, University of Michigan, Ann Arbor, MI, USA

**Daniel Breitenstein** Tascon GmbH, Münster, Germany

**David G. Castner** National ESCA and Surface Analysis Center for Biomedical Problems, Department of Bioengineering, and Department of Chemical Engineering, University of Washington, Seattle, WA, USA

**Zhan Chen** Department of Chemistry, University of Michigan, Ann Arbor, MI, USA

**Nicholas E. Dickenson** Department of Chemistry, Ralph N. Adams Institute for Bioanalytical Chemistry, The University of Kansas, Lawrence, KS, USA

**Robert C. Dunn** Department of Chemistry, Ralph N. Adams Institute for Bioanalytical Chemistry, The University of Kansas, Lawrence, KS, USA

**Christopher D. Easton** CSIRO Molecular and Health Technologies, Clayton South, VIC, Australia

**Elizabeth S. Erickson** Department of Chemistry, Ralph N. Adams Institute for Bioanalytical Chemistry, The University of Kansas, Lawrence, KS, USA

**Lara J. Gamble** National ESCA and Surface Analysis Center for Biomedical Problems and Department of Bioengineering, University of Washington, Seattle, WA, USA

**I.S. Gilmore** Analytical of Life Division, National Physical Laboratory, Teddington, Middlesex, UK

**Bernhard Goetze** Director of Research and Development, Carl Zeiss Microscopy in Peabody, Peabody, MA, USA

**Ping Gong** Department of Pharmaceutics and Pharmaceutical Chemistry, University of Utah, Salt Lake City, UT, USA  
Seventh Sense Biosystems, Cambridge, MA, USA

**David W. Grainger** Department of Bioengineering and Department of Pharmaceutics and Pharmaceutical Chemistry, University of Utah, Salt Lake City, UT, USA

**F.M. Green** Analytical Science Division, National Physical Laboratory, Teddington, Middlesex, UK

**Birgit Hagenhoff** Tascon GmbH, Münster, Germany

**Gregory M. Harbers** Replenish, Inc., Pasadena, CA, USA

Department of Pharmaceutics and Pharmaceutical Chemistry, University of Utah, Salt Lake City, UT, USA

**Ron M.A. Heeren** FOM-Institute for Atomic and Molecular Physics, Amsterdam, The Netherlands

**J.K. Heinrich Hoerber** H.H. Wills Physics Laboratory, University of Bristol, Bristol, UK

**Joseph Kozole** Department of Chemistry, Penn State University, University Park, Philadelphia, PA, USA

DuPont, Philadelphia, PA, USA

**Chi-Ying Lee** National ESCA and Surface Analysis Center for Biomedical Problems and Department of Chemical Engineering, University of Washington, Seattle, WA, USA

**Sally L. McArthur** Biointerface Engineering Group, IRIS, Faculty of Engineering and Industrial Sciences, Swinburne University of Technology, Hawthorn, VIC, Australia

**Gautam Mishra** Kratos Analytical, Wharfside, Manchester, UK

**Olivia L. Mooren** Department of Chemistry, Ralph N. Adams Institute for Bioanalytical Chemistry, The University of Kansas, Lawrence, KS, USA

**John Notte** Director of Research and Development, Carl Zeiss Microscopy in Peabody, Peabody, MA, USA

**Albert Schnieders** Tascon USA, Inc., Chestnut Ridge, NY, USA

Managing Director, CNM Technologies, Bielefeld, Germany

**M.P. Seah** Analytical Science Division, National Physical Laboratory, Teddington, Middlesex, UK

**Vincent S. Smentkowski** Nanostructures and Surfaces Laboratory, GE Global Research, Niskayuna, NY, USA

**J. Stauber** FOM-Institute for Atomic and Molecular Physics, Amsterdam, The Netherlands

**Nicholas Winograd** Department of Chemistry, Penn State University, University Park, Philadelphia, PA, USA

# Chapter 1

## Introduction

Vincent S. Smentkowski

**Abstract** The outer layer of bulk samples is referred to in the scientific community as the surface of the sample or material. At the surface, the composition, microstructure, phase, chemical bonding, electronic states, and/or texture can be different than that of the bulk material. The outer surface is where many material interactions/reactions take place; this is especially true for biomaterials as biomaterials are intended to interact with the biological system. Breakthroughs in biomaterials and biomedical devices will require novel approaches to tailoring biological surfaces in order to generate surfaces with desired properties. Analytical techniques are required to characterize the surface of biological materials and quantify their impact in real-world biological systems. Surface analysis of biological materials started in the 1960s, and the number of researchers working in this area has increased rapidly since then. Surface analysts are being asked to detect and image species present in lower concentrations and within smaller spatial dimensions in biomaterials. Biological samples, which can be highly irregular in shape, can be chemically and morphologically altered during sample preparation, storage, and/or placement under high vacuum; the molecules can become damaged when energetic surface probes are used to analyze them. The complexity of the biological system complicates the analysis of biological samples. The desire to analyze biological samples is driving the development of new and/or improved surface analysis instrumentation and data analysis tools. The surface analysis instruments which are most often used to analyze biological samples are reported in this book.

The outer layer of bulk solid or liquid samples is referred to in the scientific community as the surface of the sample or material. At the surface, the composition, microstructure, phase, chemical bonding, electronic states, and/or texture is often different than that of the bulk material. The outer surface is where many material

---

V.S. Smentkowski, Ph.D (✉)  
Nanostructures and Surfaces Laboratory, GE Global Research, 1 Research Circle,  
Niskayuna 12309, New York, USA  
e-mail: [smenkow@ge.com](mailto:smenkow@ge.com)

interactions/reactions take place (for instance, corrosion of metals and/or catalysis) [1, 2]. In 1984, Charles B. Duke wrote a paper entitled “Atoms and electrons at surfaces: A modern scientific revolution,” where he summarized the importance of surface and interfacial phenomena. In the abstract, he stated, “Whereas in the mid-1960s an interface was regarded merely as the boundary between two bulk media, today it is seen as an independent entity: a state of matter determined by its history and exhibiting its own unique composition, structure, and electronic properties” [1].

Traditionally, surface scientists and analysts have been grouped into three different categories: (1) researchers who perform a complete characterization of clean, single crystal surfaces; (2) researchers who study the interaction of adsorbates onto clean surfaces under ultrahigh-vacuum conditions; and (3) researchers who are analyzing as-received, real-life parts. The first two groups of scientists are often trying to understand fundamental phenomena under well-controlled conditions. The last group of researchers are often found in an industrial setting and are usually classified as applied surface scientists/analysts. Often times, their samples contain multiple components and because the samples are transferred from ambient conditions into the surface analysis instrument, they are not “clean,” in contrast with the samples analyzed by groups 1 and 2 above.

The field of surface analysis rapidly grew in the late 1960s and early 1970s with the introduction of commercial surface analysis instrumentation [1, 2]. It is of interest and importance to note that the first surface analysis instruments, such as Auger electron spectroscopy (AES) [3–5], X-ray photoelectron spectroscopy (XPS) [6], ion scattering spectroscopy (ISS) [7], and secondary ion mass spectroscopy (SIMS) [8, 9], were developed at, or in collaboration with, industrial research laboratories such as General Electric [3–5], Hewlett-Packard [6], 3M [7], and Knolls Atomic Power Laboratory–General Electric [8, 9], respectively. These first surface analysis instruments were designed and built in order to study practical phenomena such as metallurgy [10–13], corrosion science [14–16], electronic devices [17, 18], tribology [19–22], polymers [23–26], adhesives and resins [27], and catalysis [2, 28–30] in real material systems. The applications of surface analysis reported at conferences, as well as in the literature, have grown (and changed) with time, reflecting priorities and research interests. Surface analysts are now being asked to detect and image species present in lower concentrations and within a smaller spatial dimension in a new class of materials—biological samples. Biological samples, which can be highly irregular in shape, can be chemically and morphologically altered during sample preparation, storage, and/or placement under high vacuum; the molecules can become damaged when energetic surface probes are used to analyze them. The overall complexity of the biological system complicates the analysis of many biological samples [31]. The desire to analyze biological samples is driving the development of new and/or improved surface analysis instrumentation and data analysis tools. The most commonly used surface analysis instruments are reported in this book.

A biomaterial is defined as a material used in a medical device; a biomaterial is intended to interact with the biological system [32]. Biomaterials are fabricated into bio-devices, which are often implanted into tissues and organs. Surfaces of

biomaterials (synthetic or modified natural materials) are of critical importance since the surface is typically the only part of a biomaterial/bio-device that comes in contact with the biological system (e.g., tissues and organs for implanted biomaterial/bio-devices); surfaces are where reaction and/or adsorption occurs in biomedical assemblies [31, 33]. For certain applications, adsorption is detrimental and should be minimized [e.g., protein adhesion within microfluidic channels, and formation of a thrombus (an aggregation of blood cells) upon insertion of a biomaterial into the body], while for other applications, adsorption is needed to facilitate repair or growth (e.g., adherent cells) [31, 33]. Breakthroughs in biomedical devices will require novel approaches to tailoring biological surfaces in order to generate surfaces with desired properties. Analytical techniques are required to characterize the surface of biological materials and quantify their impact in real-world biological systems. Surface analysis of biological materials started in the 1960s, and the number of researchers working in this area has increased very rapidly since then. Today there are journals devoted to the surface analysis of biological materials and systems [34].

There are numerous exceptional books on practical surface analysis [35–43]; however, these books do not have much information regarding biological surface analysis. Books specific to a single technique often contain a chapter on biological surface analysis. In 1988, Buddy D. Ratner edited a book, *Progress in Biomedical Engineering 6, Surface Characterization of Biomaterials* [44], which summarized a symposium, sponsored by the American Chemical Society (ACS), that was attended by biologists, surface scientists, chemists, physicists, materials scientists, and physicians in Ann Arbor, Michigan, in June of 1987. In the preface to the book, Ratner compared a surface scientist's perception of a surface to that of a biologist. He concluded that “on the whole, biologist will not invoke surface-induced effects in their hypotheses. The surface scientist, on the other hand, will consider the problems of biology as being too complex and disorderly to be dealt with using the tools available. There is a wide gap in understanding between these two disciplines, but there are signs that it is narrowing.” About 25 years later, many of these gaps still remain although biologists are now realizing the importance of the outer surface of biomaterials and surface analysts are starting to analyze biomaterials. Most important, research teams are being formed that have members from both disciplines, and they are working together and cross-training each other. Since the release of the Ratner book, there have been a number of new surface analysis instruments, as well as numerous improvements to the traditional surface analysis instruments, that are facilitating biological sample analysis; many of these will be outlined in this book. In 1996, John Davies edited the book *Surface Analytical Techniques for Probing Biomaterial Processes*, which summarized four techniques commonly used by biologists for probing dynamic, in situ processes at the biomaterial interfaces [45]. The book described total internal reflection fluorescence spectroscopy (TIRFS), surface plasmon resonance (SPR), ellipsometry, and dynamic contact angle (DCA). To date, the Ratner and Davis books are the only two books that have been published on the surface analysis of biological materials.

The concept for the present book originated from numerous discussions with surface analysts who are now starting to analyze biological samples as well as

researchers in the medical and biological communities who have indicated that they are not aware of surface analysis techniques and that having one comprehensive book on the most commonly used surface analysis techniques being used to analyze biological materials would be very useful. It is anticipated that this book will result in an increase in the use of surface analysis techniques by researchers in the medical and biological communities. Although the examples described in this book are biological, the book will also be useful for researchers analyzing other materials (metals, alloys, ceramic, etc.) since this book represents a compilation of the current, state-of-the-art surface analysis techniques.

This book starts with a chapter on X-ray photoelectron spectroscopy (XPS), which is a widely used instrument as it detects all elements except hydrogen and helium; changes in peak position (binding energy) provide information about the chemical environment of the elements. The second chapter is on secondary ion mass spectrometry (SIMS). SIMS allows for the detection of all elements, with a high (ppm or better) chemical sensitivity; most state-of-the-art SIMS instruments allow for 3D analysis as well as the collection of a full mass spectrum at every voxel. In order to maximize the yield of high-mass molecular information and minimize degradation of the molecular information during SIMS analysis, the time-of flight secondary ion mass spectrometry (ToF-SIMS) community is devising novel cluster ion sources. Chapter 3 describes the benefits of these new cluster SIMS ion sources via examples. A number of research groups have also shown that the application of a metal or matrix to a biological specimen prior to SIMS analysis can also increase the amount of molecular information available. Chapter 4 describes metal-enhanced and matrix-enhanced SIMS and compares these approaches to matrix-assisted laser desorption ionization (MALDI) mass spectroscopy. Compared to SIMS, MALDI is able to detect higher mass species but has degraded lateral resolution. SIMS and MALDI provide complementary information about samples. Both SIMS and MALDI data sets are very complex and contain a wealth of information about the sample that was analyzed. The scientific community is devising data analysis strategies to facilitate data reduction. Multivariate statistical analysis (MVSA) algorithms are proving to be very valuable in this regard; readers interested in MVSA are referred to a special, two-issue series on MVSA that was published in *Surface and Interface Analysis* (SIA) in 2009 [46, 47]. Chapter 5 introduces the reader to gentle secondary ion mass spectrometry (G-SIMS) and SMILES (simplified molecular input line entry specification). G-SIMS provides information about the molecular structure that is not directly available from the as-collected mass spectrum. G-SIMS often allows the identification of unknown materials without the need for experimental library spectra. SMILES is used to simulate the fragmentation pathways that occur in G-SIMS. Helium ion microscopy (HIM) is a relatively new technique that is showing benefits compared to scanning electron microscopy (SEM) imaging, including the ability to analyze insulating samples without an overcoat, a higher lateral resolution, and a higher depth of field. HIM is described in Chap. 6. Chapter 7 summarizes scanning probe microscopy (SPM), which is a general term that is used to describe a family of instruments that measure the interaction of a small tip with a sample surface at close distances in order to provide the topography of the surface.

Many SPM instruments can provide information on a material's phase, capacitance, magnetic properties, and electrochemical properties (to name a few) while simultaneously recording the topography. Near-field scanning optical microscopy (NSOM), also referred to as scanning near-field optical microscopy (SNOM), instruments use specially fabricated probes to deliver light down to the nanometric dimension, enabling optical microscopy with a spatial resolution of tens of nanometers. NSOM instruments can simultaneously map sample fluorescence and topography with a high spatial resolution and single-molecule detection limits. NSOM is summarized in Chap. 8. Sum frequency generation (SFG) is a nonlinear optical vibrational spectroscopic technique with excellent sensitivity to interfacial molecules and molecular ordering; SFG is well suited to probing biomolecules in a native interfacial environment in order to provide information on biomolecular orientation and conformation at interfaces. SFG is summarized in Chap. 9.

Chapter 10 describes the benefits of using complementary surface analysis techniques—X-ray photoelectron spectroscopy (XPS), near-edge X-ray absorption fine structure (NEXAFS), time-of-flight secondary ion mass spectrometry (ToF-SIMS), and surface plasmon resonance (SPR)—to characterize the structure and composition of DNA-modified surfaces.

Importantly, new instruments and data analysis protocol are being designed and tested with the aim of providing more molecular information about biological samples—the future looks very encouraging. A final significant point to be made is that the most successful groups working in the field of surface analysis of biological materials have biologists as part of their research team. The biologists are bringing their surface analysis colleagues up to speed on their terminology, experimental methods, and so forth, and the surface analysts are then able to relate their findings back to the biologists using the terminology the biologists are accustomed to using. Having a common language that is understood by both parts of the team is beneficial. The biologists and the surface analysts are also working together to determine the best sample preparation methods. The gap that Ratner mentioned between these two disciplines [44] is indeed narrowing.

## References

1. Duke CB. Atoms and electrons at surfaces: a modern scientific revolution. *J Vac Sci Technol A*. 1984;2(2):139.
2. Somorjai GA, Li Y, editors. *Introduction to surface chemistry and catalysis*. 2nd ed. Hoboken: Wiley; 2010.
3. Harris LA. General electric report no 67-C-201 (1967). *J Appl Phys*. 1968;39:1419.
4. Harris LA. Miscellaneous topics in Auger electron spectroscopy. *J Vac Sci Technol*. 1974;11:23.
5. Gergely G. Vacuum. Commemoration of the 25th anniversary of Auger electron spectroscopy. 1994;45(2/3):311.
6. In cooperation with Siegbahn, a group of engineers from Hewlett-Packard in the USA (Mike Kelly, Charles Bryson, Lavier Faye, Robert Chaney) produced the first commercial monochromatic XPS instrument in 1969. [http://en.wikipedia.org/wiki/X-ray\\_photoelectron\\_spectroscopy](http://en.wikipedia.org/wiki/X-ray_photoelectron_spectroscopy). Kelly MA. *J Chem Educ*. 2004;81(12):1726.



7. Smith DP, Wang PS, Moddeman WE, Haws LD, Wittberg TN, Peters JA. Surface studies of plastic-bonded E $\epsilon$ TN and RDX by X-ray photoelectron spectroscopy (XPS) and ion-scattering spectroscopy (ISS). *J Appl Phys.* 1967;38:340; <http://www.osti.gov/bridge/servlets/purl/6254094/6254094.pdf>
8. McHugh JA, Sheffield JC. Secondary positive ion emission from a tantalum surface. *J Appl Phys.* 1964;35(3):512.
9. McHugh JA, Sheffield JC. Mass spectrometric determination of beryllium at the sub-nano-gram level. *Anal Chem.* 1967;39(3):377.
10. Lea C. Boron inhibition of oxidation on Fe-10%Cr studied by Auger electron spectroscopy. *Met Sci.* 1979;13:301.
11. Edmons DV, Jones PN. Interfacial embrittlement in liquid-phase sintered tungsten heavy alloys. *Metall Trans.* 1979;10A:289.
12. Stoddart CTH, Lea C, Dench WA, Green P, Pettit HR. Relationship between lead content of Cu-40Zn, machinability, and svvarf surface composition determined by Auger electron spectroscopy. *Met Technol.* 1979;6:176.
13. Waters RE, Charles JA, Lea C. Prior particle boundaries in hot isostatically pressed nickel-based superalloy, studied by Auger electron spectroscopy. *Met Technol.* 1981;8:194.
14. Castle JE. The use of X-ray photoelectron spectroscopy in corrosion science. *Surf Sci.* 1977;68:583.
15. Stout DA, Gavelli G, Lumsden JB, Staehle RW. In Situ AES and ESCA Analysis of Iron Oxides Formed by a Galvanic Cell. *Appl Surf Anal ASTM STP.* 1980;699:42.
16. Mathieu JB, Mathieu HJ, Landolt D. Electropolishing of titanium in perchloric acid-acetic acid solution: I. Auger electron spectroscopy study of anodic films. *J Electrochem Soc.* 1978;125:1039.
17. Holloway PH. Characterization of electronic devices and materials by surface-sensitive analytical techniques. *Surf Sci.* 1980;4:410.
18. Pignataro S. Surface analysis in microelectronics. *Anal Bioanal Chem.* 1995;353(3-4):227.
19. Buckley DH. Friction-induced surface activity of some simple organic chlorides and hydrocarbons with iron. *ASLE Trans.* 1974;17:36.
20. Jones RG. Halocarbon adsorption on Fe(100): The adsorption of CCl<sub>4</sub> studied by AES, LEED, work function change and thermal desorption. *Surf Sci.* 1979;88:367.
21. Buckley DH. Surface effects in adhesion, friction, wear, and lubrication. New York: Elsevier; 1981 and Dorinson A, Ludema KC. *Mechanics and chemistry in lubrication.* New York: Elsevier; 1985.
22. Smentkowski VS, Cheng CC, Yates Jr JT. *Langmuir.* 1990;6(1):147.
23. Clark DT. In: Briggs D, editor. *Handbook of X-ray and ultraviolet photoelectron spectroscopy.* London: Heyden; 1977. p. 2-12.
24. Wheeler DR, Pepper SV. *J Vac Sci Technol.* 1982;20:226.
25. Briggs D, editor. *Surface analysis of polymers by XPS and static SIMS.* Cambridge, UK: Cambridge University Press; 1998.
26. Castner DG, Ratner BD. Surface characterization of butyl methacrylate polymers by XPS and static SIMS. *Surf Interface Anal.* 1990;15(8):479.
27. Ebnesajjad S. Surface and material characterization techniques, page 32. In: Ebnesajjad S, editors. *Handbook of adhesives and surface preparation: technology, applications and manufacturing.* Elsevier; 2011.
28. Siegbahn K. *Electron Spectroscopy – An Outlook.* *J. Electron Spectrosc. Relat. Phenom.* 1974;5:3.
29. Yates Jr JT. *Catalysis Chem Eng News. Catalysis.* 1974;19-22.
30. Fischer TE. *Catalysis and surfaces.* *J Vac Sci Technol.* 1974;11:252.
31. Castner DG, Ratner BD. *Surf Sci. Biomedical surface science: Foundations to frontiers.* 2002;500:28.
32. <http://en.wikipedia.org/wiki/Biomaterial>
33. Kasemo B. *Biological Surface Science.* *Surf Sci.* 2002;500:656.
34. Grunze M, Exarhos G. A surface scientist's perspective on biointerphases, or "Out of the vacuum, into the liquid". *Biointerphases.* 2006;1(1):CL1.

35. Briggs D, Seah MP, editors. Practical surface analysis by Auger and X-ray photoelectron spectroscopy. Wiley; 1983; also see Briggs D, editors. Practical surface analysis by Auger and X-ray photoelectron spectroscopy. 2nd ed. Wiley; 1992.
36. Briggs D, Seah MP. Practical surface analysis: volume 2—ion and neutral spectroscopy. 2nd ed. Chichester: Wiley; 1993.
37. Vickerman JC, Gilmore I, editors. Surface analysis the principal techniques. 2nd ed. Chichester: Wiley; 2009.
38. Riviere JC, editor. Surface analytical techniques, Monographs on the physics and chemistry of materials. Oxford, UK: Oxford Science Publications; 1990.
39. Walls JM, editor. Methods of surface analysis. Cambridge, UK: Cambridge University Press; 1989.
40. Brewis SM, Briggs D, editors. Industrial adhesion problems. New York: Wiley Interscience; 1985.
41. Casper LA, Powell CJ, editors. Industrial applications of surface analysis, ACS symposium series, vol. 199. Washington, DC: American Chemical Society; 1982.
42. Vickerman JC, Briggs D, editors. ToF-SIMS surface analysis by mass spectrometry. Chichester: SurfaceSpectra/IMPublications; 2001.
43. Grams J, editor. New trends and potentialities of ToF-SIMS in surface studies. New York: Nova Science Publishers; 2007.
44. Ratner BD, editor. Surface characterization of biomaterials, Progress in biomedical engineering, vol. 6. Amsterdam: Elsevier; 1988.
45. Davies J, editor. Surface analytical techniques for probing biomaterial processes. Boca Raton: CRC Press; 1996.
46. Surface and interface analysis, Special issue on multivariate analysis. 2009;41(2).
47. Surface and interface analysis, Special issue on multivariate analysis II. 2009;41(8).

# Chapter 2

## Applications of XPS in Biology and Bionterface Analysis

Sally L. McArthur, Gautam Mishra, and Christopher D. Easton

**Abstract** XPS has been used extensively to characterize the surface chemistry of materials used in bioengineering and is increasingly finding a role in biology. Its ability to characterize both the elemental and chemical structures of the surface makes it particularly useful, as it can be used to identify and image the chemical functional groups present on the surface of virtually any material. This review is intended both to profile traditional applications of XPS in bioengineering and biology as well as to discuss advances in XPS instrumentation aimed at enabling the characterization of biological and organic materials.

### 2.1 Introduction

The past 15 years have seen a rapid rise in techniques capable of probing both biology and its interface with materials. Techniques such as surface plasmon resonance (SPR), optical waveguide lightmode spectroscopy (OWLS), and quartz crystal microbalance (QCM) are all used to give insight into the kinetics of protein–protein interactions and the interactions that occur between biomolecules and materials. Atomic force microscopy (AFM) can be used to image single molecules, unfold proteins, monitor surface topography, and measure the forces that hold biological structures together. While all of these techniques give invaluable

---

S.L. McArthur (✉)

Bionterface Engineering Group, IRIS, Faculty of Engineering and Industrial Sciences,  
Swinburne University of Technology, Hawthorn, VIC 3122, Australia  
e-mail: [SMcArthur@swin.edu.au](mailto:SMcArthur@swin.edu.au)

G. Mishra

Kratos Analytical, Wharfside, Trafford Wharf Road, Manchester, M17 1GP, UK

C.D. Easton

CSIRO Molecular and Health Technologies, Bag 10, Clayton South, VIC 3169, Australia

insight into specific biological processes, none of them provides chemically specific information. To fill this gap in our knowledge, surface chemical analysis techniques more commonly associated with pure materials science have been applied to study both biological events and the interactions that occur at the interface between biology and engineering.

X-ray photoelectron spectroscopy (XPS), also called electron spectroscopy for chemical analysis (ESCA), is the most widely used ultrahigh-vacuum (UHV) surface analysis technique. In an XPS experiment, the sample is placed in a UHV chamber and irradiated with X-rays of a specific wavelength. The adsorption of the X-rays by atoms in the sample leads to the ejection of core and valence electrons (photoelectrons). These photoelectrons have energies that are unique to each element and sensitive to their chemical states. Significantly, the intensities of the photoelectrons are proportional to the concentration of the element from which they are ejected. Of course, X-rays are capable of penetrating the sample surface up to many micrometers, but a small fraction of the photoelectrons generated relatively close to the surface (~10 nm) have sufficient energy to escape into the vacuum system without being scattered. These are the photoelectrons that are detected in XPS.

There are a number of key characteristics that make XPS suitable for the analysis of biological materials and biointerface analysis, which we discuss next.

### ***2.1.1 Range of Elements Analyzed***

XPS detects all elements except H and He. In general, for the detection of proteins, the nitrogen content of the protein is utilized to determine the presence and quantify the amount of protein on a surface [1]. The presence of nitrogen in the substrate can complicate quantification; however, monitoring other elements that are present in the protein and not in the substrate (such as Fe, Zn, or S) can overcome this complication. In addition, if the substrate contains an element not found in the protein, signal attenuation may be used to quantify the amount of adsorbed or immobilized protein. Similar approaches can be utilized to detect other biomolecules, including DNA [2], lipids, and mucins [3]. Critically, XPS can be used in the detection of adventitious contaminants such as silicones, hydrocarbons, and other chemical species that may affect the biological interactions or the function of a biomaterial or medical device [4].

In addition to detecting elements, XPS can be used to characterize specific functional groups associated with a specific element. For carbon,  $\text{CH}_x$ ,  $\text{C-O}$ ,  $\text{C=O}$ , and  $\text{O-C=O}$  may all be differentiated due to variations in the functional group's electronegativity, shifting the relative energy of their ejected photoelectron. In some instances, the binding energy differences between some functional groups are too small to be resolved clearly by XPS; however, chemical derivatization can be used to overcome this problem. In this case, the functional group is tagged with a unique element that has a high photoionization cross section and is stable in the analysis conditions, such as F or Br [5]. Common compounds utilized include trifluoroacetic

anhydride for hydroxyl tagging [6], trifluoroethanol for carboxyl groups [7], and pentafluorobenzaldehyde for amine detection [8]. Independent of complications associated with small shifts in binding energy, derivatization also enables the identification and quantification of the functional group present at the interface (e.g., acids or amines) and can be used to assess relative activities in specific applications or reaction conditions [7, 9].

### 2.1.2 Surface Sensitivity

XPS is a surface-sensitive technique because it monitors unscattered photoelectrons, approximately 95% of which arise from within a distance of three times the inelastic mean free path ( $3\lambda$ ) of the element being detected. For carbon, with  $\lambda=3.3$  nm, this means that the XPS sampling depth is  $\sim 10$  nm when the sample surface is positioned normal to the detector. It is the sampling depth for carbon that is commonly quoted as the XPS sampling depth. This means that the sampling depth is larger than the dimensions of many adsorbed proteins and biomolecules. This allows for signals from a substrate and an adsorbed (i.e., protein) overlayer to be detected simultaneously.

Attenuation of a specific element from the substrate, or the introduction of a specific element by the adsorption of a protein, can be utilized to calculate the adsorbed film thickness or determine the intercalation of protein into a porous substrate. Algorithms utilizing the X-ray emission angle ( $\theta$ ), theoretical composition of the protein film or substrate ( $I_\infty$ ), and inelastic mean free path of the emitted photoelectron of a specific element ( $\lambda$ ) enable the calculation of the protein film thickness ( $d$ ) using Eq. 2.1.

**Equation 2.1**, XPS overlayer algorithm.

$$I = I_\infty \exp^{-d/\lambda \cos \theta} \quad (2.1)$$

A number of other algorithms exist, but most assume that the protein film is homogeneous and continuous. If the XPS data do not fit the form of Eq. 2.1, this indicates that the protein film is incomplete or patchy. Paynter and Ratner have shown that it is possible to incorporate a fractional coverage term into Eq. 2.1, but the quantity of protein adsorbed to the surface must be established from another technique, such as radiolabeling [10].

### 2.1.3 Angle-Dependent XPS (ADXPS) and Depth Profiling

As stated earlier, the sampling depth of XPS is dependent on the inelastic mean free path of the emitted photoelectron of the specific element ( $\lambda$ ) and the X-ray emission angle ( $\theta$ ) via Eq. 2.2.

**Equation 2.2**, XPS sampling depth.

$$d = 3\lambda \cos\theta \quad (2.2)$$

Thus, by varying the angle between the X-ray source and the sample by simply tilting the sample stage, one can vary the XPS analysis depth from ~2 to 10 nm, depending on the element being analyzed. ADXPS enables the detection of compositional variations as a function of depth from the sample surface in a nondestructive fashion and allows the continuity and depth distribution of the coating to be probed.

Traditionally, ion beam depth profiling of materials in XPS has been limited to inorganic materials due to ion beam-induced sample damage. In recent years, there have been significant developments in the ion sources for depth profiling of organic materials. Driven by the ToF-SIMS community, cluster ion sources (including  $C_{60}^+$  [11] and coronene [12]) have become available for integration into XPS instruments. While the use of these sources is still in its infancy for biology, they have been successfully implemented to explore drug distributions in pharmaceuticals [12] and depth profiling of organic materials [13].

### 2.1.4 Freeze Hydration XPS

As many of the materials used in bioengineering and all biomolecules operate in a hydrated environment, questions about the relevance of XPS data to bioengineering applications and biological interactions are often raised [14, 15]. Freeze hydration XPS, developed by Lewis and Ratner in the early 1990s [16], involves the rapid freezing of a wet sample within the XPS entry chamber and can be used to both circumvent and investigate issues associated with sample dehydration. Once a sample is frozen, subsequent exposure to UHV at a temperature of approximately  $-100\text{ }^\circ\text{C}$  etches the ice from the surface via sublimation. The sample temperature is then lowered below  $-120\text{ }^\circ\text{C}$  for XPS analysis. Both the study by Lewis [16] and a number of subsequent investigations [17, 18] have shown that “freeze hydration” XPS enables the hydrated surface chemistry of polymers to be probed and the processes of polymer reorganization at interfaces investigated.

There were a number of XPS protein adsorption studies using cryogenic sample preparation that predate the work by Lewis and Ratner and investigated the role of substrate chemistry in the distribution and orientation of protein films [19, 20]. A review of the more recent literature illustrates that there has been very little work on biological or bioengineering applications published since 1993. The work that has been published has focused on the analysis of bacterial cells and cell membranes [21]. Some of this may be due to the complex nature of the sample preparation and the extended amount of instrument time required in preparing for and performing the experiments. In addition, as noted by Lewis, surface contamination is a major issue as cryogenic temperatures increase the rate of condensation of contaminants onto the sample surface in both air and vacuum [16]. As cryogenic sample preparation becomes more commonplace for the ToF-SIMS analysis of biological samples, there may be renewed interest in cryogenic XPS.

### 2.1.5 XPS Imaging and Mapping

The increasing interest in spatial control of cells and biomolecules for applications such as tissue engineering and array technologies has seen the requirement for small spot analysis and chemical state imaging move to the forefront of XPS research. Recent advances in instrumentation have seen the spatial resolution of XPS imaging improve significantly. Today, imaging can be achieved with spatial resolutions below 10  $\mu\text{m}$  as the standard; in some cases, a near-micron resolution can be achieved [22]. A number of groups have used standard spot size analysis (300  $\times$  700  $\mu\text{m}$ ) to characterize both chemical and thickness gradients over relatively large areas ( $\sim$ 10 mm) [7, 23], producing two- and three-dimensional maps of the material. Unlike ToF-SIMS, quantitative XPS imaging is also possible. While the process is not trivial, there are an increasing number of papers being published that detail methods for both producing and processing quantifiable images [24–26].

This chapter aims to explore the increasing number of areas where XPS is applied to address issues in biology and its engineering cousin, bioengineering. After an introduction to the instrumentation involved, we will focus on a number of the specific applications where XPS is in use today to investigate biological processes and the interface between materials and biology.

## 2.2 Instrumentation

XPS instrumentation has advanced significantly in the last three to four decades, largely driven by the demand of quantitative surface analysis in the fields of catalysis [27, 28], microelectronics [29–31], corrosion science [32, 33], and biomaterials [34–36]. In most common cases, the samples studied by this surface analysis method are durable and robust. When interest developed in applying XPS to organic and biological systems, special instrument designs and experimental considerations were needed. In particular, concerns about the effect of the ultrahigh-vacuum environment on traditionally hydrated biological surfaces needed to be addressed. Alongside this, issues including X-ray and electron damage, surface charge accumulation, narrow X-ray line widths required for higher energy resolution and finer chemical discrimination, high sample throughput, and better signal-to-noise ratios needed to be addressed. Advances in instrument manufacturing and the availability of cutting-edge electronics led to the development of instruments that are precisely tuned to address many of these specific issues. Nowadays, monochromatic X-ray probes are standard in most commercial laboratory instruments, with a probe diameter down to less than 10  $\mu\text{m}$ . The energy resolution and signal-to-noise ratio of the analyzer system have improved with the introduction of position-sensitive multi-channel detectors. Imaging analyzers and sophisticated lens systems, such as a magnetic immersion lens, have contributed significantly to the improvement in small-area imaging XPS performance and, most importantly, surface charge

neutralization. A 1–3- $\mu\text{m}$  chemical state image resolution can now be routinely achieved on a laboratory XPS instrument, thus enabling researchers to examine small features often studied in the fields of biology and medicine.

### **2.2.1 Overview of XPS Instrumentation**

Most commercial XPS systems are divided into two main chambers, one in which the XPS analysis is carried out (sample analysis chamber, or SAC). This is directly linked to a second chamber (sample entry chamber, or SEC), a sample introduction chamber consisting of anything from a simple introduction vacuum lock or a more complicated vacuum lock with other specialized preparation or treatment equipment attached to it. Stepper motor-controlled automatic or manual mechanisms are available to transfer the sample from one chamber to another.

As shown in Fig. 2.1, the sample introduction chamber is usually pumped by turbomolecular pumps capable of attaining vacuum levels of  $\sim 5 \times 10^{-8}$  Pa (or  $\sim 5 \times 10^{-10}$  mbar). Roughing and backing of the turbomolecular pumps are provided by well-trapped rotary pumps, although novel “dry” backing and roughing pumps such as diaphragm and scroll pumps are now becoming more common, particularly where hydrocarbon contamination must be avoided. The sample is introduced directly into the load lock by venting this chamber to dry nitrogen. For more complicated load lock designs, often the sample is introduced, as shown in Fig. 2.1, in a relatively smaller chamber (often referred to as fast-entry load lock), where specific treatments, such as sample cooling, are performed. Temperature measurements are made by a thermocouple in direct contact with the sample stub in the introduction chamber. Once a good level of vacuum is achieved, the sample is then transferred into the main analysis chamber or other attached preparation or treatment chambers. The use of fast-entry lock arrangements allows the main load lock to remain under ultrahigh vacuum at all times. The fast-entry lock arrangements can also be fitted with glove boxes for specialized sample treatment. Stainless steel is generally used for the vacuum lock and preparation chambers, although high-grade aluminum alloys are being used more, especially for locks. The sample-handling arrangement in the analysis chamber is also equipped with heating and cooling arrangements. The temperature is monitored by a thermocouple in direct contact with the sample stubs, and a feedback loop is used to program rates of heating and cooling. The temperature range for heating and cooling in the analysis chamber is typically in the range of  $+600$  to  $-150$  °C.

The samples are often transferred between the introduction and analysis chamber by using an automated or manual sample insertion probe. Various vacuum interlocks operate between the connecting chambers in a fail-safe mode to prevent loss of UHV conditions.

The SAC is generally constructed of mu-metal for effective magnetic screening and is designed with numerous vacuum ports that have a “line of sight” to the



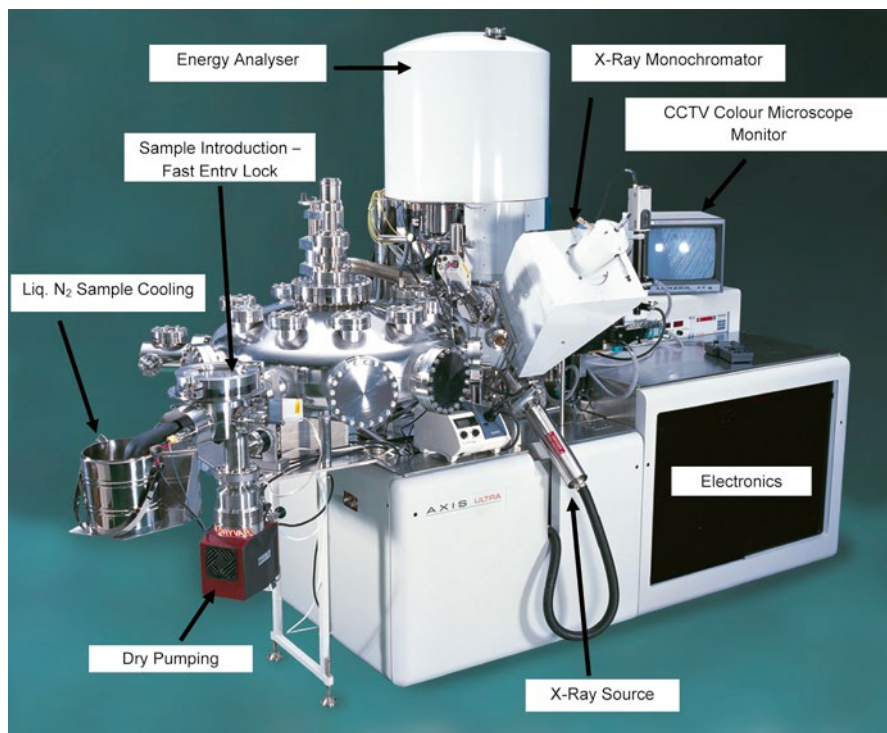


**Fig. 2.1** An example of a commercial XPS instrument—the Kratos Axis Ultra DLD. This version of the instrument has been fitted with a radial distribution chamber (RDC) permitting the transfer of a sample to and from other equipment under vacuum. The computerized user interface is not shown in this figure (Reproduced with permission from Kratos Analytical Ltd.)

sample in order to accept a comprehensive set of accessories, including ion guns. The analysis chamber is generally pumped by ion and titanium sublimation pumps, and the pressure is maintained below  $\sim 1 \times 10^{-8}$  Pa during analysis.

### 2.2.2 Charge Neutralization

As discussed earlier, the basic XPS experiment involves bombardment of a material in vacuum with soft X-rays that are capable of penetrating the sample surface up to many micrometers. Absorption of X-ray energy by an atom in a solid leads to ejection of an electron, in a process termed “photoionization,” from either from the core level or valance bands. A small fraction of these photoelectrons generated relatively close to the surface (depth  $\sim 10$  nm) have sufficient energy to escape into the vacuum system (i.e., photoemission); the process is termed the “photoelectric effect.” The photoelectric emission is the energy analyzed to produce a signature spectrum of electron intensity as a function of energy.

For a conducting sample, conservation of energy leads to the following equation:

$$E_k = h\nu - E_B^F - \phi_{sp}$$

where  $E_k$  is the measured kinetic energy of the emitted photoelectron,  $h\nu$  is the energy of the exciting X-ray photon,  $E_B^F$  is the electron binding energy relative to the Fermi level ( $E^F$ ) of the sample, and  $\phi_{sp}$  is the work function of the spectrometer. Since the binding energy is generally of interest to the user, the spectrometer is set up to record the spectrum on this energy scale directly.

For insulating samples that do not have a well-defined Fermi level, and to deal with uncertainty in surface potential developed by emission of the photoelectrons, we modify the above equation as

$$E_k = h\nu - E_B - \phi$$

where  $\phi$  is now the term that captures these surface potential uncertainties and the actual reference point for  $E_B$ . If the binding energies for different insulating samples are to be meaningfully compared, a common reference point needs to be established. For polymers, biological samples, and organic samples, the hydrocarbon component (C–C/C–H) of the C 1s peak is typically set to 285.0 eV and used as an internal reference.

Non-monochromatic XPS instruments do not generally require a dedicated charge compensation system. The X-ray flux in these systems is relatively uniform, and there are usually enough secondary electrons in the vicinity of the sample induced by the X-ray beam's striking the X-ray window and the spectrometer surface to produce adequate charge compensation.

For monochromatic XPS systems, two major advances in charge compensation systems are commonly available in commercial instruments. The first operates with spectrometers using a magnetic immersion lens often referred to as a “snorkel lens” [37]. The magnetic field intersecting the sample traps photoemitted electrons, causing them to spiral about the field lines. The charge balance plate causes lower-energy electrons to be reflected back to the sample, greatly reducing the number of additional electrons needed to reach equilibrium. As all of the reflected electrons come from the sample, the surface never becomes overcharged. The design of the neutralizer enables excess electrons to become trapped in the magnetic field until required for the neutralization process. This creates a sufficiently high flux of electrons and ensures that the whole analyzed area has a uniform surface charge, providing optimal XPS performance. A second approach of charge compensation relies on the use of a low-energy ion beam for neutralization. A stream of low-energy ions discharges the peripheral regions of the sample, and so electrons from the flood gun are not reflected before they can reach the illuminated area. In absence of the ion flux, the sample surface approaches the potential of the most energetic electron striking it, thus producing an unstable, repulsive potential. This process ensures that the potential of this peripheral region, which can be charged several volts negative, is kept close to the potential of the illuminated region so more flooding electrons can

reach the illuminated region. When the ion beam energy has been kept below 50 eV, little or no sample damage or implantation has been observed. It has also been shown that by using a low-work-function metal oxide cathode in the flood gun, a narrow energy distribution of flooding electrons can be used, making the potential across the illuminated region more uniform [38].

Biological samples can often have surface topography, and this can be a major issue for charge compensation. In the case where collimated low-energy ion beams are used, one would only expect partial neutralization of the sample surface, because of surface roughness and shadowing effects. This can be overcome using a magnetic immersion lens system, as the spiral trajectory of the neutralizing electrons allows them to evenly reach the sample's surface irrespective of topography.

### 2.2.3 Depth Profiling

As discussed earlier, the sampling depth achieved by XPS is approximately 10 nm. However, it is common to have samples composed of a much larger (>10-nm) compositional gradient. Furthermore, the chemical information generated from the top ~10 nm is a convolution of information from all the layers contained within this region. The chemical distribution as a function of depth from the outermost ~10 nm of the surface can be converted into depth profiles by using data acquired in an angular-dependent XPS (ADXPS) experiment. A number of different algorithms exist, but many, like that shown in Eq. 2.2, assume that the overlayer is homogeneous and continuous. More realistic models that do not rely on oversimplifying assumptions exist (e.g., Tougaard [39, 40]) and allow noncontinuous coatings and nanostructured surfaces to be characterized. Compositional depth profiles can also be established using these methods. By combining ARXPS with  $^{125}\text{I}$  radiolabeling, the homogeneity and distribution of protein on the surface can also be assessed. If the surface is porous, the distribution of protein *within* the outer 10 nm of the material may also be monitored. Paynter produced an algorithm for biological systems in the early 1980s [10], and software is now readily available for producing depth profiles from ARXPS data (e.g., The National Physics Laboratory (NPL) ARctick freeware available from <http://www.npl.co.uk/nanoanalysis/arctick.html>).

To investigate chemical distributions at greater depths (i.e., more than 20 nm from the top surface), destructive depth profile experiments (i.e., ion etching) are performed. Conventionally in this approach, monoatomic ions such as  $\text{Ar}^+$  or  $\text{Cs}^+$  are used to etch a few nm (2–10 nm) of the sample surface, and the bottom of the etching crater is analyzed at regular intervals. Although this depth profile approach was found to be very useful for inorganic systems, application in the field of organic, polymer, and biological materials is limited, as the structural information of the organic systems is very susceptible to damage from the monoatomic ion beams. The accuracy of analysis is further compromised by intermixing and knock-in of atoms at the bottom of the crater. Recently, it has been shown that minimally destructive XPS depth profiles of organic materials can be obtained by sputtering with large cluster ions beams (e.g.,  $\text{C}_{60}$  [11], coronene [12]).

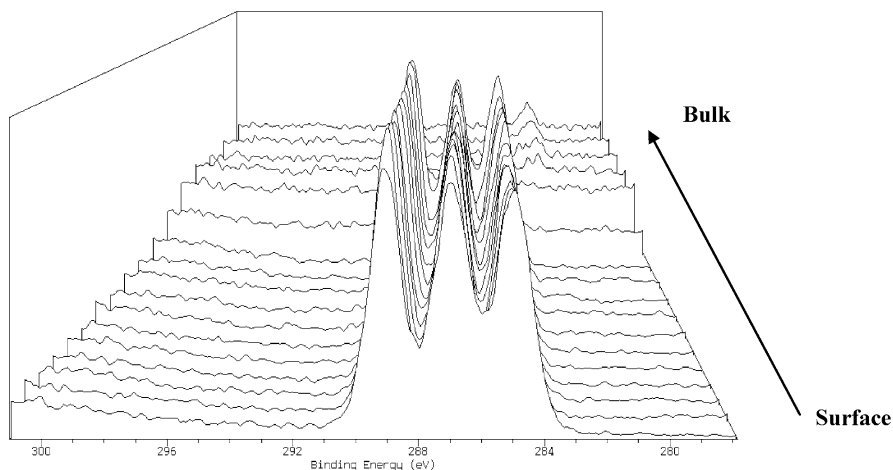


**Fig. 2.2** The C 1s spectra of spun-cast PLGA during a depth profile experiment using the coronene gun developed by Kratos

Coronene – ( $C_{24}H_{12}$ ) is a polycyclic aromatic hydrocarbon (PAH) consisting of six carbon rings. Within the ion gun, coronene powder is loaded into the oven assembly and heated to sublime coronene molecules into the gas phase. Coronene vapor passes into the source region and is ionized by electron-impact ionization. Coronene ions are formed into a beam by the condenser lens and projected into a high-resolution Wien filter to mass-/energy-select a specific ion species. The ion gun is designed to operate with ion acceleration voltages up to 20 keV, but the voltage may be set to choose either singly or doubly charged ions. If doubly charged ions are selected, then the effective ion energy available can be increased to 40 keV.

Results show that organic systems can be successfully depth-profiled using the coronene cluster ion beam. Success is defined in terms of two requirements: (1) a depth profile with a constant etch rate through the sputtered layer; and (2) a minimum amount of chemical damage to the sample during the sputter depth profile. Model polymers [e.g., PLGA, poly(lactic-co-glycolic acid)] spun-cast onto silicon substrate (thickness – 85 nm) were used to better understand the performance of this cluster ion gun on organic systems. C 1s spectra recorded at regular intervals during coronene depth profile are shown in Fig. 2.2. Prior to exposure to the coronene source, three distinct chemical environments were detected in the C 1s spectrum, a hydrocarbon peak at 285.0 eV, a carbon singly bonded to oxygen peak at 286.8 eV and a C peak for the ester group at 289.2 eV. During the coronene profile (16-keV beam energy), the chemical structure of the polymer was found to be conserved throughout the film to the sample-substrate interface.

In another study, the coronene cluster ion source was used to study the distribution of a model drug codeine ( $C_{18}H_{21}NO_3$ ) in poly(L-lactic) acid matrix as a model for a drug-loaded polymer coating [12]. The controlled release of such active

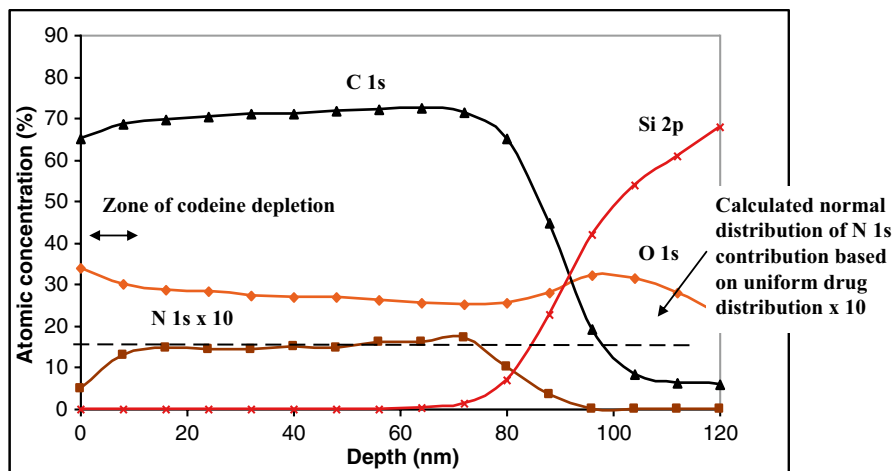


**Fig. 2.3** XPS depth profile from coronene-etched drug-loaded PLA film showing C 1s, O 1s, N 1s  $\times 10$  and Si 2p signal and calculated nitrogen concentration assuming a uniform drug distribution through the film thickness. The N 1s signal was used as a unique indicator for the presence of drug in the sample (Reprinted with permission from Ref. [12]. Copyright © Elsevier Ltd. 2009)

pharmaceutical ingredients from polymers over prolonged periods of time is vital for their application in drug-eluting stents and other drug-loaded delivery devices. Figure 2.3 shows the coronene ion depth-profile data from the drug-polymer binary system where the N 1s signal was used to monitor the distribution of the drug as a function of depth. XPS analysis of the bottom of the sputter crater with sputter time indicated that codeine was depleted from the surface and segregated to the bulk of the polymer films by comparison with a uniform distribution calculated from the bulk loading. This serves to illustrate that surface depletion of drug occurs, which poses important implications for drug-loaded polymer delivery.

## 2.2.4 Small Spot Spectroscopy

It is often necessary to analyze a small feature of interest on the surface of a specimen. For the analysis to be effective and accurate, the signal from the surrounding area should be eliminated. Two main approaches are used in current research-grade instruments to achieve this.

The first approach relies on flooding the sample with X-rays but limiting the area from which the photoelectrons are collected, generally by using the transfer lens. In most spectrometers, the electron optic lenses are fitted to the analyzer and operated in a way to produce a photoelectron image at some point in the electron optical column. By placing a small aperture at this point, only the electrons emitted from a defined area are allowed to pass through the aperture and reach the analyzer.

Usually in these instruments, a choice of aperture is available for selection, thus enabling analysis from a wide range of areas. Another variant of this instrument uses an iris to provide a continuous range of analysis areas. Quite often fixed apertures or an additional iris is positioned in the lens column to correct for spherical aberrations in the electron optical system by limiting the acceptance angle of the lens. Using this technique, commercial instruments can provide small-area analysis down to about 10  $\mu\text{m}$ .

In the second approach, a monochromatic beam of the X-ray is focused into a smaller area to analyze the feature of interest on the sample surface. Here, a quartz crystal is bent so that it can focus a beam of X-rays and provide monochromatic X-rays by diffraction. In this respect, it behaves rather like a concave mirror. The focusing is usually achieved using a magnification of unity, which means that the size of the X-ray spot on the specimen is approximately equal to the size of the electron spot on the X-ray anode. Analysis areas down to about 10  $\mu\text{m}$  can be achieved in commercially available instruments using this method.

### ***2.2.5 XPS Imaging and Mapping***

Another area where XPS instrumentation has improved significantly is photoelectron imaging. Manufacturers use two distinct approaches to obtain XPS maps: serial acquisition, in which each pixel of the image is collected in turn (mapping mode); and parallel acquisition, where data from the entire analysis area is collected (direct or real-time imaging).

Serial acquisition of images is based on a 2D rectangular array of small-area XPS analysis. In this approach, the micro-focused beam of X-rays is scanned over the sample and an image is built one pixel at a time in a point-by-point acquisition. The ultimate spatial resolution of the image is thus determined by the size of the smallest analysis area. Typically, the spatial resolution obtained by this method of image acquisition is limited to the focus of the X-ray beam, such as  $\sim 10$   $\mu\text{m}$  based on 80–20 % (or 84–16 %) edge resolution measurements. Serial acquisition is generally slower than the parallel acquisition but has the advantage that one can collect a range of energies.

In parallel acquisition of photoelectron images, the entire field of view is imaged simultaneously without scanning voltages being applied to any component of the spectrometer (imaging mode). Obtaining images in this way requires additional lenses in the spectrometer and the use of a 2D detector in the image plane. The image resolution has been significantly improved by limiting the angular acceptance of the lens, thus reducing spherical aberrations. The use of a magnetic immersion lens in the specimen region also reduces aberrations and therefore allows higher sensitivity at a given resolution. This method of imaging is relatively fast; commercial instruments can produce images with an image resolution as low as 3  $\mu\text{m}$ .

Parallel imaging clearly provides better image resolution and is faster than the serial methods, but it collects an image at a single energy only. Obtaining more

accurate image measurements using the parallel image acquisition mode thus requires a second measurement at some energy remote from the peak, where the signal intensity is approximately equal to the estimated background signal under the peak maximum. By mathematically subtracting the background signal from the signal at the peak's maximum, we can routinely make more accurate measurements.

## 2.3 Characterization of Biomolecules

### 2.3.1 *Proteins and Peptides*

A significant amount of work exists on the use of XPS to study proteins. Due to similarities in the chemical composition of most proteins, XPS cannot be used to differentiate individual components within a complex mixture of proteins. Coupled with the fact that analyzing these biomolecules requires them to be immobilized onto a surface, which can contribute to the analyzed spectra, XPS is not ideal for a fundamental chemical analysis of proteins and peptides. The strength of XPS is realized when applied to examine the immobilization of these biomolecules onto surfaces. Fundamental knowledge of the adsorption process of proteins to surfaces at the molecular level is vital for the development of interfaces that exhibit specific biophysical properties [41]. XPS provides the opportunity to examine adsorbed proteins and elucidate information regarding the orientation, surface coverage, and layer thickness [1, 10, 42].

Proteins are composed of mostly carbon, oxygen, and nitrogen and can contain low levels of other elements, including sulfur, phosphorus, and metals. Detection using XPS is typically achieved by monitoring changes in the nitrogen signal and attenuating the substrate signal. The highest sensitivity to protein adsorption can be achieved on nitrogen-free substrates or in situations where the substrate is rich in an element not found in the protein, such as fluorine. Biochemical assays, such as radiolabeling using  $^{125}\text{I}$  or detection using a fluorescent or enzyme-labeled antibody, are often used in conjunction with XPS to provide a complete picture of the absorption characteristics of the system under examination [1, 43, 44]. Figure 2.4 demonstrates the correlation of  $^{125}\text{I}$  data with XPS results, for the adsorption of fibrinogen onto mica [1]. These results compare the XPS detection limit for proteins as calculated by using the At% N signal (open circles) or attenuation of a unique substrate signal (Al) shown here as the N(1s)/Al(2s) ratio ( $x$ ). In both cases, the detection limit for the protein is shown to be  $\sim 10 \text{ ng/cm}^{-2}$ . Much of the early work and related theory about the detection of proteins has been summarized by Paynter and Ratner [45] and updated in papers by Castner and Ratner [42] and Wagner et al. [1].

Even when the substrate contains nitrogen, it is still possible to detect protein although the limits of detection are reduced. Figure 2.5 shows the high-resolution C 1s spectrum of a nitrogen-containing plasma-polymerized heptylamine thin film (HApp) before (solid line) and after the adsorption of IgG (dashed line). While the

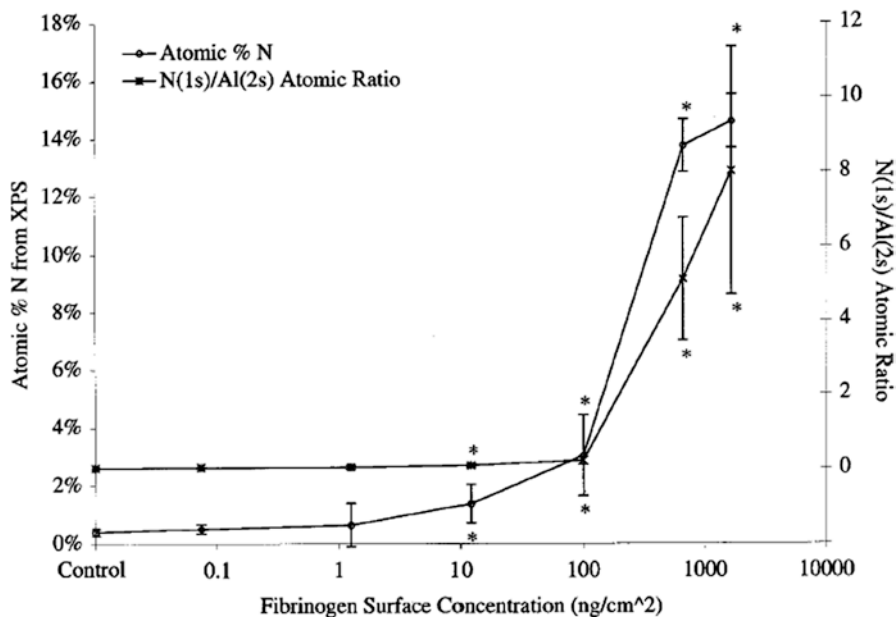


**Fig. 2.4** Surface nitrogen detected by XPS analysis of fibrinogen adsorbed onto mica. N/Al atomic ratios are also given for mica. Asterisks (\*) indicate samples that are significantly different from the control samples ( $p \leq 0.01$ ) (Reprinted with permission from Ref. [1]. Copyright © Koninklijke Brill NV 2002)

HApp contains nitrogen, it is in the form of amines and imines, whereas the protein contains amides as well as amines. XPS is able to differentiate between the amine and amide groups present on the surface, as the photoelectrons produced by the carbons found in these species have distinct energy shifts. The C–N related species are shifted to 286.5 eV, while the electronegativity of the amide (O–C–N) groups shifts the binding energy of the carbon associated with these groups to a higher binding energy of  $\sim 288$  eV. Changes in the amine and amide content of the surface have been utilized to detect proteins on nitrogen-containing surfaces with a sensitivity of  $\sim 100$  ng/cm<sup>2</sup> [1].

Peptides provide a simplified model system for examining protein adsorption processes to various surfaces. In addition, adsorbed peptides provide an opportunity to create a biologically specific interface for tissue engineering [46, 47] and bio-sensing [48]. As a result, there has been a significant increase in the research on peptide adsorption in recent years to surfaces such as gold, self-assembled monolayers, TiO<sub>2</sub>, sol-gel silica, and a range of polymers [46–53]. The analysis of peptides on surfaces creates its own challenges due to the size of the molecules and the often low density of their surface coverage. These factors combine to create what are often small changes in the chemical composition of a surface [46]. To some extent, ARXPS can be used to reduce the analysis depth and increase the relative



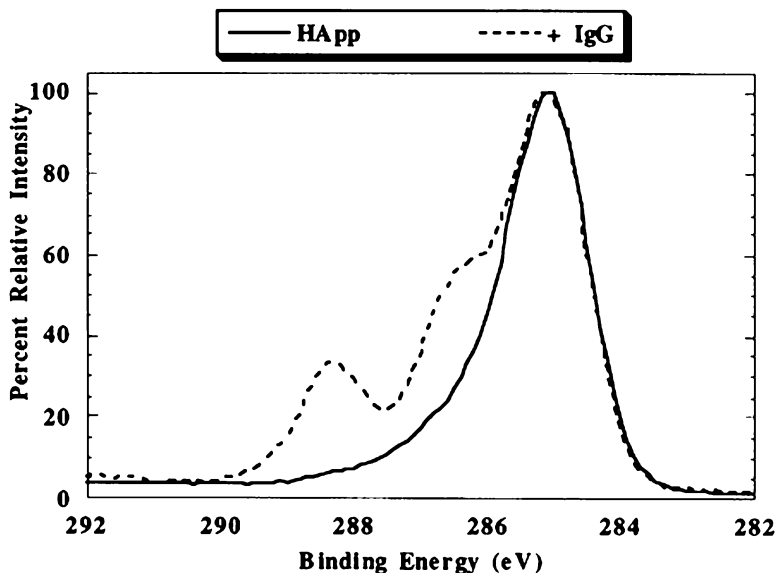


**Fig. 2.5** High-resolution XPS C 1s spectra recorded on a plasma-polymerized heptylamine (HA<sub>pp</sub>)-coated fluorinated ethylene propylene sample before (*solid line*) and after (*dashed line*) immersion in an IgG solution (Reprinted with permission from Ref. [43]. Copyright © Elsevier Ltd. 2000)

proportion of the surface chemistry that is due to the peptide, enabling the peptide to be differentiated from the substrate, which aids in limiting their impact on the surface chemistry [54]. An alternative approach is to use a process similar to derivatization to label the peptide with a specific chemical marker either prior to immobilization or once it is on the surface [48].

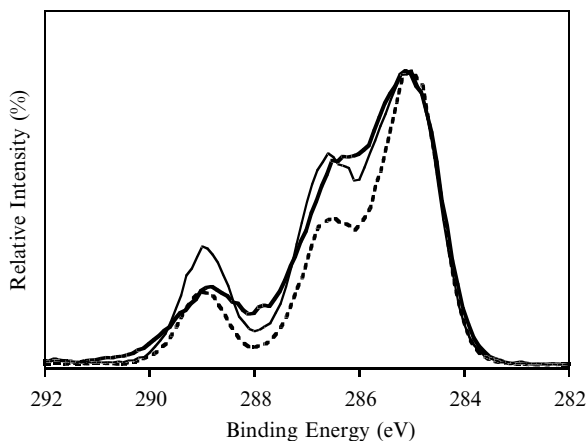
While the examples to date have been from model or laboratory systems, the same approaches have been used to implement XPS in the characterization of biomaterials and devices after *in vivo* experimentation [3, 55–58]. Table 2.1 presents the XPS atomic concentration data for Etafilcon A (Acuvue®) contact lenses before and after 10 min and 1 h of patient wear. These results show that a significant increase in nitrogen occurs after 10 min of wear, while after 1 h, a further increase in nitrogen in addition to oxygen was detected. An analysis of the high-resolution C 1s spectra from the lenses shown in Fig. 2.6 clearly demonstrates at 10 min the introduction of peak shifts associated with C–O/C–N species (~286.5 eV) and O–C–N species at 288 eV. After 1 h, the contributions have altered slightly again, with an increase in the O–C=O contributions at 289 eV, in line with the increased level of oxygen detected in the survey spectrum. From this data, researchers deduced that the adsorption processes were initially dominated by proteins (e.g., after 10 min of wear), but as the wear time increased to an hour, oxygen-rich species (e.g., mucins or polysaccharides) adsorbed alongside the proteins [3].

**Table 2.1** XPS atomic concentrations of Etafilcon A (Acuvue®) contact lenses before and after wear for 10 min and 1 h. Numbers in parentheses are standard deviations (Reprinted with permission from Ref. [3]. Copyright © Elsevier Ltd. 2001)

	Atomic concentration (%)				Atomic ratios	
	C	O	N	Si	N:C	O:C
Unworn ( $n=4$ )	72.5 (1.2)	27.0 (1.6)	0.4 (0.2)	0.1 (0.1)	0.01 (0.00)	0.37 (0.03)
10 min ( $n=10$ )	72.6 (2.3)	24.5 (2.7) <sup>a</sup>	2.3 (0.8) <sup>a</sup>	0.1 (0.0)	0.03 (0.01)	0.34 (0.04)
1 h ( $n=8$ )	67.9 (1.0) <sup>a</sup>	28.2 (1.7) <sup>a</sup>	3.7 (1.6) <sup>a</sup>	0.2 (0.3)	0.05 (0.02)	0.42 (0.03)

<sup>a</sup>Indicates an atomic concentration statistically different from the unworn lens (Student  $t$ -test,  $p < 0.01$ )

**Fig. 2.6** High-resolution XPS C 1 s spectra from an Etafilcon A (Acuvue®) contact lens before (*dotted line*) and after 10 min (*solid line*) and 1 h of wear (*thin line*) ( $0^\circ$  take-off angle) (Reprinted with permission from Ref. [3]. Copyright © Elsevier Ltd. 2001)



### 2.3.2 Other Biomolecules: Lipids, Mucins, Enzymes, and DNA

Proteins and peptides are not the only biomolecules that play a significant role in various biological processes. As a result, a number of studies have utilized XPS to detect and analyze the behavior of a range of biomolecules, including lipids [59–63], mucins and sugars [64, 65], enzymes [66–68], and DNA [2, 69–73]. Examining the chemical functionality and adsorption of these biomolecules to different surfaces is critical for advancing our fundamental understanding of their behaviors, developing bioarrays [2, 69–71, 73] and biosensors [66, 74], and controlling medical biofouling [3, 56, 75].

Table 2.2 demonstrates the elemental compositions of typical biomolecules [3]. From this data, it is apparent that adsorption of these biomolecules to a surface would induce a specific and measurable change in the surface composition of the substrate. As mentioned previously, a change in the nitrogen-to-carbon ratio (N:C) is often used as a detection marker for proteins, while a change in the oxygen-to-carbon ratio (O:C) is expected when lipids (ratio decrease) and mucins and sugars

**Table 2.2** Elemental compositions of common biomolecules (Reprinted with permission from Ref. [3]. Copyright © Elsevier Ltd. 2001)

	Atomic % composition			Atomic ratios	
	C 1s	O 1s	N 1s	N:C	O:C
Protein <sup>a</sup>	63.0	20.1	16.0	0.25	0.32
Protein <sup>b</sup>	65.3	18.1	14.2	0.22	0.28
Lipid <sup>c</sup>	95.0	5.0	0.0	0.00	0.05
Mucin <sup>d</sup>	58.0	31.0	9.8	0.17	0.53

<sup>a</sup>Theoretical composition of human albumin

<sup>b</sup>Data derived from XPS spectra of thick human albumin film

<sup>c</sup>Theoretical composition of cholesterol (C<sub>27</sub>H<sub>48</sub>O)

<sup>d</sup>Data derived from XPS spectra of the glycosylated region of porcine submaxillary mucin (PSM, MUC1)

(ratio increase) adsorb to surfaces. The contrast between the adsorbed biomolecules and the substrate can be further enhanced using angle-resolved XPS (ARXPS), where the depth of analysis is varied to analyze a larger portion of the adsorbed or immobilized material.

The introduction of DNA microarray technology provides researchers a tool to study multiple cellular processes in parallel and thus is significant to fundamental biological research and biomedical applications [76–78]. In papers that have appeared between 2007 and 2009, Lee [2], Liu [69], and others [73, 78] have examined how XPS could be used to interrogate DNA arrays and provide a quantitative interpretation of DNA hybridization efficiencies and base-pair mismatch detection. Overlays of XPS images of phosphorus, nitrogen, and sodium onto the silicon image before and after hybridization from Lee's study clearly demonstrated an increase in signal intensity upon hybridization for microspots containing complementary probe sequences (Fig. 2.7) [2]. Liu's work was able to detect a single base mismatch as well as give valuable insight into hybridization efficiencies of the arrays [69]. These studies, together with others from groups around the world, have clearly demonstrated the applications of XPS in both the development and analysis of DNA arrays without the need for radioactive or fluorescent labels [73, 78, 79]. Significantly, many of these studies have also demonstrated the ability of XPS to detect variations and surface-induced problems within the hybridization processes of a wide range of commercial and noncommercial arrays [73, 79].

## 2.4 Cell, Bacteria, and Tissue Analysis

There are many types of cells, each containing a unique combination of components within the cell membrane, including phospholipids, proteins, glycosaminoglycans (GAGs), and cholesterol. XPS provides the opportunity to probe the cell surface and elucidate information regarding their composition and responses to environmental stimulation. As detailed earlier, all of the individual components of a cell have been

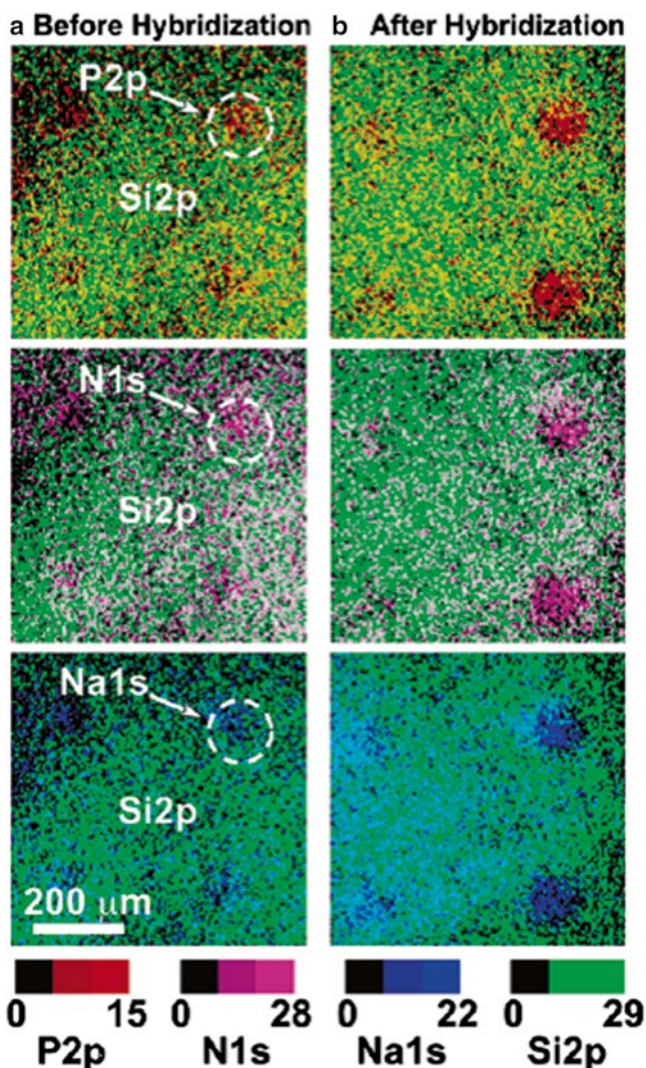


**Fig. 2.7** XPS overlay of phosphorus (P 2p), nitrogen (N 1s), and sodium (Na 1s) with the substrate silicon's (Si 2p) signal intensity images ( $800 \times 800 \mu\text{m}$ ) from printed DNA probes on CodeLink microarray slides (a) before and (b) after target hybridization (Reprinted with permission from Ref. [2]. Copyright © ACS 2007)

investigated on surfaces using XPS. When combined within a cell membrane, it becomes difficult to distinguish the individual components within the resultant XPS spectrum and quantitatively determine the amount of each component. As a result, the total element compositions obtained from survey spectra are typically employed to provide a semiquantitative comparison of cells [80]. In addition, the peak fitting

of high-resolution components (e.g., C 1s, N 1s, and O 1s) is typically undertaken. Postprocessing techniques can then be used to gain further insight. For example, the surface composition of bacteria can be modeled by three classes of components, specifically polysaccharides, peptides, and hydrocarbon-like compounds (lipidic compounds) [21].

The major focus of XPS analysis of cells has been in the investigation of microbial cells, including yeast, fungi, diatoms, and bacteria [81–84]. A number of studies have used XPS to explore changes in the chemical composition of the cell wall with changes in media (for suspended cells) or changes in substrate and media (for adhesive cells) [85, 86]. These types of studies are highly relevant for the minerals [87] and engineering industries, where specific microbial events are central to the success or failure of a process. In some instances, it enables industries to understand and prevent events such as biocorrosion [88–90], while in others it enables them to understand how surface characteristics of the bacteria or their extracellular polymeric substance (EPS) change in response to the environment [91, 92]. Properties that have been investigated include bacteria attachment and adhesion, with the aim of addressing biofouling [75, 85, 88], bioremediation [87, 93], and environmental applications [84, 94, 95].

An example of employing XPS to investigate the surface chemical structure of microbial cells is found in the work of Ahimou et al. [96]. The authors focused on the fitting of high-resolution peaks to elucidate the chemical functions of nine strains of *Bacillus subtilis*. Figure 2.8 presents high-resolution spectra of oxygen, nitrogen, and carbon for three *B. subtilis* strains. It is apparent that the spectral components assigned to the carbon peak vary considerably among strains, while the degree of variation is less significant for the nitrogen and oxygen peaks. Based on the peak position of the spectra components, the authors were able to determine the presence of individual components within the cell membrane. For example, the peak centered at 285 eV [carbon bound to carbon and hydrogen; C–(C,H)] was considered to originate from lipids or from side chains of amino acids, while the peak at ~289 eV (carboxylate and carboxyl groups) was the result of proteins and uronic acids. Further data interpretation of molar concentrations provided additional evidence; however, the authors did acknowledge that such modeling can lose significance as the number of unknown variables increases.

Another example of utilizing XPS to analyze *B. subtilis* was reported by Leone et al. [80]. In this study, a single strain (ATCC code: 6633) was analyzed using the standard freeze-dried technique and compared to frozen wet-paste samples suspended at different pH values. Applying this alternative sample-preparation technique allowed the authors to investigate protonation/deprotonation reactions of amine groups at the cell–water interface and elucidate information regarding the activity of the cell at specific pH values. It is interesting to note that different sample-preparation techniques were explored in this study, as the choice of sample-preparation and sample-handling techniques for XPS analysis of cells has long been a subject of some debate [14].

As XPS is a UHV technique, there has always been considerable concern as to whether the preparation techniques required and resultant dehydration disrupt the

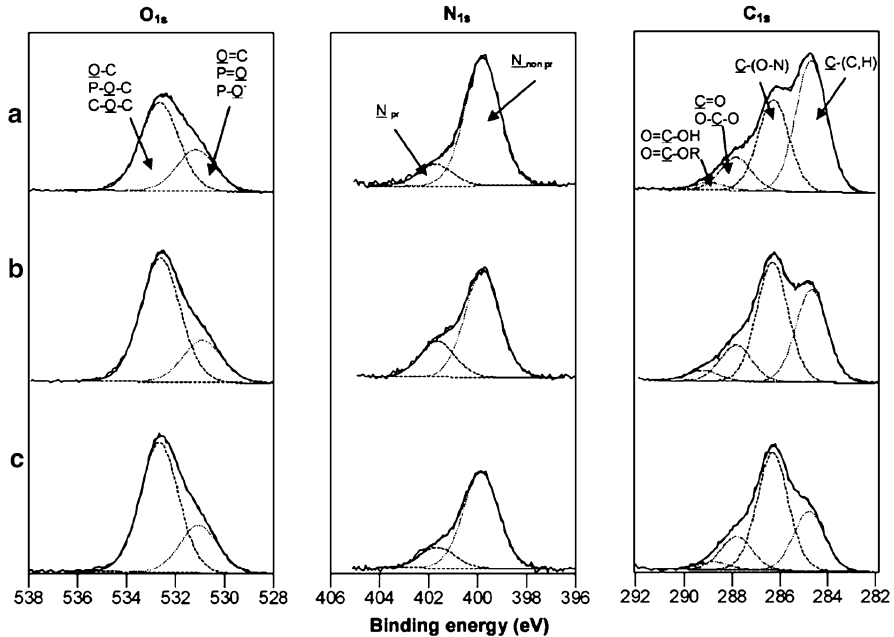


**Fig. 2.8** Representative O 1s, N 1s, and C 1s XPS peaks of three *B. subtilis* strains: (a) ATCC code: 7058; (b) ATCC code: 15476; (c) S 499 (Reprinted with permission from Ref. [96]. Copyright © Elsevier Ltd. 2007)

cell surface [14, 97]. In light of these concerns, a substantial amount of work has been undertaken to confirm XPS results by drawing comparisons with complementary data, including infrared absorption, water contact angle, and electrophoretic mobility, which are techniques that do not require ultrahigh vacuum [85, 86, 98]. These studies have shown a correlation between changes in the cell wall chemical composition with changes in the media or substrate and media, dependent on whether the cell was suspended or adhered to a surface prior to analysis. Despite these results, it is apparent that a significant amount of care must be taken when preparing microbial cells for XPS analysis. A number of reviews on the field exist and include critical assessment of the issues associated with sample preparation as well as details of the cell types that have been analyzed to date [14, 86].

### 2.4.1 Hard Tissue

Hard tissues include bone, dentin, cementum, and dental enamel; these represent the group of tissues that have undergone various degrees of mineralization during development. This mineralization is typically in the form of hydroxyapatite, which

is often applied as a biomaterial for bone implants. Within the literature, application of XPS to the analysis of hard tissue has focused on preventive and restorative dentistry. This has included analyzing the effects of various treatments, including laser irradiation [99, 100] and mouth rinses [101], and the effects of environmental exposure to chemical agents on the health of tooth enamel [102]. XPS has also been employed to examine bonding of materials and mechanisms of interactions between hard tissues and biomaterials [57, 103, 104]. In 2008, Lou et al. used XPS to investigate the surface chemical composition of 98 human maxillary first premolars to determine the compositional differences between right and left premolars [104]. The descriptive statistics of the percentage atomic concentration for all 12 elements detected were determined. The percentage of carbonate ( $\text{CO}_3$ ) was derived from high-resolution carbon spectra; the ratio  $\text{CO}_3/\text{P}$  is considered to be a measure of the susceptibility of enamel to acid attack. While no statistically significant difference was observed between right and left premolars, the authors considered the observed variation in  $\text{CO}_3/\text{P}$  potentially significant in terms of bond strength, as acid etching is typically performed prior to orthodontic bonding.

## 2.5 Biointerface Engineering

Biointerface engineering aims to bring together biology with surface engineering/science to unlock the fundamental properties driving biomolecule interactions with surfaces and to address key issues relating to biomaterials, tissue engineering, medical diagnostics, and many biotechnology applications, including sensors, bioarrays, and microfluidics. As XPS is a surface-sensitive technique, it is no surprise that it has become a core characterization tool within the discipline.

Differences between surface and bulk properties can arise via a number of different processes, including surface contamination, processing additives, blooming of plasticizers, and oxidation. Adventitious contaminants such as silicones and hydrocarbons can prevent adhesion of components, may influence the biological interactions of a biomaterial or tissue scaffold, and can interfere with the function of surface-immobilized proteins, peptides, and DNA. As such, it is critical that the surface chemistry of a material is verified at some point in the testing cycle prior to ascribing relationships between biological performance and surface chemistry or evaluating a specific immobilization strategy. There is a dearth of literature related to the detection of surface contamination via XPS, and a number of reviews exist that specifically focus on biomedical applications and issues [42, 105].

A key issue facing the integration of biomaterials is the stability of the surface when exposed to biological media; thus, an examination of how biological systems impact surfaces is paramount. XPS allows changes in the chemical composition of interfaces to be examined and has been used previously to examine the influence of microbiological corrosion (MIC) by marine aerobic bacterium on stainless steel [89] and the effects of cell culture medium on Ti, stainless steel, and a range of polymers, to name but a few examples [58, 106, 107].

As materials used in biology and bioengineering are often chosen for their mechanical or optical properties, there is an array of techniques and treatments designed to modify the material's surface for specific applications [42, 108]. Because the modifications are generally designed not to affect the bulk properties, the surface sensitivity of XPS is paramount, and angle-dependent XPS (ADXPS) is also regularly used to produce compositional depth profiles.

### ***2.5.1 The Future of XPS***

While XPS is a fundamental method for probing interfacial interactions in bioengineering, research is increasingly focusing on using XPS as part of a suite of characterization tools [42]. Obvious synergies exist between XPS and ToF-SIMS, as evidenced by the large number of papers currently in the literature that use both of these techniques. More fundamental insight into, and improvements in, devices and technology are progressively coming from combining UHV surface analysis with techniques commonly used in colloids and surface science (e.g., AFM[109]) and biological assays, such as ELISA [110], immunostaining [111], and polymerase chain reactions (PCR) [94]. This is where XPS can be used for its strengths in quantifying surface contamination, verifying surface chemistry [47, 109], and determining changes in surface chemistry after biological contact [94, 95, 111].

However, this is not to say that there are no opportunities for developments in XPS. Today multivariate statistical analysis (MVSA) routines are increasingly being developed today to assist in the interpretation of XPS data, particularly with results from imaging studies. Multivariate image analysis (MIA) methods such as scatter diagrams, principal component analysis (PCA), and classification methods are used to extract maps of pure components from degradation and images-to-spectra data sets [112]. Walton and Fairley have shown that by maintaining the relationship between images and spectra, it is possible to progress beyond the application of spectroscopic processing to multispectral imaging data sets, by utilizing the three-dimensional information contained in such data sets, to therefore improve both the processing and the visualization of the data [113]. With the ongoing development of depth profiling of biological materials being made possible by the introduction of the polyatomic ion guns, groups are just beginning to explore the applications of MVSA to explore biological systems. Studies from Artyushkova have used principal component analysis (PCA) to analyze quantitative XPS data, combining elemental and chemical species data as a function of sputter time to explore the structure of a yeast cell, with the final aim of exploring cell-directed assembly [113]. Of course, the ongoing close relationship between XPS and ToF-SIMS development will be of significant benefit as the sample-preparation techniques and cryogenic stages that have been developed for ToF-SIMS can be directly translated to XPS analysis.



## 2.6 Conclusions

Today XPS has established itself as a workhorse tool for biointerface analysis. While the key features of surface sensitivity and wide elemental analysis are at the heart of the technique, improvements in the imaging and depth-profiling capabilities of the instruments are increasingly drawing in new biological applications. But at the core, it is the relative ease of XPS data interpretation compared to ToF-SIMS and spectrometry techniques that will ensure that XPS retains its position well into the future.

## References

1. Wagner MS, McArthur SL, Shen MC, Horbett TA, Castner DG. Limits of detection for time of flight secondary ion mass spectrometry (ToF-SIMS) and X-ray photoelectron spectroscopy (XPS): detection of low amounts of adsorbed protein. *J Biomater Sci-Polym Ed.* 2002;13:407–28.
2. Lee CY, Harbers GM, Grainger DW, Gamble LJ, Castner DG. Fluorescence, XPS, and TOF-SIMS surface chemical state image analysis of DNA microarrays. *J Am Chem Soc.* 2007;129:9429–38.
3. McArthur SL, McLean KM, St John HAW, Griesser HJ. XPS and surface-MALDI-MS characterisation of worn HEMA-based contact lenses. *Biomaterials.* 2001;22:3295–304.
4. Foley JO, Fu E, Gamble LJ, Yager P. Microcontact printed antibodies on gold surfaces: function, uniformity, and silicone contamination. *Langmuir.* 2008;24:3628–35.
5. St John HAW, Gengenbach TR, Hartley PG, Griesser HJ. Surface analysis of polymers. In: O'Connor D, Sexton B, Smart RC, editors. *Surface analysis methods in material science.* Heidelberg: Springer-Verlag Berlin; 2000.
6. Beamson G, Alexander MR. Angle-resolved XPS of fluorinated and semi-fluorinated side-chain polymers. *Surf Interface Anal.* 2004;36:323–33.
7. Alexander MR, Whittle JD, Barton D, Short RD. Plasma polymer chemical gradients for evaluation of surface reactivity: epoxide reaction with carboxylic acid surface groups. *J Mater Chem.* 2004;14:408–12.
8. Ratner BD, Castner DG. Advances in X-ray photoelectron spectroscopy instrumentation and methodology: instrument evaluation and new techniques with special reference to biomedical studies. *Colloid Surf B.* 1994;2:333–46.
9. Whittle JD, Barton D, Alexander MR, Short RD. A method for the deposition of controllable chemical gradients. *Chem Commun.* 2003;14:1766–7.
10. Paynter RW, Ratner BD. The study of interfacial proteins and biomolecules by X-ray photoelectron spectroscopy. In: Andrade JD, editor. *Surface and interfacial aspects of biomedical polymers.* New York: Plenum Press; 1985. p. 189–216.
11. Chen Y-Y, Yu B-Y, Wang W-B, Hsu M-F, Lin W-C, Lin Y-C, et al. X-ray photoelectron spectrometry depth profiling of organic thin films using C60 sputtering. *Anal Chem.* 2007;80:501–5.
12. Rafati A, Davies MC, Shard AG, Hutton S, Mishra G, Alexander MR. Quantitative XPS depth profiling of codeine loaded poly(L-lactic acid) films using a coronene ion sputter source. *J Control Release.* 2009;138:40–4.
13. Yu BY, Chen YY, Wang WB, Hsu MF, Tsai SP, Lin WC, et al. Depth profiling of organic films with X-ray photoelectron spectroscopy using C-60(+) and Ar+ co-sputtering. *Anal Chem.* 2008;80:3412–5.

14. Pembrey RS, Marshall KC, Schneider RP. Cell surface analysis techniques: what do cell preparation protocols do to cell surface properties? *Appl Environ Microbiol.* 1999; 65:2877–94.
15. Vogler EA. On the biomedical relevance of surface spectroscopy. *J Electron Spectrosc Relat Phenom.* 1996;81:237–47.
16. Lewis KB, Ratner BD. Observation of surface restructuring of polymers using ESCA. *J Colloid Interface Sci.* 1993;159:77–85.
17. Lukas J, Sodhi RNS, Sefton MV. An XPS study of the surface reorientation of statistical methacrylate copolymers. *J Colloid Interface Sci.* 1995;174:421–7.
18. Magnani A, Barbucci R, Lewis KB, Leachscampavia D, Ratner BD. Surface-properties and restructuring of a cross-linked polyurethane-poly(amido-amine) network. *J Mater Chem.* 1995;5:1321–30.
19. Paynter RW, Ratner BD, Horbett TA, Thomas HR. XPS studies on the organisation of adsorbed protein films on fluoropolymers. *J Colloid Interface Sci.* 1984;101:233–45.
20. Ratner BD, Thomas TA, Shuttleworth D, Horbett TA. Analysis of the organisation of protein films on solid surfaces by ESCA. *J Colloid Interface Sci.* 1981;83:630–42.
21. Dufrene YF, VanderWal A, Norde W, Rouxhet PG. X-ray photoelectron spectroscopy analysis of whole cells and isolated cell walls of gram-positive bacteria: comparison with biochemical analysis. *J Bacteriol.* 1997;179:1023–8.
22. Vohrer U, Blomfield C, Page S, Roberts A. Quantitative XPS imaging – new possibilities with the delay-line detector. *Appl Surf Sci.* 2005;252:61–5.
23. Wang XJ, Haasch RT, Bohn PW. Anisotropic hydrogel thickness gradient films derivatized to yield three-dimensional composite materials. *Langmuir.* 2005;21:8452–9.
24. Tougaard S. Algorithm for automatic X-ray photoelectron spectroscopy data processing and X-ray photoelectron spectroscopy imaging. *J Vac Sci Technol A.* 2005;23:741–5.
25. Walton J, Fairley N. Quantitative surface chemical-state microscopy by X-ray photoelectron spectroscopy. *Surf Interface Anal.* 2004;36:89–91.
26. Walton J, Fairley N. Transmission-function correction for XPS spectrum imaging. *Surf Interface Anal.* 2006;38:388–91.
27. Steinmiller EMP, Choi K-S. Photochemical deposition of cobalt-based oxygen evolving catalyst on a semiconductor photoanode for solar oxygen production. *Proc Natl Acad Sci U S A.* 2009;106:20633–6.
28. Grünert W, Stakheev AY, Mörke W, Feldhaus R, Anders K, Shpiro ES, et al. Reduction and metathesis activity of MoO<sub>3</sub>/Al<sub>2</sub>O<sub>3</sub> catalysts: I. An XPS investigation of MoO<sub>3</sub>/Al<sub>2</sub>O<sub>3</sub> catalysts. *J Catal.* 1992;135:269–86.
29. Finster J, Klinkenberg ED, Heeg J, Braun W. ESCA and SEXAFS investigations of insulating materials for ULSI microelectronics. *Vacuum.* 1990;41:1586–9.
30. Casper L. Microelectronics processing: inorganic materials characterization. Washington DC: American Chemical Society; 1986.
31. Stinger G. The challenge of microelectronics for analytical chemistry. *Fresenius J Anal Chem.* 1992;343:771–2.
32. Heung WF, Yang YP, Wong PC, Mitchell KAR, Foster T. XPS and corrosion studies on zinc phosphate coated 7075-T6 aluminium alloy. *J Mater Sci.* 1994;29:1368–73.
33. Windisch C, Baer D, Engelhard M, Jones R. Analyzing localized corrosion in ion-implanted metals via XPS/AES. *JOM J Miner Met Mater Soc.* 2001;53:37–41.
34. Chang MC, Tanaka J. XPS study for the microstructure development of hydroxyapatite-collagen nanocomposites cross-linked using glutaraldehyde. *Biomaterials.* 2002;23:3879–85.
35. Pan J, Thierry D, Leygraf C. Electrochemical and XPS studies of titanium for biomaterial applications with respect to the effect of hydrogen peroxide. *J Biomed Mater Res.* 1994;28:113–22.
36. Ratner B. Surface characterization of biomaterials by electron spectroscopy for chemical analysis. *Ann Biomed Eng.* 1983;11:313–36.
37. Walker AR. Charged particle energy analyser. US Patent: 4810879. 1989.

38. Paul EL, Michael AK. Surface charge neutralization of insulating samples in X-ray photoemission spectroscopy. *J Vac Sci Technol A*. 1998;16:3483–9.
39. Tougaard S. Universality classes of inelastic electron scattering cross-sections. *Surf Interface Anal*. 1997;25:137–54.
40. Hajati S, Tougaard S. XPS for non-destructive depth profiling and 3D imaging of surface nanostructures. *Anal Bioanal Chem*. 2010;396:2741–55.
41. Horbett TA, Brash JL. *Proteins at interfaces II: fundamentals and applications*. Washington D. C.: American Chemical Society; 1995.
42. Castner DG, Ratner BD. *Biomedical surface science: foundations to frontiers*. *Surf Sci*. 2002;500:28–60.
43. McArthur SL, McLean KM, Kingshott P, St John HAW, Chatelier RC, Griesser HJ. Effect of polysaccharide structure on protein adsorption. *Colloid Surf B-Biointerfaces*. 2000;17:37–48.
44. Salim M, O'Sullivan B, McArthur SL, Wright PC. Characterization of fibrinogen adsorption onto glass microcapillary surfaces by ELISA. *Lab Chip*. 2007;7:64–70.
45. Johnson G, Jenkins ML, McLean KM, Griesser HJ, Kwak J, Goodman M, et al. Peptoid-containing collagenmimetics with cell binding activity. *J Biomed Mater Res*. 2000;51:612–24.
46. Massia SP, Stark J. Immobilized RGD peptides on surface-grafted dextran promote biospecific cell attachment. *J Biomed Mater Res*. 2001;56:390–9.
47. Chow E, Wong ELS, Bocking T, Nguyen QT, Hibbert DB, Gooding JJ. Analytical performance and characterization of MPA-Gly-Gly-His modified sensors. *Sens Actuator B-Chem*. 2005;111:540–8.
48. Weidner T, Samuel NT, McCrean K, Gamble LJ, Ward RS, Castner DG. Assembly and structure of alpha-helical peptide films on hydrophobic fluorocarbon surfaces. *Biointerphases*. 2010;5:9–16.
49. Apte JS, Collier G, Latour RA, Gamble LJ, Castner DG. XPS and ToF-SIMS investigation of alpha-helical and beta-strand peptide adsorption onto SAMs. *Langmuir*. 2010;26:3423–32.
50. Feyer V, Plekan O, Tsud N, Chab V, Matolin V, Prince KC. Adsorption of histidine and histidine-containing peptides on Au(111). *Langmuir*. 2010;26:8606–13.
51. Iucci G, Battocchio C, Dettin M, Gambaretto R, Polzonetti G. A NEXAFS and XPS study of the adsorption of self-assembling peptides on TiO<sub>2</sub>: the influence of the side chains. *Surf Interface Anal*. 2008;40:210–4.
52. Jedlicka SS, Rickus JL, Zemyanov DY. Surface analysis by X-ray photoelectron spectroscopy of sol-gel silica modified with covalently bound peptides. *J Phys Chem B*. 2007;111:11850–7.
53. Charnley M, Fairfull-Smith K, Haldar S, Elliott R, McArthur SL, Williams NH, et al. Generation of bioactive materials with rapid self-assembling resorcinarene-peptides. *Adv Mater*. 2009;21:2909–15.
54. Shen MC, Martinson L, Wagner MS, Castner DG, Ratner BD, Horbett TA. PEO-like plasma polymerized tetraglyme surface interactions with leukocytes and proteins: in vitro and in vivo studies. *J Biomater Sci-Polym Ed*. 2002;13:367–90.
55. Thissen H, Gengenbach T, du Toit R, Sweeney DF, Kingshott P, Griesser HJ, et al. Clinical observations of biofouling on PEO coated silicone hydrogel contact lenses. *Biomaterials*. 2010;31:5510–9.
56. Zinelis S, Thomas A, Syres K, Silikas N, Eliades G. Surface characterization of zirconia dental implants. *Dent Mater*. 2009;26:295–305.
57. Leitao E, Barbosa MA, deGroot K. XPS characterization of surface films formed on surface-modified implant materials after cell culture. *J Mater Sci-Mater Med*. 1997;8:423–6.
58. Liu YT, Li K, Pan J, Liu B, Feng SS. Folic acid conjugated nanoparticles of mixed lipid monolayer shell and biodegradable polymer core for targeted delivery of Docetaxel. *Biomaterials*. 2010;31:330–8.

59. Daniel C, Sohn KE, Mates TE, Kramer EJ, Radler JO, Sackmann E, et al. Structural characterization of an elevated lipid bilayer obtained by stepwise functionalization of a self-assembled alkenyl silane film. *Biointerphases*. 2007;2:109–18.
60. Kim HK, Kim K, Byun Y. Preparation of a chemically anchored phospholipid monolayer on an acrylated polymer substrate. *Biomaterials*. 2005;26:3435–44.
61. Michel R, Subramaniam V, McArthur SL, Bondurant B, D'Ambruoso GD, Hall HK, et al. Ultra-high vacuum surface analysis study of rhodopsin incorporation into supported lipid bilayers. *Langmuir*. 2008;24:4901–6.
62. McArthur SL, Halter MW, Vogel V, Castner DG. Covalent coupling and characterization of supported lipid layers. *Langmuir*. 2003;19:8316–24.
63. Russell BG, Moddeman WE, Birkbeck JC, Wright SE, Millington DS, Stevens RD, et al. Surface structure of human mucin using X-ray photoelectron spectroscopy. *Biospectroscopy*. 1998;4:257–66.
64. Lundin M, Sandberg T, Caldwell KD, Blomberg E. Comparison of the adsorption kinetics and surface arrangement of “as received” and purified bovine submaxillary gland mucin (BSM) on hydrophilic surfaces. *J Colloid Interface Sci*. 2009;336:30–9.
65. Libertino S, Giannazzo F, Aiello V, Scandurra A, Sinatra F, Renis M, et al. XPS and AFM characterization of the enzyme glucose oxidase immobilized on SiO<sub>2</sub> surfaces. *Langmuir*. 2008;24:1965–72.
66. Abbas A, Vercaigne-Marko D, Supiot P, Bocquet B, Vivien C, Guillochon D. Covalent attachment of trypsin on plasma polymerized allylamine. *Colloid Surf B-Biointerphases*. 2009;73:315–24.
67. Debenedetto GE, Malitesta C, Zamboni CG. Electroanalytical X-ray photoelectron-spectroscopy investigation on glucose-oxidase adsorbed on platinum. *J Chem Soc-Faraday Trans*. 1994;90:1495–9.
68. Liu ZC, Zhang X, He NY, Lu ZH, Chen ZC. Probing DNA hybridization efficiency and single base mismatch by X-ray photoelectron spectroscopy. *Colloid Surf B-Biointerphases*. 2009;71:238–42.
69. Zhang XC, Kumar S, Chen JH, Teplyakov AV. Covalent attachment of shape-restricted DNA molecules on amine-functionalized Si(111) surface. *Surf Sci*. 2009;603:2445–57.
70. May CJ, Canavan HE, Castner DG. Quantitative X-ray photoelectron spectroscopy and time-of-flight secondary ion mass spectrometry characterization of the components in DNA. *Anal Chem*. 2004;76:1114–22.
71. Petrovykh DY, Kimura-Suda H, Tarlov MJ, Whitman LJ. Quantitative characterization of DNA films by X-ray photoelectron spectroscopy. *Langmuir*. 2004;20:429–40.
72. Graf N, Gross T, Wirth T, Weigel W, Unger WES. Application of XPS and ToF-SIMS for surface chemical analysis of DNA microarrays and their substrates. *Anal Bioanal Chem*. 2009;393:1907–12.
73. Dhayal M, Ratner DA. XPS and SPR analysis of glycoarray surface density. *Langmuir*. 2009; 25:2181–7.
74. Tyler BJ. XPS and SIMS studies of surfaces important in biofilm formation – three case studies. In: Prokop A, Hunkeler D, Cherrington AD, editors. *Bioartificial organs – science, medicine, and technology*. New York: New York Acad Sciences; 1997. p. 114–26.
75. Bejjani BA, Shaffer LG. Application of array-based comparative genomic hybridization to clinical diagnostics. *J Mol Diagn*. 2006;8:528–33.
76. Lamartine J. The benefits of DNA microarrays in fundamental and applied bio-medicine. *Mater Sci Eng C-Biomim Supramol Syst*. 2006;26:354–9.
77. Wu P, Castner DG, Grainger DW. Diagnostic devices as biomaterials: a review of nucleic acid and protein microarray surface performance issues. *J Biomater Sci-Polym Ed*. 2008;19:725–53.
78. Gong P, Harbers GM, Grainger DW. Multi-technique comparison of immobilized and hybridized oligonucleotide surface density on commercial amine-reactive microarray slides. *Anal Chem*. 2006;78:2342–51.

79. Leone L, Loring J, Sjooberg S, Persson P, Shchukarev A. Surface characterization of the Gram-positive bacteria *Bacillus subtilis* – an XPS study. *Surf Interface Anal.* 2006;38:202–5.
80. Rouxhet PG, Mozes N, Dengis PB, Dufrene YF, Gerin PA, Genet MJ. Application of X-ray photoelectron-spectroscopy to microorganisms. *Colloid Surf B-Biointerfaces.* 1994;2:347–69.
81. Tesson B, Genet MJ, Fernandez V, Degand S, Rouxhet PG, Martin-Jezequel V. Surface chemical composition of diatoms. *ChemBioChem.* 2009;10:2011–24.
82. Dague E, Delcorte A, Latge JP, Dufrene YF. Combined use of atomic force microscopy, X-ray photoelectron spectroscopy, and secondary ion mass spectrometry for cell surface analysis. *Langmuir.* 2008;24:2955–9.
83. Ojeda JJ, Romero-Gonzalez ME, Bachmann RT, Edyvean RGJ, Banwart SA. Characterization of the cell surface and cell wall chemistry of drinking water bacteria by combining XPS, FTIR spectroscopy, modeling, and potentiometric titrations. *Langmuir.* 2008;24:4032–40.
84. Boonaert CJP, Rouxhet PG. Surface of lactic acid bacteria: relationships between chemical composition and physicochemical properties. *Appl Environ Microbiol.* 2000;66:2548–54.
85. van der Mei HC, de Vries J, Busscher HJ. X-ray photoelectron spectroscopy for the study of microbial cell surfaces. *Surf Sci Rep.* 2000;39:3–24.
86. Sharma PK, Rao KH. Surface characterization of bacterial cells relevant to the mineral industry. *Miner Metall Process.* 2005;22:31–7.
87. Beech IB, Zinkevich V, Tapper R, Gubner R, Avci R. Study of the interaction of sulphate-reducing bacteria exopolymers with iron using X-ray photoelectron spectroscopy and time-of-flight secondary ionisation mass spectrometry. *J Microbiol Methods.* 1999;36:3–10.
88. Yuan SJ, Pehkonen SO. Microbiologically influenced corrosion of 304 stainless steel by aerobic *Pseudomonas NCIMB 2021* bacteria: AFM and XPS study. *Colloid Surf B-Biointerfaces.* 2007;59:87–99.
89. Sahrani FK, Aziz MA, Ibrahim Z, Yahya A. Surface analysis of marine sulphate-reducing bacteria exopolymers on steel during biocorrosion using X-ray photoelectron spectroscopy. *Sains Malays.* 2008;37:131–5.
90. Omoike A, Chorover J. Spectroscopic study of extracellular polymeric substances from *Bacillus subtilis*: aqueous chemistry and adsorption effects. *Biomacromolecules.* 2004;5:1219–30.
91. Rodrigues LR, Teixeira JA, van der Mei HC, Oliveira R. Isolation and partial characterization of a biosurfactant produced by *Streptococcus thermophilus* A. *Colloid Surf B-Biointerfaces.* 2006;53:105–12.
92. Fantauzzi M, Rossi G, Elsener B, Loi G, Atzei D, Rossi A. An XPS analytical approach for elucidating the microbially mediated enargite oxidative dissolution. *Anal Bioanal Chem.* 2009;393:1931–41.
93. Magnuson TS, Neal AL, Geesey GG. Combining in situ reverse transcriptase polymerase chain reaction, optical microscopy, and X-ray photoelectron spectroscopy to investigate mineral surface-associated microbial activities. *Microb Ecol.* 2004;48:578–88.
94. Kalinowski BE, Liermann LJ, Brantley SL, Barnes A, Pantano CG. X-ray photoelectron evidence for bacteria-enhanced dissolution of hornblende. *Geochim Cosmochim Acta.* 2000;64:1331–43.
95. Ahimou F, Boonaert CJP, Adriaensen Y, Jacques P, Thonart P, Paquot M, et al. XPS analysis of chemical functions at the surface of *Bacillus subtilis*. *J Colloid Interface Sci.* 2007;309:49–55.
96. Marshall KC, Pembrey R, Schneider RP. The relevance of X-ray photoelectron-spectroscopy for analysis of microbial cell-surfaces – a critical-view. *Colloid Surf B-Biointerfaces.* 1994;2:371–6.
97. Leone L, Ferri D, Manfredi C, Persson P, Shchukarev A, Sjooberg S, et al. Modeling the acid-base properties of bacterial surfaces: a combined spectroscopic and potentiometric study of the gram-positive bacterium *Bacillus subtilis*. *Environ Sci Technol.* 2007;41:6465–71.
98. Mine A, Yoshida Y, Suzuki K, Nakayama Y, Yatani H, Kuboki T. Spectroscopic characterization of enamel surfaces irradiated with Er: YAG laser. *Dent Mater J.* 2006;25:214–8.

99. Ziglo MJ, Nelson AE, Heo G, Major PW. Argon laser induced changes to the carbonate content of enamel. *Appl Surf Sci.* 2009;255:6790–4.
100. Busscher HJ, Vandermei HC, Genet MJ, Perdok JF, Rouxhet PG. XPS determination of the thickness of adsorbed mouthrinse components on dental enamel. *Surf Interface Anal.* 1990;15:344–6.
101. Taube F, Ylmen R, Shchukarev A, Nietzsche S, Noren JG. Morphological and chemical characterization of tooth enamel exposed to alkaline agents. *J Dent.* 2010;38:72–81.
102. Yoshida Y, Van Meerbeek B, Nakayama Y, Snauwaert J, Hellemans L, Lambrechts P, et al. Evidence of chemical bonding at biomaterial-hard tissue interfaces. *J Dent Res.* 2000;79:709–14.
103. Lou L, Nelson AE, Heo G, Major PW. Surface chemical composition of human maxillary first premolar as assessed by X-ray photoelectron spectroscopy (XPS). *Appl Surf Sci.* 2008;254:6706–9.
104. Andrade JD. X-ray photoelectron spectroscopy. In: Andrade JD, editor. *Surface and interfacial aspects of biomedical polymers.* New York: Plenum Press; 1985.
105. Burgos-Asperilla L, Garcia-Alonso MC, Escudero ML, Alonso C. Study of the interaction of inorganic and organic compounds of cell culture medium with a Ti surface. *Acta Biomater.* 2010;6:652–61.
106. Zelzer M, Alexander MR. Nanopores in single- and double-layer plasma polymers used for cell guidance in water and protein containing buffer solutions. *J Phys Chem B.* 2010;114:569–76.
107. Chung DJ. Surface modification of polymers for biomaterials. *J Dent Res.* 2001;80:1348.
108. Hartley PG, McArthur SL, McLean KM, Griesser HJ. Physicochemical properties of polysaccharide coatings based on grafted multilayer assemblies. *Langmuir.* 2002;18:2483–94.
109. Griesser HJ, Hartley PG, McArthur SL, McLean KM, Meagher L, Thissen H. Interfacial properties and protein resistance of nano-scale polysaccharide coatings. *Smart Mater Struct.* 2002;11:652–61.
110. Canavan HE, Cheng XH, Graham DJ, Ratner BD, Castner DG. Surface characterization of the extracellular matrix remaining after cell detachment from a thermoresponsive polymer. *Langmuir.* 2005;21:1949–55.
111. Artyushkova K, Fulghum JE. Multivariate image analysis methods applied to XPS imaging data sets. *Surf Interface Anal.* 2002;33:185–95.
112. Walton J, Fairley N. XPS spectromicroscopy: exploiting the relationship between images and spectra. *Surf Interface Anal.* 2008;40:478–81.
113. Artyushkova K. Structure determination of nanocomposites through 3D imaging using laboratory XPS and multivariate analysis. *J Electron Spectrosc Relat Phenom.* 2010;178:292–302.

# Chapter 3

## Biomolecular Analysis by Time-of-Flight Secondary Ion Mass Spectrometry (ToF-SIMS)

Daniel Breitenstein, Birgit Hagenhoff, and Albert Schnieders

**Abstract** The use of time-of-flight secondary ion mass spectrometry (ToF-SIMS) for biomolecular analysis has made tremendous progress in recent years. This chapter will outline the principal aspects of ToF-SIMS as well as recent technical developments that have made surface mass spectrometry so valuable for this field. Furthermore, an overview on relevant biochemical applications based on the four essential operational modes—spectrometry, imaging, depth profiling, and 3D analysis—will be given. The applications range from the analysis of Langmuir–Blodgett films and tissue sections to the analysis of whole cells. With these results in mind, we will discuss the chances and limitations of the technique.

### 3.1 Introduction

Time-of-flight secondary ion mass spectrometry (ToF-SIMS) enables the analysis of the elemental as well as molecular composition of a sample's surface. The fundamental process involved is the impact of primary ions, leading to, among other things, the desorption of secondary ions, which are characteristic for the composition of the analyzed surface. Recent progress in instrumentation development has facilitated the considerable use of this technique for the analysis of biological samples.

The tremendous development of time-of-flight secondary ion mass spectrometry (ToF-SIMS) in the field of biological applications within recent becomes clear when one compares the comprehensive review by Pacholski and Winograd published in

---

D. Breitenstein (✉) • B. Hagenhoff

Tascon GmbH, Heisenbergstr. 15, Münster 48155, Germany

e-mail: [daniel.breitenstein@tascon-gmbh.de](mailto:daniel.breitenstein@tascon-gmbh.de); [birgit.hagenhoff@tascon-gmbh.de](mailto:birgit.hagenhoff@tascon-gmbh.de)

A. Schnieders

Tascon USA, Inc., 100 Red Schoolhouse Road, Chestnut Ridge, NY 10977, USA

Managing Director, CNM Technologies, Bielefeld, Germany

e-mail: [albert@tasconusa.com](mailto:albert@tasconusa.com)

1999 [1] with other, more recent reviews [2–4], including this chapter. Pacholski and Winograd had to point out just over a decade ago that in so-called static ToF-SIMS experiments, “images are usually acquired with only a few counts/pixel (p. 2979).” They emphasized that “most of the examples [at that time] involved the detection of elemental species (...) rather than molecular species (...) (p. 3001)”. However, they also stated that “this trend will surely change in the future (p. 3001).”

The aim of this chapter is to outline the principal aspects of ToF-SIMS as well as recent technical developments that made this prediction become true and that have made ToF-SIMS a useful method in the field of biochemistry.

Among the aspects that make ToF-SIMS in principle a beneficial tool for bioanalysis are the following: First, ToF-SIMS just probes the uppermost three monolayers of a sample. Second, it is especially well suited for the detection and identification of molecules with a mass of several hundred atomic mass units (u), which make up a majority of biologically relevant compounds. Third, it offers imaging capabilities with a lateral resolution as good as a few hundred nanometers. (Recently, even a 3D-imaging option for biological samples was established, which allows a vertical resolution of 30 nm [5].) The most important technical development in the last decade making these principal aspects of SIMS accessible to the field of biochemistry is the use of polyatomic primary ions for desorption. Additional details on polyatomic primary ion sources can be found in Sect. 3.2.1.2 as well as Sect. 3.3.1.

Besides a short review of the fundamental SIMS process and the presentation of the current technology of ToF-SIMS, this chapter will also give an overview of relevant biochemical applications based on the four essential operational modes: spectrometry, imaging, depth profiling, and 3D analysis. The applications range from the analysis of Langmuir–Blodgett films and tissue sections to the analysis of whole cells. With these results in mind, we discuss the chances and limitations of the technique.

Due to limited space, we cannot address a number of aspects: One of them is the historical development of ToF-SIMS. This aspect has been described in detail by Benninghoven [6]. Furthermore, as stated in the title of this chapter, biomolecular analysis by ToF-SIMS—not the detection of elements or isotopes—is the focus of this chapter. Therefore, ToF-SIMS studies focusing on this aspect, such as “classical dynamic” SIMS studies (SIMS-microscopy, recently reviewed by Guerquin-Kern et al. [7]), are excluded from this review.

The chapter is divided into seven sections: Following the introduction (Sect. 3.1), the basic principle of the ionization process is explained (Sect. 3.2). More detailed information on the technical setup of ToF-SIMS instruments that makes them uniquely useful for biomolecular applications are available in the third section. Examples of applications are discussed using the four ToF-SIMS operational modes in Sect. 3.4. Section 3.5 deals with strategies to improve the data quality. Following a brief summary of the information provided (Sect. 3.6), the final section gives an outlook of the future development of ToF-SIMS in the field of biomolecular analysis.



## 3.2 Principle of the Ionization Process

The three fundamental processes of any mass-spectrometric technique are the formation, separation, and detection of analyte ions. Since in the case of surface mass spectrometry, the analyte is present on or in a solid or liquid sample, the ion formation not only consists of ionization, but also involves the desorption of the respective particles from the surface. In ToF-SIMS, the formation of secondary ions is a result of the impact of primary ions onto the surface of the sample, whereas the separation and detection are performed by a time-of-flight (ToF) analyzer. Because of its importance, the ion-formation process will be discussed in more detail in the following section.

### 3.2.1 Formation of Secondary Ions

The fundamental event in a ToF-SIMS experiment is the desorption (sputtering) and ionization of surface components after the impact of primary ions. Whereas the desorption of particles (neutral and charged) can be described fairly well on the basis of the results of practical experiments as well as molecular dynamics calculations [8], the intrinsic effects leading to the ionization of some of these sputtered species (secondary ions) are not yet understood.

In the following section, first the linear collision cascade model of Sigmund [9–11] and Thompson [12] will be shortly introduced, because this concept has had the greatest success in quantitatively explaining observed features of sputtering, such as total yields, energy distributions of ejected particles, and the yield dependence on energy, atomic number, angle of incidence, and mass of the primary particle, as well as mass and atomic number of the target atoms. Even if the model strictly applies to the bombardment of mono-elemental, polycrystalline targets, its concepts and ideas are the basis for many other models of sputtering, including of organic systems. The question of the charge of the sputtered particles is not within the scope of Sigmund's theory. In an additional section, a short overview of the use of polyatomic primary ions will be given because of its importance for the analysis of organic, especially biomolecular, samples. For a more detailed introduction, see the next chapter in this book.

#### 3.2.1.1 Collision Cascade (Monoatomic Bombardment)

It is consensually believed that elastic collisions of a primary ion with surface atoms displace these surface atoms (primary recoils) and that this movement induces a movement of further particles (secondary recoils) [13]. In the target, the recoils will first have a directional distribution peaked in the direction of the incoming primary particle. After a few collisions, however, their motion in the cascade will be

essentially isotropic. Some recoils arrive at the target surface. They can leave the sample when their energy is high enough to overcome the surface-binding energy of the solid. Therefore, 95% of the particles desorbed by the impact of a monomolecular primary ion originate from the first to third outermost monolayers of the sample [14]. Under conditions prevailing in SIMS, the lifetime of a cascade is of the order of  $10^{-11}$  to  $10^{-12}$  s and its dimension is of the order of 10 nm [15]. The collision cascades may be considered independent events under typical conditions (primary ion currents and beam sizes) used in ToF-SIMS.

As long as the energy of the moving particle in the collision cascade is large relative to the binding energy of the target atoms, the collision partners can be considered free particles. Therefore, close to the track of the impacting projectile penetrating into the bulk of the sample, a massive fragmentation of molecules takes place, resulting in the destruction of organic material and the emission of mainly atoms. As the distance from the point of impact increases, more intact organic molecules survive. Some of these molecules may be emitted, mainly as (secondary) neutrals but partly as positively or negatively charged secondary ions [16]. Most of the secondary ions obtained in ToF-SIMS experiments are singly charged [15]. More details on the collision cascade under monoatomic bombardment are provided by Urbassek [17].

As detailed before, emitted particles could be atoms, fragments of molecules, intact molecules, or even clusters of these particles. The type of particles present in the final mass spectrum is the same as in classical mass spectrometry, such as electron impact, or gas chromatography mass spectrometry. However, due to the additionally needed step of desorption by sputtering, secondary ion mass spectra tend to show more fragmentation than those particles. A good review of the rules governing the formation and stability of ions present in mass spectra is given by McLafferty and Turecek [18].

Especially with the use of polyatomic primary ions, ToF-SIMS is well suited for the detection and identification of molecules in a medium mass range of several hundred microns. This makes ToF-SIMS particularly well suited for biomolecular work, as many important molecules (e.g., drugs) are in this mass range.

Considering the massive fragmentation of the near-surface molecules under monoatomic bombardment, it is mandatory for an artifact-free measurement to avoid collecting data from already damaged surface areas. In other words, the probability for a particular surface site to receive more than one primary ion has to be negligibly small. This can statistically be ensured by keeping the primary ion dose density below a value guaranteeing that only 1% of the surface structure is influenced. The value of this so-called static SIMS limit depends on the particular secondary ion species but typically ranges from a primary ion dose density of  $10^{11}$ - $10^{13}$  ions/cm<sup>2</sup>. Upon exceeding this static limit, one reaches “dynamic” SIMS conditions, including operational modes that are based on the removal of surface material by sputtering [19, 20]. However, with monoatomic bombardment, most organic secondary ions are highly fragmented in such an approach [21, 22]. Therefore, these “dynamic SIMS” experiments allow predominantly the detection of elements and their distribution within the sample [7].

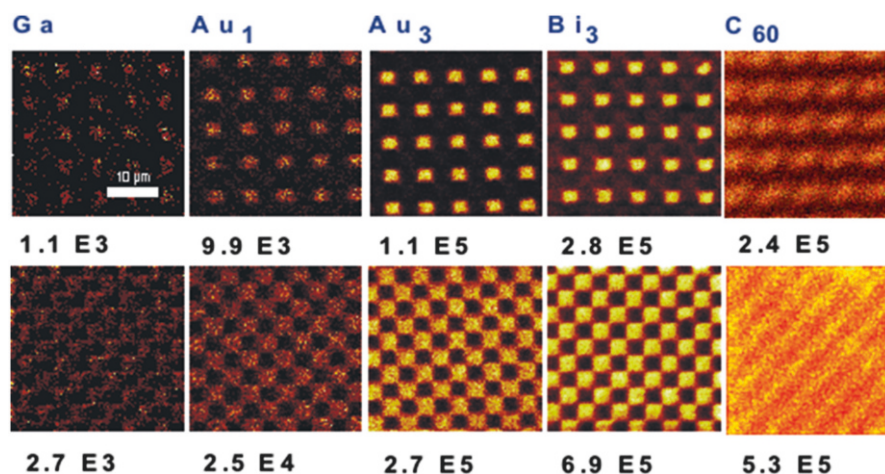


**Fig. 3.1** ToF-SIMS mass-resolved images of a blue pigment ( $m=416$  u, *top row*) and a green pigment ( $m=641$  u, *bottom row*) in a color filter array. The numbers indicate the total counts integrated over the whole image. All images were acquired with the respectively indicated singly charged primary ion species until the signal intensity dropped to  $1/e$  of the initial value—corresponding to identical sample consumption. Without going into details, which can be found elsewhere [24], this figure may serve as a qualitative example for the statements given in the text on the different types of primary ion species and primary ion sources

### 3.2.1.2 Effect of Cluster Primary Ions (Polyatomic Bombardment)

Cluster ions, such as  $SF_5^+$  [23, 24],  $C_{60}^+$  [25–27],  $Au_3^+$  [28], or  $Bi_3^+$  [29], consist of multiple atoms. Upon impact on the sample, these clusters break apart [30, 31], leading to a multiple, simultaneous bombardment of a small spot. One of the observations possible under these conditions is that the secondary ion yield, namely, the number of secondary ions generated per impacting primary ion, is drastically increased compared to monoatomic bombardment [32, 33]. The increase is nonlinear with respect to the number of projectile particles: For instance, changing the primary ion from  $Au_1^+$  to  $Au_3^+$  on an organic polymer additive sample (Irganox 1010) does not lead to a threefold but to an almost 45-fold increase of the secondary ion yield for the intact molecule (quasi-molecular ion) on thick organic substrates [34]. The key observation for the use of cluster primary ions in molecular ToF-SIMS analysis is that the yield enhancement is not accompanied by a likewise increase in surface damage [31, 34–38]. This increase in efficiency corresponds to an increase in the ultimate number of secondary ions, which can be desorbed from a surface area before they are completely destroyed by ion bombardment. A comparison of the use of monoatomic and polyatomic primary ions on identical organic samples appears in Fig. 3.1. The example is from a study highlighting the differences in performance of various primary ion species [24]. One can clearly see how the image quality improves from monoatomic to polyatomic primary ions.

The nonlinear effects (increase in yield and efficiency) are assumed to originate on the one hand from the deposition of the collision energy closer to the surface, as cluster ions have a lower kinetic energy per constituent than atomic primary ions have [31, 39]. On the other hand, it is additionally and/or alternatively explained by the overlap of the collision cascades caused by the individual constituents of the polyatomic projectile [8]. Finally, there are results indicating a more efficient protonation (i.e., ionization by attachment of a proton) of originally neutral molecules [40, 41]. The anticipated accumulation of available protons on the sample surface is expected to be the result of differences in bond-breaking mechanisms in polyatomic bombardment compared to monoatomic bombardment [40, 42].

A number of groups (such as Gillen and Roberson [23]; for a more complete list and discussion, see the review of Mahoney [43]) have reported the detection of molecular secondary ions during depth profiling, that is, sputter removal of sample surface layers (see Sects. 3.4.4 and 3.4.5), in favorable cases. The results can be explained simplistically by assuming that all molecules damaged during sputtering are removed under polyatomic sputtering in the same event, therefore exposing an “undamaged” surface [44]. The traditional distinction between “static” and “dynamic” ToF-SIMS conditions therefore does not play such a critical role for polyatomic projectiles and thick organic layers.

More details on the effect of the use of cluster ions on ToF-SIMS results can be found in the substantial review by Wucher [32] and in the next chapter in this book. Nevertheless, the physics and chemistry of cluster ion bombardment are far from being well understood and are currently widely discussed in the SIMS community.

### 3.3 Instrumentation

This section will discuss some technological aspects of ToF-SIMS instrumentation. We place special emphasis on the consequences of certain design features on the analysis of biomolecular samples.

#### 3.3.1 Primary Ion Guns

To enable the sputtering and ionization process on the surface, primary ions have to be generated, accelerated, and focused onto the target surface. Two types of ion sources are used for primary ion generation in ToF-SIMS: the liquid metal ion source and the electron impact ion source (see Sect. 3.3.1.1). Other ion sources, including surface ionization sources and duoplasmatron sources, which are also used on SIMS instrumentations, are of minor importance for biological applications. Their description goes beyond the scope of this review and can be found elsewhere [45]. Section 3.3.1.2 discusses the mass separation and pulsing of primary ions, and Sect. 3.3.1.3 describes the focusing of primary ion beams.

### 3.3.1.1 Primary Ion Sources

#### 3.3.1.1.1 Liquid Metal Ion Source (LMIS)

Primary ion guns using a liquid metal ion source for ion generation offer the highest spatial resolution of all available ion guns. In an LMIS, the source consists of a needle with a tip radius of a few microns. The needle is covered with a thin layer of a liquid metal provided from a reservoir. If the metal is not liquid at room temperature, it can be melted by a heating filament. Primary ions are extracted from the tip of the needle by an extraction voltage (in the range of 5–10 keV) applied to an opposing electrode. The emitter itself is typically at a potential of 5–30 keV above ground, resulting in a corresponding energy of the primary ions when they reach the target. Similar to the ionization process in electrospray mass spectrometry, the liquid metal forms a Taylor cone at the tip of the needle and the primary ions can be continuously extracted toward the sample.

The advantage of the LMIS against other ion sources lies in the well-defined point of primary ion extraction. Ions are formed from the Taylor cone, which is much better defined than the tip itself. The ion source therefore has a virtual size down to 10 nm in diameter [45]. This small virtual size allows exceptional focusing of the primary ion beam onto the target. Focusing is optimized by an ion-optical lens system inside the primary ion column (see Sect. 3.3.1.3). In state-of-the-art liquid metal ion guns, the beam can be focused down to some 10 nm in DC operation or approximately 100 nm in pulsed operation (see also Sect. 3.3.1.2).

The metal and therefore the primary ion species used in an LMIS depend on several critical parameters: First, the material has to be ionized easily in the field-emission process. Moreover, as the primary ions have to be created from a liquid phase, a low melting point is of high interest from a technological point of view. Furthermore, as a consequence of the time-of-flight principle within the ion gun (see Sect. 3.3.1.2), the element used as primary ion should either be monoisotopic or be easily available in isotopically separated species. In this perspective, the price of the material is also of interest. Finally, it has been shown (as discussed above) that a high mass and a polyatomic nature of the primary ion are of high interest for improved results on organic samples.

The “traditional” metal used in an LMIS is gallium [ $^{69}\text{Ga}$ , two Ga isotopes, melting point (mp): 302.9 K]. It has many benefits, including a low melting point and the availability as isotopically enriched  $^{69}\text{Ga}$ . Furthermore, it is widely used in other applications, such as focused ion beam (FIB) bombardment for material processing. However, Ga has a relatively low atomic mass, resulting in a low efficiency for secondary ion emission. Indium ( $^{115}\text{In}$ , two In isotopes, mp: 429.8 K) can be seen as a developing step because of its higher mass. More recently, gold ( $^{197}\text{Au}$ , monoisotopic, used as a eutectic mixture with germanium; mp: ~400 K [28]; or pure gold, mp: 1,337.3 K) and bismuth ( $^{209}\text{Bi}$ , monoisotopic, mp: 544.4 K) were introduced; gold and bismuth primary ion sources have been a breakthrough for the analysis of both organic and biological samples. Gold and bismuth sources already profit from the high mass of the monoatomic primary ion; however, the main improvement

compared to the other elements listed above is the formation of polyatomic cluster ions ( $M_y^{x+}$ , with  $x=1, 2$  and  $y=1, 3, 5, 7$ ). The benefits of both aspects (higher primary ion mass and polyatomic primary ion species) for organic analysis are visualized in Fig. 3.1 and were discussed in Sect. 3.2.1.2. The use of a Bi-cluster LMIS typically is preferable to an Au-LMIS because of a better performance in terms of achievable cluster currents and beam quality (focus, pulse width) and the wider variety of available cluster species [29].

### 3.3.1.1.2 Electron Impact Ion Source

In an electron impact (EI) ion source, gas-phase atoms or molecules are impacted by electrons with an energy high enough to ionize them. This process requires the continuous leaking of a gas or vapor into the ionization chamber of the source. Electrons are emitted from a heated filament and are accelerated into this chamber, where they interact with the gas or vapor particles. Ionized gas or vapor particles are captured by an electrical extraction field and are accelerated through an ion-optical system onto the target.

Traditionally, noble gases, oxygen, and  $SF_5^+$  were used in EI sources. Oxygen became one of the dominant primary ions often used for depth-profiling of inorganic samples [46]. In the field of biological applications, the recent development of a  $C_{60}$  source [27] is of great interest: Applying the ionization process to sublimed buckminsterfullerenes opens the possibility to generate a high-mass (720-u) multi-atomic ion species.

While the polyatomic nature of the  $C_{60}^+$ ,  $C_{60}^{++}$ , and  $C_{60}^{+++}$  ions is reported to be advantageous for biochemical applications, the ionization process in the EI source only allows focusing of the primary ion beam down to a diameter of a few microns in the best case. Thus, the imaging capabilities of a  $C_{60}$  source are (to date) inferior to the LMIG sources (see also Fig. 3.1) [29].

### 3.3.1.2 Separation and Pulsing of Primary Ions

The continuous extraction of primary ions from an ion source without further manipulation of the beam would lead to a continuous bombardment of the sample surface and therefore to the continuous generation of secondary particles. In such a scenario, the mass separation of secondary ions by a ToF analyzer (see Sect. 3.3.2) does not easily work. Thus, for ToF-SIMS analysis, the surface bombardment with primary ions is pulsed, which is often performed by deflecting the primary ion beam in and out of the optical axis of the primary ion gun and blanking it with appropriately placed apertures.

In most primary ion sources, a broad range of ions are generated. For example, an Au-LMIS operating with an AuGe alloy produces  $Ge_x^{y+}$  and  $Au_x^{y+}$  ions, with  $x$  and  $y$  being a natural number between 1 and 5 and 1 and 3, respectively, as well as mixed AuGe cluster ions. Similarly, a  $C_{60}$ -EI source produces  $C_{60}^{y+}$ , with  $y$  being a natural number between 1 and 3, as well as a wide variety of fragments of the

buckminsterfullerene molecules. All these ions are accelerated by the extraction field with the same energy into the primary ion gun column. Due to their different mass-to-charge ratios, they then have various velocities. Thus, different species in a pulsed ion beam would hit the sample surface at different times, leading to a widening of the primary ion pulse. Three methods can be used (sometimes together) to separate the different species in a primary ion pulse. First, the time-of flight principle (see also Sect. 3.3.2) can be used. After a beam is pulsed, an additional set of blanking plates further down the ion column is used to select a distinct ion package from a primary ion pulse at the time when these ions pass the blanking plates. At all other times, the beam would be blanked. A second method uses a Wien filter, which consists of perpendicular electric and magnetic fields. Only ions of a certain velocity (i.e., charge-to-mass ratio) can pass through such a filter. The third method uses a 90°-deflection unit for pulsing and mass-separating the beam [47].

In order to achieve the highest possible mass resolution in a time-of-flight mass analyzer, primary ion pulses should be as short as possible. Ion packages of several tens of nanoseconds in length can be further compressed in time by using an axial buncher (two plates perpendicular to the ion-optical axis). When the ion package is in the center of the two plates, a high-voltage pulse is switched to the back plate, accelerating the ions at the end of the package more than those in the front. By adjusting the amplitude of the bunching pulse, it is possible to shorten the pulse width at the target to less than 1 ns. This allows one to achieve mass resolutions (FWHM) of more than 10,000 on commercially available ToF-SIMS instruments [48]. However, the shortest pulse lengths are achieved at the expense of either the focus quality or the measuring time.

### 3.3.1.3 Focusing of Primary Ions

The ion beam is focused by an ion-optical lens systems. As the setup of the lens systems varies among manufacturers and depends on the analytical goal of the analysis, just a brief general overview is given here. More details can be found elsewhere [45].

The main components of the ion-optical system are the apertures and the electrostatic lenses. Apertures are used to blank part of the beam, while electrostatic lenses are used to focus the primary ion beam. Similar to optical lenses, aberrations should be avoided upon use of the lens system. In this review, only two types of aberrations are discussed, spherical and chromatic.

The most important aberration in an ion-optical system is the spherical aberration, meaning that ions with a movement parallel with but far from the axis of the beam are focused to a different spot than those moving on the axis of the beam. To avoid this type of aberration, one can use a circular aperture on the axis of the beam. Such a pupil allows only those primary ions that are close to the beam axis to pass. Thus, ions that would lead to a spherical aberration of the focus (i.e., those far away from the beam axis) are blanked. It should be noted that removing these primary ions increases the focus quality but decreases the number of primary ions hitting the sample—and thus increases the measuring time needed for the same sensitivity or dynamic range of a measurement.

The second important aberration to deal with is the chromatic aberration: Ions with different velocities are brought to a different focus. One instance where the chromatic aberration limits the focus of the analysis beam occurs during the electrodynamic bunching of an ion pulse in order to reduce its pulse length (see Sect. 3.3.1.2). Bunching leads to an increase in the energy spread, making it difficult to optimize the focus and mass resolution at the same time.

In dealing with these limitations, it is important to choose the correct operational mode of a primary ion gun for a certain application. In general, it is possible to optimize only two of the three following beam characteristics at the same time: pulse current (a high pulse current corresponds to high sensitivity, high dynamic range of a measurement, or short acquisition times), pulse width (a short pulse width is necessary for a good mass resolution), and focus. A typical operational mode is the “spectroscopy” or “bunched” mode (pulse width less than 1 ns; pulsed ion currents of a few pA, focus of some microns). If a better lateral resolution is needed, one can either sacrifice beam current while still maintaining a short pulse width (good mass resolution) or work with long ion pulses (effectively unit mass resolution) while maintaining a high pulse current.

### ***3.3.2 Secondary Ion Separation and Detection: Time-of-Flight Analyzer***

In general, surface material is limited. There are only approximately  $10^6$  molecules in an area of a square micron, and the analyte of interest is usually a minor component in the sample (as it is often in biological applications, such as when tracing the active ingredient of a drug in a cell). Knowing that the secondary ion yield—the portion of molecules that are successfully transformed from their state in the sample into secondary ions, which then can be detected by a mass spectrometer—is in the best cases in the percent range, but more often several orders of magnitude smaller, makes the task of ion separation and detection even more demanding. In order not to lose any information, an efficient and parallel detection of almost all generated secondary ions is of high interest. For this purpose, the time-of-flight (ToF) analyzer is superior to most other mass-spectrometric analyzer systems [49].

A linear ToF analyzer typically consists of an accelerating section and a drift section. In the accelerating section, all generated secondary ions of a given polarity are accelerated to the same nominal kinetic energy. The resulting velocities of these secondary ions depend on their mass-to-charge ratio. The accelerated ions are then transferred into the drift section. The drift section allows for a field-free drift of the ions. As the velocity of the secondary ions differs, they are mass-separated on their way to the detector: Faster (i.e., lighter) secondary ions arrive earlier at the detector than slower (i.e., heavier) ions.

Due to the strength and the direction of the individual recoils responsible for desorption, secondary ions already have initial velocities, which are added to the velocity they gain in the acceleration section of the mass spectrometer. As these



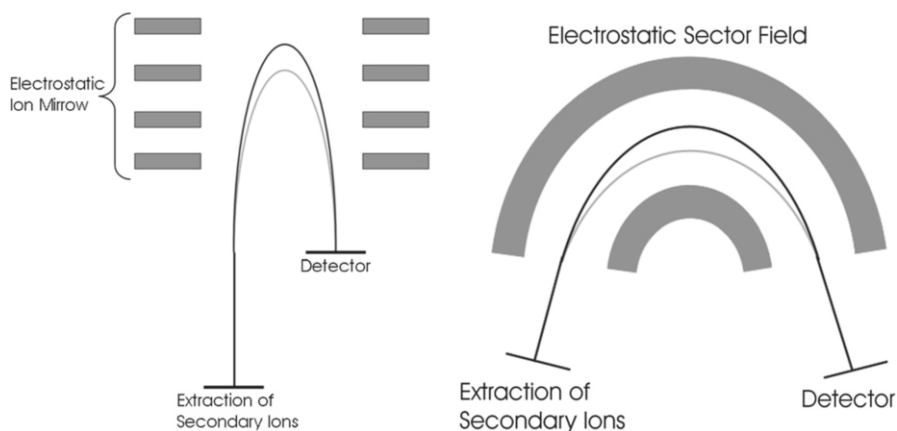


**Fig. 3.2** Schematic designs of a reflectron (electrostatic mirror) analyzer (*left*) and a sector field analyzer (*right*). Secondary ions with a higher initial kinetic energy (*dark trace*) are sent on a longer path compared to ions with a lower initial kinetic energy (*light trace*)

initial velocities are not all the same, the separation process is hampered. To compensate for this effect, most ToF-SIMS instruments today are equipped with an energy-focusing analyzer. The basic idea of such a device is to increase the flight path of ions with a higher initial velocity compared to ions of the same mass-to-charge ratio with a lower initial velocity. For this purpose, electrostatic fields can be used that act as an ion mirror (a so-called reflectron; Fig. 3.2). As high-energy ions of one species penetrate deeper into this electrostatic field, their flight paths are longer than those of ions of a lower initial energy. Under optimal alignment of the reflectron, all secondary ions of the same mass-to charge ratio arrive at the detector after the same flight time. A second option for energy focusing used in ToF-SIMS is the electrostatic sector analyzer (Fig. 3.2). Within the radius of the electrostatic sector analyzer, the drift paths of higher-energy ions are longer than those of lower-energy ions [49]. Modern ToF-SIMS instruments equipped with either of these devices achieve mass resolutions (FWHM) of more than 10,000.

Ion detection is performed using a multichannel plate configuration. The individual design—for instance, a double-channel plate arrangement (Chevron) or a combination of channel plate, scintillator, and photomultiplier (Daly–Thompson)—can vary, but the basic principle is the same: Each impact of an incoming ion causes an electrical signal, which is amplified and then registered.

### 3.3.3 Charge Compensation

The impact of primary ions and the desorption of charged particles (secondary ions and even to a greater extent secondary electrons) lead to charging of the bombarded area. On conductive samples, this net charge is instantly dissipated. However,

insulating samples can keep a localized charge for a long time, which affects the analysis. Not only is the primary beam deflected, which can degrade the lateral resolution, but—even more important—charging affects the extraction of secondary ions by nonuniformly changing the extraction field close to the analyzed surface. Depending on the sample's conductivity, the path of secondary ions is deflected from the default path through the mass spectrometer, resulting in a poor mass resolution or, in the worst case, in a complete loss of transmission to the detector.

To avoid such artifacts, charge compensation is included in modern ToF-SIMS instruments. The sample is flooded with low-energy electrons supplied by a heated filament between the primary ion pulses. The low-energy electrons are attracted by positively charged sample regions, leading to a self-adjustment of the whole surface to a uniform potential. It should be noted that even electrons of some 10 eV of energy can destroy certain organic bonds and change the sample being analyzed. Thus, minimizing the charge compensation is desired [50, 51].

### 3.3.4 Technology of Sputtering (Depth Profiling)

Depth-profiling methods are used to sample subsurface regions of samples. Depth profiles are generated by using a sputter source to erode the topmost layer of the sample surface using massive ion bombardment between analysis cycles. It is of importance to note that the pulsed nature of ToF-SIMS spectral or image analysis does not (significantly) erode the sample; thus, erosion during a depth profile is often performed using a quasi-DC ion beam. For the sputter erosion, either the primary ion beam utilized for analysis can be used or, in the more convenient case, the instrument is equipped with a second ion beam system, which is optimized for material removal (dual-beam approach [46]). There are two advantages of dual-beam depth profiling compared to single-beam depth profiling, described next.

First, the number of primary ions in an analysis mode is not adequate for a quick sputtering of the surface. Thus, in the single-beam setup, a second setting for the voltages and timing of the primary ion gun has to be used, allowing an enhanced bombardment of the surface. Constant switching from one setting to another is time-consuming. In contrast, in dual-beam mode, the time needed for analyzing the secondary ions (while they are drifting through the ToF-MS) can already be used in many cases for sputtering (interlaced mode).

Second, the sputter ion species, energy, and angle of incidence can be chosen independently from the analysis ion in the dual-beam approach. Thus, low-energy ions or a cluster ion beam such as  $C_{60}$  can be used for sputtering in order to obtain a high depth resolution and/or low damage of the remaining material on the sputtered surface, whereas high-energy ions (e.g., from an LMIS), which can be well focused, are used to analyze the center of the crater. A typical setup for the analysis of biological systems uses  $C_{60}^{y+}$  ions for sputtering and  $Bi_3^+$  for high-lateral resolution analysis of the sample [52] (see also the advantages and disadvantages of the different ion sources as discussed in Sect. 3.3.1.1).

## 3.4 Operational Modes

### 3.4.1 Overview

As shown in Table 3.1, ToF-SIMS analysis can be performed in four different operational modes, which are demonstrated on different samples in Figs. 3.3, 3.4, 3.5, and 3.6. One differentiation among operational modes is between those where (almost) no sample erosion takes place (static SIMS) and those where sample erosion is performed (dynamic SIMS). Furthermore, one can distinguish between measurements where lateral distributions of analytes are probed or not.

The simplest operational mode is the spectrometry mode (low sample erosion, no lateral probing). The result of this type of measurement is displayed as a mass spectrum, as is well known from other mass-spectrometric techniques (Fig. 3.3). Information on the chemical composition of a surface can be gained from such a spectrum. All ToF-SIMS measurements start by using this mode.

More complex is the imaging mode (low sample erosion, lateral probing). In most cases, a focused primary ion beam is rastered in both the  $x$ - and  $y$ -directions over the sample surface. A full mass spectrum is collected at every pixel, and a few user-selected species are monitored during data collection. A square of  $256 \times 256$  pixels leads to a data set of 65,536 individual spectra. The raw data taken from this kind of experiment can be presented in various ways; for instance, spectra can be retrospectively generated from any subset of pixels. Most frequently, the data are presented in mass-resolved images (Fig. 3.4). The intensity of one secondary ion species in each of the pixels is represented according to a color scale, leading to a two-dimensional image of the surface. It is noteworthy that ToF-SIMS allows the simultaneous generation of a mass-resolved image for any detected secondary ion.

When a depth profile is being performed, the spectrometric data acquisition is alternately interrupted by a sputter process eroding the surface. Thus, a small region of the sample is destroyed when this process is used: The erosion process leads to the formation of a sputter crater. The analysis area is typically centered in this crater. For every analysis cycle, the complete spectrum is stored in a raw data stream. Therefore, mass spectra from different depths of the sample can be gained. The intensity of an analyte can be plotted against the time needed for sputtering (Fig. 3.5). Thus, the vertical distribution of any detected secondary ion within the sample can be probed.

Three-dimensional analysis is performed by combining the imaging mode with sputtering of the sample. Thus, a three-dimensional representation of the detected

**Table 3.1** Operational modes in ToF-SIMS

	With low erosion (static SIMS)	With erosion (sputtering) (dynamic SIMS)
Without lateral resolution	Spectrometry (Fig. 3.3)	Depth profiling (Fig. 3.5)
With lateral resolution	Imaging (Fig. 3.4)	3D microarea analysis (Fig. 3.6)

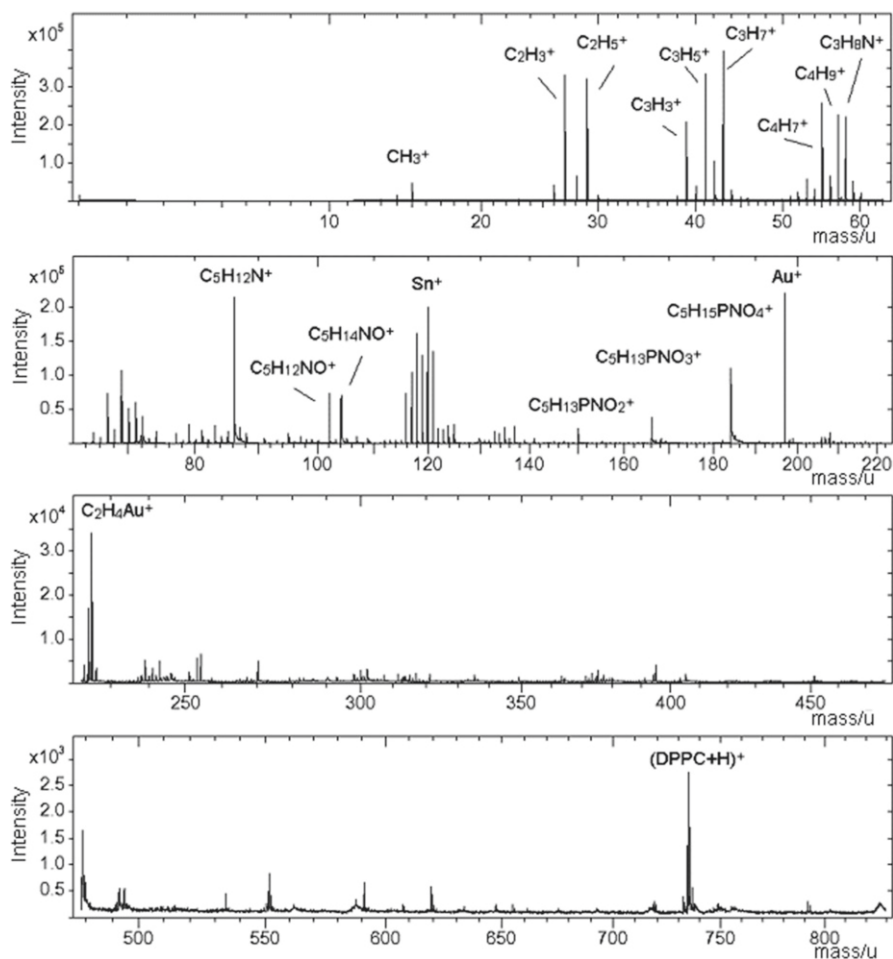


**Fig. 3.3** ToF-SIMS spectrum of positively charged secondary ions detected on a pure monolayer of the lipid DPPC (dipalmitoyl phosphatidylcholine) on a gold- and tin-containing substrate

analytes can be obtained (Fig. 3.6). The amount of data generated in this approach is enormous: For each depth, a complete set of image data (e.g., 65,536 spectra for a raster of  $256 \times 256$  pixels) is acquired. In the example shown in Fig. 3.6, image acquisition was performed in 120 depths. Thus, almost 7.9 million spectra were generated. To present the data, virtual  $xy$ -,  $xz$ -, and  $yz$ -sections can be reconstructed from the raw data stream. One must keep in mind when interpreting the 3D data that the sections are not one-to-one representations of the spatial distribution of analytes. This is due to the fact that even in the ideal case of uniform erosion by the sputter process, which is not always true especially for nonhomogeneous materials, the original sample surface is quite often not flat. Thus, for example, the sodium signal

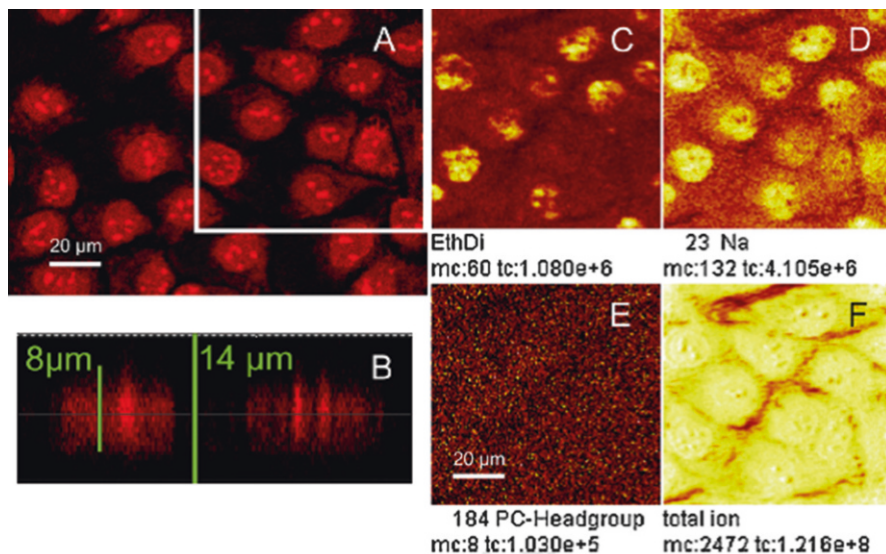


**Fig. 3.4** The DNA-staining fluorophore ethidium homodimer (“EthDI”) was detected by confocal scanning microscopy (a, b) as well as by ToF-SIMS imaging (c). Due to the low information depth, the lipids covering the nuclei had to be removed by appropriate fixation protocols in order to allow a ToF-SIMS 2D imaging of the nuclei (Reprinted from Ref. [79] with permission)

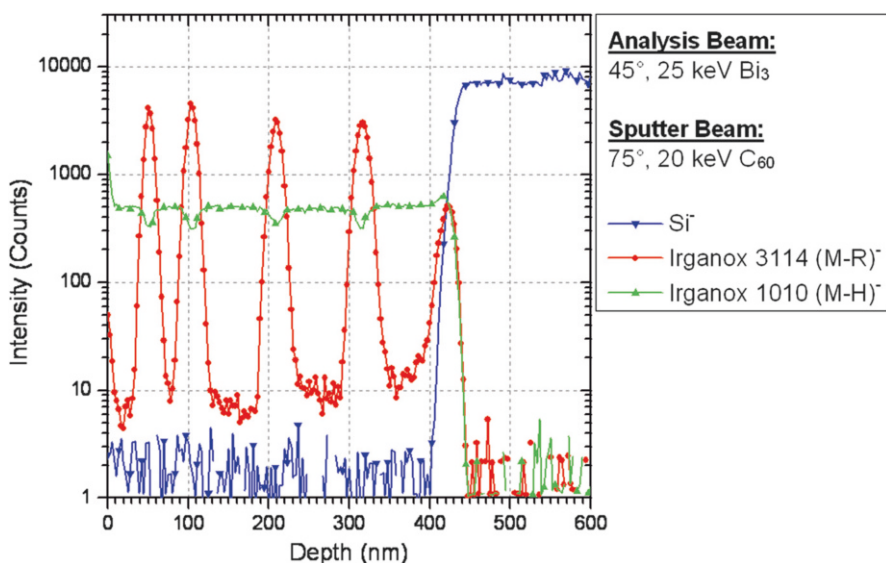


**Fig. 3.5** Depth profile of a layered polymer system (5 Irganox 3114 delta layers in an Irganox 1010 matrix) obtained in dual-beam mode, sputtering with a 20-keV C<sub>60</sub> beam, analysis with a 25-keV Bi<sub>3</sub> beam, sputter angle: 45°; sample rotation

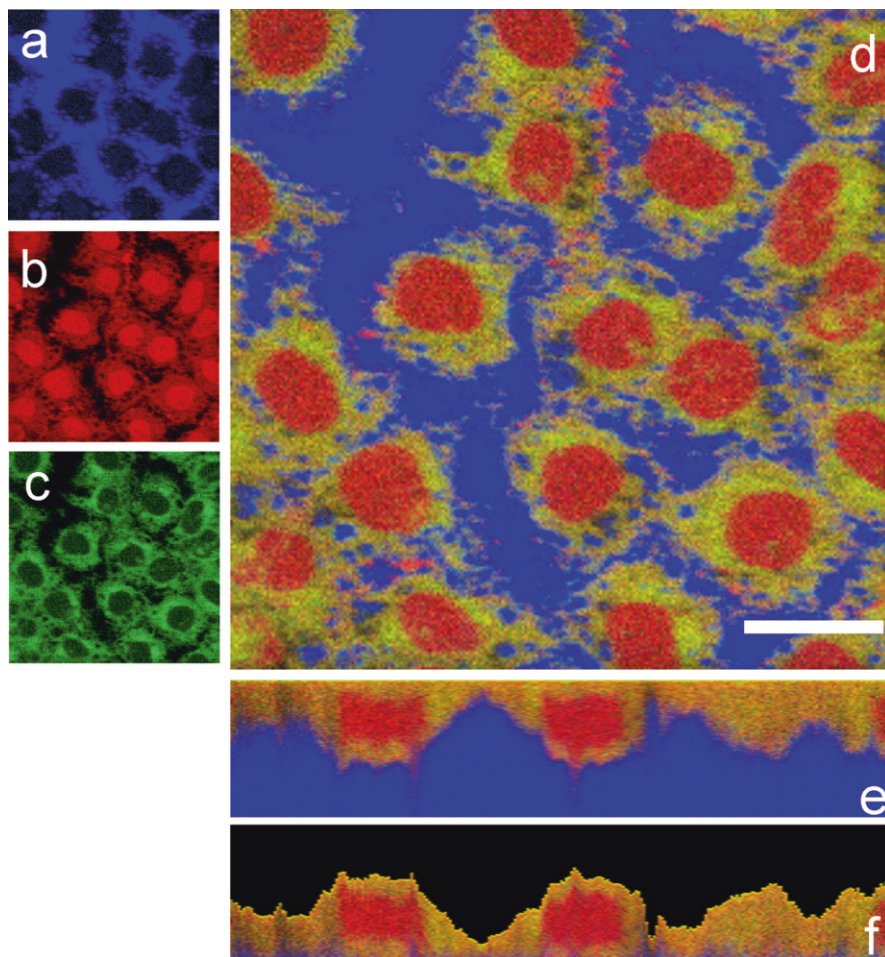


**Fig. 3.6** Three-dimensional ToF-SIMS analysis of glutaraldehyde-fixed normal rat kidney (NRK) cells (*red–green–blue* color overlay for a correlation analysis). **(a)–(d)** Horizontal *xy*-sections. The scale bar in **(d)** corresponds to 20  $\mu\text{m}$ . Pooled signals of amino acid fragment ions are represented in *red* **(b)**, those of phospholipids in *green* **(c)**, and substrate-derived secondary ions are depicted in *blue* **(a)**. **(e)** Vertical *xz*-sections; and **(f)** mathematically corrected *xz*-section showing the topography of the cells on the substrate, which is assumed to be flat (Reproduced with permission from Ref. [169])

in Fig. 3.6e derived from the plain glass substrate does not show up in an even *z*-layer but rather reflects the initial inhomogeneous topography of the surface. Software algorithms are being developed to correct for these effects.

In the following sections, the operational modes will be discussed in more detail. The discussion will focus on their use for biochemical applications.

### 3.4.2 Spectrometry

Analyzing the sample in spectrometry mode is reasonable if the aim of the analysis is to obtain laterally non-resolved information on the first three outermost monolayers of the sample. A ToF-SIMS spectrum of a pure monolayer of the lipid dipalmitoyl phosphatidylcholine (DPPC) on an Au- and Sn-containing substrate is shown as an example in Fig. 3.3. Besides the inorganic substrate ions (e.g., Au<sup>+</sup> and Sn<sup>+</sup>), quasi-molecular ions (e.g., DPPC+H<sup>+</sup>) and fragment ions of the analyte can be detected. The strength of ToF-SIMS analysis in spectrometry mode is that it allows a simultaneous detection of various types of analytes. It is limited to neither one-component systems nor to a certain type of species. In the following, a short overview of spectrometric studies of biological systems with ToF-SIMS is given.

Since the molecular mass of typical lipid molecules is ideal for detection with ToF-SIMS, the analysis of all types of lipids is a focus of ToF-SIMS research. Whereas high-mass biopolymers usually fragment during ToF-SIMS analysis, and most often statistical evaluation procedures have to be used for identification, lipids can routinely be detected as quasi-molecular ions. More information on lipid detection can be found in the imaging section (see Sect. 3.4.3).

ToF-SIMS spectra of proteins are typically dominated by amino acid fragments (NH<sub>2</sub>CHR<sup>+</sup>, with R = amino acid residue) [53–55].<sup>1</sup> However, protein analysis is not limited to the detection of these fragments; larger ions [56] and even intact small proteins and peptides up to a mass of approximately 10,000 u can be detected when adequate sample preparation and analysis protocol are followed. Examples for intact protein detection are found for angiotensin ( $M=1,045$  u) and its derivatives [54], the B-chain ( $M=3,496$  u) as well as the complete molecule ( $M=5,778$  u) of insulin [57], porcine renin ( $M=1,759$  u), and bovine ubiquitin ( $M=8,563$  u) [58]. Besides these single-component systems, protein mixtures of adsorbed multicomponent protein films were analyzed by Wagner et al. [59]. A very interesting approach is the detection and identification of tryptic peptides of a protein by ToF-SIMS [60–62].

Although DNA oligomers were found to fragment [58, 63, 64], May et al. [65] were able to distinguish representatives of this molecular species by statistical evaluation procedures (see Sect. 3.5). In addition, they give a comprehensive overview of the ToF-SIMS fragmentation patterns of nucleobases, nucleosides, and nucleotides. Another example for analyzing multiple-component systems of nucleic acids is the analysis of combined DNA and peptide nucleic acid (PNA) samples by Arlinghaus et al. [66].

In addition to lipid, protein, and DNA samples, other biotic and xenobiotic substances have also been analyzed: The analysis of different monosaccharides leads to the detection of quasi-molecular ions as well as typical fragmentation patterns [67]. In other studies, spectra of fluorophores [68–70], bone minerals [71], or pharmaceuticals [29, 72, 73] are presented.

---

<sup>1</sup>Lists of the composition and mass-to-charge ratio of typical secondary ions characteristic of amino acids can be found, for example, in a study by Michel et al. [55].

In principle, any biochemically relevant substance that is vacuum-sustainable can be analyzed. Whereas molecules larger than 2,000 u most often fragment, the chance to detect quasi-molecular ions of smaller molecules is high when polyatomic primary ion sources are used. Of note, in some cases spectrometric data can be used for semiquantitative evaluation. A striking example is the determination of an enzyme activity in correlation with the ToF-SIMS signal intensities of its substrate and product [74]. Good examples are also found for self-assembled monolayers [75], ethanolamin [76], and proteins [77].

### 3.4.3 *Imaging*

Mass-resolved images are most often interpreted to represent at least semiquantitatively the distribution of the analyte on the surface of the sample. In doing so, it has to be kept in mind that the simple approach of assuming a linear correlation of the secondary ion signal with the surface concentration of a species may lead to misinterpretation. This is due to the fact that in SIMS the number of desorbed secondary ions is a function not only of the surface concentration but also of the respective chemical environment (matrix effect), which can influence the ionization probability [15] as well as the sputter yield [78] by up to several orders of magnitude. However, a semiquantitative interpretation of images in biomolecular applications is still often possible, because the general matrix does not radically change over the area of an image. Since secondary ion yields of different species can vary by several orders of magnitude, the information accompanying a secondary ion image should include not only the field of view but also the number of ions detected in the complete image as well as in the brightest pixel in order to allow data interpretation with respect to statistical consideration.

An example for mass-resolved secondary ion images is shown in Fig. 3.4 [79]. The DNA of epithelial cells [normal rat kidney (NRK) cells] has been stained with the fluorophore ethidium homodimer (“EthDI”), which allows the localization of the nuclei by confocal scanning microscopy (Fig. 3.4a, b). The corresponding secondary ion maps (Fig. 3.4c) demonstrate that ToF-SIMS is also able to detect EthDI, showing the same lateral distribution. Due to the low information depth, the lipids covering the nuclei had to be removed by appropriate fixation protocols in order to allow a ToF-SIMS 2D imaging of the nuclei. For a more detailed discussion of this example, see [79]. It is of importance to note that staining or labeling is not required for ToF-SIMS. For the study mentioned here, it was required for the confocal scanning microscopy analysis only.

In the following, three areas of biochemical imaging applications in which ToF-SIMS has been delivering important results are discussed in more detail: the analysis of thin monolayer films (Langmuir–Blodgett films or self-assembled monolayers, Sect. 3.4.3.1); the analysis of tissue sections (Sect. 3.4.3.2); and the analysis of cell culture samples (Sect. 3.4.3.3).



### 3.4.3.1 Langmuir–Blodgett Films/Self-Assembled Monolayers

Langmuir–Blodgett (LB) films and self-assembled monolayers (SAM) are comparatively well-defined organic systems that came early in the scope of molecular imaging by ToF-SIMS [1] because of the perfect match of the surface sensitivity of ToF-SIMS with the monolayer nature of LB films and SAMs.

Generating Langmuir–Blodgett films is comparatively easy: Lipid mixtures are spread onto the water or buffer surface of a film balance, where their hydrophilic end is oriented to the water/buffer. These layers are subsequently transferred onto a substrate [80]. Usually, gold-coated glass [81, 82] or mica [83, 84] substrates are used for ToF-SIMS applications in order to allow an easier ionization (see Sect. 3.5.1) and to avoid a charging of the surface. Alternatively, SiO<sub>2</sub>/Si substrates can be used [85]. ToF-SIMS analysis of LB systems allows a view of the mixing behavior as well as on the phase behavior of the involved materials: One early publication observing both phenomena was published by Leufgen et al. [69], which describes the distribution of a native lipid (DPPC) and one of its fluorescent dye analogs. Thus, the distribution of the dye could be probed by two different techniques: by fluorescent light microscopy as well as by ToF-SIMS. As can be seen in this and other studies, fluorescence microscopy [81, 86, 87] and also atomic force microscopy [86, 88, 89] can be used to validate ToF-SIMS results.

A close correlation of a model system to the real-world environment is found for studies on LB films of pulmonary surfactants [81, 82, 86, 90, 91]. A pulmonary surfactant is a lipid/protein mixture preventing alveolar collapse in the mammalian lung. These studies aim to detect a protein-induced lipid demixing, necessary for lipid-enrichment processes in the mammalian body. They are accompanied by experiments where the complete extract of lipids and hydrophobic proteins from bovine lungs is analyzed [87].

The use of deuterated lipids in Langmuir–Blodgett studies has also been demonstrated [83, 86]. Here, hydrogen atoms in certain lipids have been replaced with the heavier isotope of hydrogen (deuterium), thereby placing a unique marker into one of the lipids. Using this strategy, researchers have distinguished similar lipids during ToF-SIMS analysis by their isotopic label, using care so that the mixing and phase behavior do not significantly change upon isotopic labeling [86].

The so-called raft theory, which, in short, predicts that cell membrane contains cholesterol-rich micro domains [92], increased the interest in protein/lipid model systems. Therefore, recent studies have dealt with lipid and lipid/protein model systems expected to be relevant for raft formation [93]. Nevertheless, it has to be pointed out that the expected size of rafts (down to 25 nm [94]) is smaller than the lateral resolution of ToF-SIMS (down to 100 nm, [29]).

It is noteworthy that artifacts were observed using ToF-SIMS for imaging and semiquantitative analysis of Langmuir–Blodgett films. Sostarecz et al. reported higher yields of DPPC-specific fragments in an expanded film, where the molecules are loosely packed, compared to a condensed film, where the molecules are densely packed in a well-ordered manner [85]. This finding does not correlate with the expected molecule density, which is higher in a condensed film. Biesinger et al. reported an

inversion of yield contrast upon exceeding the static limit on Langmuir–Blodgett films [84]. Both studies were performed under monoatomic bombardment, and thus further studies under polyatomic bombardment would be of interest.

Self-assembled mono- and multilayer systems offer another opportunity to benefit from the surface sensitivity of ToF-SIMS [95–99]. Most often they are used as model systems for the determination of ToF-SIMS-specific features. Nevertheless, other analytical questions, such as the temperature dependence of the stability of these systems [100], can be addressed. Finally, it is also possible to analyze freeze-dried supported bilayers and compare the respective ToF-SIMS results to those obtained from Langmuir–Blodgett films and bulk material of identical composition [101].

### 3.4.3.2 Tissue Sections

Tissue sections are found to be good ToF-SIMS samples because they expose the area of interest and the analyte and make them directly available for analysis. The avoidance of sample contamination by lubricants or other unwanted substances during the preparation of the tissue section is critical for a successful analysis—this is not unique to ToF-SIMS. For this reason, the use of fixatives and cryoprotectives is also not reasonable. As summarized by Richter et al. [102], to date two preparation methods are available: (1) cryofixation followed by freeze-fractioning and freeze-drying or (2) plunge-freezing and cryostat slicing followed by freeze-drying are applied to the sample. From a technological point of view, the recent development of a combined cryosectioning and ToF-SIMS instrument is interesting [103] because the dehydration step can be avoided.

Meanwhile, a noticeable number of ToF-SIMS imaging studies on tissue sections have been published: For example, the distributions of triglycerides, phospholipids, cholesterol, and fatty acids in mouse brain [104–106] and freshwater snail brain [107] sections were analyzed. In other studies, a part of a rat brain, the cerebellar cortex, was probed by ToF-SIMS imaging. It has been possible to detect the distribution of cholesterol and galactosylceramides in different cell types of these tissue sections [48, 108]. In an earlier work, Nygren et al. were able to visualize the distribution of phosphatidylcholine [109], among other substances, and with the help of metal-enhanced SIMS (see Sect. 3.5.1) the distribution of cholesterol [110] in rat kidney. Another group obtained information on the cellular metabolism in the leg section of model mice with Duchenne muscular dystrophy by identifying the distribution of various lipids within the sample [111]. Furthermore, the identification of different tissue types in human adipose tissue gained by biopsy was possible by determining the lipid distribution [112]. Finally, the distribution of different types of diacylglycerides was detected inside and outside certain vesicles in steatotic (i.e., fatty) liver samples [113].

A noteworthy paper by Brunelle et al. [3], which also includes a review of biological tissue imaging by ToF-SIMS, describes a study comparing ToF-SIMS and MALDI-MS results on a single rat brain section. This study and a later study by Monroe on a spinal cord section [114] show the complementary nature of these two

techniques: Whereas first a number of (small-sized) lipids could be probed by ToF-SIMS, MALDI-MS was able to detect (larger-sized) peptides on the same sample. It is noteworthy that while ToF-SIMS was performed without further sample treatment and basically nondestructively, MALDI analysis required the application of a matrix and consumed the sample by ablation of surface material.

### 3.4.3.3 Single-Cell Analysis

Similar to the analysis of tissue sections, the adequate preparation of the sample is the crucial step in the analysis of single cells. One approach is the freeze-drying of cells, with subsequent analysis of their surfaces [115, 116], resulting in the visualization of the distribution of cholesterol on the respective cell surfaces. However, such approaches may lead to artifacts due to contaminations derived from the cell culture medium. Additional washing steps, as shown by Berman et al. [117], may better help to circumvent this challenge.

In another approach, Fartmann et al. analyzed freeze-fractured and freeze-dried osteoblasts, which were cultured on silicon, thus obtaining hydrocarbon signals [118]. The freeze fracturing was performed using a sandwich method and is similar to the protocol used in other studies: Polystyrene beads were added to the buffer solution before a second silicon wafer was placed on top of the sample. After rapid cool down in nitrogen-cooled propane, the fracturing was performed by disruption of the two silicon wafer pieces [70, 119, 120]. It is worth noting that some research groups [121] can perform the critical preparation steps under vacuum conditions within a ToF-SIMS instrument, minimizing the risk of contamination.

Vaidyanathan et al. [122] go to the other extreme: They were able to image heat-fixed bacteria populations. Other groups preserved the cell by vitrification in trehalose [123]. Monroe et al. successfully detected the distribution of vitamin E on a single neuron [124], not giving information on their sample preparation procedure.

Sjövall and coworkers used an imprinting method for the preparation of leukocyte samples. Following a rinsing and freeze-drying procedure, Sjövall and his group obtained imprints of cells by applying pressure to a silver foil covering the sample. Thus, they were able to detect phosphocholine- and cholesterol-derived signals [125].

Finally, chemical fixation procedures allow a ToF-SIMS view into the cell. The incubation of methanol/acetic acid into cells flushes away the lipidic membrane components [126]. This approach was first introduced by Levi-Setti for dynamic SIMS [22, 127]. In 2009, a combined analysis of a xenobiotic fluorophore inside a cell by confocal laser scanning microscopy and (static) ToF-SIMS [79] was reported.

The choice of a specific preparation procedure is often based on the analytical question. However, quite often it is also governed by the abilities and equipment of the respective laboratories. Unfortunately, comparative studies on preparation procedures are not yet available. Those studies could improve our understanding of how the different abilities of individual preparation procedures influence analytical results. In particular, they would give valuable information on possible chemical changes of the specimen during preparation.

#### 3.4.3.4 Other Imaging Applications

A number of studies deal with model systems or real-world samples different than those discussed in the previous sections. Among those are the analyses of pulp [128] and paper [129], which are of interest for their respective industries. Also, wood-containing artwork has been analyzed [130]. Other sample systems analyzed with ToF-SIMS comprise biochips [131, 132] and micropatterned biomolecular surfaces [133]. Protein adsorption on surfaces relevant for medical applications [134] or cell culturing [135] has also been studied.

#### 3.4.4 Depth Profiling

In ToF-SIMS, the term “depth profiling” is used for the in-depth probing of a sample without obtaining information on the lateral distribution of the analyte. Thus, this approach is useful for well-defined layered samples. As most biological samples do not belong to this class, this application mode is rarely used in the biochemical field. To get an idea on the type of data usually obtained by depth profiling, the results of the analysis of a layered polymer system are shown in Fig. 3.5 [136]. The sample consists of five Irganox 3114 delta layers at depths of 50 nm, 100 nm, 200 nm, 300 nm, and 400 nm in an Irganox 1010 matrix. It has been produced and provided by NPL and is described in detail elsewhere [137]. The profile was acquired under sample rotation while sputtering with  $C_{60}$  and performing parallel analysis with  $Bi_3$  cluster primary ions. Many different parameters (sputter ion species and energy, sample temperature, etc.) determine the success of an organic depth profile. To describe the details is beyond the scope of this chapter. An up-to-date review was given by Mahoney [43].

Although—as stated—depth profiling is not ideally suited for biochemical analysis, a limited number of publications dealing with it are available. Most of these studies focus on the investigation of ToF-SIMS-specific properties. For example, Sostarecz et al. [138] analyzed multiple Langmuir–Blodgett film of barium arachidate by  $C_{60}$  depth profiling, finding the sputter yield to be higher by a factor of 100 compared to that of gallium. Cheng and Winograd depth-profiled a peptide-doped trehalose film with a  $C_{60}$  source that was spin-coated on silicon [44, 139]. They were able to detect intact peptide ions up to a mass of 500 u after sputtering. Although the intensities of the secondary ions characteristic for the peptide decrease upon continuous  $C_{60}$  bombardment, these results suggest the possibility of 3D analysis of biological samples.

#### 3.4.5 3D Microarea Analysis

In recent years, the first examples for three-dimensional analyses of biological samples have been presented. Most studies show the general possibility for the detection

of organic molecules in deeper layers without being able to accurately represent the expected distribution of molecular components in a cell, for example [140]. Breitenstein et al. [52] developed and published a protocol to provide the correct 3D distribution of components in glutardialdehyde-fixed normal rat kidney (NRK) cells (see Fig. 3.6). The spatial distributions of amino acids (fragments of proteins in the nuclei) and phospholipids (cell walls) as detected by ToF-SIMS correspond well to control experiments by confocal light microscopy, a well-established technique in the biological field after the ToF-SIMS data are corrected in 3D. There are a number of other 3D analyses of biological samples: In one study, Vaidyanathan et al. [122] show images of the surface as well as of a deeper layer of a bacteria sample. Another example deals with the analysis of thyroid tumor cells [141].

There are certainly a number of aspects that can be criticized in all 3D analyses of biological material with ToF-SIMS. To date, the scientific output is limited. While it is possible to detect the phosphatidylcholine and amino acid distribution in cells, other components were not detected or at least not shown in the publications. In addition, recent studies on trehalose films indicate that the sputtering process does not uniformly erode the samples [142]. As the representation of the data in all studies is based on the estimation of uniform erosion, the results are most likely displayed in a distorted way. Nevertheless, from a technological point of view, these first results are very promising. A condensed overview of 3D molecular imaging is given by Delcorte [143].

## 3.5 Improvement of Data Quality

In addition to further developments in instrumentation, two major strategies for improving data acquisition and data evaluation are currently being considered: On the one hand, the secondary ionization probability of ToF-SIMS is relatively low. An enhancement of ionization would be beneficial for ToF-SIMS analysts. On the other hand, the enormous wealth of data—even with these low ionization probabilities—is hampering an easy (manual) evaluation of the data. Therefore, statistical methods are applied to facilitate data evaluation and interpretation.

### 3.5.1 *Enhancement of Secondary Ionization Probability*

Only approximately 1%—and in many cases even less—of the ejected particles upon primary ion impact are charged and thus available for mass-spectrometric analysis. The increase in the secondary ionization probability is therefore a useful strategy to obtain better results. Three approaches will be briefly discussed in this section. However, the reader should keep in mind that these approaches are not generally applicable and are therefore limited to special conditions and samples.

One option for improvement is given by the postionization of the ejected neutral particles, which constitute the majority of the sputtered particles. Postionization can be achieved either by electrons (e-beam or plasma) or, more promisingly, by photons (laser secondary neutral mass spectrometry, laser-SNMS). While laser-SNMS is often able to selectively increase the ionization probability of certain species by several orders of magnitude (e.g., one element or a certain class of molecules in a resonant ionization scheme), it has not yet been possible to universally increase the ionization probability for all species in parallel. Since a full discussion is beyond the focus of this article, the reader is referred to some (rather old but still comprehensive) book sections [144, 145] and a more recent research article [146] for further information.

The following two strategies can be employed using standard ToF-SIMS instrumentation. An enhancement of the secondary ionization probability can be achieved in several cases using matrices known from MALDI (matrix-enhanced SIMS, ME-SIMS) [57, 73, 107, 116, 147]. Another approach to enhance the secondary ionization probability is the use of metal cationization, where a metal ion combines with a sputtered (neutral) molecule ([molecule + metal]<sup>+</sup>) (meta-SIMS) [48, 72, 115, 116, 148–151]. This can be achieved with the use of thin gold or silver coatings on the samples or by the preparation of an analyte as a (sub-) monolayer on a suitable metal substrate. Whereas in meta-SIMS the cationization of a molecule by a sputtered metal ion leads to a higher efficiency, the effects of MALDI matrices are more multifaceted [152]. Nevertheless, many of these effects can be directly or indirectly allocated to an increased sputter desorption of surface material. Most of the ME- and meta-SIMS studies were performed under monoatomic primary ion bombardment. Therefore, the question of whether the enhancement is still detectable under polyatomic bombardment is currently under investigation. The state of the art in ME- and meta-SIMS was described by Delcorte in 2006 [152].

### 3.5.2 *Statistical Evaluation*

The extraordinary wealth of data collected in each ToF-SIMS experiment requires elaborate evaluation routines. While in most cases data evaluation is still performed manually and relies heavily on the user's expertise, the use of multivariate statistical methods is becoming more and more relevant. An idea about the different mathematical approaches used for ToF-SIMS data evaluation can be gained by reading the introductory articles by Graham et al. [153], Tyler [154, 155], Milillo and Gardella [156], as well as Smentkowski et al. [157]. In the following, some examples for biochemical analytical questions, which were addressed using statistical tools, are given.

Kulp et al. were able to differentiate cell lysates by principal component analysis (PCA) [158]. Berman et al. could distinguish a number of monosaccharides from their spectra using PCA [67]. May et al. performed PCA on DNA oligomers [65], and Thompson et al. were able to discern bacilli by statistical methods [159].

Another interesting approach is the determination of conformational changes in proteins. For example, in native proteins, the hydrophobic amino acids are more commonly found in the interior of the protein than in denatured proteins. Thus, the spectral intensities of characteristic ions of these amino acids give an indication of the conformational state of a protein [160]. Nowadays, this kind of analysis can be nicely addressed by PCA [55].

The statistical tools are useful in the hands of an expert who understands the SIMS process and the mathematics behind the data evaluation, in order to validate or generate hypotheses. However, it has to be pointed out that without a thorough understanding, the tools might lead to misinterpretation of the data.

### 3.6 Specifications of TOF-SIMS

A scientist should always be aware of the physical and practical limits of an analysis by ToF-SIMS when addressing a problem with this technique. Many of these limits have been mentioned earlier in this chapter. Nevertheless, a condensed overview might (have) save(d) time for the “scan and skim” reader. Most of the limitations mentioned are matters of further scientific and engineering research and development.

ToF-SIMS is a vacuum technique. Therefore, the sample has to sustain the vacuum environment inside the instrument. For many volatile samples, this can be achieved by cooling. The sample size is usually limited by the size of the introduction chamber and the analysis chamber of the instrument. It is typically in the range of several cm in length and width and up to some 10 mm in height. However, for outgassing samples, the pumping rate of the vacuum system has to be considered, too. The actual analysis area is routinely up to  $500 \times 500 \mu\text{m}^2$ . In macro scan mode (when the stage with the sample is scanned under the primary ion beam and the mass analyzer), the analysis area can be up to several  $\text{cm}^2$  in size. However, samples have to be flat for this analysis mode. The mass range of ToF-SIMS—as of all time-of-flight mass-spectrometric techniques—is principally unlimited although the desorption and ionization process limits the practical achievable mass range to about 10,000 u [15]. The real strength of ToF-SIMS is in the detection of molecules in the range of several 100 to 2,000 u. The detection limit for these kinds of species is routinely in the femtomol to attomol per  $\mu\text{m}^2$  range. That means, for example, that  $2 \times 10^{-20}$  mol on an area of  $100 \times 100 \text{ nm}$  can be detected [28]. Some authors even claim to be able to detect an amount of a substance in the zeptomol range (4 attomol on a spot approximately 2 mm in diameter) [160]. Others have shown that proteins on a surface can be detected in an amount of size  $0.1 \text{ ng/cm}^2$  [161]. Thus, it can be estimated that detection limits in the picomol/ $\mu\text{m}^2$  range can be routinely obtained.

ToF-SIMS is a surface-sensitive analysis technique. The information depth is limited to the three uppermost monolayers [13], making ToF-SIMS useful for many analytical problems. However, this fact also necessitates—especially for biochemical samples—a contamination-free sample preparation. Quantification is difficult with ToF-SIMS. In general, semiquantitative information can be gained upon

comparison of two similar samples or different positions on one sample. The mass resolution [defined as the ratio of a mass  $m$  to the mass difference  $\Delta m$  of the next neighboring peak that can be resolved ( $R=m/\Delta m$ )] is in the range of 10,000. This means that a peak at mass 100.00 u can be distinguished from a peak at mass 100.01 u. The lateral resolution, which can be routinely obtained in imaging modes, is in the order of a few hundred nanometers [105]. Meanwhile, unpublished studies show better resolutions of down to 50 nm. Ultimately, the size of the collision cascade limits the lateral resolution in SIMS to approximately 30 nm [14]. The vertical resolution in depth profiling and 3D imaging was found to be some 10 nm in organic samples [135, 162]. For well-defined inorganic samples (e.g., in the semiconductor industry), a depth resolution of less than 1 nm can be obtained [45]. Therefore, it is likely that the ultimate limit of the vertical resolution in organic samples has not yet been reached.

It is rarely mentioned that mass resolution, lateral resolution, and analysis time (which is often equivalent to sensitivity) are part of the so-called magic triangle in ToF-SIMS: For technical reasons, only two of these three parameters can be optimized to an acceptable value in one experiment.

### 3.7 Perspectives

The use of ToF-SIMS for biomolecular analysis has made tremendous progress in the last 10 years. This was fueled to a great extent by technical developments, such as the widespread introduction of polyatomic primary ion sources. Developments in instruments are still continuing, focusing, on the one hand, on the design of primary ion sources with new species and better specifications. In particular, the development of gas cluster ion beam (GCIB) sources appears to be opening new perspectives on the field of biomolecular analysis [163, 164]. On the other hand, the instrumentation development is focused on the introduction of different analyzer systems (e.g., MS/MS [165]). This work is accompanied by more sample-focused research, including approaches to simplify cell tissue sample handling or treatments to increase ionization efficiencies (see also Sect. 3.5.1). The use of more sophisticated data evaluation routines should also be mentioned. Also promising is the increasing number of instruments available that combine ToF-SIMS with other surface-analytical techniques, making the immediate control of experimental results by complementary—and sometimes more established—techniques possible. Combination instruments with fluorescence microscopy [78], MALDI-ToF-MS [3, 113], AFM [166, 167], FTIR-microspectroscopy [112], and XPS [88] are currently available; others will certainly follow.

Beside these experimental improvements, it is agreed that there is a discrepancy between the already existing potentials of the technique and their exhaustion in the field of life sciences [168]. Certainly, biomolecular ToF-SIMS still suffers from the relatively low number of scientists applying this technique to biological samples. This is to some extent caused by the low availability of modern instruments, which



is likely related to their high cost. In addition, highly skilled personnel are needed to adequately prepare the sample and perform the ToF-SIMS measurements as well as the data workup and interpretation. In recent years, cooperation of experts from each particular field has become more common. It is likely that this type of cooperation will promote the field in upcoming years, as the different backgrounds offer a high synergy for progress.

The judgment of the potentials of ToF-SIMS in the area of life science applications is diverse: On the one hand, there are skeptics who doubt the ability of ToF-SIMS to become a standard application for answering complex questions in the life sciences. On the other hand, very optimistic views can be found, such as that in the paper entitled “The magic of cluster SIMS” in *Analytical Chemistry* [31]: “Every once in a while, a breakthrough propels a mature field into new dimensions—just as the discoveries of MALDI and ESI opened MS to biologists and, incidentally, racked up Nobel Prizes for their inventors. This sort of metamorphosis is currently under way in bioimaging because of the remarkable properties of cluster ion beam sources being used with secondary ion MS (SIMS)”. It is to hope that such ambitious goals rather propel than thwart the progress in this exciting but difficult field.

### 3.8 Acknowledgment

The authors thank Dr. Reinhard Kersting (from Tascon GmbH, Muenster) for additional proofreading. The samples shown in this review were prepared by Dr. Joachim Wegener, Dr. Christina Rommel, and Michael Seifert (all from the University of Münster in Germany). Writing this review has been financially supported by the European Union Framework Program 6 under grant number FP6-513698 (Toxdrop-Project).

### References

1. Pacholski ML, Winograd N. Imaging with mass spectrometry. *Chem Rev.* 1999;99:2977–3005.
2. Belu AM, Graham DJ, Castner DG. Time-of-flight secondary ion mass spectrometry: techniques and applications for the characterization of biomaterial surfaces. *Biomaterials.* 2003;24(21):3635–53.
3. Brunelle A, Touboul D, Laprevote O. Biological tissue imaging with time-of-flight secondary ion mass spectrometry. *J Mass Spectrom.* 2005;40:985–99.
4. McDonnell LA, Heeren RM. Imaging mass spectrometry. *Mass Spectrom Rev.* 2007;26(4):606–43.
5. Breitenstein D, et al. The chemical composition of animal cells and their intracellular compartments reconstructed from 3D mass spectrometry. *Angew Chem Int Ed Engl.* 2007;46(28):5332–5.
6. Benninghoven A. The history of static SIMS: a personal perspective. In: Vickerman JC, editor. *ToF-SIMS. Surface analysis by mass spectrometry.* Huddersfield: IM Publications; 2001. p. 41–74.

7. Guerquin-Kern J-L, et al. Progress in analytical imaging of the cell by dynamic secondary ion mass spectrometry (SIMS microscopy). *Biochim Biophys Acta*. 2005;1724:228–38.
8. Garrison BJ. Atoms, clusters and photons: energetic probes for mass spectrometry. *Appl Surf Sci*. 2006;252:6409–12.
9. Sigmund P. Theory of sputtering. I. Sputtering yield of amorphous and polycrystalline targets. *Phys Rev*. 1969;184:38.
10. Sigmund P. Erratum: theory of sputtering. I. Sputtering yield of amorphous and polycrystalline targets. *Phys Rev*. 1969;187:768.
11. Sigmund P. Collision theory of displacement damage, ion ranges, and sputtering. *Revue Roumaine de Physique*. 1972;1106(17):823.
12. Thompson MW. The energy spectrum of ejected atoms during the high energy sputtering of gold. *Philos Mag*. 1968;414(18):377.
13. Hagenhoff B, Rading D. Ion beam techniques: surface mass spectrometry. In: Rivière JC, Myhra S, editors. *Handbook of surface and interface analysis*. New York/Basel/Hong Kong: Marcel Dekker; 1998. p. 209–346.
14. Vickerman JC. TOF-SIMS: an overview. In: Vickerman JC, Briggs D, editors. *TOF-SIMS—surface analysis by mass spectrometry*. Manchester/Chichester: IM Publications; 2001.
15. Benninghoven A, Rüdenauer FG, Werner HW. Secondary ion mass spectrometry. Basic concepts, instrumental aspects, applications and trends. New York: Wiley; 1987. p. 761–949.
16. Hagenhoff B. High resolution surface analysis by TOF-SIMS. *Mikrochim Acta*. 2000;132:259–71.
17. Urbassek HM. Status of cascade theory. In: Vickerman JC, editor. *TOF-SIMS. Surface analysis by mass spectrometry*. Huddersfield: IM Publications; 2001. p. 139–60.
18. McLafferty FW, Turecek F. Interpretation of mass spectra. Mill Valley: University Science Books; 1993.
19. Chandra S. 3D subcellular imaging in cryogenically prepared single cells. *Appl Surf Sci*. 2004;231–232:467–9.
20. Galle P, et al. Subcellular localization of aluminium and indium in the rat kidney. *Appl Surf Sci*. 2004;231–232:475–8.
21. Chandra S, Smith DR, Morrison GH. Subcellular imaging by dynamic SIMS ion microscopy. *Anal Chem*. 2000;72(3):104A–14.
22. Levi-Setti R, et al. Ion microprobe imaging of  $^{44}\text{Ca}$ -labeled mammalian chromosomes. *Appl Surf Sci*. 2004;231–232:479–84.
23. Gillen G, Roberson SV. Preliminary evaluation of an SF-(5)+polyatomic primary ion beam for analysis of organic thin films by secondary ion mass spectrometry. *Rapid Commun Mass Spectrom*. 1998;12:1303–12.
24. Kötter F, Benninghoven A. Secondary ion emission from polymer surfaces under Ar<sup>+</sup>, Xe<sup>+</sup> and SF-(5)+ion bombardment. *Appl Surf Sci*. 1998;133:47–57.
25. Weibel DE, Lockyer N, Vickerman JC. C<sub>60</sub> cluster ion bombardment of organic surfaces. *Appl Surf Sci*. 2004;231–232:146–52.
26. Wong SCC, et al. Development of a C<sub>60</sub><sup>+</sup> ion gun for static SIMS and chemical imaging. *Appl Surf Sci*. 2003;203–204:219–22.
27. Weibel D, et al. A C<sub>60</sub> primary ion beam system for time of flight secondary ion mass spectrometry: its development and secondary ion yield characteristics. *Anal Chem*. 2003;75(7):1754–64.
28. Davies N, et al. Development and experimental application of a gold liquid metal ion source. *Appl Surf Sci*. 2003;203–204:223–7.
29. Kollmer F. Cluster primary ion bombardment of organic materials. *Appl Surf Sci*. 2004;231–232:153–8.
30. Russo MF, Wojciechowski IA, Garrison BJ. Sputtering of amorphous ice induced by C<sub>60</sub> and Au<sub>3</sub> clusters. *Appl Surf Sci*. 2006;252:6423–5.
31. Winograd N. The magic of cluster SIMS. *Anal Chem*. 2005;77(7):143A–9A. doi:10.1021/ac053355f.

32. Wucher A. Molecular secondary ion formation under cluster bombardment: a fundamental review. *Appl Surf Sci.* 2006;252:6482–9.
33. Benguerba M, et al. Impact of slow gold cluster on various solids: non-linear effects in secondary emission. *Nucl Instrum Meth B.* 1991;62:8–22.
34. Kersting R, et al. Influence of primary ion bombardment conditions on the emission of molecular secondary ions. *Appl Surf Sci.* 2004;231/232:261–4.
35. Castner D. Surface science: view from the edge. *Nature.* 2003;422:129–30.
36. Kötter F, Benninghoven A. Secondary ion emission from polymer surfaces under  $\text{Ar}^+$ ,  $\text{Xe}^+$  and  $\text{SF}_5^+$  ion bombardment. *Appl Surf Sci.* 1998;133:47–57.
37. Stapel D, Brox O, Benninghoven A. Secondary ion emission from arachidic acid LB-layers under  $\text{Ar}^+$ ,  $\text{Xe}^+$ ,  $\text{Ga}^+$  and  $\text{SF}_5^+$  primary ion bombardment. *Appl Surf Sci.* 1999;140:156–67.
38. Stapel D, Benninghoven A. Application of atomic and molecular primary ions for TOF-SIMS analysis of additive containing polymer surfaces. *Appl Surf Sci.* 2001;174:261–70.
39. Appelhans AD, Delmore JE. Comparison of polyatomic and atomic primary beams for secondary ion mass spectrometry of organics. *Anal Chem.* 1989;61:1087–93.
40. Conlan XA, Lockyer NP, Vickerman JC. Is proton cationization promoted by polyatomic primary ion bombardment during time-of-flight secondary ion mass spectrometry analysis of frozen aqueous solutions? *Rapid Commun Mass Spectrom.* 2006;20:1327–34.
41. Wucher A, et al. Molecular depth profiling in ice matrices using C-60 projectiles. *Appl Surf Sci.* 2004;231–232:68–71.
42. Cheng J, et al. Direct comparison of  $\text{Au}_3^+$  and  $\text{C}_{60}^+$  cluster projectiles in SIMS molecular depth profiling. *J Am Soc Mass Spectrom.* 2007;18:406–12.
43. Mahoney CM. Cluster secondary ion mass spectrometry of polymers and related materials. *Mass Spectrom Rev.* 2009;29(2):247–93.
44. Cheng J, Wucher A, Winograd N. Molecular depth profiling with cluster ion beams. *J Phys Chem B.* 2006;110:8329–36.
45. Hill R. Primary ion systems. In: Vickerman JC, editor. *ToF-SIMS. Surface mass spectrometry.* Huddersfield: IM Publications; 2001. p. 95–112.
46. Niehuis E, Grehl T. Dual beam depth profiling. In: Vickerman JC, Briggs D, editors. *TOF-SIMS: surface analysis by mass spectrometry.* Charlton: IM Publications; 2001. p. 753–78.
47. Niehuis E, et al. Design and performance of a reflectron based time-of-flight secondary ion mass spectrometer with electrodynamic primary ion mass separation. *J Vac Sci Technol A.* 1987;A5:1243–6.
48. Nygren H, et al. Localization of cholesterol, phosphocholine and galactosylceramide in rat cerebellar cortex with imaging TOF-SIMS equipped with a bismuth cluster ion source. *Biochim Biophys Acta.* 2005;1737(2–3):102–10.
49. Schueler BW. Time-of-flight mass analysers. In: Vickerman JC, editor. *ToF-SIMS. Surface analysis by mass spectrometry.* Huddersfield: IM Publications; 2001. p. 75–94.
50. Hagenhoff B, et al. Time-of-flight secondary ion mass-spectrometry of insulators with pulsed charge compensation by low-energy electrons. *J Vac Sci Technol A.* 1989;10(5):3056–64.
51. Gilmore IS, Seah MP. Electron flood gun damage in the analysis of polymers and organics in time-of-flight SIMS. *Appl Surf Sci.* 2002;187:89–100.
52. Breitenstein D, et al. The chemical composition of animal cells and their intracellular compartments reconstructed from 3D mass spectrometry. *Angew Chem Int Edit.* 2006. Submitted for publication.
53. Mantus DS, et al. Static secondary ion mass spectrometry of adsorbed proteins. *Anal Chem.* 1993;65:1431–8.
54. McArthur SL, et al. Methods for generating protein molecular ions in ToF-SIMS. *Langmuir.* 2004;20:3704–9.
55. Michel R, et al. Influence of PEG architecture on protein adsorption and conformation. *Langmuir.* 2005;21(26):12327–32. doi:10.1021/la051726h. Research article.
56. Sole-Domenech S, et al. Analysis of opioid and amyloid peptides using time-of-flight secondary ion mass spectrometry. *Anal Chem.* 2010;82(5):1964–74.

57. Wittmaack K, et al. Time-of-flight secondary ion mass spectrometry of matrix-diluted oligo- and polypeptides bombarded with slow and fast projectiles: positive and negative matrix and analyte ion yields, background signals, and sample aging. *J Am Soc Mass Spectrom.* 2000;11: 553–63.
58. Wu KJ, Odom RW. Biological material analysis by matrix-enhanced SIMS. In: Gillen G et al., editors. *Secondary ion mass spectrometry XI*. Chichester: Wiley; 1998. p. 525–8.
59. Wagner MS, Horbett TA, Castner DG. Characterizing multicomponent adsorbed protein films using electron spectroscopy for chemical analysis, time-of-flight secondary ion mass spectrometry, and radiolabeling: capabilities and limitations. *Biomaterials.* 2003;24(11): 1897–908.
60. Jabs HU, et al. High performance liquid chromatography and time-of-flight secondary ion mass spectrometry: a new dimension in structural analysis of apolipoproteins. *J Lipid Res.* 1986;27(6):613–21.
61. von Eckardstein A, et al. Site-specific methionine sulfoxide formation is the structural basis of chromatographic heterogeneity of apolipoproteins A-I, C-II, and C-III. *J Lipid Res.* 1991;32(9):1465–76.
62. von Eckardstein A, et al. Apolipoprotein A-I variants. Naturally occurring substitutions of proline residues affect plasma concentration of apolipoprotein A-I. *J Clin Invest.* 1989;84(6): 1722–30.
63. Cheran L-E, Vukovich D, Thompson M. Imaging TOF-SIMS analysis of oligonucleotide microarrays. *Analyst.* 2003;128:126–9.
64. Lee C-Y, et al. Evidence of impurities in thiolated single-stranded DNA oligomers and their effect on DNA self-assembly on gold. *Langmuir.* 2005;21:5134–41.
65. May CJ, Canavan HE, Castner DG. Quantitative X-ray photoelectron spectroscopy and time-of-flight secondary ion mass spectrometry characterization of the components in DNA. *Anal Chem.* 2004;76(4):1114–22.
66. Arlinghaus HF, et al. DNA sequencing with ToF-SIMS. *Surf Interface Anal.* 2002;33:35–9.
67. Berman ES, et al. Distinguishing monosaccharide stereo- and structural isomers with TOF-SIMS and multivariate statistical analysis. *Anal Chem.* 2006;78(18):6497–503.
68. Roddy TP, et al. Imaging of freeze-fractured cells with in situ fluorescence and time-of-flight secondary ion mass spectrometry. *Anal Chem.* 2002;74(16):4011–9.
69. Leufgen KM, et al. Imaging time-of-flight secondary ion mass spectrometry allows visualization and analysis of coexisting phases in Langmuir–Blodgett films. *Langmuir.* 1996;12: 1708–11.
70. Roddy TP, et al. Identification of cellular sections with imaging mass spectrometry following freeze fracture. *Anal Chem.* 2002;74(16):4020–6.
71. Malmberg P, et al. Analysis of bone minerals by time-of-flight secondary ion mass spectrometry: a comparative study using monoatomic and cluster ions sources. *Rapid Commun Mass Spectrom.* 2007;21(5):745–9.
72. Adriaensen L, Vangaever F, Gijbels R. Metal-assisted secondary ion mass spectrometry: influence of Ag and Au deposition on molecular ion yields. *Anal Chem.* 2004;76(22): 6777–85.
73. Adriaensen L, et al. Matrix-enhanced secondary ion mass spectrometry: the influence of MALDI matrices on molecular ion yields of thin organic films. *Rapid Commun Mass Spectrom.* 2005;19:1017–24.
74. Kim YP, et al. Activity-based assay of matrix metalloproteinase on nonbiofouling surfaces using time-of-flight secondary ion mass spectrometry. *Anal Chem.* 2008;80(13):5094–102.
75. Breitenstein D, Vohnhören B, Reihs K. Semiquantitative analysis of self assembled monolayers by LEIS as well as SIMS. Submitted.
76. Hull JR, Tamura GS, Castner DG. Interactions of the streptococcal C5a peptidase with human fibronectin. *Acta Biomater.* 2008;4(3):504–13.
77. Kim Y-P, et al. Protein quantification on dendrimer-activated surfaces by using time-of-flight secondary ion mass spectrometry and principal component regression. *Appl Surf Sci.* 2008;255(4):1110–2.

78. Schnieders A, Möllers R, Benninghoven A. Molecular secondary particle emission from molecular overlayers under 10 keV Ar<sup>+</sup> primary ion bombardment. *Surf Sci.* 2001;471:170–84.
79. Breitenstein D, et al. The chemical composition of animal cells reconstructed from 2D and 3D ToF-SIMS analysis. *Appl Surf Sci.* 2008;46(28):5332–5.
80. Ulman A. *Ultrathin organic films.* San Diego: Academic; 1994.
81. Bourdos N, et al. Analysis of lung surfactant model systems with time-of-flight secondary ion mass spectrometry. *Biophys J.* 2000;79(1):357–69.
82. Bourdos N, et al. Imaging of domain structures in a one-component lipid monolayer by time-of-flight secondary ion mass spectrometry. *Langmuir.* 2000;16:1481–4.
83. Biesinger MC, et al. Imaging lipid distributions in model monolayers by ToF-SIMS with selectively deuterated components and principal component analysis. *Appl Surf Sci.* 2006;252:6957–65.
84. Biesinger MC, et al. Principal component analysis of TOF-SIMS images of organic monolayers. *Anal Chem.* 2002;74(22):5711–6.
85. Sostarecz AG, et al. Influence of molecular environment on the analysis of phospholipids by time-of-flight secondary ion mass spectrometry. *Langmuir.* 2004;20(12):4926–32.
86. Breitenstein D, et al. Lipid specificity of surfactant protein B studied by time-of-flight secondary ion mass spectrometry. *Biophys J.* 2006;91(4):1347–56.
87. Harbottle RR, et al. Molecular organization revealed by time-of-flight secondary ion mass spectrometry of a clinically used extracted pulmonary surfactant. *Langmuir.* 2003;19:3698–704.
88. Sostarecz AG, et al. Phosphatidylethanolamine-induced cholesterol domains chemically identified with mass spectrometric imaging. *J Am Chem Soc.* 2004;126(43):13882–3.
89. Hansson M, et al. Iodine content and distribution in extratumoral and tumor thyroid tissue analyzed with X-ray fluorescence and time-of-flight secondary ion mass spectrometry. *Thyroid.* 2008;18(11):1215–20.
90. Seifert M, et al. Solubility vs. electrostatics: what determines the lipid/protein interaction in the lung surfactant. *Biophys J.* 2007;93(4):1192–203.
91. Keating E, et al. Effect of cholesterol on the biophysical and physiological properties of a clinical pulmonary surfactant. *Biophys J.* 2007;93(4):1391–401.
92. Simons K, van Meer G. Lipid sorting in epithelial cells. *Biochemistry.* 1988;27(17):6197–202.
93. McQuaw CM, et al. Investigating lipid interactions and the process of raft formation in cellular membranes using ToF-SIMS. *Appl Surf Sci.* 2006;252:6716–8.
94. Munro S. Lipid rafts: elusive or illusive? *Cell.* 2003;115(4):377–88.
95. Wolf KV, Cole DA, Bernasek SL. High-resolution TOF-SIMS study of varying chain length self-assembled monolayer surfaces. *Anal Chem.* 2002;74(19):5009–16.
96. Wong SCC, Lockyer NP, Vickerman JC. Mechanisms of secondary ion emission from self-assembled monolayers and multilayers. *Surf Interface Anal.* 2005;37:721–30.
97. Francis JT, et al. ToF-SIMS investigation of octadecylphosphonic acid monolayers on a mica substrate. *Langmuir.* 2006;22:9244–50.
98. Schröder M, et al. Influence of primary ion species on the secondary cluster ion emission process from SAMs of hexadecanethiol on gold. *Appl Surf Sci.* 2006;252(19):6566–9.
99. Rading D, Kersting R, Benninghoven A. Secondary ion emission from molecular overlayers: Thiols on gold. *Proc SIMS XI Conf.* 1997;11:455–8.
100. Francis JT, et al. ToF-SIMS investigation of octadecylphosphonic acid monolayers on a mica substrate. *Langmuir.* 2006;22(22):9244–50.
101. Prinz C, et al. Structural effects in the analysis of supported lipid bilayers by time-of-flight secondary ion mass spectrometry. *Langmuir.* 2007;23(15):8035–41.
102. Richter K, et al. Localization of fatty acids with selective chain length by imaging time-of-flight secondary ion mass spectrometry. *Microsc Res Tech.* 2007;70(7):640–7.
103. Möller J, et al. Introduction of a cryosectioning-ToF-SIMS instrument for analysis of non-dehydrated biological samples. *Appl Surf Sci.* 2006;252(19):6709–11.
104. Touboul D, et al. Tissue molecular ion imaging by gold cluster ion bombardment. *Anal Chem.* 2004;76(6):1550–9.

105. Sjövall P, Lausmaa J, Johansson B. Mass spectrometric imaging of lipids in brain tissue. *Anal Chem.* 2004;76(15):4271–8.
106. Touboul D, et al. Improvement of biological time-of-flight secondary ion mass spectrometry imaging with bismuth cluster ion source. *J Am Soc Mass Spectrom.* 2005;16:1608–18.
107. McDonell LA, et al. Subcellular imaging mass spectrometry of brain tissue. *J Mass Spectrom.* 2005;1005(40):160–8.
108. Borner K, et al. Distribution of cholesterol and galactosylceramide in rat cerebellar white matter. *Biochim Biophys Acta.* 2006;1761(3):335–44.
109. Nygren H, et al. Imaging TOF-SIMS of rat kidney prepared by high-pressure freezing. *Microsc Res Tech.* 2005;68(6):329–34.
110. Nygren H, et al. Bioimaging TOF-SIMS: localization of cholesterol in rat kidney sections. *FEBS Lett.* 2004;566(1–3):291–3.
111. Touboul D, et al. Lipid imaging by gold cluster time-of-flight secondary ion mass spectrometry: application to Duchenne muscular dystrophy. *J Lipid Res.* 2005;46(7):1388–95.
112. Malmberg P, et al. Imaging of lipids in human adipose tissue by cluster ion TOF-SIMS. *Microsc Res Technol.* 2007;70(9):828–35. doi:10.1002/jemt.20481.
113. Le Naour F, et al. Chemical imaging on liver steatosis using synchrotron infrared and ToF-SIMS microspectroscopies. *PLoS One.* 2009;4(10):e7408.
114. Monroe EB, et al. SIMS and MALDI MS imaging of the spinal cord. *Proteomics.* 2008;8(18):3746–54.
115. Nygren H, Malmberg P. Silver deposition on freeze-dried cells allows subcellular localization of cholesterol with imaging TOF-SIMS. *J Microsc.* 2004;215(Pt 2):156–61.
116. Altelaar AF, et al. Gold-enhanced biomolecular surface imaging of cells and tissue by SIMS and MALDI mass spectrometry. *Anal Chem.* 2006;78(3):734–42.
117. Berman ES, et al. Preparation of single cells for imaging/profiling mass spectrometry. *J Am Soc Mass Spectrom.* 2008;19(8):1230–6.
118. Fartmann M, et al. Characterization of cell cultures with ToF-SIMS and laser-SNMS. *Surf Interface Anal.* 2002;34:63–6.
119. Wittig A, et al. Preparation of cells cultured on silicon wafers for mass spectrometry analysis. *Microsc Res Tech.* 2005;66(5):248–58.
120. Ostrowski SG, et al. Mass spectrometric imaging of highly curved membranes during Tetrahymena mating. *Science.* 2004;305(5680):71–3.
121. Piehowski PD, et al. Freeze-etching and vapor matrix deposition for ToF-SIMS imaging of single cells. *Langmuir.* 2008;24(15):7906–11.
122. Vaidyanathan S, et al. Subsurface biomolecular imaging of *Streptomyces coelicolor* using secondary ion mass spectrometry. *Anal Chem.* 2008;80(6):1942–51.
123. Parry S, Winograd N. High-resolution TOF-SIMS imaging of eukaryotic cells preserved in a trehalose matrix. *Anal Chem.* 2005;77(24):7950–7.
124. Monroe EB, et al. Vitamin E imaging and localization in the neuronal membrane. *J Am Chem Soc.* 2005;127(35):12152–3.
125. Sjövall P, et al. Imaging of membrane lipids in single cells by imprint-imaging time-of-flight secondary ion mass spectrometry. *Anal Chem.* 2003;75(14):3429–34.
126. Hoetelmans RW, et al. Effects of acetone, methanol, or paraformaldehyde on cellular structure, visualized by reflection contrast microscopy and scanning electron microscopy. *Appl Immunohistochem Mol Morphol.* 2001;9(4):346–51.
127. Levi-Setti R, Gavrilow KL, Neilly ME. Cations in mammalian cells and chromosomes: sample preparation protocols affect elemental abundances by SIMS. *Appl Surf Sci.* 2005;252:6765–9.
128. Fardim P, et al. Extractives on fiber surfaces investigated by XPS, ToF-SIMS and AFM. *Colloid Surface A.* 2005;255:91–103.
129. Fardim P, Holmbom B. ToF-SIMS imaging: a valuable chemical microscopy technique for paper and paper coatings. *Appl Surf Sci.* 2005;249:393–407.

130. Mazel V, et al. Chemical imaging techniques for the analysis of complex mixtures: new application to the characterization of ritual matters on African wooden statuettes. *Anal Chim Acta*. 2006;570(1):34–40.
131. Aoyagi S, Kudo M. Effective monitoring of protein reaction on glass plate surfaces by TOF-SIMS. *Biosens Bioelectron*. 2005;20(8):1626–30.
132. Hellweg S, et al. Mass spectrometric characterization of DNA microarrays as a function of primary ion species. *Appl Surf Sci*. 2006;252:6742–5.
133. Belu AM, et al. Enhanced TOF-SIMS imaging of a micropatterned protein by stable isotope protein labeling. *Anal Chem*. 2001;73(2):143–50.
134. Aoyagi S, et al. TOF-SIMS imaging of protein adsorption on dialysis membrane by means of information entropy. *Surf Sci Nanotechnol*. 2003;1:67–71.
135. Canavan HE, et al. Surface characterization of the extracellular matrix remaining after cell detachment from a thermoresponsive polymer. *Langmuir*. 2005;21(5):1949–55.
136. Rading D, et al. Dual beam depth profiling of organic materials: variations of analysis and sputter beam conditions. *Surf Interface Anal*. 2010. doi:10.1002/sia.3422.
137. Shard AG, et al. Measurement of sputtering yields and damage in C<sub>60</sub> SIMS depth profiling of model organic materials. *Surf Interface Anal*. 2007;39:294–8.
138. Sostarecz AG, et al. Depth profiling of Langmuir–Blodgett films with a buckminsterfullerene probe. *Anal Chem*. 2004;76(22):6651–8.
139. Cheng J, Winograd N. Depth profiling of peptide films with TOF-SIMS and a C<sub>60</sub> probe. *Anal Chem*. 2005;77:3651–9.
140. Fletcher JS, et al. TOF-SIMS 3D biomolecular imaging of *Xenopus laevis* oocytes using buckminsterfullerene (C<sub>60</sub>) primary ions. *Anal Chem*. 2007;79:2199–206.
141. Nygren H, et al. Bioimaging TOF-SIMS: high resolution 3D imaging of single cells. *Microsc Res Tech*. 2007;70(11):969–74.
142. Wucher A, Cheng J, Winograd N. Protocols for three-dimensional molecular imaging using mass spectrometry. *Anal Chem*. 2007;79(15):5529–39. doi:10.1021/ac070692a.
143. Delcorte A. On the road to high-resolution 3D molecular imaging. *Appl Surf Sci*. 2008;255(4):954–8.
144. Arlinghaus HF. Laser-SNMS. In: Bubert H, Jenett H, editors. *Surface and thin film analysis. Principles, instrumentation, applications*. Weinheim: Wiley-VCH; 2002. p. 132–9.
145. Wucher A. Laser post-ionisation: fundamentals. In: Vickerman JC, editor. *ToF-SIMS—surface analysis by mass spectrometry*. Manchester/Chichester: IM Publications; 2001. p. 347–74.
146. Arlinghaus HF, et al. Subcellular imaging of cell cultures and tissue for boron localization with laser-SNMS. *Surf Interface Anal*. 2004;36:698–701.
147. Altelaar AF, et al. Direct molecular imaging of *Lymnaea stagnalis* nervous tissue at subcellular spatial resolution by mass spectrometry. *Anal Chem*. 2005;77(3):735–41.
148. Nygren H, Johansson BR, Malmberg P. Bioimaging TOF-SIMS of tissues by gold ion bombardment of a silver-coated thin section. *Microsc Res Tech*. 2004;65(6):282–6.
149. Delcorte A, Medard N, Bertrand P. Organic secondary ion mass spectrometry: sensitivity enhancement by gold deposition. *Anal Chem*. 2002;74(19):4955–68.
150. Delcorte A, et al. Sample metallization for performance improvement in desorption/ionization of kilodalton molecules: quantitative evaluation, imaging secondary ion MS, and laser ablation. *Anal Chem*. 2003;75(24):6875–85.
151. Kim YP, et al. Gold nanoparticle-enhanced secondary ion mass spectrometry imaging of peptides on self-assembled monolayers. *Anal Chem*. 2006;78(6):1913–20.
152. Delcorte A. Matrix-enhanced secondary ion mass spectrometry: the alchemist's solution? *Appl Surf Sci*. 2006;252(19):6582–7.
153. Graham DJ, Wagner MS, Castner DG. Information from complexity: challenges of TOF-SIMS data interpretation. *Appl Surf Sci*. 2006;252(19):6860–8.
154. Tyler BJ. Multivariate statistical image processing for molecular specific imaging in organic and bio-systems. *Appl Surf Sci*. 2006;252(19):6875–82.

155. Tyler BJ, Rayal G, Castner DG. Multivariate analysis strategies for processing ToF-SIMS images of biomaterials. *Biomaterials*. 2007;28(15):2412–23.
156. Milillo TM, Gardella JA. Spatial statistics and interpolation methods for TOF SIMS imaging. *Appl Surf Sci*. 2006;252(19):6883–90.
157. Smentkowski VS, et al. Multivariate statistical analysis of concatenated time-of-flight secondary ion mass spectrometry spectral images. Complete description of the sample with one analysis. *Anal Chem*. 2005;77(5):1530–6.
158. Kulp KS, et al. Chemical and biological differentiation of three human breast cancer cell types using time-of-flight secondary ion mass spectrometry. *Anal Chem*. 2006;78(11):3651–8.
159. Thompson CE, et al. ToF-SIMS studies of *Bacillus* using multivariate analysis with possible identification and taxonomic applications. *Appl Surf Sci*. 2006;252(19):6719–22.
160. Tidwell CD, et al. Static time-of-flight secondary ion mass spectrometry and X-ray photoelectron spectroscopy characterization of adsorbed albumin and fibronectin films. *Surf Interface Anal*. 2001;31:724–33.
161. Quong JN, et al. Molecule-specific imaging analysis of carcinogens in breast cancer cells using time-of-flight secondary ion mass spectrometry. *Appl Surf Sci*. 2004;231–232:424–7.
162. Wagner MS, et al. Limits of detection for time of flight secondary ion mass spectrometry (ToF-SIMS) and X-ray photoelectron spectroscopy (XPS): detection of low amounts of adsorbed protein. *J Biomater Sci Polym Ed*. 2002;13(4):407–28.
163. Wagner MS. Molecular depth profiling of multilayer polymer films using time-of-flight secondary ion mass spectrometry. *Anal Chem*. 2005;77:911–22.
164. Yamada I, et al. Materials processing by gas cluster ion beams. *Mat Sci Eng: R-Reports Rev J*. 2001;34(6):231–95.
165. Ninomiya S, et al. Precise and fast secondary ion mass spectrometry depth profiling of polymer materials with large Ar cluster ion beams. *Rapid Commun Mass Spectrom*. 2009;23:1601–6.
166. Carado A, et al.  $C_{60}$  secondary ion mass spectrometry with a hybrid-quadrupole orthogonal time-of-flight mass spectrometer. *Anal Chem*. 2008;80(21):7921–9.
167. Popov J, et al. Chemical mapping of ceramide distribution in sphingomyelin-rich domains in monolayers. *Langmuir*. 2008;24(23):13502–8.
168. Heeren RMA, et al. Why don't biologists use SIMS? A critical evaluation of imaging MS. *Appl Surf Sci*. 2007;252(19):6827–35.
169. Breitenstein D, et al. The chemical composition of animal cells and their intracellular compartments reconstructed from 3D mass spectrometry. *Angew Chem Int Edit*. 2007. Published online.



# Chapter 4

## Cluster Secondary Ion Mass Spectrometry

Joseph Kozole and Nicholas Winograd

**Abstract** In principle, secondary ion mass spectrometry (SIMS) molecule-specific imaging has vast implications in biological research where submicrometer spatial resolution, uppermost surface layer sensitivity, and chemically unmodified sample preparation are essential. Yet SIMS imaging using atomic projectiles has been rather ineffective when applied to biological materials. The common pitfalls experienced during these analyses include low secondary ion yields, extensive fragmentation, restricted mass ranges, and the accumulation of significant physical and chemical damage after sample erosion beyond 1 % of the surface molecules. Collectively, these limitations considerably reduce the amount of material available for detection and result in inadequate sensitivity for most applications. In response, polyatomic (cluster) ions have been introduced as an alternate imaging projectile. Cluster ion bombardment has been observed to enhance secondary ion yields, extend the spectral mass range, and decrease the incidence of physical and chemical damage during sample erosion. The projectiles are expected to considerably increase the number of molecules available for analysis and to significantly improve the overall sensitivity. Hence, the objectives of this chapter are to describe the unique physical basis for the improvements observed during polyatomic bombardment and to identify the emerging biological applications made practical by the introduction of cluster projectiles to SIMS.

---

J. Kozole

Department of Chemistry, Penn State University, 104 Chemistry Building,  
University Park, Philadelphia, PA 16802, USA

DuPont, Philadelphia, PA, USA

N. Winograd (✉)

Department of Chemistry, Penn State University, 104 Chemistry Building,  
University Park, Philadelphia, PA 16802, USA

e-mail: [nxw@psu.edu](mailto:nxw@psu.edu)

## 4.1 Introduction

Energetic (keV) atomic projectiles were first employed to desorb intact molecules for mass-spectrometric (MS) detection nearly 40 years ago [1]. However, polyatomic ions were not identified as potentially valuable projectiles until 20 years later [2]. Appelhans et al. observed that when compared to the atomic  $\text{Cs}^+$ , the cluster  $\text{SF}_6^0$  increases secondary ion efficiency and decreases the occurrence of sample damage during SIMS molecule analysis. Similar results were achieved using aromatic hydrocarbons, massive glycerol clusters, inorganic complexes, and  $\text{SF}_5^+$  as primary sources shortly thereafter [3–6]. Despite the initial success, polyatomic projectiles were not widely adopted by the SIMS community. The reluctance was credited to a number of device performance issues, which included low beam currents, inadequate beam focusing, and poor source lifetimes [6, 7]. Furthermore, the amount of evidence identifying polyatomic projectiles as better-quality sources for SIMS experiments was not overwhelming [6]. Consequently, cluster ion sources were considered too unreliable for implementation to everyday SIMS applications, and the widespread use of well-established atomic projectiles continued.

The mainstream acceptance of polyatomic projectiles to SIMS did not occur until 10 years after the preliminary observations of Appelhans et al. The breakthrough was initiated by the development of commercially available liquid metal ion (LMIG) sources to produce  $\text{Au}_3^+$  and  $\text{Bi}_3^+$  and by the marketing of improved gas-phase ion sources to produce  $\text{C}_{60}^+$  [8–10]. LMIG technology uses a heated, field-emission tip coated in a eutectic metal alloy (AuGe for  $\text{Au}_n^+$  or Bi for  $\text{Bi}_n^+$ ) to extract a mixture of metal cluster ions. The ions are mass-selected and electrostatically aligned and focused to generate a bright, spatially defined metal cluster ion beam. On the other hand, gas-phase ion sources use conventional electron impact strategies to ionize vapor-phase  $\text{C}_{60}$ . The ions are extracted, mass-filtered, and focused using a sophisticated series of beam-minimizing apertures and electrostatic lenses to obtain an intense, laterally defined  $\text{C}_{60}$  cluster ion beam. Regardless of scheme, polyatomic ion beam technology has successfully developed high-performance ion sources characterized by 1-nA maximum beam currents, ~100–200-nm optimal beam sizes, and 1,000-h source lifetimes. Consequent to the previously observed enhancements and the aforementioned technical advances,  $\text{Au}_3^+$ ,  $\text{Bi}_3^+$ , and  $\text{C}_{60}^+$  cluster projectiles were rapidly adapted to SIMS instrumentation as potential successors to atomic counterparts.

As the number of SIMS experiments involving polyatomic projectiles increased, so did the number of observations regarding cluster ion bombardment [6, 7]. The most recent observations have led to the identification of several important properties influencing the application of cluster ions to SIMS. Included among the properties are increased neutral and secondary ion yields and decreased physical and chemical sample damage. Together, the characteristics increase the number of molecules available for SIMS analysis and improve the overall sensitivity of the imaging modality. Accordingly, the objectives of this chapter are to introduce the unique mechanism for desorption during polyatomic bombardment, to identify the special

properties of cluster ions in SIMS, and to discuss the implications of these properties to sensitivity, lateral resolution, and depth resolution during the imaging modality. Using these properties, we will show how the improved performance of cluster ions in SIMS imaging can be used to characterize the chemical composition of various biological samples. The discussion is not meant to provide an exhaustive literature review of this very large subject, but is aimed toward illustrating the important strategic advantages associated with the cluster SIMS imaging approach.

## 4.2 Physics of Cluster SIMS

Molecular dynamics (MD) computer simulations have been recognized to provide valuable insight into the energetic ion bombardment of solids [11]. Consequently, the calculations will be used as a platform to discuss the differences between the atomic desorption event and the polyatomic desorption event. As a note, neutral atoms are used as the incident projectile in MD calculations, while ions are used as the incident projectile in SIMS experiments. Therefore, for the remainder of the chapter, projectiles used in MD simulations will be described in the neutral state, while projectiles used in SIMS will be described in the ion state. Despite the discrepancy, the physical phenomena in MD simulations are still representative of the desorption event in SIMS experiments.

An understanding of the atomic bombardment event is essential for a complete appreciation of the cluster desorption mechanism to be realized. Accordingly, a representative simulation of a typical trajectory of a 15-keV Ga normal incidence impact on an Ag solid crystal is shown in Fig. 4.1a [12, 13]. The atomistic motion within the Ag crystal can be described as a complicated game of billiards. Specifically, individual atoms collide with and transfer energy to other individual atoms. The cascade of substrate atoms is predominantly influenced by the trajectory of the projectile through the solid. The large incident energy and small cross section of Ga cause the atom to penetrate deep into the Ag crystal. Therefore, a large amount of the primary energy is deposited well below the solid surface. The dissipation of significant energy into the bulk causes substantial disruption of Ag atoms within the structure. Moreover, insufficient energy at the solid surface leads to the ineffective desorption of material. Hence, a large amount of the projectile energy is wasted in terms of providing useful SIMS information.

The issue of energy deposition into solids at depths efficient for material ejection and inefficient for the accumulation of sample damage is critical to the practical behavior of primary projectiles in SIMS. Polyatomic projectiles overcome the energy dissipation pitfalls observed during atomic bombardment by distributing its total incident energy over a number of constituent atoms. For example, each C atom in a 15-keV C<sub>60</sub> projectile has 250 eV of kinetic energy [7]. The energy per C atom is significantly greater than the C–C bond strength in C<sub>60</sub>. As a result, the C<sub>60</sub> cluster dissociates into 60 separate 250-eV C atoms upon impact with the solid. Because each C atom has 250 eV of energy and initiates an individual cascade event, the

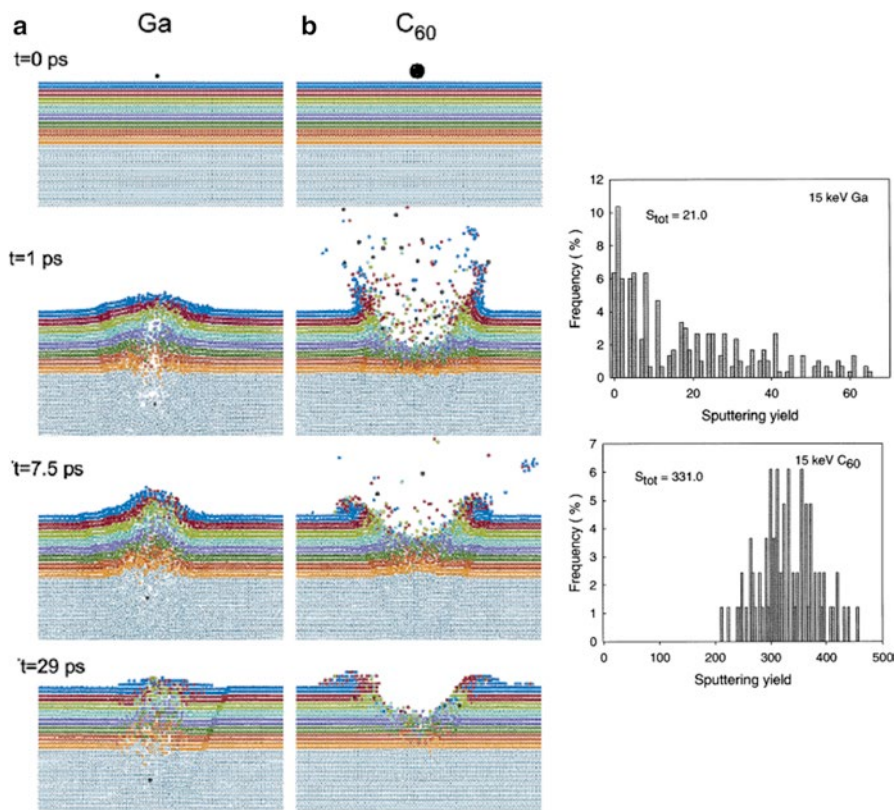


**Fig. 4.1** Cross-sectional view of the temporal evolution of a typical collision event leading to the ejection of atoms due to 15-keV Ga (a) and 15-keV C<sub>60</sub> (b) bombardment of an Ag surface at normal incidence. The dimensions of the solid are  $10 \times 10 \times 10 \text{ nm}^3$ . The Ag atoms are colored by original layers in the solid. The projectiles are in black. The bar graphs are the relative frequency of impacts leading to a given sputter yield for 15 keV Ga (top) and 15 keV C<sub>60</sub> (bottom) (This figure is from Refs. [12, 13]). The calculations in this figure can be viewed as a movie file by visiting the website <http://www.chem.psu.edu/group/bjg/sputtering-animations>)

process for the deposition of energy into the substrate is considerably different than during 15-keV Ga bombardment. Specifically, the incident energy dissipates nearer the solid surface and over a larger surface area. Therefore, the motion of atoms within the substrate is also expected to be significantly different. A representative simulation of a typical trajectory of a 15-keV C<sub>60</sub> normal-incidence bombardment of a silver solid crystal is shown in Fig. 4.1b [12, 13]. The impact event itself resembles a meteor striking the earth. The motion of substrate material consequent to the event is similar to an organized expansion of a super-heated and super-dense gas from a pressurized nozzle. The cascade results in the formation of a significant crater within the solid and the occurrence of limited sample disruption outside this immediate region. Furthermore, the impact event is characterized by the large-scale

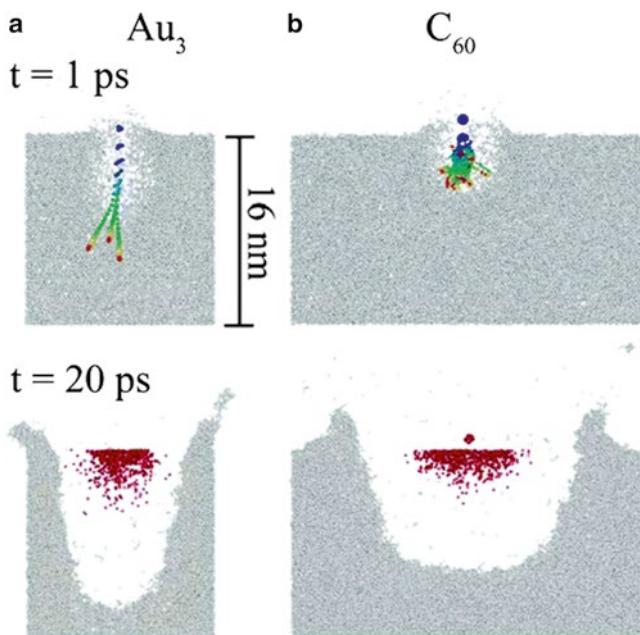


**Fig. 4.2** Cross-sectional view of the temporal evolution of a typical collision event leading to the ejection of atoms due to 5-keV  $\text{Au}_3$  (a) and 5-keV  $\text{C}_{60}$  (b) bombardment of an amorphous water surface at normal incidence. The dimensions of the solid are  $29 \times 16 \times 16 \text{ nm}^3$ . The *gray* atoms represent the water molecules. The snapshot at 1 ps contains a time-lapse overlay of the incident projectile motion within the solid. The snapshot at 20 ps displays the ejected atoms in *red* by original position in the solid (This figure is from Ref. [14]. The calculations in this figure can be viewed as a movie file by visiting the website <http://www.chem.psu.edu/group/bjg/sputtering-animations>)

ejection of material. In fact, the MD simulations illustrate a nonlinear enhancement of the number of Ag atoms removed for each incident  $\text{C}_{60}$ . That is, the yield for a 15-keV  $\text{C}_{60}$  impact is three times larger than the collective yield from 60 separate 250-eV C impacts. Thus, the polyatomic desorption event abandons linear cascade principles and enters the realm of the mesoscopic domain.

The unique mechanism for mesoscopic desorption is credited to the near-surface trajectories of the individual atoms of the cluster within the solid [14]. Specifically, the trajectories of the constituent atoms are influenced by two factors: the energy and mass per atom. Together, the factors determine the momentum of the constituent atoms and the mass-match of the constituent atoms with the substrate atoms. To illustrate this point, MD simulations of 5-keV  $\text{Au}_3$  (Fig. 4.2a) and 5-keV  $\text{C}_{60}$  (Fig. 4.2b) normal-incident trajectories on amorphous water are considered [14]. The platform is significant since  $\text{Au}_3$  and  $\text{C}_{60}$  are two commonly employed polyatomic projectiles. Moreover, the water sample consists of low-mass, weakly bound atoms comparable to organic materials. In general, the results of the  $\text{Au}_3$  and  $\text{C}_{60}$  impact events on the water sample are similar. The motion of substrate material has

a mesoscale character, and a significant crater is formed within the solid. However, the trajectories of the incident projectiles within the solid giving rise to desorption are different. The motion of the constituent atoms in the  $\text{Au}_3$  and  $\text{C}_{60}$  collision events are displayed in the time-lapse color portion of Fig. 4.2a, b, respectively. The different trajectories are attributed to each C atom in the 5-keV  $\text{C}_{60}$  particle having 83 eV of energy and a mass of 12 amu, while each Au atom in the 5-keV  $\text{Au}_3$  particle has 1.7 keV of energy and a mass of 197 amu. Therefore, the Au atoms have a momentum 11 times larger than the C atoms and a mass that is much greater than the substrate atoms ( $MW = 18$  amu). Consequently, the C atoms are promptly deflected by the substrate atoms upon impact, and the incident motion and excitation energy is confined to the near-surface region, whereas the Au atoms are slowly deflected by the much lighter substrate atoms, and the incident motion and excitation energy penetrate well beyond the near-surface region. Thus, the trajectories of the C atoms in the  $\text{C}_{60}$  collision event are more efficient for the near-surface deposition of energy into the solid. Thus, it is no surprise that the number of ice molecules removed in the  $\text{C}_{60}$  experiment ( $Y = 1,644$ ) is larger than the number removed in the  $\text{Au}_3$  experiment ( $Y = 998$ ). Despite this modest difference, the constituent atoms in both the  $\text{Au}_3$  and  $\text{C}_{60}$  clusters have significantly less momentum than a 15-keV Ga atomic projectile. Hence, polyatomic projectiles deposit their incident energy much more efficiently for providing useful SIMS information.

### 4.3 Properties of Cluster SIMS

The unique mechanism for desorption during polyatomic bombardment has led to an improved performance in SIMS. Experimental observations have identified several important properties when cluster ions are applied to SIMS. Specifically, when compared to atomic projectiles, polyatomic projectiles have been demonstrated to enhance secondary neutral and secondary ion yields—particularly in the case of large molecules—enhance surface sensitivity, reduce sample topography and inter-layer mixing, and make practical molecular depth profile and three-dimensional imaging experiments [6, 7]. Collectively, the behavior presents a unique opportunity for increased sensitivity, lateral resolution, and depth resolution during SIMS analysis. Therefore, this section will review the important characteristics of polyatomic projectiles in SIMS and comment on their implications to the imaging modality.

#### 4.3.1 Enhanced Yields

The MD simulations shown in Fig. 4.1a, b indicate the yield of a 15-keV  $\text{C}_{60}$  impact ( $Y = 331$ ) on a silver sample is 15 times larger than the yield for a 15-keV Ga impact ( $Y = 21$ ) [12, 13]. The calculations are supported by the measurement of a similar yield increase for 15 keV  $\text{C}_{60}^+$  over 15 keV  $\text{Ga}^+$  on a polycrystalline Ag substrate using a quartz crystal microbalance (QCM) to determine the mass removed for each

impact [15]. Sputter-yield enhancements have also been observed for the polyatomic bombardment of organic-like materials. Specifically, QCM measurements have determined the number of molecular equivalents sputtered from an amorphous water–ice film using 20 keV  $C_{60}^+$  ( $Y=1,800$ ) to be 18 times larger than the number sputtered using 25 keV  $Au^+$  ( $Y=100$ ) [16]. Moreover, when 40 keV  $C_{60}^{3+}$  is employed, the absolute number of water molecules removed for each impact is increased to 10,000 [17]. Additional organic materials determined to experience large yield enhancements include polymethyl methacrylate (PMMA), polylactic acid (PLA), arachidic acid, benzene, phenylalanine, gramicidin S, and trehalose, to name a few [18–24]. Regardless of the sample, the amount of material removed for each cluster ion impact is significantly larger than the material removed for each atomic ion impact.

Similar to secondary neutral yields, secondary ion yields are enhanced during cluster projectile impact events [8–10, 20, 25, 26]. However, the increase observed for ions is not as straightforward to interpret as the increase observed for neutrals [6, 7]. Particularly, the extent of the secondary ion improvement is specific to the mass of the molecule being analyzed. For the case of molecules that weigh no more than 500 amu, polyatomic projectiles typically increase ion yields by a factor of 10–100 over atomic projectiles at comparable energies [20]. The observed ion enhancement is similar in magnitude to the observed neutral enhancement. Thus, the increase in ion yield is attributed to a corresponding increase in the neutral yield, and not an increase in ionization efficiency. This idea is supported by a series of experiments performed on a barium arachidate (MW=449 amu) multilayer structure prepared using Langmuir–Blodgett techniques [20]. The experiments use the known thickness of the structure to measure the number of incident projectiles required to remove the film using both  $Ga^+$  and  $C_{60}^+$ . From the information, the neutral yield and ion yield for  $Ga^+$  and  $C_{60}^+$  can be compared. The values indicate that the enhancement for  $C_{60}^+$  over  $Ga^+$  is a factor of 100 for both neutrals and ions. Therefore, the increase in secondary ion yield can be explained by an equivalent increase in the secondary neutral yield.

On the other hand, molecules weighing at least 500 amu typically experience a 100–1,000 fold increase in secondary ion yield when polyatomic projectiles are used [8, 25]. For some examples (Fig. 4.3a, b), such as the polymer PS-2000 (MW  $\approx$  1,800 amu) and the peptide Gramicidin D (MW = 1,880 amu), a parent ion signal can only be observed if cluster projectiles are employed [8, 10]. The reason for larger enhancements at higher masses is not completely understood. However, a leading conjecture involves a larger propensity for polyatomic projectiles to “lift off” large, intact molecules while minimizing fragmentation. This proposition is supported by the MD simulations in Fig. 4.1a, b, which indicate that  $C_{60}$  has a higher probability of forming larger Ag clusters than Ga does [12, 13]. In addition to decreased fragmentation, another possible reason for the enhancement includes an improved environment for ionization under cluster bombardment [6, 7]. Experiments on amorphous ice films suggest that polyatomic projectiles are prodigious producers of protons in the impact region [27]. Thus, the ionization efficiency could potentially be increased through proton-attachment, chemical ionization of heavier, slower-moving molecules. Regardless of the scheme, polyatomic

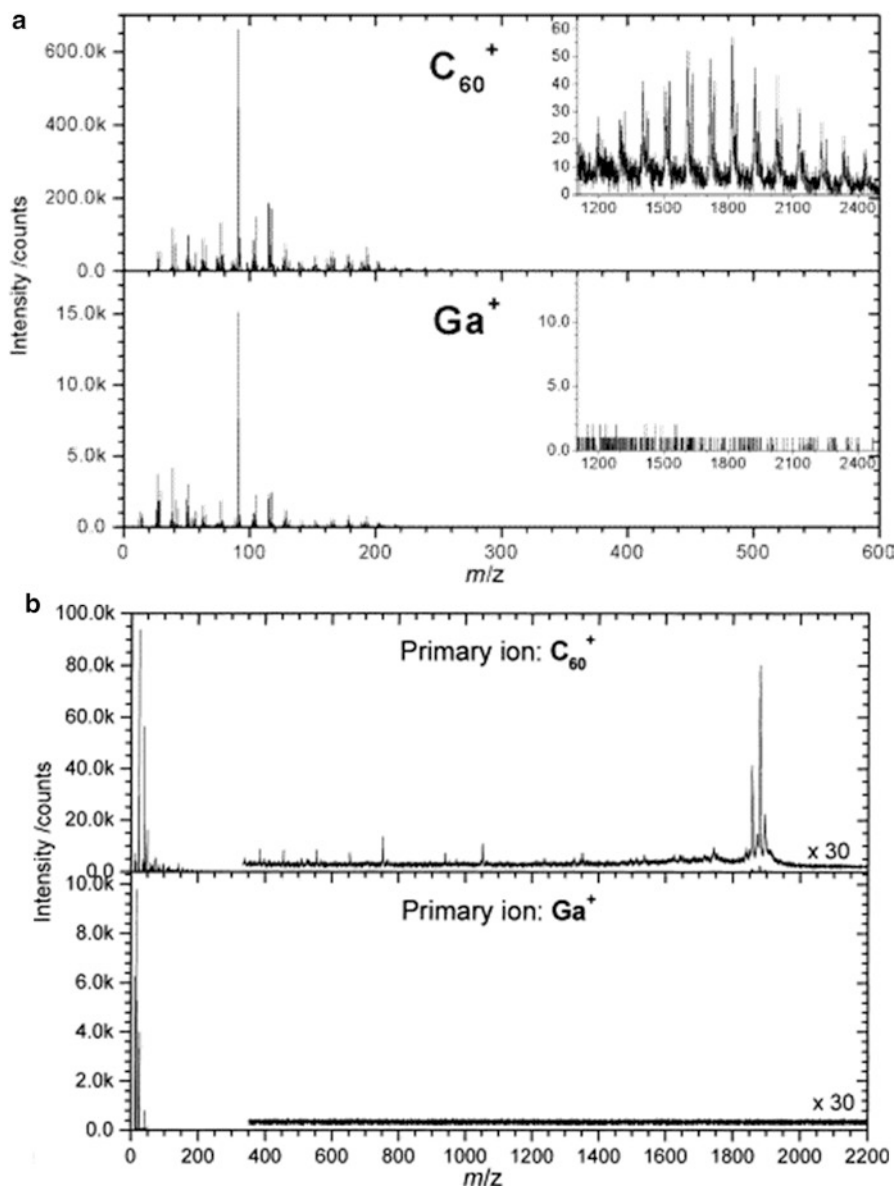


**Fig. 4.3** (a) Positive SIMS spectrum of PS-200 using 10 keV Ga (*bottom*) and 10 keV  $C_{60}$  (*top*). (b) Negative SIMS spectrum of Gramicidin D using 15 keV Ga (*bottom*) and 15 keV  $C_{60}$  (*top*). All spectra acquired using the same primary ion fluence (From Refs. [8, 10])

projectiles have been demonstrated to considerably increase the sensitivity and extend the mass range of molecules in SIMS. These properties make available a new class of molecules, which includes polymers, peptides, proteins, and lipids, for detection during SIMS.



### 4.3.2 *Reduced Physical Damage*

The MD simulations in Fig. 4.1a, b provide valuable insight into the incidence of physical damage during SIMS [12, 13]. Specifically, the calculations indicate that  $C_{60}$  disrupts the sample bulk to a lesser extent than Ga does. That is,  $C_{60}$  appears to be more sensitive to the surface material than Ga does. In fact, surface sensitivity during projectile bombardment has been measured by observing the SIMS response of an Ag substrate that is covered with water–ice overlayers of various thicknesses and bombarded with 25 keV  $Au_{1-3}^+$  and 20 keV  $C_{60}^+$  [16]. The experiments indicate the amount of silver signal attenuation is greatest when the water–ice overlayer is interrogated with  $C_{60}^+$ . Therefore,  $C_{60}^+$  transfers the largest amount of its incident energy into the water–ice overlayer and has the highest surface sensitivity of the projectiles studied. The observation of enhanced surface sensitivity has the potential to reduce ion-beam–induced topography and interlayer mixing.

The incidence of reduced physical damage during polyatomic bombardment has significant implications to depth-profile experiments. Depth-profiling measurements are achieved by alternating between erosion cycles and SIMS acquisition cycles using a single ion beam. That is, the ion beam is operated in direct current (DC) mode to systematically etch material from a sample layer by layer and operated in pulsed mode to characterize the composition of the uncovered surfaces [6, 7]. For the individual layers to be resolved in the analysis, the ion beam must erode the sample without the occurrence of significant physical damage. Atomic projectiles do not meet these requirements unless considerable changes to the analytical strategy are made [28, 29]. These changes, which include low-energy primary ion bombardment (100–500 eV), glancing incident angles, and sample rotation, add substantial complexity to the measurements and eliminate the ability to acquire images [28, 29]. Conversely, polyatomic projectiles have been demonstrated in a number of instances to meet the depth-profile requirements without method modification.

The different behaviors of 15 keV  $Ga^+$  and 15 keV  $C_{60}^+$  during the controlled erosion of alternating nickel/chromium (Ni/Cr) layers in a multilayer structure are shown in Fig. 4.4 [28, 29]. The extent of interlayer mixing during the depth-profile experiment was determined by observing the response of the metal signal as a function of sample depth and calculating the interface distance between the alternating layers within the structure. In addition to the interface width, atomic force microscope (AFM) images of the eroded sample area were acquired to evaluate the ion-beam–induced sample topography. The measurements in Fig. 4.4 provide important insight into the depth resolution achieved during the  $Ga^+$  and  $C_{60}^+$  experiments. The depth profile using  $Ga^+$  (bottom) does not resolve the individual Ni/Cr layers of the structure; the AFM measurement of the bombarded surface region (far right) indicates a 100-nm root-mean-square (rms) surface roughness. In contrast, the depth profile using  $C_{60}^+$  (top) resolves the individual Ni/Cr layers with interface widths of 10 nm and the AFM measurement (left) determines a 2.5-nm rms surface roughness. Therefore,  $C_{60}^+$  controllably erodes the Ni/Cr multilayer structure with a depth resolution of 10 nm, a value that is approaching the best resolution attained during low-energy, glancing incident, atomic projectile depth profiling. Overall, the improved

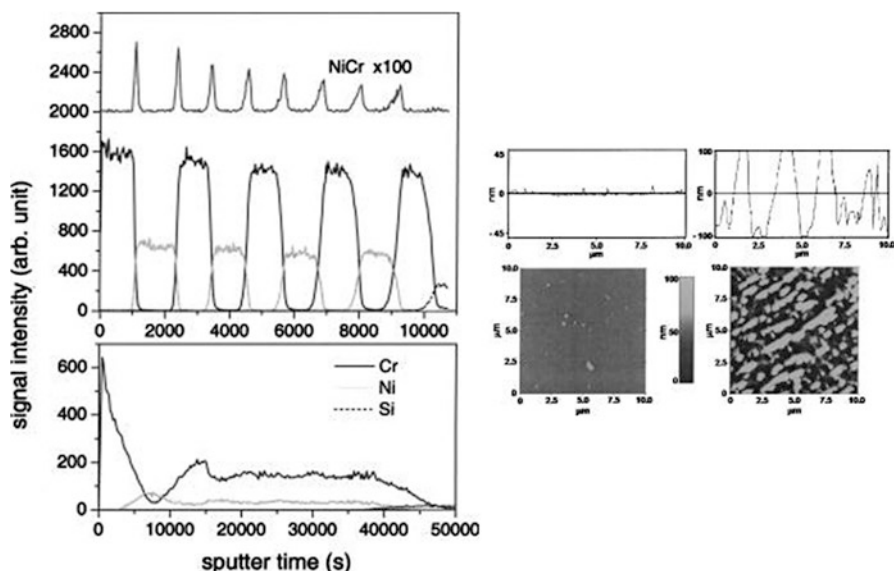


**Fig. 4.4** The integrated metal atom signal response as a function of total sputter time for depth-profile experiments on a nine-layer Ni/Cr multilayer structure. The *top panel* shows the behavior of 15 keV  $C_{60}$  and the *bottom panel* shows the behavior of 15 keV Ga. The offset graphs are AFM images of the eroded region of the Ni/Cr structure using 15 keV  $C_{60}$  (*left*) and 15 keV Ga (*right*) (From Refs. [28, 29])

behavior of  $C_{60}^+$  over  $Ga^+$  during the Ni/Cr depth-profile experiments is attributed to reduced interlayer mixing and the absence of ion-beam-induced topography as a result of enhanced surface sensitivity.

Polyatomic projectiles have been employed to successfully depth-profile a number of multilayer structures [6, 7]. The ability to probe various materials without the incidence of significant physical damage has important implications to molecular depth profiling [6, 7]. To determine the potential for these experiments, the observation of reduced topography and interlayer mixing during cluster bombardment must be extended from atomic materials to organic materials. A platform for investigating the physical damage of organic materials during sample erosion is illustrated in Fig. 4.5 [22, 30, 31]. The platform involves a spin-coated, GGYR peptide-doped, sugar trehalose film on a silicon substrate. Figure 4.5a is an AFM image of the unbombarded trehalose surface, and Fig. 4.5b is an AFM image of the same surface after  $1 \times 10^{14} \text{cm}^{-2}$  20-keV  $C_{60}^+$  bombardment. The AFM measurements indicate the rms surface roughness of the film before bombardment is 2.2 nm, while that after bombardment is 0.5 nm. Therefore,  $C_{60}^+$  bombardment does not alter the surface topography of the trehalose film; however, this observation is not consistent for all materials [32]. In addition to limited topographical effects, the depth profile in Fig. 4.5c suggests the interface region of the trehalose molecules with the silicon substrate atoms during sample erosion is 10 nm. Thus, the physical structure of the trehalose film is maintained as a function of sample depth.

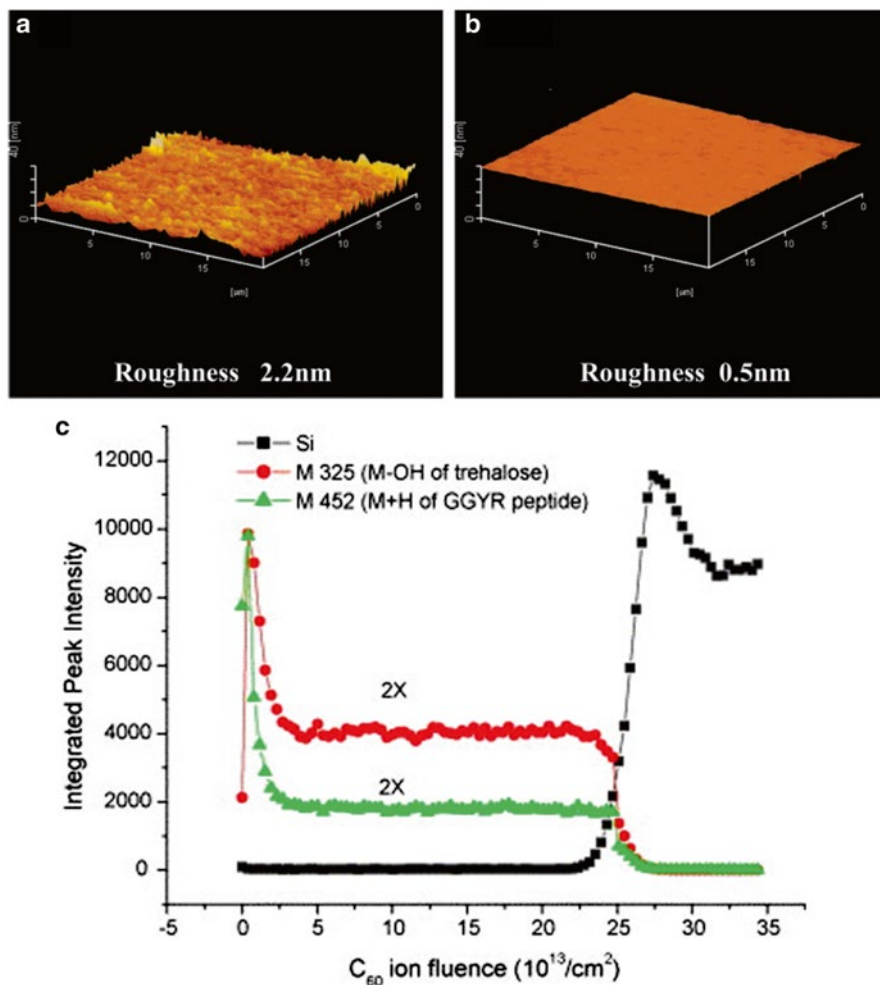


**Fig. 4.5** AFM images of (a) an unbombarded sugar trehalose film surface and (b) a  $1 \times 10^{14}$ -cm<sup>-2</sup> C<sub>60</sub><sup>+</sup> bombarded sugar trehalose film surface. The field of view is  $20 \mu\text{m} \times 20 \mu\text{m}$ . The labeled roughness corresponds to the rms values determined from statistical analysis of the entire image. (c) Depth-profile plot of secondary ion intensities of trehalose  $m/z$  325 (red circle), GGYR peptide  $m/z$  452 (green triangle), and silicon (black square) as a function of C<sub>60</sub><sup>+</sup> ion fluence. The trehalose/ GGYR film is 350 nm thick (From Ref. [22])

### 4.3.3 Molecular Depth Profiling

SIMS experiments of organic materials using atomic projectiles have traditionally been limited by the accumulation of chemical damage at the solid surface [6, 7, 11]. The chemical damage is created by the ion-beam-induced fragmentation of molecules. After extended bombardment, fragmented molecules collect at the solid

surface and cover undamaged molecules. To avoid the loss of information, ion beam erosion of the solid is often limited to 1% of the surface molecules. This restriction, known as the static limit, considerably reduces the amount of material available for analysis. Consequently, the sensitivity and lateral resolution of the SIMS imaging modality are often inadequate for most organic and biological applications when atomic projectiles are used.

Polyatomic projectiles have the potential to overcome the static limit requirement. Collectively, large yields, enhanced surface sensitivity, low topography, and reduced interlayer mixing open the door to molecular depth-profile experiments. Molecular depth-profile experiments aim to systematically remove material from an organic solid layer by layer and expose a molecularly intact surface for SIMS characterization [6, 7]. The success of the experiment relies heavily on the ability to etch the sample without the accumulation of chemical damage. The large yields and high surface sensitivities characteristic of cluster bombardment severely confine the deposition of incident energy to the solid surface. Therefore, the bulk of the ion-beam fragmented molecules are sputtered during the impact event. Moreover, residual molecule damage remains near the surface and is easily removed by subsequent bombardment. Thus, polyatomic projectiles erode organic material at a rate that prevents the accumulation of significant chemical damage at the sample surface. In addition to reduced chemical damage, decreased topography and interlayer mixing allow for the organic material to be removed without a significant physical change to the underlying solid. Thus, the pieces are in place for successful molecular depth-profile experiments.

The advantages of cluster projectiles have been used to successfully depth-profile a number of molecules. Gillen et al. have routinely demonstrated the feasibility of the experiments using 5 keV  $\text{SF}_5^+$  as a sputter projectile [3, 19, 33, 34]. An example from the research involves the controlled erosion of a polylactic acid (PLA) polymer film dosed with 5% drug molecule [19]. The depth-profile plots of secondary ion intensity versus  $\text{SF}_5^+$  primary ion fluence for the PLA polymer, the drug molecules, and the silicon substrate are illustrated in Fig. 4.6c, d. The measurements are characterized by three distinct regions: an initial period of molecule signal fluctuation often referred to as the transient region of a depth-profile measurement; an extended steady-sputter-state region, where the ion intensities do not vary as a function of erosion time; and the complete disappearance of molecular signal at the silicon interface. Most notably, the steady sputter state indicates  $\text{SF}_5^+$  can erode the material without the accumulation of significant chemical damage.

The idea of molecular stability during sample erosion has been extended to additional organic materials using  $\text{C}_{60}^+$  as a sputter projectile by Winograd et al. [18, 20, 22, 30, 31, 35–37]. An example from the research uses a spin-coated, GGYR peptide-doped, sugar trehalose film as a platform [22, 30, 31]. A depth-profile plot of secondary ion intensity versus  $\text{C}_{60}^+$  primary ion fluence for the trehalose molecule, the peptide molecule, and the silicon substrate is illustrated in Fig. 4.5c. Similar to the PLA polymer films, the trehalose signal and the peptide signal reach a steady sputter state before the silicon interface is reached. Furthermore, if the same film is eroded using 20-keV  $\text{Au}^+$ , all molecular signals immediately disappear.

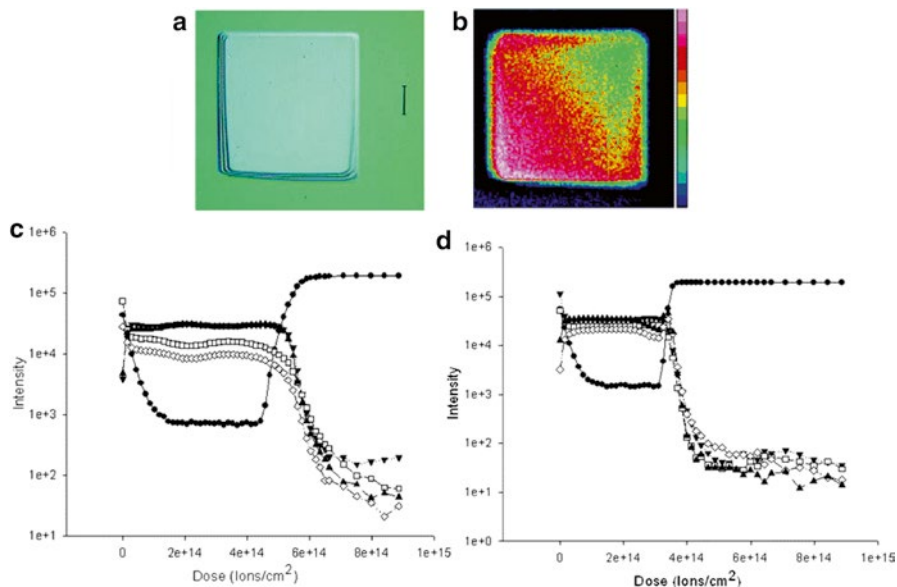


**Fig. 4.6** (a) Optical micrograph of a typical sputter crater formed after bombarding a 560-nm-thick PLA film with 5 keV  $\text{SF}_5^+$ . Scale bar represents 200  $\mu\text{m}$ . (b)  $\text{Si}^+$  molecule-specific SIMS image of a sputter crater formed after bombardment of a PLA film with  $\text{SF}_5^+$ . (c) Secondary ion intensities as a function of increasing  $\text{SF}_5^+$  primary ion dose for PLA films doped with 20% 4-acetamidophenol: ( $\blacktriangle$ )  $m/z$  152, 4-acetamidophenol ( $\text{M}+\text{H}$ ) $^+$ ; ( $\blacktriangledown$ )  $m/z$  109, 4-acetamidophenol ( $\text{M}+\text{H}-\text{COCH}_3$ ) $^+$ ; ( $\diamond$ )  $m/z$  145, PLA fragment ( $2n+\text{H}$ ) $^+$ ; ( $\square$ )  $m/z$  128, PLA fragment ( $2n-\text{O}$ ) $^+$ ; and ( $\cdot$ )  $m/z$  28,  $\text{Si}^+$ . (d) Secondary ion intensities as a function of increasing  $\text{SF}_5^+$  primary ion dose for PLA films doped with 5% theophylline: ( $\blacktriangledown$ )  $m/z$  128, PLA fragment ( $2n-\text{O}$ ) $^+$ ; ( $\square$ )  $m/z$  145, PLA fragment ( $2n+\text{H}$ ) $^+$ ; ( $\diamond$ )  $m/z$  165, theophylline ( $\text{M}+\text{H}-\text{O}$ ) $^+$ ; ( $\blacktriangle$ )  $m/z$  181, theophylline ( $\text{M}+\text{H}$ ) $^+$ ; and ( $\cdot$ )  $m/z$  28,  $\text{Si}^+$  (From Ref. [19])

Consequent to the observations, a simple analytical model was developed to explain the basic response of molecular ion intensity as a function of primary ion fluence during the erosion process [22]. The molecular depth-profile model considers a number of parameters, including the molecule sputter yield, the damage cross section of the surface molecules, and the thickness of the surface layer altered by the projectile. Specifically, the model is described by the equation

$$\frac{dc_s}{df} = \frac{Y^{\text{tot}} c_b}{nd} - \frac{Y^{\text{tot}} c_s}{nd} - \sigma_d c_s$$

where  $c_s$  is the surface concentration of intact molecules,  $c_b$  is the bulk concentration of intact molecules,  $f$  is the primary ion fluence,  $Y^{\text{tot}}$  is the total molecule sputtering yield,  $n$  is the molecular density,  $d$  is the altered layer depth beneath the surface, and  $\sigma_d$  is the area of damage on the surface [22]. The first term in the equation describes the supply of undamaged molecules from the bulk to the surface during the erosion process, the second term describes the loss of intact molecules from the surface

during sputtering, and the third term describes the damage of intact molecules remaining at the surface. Collectively, the equation indicates favorable conditions for molecular depth profiling exist when the total sputter yield is large relative to the damage cross section and altered layer thickness. The conditions have repeatedly been observed in molecular depth-profile experiments using  $\text{Au}_3^+$ ,  $\text{Bi}_3^+$ , and  $\text{C}_{60}^+$ . Molecules that have been successfully eroded include trehalose, arachidic acid, PLA polymer, PMMA polymer, amino acids in ice, cholesterol, and phospholipids, to name a few [18–20, 22, 27, 31, 33, 37–42]. Currently, the experiments are limited to a depth resolution of 10 nm. Moreover, several molecules have been identified that do not respond well during the erosion process [32]. To overcome the challenges and better generalize the strategy, the experimental variables need to be optimized to best fit the conditions of the depth-profile model. Among the variables that can be varied, the incident energy and incident angle of the cluster projectile seem most promising. Accordingly, molecular depth-profile studies investigating the effect of the projectile incident energy and projectile incident angle are currently ongoing [42–44]. The experiments are expected to provide valuable information about the optimal incident projectile energy and the optimal incident projectile angle for the deposition of primary energy into a solid—an important factor in the determination of sputter yield and damage volume [45]. Thus, the research should identify the best conditions for molecular depth profiling and extend the usefulness of the analysis.

#### ***4.3.4 Implications to SIMS Imaging***

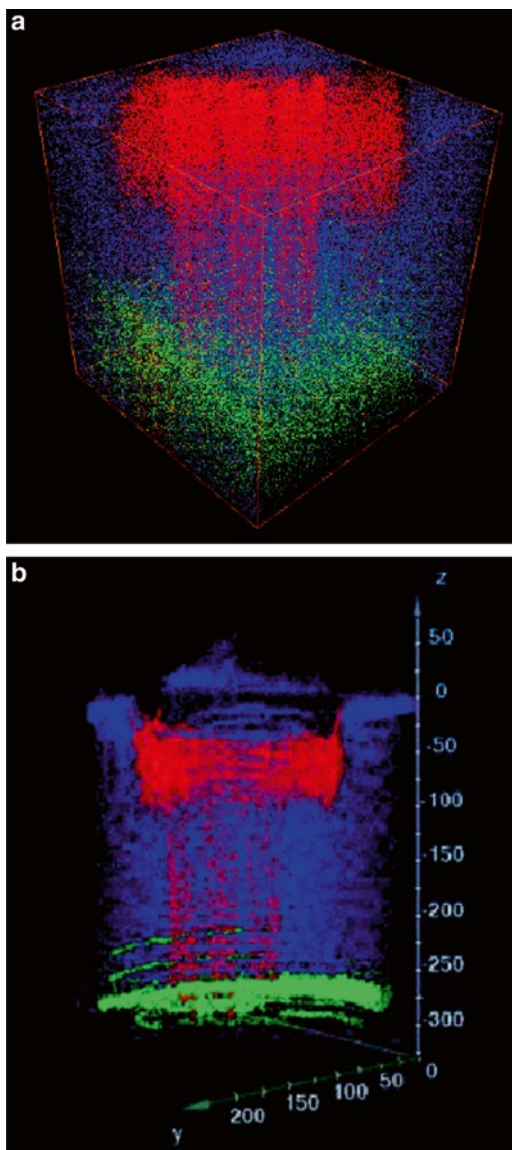
For a number of molecules, depth-profile experiments are feasible. The ability to eliminate the static limit requirement has major implications for the SIMS imaging of organic and biological materials [6, 7, 11]. SIMS images are acquired by rastering a focused ion beam across a sample surface and by collecting a mass spectrum at a sequence of surface positions. Software can be used to construct a two-dimensional (2D) image that displays ion intensity as a function of position (pixel) for a particular mass or a particular set of masses. In principle, the lateral resolution of the experiment is limited by the size of the ion beam, typically 100 nm. However, when atomic projectiles are employed, a fundamental flaw exists that causes the spatial resolution to be larger than the 100-nm beam size. The pitfall involves the accumulation of chemical damage after bombardment beyond the static limit [6, 7, 11]. Since only 1 % of the surface molecules are available for detection, the sensitivity of the SIMS measurement becomes inadequate as the pixel size approaches 100 nm  $\times$  100 nm. For instance, a molecular solid ( $1 \times 10^{22}$  molecules/cm<sup>3</sup>) has approximately  $5 \times 10^4$  surface molecules per 100-nm  $\times$  100-nm pixel. Taking into consideration the 1% static restriction, only  $5 \times 10^2$  of the molecules are available for analysis. With a typical ionization efficiency of  $1 \times 10^{-4}$ , less than 1 molecule would be detected per 100-nm  $\times$  100-nm pixel [31]. In fact, the pixel size would

have to be increased to  $1\ \mu\text{m} \times 1\ \mu\text{m}$  before 1 ion count is registered. Therefore, the lateral resolution of a static SIMS imaging experiment using atomic projectiles is fundamentally limited by sensitivity, and not by the size of the primary ion beam.

Polyatomic projectiles increase the number of molecules available for detection for samples more than one atomic layer thick. An increase in signal is attained by interrogating a pixel beyond the surface molecules and into the bulk of the solid [6, 7]. Considering the same molecular solid used in the previous example and the fact that cluster projectiles eliminate the static limit requirement, an increase in molecules over the same surface area can be achieved by changing the  $100\text{-nm} \times 100\text{-nm}$  pixel to a  $100\text{-nm} \times 100\text{-nm} \times 10\text{-nm}$ -deep voxel. The proposed three-dimensional voxel contains  $1 \times 10^6$  molecules, each of which is available for analysis. With an ionization efficiency of  $1 \times 10^{-4}$ , 100 molecules would be detected within the  $100\text{-nm} \times 100\text{-nm} \times 10\text{-nm}$  voxel. Furthermore,  $10^4$  molecules would be detected from a  $1\text{-}\mu\text{m} \times 1\text{-}\mu\text{m} \times 10\text{-nm}$  voxel. Thus, SIMS imaging using cluster projectiles has a sensitivity many orders of magnitude greater than traditional static SIMS imaging using atomic projectiles. Moreover, the effective lateral resolution is considerably better when polyatomic projectiles are used.

In addition to an improved sensitivity, molecular depth-profile experiments have the potential to construct a three-dimensional (3D) chemical map of a multicomponent solid. A 3D SIMS image of a solid is assembled by acquiring retrospective images between erosion cycles during molecular depth-profile analysis. Following data acquisition, software is used to assemble the image series in a manner in which the ion intensity of a particular mass or a particular set of masses is displayed as a function of the lateral and depth distributions within the solid. Wucher et al. have developed a protocol for 3D SIMS image reconstruction [46]. The procedure was developed using a peptide-dosed, trehalose film patterned by bombardment with a focused 15-keV  $\text{Ga}^+$  ion beam as a model. A high-resolution, image-series depth profile of this system was obtained using a focused, 40-keV  $\text{C}_{60}^+$  ion beam. In addition to the SIMS images, complementary AFM images of the system were acquired before and after the depth profile. Together, the measurements were used to calibrate a depth scale for the construction of the 3D image. However, the calibration is complicated by highly nonuniform erosion rates within different regions of the solid. The dissimilar erosion rates were attributed to the heterogeneous distribution of various materials throughout the system. Therefore, the protocol mandates that an individual depth calibration must be performed for each pixel of the imaged area for a true 3D representation of the solid to be constructed. A depth scale for each pixel was calculated using the SIMS and AFM measurements, and a new sequence of 2D images was assembled to contain the correct mass spectra for a specific depth for a specific pixel. The new images were stacked in an array to produce a 3D image of the multicomponent solid. The 3D image results of the experiment before and after depth calibration are illustrated in Fig. 4.7a, b, respectively. The images clearly demonstrate the necessity of the depth-calibration protocol for the accurate composition of the solid to be visualized. Moreover, the images provide an exciting insight into the possibly vast information that may be available during 3-D SIMS imaging.

**Fig. 4.7** (a) Uncalibrated 3D representation of a stack of sequential SIMS images with equidistant vertical spacing during a depth-profile experiment. *Red*,  $\text{Ga}^+$  ( $m/z$  69) signal from the initial  $\text{Ga}^+$  bombardment; *blue*,  $\text{M}+\text{H}^+$  ( $m/z$  452) molecular ion signal of GGYR peptide in the trehalose overlayer; *green*,  $\text{Si}^+$  ( $m/z$  28) from the Si substrate. (b) Depth-calibrated 3D representation of solid composition as constructed from the AFM-SIMS measurements. Color representation is the same as in (a). The field of view is  $200\ \mu\text{m} \times 280\ \mu\text{m}$  and the total eroded depth is 280 nm (From Ref. [46])



### 4.3.5 Comparison of Different Strategies

Before we introduce the various applications of cluster SIMS, a brief discussion for rationally selecting the optimal projectile for a specific experiment is appropriate [6, 7]. The assessment will emphasize the difference between  $\text{Au}_3^+/\text{Bi}_3^+$  and  $\text{C}_{60}^+$  projectiles in the SIMS. Other cluster projectiles, such as  $\text{SF}_5^+$ , are not yet amendable to SIMS imaging due to the poor focusing characteristics and are omitted in the



discussion for simplicity. In general,  $C_{60}^+$  provides enhanced yields and improved spectral quality as compared to  $Au_3^+/Bi_3^+$  [8, 14, 17]. Furthermore,  $C_{60}^+$  has a more surface-sensitive sampling depth and is more effective in molecular depth profiling [16, 22, 41]. The reason for these observations is attributed to each particle in the  $C_{60}^+$  cluster having less energy than each particle in the  $Au_3^+/Bi_3^+$  cluster. On the other hand, the imaging properties of  $Au_3^+/Bi_3^+$  are currently better than  $C_{60}^+$  [6, 7]. Specifically,  $Au_3^+/Bi_3^+$  provides a brighter, more laterally defined beam size, although technical advances in  $C_{60}^+$  focusing optics are rapidly narrowing the difference between these projectiles. In addition to smaller beam sizes,  $Au_3^+/Bi_3^+$  implants metal atoms into the solid during the erosion process [41]. Heavy-metal implantation changes the chemical nature of the solid and may improve the ionization efficiency during SIMS [47]. The ramification of this occurrence has yet to be determined. Overall, the larger  $C_{60}^+$  cluster is better for the acquisition of mass spectra and for molecular erosion, while the smaller  $Au_3^+/Bi_3^+$  cluster is better for high-lateral-resolution imaging applications. Perhaps a compromise for optimal 3D SIMS imaging lies in dual-beam depth-profile analysis:  $C_{60}^+$  is used for sample erosion and spectra acquisition, and  $Au_3^+/Bi_3^+$  is used for imaging acquisition.

In addition to an assessment of projectile type, comparing cluster SIMS and its principal MS imaging complement—matrix-assisted laser desorption ionization (MALDI)—is useful when optimizing an MS strategy for a particular application [48]. Briefly, MALDI uses a matrix solution to segregate analyte molecules from a complex sample. The analyte-doped matrix crystals are ablated using a UV laser and the desorbed material is directed into a mass spectrometer. In general, MALDI provides high-quality mass spectra of large-molecular-weight molecules. The spectra are characterized by little fragmentation and a nearly unlimited mass range ( $MW \geq 10^6$  amu). In addition, if a focused laser beam is used to acquire the spectra, an image of the sample can be constructed. MALDI imaging has been especially effective in the assay of large biological molecules, namely, peptides and proteins—an area SIMS imaging has been lacking. However, MALDI does not completely depict the vast range of molecules present within the sample. Specifically, the analysis is limited by little low-mass information ( $\leq 1,000$ ), a chemical background attributed to the matrix, poor surface sensitivity (100 nm), and a lateral resolution restricted by the 10–100- $\mu\text{m}$  laser beam size. The properties of cluster SIMS are an excellent complement to the MALDI pitfalls. Cluster SIMS excels in research where 0–1,000-amu target molecule mass ranges, chemically unmodified sample preparation, uppermost surface layer sensitivity, and submicrometer spatial resolution are important [6, 7, 11]. Thus, the applications of cluster SIMS emphasize research where these characteristics are essential.

#### 4.4 Applications of Cluster SIMS

The special properties of cluster projectiles make the SIMS technique an exciting option for a number of applications in a number of research fields, including semiconductors, polymers, organic, combinatorial, chemistry, nanotechnology, and

biology. Perhaps the most intriguing application is the use of cluster SIMS as a chemical microscope in the discovery of new biology. Therefore, the remainder of this chapter will discuss the biological analyses made practical by the introduction of cluster projectiles to SIMS imaging, with particular attention paid to lipid molecules within biological tissue and biological single cells.

#### 4.4.1 *Biological Tissue*

Recently, the distribution of lipid molecules in cellular membranes has become an increasingly important subject in the field of biology [49]. The interest has been prompted by the identification of lipids as key contributors in a number of cell processes, including signaling pathways, exocytosis, and endocytosis. The molecules have also been shown to play an important role in a variety of clinical diseases, namely Alzheimer's and Parkinson's. Thus, additional insight into lipid activity within cell membranes may lead to new findings in the areas of physiology, neurobiology, medicine, and pharmaceutical development.

A useful platform for investigating the function of lipids in intercellular activity is biological tissue [38, 50, 51]. Presently, strategies for *in vivo* analysis of these samples are problematic and provide little molecule specificity (i.e., magnetic resonance imaging, X-ray imaging, and microdialysis). However, procedures for dissecting, cryosecting, and preserving tissue while maintaining biological integrity for *ex vivo* analysis are better established. Unfortunately, common methods for *ex vivo* analysis offer an incomplete chemical representation of the samples. The strategies are flawed by the use of chemical labeling (i.e., fluorescence microscopy), insufficient molecule specificity (i.e., electron microscopy, Raman spectroscopy), and inadequate spatial resolution (i.e., MALDI imaging) [11, 50, 51]. In principle, SIMS is an ideal approach for overcoming these pitfalls. However, SIMS imaging using atomic projectiles of tissue samples has been limited by inadequate mass ranges ( $\leq 500$  amu), poor sensitivities, and the identification of only a few lipid molecules, namely, the phosphatidylcholine headgroup (MW = 184 amu) [50, 51]. Collectively, these pitfalls considerably reduce the amount of biologically relevant information that can be learned.

By replacing atomic projectiles with cluster projectiles, one can considerably improve the effectiveness of the SIMS imaging modality [6, 7]. The broad repertoire of lipid molecules that is detected during cluster SIMS imaging of tissue is illustrated in Fig. 4.8a [50]. The figure is a sequence of negative SIMS molecule-specific images of a mouse brain section acquired using a focused 25-keV  $\text{Au}_3^+$  ion beam and by scanning the sample target over a 9-mm  $\times$  9-mm area. Most notably, the images identify numerous lipid species ranging in mass from 0–1,000 amu, including phosphate lipid headgroups, cholesterol, palmitate, oleate, stearate, phosphosulfatide, phosphatidylinositol, and phosphatidylcholine. Moreover, the images show a distinctive lateral distribution for each lipid present within the tissue. In fact, these distributions are so unambiguous that anatomic structures of the brain are

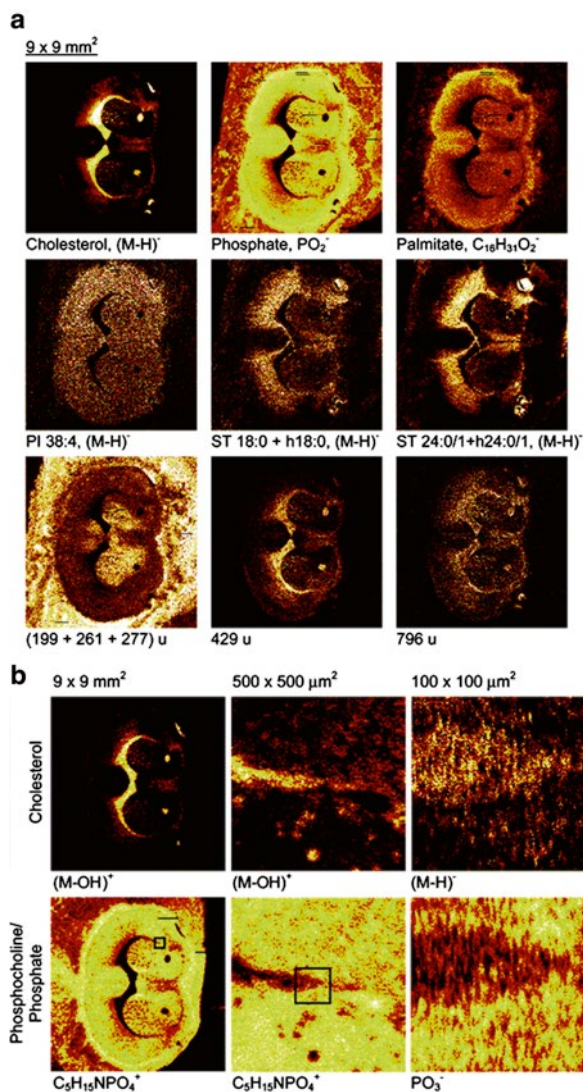


**Fig. 4.8** (a) Negative SIMS molecule-specific images of a freeze-dried, coronal-sliced, mouse brain section acquired using 25 keV Au<sub>3</sub><sup>+</sup>. The specific ions, which include cholesterol (*m/z* 385), phosphosulfatide (ST, *m/z* 806, 822, 888, 890), phosphatidylinositol (PI, *m/z* 965), and unknowns, mapped in each image are indicated below the image itself. The field of view is 9 mm×9 mm. (b) Positive and negative SIMS images of the distribution of cholesterol and phosphocholine in a mouse brain section at different fields of view. The first column of images was a positive SIMS image at a 9-mm×9-mm field of view, the second column of images was a positive SIMS image at a 500-μm×500-μm field of view, and the third column of images was a negative SIMS image at a 100-μm×100-μm field of view. The effective lateral resolution in the images is 300 nm. The magnified images were obtained from the areas indicated by the *black squares* in the phosphocholine images (From Ref. [50])

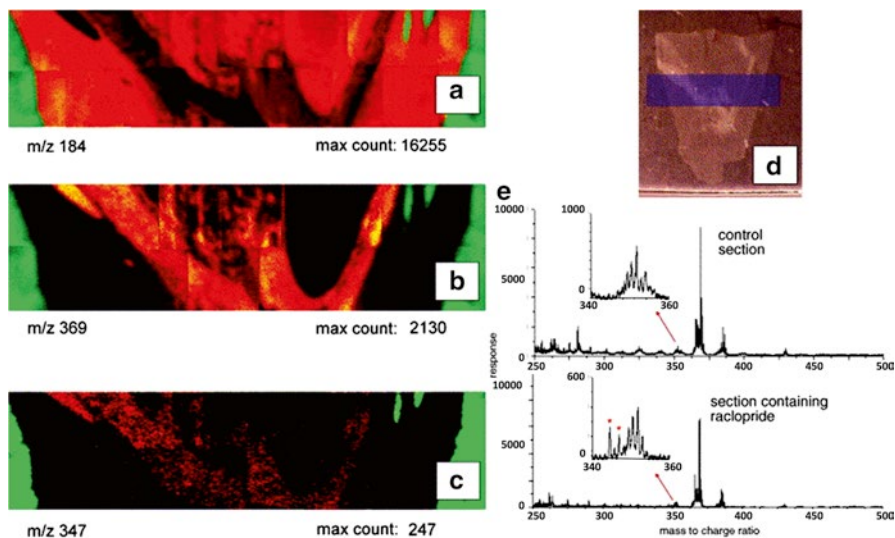


**Fig. 4.9** Positive SIMS molecule-specific images of brain section taken from a rat treated *in vivo* with the drug raclopride acquired using 40 keV  $C_{60}^+$ . The specific ions mapped include (a) phosphatidylcholine ( $m/z=184$ ), (b) cholesterol ( $m/z=369$ ), and (c) raclopride ( $m/z=247$ ). In each image, the *green intensity* represents the substrate. The field of view is 1.6 mm  $\times$  8 mm. (d) Optical image of the raclopride-treated, rat brain section. The *shaded region* illustrates the SIMS interrogated area. (e) Mass spectra illustrating the absence of the raclopride molecule in the control section and the presence of the raclopride molecule in the drug-treated section (From Ref. [39])

recognized. For instance, the images show a complementary localization between cholesterol and phosphocholine within the tissue. The heterogeneous distributions identify the cholesterol-enriched regions as white brain matter and the phosphocholine-enriched regions as gray matter. In addition, this occurrence of lipid heterogeneity is observed down to the micrometer scale (Fig. 4.8b).

An example of the improved detection levels attainable when cluster SIMS imaging is applied to tissue is shown in Fig. 4.9a–c [39]. The research uses a focused 40-keV  $C_{60}^+$  ion beam to probe the drug raclopride—a dopamine uptake inhibitor—within a brain tissue section taken from a rat dosed *in vivo*. The positive SIMS molecule-specific images of the rat brain section are shown in Fig. 4.9a–c and are constructed by stitching together a number of analyses acquired at smaller fields of view. Figure 4.9a illustrates the distribution of phosphocholine (MW=184 amu) to identify the gray-matter region of the brain, Fig. 4.9b illustrates the distribution of cholesterol (MW=369 amu) to identify the white-matter region of the brain, and Fig. 4.9c illustrates the distribution of the raclopride drug (MW=247 amu). The images indicate that raclopride can be identified from within the treated brain section and that the drug is distributed within the white-matter region of the brain (Fig. 4.9e). Unfortunately, the spatial distribution of the drug within the sample does not completely agree with the known gray-matter location of the dopamine receptors. Although the basis for the inconsistency is unknown, potential explanations include

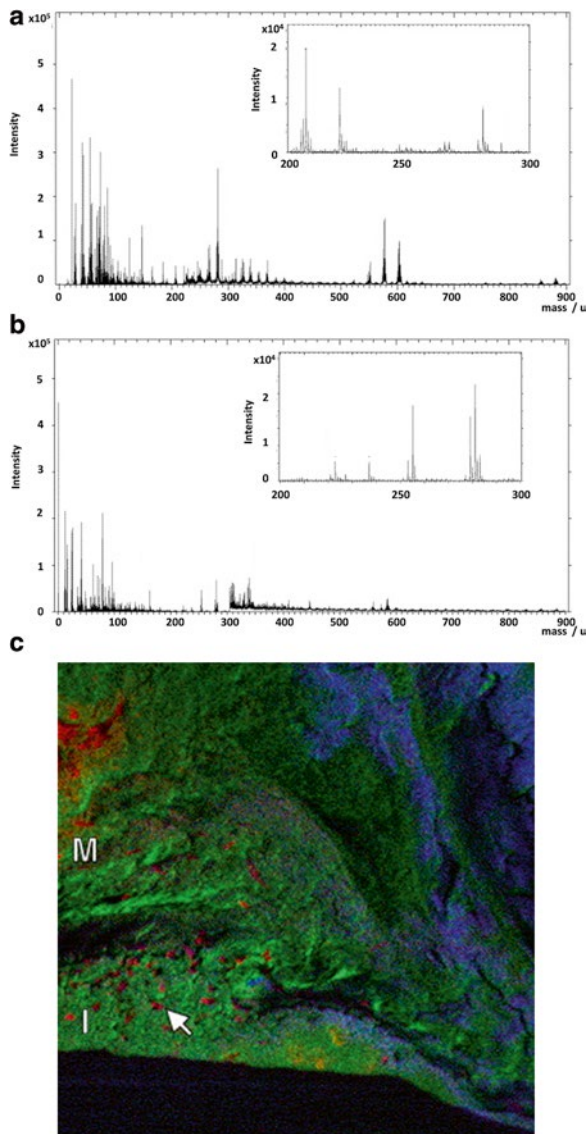
the redistribution of the drug after tissue preparation and the incidence of different ionization environments in the different regions of the tissue. Regardless of the issues, the experiment is encouraging since the raclopride-specific image demonstrates a two-part-per-million (ppm) detection level, a value that will improve even further once molecular depth profiling is applied—a feat that has already been deemed feasible on tissue homogenate when using 40 keV  $C_{60}^+$  as erosion projectile [39].

Broad ranges of lipid molecules, distinct lipid localizations, micrometer lateral resolution, 1-ppm sensitivities, and molecular depth profiling make cluster SIMS imaging a powerful technique for the analysis of tissue. A real-life biological application utilizing the strategy is illustrated in Fig. 4.11 [52]. The application involves the interrogation of human atherosclerotic plaque to determine the role of lipids in the development of cardiovascular disease. In order to analyze the unhealthy artery, SIMS spectra of healthy rat aorta were acquired as a control using a  $Bi_3^+$  ion beam (Fig. 4.10a, b). The spectra indicate that in a healthy artery, the lamellar tissue in the intima region (the innermost layer) is enriched in cholesterol, oxysterol, and diacylglycerols and that the smooth muscle tissue in the media region (the middle layer) is enriched in phosphocholine. Interestingly, the localization of lipids in the human atherosclerotic plaque shows a different distribution. Specifically, the SIMS molecule-specific image taken from the unhealthy artery shows an irregularly shaped distribution of cholesterol in the intima region and an irregularly located distribution of diacylglycerols in the media region. The unique lipid distributions suggest cholesterol and diacylglycerols play an important role in the development of cardiovascular disease. It is hypothesized that cholesterol may be an important ingredient in the apoptotic process leading to plaque formation and that diacylglycerol may be a mediator in the activation of this process. These hypotheses may be further developed by characterizing the role of these lipids in the formation of plaque at the cellular level.

#### 4.4.2 *Biological Single Cells*

A useful platform for investigating lipids at the cellular level is biological single cells [6, 7]. For reasons similar to the analysis of tissue, SIMS is an excellent strategy for analyzing these samples. An example of the biological findings that can be learned from this partnership is illustrated in Fig. 4.11 [53]. The research involves the examination of highly curved lipids during cell conjugation. Specifically, the junction region between two conjoined cells contains a large number of fusion pores. The fusion pores, which are important in a number of cellular events, including sexual reproduction, exocytosis, and endocytosis, are hypothesized to be formed through the heterogeneous redistribution of lamellar and nonlamellar lipids throughout the membrane. Particularly, increased levels of nonlamellar or high-curvature lipids and decreased levels of lamellar or rigid lipids at the junction region are expected to provide the membranes with the necessary elasticity to form the highly curved intermediate structures required for conjugation (Fig. 4.11d). To examine

**Fig. 4.10** (a) Positive and (b) negative SIMS spectra from a high-pressure, fresh-frozen, freeze-fractured, and freeze-dried rat aorta acquired using a  $\text{Bi}_3^+$  ion beam. The spectra were used as reference in the analysis of human atherosclerotic plaque. (c) An overlay of positive SIMS molecule-specific images of human atherosclerotic plaque. The field of view is  $500\ \mu\text{m} \times 500\ \mu\text{m}$ . The *red signal* in the image represents cholesterol, the *green signal* represents phosphocholine, and the *blue signal* represents diacylglycerol. The section *M* indicates the media region of the tissue and the section *I* indicates the tunica intima region (From Ref. [52])



this hypothesis, SIMS molecule-specific images of mating *Tetrahymena* cells were acquired using a focused 15-keV  $\text{In}^+$  ion beam. The images, which are illustrated in Fig. 4.11a, b, show a heterogeneous distribution of 2-aminoethylphosphonolipid (2-AEP; MW=126 amu), a nonlamellar lipid, and phosphocholine (PC; MW=184 amu), a lamellar lipid. Most notably, the fusion site between the two cells contains an elevated amount of the cone-shaped lipid 2-AEP and a depleted amount of cylindrical-shaped lipid PC (Fig. 4.11c). This observation supports the idea that

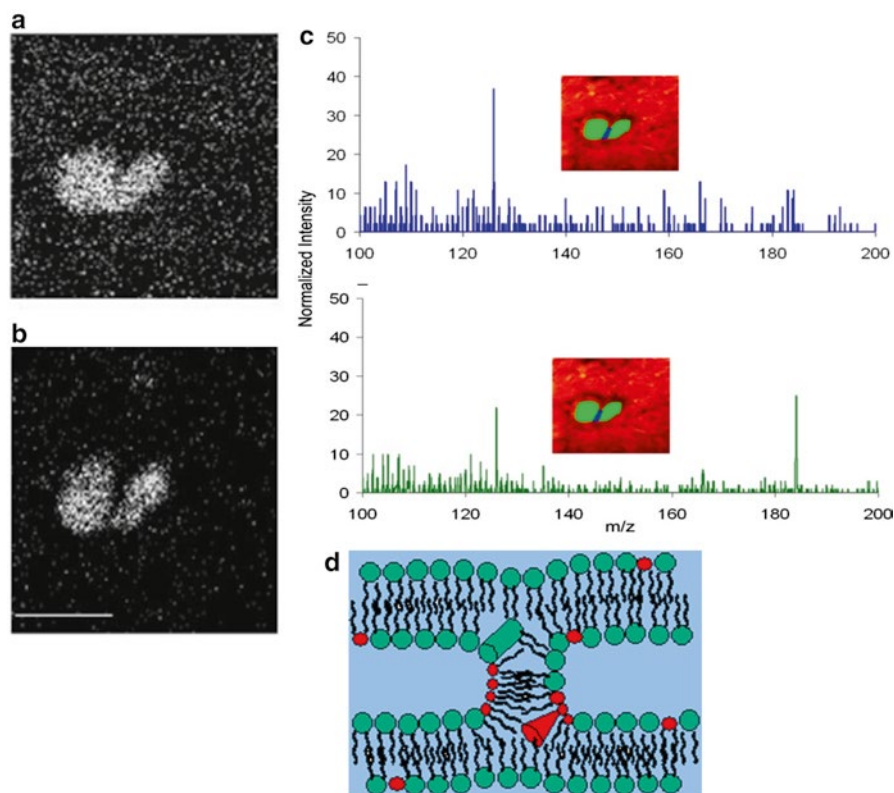


**Fig. 4.11** (a–b) Positive SIMS molecule-specific images of mating, freeze-fractured, *Tetrahymena* cells acquired using a focused 15-keV  $\text{In}^+$  ion beam. The specific ions are (a) 2-aminoethylphosphonolipid (2-AEP; MW = 126 amu), a nonlamellar lipid. The field of view is  $100\ \mu\text{m} \times 100\ \mu\text{m}$ , and (b) phosphocholine (PC; MW = 184 amu), a lamellar lipid. (c) Mass spectrum from the pixels along the conjugation junction (*top spectrum*) and from the cell body (*bottom spectrum*). (d) A schematic of the membrane fusion intermediate structure. The wavy lines depict the acyl tailgroups of the membrane phospholipids. The green circles are PC and red circles are 2-AEP, a cylinder-shaped lamellar lipid. The black circles represent the headgroup of 2-AEP, a cone-shaped nonlamellar lipid. Membrane fusion sites contain a large amount of cone-shaped lipids since these lipids fit well into contoured intermediate structures (From Ref. [53])

membrane fusion sites contain an increased concentration of nonlamellar lipids since cone-shaped lipids fit well into highly curved intermediate structures.

Future experiments using mating *Tetrahymena* aim to characterize the biological response that redistributes the lipids in preparation for the conjugation event. Unfortunately, single-cell SIMS imaging using atomic projectiles is limited to the identification of only a few lipid species. Moreover, these analyses are restricted to only the lipid molecules present within the uppermost layers of the exposed surface [54]. Therefore, a complete picture of the chemistry involved in the conjugation

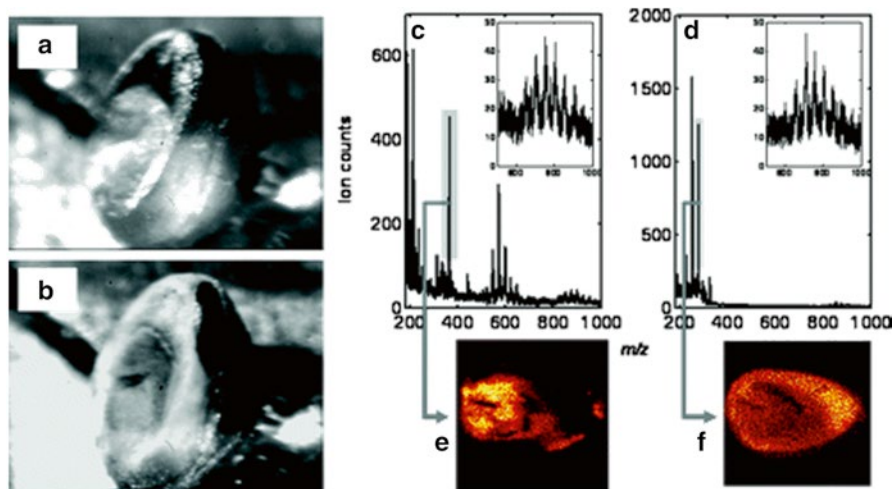


**Fig. 4.12** (a–b) Optical micrograph of a *Xenopus laevis* oocyte cell mounted on copper tape for 40-keV  $C_{60}^+$  SIMS analysis (a) before etching and (b) after etching. (c) Positive and (d) negative SIMS spectra from the oocyte cell after a  $1 \times 10^{15}$   $C_{60}^+$ /cm<sup>2</sup> etch. (e–f) SIMS molecule-specific images of the oocyte cell after a  $1 \times 10^{15}$   $C_{60}^+$ /cm<sup>2</sup> etch. The specific ions are (e) cholesterol (MW=369, positive SIMS) and oleic acid (MW=281, negative SIMS). The field of view is 1 mm  $\times$  1 mm (From Ref. [54])

event cannot be drawn using the atomic SIMS imaging modality. Nevertheless, the desired information can be attained when using cluster projectiles as both an imaging projectile and an erosion projectile in 3D SIMS imaging. An experiment demonstrating the effectiveness of this strategy is shown in Figs. 4.12 and 4.13 [54]. The research involves the 3D molecule-specific SIMS imaging of a freeze-dried *Xenopus laevis* oocyte using a 40-keV  $C_{60}^+$  ion beam (Fig. 4.12a, b). The positive and negative SIMS spectra shown in Fig. 4.12c, d demonstrate the wide array of lipid molecules that can be detected from the oocyte cell. Specifically, the lipid species identified in the spectra include phosphocholine (MW=58, 86, 166, 184 amu), cholesterol (MW=369 amu), lipid fatty acid side chains (MW: 540–720 amu), and glycosphingolipids (MW: 800–1,000 amu). In addition to lipid identification, the strategy is exciting with respect to lipid distribution as a function of the lateral and depth positions. Figure 4.13a–d display a 3D chemical representation of the oocyte cell. Of particular interest, the distribution of lipids within the image varies as a function of depth—with some species having a maximum intensity well below the sample surface. This observation is attributed to the removal of some molecules and the uncovering of others, suggesting that the 3D chemical integrity of the sample is maintained during erosion and the change in signal is representative of the molecular composition within the cell. Thus, 3D SIMS imaging using  $C_{60}^+$  is an effective means for probing the chemistry of single cells in three dimensions.



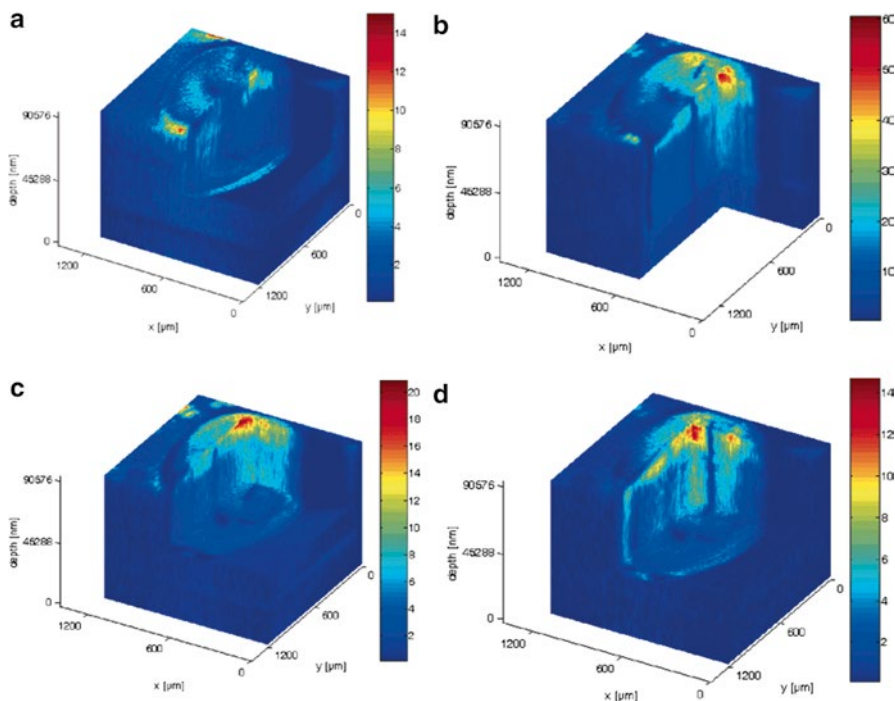


**Fig. 4.13** (a–d) Three-dimensional positive SIMS image of a oocyte cell for (a) phosphocholine (MW = 58, 86, 166, and 184), (b) signal summed over  $m/z$  range 540–650, (c) signal summed over the  $m/z$  range 815–960, and (d) cholesterol peak (MW = 369) acquired using 40 keV  $C_{60}^+$ . The 3-D representation is cut along two dimensions to display the third dimension. Color scale normalized for total counts per pixel for each mass. The field of view is 1 mm  $\times$  1 mm and the depth is 100  $\mu\text{m}$  (From Ref. [54])

## 4.5 Future Directions of Cluster SIMS

The special properties of cluster projectiles have greatly improved the usefulness of the SIMS imaging modality [6, 7]. Therefore, the future use of the technique in the characterization of real-life biological samples, such as mating *Tetrahymena*, may lead to the discovery of new and exciting biology. While the prospects for these types of experiments are promising, several issues still remain that could possibly limit the technique, including sample preparation, instrument duty cycle, and ionization probability. While these challenges are not specific to the ion beam used, cluster projectiles may be useful in overcoming them.

Sample preparation is essential when acquiring meaningful SIMS images of single cells [55–57]. In order to prepare cells for in-vacuum analysis, the 3D integrity of the sample must be preserved in the solid state with micrometer precision. Common strategies for cell preservation include freeze-drying, freeze-etching, freeze-fracturing, chemical fixation, and sugar vitrification [55–59]. Although each of the strategies

has its advantages and its disadvantages, the “gold standard” is freeze-fracturing. Specifically, freeze-fracturing involves quenching hydrated cells for in-vacuum, cryogenic fracture and analysis. Unfortunately, the usefulness of the approach is limited by the absorption of an ice contaminant overlayer. Nevertheless, the overlayer can be removed with no damage to the underlying molecules using cluster ion bombardment [59]. Therefore, a good strategy for maintaining the 3D structure of biological samples while exposing an intact, meaningful surface for SIMS imaging involves combining freeze-fracture technology and cluster ion beams.

In addition to sample preparation, SIMS imaging of biological samples is also restricted by the instrumental duty cycle of axial time-of-flight (ToF) MS [60]. For example, to analyze each of the  $10^8$  molecules in a  $1\text{-}\mu\text{m} \times 1\text{-}\mu\text{m} \times 10\text{-nm}$  voxel using a 10-pA ion beam with a 100-ns pulse width and a 10-kHz repetition rate, 10 s of instrumental time is required (assuming a sputter yield of 100). Therefore, it would take 182 h to acquire a  $256\text{-voxel} \times 256\text{-voxel}$  image. However, by eliminating the pulsed nature of the ion beam, the same image can be acquired in only 11 min, or  $10^3$  less time. Specifically, a direct current (DC) ion beam is utilized by switching from an axial ToF geometry to an orthogonal ToF (oToF) geometry. In addition to rapid sampling, the proposed design allows for tandem MS/MS, collisional focusing, collisional cooling, and ion trapping when a series of quadrupoles (q) is placed between the sampling region and the ToF region. Therefore, the instrumental scheme extends the usefulness of the SIMS imaging modality—making the quadrupole-orthogonal ToF design with a cluster ion beam a possible SIMS instrument of the future.

Perhaps the most critical of the remaining issues is the ionization probability of the SIMS technique [61, 62]. Typically, only 1 in  $10^4$  desorbed molecules is an ion, meaning the majority of the signal is lost in the neutral fraction. Postionization of the neutral molecules using light sources is a common strategy for recovering the lost signal. To date, the postionization analysis has been limited by extensive fragmentation [61, 62]. The observation is attributed to photofragmentation and photodissociation of molecules sputtered with internally excited electronic states. The pitfall may be overcome by using cluster ion bombardment to desorb electronically cooled molecules [15, 63, 64]. Specifically, molecule cooling is achieved through large-scale collision events in the dense sputter plume. Therefore, by combining cluster projectiles with light sources, such as vacuum ultraviolet (VUV) radiation, mid-infrared (IR) light sources, and femtosecond visible light sources, postionization of neutral molecules may be possible without extensive fragmentation, improving the ionization probability and overall sensitivity of the experiments.

## 4.6 Summary

Recently, cluster projectiles have been introduced as replacements to atomic projectiles in the SIMS imaging modality. Since cluster ions have less energy per atom than atomic ions, a unique mechanism for desorption is utilized during bombardment. The mechanism, which is mesoscopic in nature, has led to the observation of

several important properties when cluster projectiles are applied to SIMS, including enhanced yields, reduced damage, and the feasibility of molecular depth profiling. Together, the properties considerably extend the usefulness of the SIMS imaging modality—especially when used to interrogate lipid molecules in biological tissue and biological single cells. Specifically, the analyses are characterized by extended mass ranges, improved detection levels, submicrometer lateral resolution, and 3D molecule-specific imaging. Moreover, the usefulness of the analyses can be improved further by combing cluster ion beams with freeze-fracture technology, qq-oToF instrumental design, and postionization using light sources.

**Acknowledgments** The authors acknowledge the National Institutes of Health under grant number EB002016-13, the National Science Foundation under grant number CHE-0555314, and the Department of Energy under grant number DE-FG02-06ER15803 for financial support.

## References

1. Benninghoven A. *Zeitschrift for Physik A—Atoms Nuclei*. 1970;230:403–17.
2. Appelhans AD, Delmore JE. *Anal Chem*. 1989;61:1087–92.
3. Gillen G, Simons DS, Williams P. *Anal Chem*. 1990;62:2122–30.
4. Cornett DS, Lee TD, Mahoney JF. *Rapid Commun Mass Spectrom*. 1994;8:996–1000.
5. McMahon JM, Dookeran NN, Todd PJ. *J Am Soc Mass Spectrom*. 1995;6:1047–58.
6. Winograd N, Postawa Z, Cheng J, Szakal C, Kozole J, Garrison BJ. *Appl Surf Sci*. 2006;252:6836–43.
7. Winograd N. *Anal Chem*. 2005;77:142a–9.
8. Weibel D, Wong S, Lockyer N, Blenkinsopp P, Hill R, Vickerman JC. *Anal Chem*. 2003;75:1754–64.
9. Davies N, Weibel DE, Blenkinsopp P, Lockyer N, Hill R, Vickerman JC. *Appl Surf Sci*. 2003;203:223–7.
10. Wong SCC, Hill R, Blenkinsopp P, Lockyer NP, Weibel DE, Vickerman JC. *Appl Surf Sci*. 2003;203:219–22.
11. Vickerman JC, Briggs D, editors. *ToF-SIMS: surface analysis by mass spectrometry*. Manchester: SurfaceSpectra; 2001.
12. Postawa Z, Czerwinski B, Szewczyk M, Smiley EJ, Winograd N, Garrison BJ. *J Phys Chem B*. 2004;108:7831–8.
13. Postawa Z, Czerwinski B, Szewczyk M, Smiley EJ, Winograd N, Garrison BJ. *Anal Chem*. 2003;75:4402–7.
14. Russo MF, Garrison BJ. *Anal Chem*. 2006;78:7206–10.
15. Sun SX, Szakal C, Winograd N, Wucher A. *J Am Soc Mass Spectrom*. 2005;16:1677–86.
16. Szakal C, Kozole J, Russo MF, Garrison BJ, Winograd N. *Phys Rev Lett*. 2006;96:216104.
17. Russo MF, Szakal C, Kozole J, Winograd N, Garrison BJ. *Anal Chem*. 2007;79:4493–8.
18. Szakal C, Sun S, Wucher A, Winograd N. *Appl Surf Sci*. 2004;231–2:183–5.
19. Mahoney CM, Roberson SV, Gillen G. *Anal Chem*. 2004;76:3199–207.
20. Sostarecz AG, McQuaw CM, Wucher A, Winograd N. *Anal Chem*. 2004;76:6651–8.
21. Smiley EJ, Winograd N, Garrison BJ. *Anal Chem*. 2007;79:494–9.
22. Cheng J, Wucher A, Winograd N. *J Phys Chem B*. 2006;110:8329–36.
23. Van Stipdonk MJ, Harris RD, Schweikert EA. *Rapid Commun Mass Spectrom*. 1996;10:1987–91.
24. Tempez A, Schultz JA, Della-Negra S, Depauw J, Jacquet D, Novikov A, Lebeyec Y, Pautrat M, Caroff M, Ugarov M, Bensaoula H, Gonin M, Fuhrer K, Woods A. *Rapid Commun Mass Spectrom*. 2004;18:371–6.

25. Ostrowski SG, Szakal C, Kozole J, Roddy TP, Xu JY, Ewing AG, Winograd N. *Anal Chem.* 2006;78:973.
26. Xu JY, Szakal CW, Martin SE, Peterson BR, Wucher A, Winograd N. *J Am Chem Soc.* 2004;126:3902–9.
27. Conlan XA, Lockyer NP, Vickerman JC. *Rapid Commun Mass Spectrom.* 2006;20:1327–34.
28. Sun S, Szakal C, Roll T, Mazarov P, Wucher A, Winograd N. *Surf Interface Anal.* 2004;36:1367–72.
29. Sun S, Wucher A, Szakal C, Winograd N. *Appl Phys Lett.* 2004;84:5177–9.
30. Cheng J, Winograd N. *Appl Surf Sci.* 2006;252:6498–501.
31. Cheng J, Winograd N. *Anal Chem.* 2005;77:3651–9.
32. Shard AG, Brewer PJ, Green FM, Gilmore IS. *Surf Interface Anal.* 2007;39:294–8.
33. Mahoney CM, Fahey AJ, Gillen G. *Anal Chem.* 2007;79:828–36.
34. Wagner MS, Lenghaus K, Gillen G, Tarlov MJ. *Appl Surf Sci.* 2006;253:2603–10.
35. Wucher A, Sun S, Szakal C, Winograd N. *Appl Surf Sci.* 2004;231–2:68–71.
36. Sostarecz AG, Sun S, Szakal C, Wucher A, Winograd N. *Appl Surf Sci.* 2004;231–2:179–82.
37. Wucher A, Sun SX, Szakal C, Winograd N. *Anal Chem.* 2004;76:7234–42.
38. Touboul D, Kollmer F, Niehuis E, Brunelle A, Laprevote O. *J Am Soc Mass Spectrom.* 2005;16:1608–18.
39. Jones EA, Lockyer NP, Vickerman JC. *Int J Mass Spectrom.* 2007;260:146–57.
40. Kozole J, Szakal C, Kurczy M, Winograd N. *Appl Surf Sci.* 2006;252:6789–92.
41. Cheng J, Kozole J, Hengstebeck R, Winograd N. *J Am Soc Mass Spectrom.* 2007;18:406–12.
42. Fletcher JS, Conlan XA, Jones EA, Biddulph G, Lockyer NP, Vickerman JC. *Anal Chem.* 2006;78:1827–31.
43. Kozole J, Willingham D, Winograd N. *Appl Surf Sci.* 2007, submitted.
44. Cheng J, Wucher A, Winograd N. *Appl Surf Sci.* 2007, submitted.
45. Ryan KE, Smiley EJ, Garrison BJ. *Appl Surf Sci.* 2007, submitted.
46. Wucher A, Cheng J, Winograd N. *Anal Chem.* 2007;79:5529–39.
47. Marcus A, Winograd N. *Anal Chem.* 2006;78:141–8.
48. Karas M, Bahr U, Ingendoh A, Nordhoff E, Stahl B, Strupat K, Hillenkamp F. *Anal Chim Acta.* 1990;241:175–85.
49. Mukherjee S, Maxfield FR. *Annu Rev Cell Dev Biol.* 2004;20:839–66.
50. Sjoval P, Lausmaa J, Johansson B. *Anal Chem.* 2004;76:4271–8.
51. Sjoval P, Johansson B, Lausmaa J. *Appl Surf Sci.* 2006;252:6966–74.
52. Malmberg P, Borner K, Chen Y, Friberg P, Hagenhoff B, Mansson JE, Nygren H. *Biochim Biophys Acta-Mol Cell Biol L.* 2007;1771:185–95.
53. Ostrowski SG, Van Bell CT, Winograd N, Ewing AG. *Science.* 2004;305:71–3.
54. Fletcher JS, Lockyer NP, Vaidyanathan S, Vickerman JC. *Anal Chem.* 2007;79:2199–206.
55. Colliver TL, Brummel CL, Pacholski ML, Swanek FD, Ewing AG, Winograd N. *Anal Chem.* 1997;69:2225–31.
56. Pacholski ML, Donald M, Cannon J, Ewing AG, Winograd NJ. *Am Chem Soc.* 1999;121:4716–7.
57. Roddy TP, Donald M, Cannon J, Meserole CA, Winograd N, Ewing AG. *Anal Chem.* 2002;74:4011–9.
58. Parry S, Winograd N. *Anal Chem.* 2005;77:7950–7.
59. Kurczy ME, Piehowski P, Parry S, Ewing AG, Winograd N. *Appl Surf Sci.* 2007, submitted.
60. Carado A, Kozole J, Passerelli M, Winograd N, Loboda A, Wingate J. *Appl Surf Sci.* 2007, submitted.
61. Vorsa V, Kono T, Willey KF, Winograd N. *J Phys Chem B.* 1999;103:7889–95.
62. Vorsa V, Willey KF, Winograd N. *Anal Chem.* 1999;71:574–81.
63. Wojciechowski IA, Kutliev U, Sun SX, Szakal C, Winograd N, Garrison BJ. *Appl Surf Sci.* 2004;231–2:72–7.
64. Wojciechowski IA, Sun SX, Szakal C, Winograd N, Garrison BJ. *J Phys Chem A.* 2004;108:2993–8.

# Chapter 5

## Biological Tissue Imaging at Different Levels: MALDI and SIMS Imaging Combined

J. Stauber and Ron M.A. Heeren

**Abstract** Mass spectrometry has been employed to analyze the composition and structure of biologically relevant molecules in solution. Advances in methodology and instrumentation developments now allow the application of mass spectrometry for local biomolecular analysis directly on biological tissue surfaces; this technique is called imaging mass spectrometry (IMS). IMS is an innovative discovery tool for the biomedical sciences. This chapter describes the two main approaches relevant for molecular tissue imaging studies in the life sciences: secondary ion mass spectrometry (SIMS) imaging and matrix-assisted laser desorption and ionization (MALDI)-based imaging techniques. The benefits of imaging mass spectrometry for the fields of drug metabolism, lipidomics, and proteomics are discussed. Integrated MS imaging and proteomics protocols as well as tandem-MS imaging strategies, which are key to the identification of larger-molecular-weight compounds, are also reviewed.

### 5.1 Introduction

Imaging mass spectrometry (IMS) [1] is a very sensitive molecular imaging technique that provides combined molecular resolution and spatial resolution. It allows the identification and localization of the molecular content directly from tissue sections, single cells, and many other surfaces. The key features for biological studies are the sensitivity provided by modern mass spectrometers, the label-free nature of the technique, the ability to image posttranslational modifications, and the spatial resolution, which ranges from the organisms level (hundreds of micrometers) to the

---

J. Stauber • R.M.A. Heeren (✉)  
FOM-Institute for Atomic and Molecular Physics, Science park 104,  
1098 XG Amsterdam, The Netherlands  
e-mail: [heeren@amolf.nl](mailto:heeren@amolf.nl)

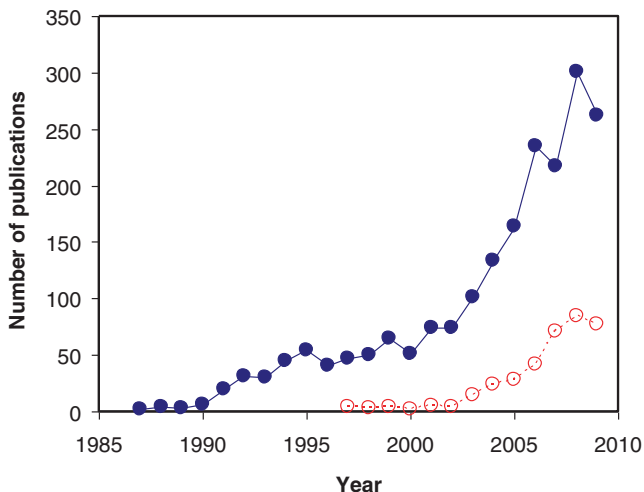


**Fig. 5.1** The number of publications resulting from a “web-of-science” search using the keywords “MALDI imaging” (*open circles*) and “imaging mass spectrometry” (*solid circles*). The results were obtained from the December 31, 2009, database

cellular level (tens of nanometers). IMS allows the simultaneous detection and imaging of thousands of species images in a single experiment. As such, it constitutes an efficient, multicomponent molecular imaging technique. The large number of new studies that include imaging mass spectrometry is evidence of the rapid growth of the field (Fig. 5.1).

IMS can be used to study different compositions and structures of surfaces in the context of biological studies. The IMS protocols and instruments have been developed to study the biodistribution of endogenous compounds, such as lipids or proteins, and exogenous compounds, such as polymers or drugs designed for tissue treatment. IMS helps to understand biological processes from subcellular to multicellular levels of spatial resolution. Moreover, it detects many different types of compounds in order to cover the large number of molecules present in the animal and vegetable kingdoms.

Compared to other molecular imaging approaches, such as magnetic resonance imaging (MRI), positron emission tomography (PET), or fluorescent immunochemistry, IMS provides unique information: IMS identifies molecules without the labeling of compounds, which allows the discovery of new localized compounds; no other technique can do this. Even though IMS is an *Ex vivo* technique and not an *in vivo* diagnosis technique such as MRI or PET, it can be coupled with them to validate molecular repartition, examine degradation of biomarkers, and/or study drug delivery, as demonstrated in recent publications [2].

Biological surface analysis with mass spectrometry has evolved around two main desorption and ionization methods: secondary ion mass spectrometry (SIMS) and matrix-assisted laser desorption ionization (MALDI). Both techniques are used

in imaging mass spectrometry and combined with different mass analyzers and detectors in order to increase the sensitivity and spatial resolution. SIMS has been in development since the early 1970s and applied to many different biological surfaces [2]. Although SIMS was initially limited to elements and small molecules, the detection and imaging of higher-molecular-weight species were realized through different surface modifications, such as metal-assisted SIMS (MetA-SIMS) and matrix-enhanced SIMS (ME-SIMS) [3–5], as well as by the use of cluster ion beam as the projectile species, as outlined in Chap. 4 of this book. MALDI imaging was developed in the late 1990s to image larger, intact molecules such as peptides and proteins. The SIMS and MALDI techniques both possess complementary characteristics in mass range, sensitivity, and spatial resolution, as will be demonstrated in this chapter.

IMS is crucially dependent on suitable and adequate sample-preparation techniques, as is any molecular analytical technique. Sample preparations, including solvent treatment, sample storage, and matrix deposition, are important for classical proteomics and lipidomics experiments directly on tissue. Reproducible sample preparations allow sensitive and high-resolution image analysis with ME-SIMS, MetA-SIMS, and MALDI imaging. Due to the different sensitivities and mass ranges accessible by SIMS and MALDI, different classes of molecules can be detected by combining these techniques [6]. Peptides and proteins, as well as lipids, metals, drugs, and metabolites, can be monitored and localized in different biological samples. Combinations of specific (bio-)markers that characterize a disease state can be identified, as IMS provides simultaneous images of different compounds found on pathological tissue sections.

In this chapter, we present the three biomolecular IMS techniques (ME-SIMS, MetA-SIMS, and MALDI), discuss different tissue-preparation methods, and summarize representative applications in different fields of research, such as lipidomics, plant studies, pharmaceuticals, proteomics, and clinical proteomics. The chapter ends with an outlook on future developments and the related applications of surface-enhanced SIMS and MALDI imaging. These high-end mass-spectrometric-based imaging methodologies are continuously under development to improve the sensitivity, resolution (both spatial and mass-resolving power), and data workup protocol, in order to increase the usage of IMS in clinical medicine.

## 5.2 Imaging Mass Spectrometry Modes

### 5.2.1 *Imaging Modes*

Many different ionization methods and mass analyzers have been used in imaging mass spectrometry (IMS) experiments. SIMS and MALDI have emerged as the two dominant methodologies in the generation of mass-resolved molecular images of surfaces. Both display different but complementary molecular imaging capabilities

and are employed in a wide variety of (biological) applications. Traditionally, SIMS targeted elements and small to medium-sized biomolecules (under 600 Da), whereas MALDI extended molecular imaging capabilities to a larger-molecular-weight domain (100 Da–80 kDa).

The two techniques combine an ion source, a mass analyzer, an ion detector, and data acquisition and processing software. They display complementary spatial resolution, sensitivity, and molecular weight ranges. Two different types of imaging modes, irrespective of the ionization method, are used: microprobe mode imaging and microscope mode imaging. The next section briefly explains the two different imaging approaches

### 5.2.2 *Microprobe Mode*

Microprobe (Fig. 5.2) is the most common imaging mode in mass spectrometry. It is a relatively straightforward technique to image a small, localized region by focusing a desorption/ionization beam on the sample. The ionization beam rasters, or scans, a selected region of the sample, and a mass spectrum is recorded for each beam shot. The mass spectra are stored along with the coordinates of the analyzed spot, as defined by the focus and position of the ionization beam. Molecular images of different ions are retrospectively reconstructed by dedicated software. This microprobe scanning mode is usually used with SIMS and MALDI imaging mass spectrometry. The spatial resolution of the ionization beam can be as high as 50 nm in SIMS and is conventionally limited by the laser spot's size (typically 50  $\mu\text{m}$ ) in MALDI. For that reason, the microscope imaging mode was developed and applied for MALDI studies in order to increase the spatial resolution [7].

### 5.2.3 *Microscope Mode*

The microscope imaging (Fig. 5.2) mode does not require position rastering with focused desorption beams. Instead, ion-optical elements in the time-of-flight mass spectrometer are used to retain the spatial organization of the ions after desorption and ionization between the ion source and the detector [7]. This results in a mass-resolved projection of the spatial origin of the ions generated at the sample surface by the defocused ionization beam and allows direct mass-resolved molecular image observation when combined with a position-sensitive detector. The magnification of the microscope elements, the quality of the ion optics, and the resolution of the position-sensitive detector determine the spatial resolution. The best spatial resolution demonstrated to date is a pixel size of 600 nm [7, 8]. The microscope mode directly analyzes a larger field-of-view (FOV) than the microprobe mode: It allows for the analysis of up to a 400- $\mu\text{m}$ -diameter area. The microscope mode is approximately 10,000 times faster than the microprobe mode.



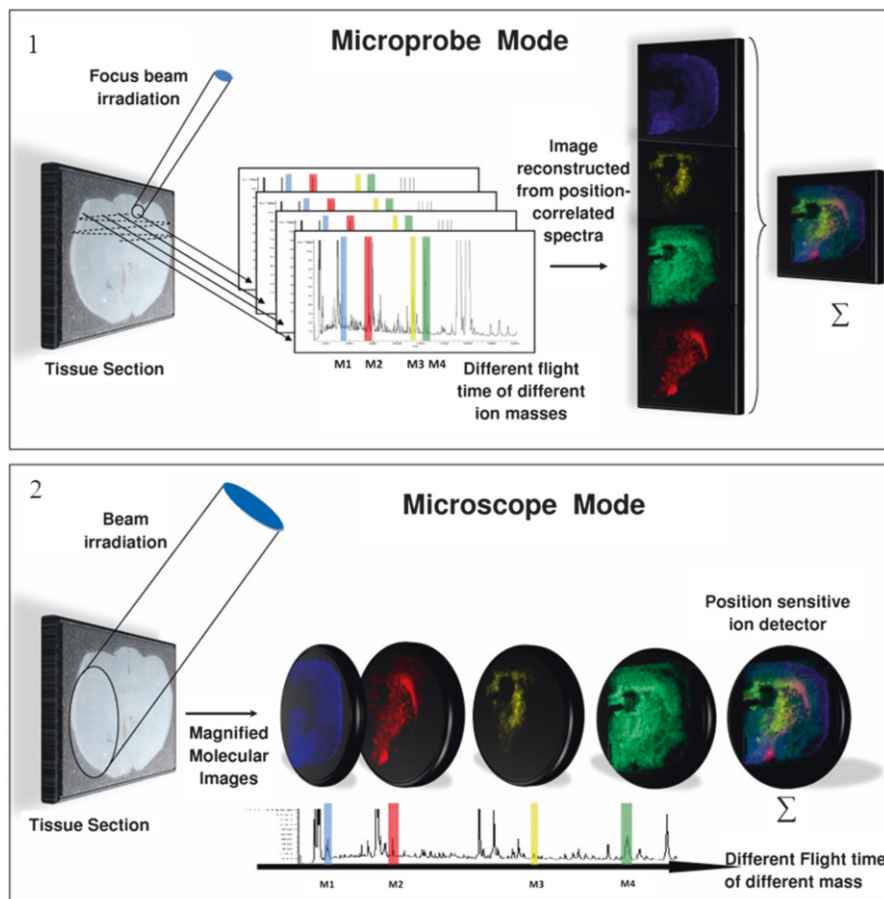


**Fig. 5.2** Schematics illustrating the two approaches in molecular imaging mass spectrometry: (1) Microprobe-mode imaging records the mass spectra in spot-by-spot ( $x, y$ ) position on the sample surface; (2) microscope-mode imaging records magnified images of mass-resolved ion distributions using a 2D detector

## 5.3 MALDI and SIMS: Two Sources of Ionization

### 5.3.1 MALDI Source

Developed by Karas and Hillenkamp in 1987 [9, 10], MALDI allows the simultaneous ionization/desorption of sample molecules, provides high sensitivity, and allows the analysis of large (up to 200 kDa) molecules. MALDI imaging was introduced in 1997 with advanced software capabilities [11, 12]. A large number of applications were presented in the last decade, with many biological applications. Most studies

use the MALDI imaging technique in a microprobe mode, by combining laser irradiation of the sample and advanced software capabilities to reconstruct images. More recently, commercial instruments with well-optimized system control and a laser spot size down to approximately a 50- $\mu\text{m}$  diameter have been developed. Important MALDI considerations include the size of the laser beam, the wavelength, the pulse width, and the matrices used. MALDI imaging traditionally uses either N<sub>2</sub> (337-nm) or Nd:YAG (335-nm) UV lasers, with the latter becoming more routinely used over the last two years, resulting in increased laser performance and stability. The laser pulse length (width) was found to have very little to no influence on MALDI mass spectra, at least up to pulse lengths of tens of nanoseconds [13]. This suggests that the desorption/ionization process is determined by the energy density supplied to the sample by the laser pulse (fluence or energy density, 100 J/m<sup>2</sup>) rather than by the rate of energy flow (irradiance, W/cm<sup>2</sup>). The fluence or energy flow required on the target is dependent on the spot size and pulse length (typically 3–5 ns).

(a) *Desorption/ionization process*

Since 1976, laser irradiation has been employed to ionize peptides from solid samples deposited on a surface [14]. Studies over the first decade of its use showed it was not efficient for large peptides. Therefore, the use of a matrix as an energy-transfer medium presented advantages in the desorption/ionization laser process.

The technique of MALDI imaging uses a pulsed beam of laser in the UV (or infrared laser source) to desorb and ionize a mixture of co-crystallized matrix and tissue. The matrix minimizes the sample degradation caused by energy absorption of the laser beam. The laser-transmitted energy is absorbed by the matrix, which acts as a resonant absorber for the photons and causes a phase explosion due to overheating of the surface. The sample molecules expand, are ejected into the gas phase, ionized, and then detected.

Partially ejected molecules are ionized by proton transfer, in the solid phase either before desorption or after desorption by collision with the excited matrix and other molecules. These processes generate different singly or multiply charged ions  $[M+nH]^{n+}$ , but the majority are singly charged ions.

No single mechanism can explain all the ions observed in a MALDI experiment. The large range of samples, matrices, and experimental parameters hinders the elucidation of ion-formation mechanisms. However, ion-formation mechanisms are described by two categories: primary and secondary ion formation [15]. The timescale for ion formation is of utmost interest, where the laser pulse typically lasts 3–5 ns, but the time required for expansion is much longer, many microseconds [16]. Primary ionization is caused by the laser pulse directly or by ion-molecule reactions within the excited matrix plume. Basic thermodynamics of ion formation, multiphoton ionization [17], energy pooling [18], and excited-state proton transfer [9] describe primary ionization. Although many primary ionization pathways have been identified, it has been hypothesized that secondary processes that occur within the expanding plume of sputtered species are the most important factor for the production of ions [19, 20]. In the expanding plume, reactions between ions and neutrals continue as long as there are collisions. Electron and proton transfer from the

matrix to the analyte is probably the most important secondary reaction and causes the predominantly detected protonated form of peptides and proteins. The gas-phase reaction of these two products is exoergic (protonation of peptide and deprotonation of matrix) since the proton affinity of the matrix is lower than the gas-phase basicity (GB) of the peptides or proteins, while the deprotonation of peptides and proteins is endoergic [20].

(b) *The matrix: The key role in a MALDI imaging experiment*

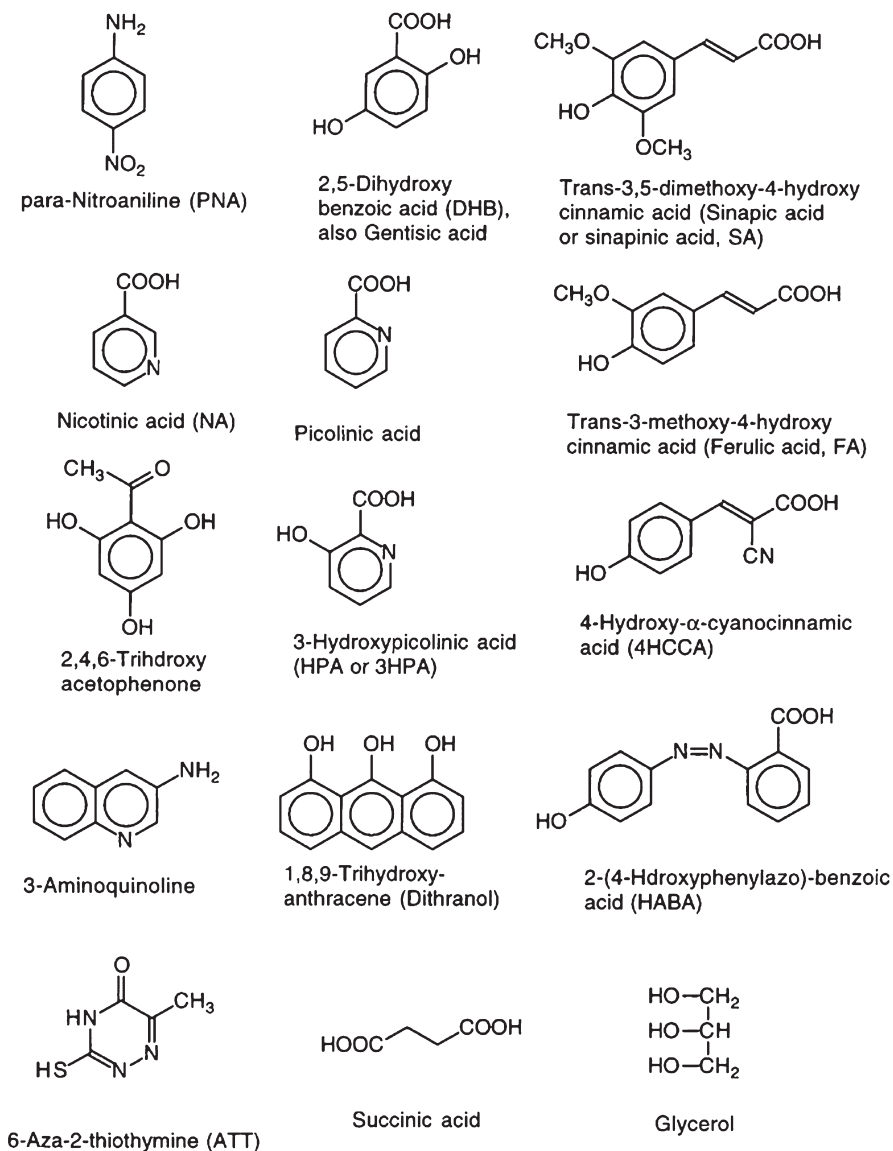
As explained above, the thermodynamics of the reaction depends on the type of matrix employed. Each matrix–analyte system exhibits different proton-transfer energetics. Therefore, different matrices are used for different types of analytes.

Figure 5.3 shows MALDI matrices and their structures. Three matrices are commonly used: 3,5-dimethoxy-4-hydroxycinnamic acid (sinapinic acid, SA),  $\alpha$ -cyano-4-hydroxycinnamic acid (HCCA), and 2,5-dihydroxybenzoic acid (DHB). SA is specially used as a more energetic matrix for the detection of proteins between 2 and 75 kDa. However, SA generates many derived ions at a low mass range, which results in a large amount of chemical noise [20]. Thus, for peptide ion detection, HCCA or DHB is often used. These cold matrices do not generate as much derived ion signal at low mass and allow easy mass spectral analysis and image reconstructions..

Recently, ionic matrices have been applied [21], to improve the signal intensities and crystal size homogeneity. These ionic matrices are obtained by a reaction between an acid matrix and a base (aniline). The comparison of images between classical matrix and ionic matrix HCCA/ANI positions them as an alternative to classical matrices (Fig. 5.4).

### 5.3.2 SIMS Source

Secondary ion mass spectrometry has been used as a high-spatial-resolution analytical microscopy technique since its inception as an imaging technique. Developed by Castaing and Slozdzian in 1962 [2], a broad beam (0.5-mm diameter of  $\text{Ar}^+$  primary ion beam) was used to desorb and ionize sample in a secondary ion and create an image resulting in a 1- $\mu\text{m}$  spatial resolution. In the microscope mode, the ultimate spatial resolution of mass-resolved images is comparable to that of the best optical microscopes (0.5  $\mu\text{m}$ ). This limitation is imposed by the energy spread of the secondary ions, causing imaging chromatic aberrations. The microprobe scanning mode, which was developed to be an alternative SIMS imaging mode [22], and the introduction of high-brightness liquid ion sources (LMIS) revolutionized SIMS imaging mass spectrometry in the 1980s. These ion sources, with suitable apertures and focusing ion optics, can be focused to small spot sizes (in the best case 20 nm) while retaining sufficient ion current for high-spatial-resolution microprobe experiments [23]. SIMS coupled with a time-of-Flight (ToF) analyzer provides a technique with high spatial resolution and high mass-resolving power and allows for the simultaneous detection of all species.



**Fig. 5.3** Structures, chemical names, trivial names, and abbreviations of frequently used MALDI matrices (From Ref. [15])

(a) *Enhancing molecular ion yield in SIMS*

SIMS is one dominant technique for surface analysis and imaging by mass spectrometry of small molecules [24]. Here, we discuss strategies that can enhance the applicability of SIMS to biological tissue surfaces. These innovative strategies, which include matrix-enhanced SIMS and metal-assisted SIMS, complement the MALDI-based imaging approaches.

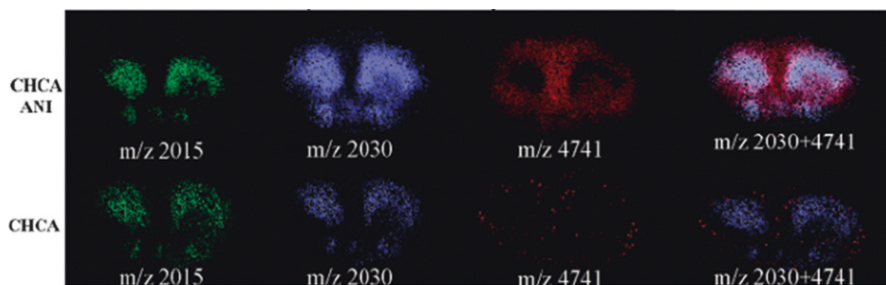


**Fig. 5.4** Comparison of HCCA classical matrix (*bottom*) and HCCA/ANI ionic matrix (*top*). The HCCA/ANI matrix shows higher signal intensities than the classical HCCA matrix [21]

The sputtering process in SIMS, generated by high-energy primary ions, results in fragmentation of almost all labile components on the surface. Increased detection sensitivity for these labile intact molecular ions has been a major research topic in organic SIMS for more than 10 years. Several strategies have been developed to minimize the internal energy deposition during desorption and ionization in SIMS.

The use of polyatomic primary ion sources, such as  $C_{60}^+$ ,  $SF_6^-$ ,  $Au_n$ , and  $Bi_n^{m+}$ , results in an increased secondary ion yield [25, 26]. Here, a beam of energetic cluster ions (up to several thousand electron volts) is directed at the surface. The cluster ions are believed to dissociate at the moment of surface impact, which results in the redistribution of the initial kinetic energy over the atoms present in the cluster [26, 27]. ME-SIMS (matrix-enhanced SIMS [28]) and MetA-SIMS (metal-assisted SIMS [3, 29]) have also been developed to increase the dynamic mass range, as outlined below.

#### (b) *Matrix-enhanced SIMS*

Odom and Wu reported the first ME-SIMS results in 1996. In their study, the sample was prepared in a solid organic matrix similar to sample preparations used for MALDI [28]. Over the past decade, ME-SIMS has been applied to a variety of biological studies [3, 5, 30]. This technique requires specific sample-preparation steps in order to optimize the signal intensity and minimize the redistribution or modification of the sample analytes.

The idea of diluting analyte molecules in a solid matrix preceded the invention of MALDI. Michl and coworkers analyzed small organic molecules by SIMS with frozen rare gas (Ar) as a matrix [31]. Other groups investigated the use of carbon as a matrix, which is particularly helpful in the analysis of polycyclic aromatic compounds [32, 33]. Barber and coworkers also popularized the use of glycerol matrices for ME-SIMS. In comparison with solid matrices, the liquid matrix refreshes the sample by evaporation and/or macroscopic flow under ion beam bombardment conditions [34]. Gillen et al. reported enhanced secondary ion signals for small molecules embedded in frozen glycerol matrix [35] and also studied gelatin matrices as a model of biological samples for secondary ion emission [36]. In addition, Cooks and coworkers embedded samples in ammonium chloride [37]. Similarly, Wu and

Odom applied a solid organic matrix similar to sample preparations used in MALDI for high-mass detection [28]. The co-crystallization of the matrix on the sample surface permits the observation of molecular ions using static secondary ion mass spectrometry (SSIMS). Matrix-enhanced SIMS yields substantial increases in the ionization efficiency of peptides, proteins, and oligonucleotides, enabling the detection of species with masses up to  $\sim 10,000$  Da.

### **5.3.3 *Characteristic of Ionization, Differences Between SIMS and Matrix-Enhanced SIMS***

Cooks and coworkers report that the use of a matrix such as  $\text{NH}_4\text{Cl}$  results in the ejection of ions with a lower internal energy since fewer fragmentation products are observed in the mass spectra [37, 38]. The authors proposed that analyte and matrix molecules are sputtered from the surface in the form of clusters. After emission, these clusters cool via evaporation, releasing analyte molecules with a low internal energy.

Other authors [28, 39] have compared a series of MALDI matrices and biological analytes with various masses (MW: 1,759–14,000 Da) in order to assess positive/negative matrix and the ion analyte yields. It is not clear what proportion of the efficiency enhancement provided by the matrix is attributable to the dynamics of desorption and to the chemistry of the molecular ion-emission ionization steps. It is proposed that the matrix plays an essential role as a strong proton donor, such as those used as MALDI matrices [37]. In the ME-SIMS process, the matrix should efficiently promote the cationization of neutral molecules sputtered from a solid mixture by an energetic ion beam, without photochemical reactions initiated by UV laser photons. In addition, a large number of molecules are sputtered per ion impact, and the analyte appears to be naturally entrained by the sputtered matrix flux. Moreover, the use of a matrix/analyte mixture yields less fragmentation, which is attributed to the excess matrix in the environment, which provides a much softer yet efficient desorption and ionization of the compound [28]. Finally, the matrix/analyte mixture has a sufficiently high concentration of analytes in the top monolayers of the surface.

### **5.3.4 *Characteristic of Metal-Assisted SIMS***

Surface metallization (MetA-SIMS) was also developed to enhance the desorption/ionization of higher-molecular-mass species [40]. For MetA-SIMS, a submonolayer coverage of a noble metal such as Au or Ag is applied to the surface of a material. Silver and gold metallization demonstrated an enhancement of nearly two orders of magnitude compared with traditional SIMS methods for the detection of polystyrene, a common organic polymer [29]. Metallization is especially useful for increasing the sensitivity for SIMS imaging of thick organic samples. Nevertheless,

ME-SIMS is still superior for the analysis of lipids and peptides. Several explanations for the sputtering mechanism of MetA-SIMS have been proposed. Metal cluster and nanoparticle formation may enhance the molecular ion yield and signal detection, by a number of proposed processes. First, the metallization of sample may eliminate sample charging due to the conducting paths created at the surface by the gold pattern. The elimination of charging effects induces a better-quality image [41]. Second, the metal clusters sitting on the surface of the sample can constitute a matrix that enhances desorption/ionization yield. Gold embedded in the sample acts as a cationing agent and may improve ion formation. Third, the metal evaporation by the primary ion beam may induce migration of mobile analytes onto metal nano-islands [29].

## 5.4 Analyzers to Improve IMS Capabilities

The mass spectrometry analytical technique combines sources and analyzers, which are interlocked and developed to increase the sensitivity and the number of parallel ion-detection events. Table 5.1 describes the different mass analyzer characteristics used for SIMS and MALDI imaging mass spectrometry. Different geometries of time-of-flight analyzers (linear, orthogonal, delayed extraction) and innovative mass analyzer instruments, such as quadrupole-TOF, ion mobility-quadrupole-TOF, and Fourier transform ion cyclotron resonance (FT-ICR), supply new perspectives and applications in imaging mass spectrometry [42–45].

In the early development of SIMS, the dynamic mode, which utilizes high-primary-ion current densities on the sample, was used due to limited sensitivity. The characteristic effect of the dynamic SIMS mode is typically increased erosion rates equivalent to the removal of up to several hundred monolayers of sample per second. Therefore, the instruments offered high detection efficiencies. Nevertheless, the dynamic mode is not suitable for the surface analysis of small areas and for long experiments. Thus, the static mode was developed by reducing the primary ion current density. At the first stage of static SIMS development, quadrupole and sector analyzers were combined to the SIMS source [46, 47]. These analyzers have a low transmission ratio (ratio of ions leaving a region of a mass spectrometer to the number of ions entering that region) and operate in a scanning mode. These properties resulted in limited sensitivity and unique  $m/z$  ion detection (low mass-resolving

**Table 5.1** Characteristic performances of different mass analyzers

Analyzer	Mass-resolving power	$m/z$ Range	Transmission	Detection	Sensitivity	Rep. rate
Quadrupole	$10^2$ – $10^3$	$10^3$	0.01–0.1	Sequential	1	<1 Hz
Sector	$10^4$	$>10^4$	0.1–0.5	Sequential	10	<1 Hz
Time-of-flight	$10^3$ – $10^4$	$10^5$	0.5–1.0	Parallel	$10^4$	>10 kHz
FT-ICR	$10^4$ – $10^6$	$10^6$	0.2–0.9	Sequential	Zmol	<1 Hz

power), which results in the loss of important information for imaging MS experiments. The increased use of static SIMS in the 1980s [48] resulted in the replacement of quadrupole and sector mass analyzers with time-of-flight analyzers (ToF). TOF analyzers offer two main advantages: a theoretically unlimited mass range and a parallel mass registration, which allows for the collection of a mass spectrum at every image pixel (rapid data collection) [49–51].

### 5.4.1 *Time-of-Flight*

Introduced by Stephens in 1946 [52], the time-of-flight analyzer has been combined with a SIMS ion source since the 1980s and with MALDI sources since its development in the early 1990s. ToF offers a good transmission ratio (50–100%), sensitivity, dynamic mass range, and repetition rate. The first high-mass-resolving power imaging with a ToF-SIMS instrument in a scanning microprobe mode was published by Schwieters' group in 1991 [53]. They reported secondary-ion images of a polymer with an average molecular weight of 1,400  $m/z$ .

Rapidly, the efficiency and the utility of ToF-SIMS imaging were demonstrated by many experts who consider mass spectrometry the most powerful technique for chemical analysis. Since the 1990s, the SIMS and MALDI sources have been combined with different configurations of time-of-flight detectors.

Time-of-flight analyzers allow the separation of ionized accelerated molecules according to their molecular masses. Generated by the ionization beam in the source, ions characteristic of the surface species are accelerated by an electric field between the conductive support (and sample) and the extraction grid (10–25 kV) to the same kinetic energy. Therefore, the ions arrive at the detector with different speeds, which are inversely proportional to their mass over charge values. Three main ToF analyzer geometries are defined in order to increase the sensitivity, mass accuracy, and mass-resolving power. These entry geometries are linear, reflectron, and orthogonal.

The linear geometry is commonly used in ToF imaging mass spectrometry and provides the highest sensitivity. As shown in Fig. 5.5, reflector mode and a delayed extraction time can be performed to provide an increase in sensitivity, mass-resolving power, and mass accuracy. The reflectron is an electrostatic ion mirror placed at the end of the drift tube. The ion mirror reflects the ions and corrects the different velocities by focusing the ions with the same  $m/z$  value and improves the mass-resolving power. The delayed extraction time or pulsed ion extraction corresponds to a short period of time delay between firing the laser and extracting the ions, which improves the sensitivity and mass-resolving power of a MALDI experiment [54, 55]. The linear geometry with reflector mode and delayed extraction is widely used in imaging mass spectrometry [55]. Nevertheless, delayed extraction must be tuned for each mass and is less effective at high mass. Therefore, a second time-of-flight geometry, orthogonal acceleration, was presented by Guilhaus and coworkers [56]. This geometry, shown in Fig. 5.5, places the ion source orthogonal



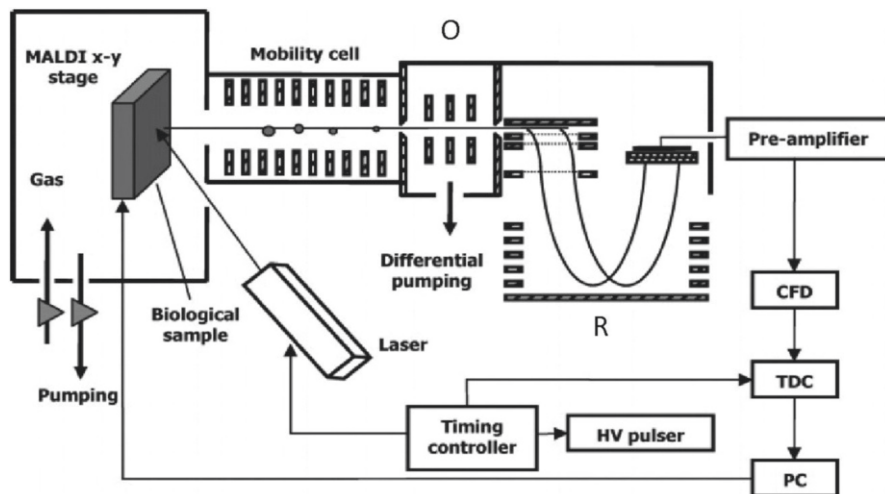


**Fig. 5.5** Mass spectrometer combined with an ion-mobility cell allows the separation of compounds according to their structure and conformation. In this example, an orthogonal time-of-flight (O) and electrostatic mirrors (R) as a reflector are used [43]

to the time-of-flight analyzer. This decoupling of the source from the mass analyzer results in an independent mass determination. The orthogonal mass analyzer allows a better mass accuracy in MALDI imaging as subtle height differences on the sample no longer influence the time-of-flight measured.

Previously used alone with a linear or orthogonal geometry, TOF mass analyzers are now combined with other mass analyzers in order to improve functionalities and capabilities. The quadrupole mass filter, developed in the mid-1950s by Wolfgang Paul, corresponds to four parallel hyperbolic rods that apply static or oscillating electrical fields to select ions. The quadrupole is well suited as an ion guide and collision cell to fragment parent ions and therefore allow molecule identification. The MALDI-Q-ToF mass spectrometer improves the capabilities of the MALDI imaging experiment by the localization, identification, and validation of molecules in tissue [44, 57].

#### 5.4.2 New Instruments for Imaging Mass Spectrometry

The goal of developing imaging mass spectrometry is not to replace existing molecular imaging technologies but to offer an alternative detection method and the possibility of molecule identification directly on the tissue. Mass spectrometry is the instrument of choice for simultaneous localization and identification. To this end, new instruments with different mass analyzers have been developed to improve the selectivity, sensitivity, and identification of detected molecules. Fourier transform

ion cyclotron resonance (FT-ICR), microscope MALDI, and ion-mobility mass spectrometers are presented and discussed as new instruments for MALDI imaging mass spectrometry. FT-ICR and ion-mobility IMS increase the number of identified molecules in tissue samples [43, 58], whereas the microscope MALDI increases MALDI image resolution, down to 4  $\mu\text{m}$  [7].

The MALDI–ion-mobility (IM)–orthogonal-time-of-flight mass spectrometer ( $\text{oTOFMS}$ ) provides a gas-phase separation before the MS experiment. IM, also called plasma chromatography, was developed in the 1970s as a technique for ion separation [59]. IM applications range from protein interaction studies to conformer differentiation. Ion-mobility mass spectrometry (IMMS) consists of an applied electric field in a buffer gas to separate individual components according to their mobility differences (collisional cross section) followed by mass-to-charge ratio discrimination in a time-of-flight instrument. Flight times in the mass spectrometer are much shorter than residence times in the drift tube; thus, it is possible to record mass-resolved ion mobilities for all ions simultaneously [60]. The combination of IM and imaging mass spectrometry is especially well suited to discriminate lipids and peptides with the same mass-to-charge ratio [45]. Therefore, this separation allows simultaneous localization and identification [61].

The ultrahigh-mass-resolving power of MALDI FT-ICR reveals novel molecular distributions that remain hidden with low-resolution mass-spectrometric techniques [58].

The FT-ICR geometry was used in the early 1930s [62] for nuclear physics experiments and 40 years later for applications [63, 64]. The FT-ICR mass spectrometer is composed of an ion cyclotron resonance cell placed in a homogeneous high magnetic field. A Lorenz force perpendicular to the magnetic field causes the ions to rotate with a frequency that is inversely proportional to their  $m/z$  ratio. This frequency of rotation is measured as the induced charge on detection electrodes located on the ICR cell. The time-domain signal is measured, amplified, and Fourier-transformed to yield frequency-domain data and then converted to  $m/z$  [65, 66]. A longer time-domain signal yields a higher mass-resolving power and a more precise frequency determination, and thus a higher mass accuracy (Table 5.1). This increased mass-resolving power for MALDI imaging allows the identification and localization of more peptides and lipids in tissue. The main difference between FT-ICR and ToF is the delay time of mass analysis. In FT-MS, this period is much longer (ms to seconds) than in the ToF-MS ( $\mu\text{s}$ ). Tissue digestion combined with ion mobility or FT-ICR mass spectrometry identifies a large number of peptides from different tissue types (formalin-fixed paraffin-embedded).

The microscope mode uses ion-optical microscope elements to project the spatial origin of the ions generated at the sample surface onto a two-dimensional position-sensitive detector [7, 67]. This approach of MALDI microscope mode imaging allows a 200- $\mu\text{m}$ -diameter area analysis with a high spatial resolution (4  $\mu\text{m}$ ). In this case, the spatial resolution is independent of the spot diameter of the ionizing beam but depends on the quality of the ion optics and the detector. A single analysis over a large area now results in a higher efficiency of ion production as well as an increase in the temporal resolution. This mass spectrometer design allows for

the detection of compounds up to 4 kDa, such as lipids, peptides, and small proteins, which are of interest in lipidomics and proteomics. These applications are detailed later in [Sect. 5.6](#) on the applications of surface-enhanced IMS.

Another technique describes a way to decrease the spatial resolution without modifying the ion optics. Microstructures of silicon wafer masks with small apertures were designed to decrease the laser diameter and the irradiated area. By application of these design masks close to the sample, 30- $\mu\text{m}$  irradiated surfaces are easily obtained and can reach 10  $\mu\text{m}$  without the loss of signal intensities [67, 68].

## 5.5 Sample Preparation and Protocols

The new fields of lipidomics and proteomics were born in the early 1980s when mass spectrometry (analytical chemistry) was applied to biological samples. The MS approach revolutionized molecular biology and biochemistry with its high sensitivity and high-throughput analysis. However, MS approaches involve stringent and precise sample preparation to avoid contaminants and false-positive detection of biomarkers. Due to the high sensitivity and the need for reproducibility, many congresses and initiatives are focused on standardizing the techniques [69, 70].

Sample preparation is one of the most important steps for sensitive, rational, and coherent analysis. The conditioning of the tissue and the timescale of the analysis are critical and were neglected in the past. Tissue samples are very sensitive to enzyme activity and surface contamination. After dissection, enzymes are still active and play a role in the degradation of the proteome and the transcriptome. New methods such as fast microwave irradiation and homogeneous heating have been used to prevent the degradation of proteins and peptides [71, 72].

Therefore, high reproducibility and standardization are essential prerequisites for any analytical approach. Moreover, maintaining the biochemical, molecular, and structural sample integrity is a crucial supplementary aspect for the field of IMS. These points are discussed here, from the tissue collection to the final analysis.

### 5.5.1 Tissue Collection

The first step of the IMS experiment is tissue collection, which is basically the application of the knowledge of anatomopathologists. The analysis of fresh tissue sections is not as difficult as that of preserved tissues. Frozen tissue and formalin-fixed and paraffin-embedded (FFPE) tissue are the two most common preparations used for the preservation of tissue integrity while avoiding molecular degradation. The analysis of archived specimens is widely restricted due to methylene cross-linkage between peptides and proteins [73]. However, recent FFPE tissue preparations have been presented and applied to proteomics studies [74, 75]. These new possibilities open the proteomics and imaging experiments to a large number of sample bibliotheca.

### 5.5.1.1 Fast Frozen Tissues

Generally, after an organ has been removed from a sacrificed animal or a biopsy has been taken, the sample is snap-frozen in isopentane (at  $-50\text{ }^{\circ}\text{C}$ ), depending on the volume of the tissue. Isopentane is preferred over liquid nitrogen ( $\text{LN}_2$ ) due to its larger heat capacity, which prevents the formation of ice crystals in the tissue. Cooling down larger tissue volumes (such as entire organs) is more cumbersome due to the introduction of large temperature gradients. In those cases,  $\text{LN}_2$  is often used. The formation of ice crystals can destroy the cellular morphology by disrupting the cell membranes. Different reports show the necessity to heat or to use microwave to inhibit the enzymatic activities and avoid protein degradation just after the animal sacrifice. In the past 10 years, an additional step of heating or microwave irradiation has been used to inactivate peptide and protein degradation [71, 72].

### 5.5.1.2 FFPE Tissue

Formalin-fixed and paraffin-embedded tissues are difficult to analyze by classical proteomics studies due to the cross-linkage between the amino and thiol groups of amino acids. A protocol with enzyme cleavage has been used to extract, detect, and localize protein fragments [76]. A dewaxing step with xylene and rehydration with graded water/ethanol baths are followed by applying enzyme on the sample surface using a microspotting technique. Enzyme spots with a  $50\text{--}80\text{-}\mu\text{m}$  diameter allow a reproducible and controlled amount of deposited enzyme [74, 75].

### 5.5.1.3 Tissue Section

The biological tissue sample is cut at a temperature of  $-18/20\text{ }^{\circ}\text{C}$  in a cryo-microtome following one of the previous sample-preparation steps. Samples embedding in embedding materials containing synthetic polymers such as polyethylene glycol (PEG) and polydimethylsiloxanes (PDMS) should preferably be avoided. These materials have a tendency to smear a thin layer of polymer over the sample surface during the sectioning procedure. This surface pollution often leads to preferential ionization and ion-suppression effects, which will reduce the resulting image quality. Clean tissue sections with a thickness of  $10\text{--}15\text{ }\mu\text{m}$  are immediately deposited onto a stainless steel plate and directly analyzed or kept at  $-80\text{ }^{\circ}\text{C}$ . The best extraction conditions and consequently the highest sensitivity and mass-resolving power are obtained when using stainless steel plates. However, other sample holders, such as a glass plate coated by a thin conductive layer, which allows staining optical image records, can be used. Just before analysis, the plates are warmed to room temperature and dried under vacuum. There is no delocalization of observed compounds (on the scale of a few hundred nanometers), regardless of their mass. Compounds such as phospholipids are unlikely to delocalize, but it is generally feared that light elements, such as  $\text{Na}^+$  or  $\text{K}^+$ , can be rapidly delocalized on a

nanometer scale [1]. Nevertheless, no such movement of alkaline or organic ions has been observed at the micrometer scale under the conditions described above. In addition, this sample-preparation method is robust, reproducible, and easy and does not limit the lateral resolution.

## 5.5.2 *Surface Modifications*

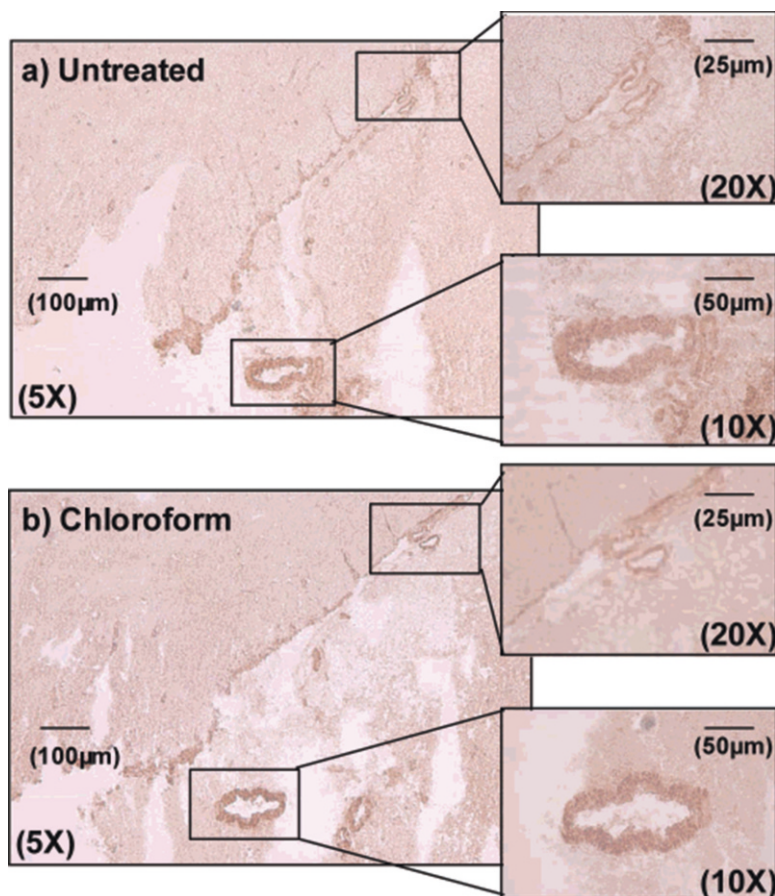
### 5.5.2.1 **Organic Solvent Treatment**

Organic treatment consists of a step of fast solution application (chloroform, cold ethanol, water) on the tissue surface to remove a particular class of compounds (lipids or peptides) according to their solubilities in the solution used. The aim of this approach is to decrease the complexity of the sample and to avoid ion-suppression effects during the MS analysis. Many different sample preparations have been developed to increase sensitivity, such as washes with chloroform, methanol, water, or ethanol [77, 78]. These washes must be performed with caution to avoid any delocalization of hydrophilic peptides. Apolar solvents, such as chloroform or xylene, are used particularly to remove lipids and deconstruct the lipids layers of the cell membrane to increase the detection of high-mass proteins [74, 79]. Each sample is a unique model, and parameters must be optimized sample to sample. As shown in Fig. 5.6, analyses must be validated with immunochemistry to demonstrate that there is no delocalization of compounds after tissue preparation and treatment [79].

### 5.5.2.2 **Matrix Deposition**

Matrix-enhanced SIMS and MALDI techniques need a matrix deposited on the surface after sample sectioning and surface treatment. A large number of matrices and deposition techniques have been tested [28]. One of the key issues associated with ME-SIMS and MALDI is the selection of appropriate matrix material for different analytes according to the type of biological sample. Table 5.2 shows different matrices and their associated applications.

Generally, matrices are freshly prepared by dissolution in 50 % H<sub>2</sub>O and 50 % acetonitrile to a concentration of 0.5 M. The goal of matrix application is to produce a very thin coating (several monolayers thick) on the tissue surface. Many techniques have been developed for matrix deposition without molecular delocalization, including spin coating, spraying, acoustic deposition, microspotting, and pipette depositing [74, 75, 85]. Pipette deposition and manual spraying were used for rapid analysis but are not suited for reproducible and accurate imaging experiments. However, the other techniques cited above (which have now been commercialized; the ImagePrep vibrational sprayer by Bruker Daltonics, the Portrait 630 acoustic spotter by Labcyte and the ChIP piezo spotting system by Shimadzu are a few

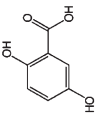
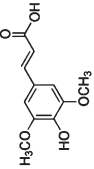
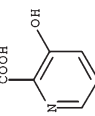
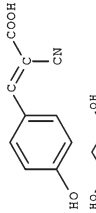
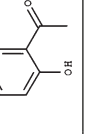


**Fig. 5.6** Images obtained after immunochemistry of oxytocin peptides before (a) and after chloroform treatment (b) showing no delocalization of the peptide [79]

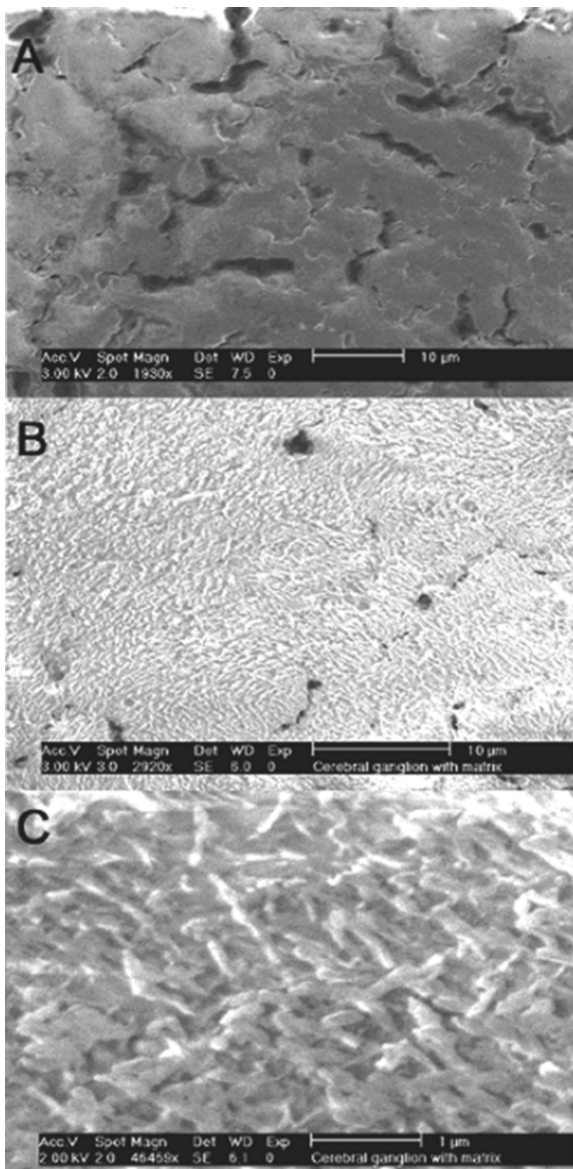
examples of available matrix-deposition systems) deposit matrix reproducibly with a well-known quantity and spot size (between 30–80-µm spot diameter). Ultimately, when a matrix deposition system is being used to enhance the molecular signal quality, the size of the matrix crystals will determine the obtainable spatial resolution and the sensitivity. Figure 5.7 provides an example where electrospray deposition was utilized to produce extremely small matrix crystals that are compatible with the spatial resolution of SIMS. Crystal sizes were smaller than 1 µm, as shown in Fig. 5.7c, allowing for the visualization of subcellular detail in these neuronal cells.

In this case of ME-SIMS, the dried droplet deposition should not be used, in order to avoid any peptide and/or biomolecule delocalization. Matrix droplets deposited on cryo-microtome cut tissue sections spread over the surface and crystallize. This leads to very large matrix crystal sizes (10 µm) and lateral analyte diffusion after wetting the tissue. Matrix solutions can be sprayed or deposited with a very small droplet diameter (90 µm) to avoid diffusion of molecules over the sample.

**Table 5.2** Common matrices used for matrix-enhanced mass spectrometry techniques and their associated applications

Compound	Name	Structure	Solvents	Applications
DHB	2,5-Hydroxybenzoic acid		Acetonitrile, water, methanol, acetone, chloroform	Peptides, proteins, lipids, glycoproteins, glycans [30, 80]
SA	3,5-Dimethoxy-4-hydroxycinnamic acid		Acetonitrile, water, methanol, acetone, chloroform	Proteins [78, 81], glycoproteins
3-HPA	3-Hydroxypicolinic acid		Ethanol	Alcalins, oligonucleotides, proteins [82, 83]
HCCA	alpha-Cyano-4-hydroxycinnamic acid		Acetonitrile, water, ethanol, acetone	Lipids, peptides [39], proteins [84]
THAP	2,4,6-Trihydroxy acetophenone		Ethanol	Oligonucleotides, peptides

**Fig. 5.7** Scanning electron microscopy images of *Lymnaea stagnalis* nervous tissue (a) prior to matrix application (scale bar 10  $\mu\text{m}$ ) and (b) after electrospray deposition of 2,5-DHB (scale bar 10  $\mu\text{m}$ ); (c) higher-magnification image showing submicron crystal dimensions (scale bar 1  $\mu\text{m}$ ) [86]



### 5.5.2.3 Metal Deposition

Metal deposition consists of a unique surface modification (MetA-SIMS) or sometimes an additional step for MALDI ionization or ME-SIMS ionization enhancement and will be discussed in detail in the next section.



Metal deposition is realized using metal-coating techniques similar to those used in electron microscopy. This provides a reproducible and accurate deposition of metal to the sample surface. Usually, a thickness of 2–5 nm is deposited and increases the ionization efficiency up to 3 kDa [40, 41]. The metal thickness is determined during the deposition process using a quartz crystal microbalance integrated in the metal-deposition system. Studies using atomic force microscopy indicated that during 1–2-nm gold deposition small islands are formed on the tissue surface. The surface becomes conductive although it is difficult to exactly assess the conductivity of the ITO–tissue–Au sandwich structure. If the thickness exceeds 5 nm, many gold clusters are formed and the molecular signal is suppressed completely. This is believed to indicate the formation of a solid, closed film that minimizes energy deposition directly in the tissue.

### 5.5.3 Comparison of Metallization and Matrix-Deposition Procedures

Metallization and matrix deposition enhance ionization and desorption, but these processes do possess drawbacks. Here, we will recapitulate a series of criteria, which are initiated from the personal interpretation of Delcorte [87] and applied to MALDI and SIMS imaging experiments. The interpretation and coherence of the imaging results are correlated to different criteria of efficiency, reproducibility, versatility, and ease of interpretation, as summarized in Table 5.3.

Efficiency is characterized by an enhanced ionization yield, which is comparatively the same in MetA-SIMS and ME-SIMS. However, the dynamic mass range of the MetA-SIMS procedure is more limited (up to ~3 kDa) than that of ME-SIMS [40].

Reproducibility is the major factor for imaging techniques to obtain coherent observations. The reproducibility of imaging MS experiments is characterized by two main aspects: the detection and localization of identical intensity signals. The reproducibility of matrix deposition is less effective than metal deposition due to the difficulty to reproduce the same deposition conditions and matrix crystal size/structure [86, 88, 89]. Nevertheless, many different matrix-deposition methods have been developed to reproduce the same quality of coverage and allow more

**Table 5.3** A comparison between surface metallization and matrix deposition for SIMS-based tissue imaging mass spectrometry

Criterion	Matrix deposition	Metal deposition
Efficiency	++	++
Reproducibility	–	+
Versatility	+/-	++
Ease of interpretation	–	+
Equipment/cost	+	–

++ very good, + good, +/- satisfactory, – limiting

reproducible images. Moreover, the crystal size (around 1–5  $\mu\text{m}$ ) does not have the same effect in SIMS and MALDI imaging, with regard to the beam diameter. In the case of MALDI, the laser beam could reach 20  $\mu\text{m}$ , and the image does not have enough spatial resolution to be affected by the crystal size. However, in SIMS a smaller beam (500 nm) is used and quality of the images is restrained to the crystal size. In addition, matrix deposition induces an increase in low-mass-range matrix signals, which interfere with sample signals, unlike metal deposition.

Versatility defines the number of possible applications of SIMS and MALDI imaging with metal or matrix deposition. Metal deposition allows a large number of applications because of its accurate deposition for any type of sample surface without any delocalization [30]. Moreover, the interpretation of their spectra is easier because only peaks from the metal are detected [90]. In the case of a matrix-enhanced SIMS experiment, the matrix produces interference in the spectra [91].

## 5.6 Applications of MALDI and Enhanced SIMS Imaging

Chemical imaging mass spectrometry provides both chemical information and the spatial organization of each component on a surface. The development of imaging mass spectrometry is revolutionizing the field of biological analysis [92]. SIMS and MALDI are the two most common techniques for the characterization and localization of compounds and provide a broad spectrum of applications.

The first analyses of biological tissue used a SIMS mass spectrometer for metal, lipids, and peptides localizations [93] with a high spatial resolution of 0.5  $\mu\text{m}$ . A high spatial resolution combined with a high sensitivity for high-mass molecules remains the goal of chemical imaging mass spectrometry. Both MALDI- and SIMS-based approaches have been developed to achieve these goals, as discussed above.

Three large families of molecules are implicated in the organization (structure and activity) of cells: proteins, lipids, and carbohydrates. These biomolecules are observed at different concentrations ( $10^6$  of magnitude) in the tissue, have different biochemical properties (molecular weight, pH iso-electric, proton affinity), and result in a different degree of desorption and ionization efficiency. The key to success is to apply appropriate imaging techniques (IMS and traditional imaging techniques) to answer a precise question.

In this section, we present different applications of molecular imaging mass spectrometry in the detection of molecules [such as pharmaceuticals, metabolites, atoms (metals), lipids, peptides, and proteins], that play a role in disease or specific conditions from plants to animal tissue. The choice of the complementary IMS technique depends on two parameters: the nature of the detected compounds (and the correlated mass) and the spatial resolution. The surface enhanced IMS helps to understand the role of each molecule in many different fields of research (lipidomics, proteomics, clinical proteomics, and pharmacology), showing a large spectra of applications.

### 5.6.1 *Single-Cell Imaging of Peptides and Lipids for Fundamental Biological Studies*

Surface-enhanced SIMS is the suitable instrument for the detection of low-mass molecules such as lipids and small peptides. Moreover, the detection of molecules in ganglia samples of small animals requires a high spatial resolution; thus, SIMS could play an important role for high spatial localization of biomolecules without chemical labeling (as is required in immunochemistry or targeted approaches).

Recent studies have combined surface-enhanced SIMS and MALDI to detect and localize compounds in biological samples. Heeren's group developed and applied surface analysis using ME-SIMS and MetA-SIMS for the detection of neuropeptides and lipids in *Lymnaea stagnalis* [86] and neuroblastoma [3].

Matrix (2,5-dihydrobenzoic acid in these examples) was deposited by an electrospray-deposition (ESD) system in order to ensure small matrix crystals compatible with the high spatial resolution of SIMS (Fig. 5.7). After tissue sectioning and pickup, the *Lymnaea stagnalis* tissue was sectioned with a cryo-microtome, placed on an indium-tin-oxide (ITO) coated glass slide, and coated with DHB matrix by ESD. The tissues were analyzed on a TRIFT-II time-of-flight SIMS (ToF-SIMS) equipped with an  $^{115}\text{In}^+$  liquid metal ion gun (LMIG), and on a MALDI equipped with 337 nm nitrogen laser VSL-337i in reflectron mode.

Different peptide and lipid profile images produced from SIMS and MALDI mass spectrometry were compared to scanning electron microscopy (SEM) images [86]. SEM was used to determine the size of the matrix crystals, thus validating ESD for ME-SIMS matrix deposition. The crystal size was  $\sim 1\ \mu\text{m}$ , which allows imaging at subcellular resolution. ME-SIMS and MALDI spectra show peaks under 3,000  $m/z$  (Fig. 5.8), which reveal the presence of the neuropeptide APGWamide in the anterior lobe of the right cerebral ganglia (Fig. 5.8) in the associated images (Fig. 5.9). This peptide regulates the male copulation behavior of *Lymnaea stagnalis* [94]. This study corroborates previous studies of matrix-enhanced SIMS and shows the power of ME-SIMS to detect and image both lipids and localized neuropeptides with a high spatial resolution ( $1.5\ \mu\text{m}$ ).

Surface metallization was used as an alternative to matrix deposition with SIMS and added (in addition to the matrix) for MALDI analysis. High-resolution images of lipids and peptides were obtained for neuroblastoma cells and rat brain tissues with MetA-SIMS, ME-SIMS, and a homemade MALDI-BioTRIFT instrument with a higher spatial resolution than commercially available MALDI instruments [7, 30].

ME-SIMS increases the signal intensities for phospholipids, phosphatidyl choline (PC), sphingomyelin (SM), cholesterol, ceramide, and di-acyl glycerol (DAG) (Fig. 5.8) compared to regular SIMS analysis. MetA-SIMS further increases the same signals ( $\sim 50\times$ ) and also increases the yield of other molecular signals, as shown in Fig. 5.10.

Lateral resolution analyte diffusion is minimized in MetA-SIMS, where only migration on gold islands at the nanometer scale may occur, which produces

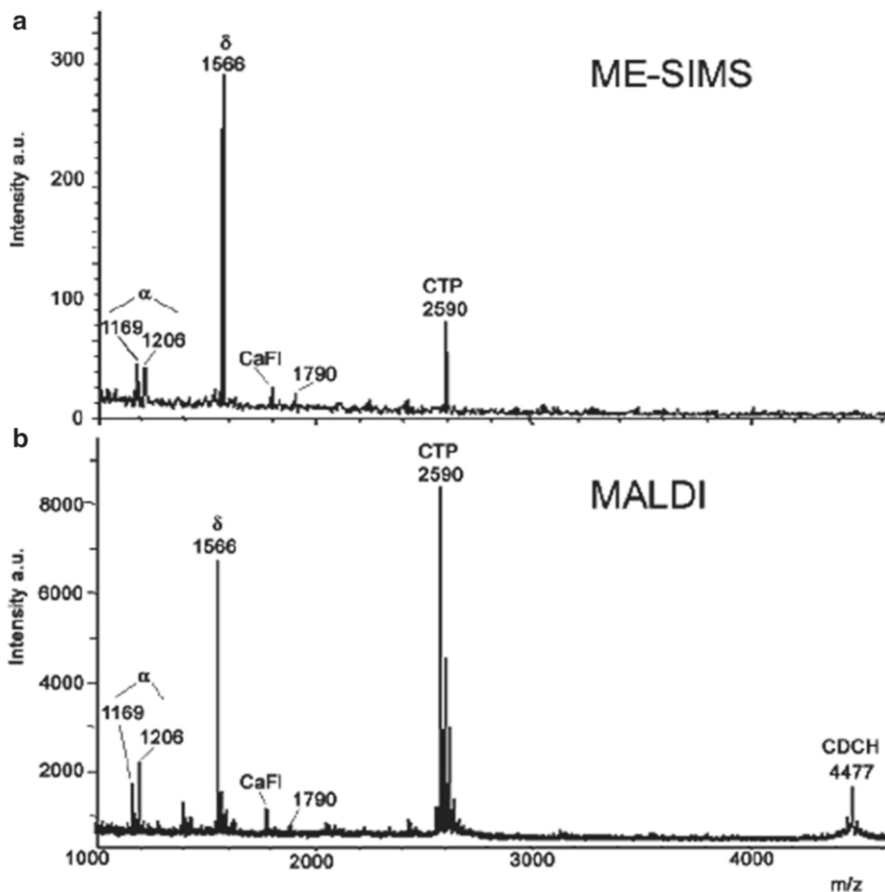


**Fig. 5.8** ME-SIMS vs. MALDI: (a) ME-SIMS and (b) MALDI spectra of a commissure extract of the pond snail *Lymnaea stagnalis*. Both spectra were obtained using standard dried droplet sample preparation with 2,5-DHB as matrix. The peptides identified are R-caudorsal cell peptide (R, protonated and cationized), ä peptide (ä), HFFYGPYDVFQRD<sub>V</sub>amide ( $m/z$  1,790), Calfluxin (CaFl), carboxyl terminal peptide (CTP), and caudorsal cell hormone (CDCH). The ME-SIMS measurements used indium primary ions (total ion dose  $8.9 \times 10^{11}$  ions/cm<sup>2</sup>) and the MALDI experiments 250 shots of the 4-ns 337-nm nitrogen laser [80]

better-quality images than ME-SIMS. Moreover, higher mass signals are observed (peptides) up to 1,400 Da. The combination of the spatial resolution and the high sensitivity for cholesterol and other ions allows the description of subcellular organization and the differentiation of cell clusters of the neuroblastoma. The membrane, nucleus, and intracellular compounds are observed to delineate the neuroblastoma.

Moreover, except for the lipids' signals, the spectrum shows no other molecular signals in ME-SIMS, while signals up to 4,000 and 1,500 Da are observed from the

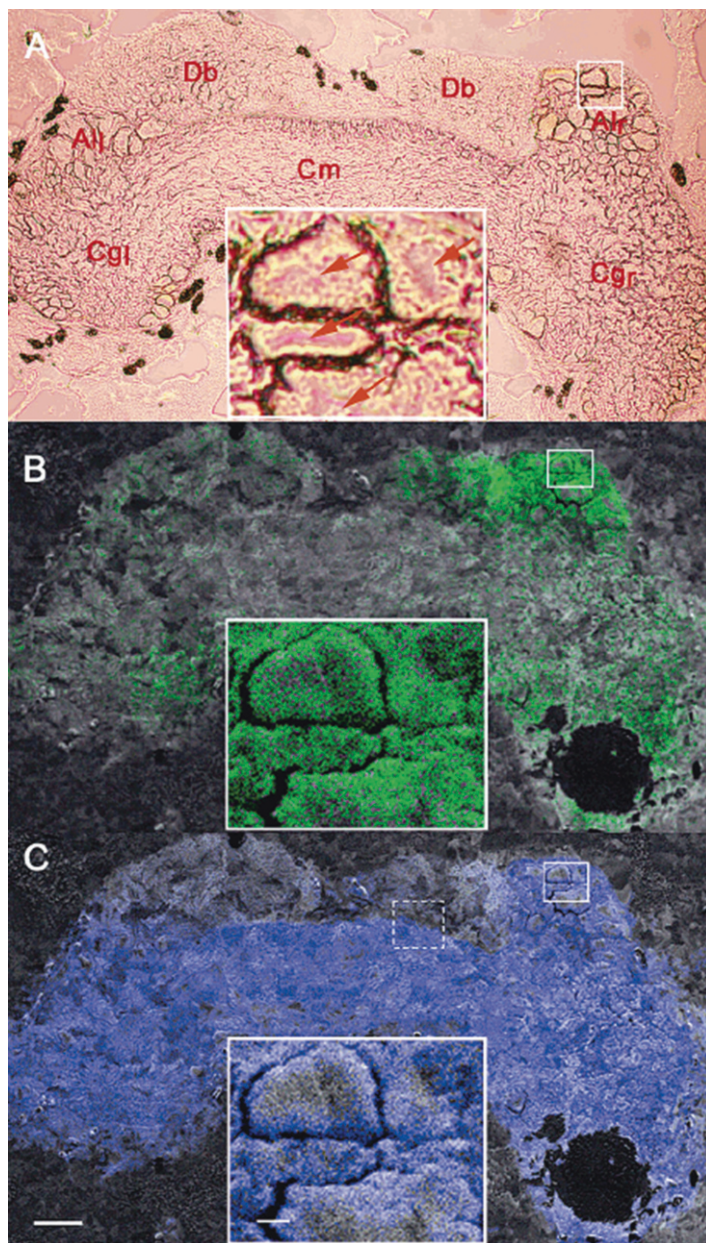


**Fig. 5.9** Direct molecular imaging of *Lymnaea stagnalis* nervous tissue by ME-SIMS: (a) optical image of the *Lymnaea* cerebral ganglia; inset shows high-magnification image of neurons in the anterior lobe (solid box); arrows indicate nuclei. Different regions in the section are right and left cerebral ganglia (Cgr and Cgl), anterior lobe (Al), commissure (Cm), and dorsal bodies (Db); (b) ME-SIMS image of APGWamide (429.0–433.2 *m/z*; green) distribution; (c) ME-SIMS image of cholesterol (368.2–371.3 *m/z*; blue) distribution. Scale bar: 200  $\mu\text{m}$ ; scale bar inset: 10  $\mu\text{m}$ . Molecular images (b and c) are presented as colored overlays on top of the gray-scale TIC (total ion count) image (mass range: 1.0–5,000 *m/z*) [3]

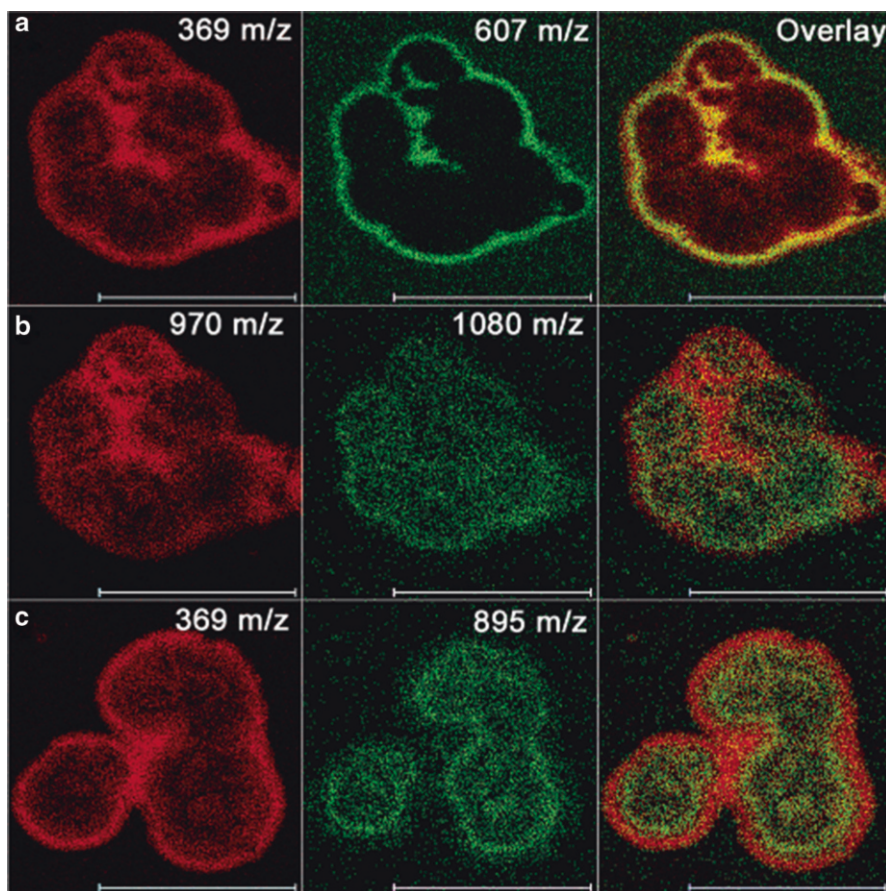


**Fig. 5.10** Cellular localization of Meta-SIMS selected ion count signals from neuroblastoma cells. Cells were imaged after deposition of 1-nm gold: (a)  $m/z$  369 (cholesterol  $[M-OH]^+$ , 0–14 counts) and 607 (DAG, 0–6 counts); (b)  $m/z$  970 (cholesterol  $[2 M + Au]^+$ , 0–4 counts) and 1,080 (0–1 counts); (c)  $m/z$  369 (cholesterol  $[M-OH]^+$ , 0–12 counts) and 895 (0–2 counts) [3]

same section by stigmatic MALDI and Meta-SIMS. These results are explained by the major difference between the two approaches, which relates to the amount of sample consumed. In MALDI, each laser shot consumes approximately 100 nm–1  $\mu$ m of sample, while the penetration depth of the SIMS is typically 10 nm. This is explained by the crystallization and segregation of lipids on the crystal surface of the matrix, while the peptides are mainly incorporated into the matrix [95].

Sample preparations of tissue with chemical modifications used with the MALDI-BioTRIFT technique show high-mass signals up to 4,000 Da, with a higher spatial resolution (approximately 2  $\mu$ m). Gold deposition results in an enhanced image quality and signal intensity, not only for SIMS but also for MALDI.

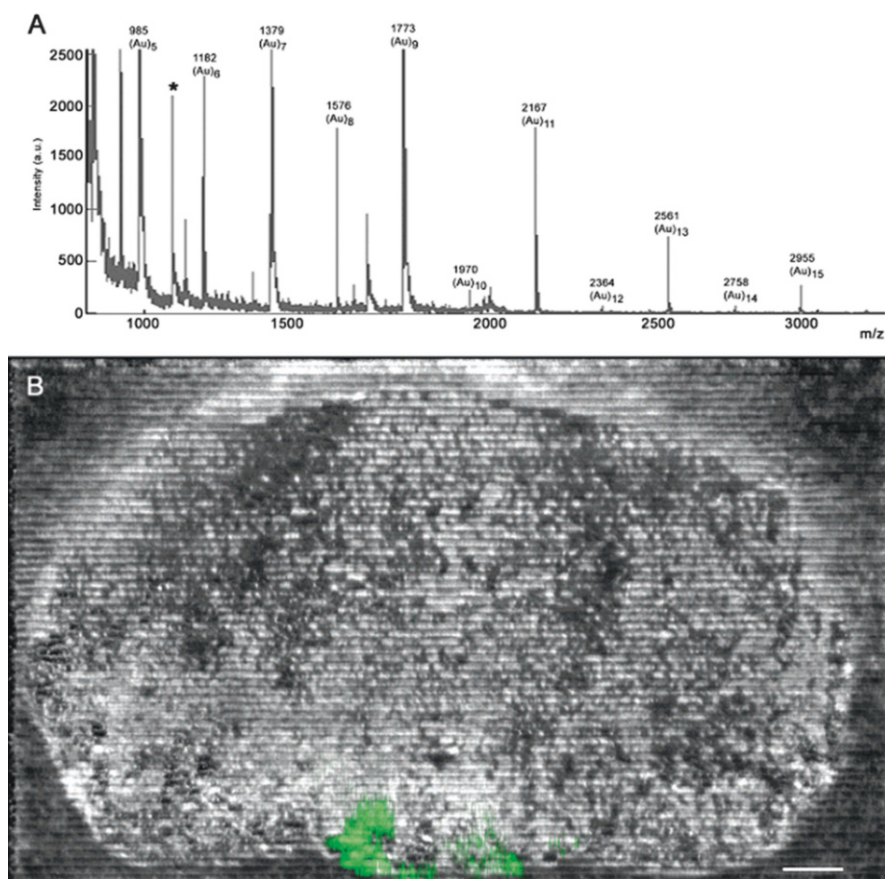


**Fig. 5.11** MALDI stigmatic imaging of a rat brain tissue section: (a) a line scan summed mass spectrum showing gold cluster peaks and several peptide peaks, with the vasopressin mass at  $m/z$  1,085 (\*); (b) TIC image (gray scale) of an HCCA-coated rat brain tissue section overlaid with the selected ion image for vasopressin (green). Scale bar: 1 mm [3]

Figure 5.11 shows images of a localized vasopressin (1,085-Da) protein obtained from matrix-enhanced MALDI.

ME- and MetA-SIMS describe localized low-mass signals from lipids and peptides by the assistance of chemical modifications. The matrix deposition for ME-SIMS is the prerequisite for MALDI analysis as well. MALDI allows the multimolecular imaging of peptides and proteins up to 75 kDa. The large dynamic mass range allows for the analysis of complex mixtures of compounds in tissues and has many biological applications. Applications include imaging of organs or whole animal body slices as well as vegetable models [11, 96], with the detection and localization of drugs, metabolites, peptides, proteins, and carbohydrates.

### 5.6.2 *Peptide and Protein Detection: MALDI Imaging Applications*

The first direct image construction by MALDI was initiated by Caprioli's group [11]. At this juncture, in 1997, MALDI was described as a technique to analyze a biological solution with proteins and peptides. Different groups have applied this technique to a direct analysis of tissue by matrix droplet deposition followed by MALDI-ToF MS analysis [97–99]. Different average spectra for regions of interest (ROI) are compared and allow differentiation of the proteome and lipidome in certain regions.

In the past decade, many developments for sample preparation, instrumentation optimization, and software have enabled MALDI imaging at a subcellular resolution with good sensitivity [80].

### 5.6.3 *Proteomics and Clinical Proteomics*

No specific sample-preparation methods were used for the first MALDI imaging experiments. The matrix was applied directly with a pipette or sprayed onto the tissue in order to make a reproducible procedure to detect some standard peptides and proteins [11, 100, 101]. The choice of a spraying system or microspot deposition of matrix is crucial for the spatial resolution and the reproducibility of experiments. The mass range detectable with MALDI imaging is approximately 0–80 kDa. The first application of MALDI on a biological surface was to detect large molecules for proteomics studies (Fig. 5.12) [102]. In this case, human glioblastoma cells were implanted into a hind limb of a nude mouse model and specific markers (T $\beta$ .4 protein,  $m/z=43,965$ ) were observed in the tumor proliferation area (Fig. 5.12). These first publications illustrate the interest in MALDI imaging for proteomics and clinical proteomics research: detecting proteins implicated in disease pathologies, that discriminate different cell or organ states.

The work of the Sweedler group illustrates the usefulness of MALDI imaging in the neuroscience field [103–105]. The Sweedler group has developed methodologies and sample preparations for invertebrate ganglia cell imaging. The application of matrix onto the *Aplysia californica* exocrine gland and neuronal tissue shows the ability to spatially image neuropeptides and proteins. Two different approaches have been used. First, a microspotted matrix deposition on different ganglia slides (every 30  $\mu\text{m}$ ) demonstrated the ability to profile neurons without removing cells from the ganglion matrix from the ventral to the dorsal side. Another approach uses total laser ablation of the matrix and moves the plate a distance (25  $\mu\text{m}$ ) smaller than the laser spot size, a so-called oversampling approach. In this manner, even with a large laser spot, a small analytical area can be studied, improving the spatial resolution of the resulting image. The use of an adequate bioinformatics tool to reconstruct the image allows the imaging of molecules with a resolution of 50  $\mu\text{m}$ .



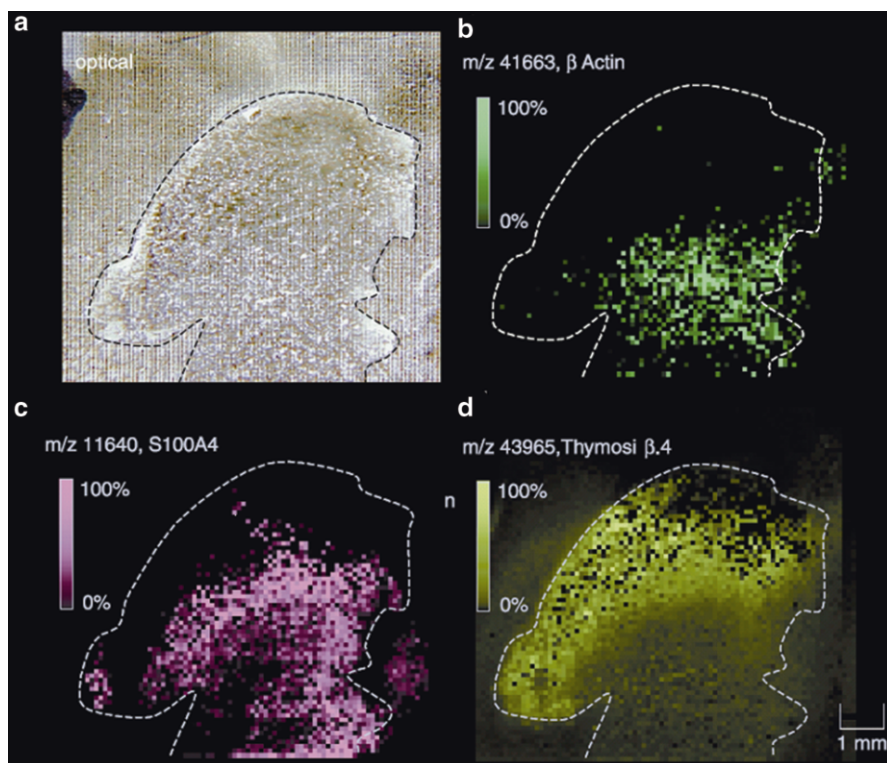


**Fig. 5.12** Selected protein images from a glioblastoma section: (a) human glioblastoma slice mounted on a metal plate, coated with matrix (the lines are from ablation of matrix with the laser); (b–d) mass-spectrometric images of proteins showing a high concentration in the proliferating area of the tumor (d) and other proteins present specifically in the ischemic and necrotic areas (b and c) [102]

At the same time, other groups have applied MALDI imaging to different diseases by integrating sample comparisons [78, 81, 106, 107]. As illustrated in these papers, MALDI mass-spectrometric imaging on tissues is used in endogen biomarker discovery by determining under- and overexpressed peptides/proteins of a disease state versus a healthy control (AD). MALDI mass-spectrometric imaging has also been applied to the study of amyloid beta peptide distribution in brain sections from mice and shows features reminiscent of Alzheimer's disease.

#### 5.6.4 Drug Distribution and Quantification

IMS has also been used to observe the elimination and repartition of drug distributions on tissue sections [44, 78, 96, 108–111]. The drug profile and ADME (adsorption, distribution metabolism, and excretion) studies appear to be particularly well

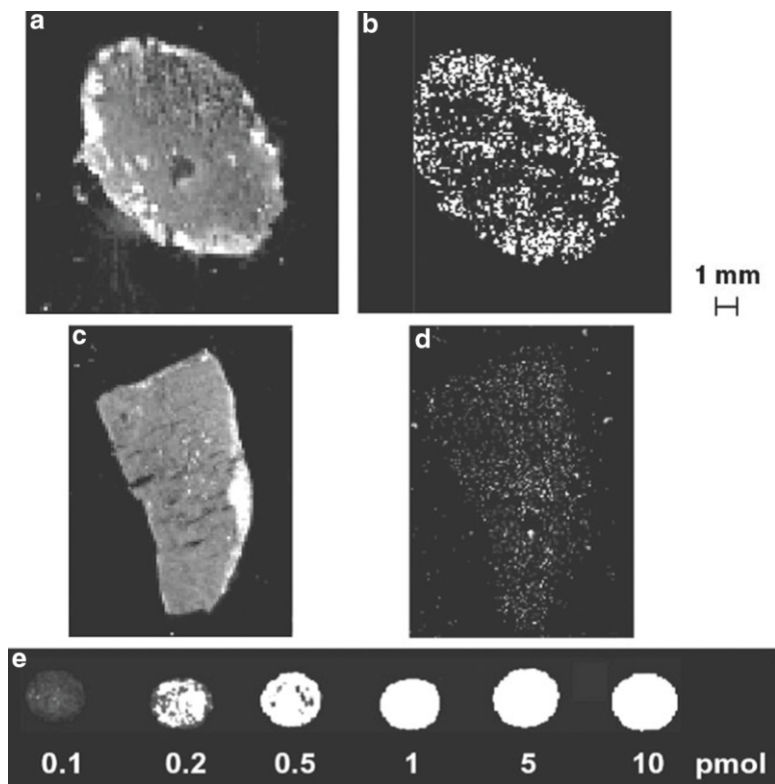


**Fig. 5.13** Drug distribution of erlotinib in rat liver (a, b) and spleen (c, d) tissue section. (a) and (c) represent the optical image, while (b) and (d) represent the MALDI image of erlotinib at  $m/z=278.1$ . (e) represents the dilution series of erlotinib on target plate as a calibration (the HCCA matrix was deposited by hand) [78]

suited with IMS [57, 109, 112]. In these articles, different drugs are injected into the animals, and monitored by single-MS or tandem-MS imaging to visualize the drug incorporation. Signor et al. compared the quantification of erlotinib by autoradiography, LC-MS, and MALDI imaging experiments. As shown in Fig. 5.13, at a concentration of 3.76 ng/mg, erlotinib and its metabolites are observed in the rat liver and spleen sections. The comparison of quantification techniques (autoradiography and LC-MS/MS) was also similar with MALDI analysis as a quantitative approach [78].

However, signal intensities may vary even in the same sample; thus, MALDI MS is not the method of choice for absolute quantification. In this study [112], the drug distributions and the intensity ratios could be reproduced within a range of 20 % (if the sample-preparation procedure as well as instrument settings and laser intensity are kept constant). An internal calibration and reproducible deposition of matrix enable relative quantification with the comparison of peak areas instead of height peaks.

Several groups have shown that this method allows a quantification error variation of about 2–3 % [96, 113, 114]. New methods such as multiple reaction monitoring (MRM)–based imaging on triple quad systems provide a rapid, more sensitive targeted analysis of drug distributions in whole body tissue sections [115]. Although these methods are relevant to quantify sample-to-sample variations, validation processes are still used with established methods such as Western blot and immunochemistry for determining accurate concentrations. It is necessary to combine IMS with HE staining and immunohistochemistry to validate IMS as an approach for the identification of molecules from tissue [116]. Thus, a validation method was developed with a tag-mass, called specific mass spectrometry imaging. This approach allows the simultaneous detection and validation of molecules of interest using IMS [81, 83, 107].

### ***5.6.5 Specific Mass Spectrometry Imaging***

Specific mass spectrometry imaging is used to image different types of molecules, such as proteins and nucleotides, with a combination of mass spectrometry imaging and immunohistochemistry. A tag-mass is used, which is a tagged antibody or aptamer that can be observed in the IMS experiment. This concept was developed to detect compounds such as nucleotides and large proteins, which are difficult to ionize by classical IMS experiments. A specific mass spectrometry imaging experiment is shown in Fig. 5.14 along with the different steps of tag-mass multiplexing.

### ***5.6.6 Application with Carbohydrates and Metabolites in Plants***

IMS applications in the vegetable kingdom, including MALDI imaging of oligosaccharides and primary metabolites in a plant system, have recently been presented [117]. MALDI imaging was used to identify metabolites, namely, glucose-6-phosphate, in potato tubers [118] and to determine agrochemical compounds in soybeans [119]. In these examples, the sensitivity of MALDI imaging and the semi-quantitative evaluation allow the detection of hundreds of metabolites with a concentration of around 1  $\mu\text{g/g}$ . Other approaches, including electrospray mass spectrometry and enzyme-linked assay, could be combined with IMS, but the sensitivity of IMS offers the potential of simultaneous metabolite assays. Nevertheless, there are over 100,000 plant metabolites, and MS/MS is necessary for accurate identification. Combined IMS and MS/MS approaches have been developed for frozen, fixed, and embedded tissues [120]. These methods will be discussed in the section entitled “Perspectives” ahead.

Recently, Thomas-Oates published a study on the localization of carbohydrate metabolites as an indicator of grain yield. Cross and longitudinal sections from the

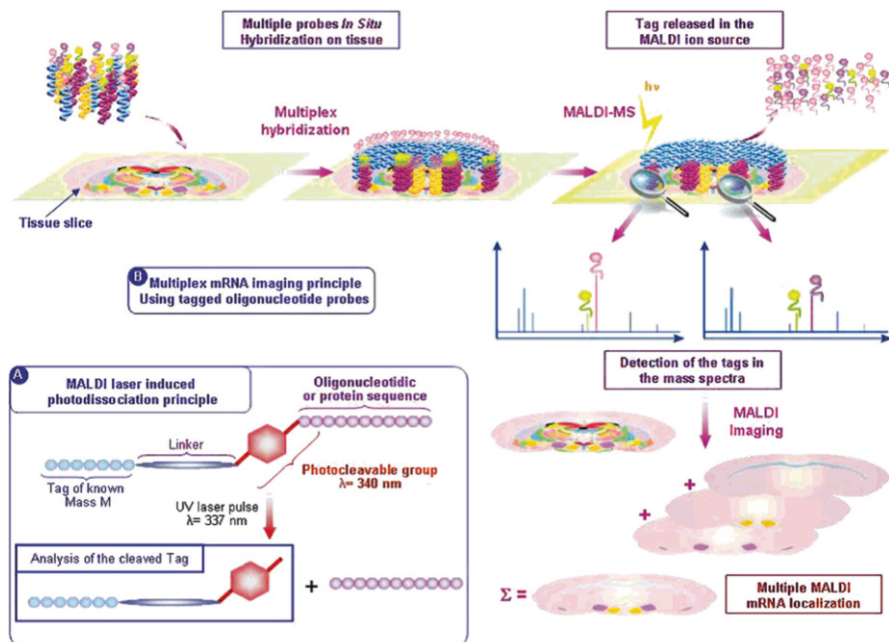


**Fig. 5.14** Specific mass spectrometry imaging approach uses a tagged reporter, which allows the multiplex detection of a large number of molecules, including nucleotides and proteins. In this example, the tag-mass is a complementary oligonucleotide sequence, which has a high affinity to the complementary sequence of interest in the tissue. This affinity and the IMS experiment allow the localization of the interest sequence of DNA, RNA, or proteins in a more general aspect [83]

wheat stems of *Triticum aestivum* were used to localize water-soluble carbohydrates [121]. They demonstrated the sensitivity of IMS and verified the results using complementary techniques, including LC-MS. An advantage of IMS over the other techniques included the ability to determine *in situ* localization.

### 5.6.7 MALDI Imaging of Lipids

Lipid distributions are usually detected and mapped by SIMS mass spectrometry, especially because of the sensitivity to SIMS in the low-mass range. Lipids can also be detected and localized by MALDI with special matrices to minimize interference from matrix peaks. In this context, the MALDI ion-mobility mass spectrometry imaging technique was developed. MALDI-Q-ToF, coupled with an ion-mobility cell, developed by the groups of Woods and Schultz, allows for the separation of lipids, matrix, and peptide species [43, 45, 122]. This separation allows a differentiation between species, with a higher signal-to-noise ratio, as shown in Fig. 5.15.

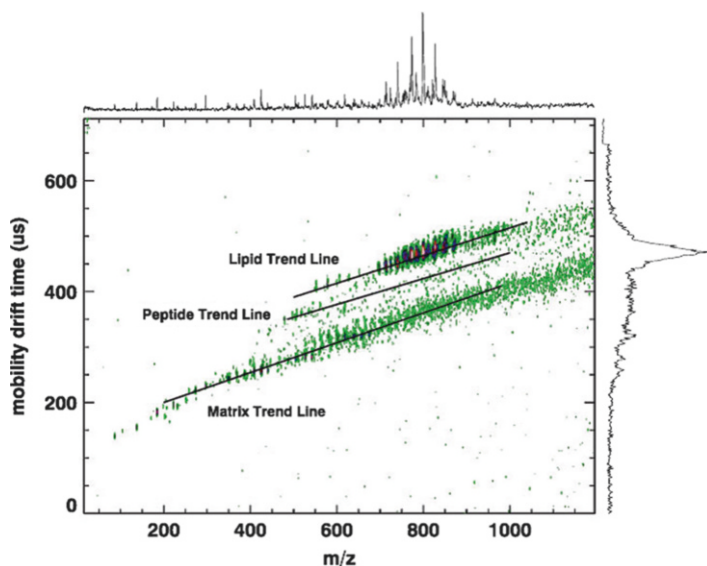


**Fig. 5.15** Ion-mobility diagram obtained by MALDI-IM imaging of a rat brain section. The y-axis is the time separation in the drift cell, and the x-axis is mass-to-charge ratio. Different species (here, DHB matrix, peptides, and lipids) fall on unique trend lines [45]

### 5.6.8 Element/Metal Detection

One other dedicated application of IMS is the localization of contrast agents used for MRI imaging [123–125]. Contrast agents, used to increase the contrast of images during *in vivo* imaging by MRI or PET instruments, were studied by IMS to accurately localize their distributions in organs and cells with a better sensitivity and spatial resolution than classical MRI. In these examples, IMS allowed the detection of contrast agents in their native or degraded form [126].

## 5.7 Perspectives

As presented here, surfaced-enhanced SIMS and MALDI imaging are two recent approaches to detect and image macromolecular compounds directly in biological samples. Important recent developments include sample-preparation protocols and, in particular, instrument combinations of SIMS and/or MALDI ionization sources with different mass analyzers. These developments are correlated to the same developments observed in classical proteomics studies many years ago. In that sense, it is easy to foresee the inclusion of IMS into biological studies.

In a general view, IMS is able to visualize different compounds with a spatial resolution of 50 nm–100  $\mu\text{m}$  with good sensitivity. Nevertheless, the accurate identification and validation of these compounds is still difficult. In this way, many different approaches, such as immunochemistry and autoradiography, validate the presence of biomolecules. In the past decade, different tandem mass spectrometry (MS/MS) approaches were developed with instruments with new geometries to directly identify molecules in tissue [127]. These new geometries allow a better separation and possible *in situ* identification of compounds such as lipids and digested proteins. Thus, two groups have developed *in situ* enzymatic digestion to map large proteins in frozen and formalin-fixed and paraffin-embedded (FFPE) tissues [74, 75, 128].

Trypsin digestion (from classical proteomics experiments) on FFPE tissues allows proteomics studies on archived tissues from hospital libraries [76]. This method of digestion requires a micro-deposition instrument to avoid any delocalization of digested peptides, where trypsin deposition comes before matrix deposition. Digestion on tissue allows the identification and localization of thousands of digested peptides. Nevertheless, it is difficult to identify all of the fragments because of the high concentration of peptides and lipids in the mass range of 350–950  $m/z$ . In this perspective, digested FFPE and frozen tissues were analyzed with an ion-mobility mass spectrometer [128]. This approach separates molecules (e.g., peptides, drugs, and proteins) according to their conformation (cross section) and offers better identification. Moreover, MALDI ion-mobility imaging allows the separation of drugs from lipids, saccharides, nucleotides, and peptides. The use of standard protocols, coupled with sensitive instruments that can separate ions in the gas phase prior to mass analysis, could be the way to improve the field of imaging mass spectrometry.

## 5.8 Conclusion

As shown in this chapter, surface-enhanced imaging mass spectrometry and IMS are technologies based on fundamental innovations in physics and chemistry. Their applicability to biological and biomedical studies has been shown. SIMS and MALDI combined offer complementary surface-analysis approaches to study a range of species, from elements to proteins (Fig. 5.16). Applications include biomarker discovery or drug assessment (ADMET: absorption, distribution, metabolism, elimination, toxicology) on biopsy surfaces. As a result, this method can be involved in each step of drug discovery: for target identification, lead optimization, assessment of drug-delivery systems, and profiles of the biodistribution and metabolism.

These young techniques are under development to increase their sensitivity, speed of analysis, reproducibility, and spatial resolution. The numbers of papers published recently demonstrate the power and potential of these approaches to overcome “classical” imaging problems. Initially developed to localize lipids, peptides,

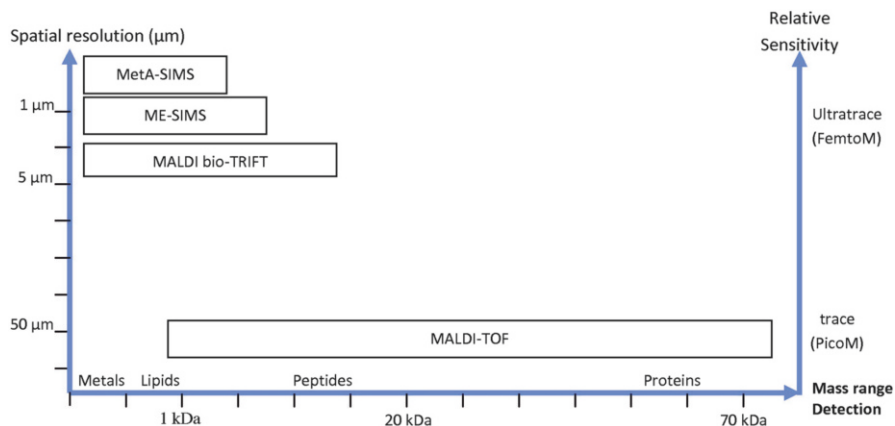


**Fig. 5.16** Description of the different enhanced-surface IMS techniques according to their spatial resolution, mass-range detection, and sensitivity

and proteins, MALDI imaging and surface-enhanced SIMS allow the detection of biomarkers related to specific tissue conditions.

Imaging mass spectrometry is a label-free imaging technique for molecular pathology that complements existing, less specific imaging modalities in biomedical research. This innovative MS-based technique, together with such techniques as MRI, CT, PET, or ICC imaging, will visualize the fundamentals of diseases in future biomedical imaging research.

## References

1. McDonnell LA, Heeren RMA. Imaging mass spectrometry. *Mass Spectrom Rev.* 2007;26: 606–43.
2. Castaing R, Slodzian G. Microanalyse par emission ionique secondaire. *J Microsc.* 1962;1: 395–410.
3. Altelaar AFM, Klinkert I, Jalink K, De Lange RPJ, Adan RAH, Heeren RMA, Piersma SR. Gold-enhanced biomolecular surface imaging of cells and tissue by SIMS and MALDI mass spectrometry. *Anal Chem.* 2006;78:734–42.
4. McDonnell LA, Heeren RMA, de Lange RPJ, Fletcher IW. Higher sensitivity secondary ion mass spectrometry of biological molecules for high resolution, chemically specific imaging. *J Am Soc Mass Spectrom.* 2006;17:1195–202.
5. Altelaar AFM, Luxembourg SL, McDonnell LA, Piersma SR, Heeren RMA. Imaging mass spectrometry at cellular length scales. *Nat Protoc.* 2007;2:1185–96.
6. Heeren RMA, McDonnell LA, Amstalden ER, Altelaar AFM, Piersma SR. Why don't biologists use SIMS; a critical evaluation of imaging MS. *Appl Surf Sci.* 2006;252:6827–35.
7. Luxembourg SL, Mize TH, McDonnell LA, Heeren RMA. High-spatial resolution mass spectrometric imaging of peptide and protein distributions on a surface. *Anal Chem.* 2004;76: 5339–44.

8. Klerk LA, Lockyer NP, Kharchenko A, MacAleese LP, Dankers PYW, Vickerman JC, Heeren RMA.  $C_{60}^+$  secondary ion microscopy using a delay line detector. *Anal Chem.* 2010;82:801–7.
9. Karas MI, Bachmann D, Bahr U, Hillenkamp F. Matrix-assisted ultraviolet laser desorption of non-volatile compounds. *Int J Mass Spectrom.* 1987;78:53–68.
10. Hillenkamp F, Karas M. Matrix-assisted laser desorption/ionisation, an experience. *Int J Mass Spectrom.* 2000;200:71–7.
11. Caprioli RM, Farmer TB, Gile J. Molecular imaging of biological samples: localization of peptides and proteins using MALDI-TOF MS. *Anal Chem.* 1997;69:4751–60.
12. Stoeckli M, Farmer TB, Caprioli RM. Automated mass spectrometry imaging with a matrix-assisted laser desorption ionization time-of-flight instrument. *J Am Soc Mass Spectrom.* 1999;10:67–71.
13. Dreisewerd K, Schürenberg M, Karas M, Hillenkamp F. Influence of the laser intensity and spot size on the desorption of molecules and ions in matrix-assisted laser desorption/ionization with a uniform beam profile. *Int J Mass Spectrom.* 1995;141:127–48.
14. Posthumus MA, Kistemaker PG, Meuzelaar HLC, Ten Noever de Brauw MC. Laser desorption-mass spectrometry of polar nonvolatile bio-organic molecules. *Anal Chem.* 1978;50:985–91.
15. Zenobi R, Knochenmuss R. Ion formation in MALDI mass spectrometry. *Mass Spectrom Rev.* 1998;17:337–66.
16. Zhigilei LV, Garrison BJ. Molecular dynamics simulation study of the fluence dependence of particle yield and plume composition in laser desorption and ablation of organic solids. *Appl Phys Lett.* 1999;74:1341–3.
17. Ehring H, Karas M, Hillenkamp F. Role of photoionization and photochemistry in ionization processes of organic molecules and relevance for matrix-assisted laser desorption ionization mass spectrometry. *Org Mass Spectrom.* 1992;27:472–80.
18. Preston-Schaffter LM, Kinsel GR, Russell DH. Effects of heavy-atom substituents on matrices used for matrix-assisted laser desorption-ionization mass spectrometry. *J Am Soc Mass Spectrom.* 1994;5:800–6.
19. Knochenmuss R, Zenobi R. MALDI ionization: the role of in-plume processes. *Chem Rev.* 2003;103:441–52.
20. Breuker K, Knochenmuss R, Zhang J, Stortelder A, Zenobi R. Thermodynamic control of final ion distributions in MALDI: in-plume proton transfer reactions. *Int J Mass Spectrom.* 2003;226:211–22.
21. Lemaire R, Tabet JC, Ducoroy P, Hendra JB, Salzert M, Fournier I. Solid Ionic matrixes for direct tissue analysis and MALDI imaging. *Anal Chem.* 2006;78:809–19.
22. Liebl H. Ion microprobe mass analyzer. *J Appl Phys.* 1967;38:5277–83.
23. Chabala JM, Soni KK, Li J, Gavrilov KL, Levi-Setti R. High-resolution chemical imaging with scanning ion probe SIMS. *Int J Mass Spectrom.* 1995;143:191–212.
24. Benninghoven A. Die Analyse monomolekularer Festkörperoberflächenschichten mit Hilfe der Sekundärionenemission. *Z Physik.* 1970;230:403–17.
25. Appelhans AD, Delmore JE. Comparison of polyatomic and atomic primary beams for secondary ion mass spectrometry of organics. *Anal Chem.* 1989;61:1087–93.
26. Winograd N. The magic of cluster SIMS. *Anal Chem.* 2005;77:142A–9.
27. Gillen G, Fahey A. Secondary ion mass spectrometry using cluster ion beams. *Appl Surf Sci.* 2002;203:209–13.
28. Wu KJ, Odom RW. Matrix-enhanced secondary ion mass spectrometry: a method for molecular analysis of solid surfaces. *Anal Chem.* 1996;68:837–82.
29. Delcorte A, Bour J, Aubriet F, Muller JF, Bertrand P. Sample metallization for performance improvement in desorption/ionization of kilodalton molecules: quantitative evaluation, imaging secondary ion MS, and laser ablation. *Anal Chem.* 2003;75:6875–85.
30. McDonnell LA, Piersma SR, Altelaar AFM, Mize TH, Luxembourg SL, Verhaert PDEM, van Minnen J, Heeren RMA. Subcellular imaging mass spectrometry of brain tissue. *J Mass Spectrom.* 2005;40:160–8.



31. Jonkman HT, Michl J, King RN, Andrade JD. Low-temperature secondary positive ion mass spectrometry of neat and argon-diluted organic solids. *Anal Chem.* 1978;50:2078–82.
32. Ross MM, Colton RJ. Summary abstract: secondary ion mass spectrometry of organic adsorbates on carbon particles and liquid metal surfaces. *J Vac Sci Technol A.* 1983;1:441–2.
33. Ross MM, Colton RJ. Carbon as a sample substrate in secondary ion mass spectrometry. *Anal Chem.* 1983;55:150–3.
34. Barber M, Bordoli RS, Sedgwick RD, Tyler AN. *J Chem Soc Chem Comm.* 1981;325–327.
35. Gillen G, Christiansen JW, Tsong IST, Kimball B, Williams P, Cooks RG. Sputter yields of ammonium chloride and solid glycerol. *Rapid Commun Mass Spectrom.* 1988;2:67–8.
36. Bennett J, Gillen G. Formation and emission of tetraalkylammonium salt molecular ions sputtered from a gelatin matrix. *J Am Soc Mass Spectrom.* 1993;4:930–7.
37. Busch KL, Hsu BH, Xie YX, Cooks RG. Matrix effects in secondary ion mass spectrometry. *Anal Chem.* 1983;55:1157–60.
38. Liu LK, Busch KL, Cooks RG. Matrix-assisted secondary ion mass spectra of biological compounds. *Anal Chem.* 1981;53:109–13.
39. Wittmaack K, Szymczak W, Hoheisel G, Tuszynski W. Time-of-flight secondary ion mass spectrometry of matrix-diluted oligon- and polypeptides bombarded with slow and fast projectiles: positive and negative matrix and analyte ion yields, background signals, and sample aging. *J Am Soc Mass Spectrom.* 2000;11:553–63.
40. Delcorte A, Medard N, Bertrand P. Organic secondary ion mass spectrometry: sensitivity enhancement by gold deposition. *Anal Chem.* 2002;74:4955–68.
41. Delcorte A, Bertrand P. Interest of silver and gold metallization for molecular SIMS and SIMS imaging. *Appl Surf Sci.* 2004;231–2:250–5.
42. Taban IM, Altelaar AFM, Fuchser J, van der Burgt YEM, McDonnell LA, Baykut G, Heeren RMA. Imaging of peptides in the rat brain using MALDI-FTICR mass spectrometry. *J Am Soc Mass Spectrom.* 2007;18:145–51.
43. Tempez A, Ugarov M, Egan T, Schultz JA, Novikov A, Della-Negra S, Lebeyec Y, Pautrat M, Caroff M, Smentkowski VS, Wang H-YJ, Jackson SN, Woods AS. Matrix implanted laser desorption ionization (MILDI) combined with ion mobility-mass spectrometry for bio-surface analysis. *J Proteome Res.* 2005;4:540–5.
44. Bunch J, Clench MR, Richards DS. Determination of pharmaceutical compounds in skin by imaging matrix-assisted laser desorption/ionisation mass spectrometry. *Rapid Commun Mass Spectrom.* 2004;18:3051–60.
45. Jackson SN, Ugarov M, Egan T, Post JD, Langlais D, Schultz JA, Woods AS. MALDI-ion mobility-TOFMS imaging of lipids in rat brain tissue. *J Mass Spectrom.* 2007;42:1093–8.
46. Müller A, Benninghoven A. Investigation of surface reactions by the static method of secondary ion mass spectrometry: III. The oxidation of vanadium, niobium and tantalum in the monolayer range. *Surf Sci.* 1973;39:427–36.
47. Plog C, Wiedmann L, Benninghoven A. Empirical formula for the calculation of secondary ion yields from oxidized metal surfaces and metal oxides. *Surf Sci.* 1977;67:565–80.
48. Standing KG. Timing the flight of biomolecules: a personal perspective. *Int J Mass Spectrom.* 2000;200:597–610.
49. Wirth A, Thompson G, Gregory SP, editors. In: Benninghoven A, editor. *Secondary ion mass spectrometry SIMS VI.* New York: Wiley;. 1987. 639 pp.
50. Waugh AR, Kingham DR, Hearn MJ, Briggs DA, editors. In: Benninghoven A, editor. *Secondary ion mass spectrometry SIMS VI.* New York: Wiley; 1987. 231 pp.
51. Mullock SJ, Reich DF, Dingle T, editors. In: *Secondary ion mass spectrometry SIMS VII.* New York: Wiley; 1989. 847 pp.
52. Stephens WE, Serin B, Meyerhof WE. A method for measuring effective contact e.m.f. between a metal and a semi-conductor. *Phys Rev.* 1946;69:42.
53. Schwieters J, Cramer HG, Heller T, Jurgens U, Niehuis E, Zehnpfenning J, Benninghoven A. High mass resolution surface imaging with a time-of-flight secondary ion mass-spectroscopy scanning microprobe. *J Vac Sci Technol A.* 1991;9:2864–71.

54. Brown RS, Lennon JJ. Mass resolution improvement by incorporation of pulsed ion extraction in a matrix-assisted laser desorption/ionization linear time-of-flight mass spectrometer. *Anal Chem.* 1998;1995:67.
55. Vestal ML, Juhasz P, Martin SA. Delayed extraction matrix-assisted laser desorption time-of-flight mass spectrometry. *Rapid Commun Mass Spectrom.* 1995;9:1044.
56. Laiko VV, Dodonov AF. Resolution and spectral-line shapes in the reflecting time-of-flight mass-spectrometer with orthogonally injected ions. *Rapid Commun Mass Spectrom.* 1994;8:720–6.
57. Hsieh Y, Casale R, Fukuda E, Chen J, Knemeyer I, Wingate J, Morrison R, Korfmacher W. Matrix-assisted laser desorption/ionization mass spectrometry for direct measurement of clozapine in rat brain tissue. *Rapid Commun Mass Spectrom.* 2006;20:965–72.
58. Taban IM, Altelaar AFM, van der Burgt YEM, McDonnell LA, Baykut G, Heeren RMA. Imaging of peptides in the rat brain using MALDI-FTICR mass spectrometry. *J Am Soc Mass Spectrom.* 2007;18:145–51.
59. Kanu AB, Dwivedi P, Tam M, Matz L, Hill Jr HH. Ion mobility-mass spectrometry. *J Mass Spectrom.* 2008;43:1–22.
60. Gillig KJ, Ruotolo B, Stone EG, Russell DH, Fuhrer K, Gonin M, Schultz AJ. Coupling high-pressure MALDI with ion mobility/orthogonal time-of-flight mass spectrometry. *Anal Chem.* 2000;72:3965–71.
61. Stauber J, Lemaire R, Wisztorski M, Ait-Menguellat S, Lucot JP, Vinatier D, Desmond A, Deschamps M, Proess G, Rudloff I, Salz M, Fournier I. New developments in MALDI imaging mass spectrometry for pathological proteomic studies; introduction to a novel concept, the specific MALDI imaging. *Mol Cell Proteomics.* 2006;5:S247.
62. Lawrence EO, Livingston MS. The production of high speed light ions without the use of high voltages. *Phys Rev.* 1932;40:19.
63. Comisarow MB, Marshall AG. Fourier transform ion cyclotron resonance spectroscopy. *Chem Phys Lett.* 1974;25:282–3.
64. Marshall AG, Hendrickson CL, Jackson GS. Fourier transform ion cyclotron resonance mass spectrometry: a primer. *Mass Spectrom Rev.* 1998;17:1–35.
65. Ledford Jr EB, Rempel DL, Gross ML. Space charge effects in Fourier transform mass spectrometry. Mass calibration. *Anal Chem.* 1984;56:2744–8.
66. Shi SDH, Drader JJ, Freitas MA, Hendrickson CL, Marshall AG. Comparison and interconversion of the two most common frequency-to-mass calibration functions for Fourier transform ion cyclotron resonance mass spectrometry. *Int J Mass Spectrom.* 2000;195–196:591–8.
67. Wisztorski M, Verplanck N, Thomy V, Stauber J, Camart JC, Salz M, Fournier I. Use of masks in MALDI-MSI: an easy tool for increasing spatial resolution of images by decreasing irradiated area. Indianapolis: American Society of Mass Spectrometry; 2007.
68. Wisztorski M, Croix D, Macagno E, Fournier I, Salz M. Molecular MALDI imaging: an emerging technology for neuroscience studies. *Dev Neurobiol.* 2008;68:845–58.
69. Taylor CF, Paton NW, Lilley KS, Binz P-A, Julian RK, Jones AR, Zhu W, Apweiler R, Aebersold R, Deutsch EW, Dunn MJ, Heck AJR, Leitner A, Macht M, Mann M, Martens L, Neubert TA, Patterson SD, Ping P, Seymour SL, Souda P, Tsugita A, Vandekerckhove J, Vondriska TM, Whitelegge JP, Wilkins MR, Xenarios I, Yates JR, Hermjakob H. The minimum information about a proteomics experiment (MIAPE). *Nat Biotechnol.* 2007;25:887–93.
70. Orchard S, Hermjakob H. The HUPO proteomics standards initiative—easing communication and minimizing data loss in a changing world. *Brief Bioinform.* 2008;9:166–73.
71. Sköld K, Svensson M, Norrman M, Sjögren B, Svenningsson P, Andrén PE. The significance of biochemical and molecular sample integrity in brain proteomics and peptidomics: Stathmin 2–20 and peptides as sample quality indicators. *Proteomics.* 2007;7:4445–56.
72. Theodorsson E, Stenfors C, Mathé AA. Microwave irradiation increases recovery of neuropeptides from brain tissues. *Peptides.* 1990;11:1191–7.

73. Metz B, Kersten GFA, Hoogerhout P, Brugghe HF, Timmermans HAM, de Jong A, Meiring H, ten Hove J, Hennink WE, Crommelin DJA, Jiskoot W. Identification of formaldehyde-induced modifications in proteins: reactions with model peptides. *J Biol Chem.* 2004;279:6235–43.
74. Stauber J, Lemaire R, Franck J, Bonnel D, Croix D, Day R, Wisztorski M, Fournier I, Salzet M. MALDI imaging of formalin-fixed paraffin-embedded tissues: application to model animals of Parkinson disease for biomarker hunting. *J Proteome Res.* 2008;7:969.
75. Lemaire R, Desmons A, Tabet JC, Day R, Salzet M, Fournier I. Direct analysis and MALDI imaging of formalin-fixed, paraffin-embedded tissue sections. *J Proteome Res.* 2007;6:1295–305.
76. Crockett DK, Lin Z, Vaughn CP, Lim MS, Elenitoba-Johnson KSJ. Identification of proteins from formalin-fixed paraffin-embedded cells by LC-MS//MS. *Lab Invest.* 2005;85:1405–15.
77. Chaurand P, Caprioli RM. Direct profiling and imaging of peptides and proteins from mammalian cells and tissue sections by mass spectrometry. *Electrophoresis.* 2002;23:3125–35.
78. Stoeckli M, Staab D, Staufenbiel M, Wiederhold KH, Signor L. Molecular imaging of amyloid beta peptides in mouse brain sections using mass spectrometry. *Anal Biochem.* 2002;311:33–9.
79. Lemaire R, Wisztorski M, Desmons A, Tabet JC, Salzet M, Fournier I. MALDI-MS direct tissue analysis of proteins: improving signal sensitivity using organic treatments. *Anal Chem.* 2006;78:7145–53.
80. Altelaar AFM, van Minnen J, Jiménez CR, Heeren RMA, Piersma SR. Direct molecular imaging of *Lymnaea stagnalis* nervous tissue at subcellular spatial resolution by mass spectrometry. *Anal Chem.* 2005;77:735–41.
81. Lemaire R, Aït-Menguellat S, Stauber J, Marchaudon V, Lucot JP, Collinet P, Farine MO, Vinatier D, Day R, Ducoroy P, Salzet M, Fournier I. Specific MALDI imaging and profiling for biomarker hunting and validation: fragment of the 11S proteasome activator complex, Reg alpha fragment, is a new potential ovary cancer biomarker. *J Proteome Res.* 2007;6:4127–34.
82. Armin Holle AH, Kayser M, Höhdorf J. Optimizing UV laser focus profiles for improved MALDI performance. *J Mass Spectrom.* 2006;41:705–16.
83. Lemaire R, Stauber J, Wisztorski M, Van Camp C, Desmons A, Deschamps M, Proess G, Rudlof I, Woods AS, Day R, Salzet M, Fournier I. Tag-mass: specific molecular imaging of transcriptome and proteome by mass spectrometry based on photocleavable tag. *J Proteome Res.* 2007;6:2057–67.
84. Groseclose MR, Andersson M, Hardesty WM, Caprioli RM. Identification of proteins directly from tissue: in situ tryptic digestions coupled with imaging mass spectrometry. *J Mass Spectrom.* 2007;42:254–62.
85. Chaurand P, Rahman MA, Hunt T, Mobley JA, Gu G, Latham JC, Caprioli RM, Kasper S. Monitoring mouse prostate development by profiling and imaging mass spectrometry. *Mol Cell Proteomics.* 2008;7:411–23.
86. Luxembourg SL, McDonnell LA, Duursma M, Guo X, Heeren RMA. Effect of local matrix crystal variations in matrix-assisted ionization techniques for mass spectrometry. *Anal Chem.* 2003;75:2333–41.
87. Delcorte A. Matrix-enhanced secondary ion mass spectrometry: the alchemist's solution? *Appl Surf Sci.* 2006;252:6582–7.
88. Wilfried Szymczak KW. Effect of water treatment on analyte and matrix ion yields in matrix-assisted time-of-flight secondary ion mass spectrometry: the case of insulin in and on hydroxycinnamic acid. *Rapid Commun Mass Spectrom.* 2002;16:2025–33.
89. McArthur SL, Vendettuoli MC, Ratner BD, Castner DG. Methods for generating protein molecular ions in ToF-SIMS. *Langmuir.* 2004;20:3704–9.
90. Adriaensen L, Vangaever F, Gijbels R. Metal-assisted secondary ion mass spectrometry: influence of Ag and Au deposition on molecular ion yields. *Anal Chem.* 2004;76:6777–85.
91. Adriaensen L, Vangaever F, Lenaerts J, Gijbels R. Matrix-enhanced secondary ion mass spectrometry: the influence of MALDI matrices on molecular ion yields of thin organic films. *Rapid Commun Mass Spectrom.* 2005;19:1017–24.

92. Aebersold R, Mann M. Mass spectrometry-based proteomics. *Nat Insights*. 2003;422:198–207.
93. Garrison BJ, Winograd N. Ion beam spectroscopy of solids and surfaces. *Science*. 1982;216:805–12.
94. Li KW, Smit AB, Geraerts WPM. Structural and functional characterization of neuropeptides involved in the control of male mating behavior of *Lymnaea stagnalis*. *Peptides*. 1992;13:633–8.
95. Hanton SD, Clark PAC, Owens KG. Investigations of matrix-assisted laser desorption/ionization sample preparation by time-of-flight secondary ion mass spectrometry. *J Am Soc Mass Spectrom*. 1999;10:104–11.
96. Stoeckli M, Staab D, Schweitzer A, Gardiner J, Seebach D. Imaging of a [beta]-peptide distribution in whole-body mice sections by MALDI mass spectrometry. *J Am Soc Mass Spectrom*. 2007;18:1921–4.
97. van Veelen P, Jimenez C, Li K, Wildering W, Geraerts W, Tjaden U, van der Greef J. Direct peptide profiling of single neurons by matrix-assisted laser-desorption ionization mass-spectrometry. *Org Mass Spectrom*. 1993;28:1542–6.
98. Garden RW, Moroz LL, Moroz TP, Shippy SA, Sweedler JV. Excess salt removal with matrix rinsing: direct peptide profiling of neurons from marine invertebrates using matrix-assisted laser desorption/ionization time-of-flight mass spectrometry. *J Mass Spectrom*. 1996;31:1126–30.
99. Redeker V, Toullec J-Y, Vinh J, Rossier J, Soyey D. Combination of peptide profiling by matrix-assisted laser desorption/ionization time-of-flight mass spectrometry and immunodetection on single glands or cells. *Anal Chem*. 1998;70:1805–11.
100. Stoeckli M, Chaurand P, Caprioli RM. Direct profiling of proteins in biological tissue sections by MALDI mass spectrometry. *Anal Chem*. 1999;71:5263–70.
101. Garden RW, Sweedler JV. Heterogeneity within MALDI samples as revealed by mass spectrometric imaging. *Anal Chem*. 2000;72:30–6.
102. Stoeckli M, Chaurand P, Hallahan DE, Caprioli RM. Imaging mass spectrometry: a new technology for the analysis of protein expression in mammalian tissues. *Nat Med*. 2001;7:493–6.
103. Rubakhin SS, Greenough WT, Sweedler JV. Spatial profiling with MALDI MS: distribution of neuropeptides within single neurons. *Anal Chem*. 2003;75:5374–80.
104. Kruse R, Sweedler JV. Spatial profiling invertebrate ganglia using MALDI MS. *J Am Soc Mass Spectrom*. 2003;14:752–9.
105. Monroe EB, Jurchen JC, Lee J, Rubakhin SS, Sweedler JV. Vitamin E imaging and localization in the neuronal membrane. *J Am Chem Soc*. 2005;127:12152.
106. Hintersteiner M, Enz A, Frey P, Jatou A-L, Kinzy W, Kneuer R, Neumann U, Rudin M, Staufenbiel M, Stoeckli M, Wiederhold K-H, Gremlich H-U. In vivo detection of amyloid-beta deposits by near-infrared imaging using an oxazine-derivative probe. *Nat Biotechnol*. 2005;23:577–83.
107. Stauber J, Lemaire R, Wisztorski M, Ait-Menguellet S, Lucot JP, Vinatier D, Desmond A, Deschamps M, Proess G, Rudlof I, Salzet M, Fournier I. New developments in MALDI imaging mass spectrometry for pathological proteomic studies; introduction to a novel concept, the specific MALDI imaging. *Mol Cell Proteom*. 2006;5:S247.
108. Baluya DL, Garrett TJ, Yost RA. Automated MALDI matrix deposition method with Inkjet printing for imaging mass spectrometry. *Anal Chem*. 2007;79:6862–7.
109. Hsieh Y, Chen J, Korfmacher WA. Mapping pharmaceuticals in tissues using MALDI imaging mass spectrometry. *J Pharmacol Toxicol Meth*. 2007;55:193–200.
110. Atkinson SJ, Loadman PM, Sutton C, Patterson LH, Clench MR. Examination of the distribution of the bioreductive drug AQ4N and its active metabolite AQ4 in solid tumours by imaging matrix-assisted laser desorption/ionisation mass spectrometry. *Rapid Commun Mass Spectrom*. 2007;21:1271–6.
111. Signor L, Varesio E, Staack RF, Starke V, Richter WF, Hopfgartner G. Analysis of erlotinib and its metabolites in rat tissue sections by MALDI quadrupole time-of-flight mass spectrometry. *J Mass Spectrom*. 2007;42:900–9.

112. Rohner TC, Staab D, Stoeckli M. MALDI mass spectrometric imaging biological tissue sections. *Mech Ageing Dev.* 2004;126:177–85.
113. Gusev AI, Wilkinson WR, Proctor A, Hercules DM. Direct quantitative analysis of peptides using matrix assisted laser desorption ionization. *Fresenius J Anal Chem.* 1996;354:455–63.
114. Wilkinson WR, Gusev AI, Proctor A, Houalla M, Hercules DM. Selection of internal standards for quantitative analysis by matrix-assisted laser desorption-ionization (MALDI) time-of-flight mass spectrometry. *Anal Bioanal Chem.* 1997;357:241–8.
115. Hopfgartner G, Varesio E, Stoeckli M. Matrix-assisted laser desorption/ionization mass spectrometric imaging of complete rat sections using a triple quadrupole linear ion trap. *Rapid Commun Mass Spectrom.* 2009;23:733–6.
116. Amann JM, Chaurand P, Gonzalez A, Mobley JA, Massion PP, Carbone DP, Caprioli RM. Selective profiling of proteins in lung cancer cells from fine-needle aspirates by matrix-assisted laser desorption ionization time-of-flight mass spectrometry. *Clin Cancer Res.* 2006;12:5142–50.
117. Burrell MM, Earnshaw CJ, Clench MR. Imaging matrix assisted laser desorption Ionization mass spectrometry: a technique to map plant metabolites within tissues at high spatial resolution. *J Exp Bot.* 2007;58:757–63.
118. Bunch J, Burrell MM, Clench MR. MALDI imaging to reveal metabolite profiles in potato tubers. *Abstract/Comp Biochem Physiol A.* 2004;137:147–60.
119. Mullen AK, Clench MR, Crosland S, Sharples KR. Determination of agrochemical compounds in soya plants by imaging matrix-assisted laser desorption/ionization mass spectrometry. *Rapid Commun Mass Spectrom.* 2005;19:2507–16.
120. Jonathan Stauber, Luke MacAleese J, Franck, Marten Snell, Emmanuelle Claude, basak Kükreer Kaletas, Ingrid van der Wiel, Maxensce Wisztorski, Isabelle Fournier and Ron M.A. Heeren JASMS. On-Tissue Protein Identification and Imaging by MALDI-Ion Mobility Mass Spectrometry. 2010;21:338–47.
121. Robinson S, Warburton K, Seymour M, Clench M, Thomas-Oates J. Localization of water-soluble carbohydrates in wheat stems using imaging matrix-assisted laser desorption/ionization mass spectrometry. *New Phytol.* 2006;173:428–44.
122. Woods AS, Wang HY, Jackson SN. A snapshot of tissue glycerolipids. *Curr Pharm Des.* 2007;13:3344–56.
123. Kahn E, Tessier C, Lizard G, Petiet A, Brau F, Clement O, Frouin F, Jourdain JR, Guiraud-Vitoux F, Colas-Linhart N, Siauve N, Cuenod CA, Frija G, Todd-Pokropek A. Distribution of injected MRI contrast agents in mouse livers studied by confocal and SIMS microscopy. *Anal Quant Cytol Histol.* 2002;24:295–302.
124. Langstrom B, Andren PE, Lindhe O, Svedberg M, Hall H. In vitro imaging techniques in neurodegenerative diseases. *Mol Imaging Biol.* 2007;9:161–75.
125. Kahn E, Tessier C, Lizard G, Petiet A, Bernengo GC, Coulaud D, Fourré C, Frouin F, Clément O, Jourdain JR, Delain E, Guiraud-Vitoux F, Colas-Linhart N, Siauve N, Cuenod CA, Frija G, Todd-Pokropek A. Analysis of the distribution of MRI contrast agents in the livers of small animals by means of complementary microscopies. *Cytometry.* 2003;51A:97–106.
126. Acquadro E, Cabella C, Ghiani S, Miragoli L, Bucci EM, Corpillo D. Matrix-assisted laser desorption ionization imaging mass spectrometry detection of a magnetic resonance imaging contrast agent in mouse liver. *Anal Chem.* 2009;81:2779–84.
127. Shimma S, Sugiura Y, Hayasaka T, Zaima N, Matsumoto M, Setou M. Mass imaging and identification of biomolecules with MALDI-QIT-TOF-based system. *Anal Chem.* 2008;80:878–85.
128. Stauber J, Kükreer Kaletas B, van der Wiel IM, Snel MF, Claude E, Heeren RMA. Ion mobility imaging mass spectrometry: a new tool for in situ identification proceedings, ASMS Denver. 2008.

# Chapter 6

## Molecular Structure and Identification Through G-SIMS and SMILES

F.M. Green, I.S. Gilmore, and M.P. Seah

**Abstract** In this chapter, we discuss the use of G-SIMS (gentle secondary ion mass spectrometry) and SMILES (simplified molecular input line entry specification) for analyzing biologically relevant materials and molecules. G-SIMS is an easy-to-use method that considerably simplifies complex static secondary ion mass spectrometry (SSIMS) spectra into spectra with only those ions that are highly characteristic of the surface. G-SIMS provides information about the molecular structure that is not directly available from the mass spectrum, allowing the identification of unknown materials without the need for experimental library spectra. For complex molecules such as biomolecules, identification of the most characteristic fragment ions alone may be insufficient to uniquely identify a molecule because of the combinatorial chemical possibilities available within the achievable mass accuracy. The molecular structure can be reassembled by following the fragmentation pathways (by varying the G-SIMS surface plasma temperature); this technique is known as G-SIMS-FPM (G-SIMS fragmentation pathway mapping). This provides powerful capability analogous to MS/MS experiments traditionally used in mass spectrometry. A simple method, using SMILES, is used to simulate the fragmentation pathways that occur in G-SIMS. These pathways are found to have good agreement with the G-SIMS fragmentation pathways. The simulated pathways help analysts deduce the molecular structure, leading to refined identification. A rapid method to establish a foundational database of simulated pathways using the SIMS community and a web-based system is being developed.

---

F.M. Green (✉) • I.S. Gilmore • M.P. Seah  
Analytical Science Division, National Physical Laboratory,  
Teddington, Middlesex TW11 0LW, UK  
e-mail: [Felicia.Green@npl.co.uk](mailto:Felicia.Green@npl.co.uk)

## 6.1 Introduction

The strength of SSIMS, and also one of its drawbacks, is that the mass spectra are extremely rich, with hundreds of mass peaks, many of which clearly contain aspects of the molecular information. As we shall see later, many of these peaks are degraded fragment ions that, unfortunately, do not relate directly to parent molecules. These ions confuse the spectral interpretation. Figure 6.1 illustrates the issue with a mass spectrum of an industrial antioxidant, Irganox 1010, used in the polymer industry, on a silver substrate. It is clear that there are many peaks, and by progressively zooming in on smaller and smaller regions, we see the complexity of the spectrum.

Traditionally, to identify a material, the SSIMS spectrum is used as a fingerprint for comparison with library spectra. Such libraries [1–3] are excellent and—through the pioneering work of Vickerman and Briggs—are of great benefit to the whole community and widely used. However, the growth and coverage of experimental libraries are, by necessity, limited. Twenty years after the publication of the first

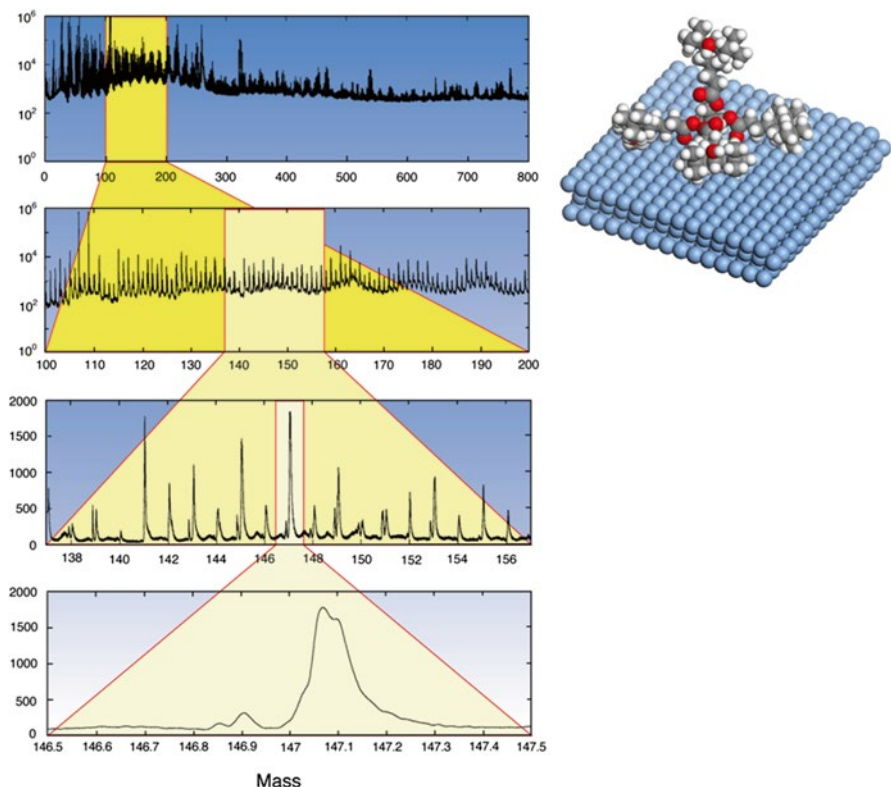


**Fig. 6.1** The positive-ion static SIMS spectrum of a surface layer of Irganox 1010 molecules on silver (*inset*), illustrating the complexity of the mass spectrum. Note, for clarity, the *inset* only shows one molecule on the surface, whereas the spectrum is for a monolayer of molecules

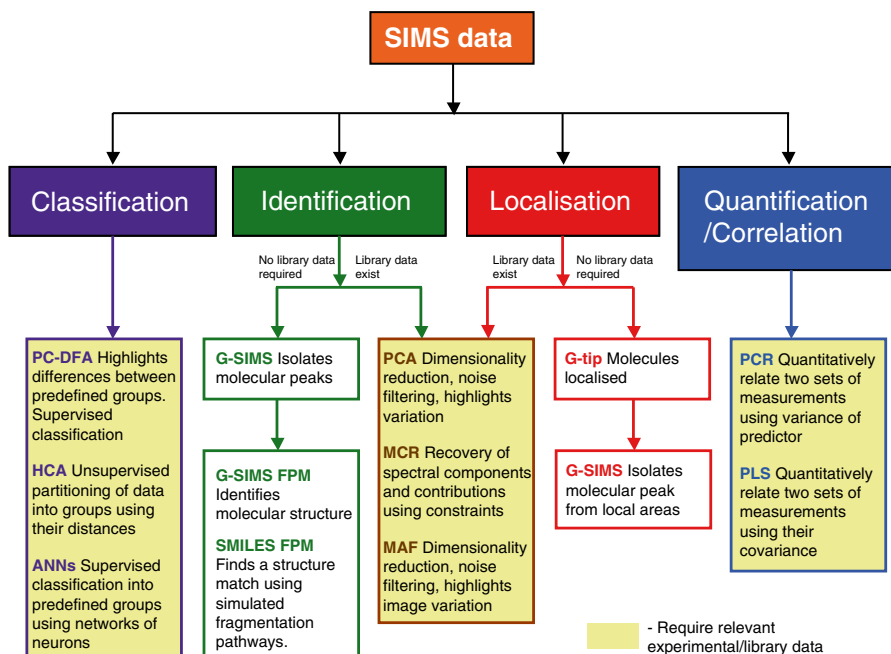


**Fig. 6.2** The complementarity of G-SIMS with multivariate methods. Note: *PC-DFA* principal component discrimination analysis, *HCA* hierachal cluster analysis, *ANNs* artificial neural networks, *PCA* principal component analysis, *MCR* multivariate curve resolution, *MAF* maximum autocorrelation factors, *PCR* principal component regression, *PLS* partial least squares

library in 1989, the combined content contains spectra for 500 materials only. In comparison to the range of industrially relevant materials, this is a tiny fraction. For new and rapidly growing industrial sectors such as pharmaceuticals, biomaterials, and biotechnology, the problems are acute. A library-independent method was required that provides direct interpretation and accesses the full range of required materials. Hence, G-SIMS was developed.

Multivariate analytical methods are very powerful for the identification, quantification, classification, and development of models for prediction. These methods are described in detail in the previous chapter and also in Ref. [4]. In Fig. 6.2, we illustrate the complementarity between multivariate methods and G-SIMS. Both methods simplify the mass spectra; multivariate methods reduce the complexity of the data using statistical methods (i.e., the variance), while G-SIMS simplifies the spectra by eliminating heavily fragmented and degraded molecules, leaving the more intact structurally significant ions. This utilizes the underlying chemistry of the molecules and the physics of the fragmentation process. This latter characteristic enables G-SIMS to extract information that is otherwise not directly accessible from the spectra, thus providing powerful information on the molecular structure. Multivariate methods are excellent to identify trends and correlations in spectra and



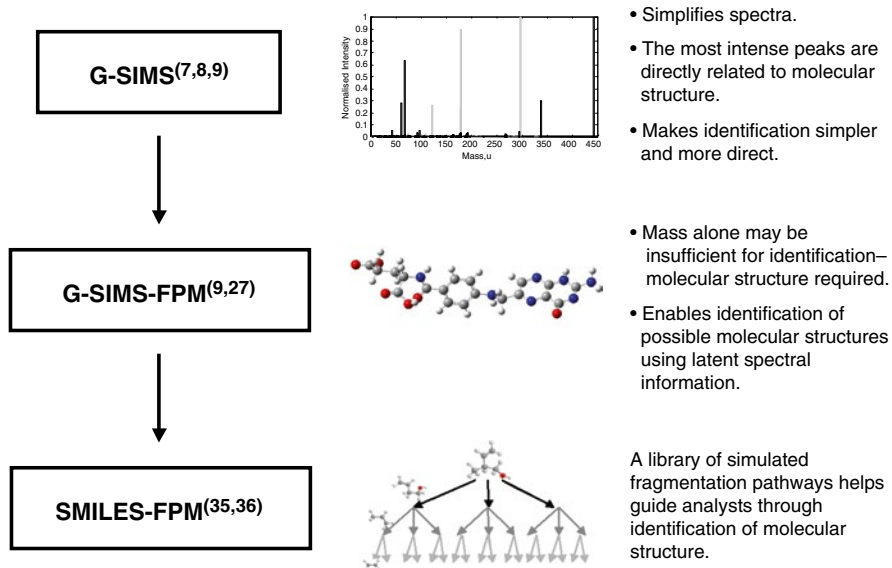


**Fig. 6.3** Information available from G-SIMS, G-SIMS-FPM, and G-SIMS SMILES—a quick reference guide for analysts

images with other experimental variables, such as composition or, for example, production methods, and, coupled with a priori information, for quantification, classification, and prediction [4]. G-SIMS spectra are not used directly for quantification but for identification; however, the G-SIMS peaks are good peaks to select for quantification. For example, for the quantification of polystyrene materials, the tropyllium ion ( $C_7H_7^+$ ) is the most intense ion, but quantification is poorer than if the structurally significant ions identified by G-SIMS (e.g.,  $C_{15}H_{13}^+$ ) are used [5].

In Sect. 6.2, we review the G-SIMS concept and the practicalities of acquiring G-SIMS spectra with a simple guide. Examples of the effectiveness of G-SIMS for a variety of biologically relevant polymers and molecules are given in Sect. 6.3. In Sect. 6.4, the use of G-SIMS to elucidate the molecular structure, by examining the fragmentation pathways, is described. This is known as G-SIMS fragmentation pathway mapping (FPM). A novel approach based on SMILES (simplified molecular input line entry specification) [6], to simulate fragmentation pathways and help identify the molecular structure, is given in Sect. 6.5. Section 6.6 is a short outline of recent innovations for G-SIMS imaging. Finally, in Sect. 6.7, we discuss the future outlook.

A summary of the increasing molecular information now available to the analyst as we progress from a basic G-SIMS analysis through G-SIMS-FPM to G-SIMS with SMILES is given in Fig. 6.3. This indicates the method to select, depending on the level of information required for any particular analytical situation.

## 6.2 G-SIMS

In this section, we give an overview of the principles of G-SIMS and the role of fragmentation in SIMS, as well as practical help for analysts. The section begins with an overview of the G-SIMS concept and follows with an easy guide to obtaining G-SIMS spectra. This includes an examination of the way fragmentation varies for ions of different energy and species and helps the analyst choose suitable primary ions to obtain G-SIMS.

### 6.2.1 Overview of the G-SIMS Concept

We envisage the impact of a single primary ion schematically in Fig. 6.4. Typically, for efficient ion beams, the ion energy is approximately 10–25 keV; that energy is dissipated in the surface of the material over a depth range of approximately 25 nm (around 100 atom layers). The energy distribution of excited atoms at the surface may be approximated by a 2D Gaussian, centered around the original impact site with an FWHM of around 2 nm. In this scheme, we consider a monolayer of molecules, such as folic acid, covering the surface. It is clear that those folic acid molecules along the peripheral zone of the impact site are more gently liberated from the surface and have a higher probability of remaining intact. As we move closer to the center of the impact site, the energy rises and the molecules begin to

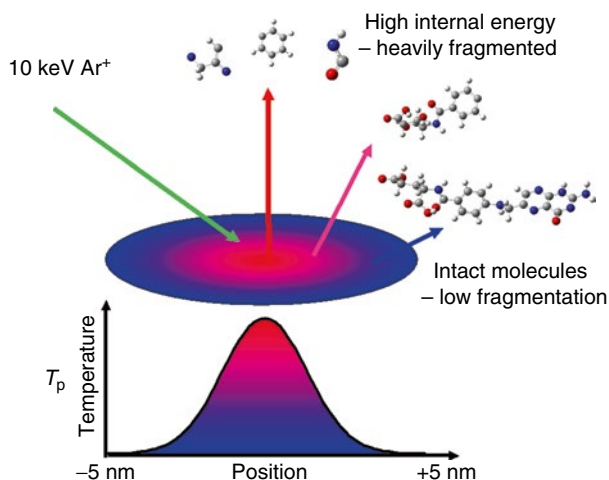


**Fig. 6.4** Illustration of the surface-energy distribution from a single-ion impact on a target material with a surface monolayer of folic acid molecules. Typical fragmentation products for folic acid are shown

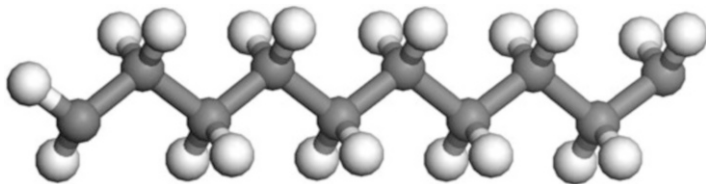


Fig. 6.5 Schematic of a hydrocarbon molecule of the series  $C_nH_{2n}$

fragment more, so that, at the center, the emitted ions have a high internal energy and most probably consist of small degraded fragments. The measured SIMS spectrum is the volume integral of all these fragment ions and thus contains some intact molecular ions among a dominant background of smaller degraded ions. We see an example of this in Fig. 6.1. The small fragment ions are not helpful for identification, as they are ubiquitous among many different material types. In many cases, larger, more stable ions, such as polycyclic aromatic ions, may form in this area. These ions may be misleading and, if used, give poor quantification.

We now consider how fragmentation of a molecule leads to daughter products and how their intensities are related. In the recoil from the primary ion impact, the surface zone may be characterized by a surface plasma temperature,  $T_p$ . This is a function of the radius,  $r$ , from the point of impact. The plasma temperature is also a function of the bombarding ion species and the impact energy,  $E$ . If we reduce the plasma temperature by adjusting the primary beam energy, the relative intensities of the more intact molecular fragments would be expected to increase. In principle, given the relative intensities of ions at two different values of  $T_p$ , it is possible to extrapolate to the relative spectral intensities at a lower surface plasma temperature. This is the basic principle of G-SIMS, which is explained below and in more detail in Refs. [7–9].

We consider the fragmentation of a hydrocarbon molecule, as shown in Fig. 6.5, into the series  $C_nH_{2n}$ ,  $C_nH_{2n-1}$ ,  $C_nH_{2n-2}$ , and so on, and note that the energy,  $\Delta u$ , to remove each successive hydrogen atom is approximately the same. Thus, the number of fragments,  $N_i$ , of composition  $C_nH_{2n-i}$ , derived from  $N_0$  components of composition  $C_nH_{2n}$ , is given by the simple partition function relation

$$N_i = N_0 \exp\left(\frac{-i\Delta u}{kT_p}\right). \quad (6.1)$$

If we now consider these at the two ion beam energies,  $E_1$  and  $E_2$ , with associated fragment surface plasma temperatures  $T_{p1}$  and  $T_{p2}$ , we get

$$\frac{N_i(E_2)}{N_i(E_1)} = \frac{N_0(E_2)}{N_0(E_1)} \exp\left[\frac{-i\Delta u}{k} \left(\frac{1}{T_{p2}} - \frac{1}{T_{p1}}\right)\right]. \quad (6.2)$$

The ratio of  $N_i(E_2)$ , for a low ion beam energy,  $E_2$ , to those at high energy,  $N_i(E_1)$ , gives a factor,  $F_x$ , where  $x$  is the index related to each mass peak. This  $F_x$  term is

related to the effective surface plasma temperatures  $T_{p1}$  and  $T_{p2}$  from Eq. 6.2. Since  $T_{p1}$  and  $T_{p2}$  are of a similar magnitude and  $T_{p2}$  is less than  $T_{p1}$  by  $\Delta T$ , we may first consider the factor  $F_x^2$ , which would be the  $F_x$  value for surface plasma temperatures  $T_{p1} - 2\Delta T$  and  $T_{p1}$ . Thus, one could use  $F_x^{13}$  or some high power to deduce the result at a significantly lower surface plasma temperature than that relevant to either of the recorded spectra.

We may now generate a low surface plasma temperature SSIMS spectrum by multiplying an existing spectrum,  $N_x$ , with the factor  $F_x^g$ . This forms the G-SIMS spectrum with intensities  $I_x$  given by

$$I_x = M_x N_x F_x^g, \quad (6.3)$$

where  $g$ , the G-SIMS index, is often set at 13. The additional factor  $M_x$ , the mass of the emitted fragment, is found useful to enhance the natural fall in emission with mass. In Ref. [8], a simple method is described that constructs a tangent line passing through the two most significant high-mass fragments. A new ratio,  $F_x^*$ , is then calculated by dividing  $F_x$  by the function of the tangent line.

It is useful to look in a little more detail at the spectral intensity ratio,  $F_x$ , as this will help with later understanding of the method. The intensity ratio on the left of Eq. 6.2 can be rewritten as  $F_{x,i}$ , where

$$F_{x,i} = F_{x,0} \exp(-\beta i) \quad (6.4)$$

and  $-\beta i$  is given by the items in square brackets on the right of Eq. 6.2. Thus, an intensity ratio plot of  $\log_e(F_{x,i})$  versus mass will show data for a given  $C_nH_{2n-1}$  series falling on a straight line with gradient  $\beta$  per increment in  $i$ . In the case used here, where the increment in  $i$  is a hydrogen atom, the gradient is simply per unified atomic mass units, u, or Dalton, Da. If  $\Delta u$  is positive and if the surface plasma temperature,  $T_{p1}$ , at energy  $E_1$  is greater than the surface plasma temperature,  $T_{p2}$ , at energy  $E_2$ ,  $\beta$  will be positive, and vice versa. Note that the energy to remove a hydrogen atom from  $C_{12}H_{24}$  will be very similar to that from  $C_6H_6$ , so that the gradients,  $\beta$ , will be the same for the hydrogen loss series in the intensity ratio plot for many values of  $n$ .

Figure 6.6 shows the intensity ratio plot ( $F_{x,i}$  vs. mass) for the  $E_2$  spectra for primary ion  $Ar^+$  with  $E_2 = 4$  keV and the  $E_1$  spectrum an average for  $Ar^+$  with 4–10 keV energies, with the  $C_xH_y$  ions plotted with a filled circle, distinguishing the gradients,  $\beta$ , for different hydrocarbon cascades. This intensity ratio plot clearly shows the fragmentation cascades and so will be termed a fragment cascade plot in the rest of the chapter. Observing the parallelism of the gradients in Fig. 6.6 shows that, for  $x > 3$ , a single value of  $\Delta u$  or  $\beta$  may be used to describe the fragmentation process. We will later return to the value of  $\beta$  for the selection of optimum ion beam parameters. Fortunately for the analysts, we do not need to calculate the value of  $\beta$  for G-SIMS or indeed any other parameter—all that is needed is the ratio of spectral intensities,  $F_x$ , as shown above in Eq. 6.4.

The G-SIMS procedure blends information about the amount of fragmentation each peak has undergone (from the fragment cascade plot) with the original spectral

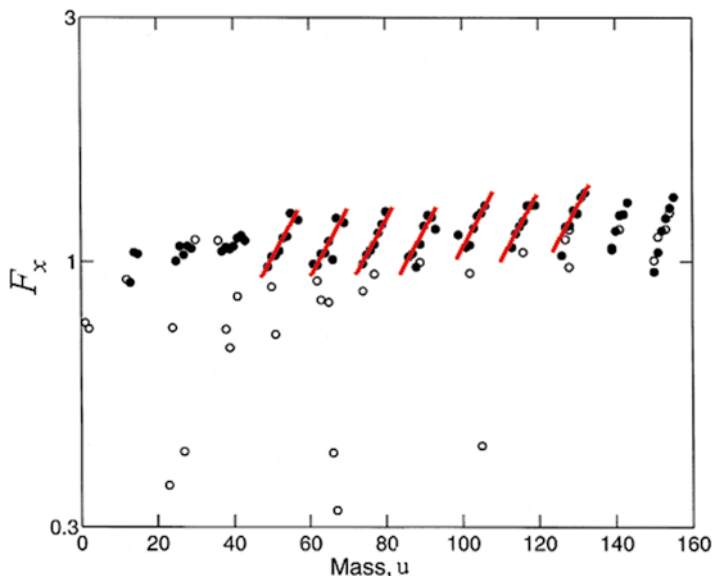


**Fig. 6.6** Fragment cascade plot showing the ratio of polystyrene (PS) spectral intensities  $F_x$ , for 4 and an average of 4–10-keV argon primary ions. The *filled circles* represent fragments of the type  $C_xH_y$ , whereas the *empty circles* are peaks for contaminants (After Ref. [7])

intensities. Those fragments that have little degradation are boosted in intensity and those with significant degradation are suppressed. This is what would be observed if one could do static SIMS with a very low  $T_p$  value (or very low energy). As an example of the power of G-SIMS for direct analysis, we show in Fig. 6.7 the SSIMS and G-SIMS spectra for polystyrene (PS). The dominant intensity ions in the SSIMS spectra (Fig. 6.7b) are polycyclic aromatic ions with complex linked cyclic arrangements, which exhibit little direct relevance to the PS structure. These structures are very stable ions produced from the high-energy fragmentation cascade, either as recombination events or as the end result of a decay process for a molecule originally with excess energy. These “characteristic” peaks are common to many other materials. In contrast, the G-SIMS spectrum (Fig. 6.7a) is dominated by ions with pendant phenyl groups, exactly as would be expected from the molecular structure, giving direct identification without the need for library data. G-SIMS has been tested extensively on many materials, including polymers, such as PS [7], PC [7], PTFE [7], and PMMA [8], and complex molecules, including Irganox 1010 [8], caffeine [8], cholesterol [8], glucose [8], poly-L-lysine [8], and folic acid [9], biodegradable polymers [10–12], and adhesives [13]. Typically, for SSIMS, only one or two peaks above, say, 1 % of the maximum peak intensity provide direct interpretation out of several hundred peaks. For G-SIMS, the situation is quite different; spectra typically contain five or so peaks, which lead to direct interpretation and identification. This step change opens the door to applications in areas where the fingerprint approach of collating spectra is not practicable.

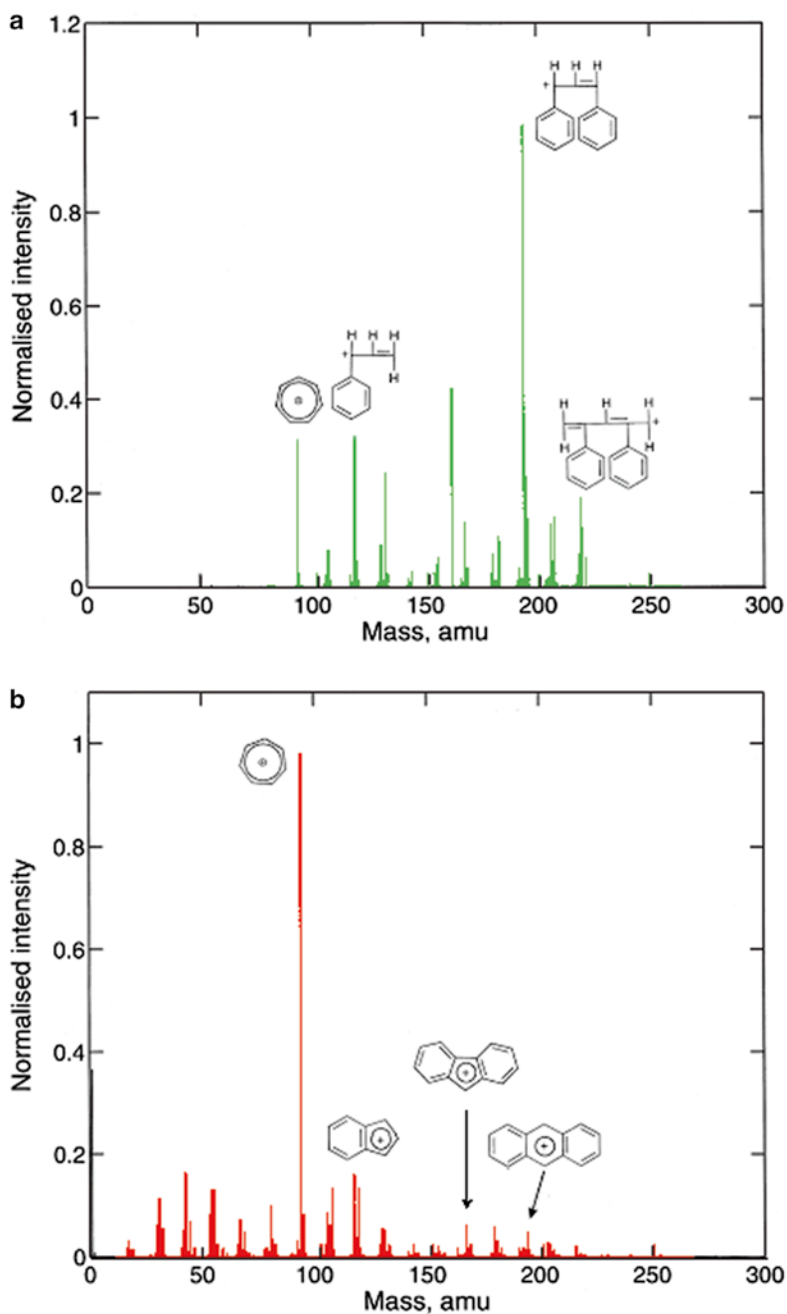


**Fig. 6.7** Positive-ion spectra of polystyrene. (a) G-SIMS spectrum using the ratio between 10- and 4-keV argon ions; (b) static SIMS spectrum using 10-keV argon ions (After Ref. [7])

## 6.2.2 Practicalities of G-SIMS: A Simple Guide

### 6.2.2.1 Optimizing Instrument Parameters

In practice, to generate G-SIMS spectra, all that is required are two sequential spectra acquired from the same area using different ion beam conditions (providing different surface plasma temperatures). An important prerequisite is that the instrument should be in good control with repeatabilities of typically better than 2 %. This is readily achievable in modern instruments. In a recent VAMAS interlaboratory study, around 90 % of 32 participating laboratories achieved better than 2 % repeatability [14]. It is recommended that analysts use the standard ISO 23830 for determining the repeatability and constancy of their instrument [15]. A spreadsheet that does all of the necessary calculations is freely available from the NPL website; see Ref. [16].

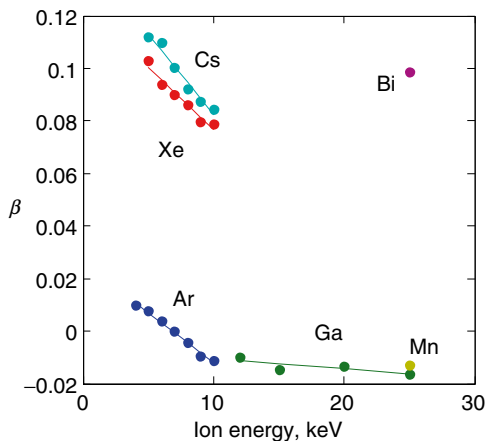
As with all mass spectrometries, for accurate identification it is critical to calibrate the mass scale accurately. In a second VAMAS interlaboratory study, it was found that the fractional mass accuracy for large molecules was typically very poor [17] (150 ppm). A procedure for improving the mass calibration, by typically a factor of 10, is given in Ref. [18]; an ISO standard for this is now available as ISO 13084:2011. Similarly, it is important to ensure that the mass resolution of the instrument is sufficient to resolve chemical differences.

### 6.2.2.2 Selecting the Ion Beam Parameters

We discussed earlier the index  $\beta$ , the gradient of the fragment cascades for  $C_xH_y$ , observed in Fig. 6.6. The larger the value of  $\beta$  is between conditions, the stronger the difference will be in surface plasma temperatures. In Fig. 6.8, we show the values of  $\beta$  for PS for different primary ion species ( $Ar^+$ ,  $Mn^+$ ,  $Ga^+$ ,  $Xe^+$ ,  $Cs^+$ ,  $Bi^+$ ) for a range of practical ion beam energies, relative to  $Ar^+$  at 7 keV. It is clear that using a  $Ga^+$  ion beam at say 12 and 25 keV gives only a small change in  $\beta$ , and therefore only a small difference in surface plasma temperatures, and consequently is not effective for G-SIMS. Selecting primary ions with high and low mass is best. A number of laboratories have found that Cs (131 u) and Ar (40 u) or Cs and Ga (69 u) provide very effective combinations for G-SIMS [17]. However, by using different primary ions, we introduce a general mass dependency in  $F_x$  (Fig. 11 of Ref. [7]). In early work, that was removed by a simple cubic fit to the data using a least-modulus minimization. More recent work shows that an erf function (a function with a sigmoidal shape giving an output rising from zero to one as the input increases) gives a more universal fit and is recommended.

For heterogeneous samples (i.e., most samples), it is important that the analyses are from the same area, and so the ion beams need to be aligned. Clearly, misalignment leads to the ratio of spectra from different areas, causing the method to be less reliable. If available, a dual-beam source sharing the same ion-optical column is preferable. This ensures co-alignment at the sample. Recently [19], a novel emitter for a Taylor cone liquid metal ion source (LMIS) was developed that consists of Bi

**Fig. 6.8** Average cascade gradient,  $\beta$ , for  $\text{Ar}^+$ ,  $\text{Ga}^+$ ,  $\text{Xe}^+$ ,  $\text{Cs}^+$ ,  $\text{Bi}^+$ , and  $\text{Mn}^+$  for various energies on polystyrene (After Ref. [19])



(208.98 u) with a small amount of Mn (54.94 u). This is a very convenient option for analysts as it may be used in all Taylor cone LMIS, which are now the dominant primary ion guns in SSIMS. In this way, the two ion beams are inherently aligned [19]. We discuss this later in Sect. 6.6. The alternative use of separate ion columns will need a careful alignment procedure.

### 6.2.2.3 Acquisition of Spectra

It is important to ensure that the total fluence of ions is kept below  $1 \times 10^{16}$  ions/m<sup>2</sup> so that ion-induced damage effects are small [20]. If the experiment requires charge compensation using an electron beam, it is also very important to ensure that the electron fluence is kept below  $6 \times 10^{18}$  electrons/m<sup>2</sup>. More details and guidance are given elsewhere [21].

Acquire two mass spectra, the first using the ion beam of lowest fragmentation (for example,  $\text{Cs}^+$ ,  $\text{Bi}^+$ , or lower-energy ions), followed immediately by a second, using the ion beam of higher fragmentation (for example,  $\text{Ar}^+$ ,  $\text{Mn}^+$ , or higher-energy ions). Most modern instruments can be programmed using a batch method, making acquisition straightforward. To improve and monitor measurement uncertainty, it is recommended that pairs of spectra are acquired from at least three separate areas, preferably five.

The next step is exactly as for any SSIMS experiment: The peak intensities need to be measured from the mass spectrum. Use the low-fragmentation spectrum to choose the peaks. Most commercial software can perform this automatically by identifying the peak centroid and width data. When applied to the mass spectrum, these data yield a data matrix of peak centroid mass and peak intensities. When using an automatic peak-search method, it is important to review the peaks identified to check that metastables [22] and other background artifacts are excluded. Metastables actually provide valuable information about the molecular structure that is very



complementary to G-SIMS. We will not discuss this further here, but interested readers are directed to Ref. [22], which provides an easy-to-use method to identify metastable peaks and their parent ions. If peaks are not resolved into separate components, this can cause problems with identification—as with any analysis.

Use the same table of peak positions and widths to measure the peak intensities for all the spectra. G-SIMS spectra are then calculated directly using Eq. 6.3. To make it easier, a simple Excel spreadsheet “Easy G-SIMS” is freely available on the web at Ref. [23]. This spreadsheet simply requires input of the peak masses and spectral intensities for matching low- and high-fragmentation data in columns. The spreadsheet also gives the repeatability of the data and incorporates the “tangent gradient” method, which is very useful for large molecules although generally is not required for polymers. The index  $g$  may be altered, effectively allowing the surface plasma temperature to be adjusted. We shall come back to this later for the analysis of molecular structure. G-SIMS may be conducted for both positive and negative secondary ions.

### 6.3 G-SIMS Examples

In the previous section, we outlined the G-SIMS concept and the practicalities of producing G-SIMS spectra. We now provide examples to illustrate the utility of the method. The static SIMS spectrum of polycarbonate (PC) is dominated by polycyclic aromatic hydrocarbon ions and other hydrocarbons that do not relate directly to the PC monomer repeat unit structure but instead are degraded fragments and rearrangement product ions (see Fig. 12a of Ref. [7]). In contrast, the G-SIMS spectrum exhibits a dominant ion at  $C_9H_{11}O^+$ , which is directly related to the parent structure, as well as other structurally significant ions:  $C_2H_3O^+$ ,  $C_3H_3O^+$ ,  $C_7H_7O^+$ , and  $C_8H_9O^+$ . The degradation fragments such as polycyclic aromatic hydrocarbon ions are absent from the G-SIMS spectrum (see Fig. 12b of Ref. [7]). Therefore, the PC reference material provides a good and clear test for the successful operation of G-SIMS [17]. For G-SIMS to be judged successful for this reference material, each of the following requirements must be met: the presence of a strong  $C_9H_{11}O^+$  peak; the absence of polycyclic aromatic peaks; good repeatability; and low- and high-fragmentation conditions that give a well-separated surface plasma temperature (observed by a clear structure in the ratio  $F_x$  values, shown in Fig. 6.6 for PS).

Earlier, in the introduction, we illustrated the complexity of the static SIMS spectrum with the Irganox molecule, shown in Fig. 6.1. For comparison, we show in Fig. 6.9 the G-SIMS spectra, using the tangent gradient, for positive and negative ions. It is clear that these spectra are much simpler than Fig. 6.1 and the peaks are directly related to the parent structure.

In 2006, Ogaki et al. [11] successfully used G-SIMS to study a series of biodegradable polyesters; these are medically important, particularly in drug-delivery systems and biomedical implants. These materials include polyglycolic acid (PGA), poly-L-lactic acid (PLA), poly- $\beta$ -hydroxybutyrate (PHB), and poly- $\epsilon$ -caprolactone

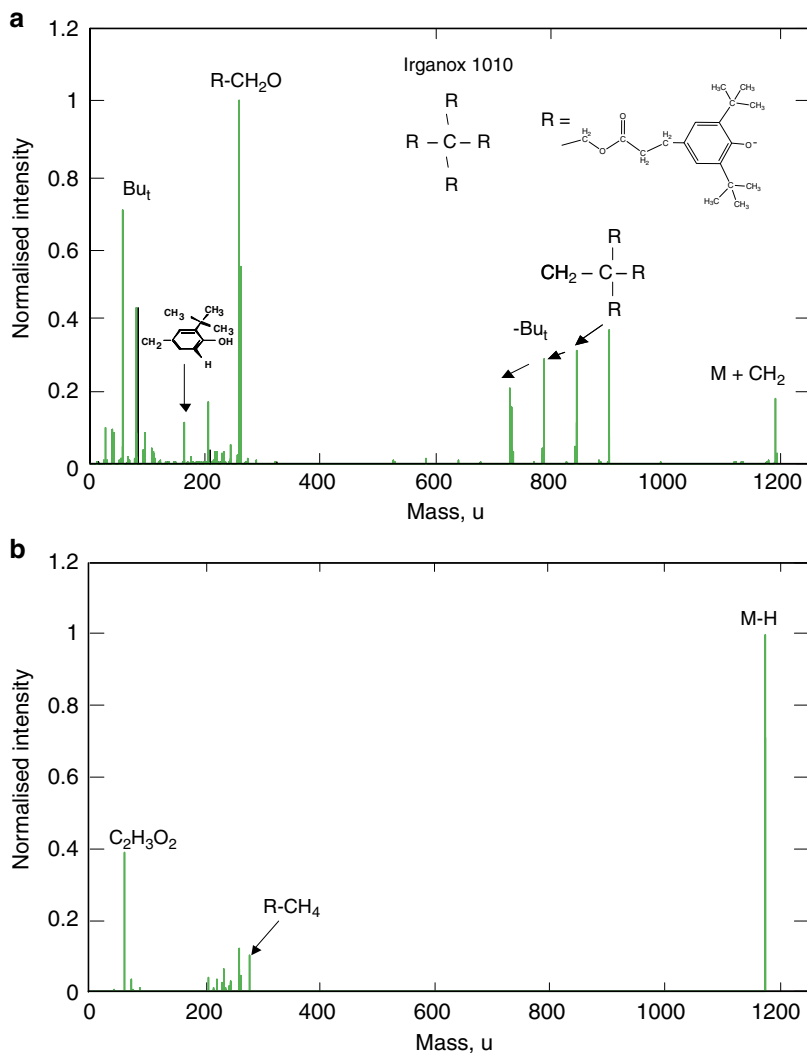


**Fig. 6.9** G-SIMS spectra of Irganox 1010: (a) positive ions; (b) negative ions, using the ratio between 10-keV argon and cesium ions (After Ref. [27])

(PCL) [10–12]. They have also used G-SIMS to study PLA end-group contribution to SIMS spectra [12] and random poly (lactic-co-glycolic acid) copolymers. As a typical example of this series of materials, we show in Fig. 6.10 the G-SIMS spectrum for an 80:20 PLGA co-polymer from Ref. [12]. All of the peaks are directly related to the molecular structure and can easily be attributed to lactide, glycolide, and combined fragments. The G-SIMS analysis also provides additional information on the formation of the secondary ions, which agrees with deuteration studies.

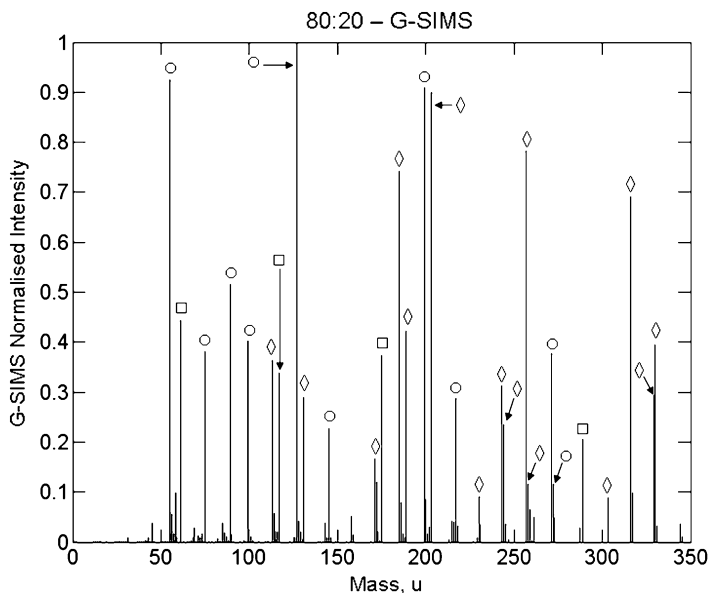


**Fig. 6.10** G-SIMS spectrum of 80:20 PLGA co-polymer. Repeat unit of lactide-only fragments are marked “O,” glycolide-only fragments are marked “□,” and mixed fragments are marked “◇” (From Ref. [12], reproduced with permission)

In Fig. 6.11, we show the G-SIMS spectrum of cholesterol ( $C_{27}H_{46}O$ ), with mass 386.3549 u. The spectrum is very simple, with a dominant  $[M-OH]^-$  ion that is more similar to traditional electron impact gas-phase mass spectra than the complementary SSIMS spectrum shown in Fig. 6.11b. Similarly, in Fig. 6.11c, the G-SIMS spectrum of caffeine ( $C_8H_{10}N_4O_2$ ) is much simpler than the SSIMS spectrum of Fig. 6.11d. The G-SIMS spectrum consists of molecular peaks  $[M-CH]^+$ ,  $[M+H]^+$ ,  $[M+2H]^+$ ,  $[M+CH]^+$ , and  $[2M+H]^+$ . Figure 6.11e, f show the G-SIMS and SSIMS spectra of the polyamino acid poly-L-lysine. The poly-L-lysine static SIMS spectrum is dominated by high intensities of fragmentation products in the low-mass range. The power of G-SIMS is illustrated by the unambiguous peaks representing the functional group of the amino acid and a dimer fragment at higher mass. The intense double peak in between is a separate bromide compound—the material is supplied as a salt. Samples of bovine serum albumin have also been analyzed [9], showing the correct fragmentation behavior and allowing identification of individual amino acid groups.

The molecular structure of folic acid is shown in Fig. 6.12 together with six possible subunits that could assemble to form the molecule, denoted by  $\alpha$ ,  $\beta$ ,  $\gamma$ ,  $\delta$ ,  $\epsilon$ , and  $\zeta$ . The total molecular weight using the main isotopes is 441.1396 u. Folic acid is composed of C, H, N, and O arranged in the chemically rather different subunits that make a chemical composition assignment from the measured fragment mass difficult, even for time-of-flight systems with typically 10-ppm mass-scale accuracy.

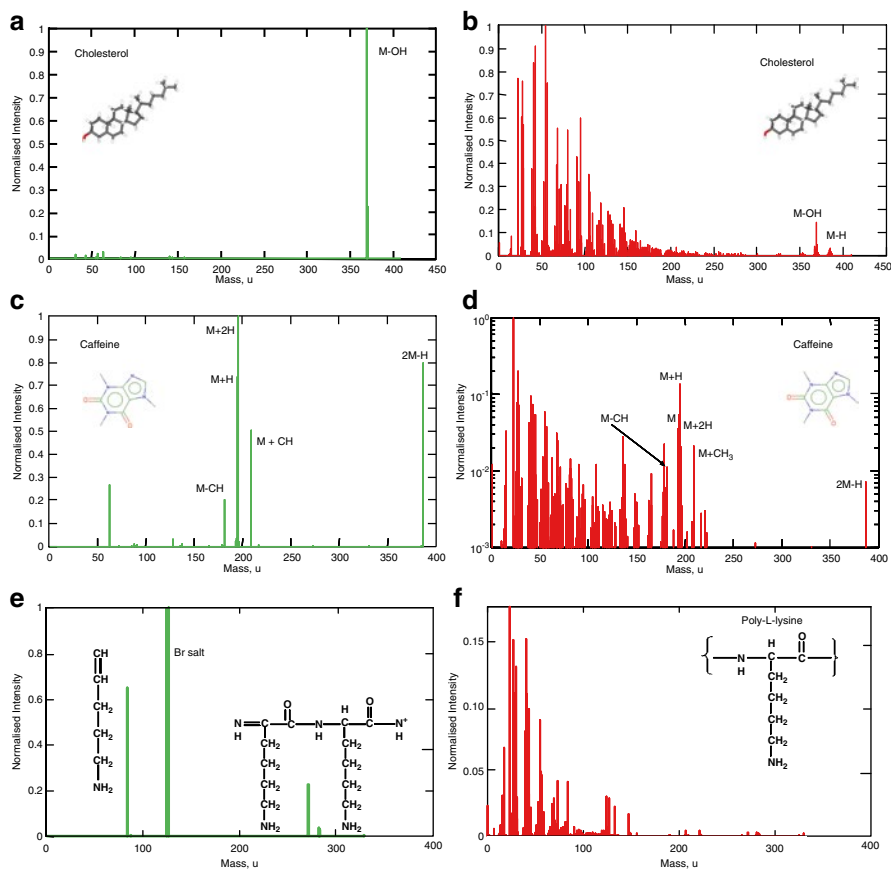


**Fig. 6.11** Positive G-SIMS spectra (*left*) and static SIMS (*right*) for (a) and (b) cholesterol, (c) and (d) caffeine, and (e) and (f) poly-L-lysine using the ratio between 10-keV argon and cesium ions (Here and elsewhere, G-SIMS spectra are often shown in *green* and the complementary static SIMS in *red*.) (After Ref. [8])

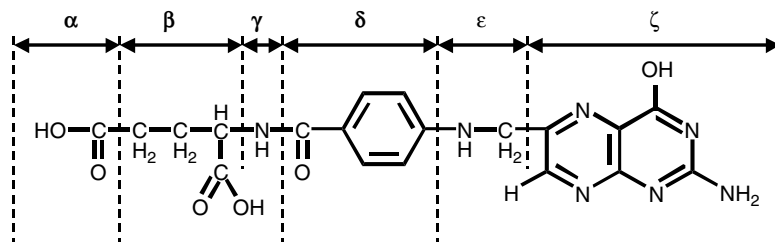


**Fig. 6.12** The molecular structure of folic acid; different subsections have been labeled

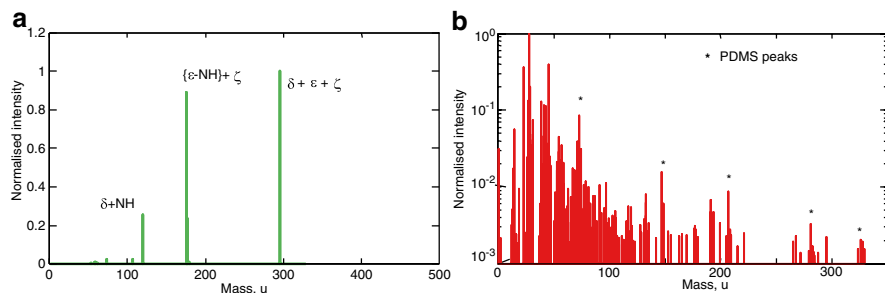


**Fig. 6.13** (a) G-SIMS spectrum for folic acid using the ratio between 10-keV argon and cesium ions and (b) SSIMS spectrum (After Ref. [27]). In (b) peaks marked with an *asterisk* are characteristic of PDMS

Figure 6.13b shows the SSIMS spectrum for 10 keV  $\text{Cs}^+$  primary ions and Fig. 6.13a the G-SIMS spectrum. The SSIMS spectrum is displayed with a logarithmic intensity scale that clearly shows the large population of degraded fragment products. The five distinct molecular fragments shown with an asterisk in Fig. 6.13b, and observed at masses 73.054 u, 147.079 u, 207.043 u, 281.067 u, and 324.996 u, are the well-known fragments from polydimethylsiloxane (PDMS) contamination. The G-SIMS spectrum is much simpler, with four dominant peaks at masses 120.051 u, 176.065 u, 177.077 u, and 295.094 u. It is interesting that the PDMS peaks are no longer dominant in the spectrum. The accuracy of the mass-scale calibration is sufficient to assign the fragment formula  $\text{C}_7\text{H}_6\text{NO}^+$  to the peak at mass 120.051. However, it is not possible to assign a unique fragment formula to the mass peak 295.094. It could be a number of possibilities from the folic acid molecule. For example, it could be subunits  $\alpha + \beta + \gamma + \delta + \epsilon$  and an additional oxygen giving the composition  $\text{C}_{13}\text{H}_{15}\text{N}_2\text{O}_5^+$  with a mass of 295.0930, or alternatively it could be subunits  $\delta + \epsilon + \zeta$  with a chemical composition  $\text{C}_{14}\text{H}_{11}\text{N}_6\text{O}_2^+$  and a mass of 295.0940. A mass-calibration accuracy of better than 4 ppm would be necessary to interpret this difference. What is needed to identify this peak is structural information, and we show how this can be done in the following section.

## 6.4 G-SIMS Fragmentation Pathway Mapping (G-SIMS-FPM)

With a careful calibration of the mass scale [18] and instrument optimization, in tof-SIMS one can achieve a 10-ppm accuracy of the mass scale [18]. Unfortunately, this is insufficient to separate the many chemical permutations accommodated by this level of uncertainty. Traditionally in mass spectrometry, an MS/MS experiment would be performed, fragmenting the molecular ion of interest. This is usually achieved via a low-energy collision with target atoms, typically of an inert gas,

followed by a mass analysis of the fragmentation products. In ion-trap systems, this process may be repeated many times depending on the number of initial ions available and is thus called  $MS^n$ . This is a very powerful method and is routine for molecular identification. Unfortunately, at the present time none of the commercial ToF-SIMS instruments, widely used by industry and academia, has MS/MS capability. This is because of the need for a high repetition rate (100 us) for fast imaging and also the small volumes of material that are available from the surface. For example, in a monolayer, a 200-nm  $\times$  200-nm square pixel with 1 % ionization efficiency, only 10 molecules are available, assuming a transmission of 50 %. New opportunities now exist, with the advent of organic depth profiling using cluster ion beams such as  $C_{60}$ , where the available material for analysis is no longer constrained to the outermost molecules at the surface by the static limit (only around 1 % of surface atoms have a primary ion impact). Consequently, the available molecular signal is much higher (provided the molecule is not just at the surface!). Vickerman and coworkers are exploiting this in a pioneering new instrument incorporating ToF-ToF capability [24] in collaboration with Ionoptika Ltd. [25]. This is a very powerful instrument with a high duty cycle (rapid depth profiling) that gives molecular structure information through MS/MS and a mass-scale calibration that is decoupled from the SIMS emission process. Similarly, Winograd and coworkers have fitted a  $C_{60}$  ion source to a traditional LC-MS/MS quadrupole-ToF mass spectrometer [26]; such mass spectrometers have a very wide user base in the mass spectrometry community. These innovative approaches have a very powerful potential, especially for biological applications.

G-SIMS may also be used to provide molecular structure information. In Fig. 6.4, we illustrated the SIMS emission process with intact fragments emitted from a low surface plasma temperature (outer zone) and more degraded fragments emitted from a high-surface plasma temperature. We may explore the fragmentation behavior between these conditions by changing the parameter  $g$  in the G-SIMS equation, Eq. 6.3. This concept is illustrated with the folic acid molecule in Fig. 6.14. In the G-SIMS regime ( $g=13$ ), the spectrum is dominated by the intact parent molecules; as the plasma temperature is increased (by lowering  $g$ ), the spectrum is populated by more and more fragmentation products until at  $g=0$  or 1 the original static SIMS spectra are obtained with their high populations of fragmentation products. We may therefore map out these fragmentation pathways; the method to do this, G-SIMS fragmentation pathway mapping, is explained in the following, exemplified with folic acid.

We may investigate the effect of varying the surface plasma temperature,  $T_p$ , by changing the G-SIMS index,  $g$ , of Eq. 6.3 from high fragmentation to low fragmentation and mapping out the corresponding variation in G-SIMS intensities. Figure 6.15 shows this for values of  $g$  from 0 to 40. With  $g=0$ , we begin in the SSIMS regime. As  $g$  is increased, we progress to the G-SIMS regime (lower surface plasma temperature). First, we see the substrate and low-molecular-weight fragments decay rapidly. At the same time, the intensities of more intact fragments begin to grow, but even larger intact fragments that grow more strongly soon overtake these. Consequently, the intensities of the smaller degraded fragments begin to decay. This evolves for larger and more intact fragments until eventually the

**Fig. 6.14** Illustration of how the fragmentation pathways may be mapped out in G-SIMS-FPM by varying the surface plasma temperature using the parameter  $g$

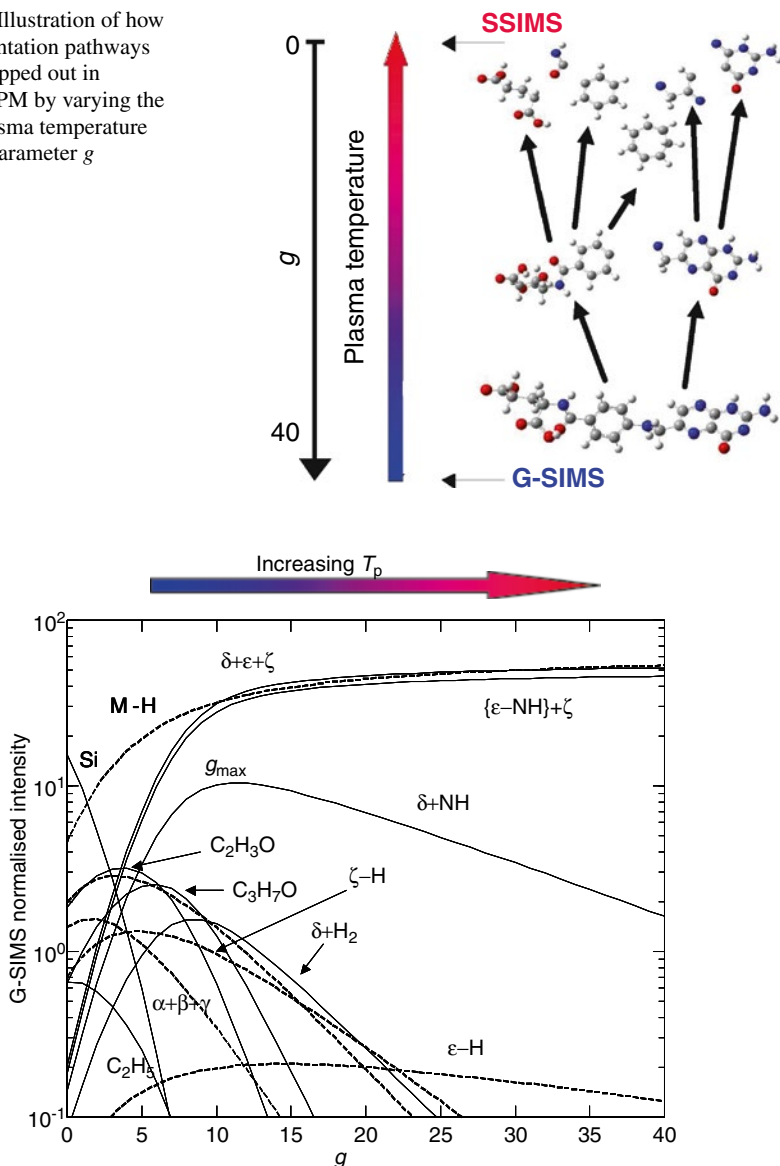
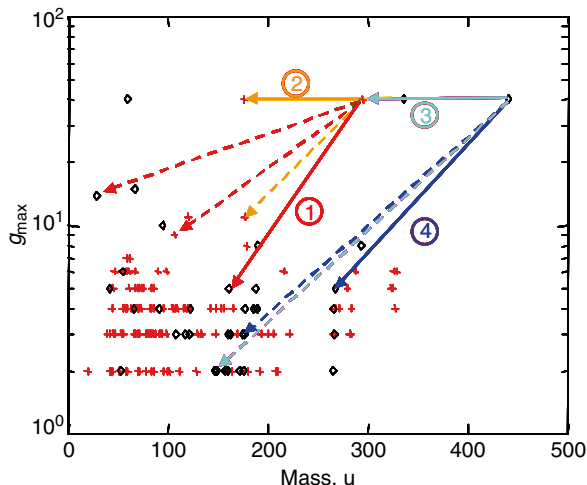


**Fig. 6.15** Effect on G-SIMS intensities using the ratio between 10-keV argon and cesium ions with increasing  $g$  from 0 to 40

dominant parent fragment has the highest G-SIMS intensity. For each fragment, the G-SIMS intensity goes through a maximum at a value  $g_{\max}$  that is characteristic of the plasma temperature [27].

This process is conducted independently for both the positive- and negative-ion data. The  $g_{\max}$  values for each fragment and for both polarities are brought together in a single plot. In Fig. 6.16, we show a plot of the  $g_{\max}$  values for folic acid, with

**Fig. 6.16** Reassembly plot of  $g_{\max}$  for folic acid using the ratio between 10-keV argon and cesium ions. Two assembly pathways with sets of co-daughters are shown as *solid* and *dashed* lines. One further pathway for granddaughters is shown *dashed*. That pathway must also emit a  $\gamma + \text{CH}_3\text{O}$  subunit as either a negative or neutral fragment and is not shown



positive-ion data plotted with a red plus symbol and negative-ion data with a black hollow diamond symbol. We analyze the fragmentation process by first selecting the highest-mass fragment with the highest value of  $g_{\max}$ . This is the parent fragment with a mass  $M_p$ . We next choose a fragment at a lower mass with the next-lowest value of  $g_{\max}$ . This is a trial daughter fragment with mass  $M_D$ . We now postulate that the parent fragmented into the daughter (which exhibits a higher surface plasma temperature, higher  $g_{\max}$ ) with up to two fragmentation products, co-daughters, with masses  $M_{C1}$  and  $M_{C2}$ , respectively. All possible combinations of up to two fragments are computed from those fragments present in the G-SIMS spectrum (Fig. 6.13a). The positive fragment ions in the G-SIMS spectra are likely to be protonated, and so the possibility of one or two additional hydrogen atoms with mass  $nH$  is permitted, such that

$$M_p = M_D + M_{C1} + M_{C2} + nH, \quad (6.5)$$

where  $-2 \leq n \leq 2$ .

The possible co-daughter fragments are then validated by calculating their composition from the peak centroid mass and comparing with chemically possible structures. Typically,  $M_C \ll M_p$ , and the chemical composition may therefore be assigned with higher certainty. Those postulated co-daughter fragments containing Si from the substrate or other elements known to be absent in the molecule such as Na or K may be immediately ruled out. In Fig. 6.16, we map out two of the likely principal fragmentation pathways (i.e., sets of co-daughters) elucidated using the method above. With careful mass measurement [18], we may be able to see that fragmentation pathway 1, in red, leads to three products, which are identified as  $\delta + 2H$ ,  $\epsilon - H$ , and  $\zeta - H$  (with nominal masses 106, 28, and 161 u), so that the parent ion for that pathway is  $\delta + \epsilon + \zeta$  (with mass 295 u), where the symbol order does not necessarily define the order in the molecule. This represents one end of the folic acid molecule and provides



the identity of the daughter for fragmentation pathway 3, in magenta. The co-daughter is identified as  $\alpha + \beta + \gamma$  (with mass 145 u), which then leads to the identification of the entire molecular structure  $\alpha + \beta + \gamma + \delta + \epsilon + \zeta$  (with mass 440 u). Fragmentation pathways 2 and 4, in orange and blue, respectively, support these assignments. The fragment at mass  $295.094 \pm 0.003$  is now clearly shown to be the fragment  $[\delta + \epsilon + \zeta]^+$ ; this demonstrates the importance of a combined approach with positive and negative ions and the ability of G-SIMS-FPM to identify a molecule where the mass alone is insufficient to do this [27]. By following the fragmentation pathways from a large molecular ion to smaller entities, we have identified those entities. The original parent molecular structure is then reassembled in a manner similar to traditional MS/MS experiments. So far, we see how the molecular structure may be reassembled using G-SIMS fragmentation pathway mapping for folic acid. Of course, in this example, the molecular structure of the parent molecule is known a priori. Typically, the molecular structure that must be identified is an unknown, which makes the interpretation of the fragmentation pathways significantly more challenging. In the next section, we describe the development of a system for analysts, to guide them through the reassembly process, providing suggested options.

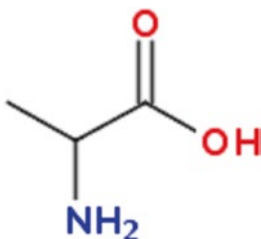
## 6.5 SMILES

In this section, we show how a novel approach based on SMILES (simplified molecular input line entry specification) [6] is used to identify the reassembly process, through evaluation of fragmentation pathways to build up molecular structures. A brief introduction to SMILES is given in Sect. 6.5.1. To assist analysts in the interpretation of the fragmentation pathways, we outline in Sect. 6.5.2 a method to simulate the fragmentation pathways. Examples of simulated pathways and their complementarities to G-SIMS are shown in Sect. 6.5.3, for a wide range of different biological molecules. Section 6.5.4 discusses how these can be used to aid the analyst in producing fragmentation pathways and reassembling molecular structures.

The prediction of mass spectra from structural information, and vice versa, has been a longstanding challenge since the mid-1960s when computers became sufficiently powerful to study small molecules. The DENDRAL project [28], which took place over the period 1965 to 1990, was the first. Gasteiger et al. [29] used a different approach, an automatic algorithm, FRANZ, to predict a mass spectrum from the molecular structure, including details of fragmentation and rearrangements occurring in the spectrometer. An excellent agreement is shown between predicted and experimental spectra for small molecules with around 10 constituents, excluding hydrogen. However, it is clear that these systems are not, as yet, readily applicable to complex molecules, as evidenced by the usage in the community. We show that our simple system based on SMILES, coupled with the under-graded G-SIMS spectra, forms a powerful combination for the identification of complex molecules.

### 6.5.1 Simplified Molecular Input Line Entry Specification (SMILES)

Simplified molecular input line entry specification (SMILES) allows the structure of a molecule to be unambiguously expressed in a logical, computer-readable way using an ASCII text string. SMILES was originally developed by Weininger et al. [30] and more recently developed by Daylight Chemical Information Systems [6]. The SMILES format is a very popular format used in informatics and is integrated into a wide range of software freely available on the Internet to give, for example, molecular structure [31, 32], chemical information, such as  $pK_A$  [33], solubility [33], molecular volume [32], and  $\log P$  values [32], as well as physical parameters such as density [33], refractive index [33], molar mass [34], and mass spectral isotope patterns [34]. The syntax and grammar of SMILES are described in detail elsewhere [6, 30]. In brief, each element is denoted by its chemical symbol, with the first letter given in the upper case. Adjacent atoms in the SMILES string (read from left to right) are considered to have a single bond unless otherwise denoted by an inserted “=” or “#” character representing double and triple bonds, respectively. Hydrogen is implicit. Branches are described using parentheses, and it is possible to nest parentheses for subbranches. Cyclic structures are defined by a number identifying which atoms open and close the ring structure, so that cyclohexane is represented by C1CCCCC1. Aromatic atoms are shown in lower case, so that benzene is represented by c1ccccc1. Ionic bonds may also be described as well as chirality (not used here). Canonical form ensures that the SMILES structure is unique for a given molecular structure. For example, CC(C(=O)O)N represents the following structure (without chirality):



### 6.5.2 Simulated Fragmentation Pathways

A computer program developed at NPL [35] using MATLAB (The MathWorks, Natick, MA, USA) simulates full fragmentation pathways for any molecule given in the SMILES format. This starts with the parent molecule of unlimited complexity and cleaves it at a bond into two parts. This is repeated for each bond in the parent molecule, and the fragment products are listed in the first level of a tree structure, as illustrated in Fig. 6.17. For example, an illustrative molecule ABCD would be fragmented into six substructures, A, BCD, AB, CD, ABC, and D. Clearly, the

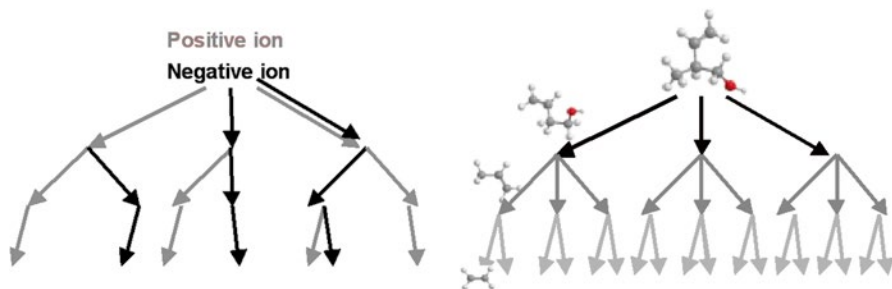
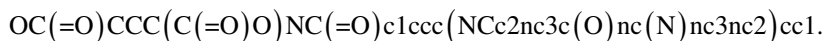


**Fig. 6.17** Illustrative example of the fragmentation pathways mapped out in G-SIMS for positive and negative ions (*left*) and the complementary simulated pathways using the SMILES fragmentation software (*right*)

fragmentation terminates for A and D, but, for example, BCD may be fragmented into four further subunits, B, CD, BC, and D, giving a second level of fragmentation. Similarly, CD and BC may be fragmented to a third level of fragmentation. In this example, the third level of fragmentation is the final level, so that at that stage, the molecule has been fragmented into its constituent elements. At the bottom, in the right-hand example in Fig. 6.17, we would usually finish with fewer possibilities in the final level and possibly, for example, just C, H, and O. It is also easy to see in the above simple example that the subunit BC will be found from both the fragmentation of BCD and of ABC. There is no need to fragment the same structure twice; to save computer time for each fragment, the computer checks in a look-up table to see if a fragment has been analyzed before. If so, a link is stored and the fragmentation is terminated. Later we shall see how this can be extended to include fragments in a larger database for many parent molecules. This method significantly reduces computational time. The computer program uses a structured array with each element, containing details of the fragment, including SMILES text string, exact mass, and links to other parts in the fragmentation pathway with the same fragment. The exact mass is calculated by a separate program that for a given SMILES text string sums the main isotope masses of all the constituent elements as well as the number of implicit hydrogen atoms through the determination of atom valency and bonding. We use these values later to compare with experimental G-SIMS data.

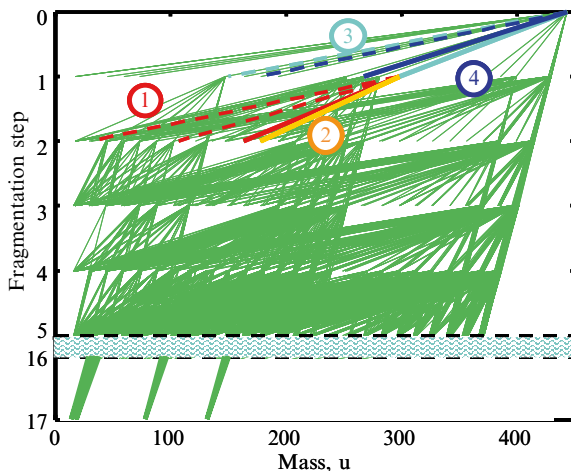
### 6.5.3 Simulated SMILES Fragmentation Pathways for Biologically Relevant Examples

The SMILES text for folic acid is readily available from the web as follows:



This structure is provided as input to the fragmentation pathway simulator software and the fragmentation pathways are calculated. On a Pentium PC with a

**Fig. 6.18** Simulated fragmentation pathways displayed on a plot of fragment mass and fragmentation level for folic acid (From Ref. [35]). For clarity, not all fragmentation levels are shown. The fragmentation pathways identified in Fig. 6.14 are also highlighted for comparison



2.66-GHz processor, this takes approximately 20 minutes. Fragmenting the molecule to the constituent atoms C, N, and O requires 34 levels of fragmentation. However, it is assumed that stable ring structures, such as benzene, are unlikely to fragment, such that folic acid only requires 17 levels of fragmentation. The output of the program contains a structured array, described earlier, containing each fragment structure in SMILES text and the main isotope accurate mass position. For this system to be useful, it must be able to describe, say, at least 75 % of the fragments observed in the key G-SIMS spectrum. For folic acid, simulated fragments account for 90 % of peaks with an intensity of  $>0.02$ . This excellent agreement between experimental G-SIMS data and our simple system for simulating fragments is because the G-SIMS spectrum consists of simple fragments that are undegraded and have not undergone postemission rearrangements [7].

The simulated fragmentation pathways stored in the structural array are essentially organized in a tree structure. However, for analytical purposes, this is not so convenient, as fragments of a similar mass are not necessarily juxtaposed. Instead, in Fig. 6.18, we show the simulated fragmentation pathways for folic acid as a mass-based tree structure with the fragmentation level on the ordinate and the fragment mass on the abscissa. So, in the top right we start with the parent molecule going through successive fragmentations until eventually we end up with the constituent structures (e.g., benzene) and elements C, N, O in the bottom left. This plot is then similar to the G-SIMS reassembly plot shown earlier in Fig. 6.16. Each of the four fragmentation pathways identified earlier may also be found on the simulated fragmentation pathway, and these are highlighted. At the 16th and 17th fragmentation levels, all of the structural information has been lost and is shown here for completeness. At the 17th level are C, N, O,  $C_6H_6$ , and  $C_6N_4H_4$ . In practice, the 10th level of fragmentation is typically required for structurally significant peaks.

The natural lexicon of amino acids in peptides and proteins provides a useful system to study the effectiveness of the simulated pathways [36] further as well as

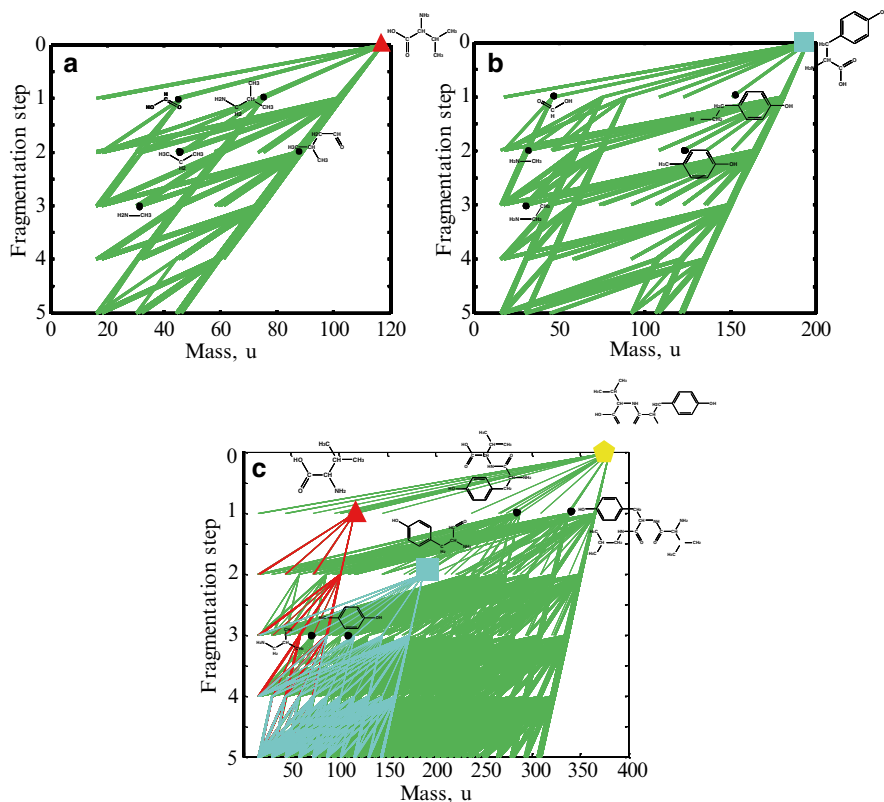


**Fig. 6.19** Simulated fragmentation pathways for (a) valine, (b) tyrosine, and (c) a simple peptide valine–tyrosine–valine (After Ref. [36]). Those fragments with strong intensities in the static SIMS library spectra [13] are marked with a *filled circle*, with the fragment structure shown directly from the SMILES text for that fragment

being of significant practical importance. In addition, the small base set of only 22 amino acids provides a good starting place for the development of a fragment library, which, if successful, will be of significant help in the identification of peptides in static SIMS. Figure 6.19a, b show the simulated SMILES fragmentation pathways for the amino acids valine, OC(=O)C(N)C(C)C, and tyrosine, OC(=O)C(N)Cc1ccc(O)cc1, respectively. For comparison with static SIMS, those fragments exhibiting strong secondary ion intensities are marked on the fragmentation pathways with filled circles. The SMILES fragmentation pathway accounts for all the major peaks identified in the SIMS library spectra [1] for both valine and tyrosine. The simulated pathways also include the characteristic ion fragments identified previously in Ref. [37]. Typically, in the SIMS analysis of proteins, the fragmentation is extensive and significant secondary ion intensities are observed for

individual amino acids rather than pluralities. The identification of pluralities of amino acids, even if weak in the SSIMS spectrum, would add significantly to the ability to identify or characterize proteins. In Fig. 6.19c, we show the simulated fragmentation pathway for a simple, three-amino-acid peptide consisting of valine–tyrosine–valine (VYV). Clearly, there are many fragments containing information about juxtaposed amino acids. Those information-rich peaks, while weak in the static SIMS spectra, are more prominent in G-SIMS spectra [35].

### **6.5.4 Interpretation of G-SIMS Fragmentation Pathways Using Simulated Fragments**

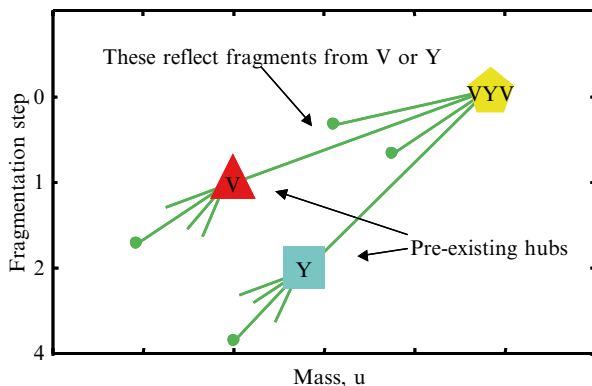
Section 6.4 shows how a molecular structure can be reassembled, by working from small fragments up fragmentation pathways to reach the molecular structure. For the illustrative example of folic acid, this was helped by already knowing the molecular structure. In the previous section, we outlined a method for simulating the fragmentation pathways for molecules without experimental data. By combining the two sections, we can produce a simple system to guide analysts through the reassembly of a molecule to reduce the possible choices for an unknown structure.

An analyst may select any fragment in the G-SIMS fragmentation pathway, and the mass of this fragment will then be automatically compared with a simulated library of fragments containing many types of parent molecules. A suite of possible fragmentation routes may then be identified to build the fragment to one of the larger masses that are contained in the experimental data. This guided process may then be followed until reaching the largest fragment in the experimental data. This may not identify a unique solution but may produce a reduced set of options. This accelerates and improves the reliability of establishing the molecular structure and molecular identity.

A great advantage of a simulated fragmentation library is that it does not rely on the contribution of experimental data from the community, which is always the rate-limiting factor. An additional advantage is the equivalence and reproducibility of data generated from a controlled computer program compared with a wide range of instrument designs and configurations in experimental data. One mechanism to grow the library very rapidly is to provide the SMILES simulation fragmentation pathway software freely on the web, for the community to use on molecules of interest to them. The generated simulated fragmentation pathways can then be added to an open-access central web library, which is freely accessible to all users. This approach is now being developed and will be tested.

In the development of a fragmentation library, it is clear that archetypal molecular entities only need to be fragmented and stored once. These become “hubs” in the library, marked in Fig. 6.19c for valine (V) and tyrosine (Y). In the case of peptides and proteins, previously fragmented amino acids or peptides will form hubs that can be directly referenced to the SMILES fragmentation library, simplifying the

**Fig. 6.20** An illustration of the way a SMILES fragmentation library will build up modules—simplifying the fragmentation maps



fragmentation map. Figure 6.20 illustrates how each new hub becomes an integral component part (i.e., module) of the SMILES fragmentation library. With more components in the library, building the library becomes increasingly easy.

## 6.6 G-SIMS Imaging

A recent innovation by ION-TOF in collaboration with NPL [19] allows G-SIMS to be conducted using the popular  $\text{Bi}^+$  liquid metal ion source. The liquid metal ion source using  $\text{Au}_n^+$  or  $\text{Bi}_n^+$  has rapidly become the standard ion gun on all new instruments, making G-SIMS accessible to a much wider user community. G-SIMS is now facilitated by a special emitter known as the G-tip, which is comprised of Bi and a small amount of Mn. This allows  $\text{Bi}_n^+$  or  $\text{Mn}^+$  primary ions to be selected and focused to the same point. In the G-tip, the two ion beams are automatically aligned, allowing G-SIMS imaging. These two primary ions produce well-separated surface plasma temperatures, as may be expected from Fig. 6.8. Indeed, recent calculations show that it would be very difficult to improve on this choice for generating G-SIMS spectra [38]. An example G-SIMS spectrum using the G-tip is shown in Fig. 6.21a for polycarbonate (PC); it shows the key characteristic  $\text{C}_9\text{H}_{11}\text{O}^+$  peak. Indeed, the G-SIMS effect is so strong that at a  $g$  of 13, this is the only peak in the spectrum! The capability of the G-tip for G-SIMS imaging is shown in Fig. 6.21c, d using a polycarbonate sample patterned with a surface coverage of Irganox 1010. The sample is prepared by thermally evaporating Irganox onto the PC sample masked with a 125- $\mu\text{m}$  mesh TEM grid. Figure 6.21c, d show that the dominant G-SIMS peaks may be found for both regions of interest, and the intensity maps of these key peaks are shown to be strongly characteristic. A line profile of the image [19] shows that the  $\text{Mn}^+$  and  $\text{Bi}^+$  images are correlated to better than the beam size that defines the resolution of the image here, in this case about 5  $\mu\text{m}$ . The ease with which G-SIMS can be conducted, extremely effectively, from a single ion-beam column using the G-tip significantly enhances the prospects for G-SIMS.

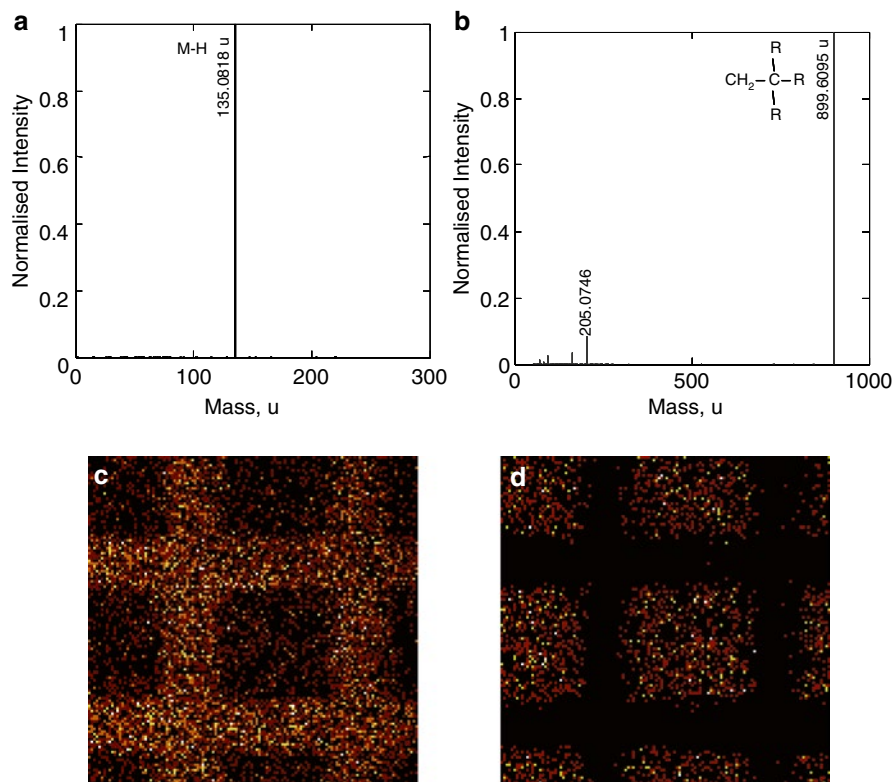


**Fig. 6.21** Positive ion G-SIMS spectra from (a) PC areas and (b) Irganox 1010 areas, of a two-phase material. Secondary ion images of the corresponding G-SIMS peaks are shown (c) for 135.0818 u, (d) for 899.6095 u (After Ref. [19]). The field of view is 250 μm × 250 μm

## 6.7 Cluster Sources

For high-ion yields from organic layers, many analysts use  $\text{Bi}_3^+$  or  $\text{Bi}_5^+$  primary ions. For the study of thicker layers of organic materials, argon cluster primary ions are often used as they lead to much less degradation of the sample. These primary ion beams may be incorporated into the G-SIMS scheme directly, replacing one of the two ion sources traditionally used for G-SIMS. The choice of  $\text{Bi}_3^+$  or  $\text{Bi}_5^+$  with  $\text{Ar}^+$  or  $\text{Mn}^+$  is a practical combination that gives very strong signals. The difference between  $\text{Bi}_3^+$  or  $\text{Bi}_5^+$  with  $\text{Ar}^+$  and a more traditional G-SIMS using  $\text{Bi}^+$  with  $\text{Ar}^+$  is quite strong, and this leads to the effect that smaller  $g$  values are required to achieve the G-SIMS result. In an example for the reference molecule of Irganox 1010 [39] comparing  $\text{Bi}_5^+$  with  $\text{Ar}$  to  $\text{Bi}^+$  with  $\text{Ar}$ , Seah and coworkers found that the effect of  $g$  is about three times stronger. More importantly, the better quality of spectra for the high-mass peaks using  $\text{Bi}_5^+$  compared with  $\text{Bi}^+$  means that the G-SIMS for the higher-mass entities is more reliable. The cluster primary ion sources thus have an important role to play in the G-SIMS for secondary ions with masses above 500 Da.



## 6.8 Future Outlook

The use of G-SIMS is growing, showing success for a widening range of materials. The largest barrier to the uptake of G-SIMS in the SIMS community has been the availability of suitable dual-source ion beams. Recent developments such as the G-tip make G-SIMS available on the most popular ion beam sold on the majority of new instruments. This will rapidly increase the accessibility. Together with easy-to-use analytical tools—such as Easy G-SIMS [23], a simple spreadsheet analysis of data—G-SIMS is becoming more accessible to analysts. Future developments may integrate G-SIMS processing into manufacturers' software.

The development of G-SIMS-FPM with SMILES could provide a powerful approach to identify molecules from the molecular structure that is not restricted by the availability of experimental libraries. The proposed community-developed SMILES simulated fragmentation library will aid rapid library development, as has been demonstrated by many user-developed knowledge resources on the web. A further advantage here is that this would all be done using a validated single algorithm.

The challenges analysts face are increasing in the world of rapidly developing, complex technologies, such as the identification and distribution of molecules at surfaces for organic electronics, displays, sensors, organically functionalized MEM devices, and nanobiotechnology. G-SIMS provides the analyst with a powerful method to simplify spectra of increasingly complex samples and move beyond this to give a more direct interpretation. The newer developments of G-SIMS-FPM and SMILES simulated fragmentation pathways show great promise for enabling analysts to obtain structural information of unknown biologically relevant materials quickly and simply.

Chapters in this book have shown the power of SIMS for the analysis of biological surfaces. G-SIMS adds to this for the identification of complex molecules and interpretation of data through access to information in the mass spectrum that would otherwise remain latent.

## References

1. Vickerman JC, Briggs D, Henderson A, editors. The Static SIMS library, version 4. Manchester: SurfaceSpectra. <http://www.surfacespectra.com/simslibrary>
2. Schwede BC, Heller T, Rading D, Niehius E, Wiedmann L, Benninghoven A. The Münster High Mass Resolution Static SIMS library. Münster: ION-TOF; 2003.
3. Briggs D, Brown A, Vickerman JC. Handbook of static secondary ion mass spectrometry (SIMS). Chichester: Wiley; 1989.
4. Lee JLS, Gilmore IS. The application of multivariate data analysis techniques in surface analysis. In: Vickerman JC, Gilmore IS, editors. Surface analysis – the principal techniques. 2nd ed. Wiley, Chichester: UK; 2008.
5. Weng LT, Bertrand P, Laver W, Zimmer R, Bussetti S. Quantitative surface analysis of styrene-butadiene copolymers using time-of-flight secondary ion mass spectrometry. *Surf Inter Anal.* 1995;23:879–886.

6. SMILES, Daylight Chemical Information Systems. <http://www.daylight.com/smiles/>
7. Gilmore IS, Seah MP. Static SIMS: Towards Unfragmented Mass Spectra - The G-SIMS Procedure. *Appl Surf Sci.* 2000;161:465–480.
8. Gilmore IS, Seah MP. G-SIMS of Crystallisable Organics. *Appl Surf Sci.* 2003;203–204: 551–555.
9. Gilmore IS, Seah MP. Organic Molecule Characterisation – G-SIMS. *Appl Surf Sci.* 2004; 231–232:224–229.
10. Ogaki R, Green FM, Lic S, Vert M, Alexander MR, Gilmore IS, Davies MC. A comparison of the static SIMS and G-SIMS spectra of biodegradable homo-polyesters. *Surf Inter Anal.* 2008; 40:1202–1208.
11. Ogaki R, Green FM, Li S, Vert M, Alexander MR, Gilmore IS, Davies MC. G-SIMS of Biodegradable Homo-Polyesters. *Appl Surf Sci.* 2006;252(19):6797–7800.
12. Ogaki R, Green FM, Gilmore IS, Shard AG, Luk S, Alexander MR, Davies MC. Study of the end-group contribution to ToF-SIMS and G-SIMS spectra of poly(lactic acid) using deuterium labelling. *Surf Inter Anal.* 2007;39(11):852–859.
13. Hawtin PN, Abel M-L, Watts JF, Powell J. G-SIMS of Thermosetting Polymers. *Appl Surf Sci.* 2006;252:6676–6678.
14. Gilmore IS, Seah MP, Green FM. Static TOF-SIMS – a VAMAS Interlaboratory Study. Part I. Repeatability and Reproducibility of Spectra. *Surf Inter Anal.* 2006;37:651–672.
15. ISO 23830, Surface chemical analysis—Secondary ion mass spectrometry—Repeatability and constancy of the relative intensity scale in static secondary ion mass spectrometry, ISO Geneva.
16. Repeatability and constancy spreadsheet. National Physical Laboratory, UK. [http://resource.npl.co.uk/docs/science\\_technology/nanotechnology/ssims/repeatabilityandconstancyspreadsheet.xls](http://resource.npl.co.uk/docs/science_technology/nanotechnology/ssims/repeatabilityandconstancyspreadsheet.xls)
17. Gilmore IS, Seah MP, Green FM. Static TOF-SIMS – a VAMAS Interlaboratory Study: part II – Accuracy of the Mass Scale and G-SIMS Compatibility. *Surf Inter Anal.* 2007;39(10):817–825.
18. Green FM, Gilmore IS, Seah MP. TOF-SIMS: Accurate Mass Scale Calibration. *J Am Soc Mass Spectrom.* 2006;17:514–523.
19. Green F, Kollmer F, Niehuis E, Gilmore I. Imaging G-SIMS: A Novel Bismuth-Manganese Source Emitter. *Rapid Commun Mass Spectrom.* 2008;22:2602–2608.
20. Gilmore IS, Seah MP. Static SIMS: A Study of Damage using Polymers. *Surf Inter Anal.* 1996;24(11):746–762.
21. Gilmore IS, Seah MP. Electron Flood Gun Damage in the Analysis of Polymers and Organics in Time of Flight SIMS. *Appl Surf Sci.* 2002;187:89–100.
22. Shard AG, Gilmore IS. Analysis of metastable ions in the ToF-SIMS spectra of polymers. *Int J Mass Spectrom.* 2008;269(1):85–94.
23. Easy G-SIMS. National Physical Laboratory, UK. <http://www.npl.co.uk/server.php?show=ConWebDoc.610>
24. Fletcher JS, Henderson A, Biddulph GX, Vaidyanathan S, Lockyer NP, Vickerman JC. Uncovering new challenges in bio-analysis with ToF-SIMS. *Appl Surf Sci.* 2008;252:1264–70.
25. Hill R, Blenkinsopp PWM, Barber AM. Ionoptika Ltd. [www.ionoptika.com](http://www.ionoptika.com)
26. Carado A, Kozole J, Passarelli M, Winograd N, Loboda A, Bunch J, Wingate J, Hawkin J, Murphy J. Biological Tissue Imaging with a Hybrid Cluster SIMS Quadrupole Time-of-Flight Mass Spectrometer. *Appl Surf Sci.* 2008;255:1572–15755.
27. Gilmore IS, Seah MP, Green FM. G-SIMS-FPM: Molecular Structure at Surfaces – A Combined Positive and Negative Secondary Ion Study. *Appl Surf Sci.* 2006;252(19):6601–6604.
28. Lindsay RK, Buchanan BG, Feigenbaum EA, Lederberg J. Applications of artificial intelligence for organic chemistry: the Dendral project. New York: McGraw-Hill; 1980.
29. Gasteiger J, Hanebeck W, Schulz K-P. Prediction of mass spectra from structural information. *J Chem Inf Comput Sci.* 1992;32:264–271.
30. Weininger D. SMILES, a Chemical Language and Information system. 1. Introduction to Methodology and Encoding Rules. *J Chem Inf Comput Sci.* 1988;28:31–36.
31. SMILES, Daylight Chemical Information Systems, Depict. [http://www.daylight.com/daycgi\\_tutorials/depict.cgi](http://www.daylight.com/daycgi_tutorials/depict.cgi)

32. Molinspiration. <http://www.molinspiration.com/cgi-bin/properties>
33. Karickhoff SW, Carreira LA, Hilal SH. SPARC on-line calculator. <http://ibmlc2.chem.uga.edu/sparc/>
34. Molar mass and mass spectral isotope pattern. <http://www.colby.edu/chemistry/NMR/scripts/smileMM.html>
35. Gilmore IS, Seah MP, Green FM. Identification of Complex Molecules at Surfaces: G-SIMS and SMILES Fragmentation Pathways. *Int J Mass Spectrom.* 2008;272:38–47.
36. Gilmore IS, Seah MP, Green FM. G-SIMS and SMILES: Simulated Fragmentation Pathways for Identification of Complex Molecules, Amino Acids and Peptides. *Appl Surf Sci.* 2008;252:852–855.
37. Wagner MS, Castner DG. Characterization of Adsorbed Protein Films by Time-of-Flight Secondary Ion Mass Spectrometry with Principal Component Analysis. *Langmuir.* 2001;17:4649–4660.
38. Seah MP, Gilmore IS, Green FM. G-SIMS: Relative Effectiveness of Different Monatomic Primary Ion Source Combinations. *Rapid Commun Mass Spectrom.* 2009;23:599–602.
39. Seah MP, Green FM, Gilmore IS. Cluster Primary Ion Sputtering: Secondary Ion Intensities in Static SIMS of Organic Materials, *J Phys Chem C.* 2010;114:5351–5359.

# Chapter 7

## Imaging with the Helium Ion Microscope

John Notte and Bernhard Goetze

**Abstract** A newly developed technology, the helium ion microscope (HIM), provides high-resolution imaging with several benefits compared to the standard scanning electron microscope (SEM). First, the images provide high resolution because the helium beam can be brought to a focused probe size that can be as small as 0.25 nm. Second, the images provide contrast mechanisms that are often markedly different from the SEM. These contrast mechanisms can reveal topographic, composition, and other types of information about the sample. Third, compared to the SEM, the HIM images tend to be more surface-specific – revealing information about the surface without the confusing subsurface information. Fourth, the HIM can obtain high-resolution images even of insulating samples that would otherwise charge excessively in the SEM. The HIM is still in its infancy compared to the SEM, having only been commercially available for 7 years; however, it has already provided several unique advantages for the imaging of biological materials.

### 7.1 Introduction: On the Importance of Surfaces

In many imaging and analysis applications, surface specificity is crucial to produce an easily interpreted image or data set. In fact, the nature of the human retina (essentially a 2D sensor) limits our eyes to gathering 2D information. Also, for uncounted years, our brains have been optimized for interpreting this 2D information as surface-specific information. The mixing of deeper information with the surface information tends to make the images harder to understand or downright deceptive (think smoke and fog). In a mathematical sense, the determination of 3D information from a 2D data set is a noninvertible problem. In other words, a single image does not

---

J. Notte (✉) • B. Goetze  
Director of Research and Development, Carl Zeiss Microscopy,  
Peabody, MA, USA  
e-mail: john.notte@zeiss.com

provide enough information to unambiguously reveal both surface information and the deeper information. Hence, an imaging technique that provides surface-specific information offers a less ambiguous interpretation.

In many applications, surface specificity is of primary importance because the interface itself is the subject of the investigation. To a large extent, this is because the interfaces define the boundary between objects, and it is through these interfaces that objects can interact. Challenging applications of this nature occur in biology (e.g., cell membranes), semiconductor physics (e.g., doped silicon junctions), and material science (e.g., catalysis and corrosion). In most of these applications, the surfaces are critical because the most interesting chemical processes are limited to interfaces between different domains.

Many of the well-established high-resolution imaging techniques provide an ambiguous image that mixes the surface information with the deeper information. The well-established techniques of transmission electron microscope (TEM) and scanning transmission electron microscope (STEM) provide excellent resolution only after preparation of a ~100 nm thick lamella through which the beam passes. The lamella preparation can be time-consuming and there is a risk of damaging the specimen in the process. Because the beam passes through the lamella, the contrast in the image represents an average along the beam path through the sample rather than the true surface information. In addition, while the atomic force microscope (AFM) provides high-resolution surface analysis, it is limited to the subset of samples that can be directly contacted and have a very limited topography – a very small subset of biological specimens. The most routinely used high-resolution imaging instrument for biological samples is the scanning electron microscope (SEM). The images it provides are high-resolution and do provide a good image contrast that reveals different properties of the specimen. However, the SEM is known to produce much of its signal from the reemergence of backscatter electrons, which reveal “SE2” information about deeper layers – a topic of discussion in later sections here. This effect can be mitigated by operating the electron beam at lower energies, but this tends to limit the lateral resolution by chromatic aberration effects. The operation of the SEM also induces charging on and under the surface of the sample – effects that can compromise the image quality and can even damage the specimen. Metal coatings are sometimes used to improve the charging and surface specificity of the SEM, but the coatings often obscure the fine-scale features of interest and even also damage the sample. Operating the SEM in the presence of gases (such as water or nitrogen) can help to mitigate the surface-charging effects, but subsurface charging is not resolved, and the gases tend to limit the resolution.

In contrast, the newly developed technology of the helium ion microscope (HIM) produces high-resolution images with *inherent* surface specificity. The surface-specific nature of the images is a direct consequence of the physics of the helium ion as it interacts with the specimen. The charging effects are also fundamentally different from the SEM and are much more readily mitigated. Figure 7.1 is an HIM image of the iron oxidizing Acidovorax Proteobacteria (strain BoFeN1). This sample was originally isolated from the anoxic freshwater sediments of Lake Constance in Germany and was provided by Martin Obst and Fabian Zeitvogel, University of

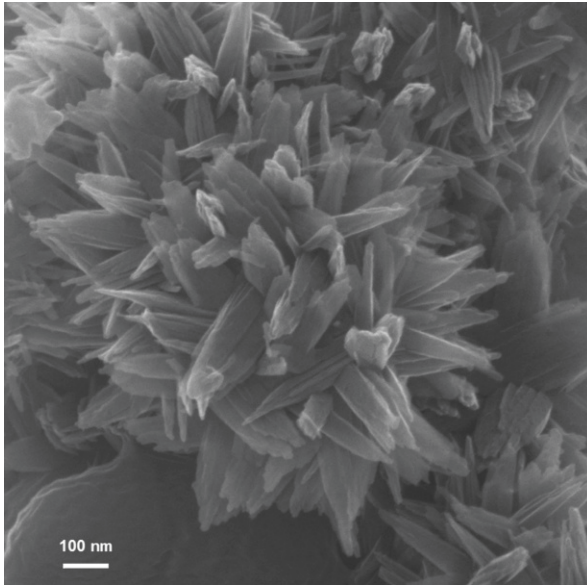


**Fig. 7.1** A high-magnification helium ion microscope image of *Acidovorax* (Sample provided by Martin Obst and Fabian Zeitvogel of the University of Tuebingen)

Tuebingen, Germany. When grown in the presence of Fe(II), some cells tend to form a crust of Fe(III) mineral needles. Imaging with an HIM reveals the structure of those mineral crusts on the cell surface for the first time. Imaging in the SEM requires platinum coatings, which incidentally adulterate the real structure and introduce artifacts [1].

In this chapter, the basic technology of the HIM is first explained. Subsequently, the unique interaction of the beam with the sample is described in detail for a range of beam energies and samples. Specifically addressed are the image formation process and the properties of the sample, which are revealed in the resulting image. The unique charging advantages and the minimal sample preparation requirements are then described in detail. Lastly, the future outlook of this technology is provided.

## 7.2 Technology of the Helium Ion Microscope

### 7.2.1 Overview

Much of the technology discussed here is contained within the Zeiss family of helium ion microscopes: the ORION Plus™ and the ORION NanoFab™. These models have only recently become commercially available [2] after many years of

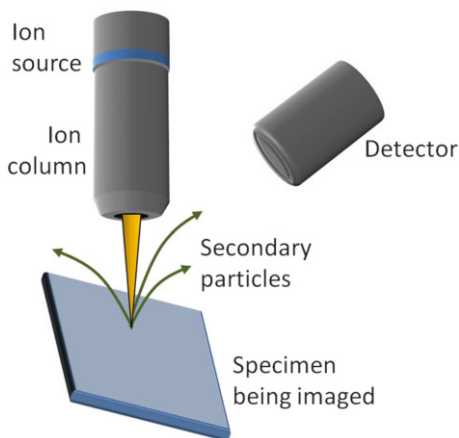


**Fig. 7.2** Diagram of the helium ion microscope showing the ion source, the ion column, the sample, the detectable particles, and the detector

development [3]. A simplified diagram of the HIM is shown in Fig. 7.2. The helium ion source produces an ion beam with a typical energy of 30 keV and an ion beam current of about 100 pA. The beam enters the ion column, which includes steering deflectors, apertures, stigmators, scanning deflectors, and focusing elements. As the beam exits the column, it is focused to a very small probe size on the surface of the specimen. Typically, this probe size is 0.5 nm although measurements as small as 0.21 nm have been attained. The specimen can be virtually any shape or size, and a mechanical stage allows the sample to be reoriented to provide alternative perspectives. The entire beam path and specimen are maintained under a vacuum of better than  $2 \times 10^{-7}$  Torr.

As the focused beam strikes the sample at a particular location, it produces a number of particles that can subsequently be detected. The properties of the generated particles (their abundance, energy, angle, etc.) reveal some property about that particular location. The beam is then advanced to a new location (perhaps just 1 nm away), and the emitted particles are again detected. The variation in the quantity or properties of the generated particles provides the contrast from location to location on the sample. The focused helium beam is advanced in a raster pattern across a rectangular region of the sample (as shown in Fig. 7.2). The image is then assembled on a pixel-by-pixel basis as the beam is advanced. The gray level of each pixel is based upon a chosen property of these generated particles. For example, the pixel may be assigned black if there are no secondary electrons produced, or white if 10 or more secondary electrons are produced at that location. The typical time to acquire such an image can vary from 5 s to 5 min, depending on the signal-to-noise ratio required and the number of pixels in the final image (Fig. 7.3).

In some respects, the HIM operates much like the traditional SEM or gallium focused ion beam (FIB). In these regards, there are excellent textbooks that detail

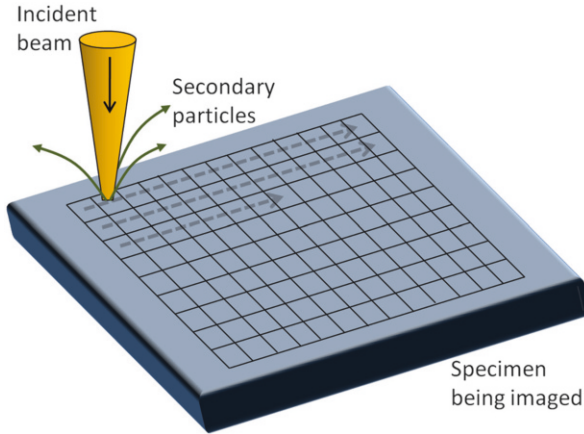


**Fig. 7.3** The focused helium beam is moved from location to location in a raster pattern across the sample. Each of the locations on the sample corresponds to a pixel in the final image. Each pixel is assigned a gray level based upon the generated particles at the corresponding position

the basic physics that is common to their operation [4]. However, in many important ways the technology of the HIM is distinctly different. Only the most significant of these differences are therefore detailed in the following sections.

### 7.2.2 *The Helium Ion Source*

The helium ion source [5] is the key enabling technology for the HIM. A fuller description of the technology can be found in the established literature [6], but a cursory description is provided here. The ion source consists of a needle that is drawn to an atomically sharp end form (Fig. 7.4). The ion source operates at a temperature of about 70 K, in an ultrahigh-vacuum (UHV) vessel, with a large positive voltage applied to it. The apex of this tip has an underlying spherical shape (radius  $\sim 1,000 \text{ \AA}$ ). Superimposed on this spherical shape is a three-sided pyramid terminating in an atomically sharp vertex. At this vertex, the single most protruding atom experiences an electric field, which can be as large as  $4 \text{ V/\AA}$ . In this otherwise UHV region, ultrapure helium gas is admitted (impurity concentrations are typically 1 part in  $10^6$ ). Although neutral, the helium atoms become polarized and are drawn in toward the tip in the presence of the field gradient. This effect creates a region of elevated pressure surrounding the apex. The helium atoms are cooled by the process of repeated collisions with the cryogenic tip and eventually come to thermal equilibrium with the tip. As the low-energy helium gas atoms pass in the vicinity of the most protruding atom, the large electric field can cause a single electron to quantum mechanically tunnel [7] out of the helium atom and into the emitter tip. The remaining positive helium ion is now repelled by the positively biased tip and is



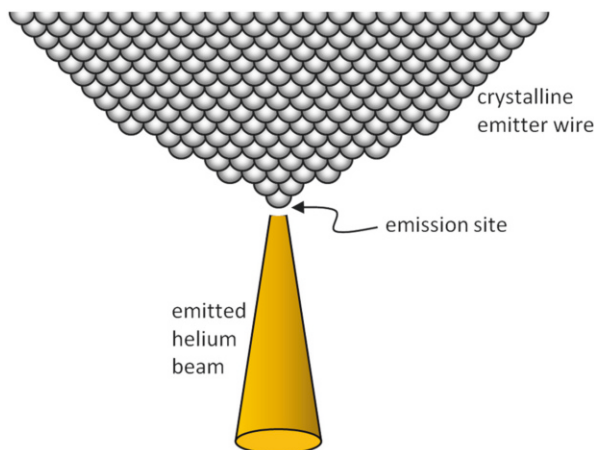


**Fig. 7.4** The helium ion source produces helium ions originating from an atomically sharp asperity at the end of a positively biased needle maintained at cryogenic temperatures

immediately accelerated away. The field ionization process, which is key to this new microscope, was discovered over 50 years ago in the context of the field ion microscope (FIM) [8, 9].

Several unique properties of this ion source make it so desirable for high-resolution microscopy. First, the generated ions are produced from a region of atomic dimensions, and the virtual source size (established from back-tracking the ion's final trajectories) is less than  $1 \text{ \AA}$  in size. Second, the beam diverges very gradually, with a typical emission cone semiangle less than  $1^\circ$ . Together, these two properties are reflected in the very high “brightness” of the ion source – routinely measured to be  $4 \times 10^9 \text{ A cm}^{-2} \text{ sr}^{-1}$  for a 25 keV beam [10]. Another important attribute is the monochromatic character of the ions. The energy spread,  $\Delta E$ , of the beam is found to be about 1 eV or less, representing less than 1 part in  $10^4$  of the beam energy [11]. The low-energy spread is important to minimize the energy-dispersive effects as the beam is shaped and steered with electrostatic lenses and deflectors.

The usage of helium ions – as opposed to lighter- or heavier-charged particles – is ideal for imaging applications and offers advantages over the competing technologies of electron and gallium ion beams. The mass of an electron is so small that its wavelike properties begin to manifest themselves as the electron beam is focused. In fact, a highly optimized SEM will have its probe size significantly limited by diffraction [12]. For the helium ion beam, the de Broglie wavelength can be as small as 100 fm – not significantly affecting the focused probe size. Compared to gallium, helium is light enough that it does not cause excessive damage to the sample. In contrast, the massive gallium atom (atomic weight  $\sim 69 \text{ amu}$ ) is very effective [13] in sputtering away any specimen in which it strikes. Helium is also optically transparent, is chemically inert, and can diffuse out of biological specimens in relatively short times. For these reasons, helium is a convenient ion species for a charged

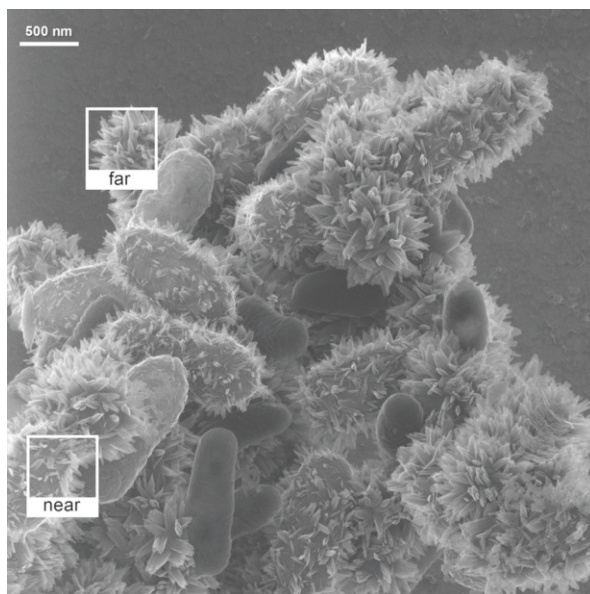


**Fig. 7.5** A larger field of view of the same specimen shown in Fig. 7.1. This image shows that the sharpness is uniform throughout the image for both near (*lower boxed region*) and far features (*upper boxed region*). These are separated by an estimated 2  $\mu\text{m}$  in depth

particle microscope. It will be mentioned in later sections that the same technology can be made to work with the heavier noble gas, neon. Such a neon beam offers a different type of sample interaction that can induce deliberate erosion of the specimen in a controlled manner with nanometer-level precision.

### 7.2.3 Probe Formation

After the ions are emitted from the ion source, they are accelerated into the optical column, which manipulates the beam to achieve the smallest attainable probe size on the sample. The beam is extracted from the ion source and emerges with an energy that varies from 15 to 45 keV. An electrostatic condenser lens is used to limit the rate of divergence of the helium beam. The column includes static deflectors for aiming the beam down the column and dynamic deflectors for scanning the beam in a raster pattern across the sample. An aperture is used to select only the central portion of the beam before it enters the final lens. Finally, the beam is focused with an electrostatic lens to achieve the smallest probe size at the surface of the sample.

As the beam is approaching the sample, it is roughly conical in its shape, with a convergence semiangle of less than 1 mrad. The small convergence angle also provides for a relatively long depth of field, making it easy to visualize samples with high aspect ratios (Fig. 7.5). The size of the imaged area (field of view) can span

from 100 nm to 1 mm, with as many as  $2048 \times 2048$  pixels per image. The sample can be mounted to a standard stub or glass slide and be positioned anywhere from 4 to 40 mm below the final lens. Under optimal conditions, the helium ion beam can be focused to a probe size as small as 0.25 nm. Such images can resolve details otherwise not seen with an SEM or FIB. The sample can also be biased positively or negatively to enhance or diminish specific contrast mechanisms.

### 7.3 Beam–Specimen Interaction

As in an SEM or gallium FIB, the image generation in the HIM depends critically on how the particles comprising the focused beam interact with the specimen. Because the helium beam interaction is distinctly different compared to an SEM or a gallium FIB, the image contrast is distinctly different. The physics of the helium beam interaction is not fully understood, but several researchers [14–16] have begun unfolding the phenomena that underlie the images. These efforts will ultimately explain the mechanisms by which the HIM produces its high-contrast, high-resolution images. But even without our having a complete theoretical understanding of the contrast mechanisms, the HIM is establishing itself through the unique images it produces.

A basic understanding of beam–specimen interaction is best approached by considering the behaviors of individual helium ions incident upon the specimen. The fate of a single helium ion impinging upon a specimen can be understood from fundamental physics – primarily electrostatics and atomic-level scattering physics. In almost all circumstances, the incident particles do arrive one at a time, and their collision cascades are completed before the next particle arrives. The behavior of individual ions can then be combined by statistical methods to provide the average behavior of the helium ion beam. Such methodologies are commonly undertaken with Monte Carlo computer simulations. The remainder of this section relies heavily upon the IoniSE [16], TRIM [17], and Casino [18] computer programs to simulate the charged particles within the specimen.

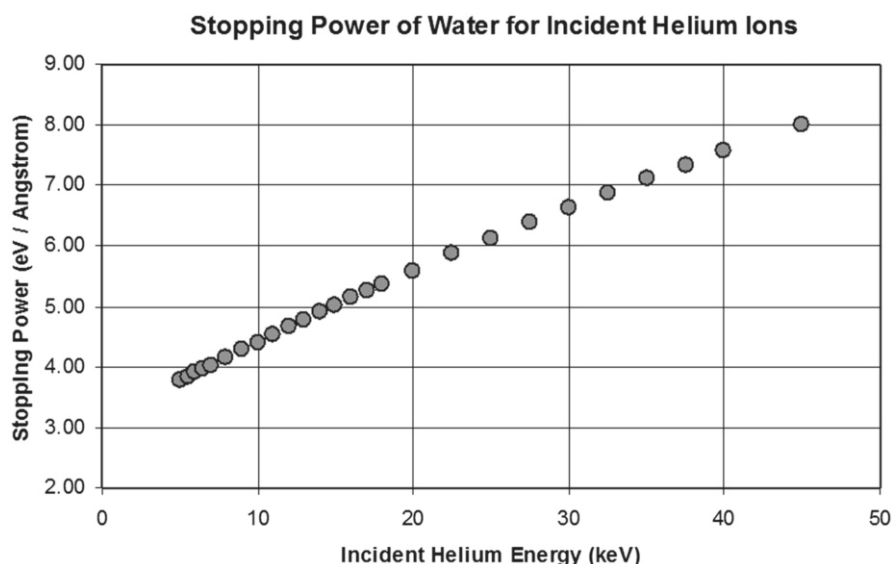
#### 7.3.1 Beam Penetration

A single helium ion interacts with the sample through a series of electrostatic interactions between the ion and the target nuclei and electrons that comprise the specimen. Most of these interactions produce small angular deflections whereby the trajectory of the helium ion is only slightly altered. These interactions tend to reduce the energy of the incident ion with a statistically averaged “stopping power” measured in energy loss per traveled path length ( $\text{eV}/\text{\AA}$ ). The stopping power determines how the particle is slowed down and eventually comes to a stop, and correspondingly how its energy is transferred to the specimen. The exact value of

**Table 7.1** The stopping power for 25 keV helium ions into select materials

Specimen	Stopping power for 25-keV incident helium (eV/Å)
Water	6.1
Adipose tissue <sup>a</sup>	7.3
Cortical bone	9.7
Zinc	13.0
Osmium	14.8
Gold	16.0

<sup>a</sup>Berger MJ. Stopping powers and ranges for protons and alpha particles, International Commission on Radiation Units – Report ICRU-49. Bethesda, MD, USA: ICRU; 1993

**Fig. 7.6** The stopping power tends to decrease with decreasing energy

the stopping power depends on the composition of the specimen and the energy of the helium ion. The stopping power for 25 keV helium ions into select materials is shown in Table 7.1.

The stopping power tends to decrease with decreasing energy, as shown in Fig. 7.6. This energy is transferred from the helium ion to the electrons and nuclei of the specimen by several mechanisms. The relative importance of the different mechanisms may vary with beam energy and with the composition of the specimen, but the following estimates are valid for 25 keV helium into silicon: About 80 % of the energy transfer is to electrons – including ionization of the atoms in the specimen. These excited electrons are responsible for the production of secondary electrons – which will be discussed in the next section. The remaining 20 % of the energy is transferred to the nuclei of the sample, resulting in lattice vibrations (phonons), recoiled target atoms, and occasional backscattering events. As the

incident ion loses energy, the energy transfer to the nuclei tends to dominate over the energy transfer to the electrons. Ultimately, the stopping power is responsible for determining the average penetration depth of the helium beam.

As the helium ions penetrate into the surface of the specimen, there is a high probability that the helium ion will capture an electron within a few nanometers of the surface. Consider that helium is the most “electron-greedy” of all the residents of the periodic table. The helium ion will spend most of the rest of its trajectory (perhaps hundreds of nanometers) as a neutral helium atom. By this process of electron capture, the incident helium produces a very thin layer of positive surface charge over the top few nanometers of the surface. This is distinctly different from electrons, which are destined to keep their charge with them wherever they go – producing a deeper and widely distributed negative charging artifact. This simple difference is a distinct advantage for the HIM over the SEM and will be discussed in greater detail in a later section.

The helium ion’s predominant interaction with electrons tends to produce a relatively small angular deflection of the incident ion, a consequence of the disparity in the masses:  $M_{\text{He}}/m_e \cong 7,300$ . But there is a nonzero probability that the helium ion’s trajectory will put it in line with the nucleus of a target atom. In this case, there is a strong electrostatic repulsion between the helium nucleus and the nucleus of the target atom. To some extent, these nuclei will be partly shielded by the remaining electrons. This resulting deflection is commonly known as Rutherford scattering [19]. In some cases, the helium atom is scattered backward out of the sample. These helium atoms are termed “backscattered,” and their detection for the purposes of imaging is a subject addressed in the next sections. The probability of backscattering is typically 0.1 to 1 %, but this number increases for higher-atomic-number targets or for lower-incident-energy helium ions.

Due to the random nature of the collisions, the trajectories of the individual helium ions in the specimen vary considerably. Using the simulation software to simulate many thousands of ion trajectories reveals the general depth and shape of the interaction. From these simulations, it is also possible to determine the statistically averaged results, such as the average penetration depth and the average sub-surface dispersion of the beam. The leftmost portion of Fig. 7.7 shows the general shape of the interaction volume for a 30 keV helium beam incident on a silicon specimen. The statistical nature of the scattering is evident in the varied trajectories (100 are shown here). Below the surface, the ions diverge in the shape of a well-defined cone (the typical cone angle is less than 5°) before broadening into a more spherical volume (not shown). The overall “teardrop” shape is common for many target materials and medium- to high-helium beam energies. In this particular case, the average incident helium beam penetrates to a depth of 350 nm. The shape of the interaction volume and the width near the surface are of critical importance for high-resolution-image formation – the topic of the next section. For comparison, the penetration of a 30 keV gallium beam is shown in the center of Fig. 7.7. For the more massive gallium beam, the nuclear scattering dominates, and the beam penetrates less deeply and broadens rapidly as it produces many displacements (shown as green dots) to the sample atoms. Surface sputtering is also quite significant for

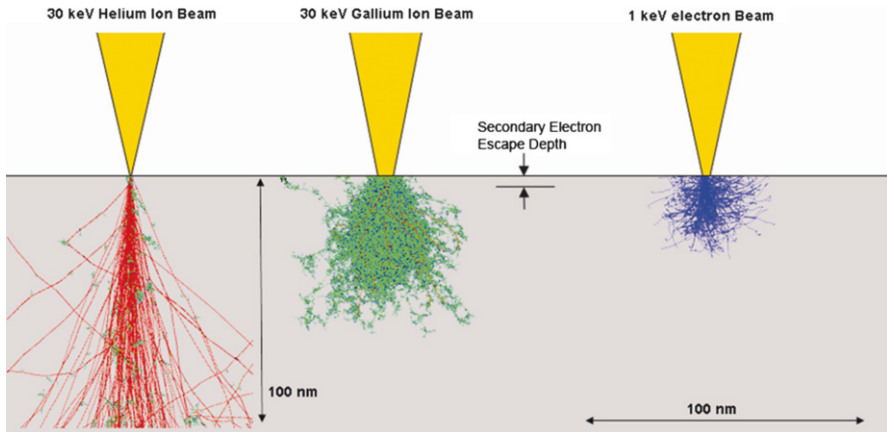


**Fig. 7.7** Monte Carlo modeling results for representative beams into silicon. The *red* shows the trajectories of the incident particles (100 are shown for each case). The *green dots* indicate atoms of the specimen that have been displaced

such heavy ion beam species, causing the sample to be eroded as it is imaged. On the right of Fig. 7.7, a low-energy electron beam is shown for comparison. The electron beam interacts predominantly with the abundant electrons in the sample, and owing to their equal mass, they can scatter through large angles. Consequently, the beam disperses under the surface, and the interaction volume can be quite wide at the surface.

### 7.3.2 *Generated Particles and Suitable Detectors*

As the helium ion beam penetrates into the specimen, there are several particles that may be ejected from the specimen. The properties of these particles (including their abundance, charge, emission angle, or energy) can reveal information about the specimen that can vary from point to point (e.g., local topography or local composition). The detection of these particles, and their assumed variation from one location to another, form the basis for the contrast in the image. In the following section, the commonly encountered detected particles are discussed in detail.

#### 7.3.2.1 *Secondary Electrons*

A secondary electron (SE) is any electron ejected from the surface with a kinetic energy below 50 eV. As with the SEM and gallium FIB, the SEs are the most commonly used detectable particle for image formation in the HIM. This is in part because of the relative abundance of SEs produced, and in part because of the

relative ease with which the SEs can be detected. Images that are based upon SE detection also reveal high-resolution and topographic information. The HIM has an advantage in producing many more SEs per incident particle (2 to 5) compared to the SEM, where the SE yield is typically less than 1.

As the helium ion enters the specimen, electrons are excited all along the ion's trajectory, but they can travel only a short distance (typically <3 nm) before their energy is dissipated. So it is only those electrons excited sufficiently close to the surface that may escape and be detected. Refer back to Fig. 7.7: The HIM has a unique advantage over the SEM or Gallium FIB in that the excited volume is quite narrow within the top few nanometers of the surface. Hence, the helium-induced SEs that can be detected will convey information about the intended location of the incident beam [20]. Compare this to the other beams, where the SEs can convey information that is less local because the near-surface excited volume is considerably wider. The result is a sharper image with the HIM.

The SEs that are generated from the incident beam as it first enters the sample are termed type-one secondary electrons, or "SE1," whereas if the SE is generated from the incident beam as it backscatters deeply and again passes near the surface, it is termed "SE2." Because of the relatively low backscatter yield of helium (~1 % for typical biomaterials), the SE signal consists almost entirely of SE1s and hence convey only surface information. For the electron beam, however, there is often considerable backscattering from deeper within the specimen, producing any number of SE2s as the incident electrons reemerges from the surface. The likelihood of the high angle scattering depends critically upon the subsurface composition, and hence the SEM's detector sees both surface and subsurface information conflated together [21].

The helium-induced SEs that escape the specimen typically have an energy [22] less than 2 eV. Due to their relatively low energy, their detection is relatively straightforward; they can easily be drawn toward any nearby electrode that is positively biased. The same technology used in the SEM, the Everhart-Thornley detector, has been adapted for usage in the helium ion microscope (Fig. 7.8). It consists of a highly transparent metal grid that is biased positively to about +500 V to attract the electrons. Once within the grid, the electrons are accelerated toward a scintillator that is biased to +10 kV. Upon striking the scintillator, a single electron will produce about 100 photons, which are optically guided down a light pipe and delivered to a photomultiplier tube (PMT). With a suitable gain, the PMT produces an easily measured electrical signal for each detected electron. The detection efficiency of such a detector depends critically upon the geometry of the sample relative to the detector grid and the final lens. The detection efficiency is commonly 80 %, but it tends to be reduced when the sample is very close to the final lens. A small positive bias can be applied to the sample to improve the performance of the detector.

The HIM images that are based upon the detection of SEs convey a detailed surface topography that is intuitively interpreted. The topographic information is evident in Fig. 7.9, which shows a complex three-dimensional arrangement of collagen fibers from a rabbit knee. Even to the untrained eye, each fiber's size, shape, banded texture, and three-dimensional arrangement are easily recognized. The visual cues that aid our interpretation include the characteristic bright-edge effect along the

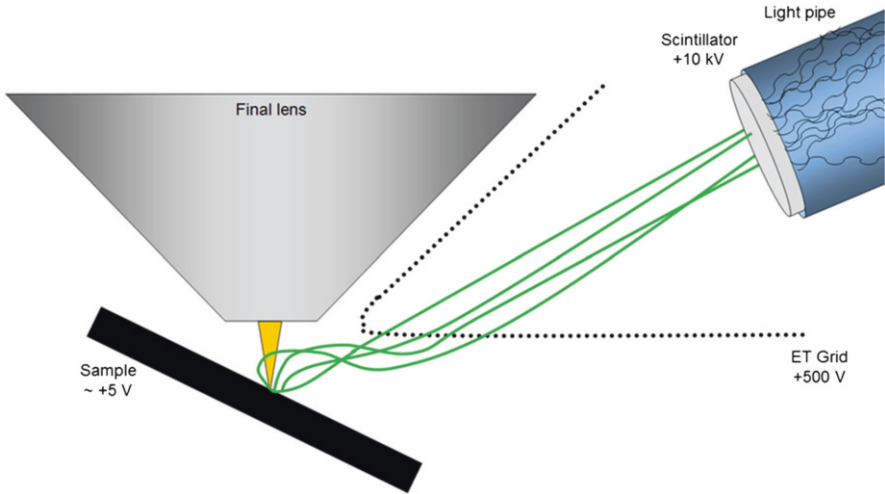


**Fig. 7.8** A standard Everhart–Thornley detector is very effective in collecting secondary electrons and producing an electrical signal

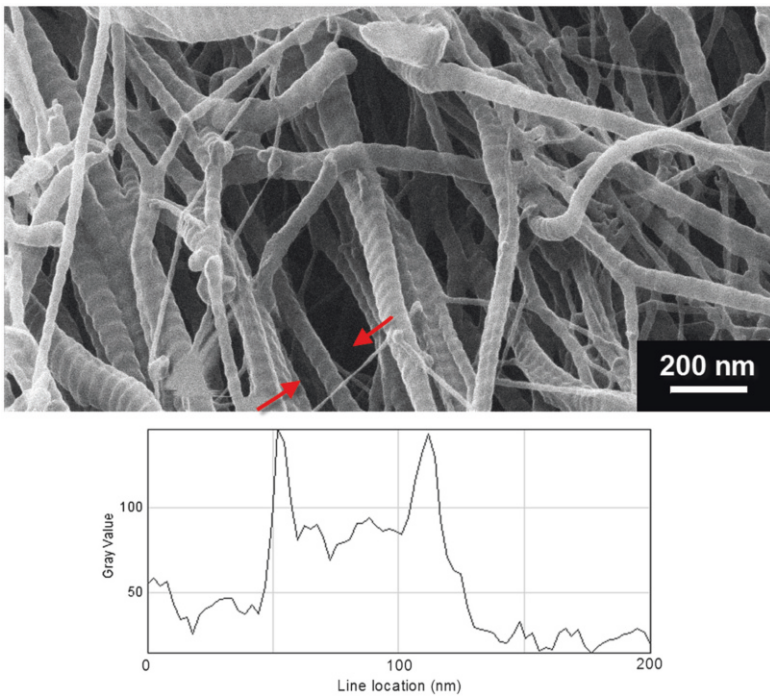
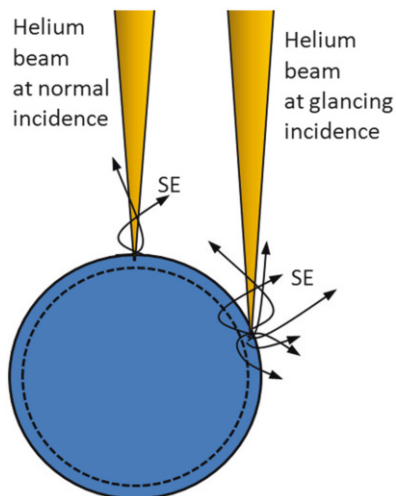


**Fig. 7.9** The three-dimensional structure of collagen fibers is readily interpreted in this SE image from the HIM. Below the image, an individual line profile between the two *arrows* shows the bright edge effect (Sample provided by Wendy van den Berg-Foels, Clemson–Medical University of South Carolina Bioengineering Program)



**Fig. 7.10** As the helium beam enters the sample, electrons are excited all along its trajectory. When the beam enters at a glancing angle, more of these can escape and become detectable SEs, leading to a bright edge effect. The *dotted line* represents the characteristic escape depth of secondary electrons



edge of each fiber and can be explained as follows (Fig. 7.10): Where the beam strikes the sample at normal incidence, a small number ( $<5$ ) of secondary electrons are produced, resulting in a darker gray pixel. In contrast, when the incident beam strikes the sample at a glancing angle, the beam remains close to the surface for a longer path length, and hence more SEs can escape and result in a brighter pixel. Experimentally, the bright-edge effect roughly corresponds to a brightness enhancement factor proportional to  $\sec(\alpha)$ , where  $\alpha=0$  corresponds to the incident beam being parallel to the local surface normal.

Figure 7.9 also demonstrates the excellent depth of field afforded by the HIM. The more deeply situated collagen fibers are inherently darker because of the lower probability of SE detection – a visual cue that provides additional spatial information. Note also that the thinnest fibers are somewhat transparent: There are detectable SEs from the front surface as well as the back surface, as well as in further portions of the sample. This can lead to a transparency-like effect where the HIM conveys front surface information, superimposed on a more diffuse back surface information, superimposed upon a further portion of the sample.

### 7.3.2.2 Backscattered Helium

The small fraction of incident helium ions that undergo large angle scattering from the nuclei of the specimen can occasionally escape from the specimen and subsequently be detected. These backscattered helium ions may still be in the form of positive ions or they may be neutralized. The probability of backscattering is directly related to the scattering cross section, which in turn depends on the atomic number of the specimen atoms. According to the simple Rutherford scattering principles, the scattering probability should increase with the target atom's atomic number squared. Thus, an embedded gold nanoparticle would be more likely to produce a

backscatter event than the lighter elements found in biological specimens. Experimentally, this general trend is readily observed, but there are additional fluctuations that are not fully understood [23]. The unexplained fluctuations seem to correlate strongly with the group number (column number) of the periodic table, with copper, silver, and gold having scattering probabilities that are higher than most other elements in the same period (row).

The outcome of helium scattering can be most simply understood by considering the conservation of momentum and energy. Solving these equations yields the following equation [24]:

$$E_B = E_0 \left( \frac{\sqrt{M_2^2 - M_1^2 \sin^2 \theta} + M_1 \cos \theta}{M_1 + M_2} \right)^2. \quad (7.1)$$

Here  $E_B$  is the energy of the helium atom just after the scattering, and  $E_0$  is the energy just before the scattering. The masses of the incident helium ion and the target atom are  $M_1$  and  $M_2$ , respectively.  $\theta$  is the angle by which the helium atom's trajectory was changed (with  $180^\circ$  corresponding to a true backscatter). The simple physics is complicated by the fact that the helium atom loses energy through its many inelastic collisions throughout its trajectory (both before the scattering event and after).

In the ORION Plus instrument, the backscattered helium can be detected by two different methods. The first is a detector that produces a signal proportional to the abundance of detected backscattered helium. This is achieved with an annular microchannel plate (MCP) detector, which can be either retracted or inserted between the sample and the final lens, as shown in Fig. 7.11. When inserted, the MCP subtends a solid angle of about 1.8 sr. Because the backscatter rate is dependent on the atomic number, this detector provides a useful contrast to distinguish between heavy and light elements, with minimal topographic information. Because of the low rate of helium backscattering, this detector requires comparatively high exposures to generate images. The second option for detection of backscattered helium is a detector capable of simultaneously measuring the angle and energy of the individual backscattered helium atoms. This is achieved with a solid-state, energy-resolving detector with a limited acceptance angle. In the ORION Plus instrument, this detector has been used to identify unknown elemental composition or to determine the thickness of thin films [25].

### 7.3.2.3 Other Detectable Particles

In addition to secondary electrons and backscattered helium ions, photons have been observed to be emitted from some types of samples (Fig. 7.12). These have been measured with a simple PMT with a borosilicate glass window and a bi-alkali photocathode. Several materials have been tested, but only a small fraction of them seem to produce photons under the helium ion beam. The mechanism is not fully understood,

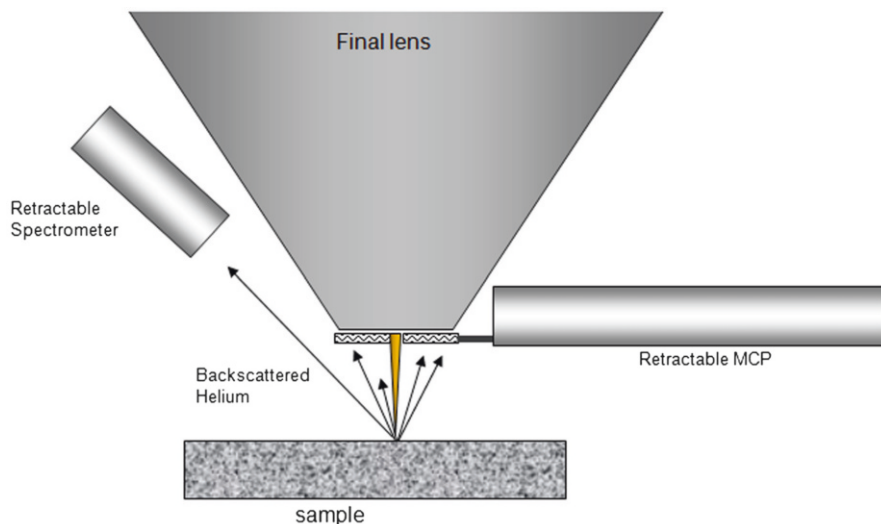


**Fig. 7.11** The MCP detector can be inserted for use and provides an electrical signal for each helium atom (ion or neutral) that strikes it. Alternatively, the spectrometer can be used to analyze the angular and energy distributions

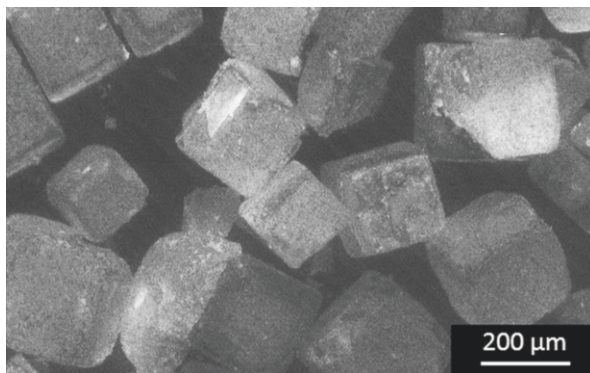


**Fig. 7.12** The specimen is a collection of table salt. In this image, the grayscale was assigned based upon the abundance of detected photons

but two classes of mechanisms have been proposed. First, the photons can be the result of relaxation of the target atoms that have been raised to a higher energy state by action of the helium beam. This is akin to the cathodoluminescence (CL) effect, similar to what has been observed with SEMs. The spectrum of this emitted light could then be used to positively identify the target atoms by their emission spectra [26]. The other proposed explanation (which has no SEM counterpart) is that the photons are the result of the incident helium ions' returning to a lower energy state. This process will produce deep UV photons ( $\sim 20$  eV) as well as a broad range of visible and infrared photons.

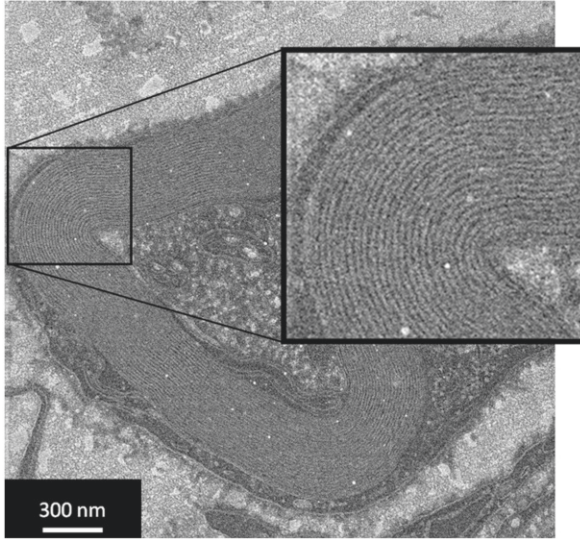


**Fig. 7.13** Myelin sheets from a mouse cell as imaged with transmitted helium (Sample provided by Prof. Schroeder from MPI Heidelberg)

For either mechanism, the detection of these photons may reveal important information about the optical properties of the specimen in question. Recently, some HIM owners have equipped their systems with optical spectrometers for collecting and analyzing the photons that are produced [27]. Of special interest are the well-established fluorescent markers used in biomedical research.

Secondary ions and neutrals are known to be ejected from the sample when exposed to the focused helium beam. These are sputtered atoms from the sample and, as such, could provide useful imaging or analysis capabilities. A detector that can measure the gross abundance of all such secondary ions (SI) can provide an alternative imaging mode with a contrast that may be complementary to the SE contrast. Beyond this, one of several mass spectrometry techniques [28] can ascertain the atomic or molecular mass of the sputtered materials at the indicated location. Although a secondary ion mass spectrometer (SIMS) is not presently available for the HIM, there is ongoing work to develop such a commercially available detector for imaging and analysis [29]. Such an analysis technique could provide a mass resolution sensitive enough to distinguish different isotopes of the same element – enabling the use of isotopic markers.

Another type of detectable particle is the transmitted helium. For samples that are prethinned (typically 100 nm or less), the helium ions have a probability of passing through it with some angular deflection. The detection of the transmitted helium at a certain angle can provide a useful contrast mechanism that could complement the standard STEM imaging modes. An example of such an image is shown in Fig. 7.13. The image shows the myelin sheets from a mouse cell after it had been prepared by microtome and imaged in the ORION HIM with a transmission

detector. In this case, the detector was configured for “brightfield mode,” collecting transmitted helium ions that suffered minimal angular deflections.

Lastly, it should be pointed out that the HIM is a relatively new instrument, and so there may be other particles that may be produced and may be detectable but have not yet been investigated. As we do with other new imaging technologies (i.e., the SEM in the 1950s), we anticipate the development of new detectors and new imaging modes as the instrument gains wider usage.

## 7.4 Sample Charging and Sample Preparation

Imaging biological specimens in the SEM requires several preparatory techniques to stabilize the materials to tolerate vacuum, to provide adequate contrast, and to minimize charging artifacts. While these preparations have been well established [30], they are known to introduce artifacts [31]. These artifacts are tolerable for some applications, but under highest magnifications, the sub 10 nm details reveal many distortions compared to the native state. In particular, the metallization of insulating samples with platinum or carbon will destroy or at least obscure the finer details. Operation of the SEM under high gas pressures (e.g., the environmental SEM) is one alternative to metal coating, but again there are resolution disadvantages that hide the sub 10 nm details.

Imaging with the helium ion microscope offers a unique advantage relative to the SEM in minimizing charging artifacts when imaging insulating samples or samples mounted to glass substrates. The first advantage is simply a result of the lower currents used in the HIM (1 pA typically) compared to the SEM (10 pA or more). A more significant difference between the HIM and SEM is in the distribution of the positive or negative charge. As mentioned earlier, the helium ions arrive in a single ionized state, and as they enter the specimen, they are apt to become neutralized and statistically spend most of the rest of their trajectory in a neutral state. Thus, beneath the surface, there is no net charge transport with the helium beam. In contrast, the electrons are deposited under the surface, where a negative space charge will accumulate. At the surface there is a relatively minor difference between the HIM and the SEM. The helium beam will produce positive surface charging because of two reasons: (1) the neutralization of the incident helium, and (2) the ejection of secondary electrons from the top few nanometers of the surface. The incident electron beam will also produce a positive surface charge, but only because of the ejection of secondary electrons from the surface. The effect is that the HIM produces only surface charging, and it is always positive in sign, whereas the electron beam induces positive surface charging *in combination with* negative subsurface charging. The net charging for the SEM can be either positive or negative depending on the relative contribution of these two effects. But even if they are exactly balanced and there is no *net* charging, there is still an electric field established between the subsurface (negative) and surface (positive) charging. The HIM comes equipped with a low-energy electron flood gun that easily mitigates the HIM’s positive surface charging. However, an electron flood

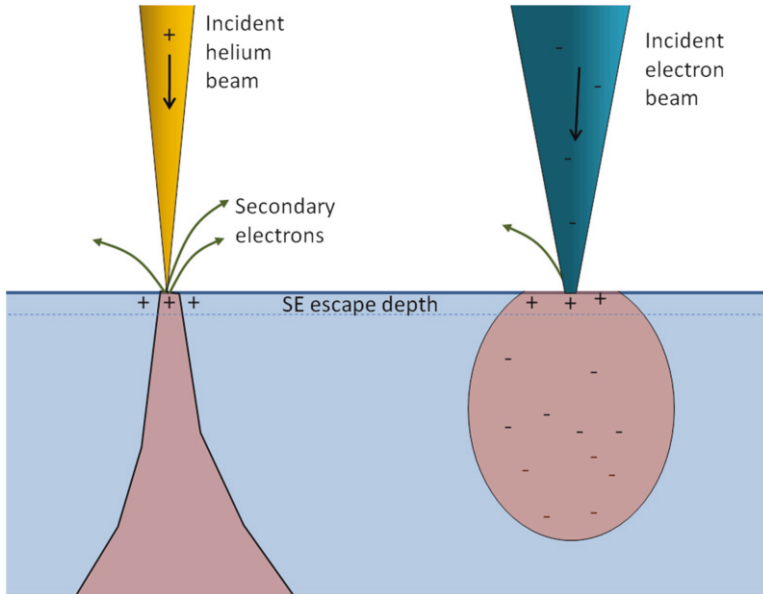


**Fig. 7.14** The charging characteristics of the HIM (*left*) and the SEM (*right*). The HIM produces only positive surface charging within a few nanometers of the surface, which is easily mitigated with an electron flood gun. The SEM's subsurface charging has no known remedy

gun, or any surface treatment, cannot resolve both the surface and subsurface accumulated charge for the SEM. Figure 7.14 is a diagram comparing the charging situation for insulating samples from the HIM (*left*) and the SEM (*right*). For these reasons, the HIM has provided some exceptional imaging results on insulating samples that otherwise provide a challenge to image in the SEM.

An example of HIM imaging of an insulating sample is shown in Fig. 7.15. This image reveals the large-scale ultrastructure of mouse tooth enamel as imaged in the HIM without any special metal coating. Tooth enamel consists of extremely long and thin crystals of carbonated hydroxyapatite. The single crystals (70 nm wide and hundreds of microns long) are arranged in bundles (so-called enamel prisms) that are oriented in a species-specific and tooth-specific way to form a hierarchical structure that is very hard, but not brittle, and lends the tooth its mechanical properties (hardness and fracture resistance). The bundles represent former pathways of cells, controlling the growth of both the crystals and the bundles. The unique three-dimensional ultrastructure of the enamel represents a frozen map of the cell migration in the early development of the tooth. An SEM microscopist might have turned to a metallization technique in order to image this sample, but this would have compromised the fine detail and would likely have produced incomplete coverage due to the wildly varying topography.

The HIM's ability to image samples with minimal charging artifacts and with high resolution and contrast offers the microscopist a chance to image his or her samples

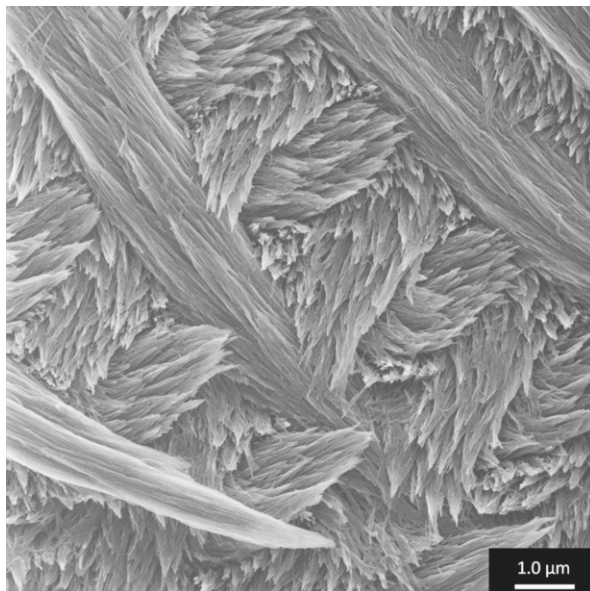


**Fig. 7.15** Ultrastructure of mouse tooth enamel imaged without any metal coating in the helium ion microscope (Samples provided by Felicitas Bidlack of the Forsyth Institute, Cambridge, MA, USA)

with much less sample preparation. For highly three-dimensional structures, this avoids possible damage. Figure 7.16 shows a collecting duct of an intercalated renal cell. The collecting duct of the kidney absorbs water and nutrients out of the primary urine – an ultra filtrate of the blood. The intercalated cells play an important role in the acid–base homeostasis of the kidney. The intense membrane system of these cells bears  $H^+$  ATPases regulating the pH of the primary urine. In the foreground (indicated by arrows), a primary cilium of the principle cells is visible. The exact function of this structure in the kidney remains unknown; one theory is that it has a role as a flow sensor in the collecting duct. HIM imaging of those structures reveals details that have not been observed before using conventional SEM.

The HIM offers the unique possibility to image biological samples with the without the necessity of conductive coatings. This capability, together with the extremely high resolution, can result in completely new insights on biological specimen. As with all microscopy techniques, improving resolution always unveils new and exciting details. It also means, though, that one enters the unknown with respect to what exactly can be observed and interpreted. Preparing a wet biological sample, fixing it, and drying it to make it vacuum-friendly inevitably changes the nature of the sample. If the sample is then imaged uncoated, it represents nothing but reality – or does it?

What happens if one can image without coatings in the sub 10 nm range is that sample preparation artifacts become obvious instantly. The difficulty one faces in omitting the well-known metal or carbon coatings is interpreting the results. Using the HIM on biological samples is rewarding in many aspects, and this chapter tries

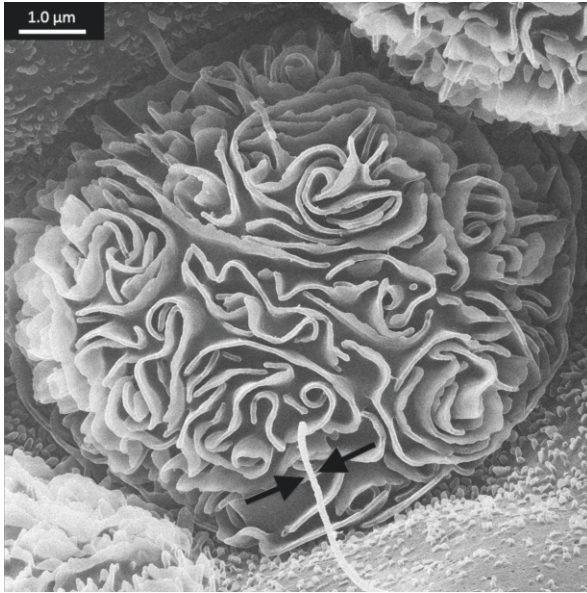


**Fig. 7.16** The intercalated and principal cells of the kidney (Sample provided by Dennis Brown and Teodor Paunescu of Massachusetts General Hospital, Boston, MA, USA)

to convince the reader that it is worthwhile. It also means that the sometimes well-established sample preparation protocols for the SEM are a good starting point for HIM imaging but need to be modified for each sample type. The imaging of the collagen fiber network (Fig. 7.9) needed extensive optimization steps [32] in the preparation of the cartilage tissue. Figure 7.16 shows a rat kidney preparation that was possible only after a thorough development of a sample preparation protocol [33] for tissue samples. This protocol has been successfully adapted in the meantime for testis, retina, and inner ear samples (unpublished). In general, one has to be extremely careful not to damage the ultrastructure of the sample; what this involves is almost always very much dependent on what type of sample is under investigation. Once this hurdle is overcome, the results are very rewarding. Researchers are only starting to investigate their structures of interest using this new technology, and the results so far are very encouraging.

## 7.5 Future Outlook

The helium ion microscope remains a relatively new technology – much as the SEM was in the 1950s. Its strengths and weaknesses are still being recognized for biological and other application areas. New detectors and new methodologies are still evolving. Already mentioned was the prospect of generating images from the



detection of specific secondary ions, characteristic photons, and transmitted helium. Other nonimaging applications include manipulation of the specimen to support imaging. For example, recent work has demonstrated that this same technology can be extended to ion beam species other than helium. A focused neon beam, for example, has been generated with the same gas field ion source by changes to the emitter and the gas supply. The heavier mass of the neon atom will sputter away materials at a rate about 50 times faster than helium. Such a nanometer-sized focused neon beam can serve as a “nanoscale scalpel,” able to remove material and expose hidden features that can be subsequently imaged. It is conceivable that three-dimensional information can be reconstructed through an alternating series of slicing and imaging procedures. In a recent publication by Joens et al. [1], the sheath of a predator nematode was removed to expose the otherwise hidden tooth.

## 7.6 Summary

The newly developed helium ion microscope offers new imaging capabilities that are distinctly different from the traditional gallium focused ion beam or scanning electron microscope. The helium beam can be focused to a smaller probe size (as small as 0.25 nm) and can provide a greater depth of focus than the competing techniques. Most importantly, the helium beam interacts with the specimen in a distinctly different manner than electrons or heavier ions. The generated particles (including secondary electrons, backscattered helium, and others) provide rich contrast mechanisms that give information about the topography, composition, and other properties of the sample. For the imaging applications in biology, the HIM offers some unique advantages. In addition to the high resolution and long depth of focus, the helium beam can provide excellent contrast even on low-atomic-number materials such as carbon. The images that are produced from secondary electrons provide information that is specific to the top several nanometers of the sample. Most importantly, the HIM can provide imaging with a minimal sample preparations, allowing the researcher to have greater confidence that preparation artifacts are not occluding the features of interest. Also, insulating samples can be easily imaged at high magnification without the usual degradations and artifacts seen in the SEM.

## References

1. Joens MS, Huynh C, Kasuboski JM, Ferranti D, Sigal YJ, Zeitvogel F, Obst M, Burkhardt CJ, Curran KP, Chalasani SH, Stern LA, Goetze B, Fitzpatrick JAJ. Helium ion microscopy (HIM) for the imaging of biological samples at sub-nanometer resolution. *Sci Rep.* 2013;3:3514.
2. Ward B, Notte J, Economou NP. Helium ion microscope: a new tool for nanoscale microscopy and metrology. *J Vac Sci Technol B.* 2006;24:2871–4.
3. Economou NP, Notte JA, Thompson WB. *Scanning.* 2012;34(2):83–9.

4. Goldstein J, Newbury DE, Joy DC, Lyman C, Echlin PE, Lifshin E, Sawyer L, Michael J. Scanning electron microscopy and X-ray microanalysis. 3rd ed. New York: Kluwer/Plenum Publishers; 2003. p. 49.
5. Tondare VN. Quest for a high brightness monochromatic noble gas ion source. *J Vac Sci Technol A*. 2005;23(6):1498–507.
6. Hill R, Notte JA, Scipioni L. In: Hawkes PW, editors. *Advances in imaging and electron physics*, vol. 170. Elsevier; 2013. p. 65–128.
7. Oppenheimer JR. Three notes on the quantum theory of aperiodic effects. *Phys Rev*. 1928;31:66–81.
8. Tsong TT. *Atom probe field ion microscopy*. New York: Cambridge University Press; 1990.
9. Müller EW, Tsong TT. *Field ion microscopy, principles and applications*. New York: Elsevier; 1969.
10. Hill R, Notte J, Ward B. The ALIS helium ion source and its application to high resolution microscopy. *Phys Procedia*. 2008;1:135–41.
11. Ernst N, Bozdech G, Schmidt H, Schmidt WA, Larkins GL. On the full-width-half-maximum of field ion energy distributions. *Appl Surf Sci*. 1993;67:111–17.
12. Reimer L. *Scanning electron microscopy*. 2nd ed. New York: Springer; 1998. p. 27.
13. Orloff J, Swanson LW, Utlaut M. Fundamental limits to imaging resolution for focused ion beams. *J Vac Sci Technol B*. 1996;14(6):3759–63.
14. Inai K, Ohya K, Ishitani T. Simulation study on image contrast and spatial resolution in helium ion microscope. *J Electron Microsc*. 2007;56:163–9.
15. Bell DC. Contrast mechanisms and image formation in helium ion microscopy. *Microsc Microanal*. 2011;17:147–53.
16. Ramachandra R, Griffin B, Joy DC. A model for secondary electron imaging in the helium ion microscope. *Ultramicroscopy*. 2009;109:748–57.
17. Ziegler JF, Biersack JP, Littmark U. *The stopping and range of ions in solids*, vol. 1, *Stopping and ranges of ions in matter*. New York: Pergamon Press; 1984. For the updated version, see SRIM Version 2013 ([www.SRIM.com](http://www.SRIM.com)).
18. Drouin D, Couture AR, Joly D, Tastet X, Aimez V, Gauvin R. CASINO V2.42 – a fast and easy-to-use modeling tool for scanning electron microscopy and microanalysis users. *Scanning*. 2007;29(3):92–101.
19. Rutherford E, Geiger H, Marsden E. The scattering of  $\alpha$  and  $\beta$  particles by matter and the structure of the atom. *Phil Mag*. 1911;Series 6, 21:669–88.
20. Sijbrandij S, Notte J, Sanford C, Hill R. Analysis of subsurface beam spread and its impact on the image resolution of the helium ion microscope. *J Vac Sci Technol B*. 2010;28(6):C6F6–9.
21. Goldstein J, Newbury DE, Joy DC, Lyman C, Echlin PE, Lifshin E, Sawyer L, Michael J. *Scanning electron microscopy and X-ray microanalysis*. 3rd ed. New York: Kluwer/Plenum Publishers; 2003.
22. Petrov YV, Vyvenko OF, Bondarenko AS. Scanning helium ion microscope: distribution of secondary electrons and ion channeling. *J Surf Invest X-Ray Synchrotron Neutron Tech*. 2010;4(5):792–5.
23. Kostinski S, Yao N. Rutherford backscattering oscillation in scanning helium ion microscopy. *J Appl Phys*. 2011;109:064311.
24. Rabalais JW. *Principles and applications of ion scattering spectroscopy*. Hoboken: Wiley Interscience; 2003.
25. Sijbrandij S, Notte J, Scipioni L, Huynh C, Sanford C. Analysis and metrology with a focused ion beam. *J Vac Sci Technol B*. 2010;28(1):73–7.
26. MacRae CM, Wilson NC. *Luminescence database I – minerals and materials*. *Microsc Microanal*. 2008;14(2):184–204.
27. Boden SA, Franklin TMW, Scipioni L, Bagnall DM, Rutt HN. Ionoluminescence in the helium ion microscope. *Microsc Microanal*. 2012;18(06):1253–62.
28. Benninghoven A, Rüdener FG, Werner HW. *Secondary ion mass spectrometry: basic concepts, instrumental aspects, applications, and trends*. New York: Wiley; 1987.

29. Wirtz T, Vanhove N, Pillatsch L, Dowsett D, Sijbrandij S, Notte J. Towards secondary ion mass spectrometry on the helium ion microscope: an experimental and simulation based study with He<sup>+</sup> and Ne<sup>+</sup> bombardment. *Appl Phys Lett*. 2012;101:041601.
30. Pawley J, Schatten H. *Biological low-voltage scanning electron microscopy*. New York: Springer; 2008.
31. Crang FE, Klomparens KL. *Artifacts in biological electron microscopy*. New York: Plenum Press; 1988.
32. Vanden Berg-Foels WS, Scipioni L, Huynh C, Wen X. Helium ion microscopy for high-resolution visualization of the articular cartilage collagen network. *J Microsc*. 2012;246(2):168–76.
33. Rice WL, Van Hoek AN, Păunescu TG, Huynh C, Goetze B, Singh B, Scipioni L, Stern LA, Brown D. High resolution helium ion scanning microscopy of the rat kidney. *PLoS One*. 2013;8(3):e57501.

# Chapter 8

## Sum Frequency Generation Vibrational Spectroscopy: A Sensitive Technique for the Study of Biological Molecules at Interfaces

Andrew P. Boughton and Zhan Chen

**Abstract** The behavior of biological molecules in interfacial environments is critical to understanding a broad range of phenomena, from biocompatibility to the functions of membrane-associated peptides and proteins. Sum frequency generation (SFG) vibrational spectroscopy is a nonlinear optical vibrational spectroscopic technique with an excellent sensitivity to interfacial molecules and molecular ordering and is well suited to probing biomolecules in a native interfacial environment. Using this technique, one can obtain unique information on the biomolecular orientation and conformation at interfaces. SFG also provides additional measurements that are complementary to other vibrational studies; more complicated protein structures and orientation distributions may be studied in greater detail when SFG is combined with other vibrational techniques.

### 8.1 Introduction

Although many biological phenomena have been studied in solution, interfaces are more difficult to probe. The structures of biomolecules at interfaces control many important phenomena—examples include blood coagulation on implant surfaces, membrane protein functions, marine biofouling, biosensing, and antimicrobial potency and selectivity [1–6]. Protein adsorption is the earliest response of the body to biomaterial implantation; depending on the properties of the material in question, this can lead to quite dramatic changes in protein structure relative to the X-ray crystal structures that have proven so valuable in biology. These structural changes mediate further body reactions and may cause unfavorable responses, such as blood clotting

---

A.P. Boughton • Z. Chen (✉)  
Department of Chemistry, University of Michigan, 930 North University Avenue,  
Ann Arbor, MI 48109, USA  
e-mail: [zhanc@umich.edu](mailto:zhanc@umich.edu)

and unnecessary immune response [3]. Biomolecules such as adhesive proteins from marine organisms can also interact with coating surfaces, leading to biofouling [4].

Proteins exist at interfaces quite naturally as well; for example, the lipid membranes that separate cells from their surroundings contain a wide range of proteins. These molecules are vital for the transport of nutrients, the survival of the cell, and the ability to sense and adapt to changes in the cell's surrounding environment. Yet high-quality crystals of many membrane proteins have proven elusive for crystallographers, and the constraints of crystallization may alter native structures in the cases where X-ray diffraction data do exist. Further, such static pictures may fail to reveal the changes in protein structure that occur during biological processes or from changes in the protein environment (such as temperature, pH, or varying charge and hydrophobicity of the lipid environment). Therefore, it is necessary to investigate the structures of membrane-associated proteins in situ. A direct probe of peptides in membranes also has applications to the rational design of antimicrobial peptides (AMPs) [1, 7], for which orientation measurements can reveal the nature of interactions with the membrane, thought to be critical to AMP function.

Surface-sensitive in situ probes of biomolecules at interfaces are needed to address these and other questions, yet such techniques are often limited—due to either a requirement for high-vacuum, interfering signals from the surrounding environment or a need for chemically added labels that may alter the native behavior of the biomolecule in question.

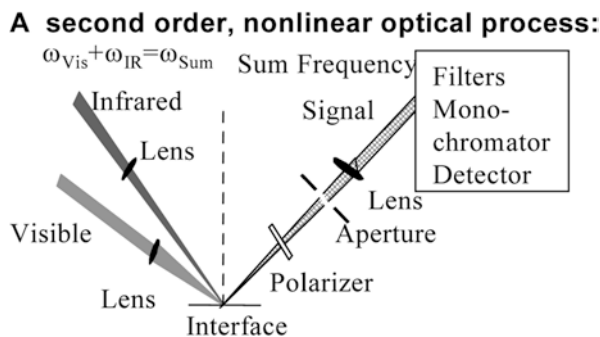
To this end, sum frequency generation vibrational spectroscopy (commonly abbreviated as SFG) has recently been applied to a range of biological systems. The focus of this chapter is on the biological applications of SFG for a broad audience in science and engineering. Here, instead of an inclusive review with an extensive discussion of SFG methodology and applications, we will summarize the method, compare advantages and disadvantages, and demonstrate examples of how this emerging technique can expand our knowledge of the interfacial behavior of important biomolecules. For further background, and details of many nonbiological applications of SFG, numerous review articles are available to the interested reader [8–14]. Examples of nonbiological systems studied using SFG include surface structures of liquids [15–18], interfacial structures of surfactants [19, 20], structures of molecules on electrodes [21–23], molecular adsorption and reaction on catalyst surfaces [24–26], chirality [27–29], and polymer surfaces and interfaces [9, 30, 31].

## **8.2 Sum Frequency Generation (SFG): Theory, Experiment, and Data Analysis**

### ***8.2.1 SFG: A Nonlinear Optical Process***

SFG is a second-order nonlinear optical process. One practical consequence of this fact is that output signals will be observed only in media that lack inversion symmetry (under the electric dipole approximation [32]). Bulk materials (such as air,

Fig. 8.1 SFG process



liquids, amorphous solids, and many crystalline solids) possess inversion symmetry. At many surfaces and interfaces, inversion symmetry is broken; thus, SFG is highly sensitive to surface-adsorbed molecules and interfacial molecular ordering.

In the typical SFG experiment, a fixed-frequency visible beam is overlapped in space and time with a frequency-tunable infrared laser, producing an output beam whose frequency is the sum of the two input beams (Fig. 8.1). This process is greatly enhanced when one of the beams (usually the infrared) is in resonance with the (vibrational) transitions of the molecule, resulting in a surface-sensitive vibrational spectroscopic technique; by using polarized beams, we can also study the molecular orientation. Data are presented as the output (sum frequency) signal intensity plotted against the frequency of the tunable infrared beam to take advantage of this fact. Therefore, SFG spectra appear similar to Fourier transform infrared (FTIR) and Raman spectra.

However, there are important differences. Vibrational modes are observed in FTIR or Raman spectra when either the dipole or polarizability transition moments change, respectively. The response of the molecule in SFG depends on a property known as the hyperpolarizability ( $\beta$ ), which is the *product* of the IR dipole and

Raman polarizability transition moments, such that  $\beta_{lmn,q} \propto \frac{\partial \alpha_{lm}^*}{\partial Q_q} \frac{\partial \mu_n}{\partial Q_q}$ . If either the

change in polarizability ( $\alpha$ ) or the change in dipole moment ( $\mu$ ) of a vibrational mode is equal to zero, then no SFG signal will be observed: The vibrational peaks observed in SFG are only those that are present in *both* infrared *and* Raman spectroscopy. This can be advantageous in the study of adsorbed proteins, as the elimination of interfering peaks simplifies the resulting spectrum. Further, the selection rule of SFG is such that the interfacial layer is probed selectively, and with good sensitivity. Both experiments and theoretical simulations indicate that SFG is submonolayer surface-sensitive. By contrast, the surface sensitivity in attenuated total reflectance Fourier transform IR spectroscopy (ATR-FTIR, a commonly used linear spectroscopy) is determined by the penetration depth of the evanescent wave (on the order of hundreds of nanometers or even microns). In practice, ATR-FTIR probes many layers of molecules, beyond those at the surface or interface. As a result, large water-bending signals must be subtracted when studying backbone signals from proteins at the surface–water interface. This background subtraction is not necessary for SFG.

Although surface-enhanced Raman scattering (SERS) has been widely applied to study the surface and interfacial structures of various molecules, it also lacks the intrinsic surface specificity of SFG and requires the use of metal substrates for the signal enhancement to occur—this is not always ideal for biological samples.

Another distinctive feature of SFG is that it is a coherent process, meaning that different vibrational modes can interfere with each other. Although this may complicate fitting in some cases, it can also provide an opportunity to measure the absolute orientation and to test the fitting results empirically. SFG spectra are fit according to the following equation:

$$I_{SFG} \propto |\chi_{\text{eff}}|^2 = \left| \chi_{\text{nr}} + \sum_q \frac{A_{SFG,q}}{\omega_2 - \omega_q + i\Gamma_q} \right|^2,$$

where  $A$  represents the strength of the  $q$ th vibrational mode,  $\Gamma$  is the damping coefficient (peak width),  $\omega_2$  is the infrared frequency,  $\omega_q$  is the vibrational frequency of the  $q$ th vibrational mode, and  $\chi_{\text{eff}}$  is the effective second-order nonlinear susceptibility (see later discussion). One practical consequence of this equation is that vibrational modes of similar energy (peaks close in frequency) can interfere with each other constructively or destructively, depending on their relative phases. This interference allows SFG to measure the *absolute* orientation, such as whether a group points up or down; such information is difficult to obtain from other commonly used vibrational techniques.

To date, much work has been done in SFG to study the CH stretching modes in various chemical groups (such as methyl, methylene, and phenyl groups). More recently, the highly informative amide I band has been studied as well, examining signals from backbone carbonyl groups in the protein [33]. The amide I peak center frequencies and peak widths are sensitive to the secondary structure and conformational changes of the protein, as in FTIR; thus, SFG studies can be thought of as a valuable extension of earlier vibrational spectroscopies, with a range of new advantages (discussed herein) that are well suited to complex biological systems. By adopting similar methods of sample preparation and combining multiple techniques, it is possible to study complex biomolecules with superb interfacial sensitivity.

## 8.2.2 SFG Data Analysis

### 8.2.2.1 SFG Orientation Analysis for CH Groups

By taking advantage of the polarized nature of the output sum, input visible, and input infrared radiation in SFG experiments, we may extract important information on molecular orientation. In addition to having the excellent surface specificity outlined earlier, SFG uses three beams, providing more combinations of polarizations and potentially more measurements than FTIR (one beam) or Raman (two beams); this allows for more complicated orientations and orientation distributions to be characterized.

The fitted signal intensity in SFG is related to the surface susceptibility tensor  $\chi_{ijk}$  in the lab-fixed coordinate system, as shown above. Different combinations of polarized beams allow the measurement of different components of this tensor [34]:

$$\begin{aligned}\chi_{eff,ssp}^{(2)} &= L_{yy}(\omega)L_{yy}(\omega_1)L_{zz}(\omega_2)\sin\beta_2\chi_{yyz}, \\ \chi_{eff,sps}^{(2)} &= L_{yy}(\omega)L_{zz}(\omega_1)L_{yy}(\omega_2)\sin\beta_1\chi_{yzy}, \\ \chi_{eff,pss}^{(2)} &= L_{zz}(\omega)L_{yy}(\omega_1)L_{yy}(\omega_2)\sin\beta\chi_{zyy}, \\ \chi_{eff,ppp}^{(2)} &= -L_{xx}(\omega)L_{xx}(\omega_1)L_{zz}(\omega_2)\cos\beta\cos\beta_1\sin\beta_2\chi_{xxz} \\ &\quad - L_{xx}(\omega)L_{zz}(\omega_1)L_{xx}(\omega_2)\cos\beta\sin\beta_1\cos\beta_2\chi_{xzx} \\ &\quad + L_{zz}(\omega)L_{xx}(\omega_1)L_{xx}(\omega_2)\sin\beta\cos\beta_1\cos\beta_2\chi_{zxx} \\ &\quad + L_{zz}(\omega)L_{zz}(\omega_1)L_{zz}(\omega_2)\sin\beta\sin\beta_1\sin\beta_2\chi_{zzz},\end{aligned}$$

where  $L_{ij}$  denotes Fresnel factors, and  $\beta$ ,  $\beta_1$ , and  $\beta_2$  are angles between the surface normal and the SFG signal, input visible, and input IR beams, respectively. The surface susceptibility tensor in the lab-fixed coordinate system is proportional to the response of the molecule as described by the molecular hyperpolarizability tensor,  $\beta_{lmn}$ , related by a coordinate transformation:

$$\chi_{ijk,q}^{(2)} = N \sum_{l,m,n} (\hat{i} \cdot \hat{l})(\hat{j} \cdot \hat{m})(\hat{k} \cdot \hat{n}) \beta_{lmn,q}.$$

Therefore, SFG measurements can be related to the orientation angle of the molecule relative to the lab frame, where  $\theta$  is typically defined as the angle between the principal axis of the molecule or function group and the  $z$ -axis perpendicular to the plane of the interface. For example, for the symmetric stretching mode of a methyl group,

$$\begin{aligned}\chi_{xzx,s} &= \chi_{yyz,s} = \frac{1}{2} N_s \beta_{ccc} [\cos\theta(1+r) - \cos^3\theta(1-r)], \\ \chi_{zxx,s} &= \chi_{yzy,s} = \chi_{zxx,s} = \chi_{zyy,s} = \frac{1}{2} N_s \beta_{ccc} [\cos\theta - \cos^3\theta](1-r), \\ \chi_{zzz,s} &= N_s \beta_{ccc} [r \cos\theta + \cos^3\theta(1-r)].\end{aligned}$$

Here,  $\beta_{aac} = r\beta_{ccc}$ . The number density,  $N_s$ , is a constant property of the surface and does not change with the polarization combination of the input laser beams. Therefore, important information on molecular orientation may be extracted from experimental measurements as a ratio of the signal strength measured in two polarizations. This approach does not require knowledge of the surface coverage, which cancels when a ratio is taken; this somewhat simplifies the experimental procedure. However, it requires the assumption that every methyl group has the same orientation angle  $\theta$ . If methyl groups adopt different orientations, then in the above equations,  $\cos\theta$  and  $\cos^3\theta$  will be replaced by their averages:  $\langle\cos\theta\rangle$  and  $\langle\cos^3\theta\rangle$ . To



characterize these average values for a distribution, it is necessary to know the surface coverage ( $N_s$ ) [35]. A number of articles discuss the mathematical relationships in greater depth [36–39].

Many SFG studies have been performed on the orientation of CH groups (such as methyl, methylene, and phenyl groups), and the details will not be repeated here; instead, our focus will be on the orientation of protein secondary structures as determined using amide I signals. However, it is worth noting that methyl ( $-\text{CH}_3$ ) signals are also of great biological utility, and their orientation can be used to study structural changes that affect protein side chains and model cell membranes.

### 8.2.2.2 SFG Amide I Protein Signals

Signals in the amide I region mainly come from the CO groups on the backbone of the protein and are sensitive to secondary structure. Two common secondary structures that form the building blocks of larger proteins are  $\alpha$ -helices [40] and  $\beta$ -sheets [41]; both have been studied using SFG. Signals from these structures give peaks at different frequencies, which in SFG can be separated and correlated to the overall orientation of  $\alpha$ -helices or  $\beta$ -sheets in interfacial biomolecules.

### 8.2.2.3 Determining the Orientation of an $\alpha$ -Helix Using SFG

If the orientation of each secondary structure of a protein at an interface can be deduced, the overall orientation and conformation of the protein can be inferred (for further discussion, see Sect. 8.3.3.4.1). As was discussed above for the simple case of a methyl group, the orientation of an  $\alpha$ -helix can be deduced from polarized SFG experiments. The different susceptibility tensor components  $\chi_{abc}$  measured in each polarization are related to various hyperpolarizability elements  $\beta_{ijk}$  as a function of the molecular orientation. For  $\alpha$ -helices, the observed signal intensity varies with the tilt angle  $\theta$  relative to the surface normal according to the following equations [42].

For the  $A$  mode:

$$\chi_{A,xxz} = \chi_{A,yyz} = \frac{1}{2} N_s \left[ (1+r) \langle \cos\theta \rangle - (1-r) \langle \cos^3\theta \rangle \right] \beta_{ccc},$$

$$\chi_{A,xxz} = \chi_{A,yzy} = \chi_{A,zxz} = \chi_{A,zyy} = \frac{1}{2} N_s \left[ (1-r) (\langle \cos\theta \rangle - \langle \cos^3\theta \rangle) \right] \beta_{ccc}, \quad (8.1)$$

$$\chi_{A,zzz} = N_s \left[ r \langle \cos\theta \rangle + (1-r) \langle \cos^3\theta \rangle \right] \beta_{ccc},$$

where  $r = \frac{\beta_{aac}}{\beta_{ccc}}$ .

For the  $E_1$  mode:

$$\begin{aligned}\chi_{E,xxz} &= \chi_{E,yyz} = -N_s \left( \langle \cos\theta \rangle - \langle \cos^3\theta \rangle \right) \beta_{aca}, \\ \chi_{E,xxx} &= \chi_{E,yyz} = \chi_{E,zxx} = \chi_{E,zyy} = N_s \left( \langle \cos^3\theta \rangle \right) \beta_{aca}, \\ \chi_{E,zzz} &= 2N_s \left( \langle \cos\theta \rangle - \langle \cos^3\theta \rangle \right) \beta_{aca}.\end{aligned}\tag{8.2}$$

Because of the limited resolution of many SFG spectrometers ( $\sim 5\text{ cm}^{-1}$  or more), it is necessary to add the response of the two vibrational modes of the helix together before taking a ratio between polarized measurements. This assumes that the two peaks are too close in frequency to be separated in the fitting, so that the total intensity of the measured peak will be a combination of both of the closely spaced modes. Experimental measurements from infrared and Raman have been used to determine the values of  $\beta$  required to determine the orientation [43–46]. Using these parameters, SFG has recently been applied to study the multiple orientations of the helical peptide melittin in a lipid bilayer, as well as the orientation distribution of helical fibrinogen coiled-coils at interfaces [42, 47]. The total hyperpolarizability of a multi-helix protein has been calculated and has also been applied to the study of more complicated proteins containing multiple distinct helices, such as the  $\beta\gamma$  subunit of a heterotrimeric G-protein in a model membrane [48].

### 8.2.2.4 Studying the Orientation of a $\beta$ -Sheet with SFG

While helices represent one of the most common secondary structural motifs,  $\beta$ -sheets represent another, and some preliminary work has been done on their orientation analysis. This is somewhat more complicated by the fact that upon averaging to calculate the surface susceptibility, one can no longer assume that the molecule is axially symmetric. The result is that the orientation of a  $\beta$ -sheet is characterized by *two* angles: a tilt angle,  $\theta$ , and a twist angle,  $\phi$  [49].

For the  $B_1$  mode:

$$\begin{aligned}\chi_{xxz} &= \chi_{yyz} = \chi_{zxx} = \chi_{zyy} = \chi_{zxx} = \chi_{zyy} = -\left( \langle \cos\theta \sin\phi \cos\phi \rangle - \langle \cos^3\theta \sin\phi \cos\phi \rangle \right) \beta_{abc}, \\ \chi_{zzz} &= 2\left( \langle \cos\theta \sin\phi \cos\phi \rangle - \langle \cos^3\theta \sin\phi \cos\phi \rangle \right) \beta_{abc}, \\ \chi_{zxy} &= -\chi_{zyx} = -\chi_{yzx} = \chi_{xzy} = \frac{1}{2}\left( \langle \sin^2\theta \cos^2\phi \rangle - \langle \sin^2\theta \sin^2\phi \rangle \right) \beta_{abc}.\end{aligned}$$

For the  $B_2$  mode:  $\chi_{zxy} = -\chi_{zyx} = -\chi_{yzx} = \chi_{xzy} = \frac{1}{2}\left( \langle \cos^2\theta \rangle - \langle \sin^2\theta \cos^2\phi \rangle \right) \beta_{acb}$ .

For the  $B_3$  mode:  $\chi_{zxy} = -\chi_{zyx} = -\chi_{yzx} = \chi_{xzy} = -\frac{1}{2}\left( \langle \cos^2\theta \rangle - \langle \sin^2\theta \sin^2\phi \rangle \right) \beta_{bca}$ .

The achiral susceptibility tensor elements for the  $B_2$  and  $B_3$  modes are identical to those for the  $B_1$  mode, except that  $\beta_{abc}$  is replaced by  $\beta_{acb}$  and  $\beta_{abc}$ , respectively.

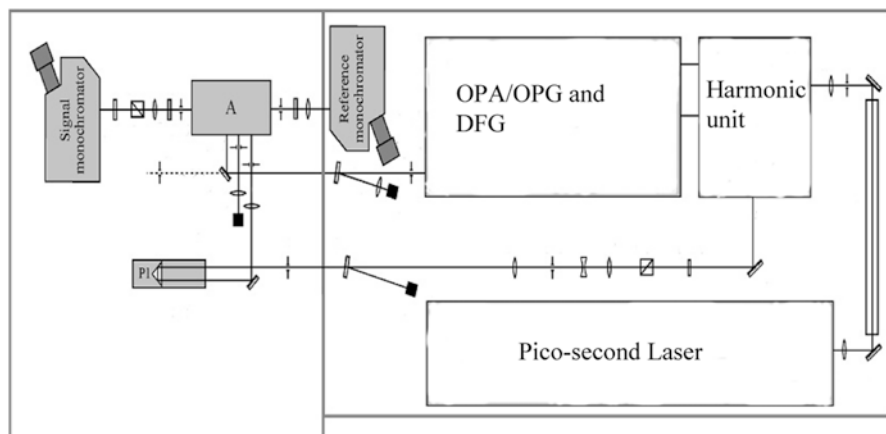


**Fig. 8.2** Layout of a typical SFG instrument

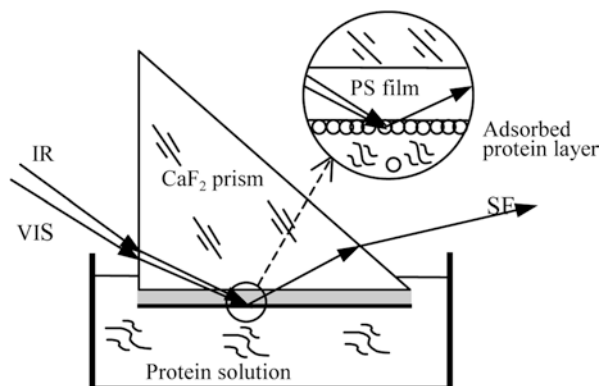
Note that unlike previous examples, the orientation of a  $\beta$ -sheet is described by additional parameters besides  $\langle \cos \theta \rangle$  and  $\langle \cos^3 \theta \rangle$ ; as we will discuss later, the availability of additional measurements can be very valuable when studying larger proteins.

Due to the symmetry of  $\beta$ -sheets, a new set of *chiral* tensor elements is available for measurement in addition to the elements measured normally. (For the chiral elements, all three indices  $i, j, k$  in the element  $\beta_{ijk}$  are different.) In fact, the  $\beta$ -sheet structure can potentially yield strong chiral signals [49, 50]. These additional measurements may make it possible to analyze the orientation of  $\beta$ -sheets at interfaces; the relevant molecular hyperpolarizability components required for quantitative orientation analysis of  $\beta$ -sheets are currently being investigated.

### 8.2.3 SFG Experimental Procedures

The typical SFG experiment employs a fixed-frequency visible beam and an infrared laser (either tunable-frequency or broadband). Representative SFG instruments have been described in Refs. [51–54], and in recent years commercial instruments have become increasingly available from several manufacturers. The input laser beams are spatially and temporally overlapped to produce the third “output” frequency, which is collected by a photomultiplier tube, CCD, or other detection scheme; since the beam sizes are quite small ( $\sim 500 \mu\text{m}$ ), sample requirements are reasonable. An example SFG system is shown in Fig. 8.2. This system has four components: (1) a pico-second Nd:YAG laser; (2) a harmonic unit with two KD\*P crystals; (3) an optical parametric generation (OPG)/optical parametric amplification (OPA) and difference frequency generation (DFG) system based on LBO and

**Fig. 8.3** The SFG “near”-total-reflection experimental geometry (Reproduced with permission from Ref. [33]. © 2003, American Chemical Society)



AgGaS<sub>2</sub> crystals; and (4) a detection system. The visible beam (532 nm) is generated by frequency-doubling the fundamental output pulses of 20-ps pulse width from the Nd:YAG laser. The tunable IR beam is generated from the OPG/OPA and DFG system and can be tuned from 1,000 to 4,300 cm<sup>-1</sup>; by replacing the AgGaS<sub>2</sub> crystal with a GaSe crystal, this range may be extended down to 650 cm<sup>-1</sup>. In this example, the output signal is collected by a photomultiplier and processed with a gated integrator. However, CCD detectors are becoming increasingly available. By monitoring the power of the visible and IR beams using photodiodes, we can normalize SFG spectra by the power of the input laser beams.

In order to collect protein signals, it is beneficial to consider the experimental geometry. As shown in Sect. 8.2.2.1, the output signal is affected by the Fresnel factors ( $L_{ij}$ ), which depend on the incident angles of the beams and the indices of refraction of the media through which the beams pass. Many existing SFG experiments employ a straightforward reflection geometry, which has the advantage of being relatively easy to align. Yet if we change it to a “near” total internal reflection right-angle prism geometry (Fig. 8.3) instead, the angle-dependent Fresnel factors are increased substantially, making it easier to observe weak signals experimentally [33, 55]. This provides advantages for fitting and quantitative analysis, as well as improved detection limits.

One important advantage of SFG in the study of biomolecules is that unlike vacuum techniques, SFG is capable of measuring protein orientation and conformation in a biologically relevant, aqueous environment. The surface sensitivity of SFG is such that as little as a few micrograms of the protein of interest are enough for reasonable signals to be observed, making it feasible to study protein behavior even at low concentrations. This is also beneficial when employing expensive isotope-labeled materials, large quantities of which are often difficult to obtain.

Lastly, dramatic signal and selectivity enhancements may be possible by employing the emerging technique of doubly resonant SFG (DR-SFG) [27, 56–59], which can enhance the signal intensities by exciting both vibrational and electronic transitions, leading to signal enhancements of several orders of magnitude. Normally, the SFG signal intensity is determined by the product of the IR absorption and

the normal Raman signal intensity. The DR-SFG signal intensity is the product of the IR absorption and the *resonance* Raman signal intensity [57, 58], and therefore signals obtained using the DR-SFG signal can be much stronger than those from normal SFG. This promises superior detection limits, among other uses. However, there have as yet been few applications of this technique to biomolecules, and so this technique will not be discussed further in this chapter.

## 8.3 Applications of SFG to Biological Molecules at Interfaces

### 8.3.1 SFG Studies of Proteins: The CH and NH Spectral Region

Partially due to limitations in the tunable frequency range of older laser instruments, many early SFG studies of proteins focused on CH stretching signals: methyl groups, phenyl rings, and other functional groups of interest in protein amino acid side chains. Although the sheer number of similar amino acids would hamper any serious attempt to study the orientation and conformation of the entire protein at the interface based on CH signals, the requirement that a medium lack inversion symmetry allows signals to be interpreted in terms of side-chain ordering at the interface. Early studies showed that protein CH signals could be detected readily on a range of biomedically important polymers [60], and these signals were interpreted as demonstrating the segregation of hydrophobic and hydrophilic residues at the polymer–water boundary. As a later test, Somorjai and coworkers used a simple peptide designed to form a facially amphiphilic helix at interfaces and found that strong CH signals could indeed be obtained [61, 62]. These results confirmed that the hydrophobic residues are strongly ordered at a hydrophobic–hydrophilic interface (e.g., polymer–solution). Such ordering of hydrophobic groups has also been seen previously for a variety of amino acids at an oil–water interface [63]. By also studying the NH stretch, Evans-Nguyen and colleagues demonstrated that specific amino acids remain buried after the conversion of fibrinogen to fibrin [64]. Water molecules can also order in the vicinity of a protein, providing additional clues about protein adsorption and the burial of hydrophobic regions [65, 66].

Side-chain ordering at an interface can be influenced by changing the contacting media of the protein [61, 67, 68]. Different spectra were collected from bovine serum albumin (BSA) at the polymer–water interface as opposed to the polymer–air interface, as a result of a different ordering of hydrophobic groups. Replacing the water with a hydrophobic solvent (such as benzene) also led to spectral changes. Stronger ordering was observed at hydrophobic–hydrophilic interfaces, whereas only weak signals were observed from hydrophilic–hydrophilic interfaces (such as SiO<sub>2</sub>–water). It is important to note that SFG is very sensitive to molecular orientation; as a result, weaker signals can sometimes be observed even in the case where more adsorbed protein is present (if those molecules are less well ordered) [69].

Changes in the interfacial environment can manifest as other changes in protein behavior as well. A difference in pH can affect side-chain ordering at an interface, as was observed for proteins such as lysozyme [70]. This may dramatically change the dominant protein–surface interactions in some cases. At normal pH values, NH groups in human fibrinogen were found to order; at acidic pH values, this interaction shifted to more favorable hydrogen bonding [71]. Thus, SFG can provide a molecular-level explanation for the pH-dependent difference in protein affinity for the surface. Such changes may also shift the balance in the process of competitive adsorption, as the nature of the favorable protein–surface interactions shifts.

A change in pH may also affect the protonation state of amino acids on the protein, which in turn will alter the net charge of the adsorbed protein layer and resulting interactions with other molecules. Urea, a common protein denaturant, was found to orient differently toward a protein layer at high and low pH values; since the actual effect of urea denaturation is not sensitive to charge, a direct interaction between the protein and the denaturant was ruled out as the mechanism [72]. The interfacial and in situ sensitivity of SFG makes it possible to directly study molecular interactions at the interface as a function of changes in the surrounding conditions, such as pH. SFG protein CH signals have also been used to study molecular recognition events such as protein binding of a ligand, of great importance to the development of biosensors [73, 74].

As the protein concentration increases, protein–protein interactions become increasingly important. Protein CH signals were found to change at a protein solution–air interface as a function of concentration, indicating that interactions between nearby proteins can be very important in determining the ordering of hydrophobic side chains (as well as the entire structure) [69, 75]. Various surfactants were likewise shown to affect protein aggregation [76].

Investigating protein structures at interfaces by SFG CH signals provides direct, in situ evidence that interfacial protein side-chain ordering can change when the environment is altered. For simpler biomolecules, such as amino acids and peptides, with well-defined structures, more detailed structural information may be inferred from such studies; this is valuable for the study of structural changes related to biocompatibility and biofouling. However, the very large number of similar hydrophobic groups in many larger proteins makes it difficult to describe the structure in detail using CH signals alone. Isotope labeling of specific amino acids is one way to gain additional information from interfacial proteins.

### ***8.3.2 Isotope Labeling***

Isotope labeling can provide a way to determine the orientation of one or a few side-chain groups, by shifting the frequency of an individually labeled vibration to a new, easily resolved position away from interfering or overlapping signals. The value of this approach has been demonstrated in linear spectroscopy, such as FTIR. Numerous labeling studies have demonstrated that isotope labeling can lead to a more accurate

determination of molecular orientation [77–79]. Labeling studies are particularly useful when dealing with proteins, as it allows the signal from one specific group or type of amino acid of interest to be isolated from other amino acids. For large and complicated proteins, this provides an additional set of measurements that allow the characterization of biomolecules in which multiple similar groups cannot be distinguished by spectral fitting alone. Thus, the use of isotope labeling, when combined with the increased polarization-dependent measurements in SFG, may prove a very valuable tool in the study of large proteins [80].

It has been demonstrated that SFG is sensitive enough to detect a single labeled amino acid in a protein at an interface. It has also been reported that SFG can selectively probe isotope-labeled segments in a protein, such as when deuteration of a certain amino acid was introduced [81]. If different segments of a protein can be isotope-labeled in succession, SFG can be used to study the structure of a protein in detail.

Another advantage of isotope labeling lies in the ability to separate signals contributed by different molecules (e.g., labeled and unlabeled). SFG studies using partially deuterated proteins and normal hydrogenated proteins have demonstrated that protein adsorption to a polymer surface is a reversible process [81] and that a protein will induce changes in polymer structure as it adsorbs [82]. The ability to separate signals from different molecules at the surface can be quite useful in monitoring competitive adsorption, namely, the Vroman effect, in which one protein is displaced by another with lower mobility but greater affinity for the surface [83]. Isotope-labeled proteins have been used to show that hydrocarbon contamination on the surface may gradually be replaced by a layer of adsorbed proteins over a period of time [84].

### 8.3.3 Studying Amide I Protein Signals with SFG

#### 8.3.3.1 Advantages of the Amide I Band

The amide I band of proteins is attractive for vibrational studies of proteins. This band can be loosely described as a stretching mode of backbone carbonyls [85], and the exact peak center frequency depends on the secondary structure and conformation of the protein. These frequencies are roughly the same as those observed via FTIR, but SFG amide I spectra do not suffer the interference from strong water-bending signals that usually obscures the amide I region in ATR-FTIR. As newer and more broadly tunable SFG instruments become increasingly available, it is expected that this informative spectral region will be increasingly studied.

Further, the unique peak center frequencies of various secondary structural elements in a protein can be combined with the orientation information obtainable by SFG to create a more complete picture of the interfacial orientation. Although vibrational spectroscopy cannot directly inform us *which* segments of the protein have adopted a given helical or  $\beta$ -sheet conformation, the increasing availability of

high-quality protein structures (via the Protein Databank, PDB) allows important conclusions to be drawn about the structural changes that occur with slight changes in the protein environment in situ. For example, if regions of the protein undergo bending or deformation, changes in the spectrum will be observed. As discussed above, CH signals are often difficult to interpret in terms of a detailed molecular orientation; in contrast, the amide I band presents a picture of the backbone molecular orientation that is well suited to the task.

### 8.3.3.2 Detection of SFG Amide I Signals

A method to probe the overall molecular orientation selectively at interfaces would be of great utility. For example, many membrane-active proteins or peptides (such as antimicrobial peptides, AMPs) are difficult to study in their native environment, yet knowing their orientation in membranes is critical for understanding the mode of action and designing more effective antimicrobial agents [1, 86, 87]. Because these peptides are generally short and adopt characteristic secondary structures (such as  $\alpha$ -helices and  $\beta$ -sheets) that form the building blocks of larger proteins, the orientation determination of small antimicrobial peptides also offers a proof-of-concept and testing ground for larger proteins.

Amide I signals have been examined by several research groups to date. The first SFG amide I signals were collected from the polymer–protein interface using the near-total-reflection geometry; a number of proteins were studied, demonstrating that SFG is sensitive enough to distinguish among proteins with different secondary structures [33]. By using antimicrobial peptides such as  $\alpha$ -helical MSI-594 and the  $\beta$ -sheet peptide tachyplesin, researchers have shown that SFG amide I signals originating from proteins can be detected from both  $\alpha$ -helices and  $\beta$ -sheets distinguishably [49, 50]. Using the thin-film optical model for the interpretation of spectra, Wang et al. proved that the signals obtained are from proteins adhered to the surface, rather than only to part of a layer [88].

### 8.3.3.3 Qualitative Studies: Amide I Spectra Demonstrating Orientation and Ordering

As we discussed above for the CH and NH spectral region, stronger signals are obtained for greater molecular ordering or certain orientations though here the signals obtained are a guide to the overall ordering and orientation of the protein backbone. Thus, strong signals were observed for long and well-aligned poly- $\gamma$ -benzyl-L-glutamate (PBLG) helices [89], yet only very weak signals were obtained from albumin despite a large number of  $\alpha$ -helical segments in the latter [33]. As with other chemical groups, this molecular ordering or orientation can be affected by the composition of the surface in question, as was demonstrated for time-dependent SFG amide I signal changes of fibrinogen on a variety of polymer surfaces [90]. The surface charge can also alter the ordering. For example, the blood protein



factor XII (FXII) can autoactivate on negatively charged surfaces, leading to blood coagulation. It was hypothesized that this activation is due to increased ordering and a more favorable orientation when adsorbed on negatively charged surfaces, but this has been difficult to directly test. Using SFG, Chen et al. have shown that (negatively charged) sulfonated polystyrene surfaces induce a net orientation and greater ordering for adsorbed FXII compared to behavior on neutral polystyrene surfaces [91]. This view of proteins at surfaces provides useful structural insights for understanding biocompatibility.

### 8.3.3.4 Quantitative Orientation Studies from SFG Amide I Signals

#### The Value of Multiple Measurements

SFG provides a number of advantages for the study of biomolecules at interfaces: It is an inherently surface-sensitive technique with many of the advantages and applications of FTIR, yet it is also capable of providing more measurements to characterize the orientation of biological systems. Even a single-helix peptide in a well-defined environment cannot always be described by assuming only a single orientation; for larger proteins with multiple similar structural elements, obtaining more measurements from additional vibrational spectroscopies is critical [80].

Different vibrational spectroscopic techniques measure different structural parameters. For example, if the tilt angle of a structural element (e.g., an  $\alpha$ -helix) is  $\theta$  versus the surface normal, ATR-FTIR can determine the angle by measuring  $\langle \cos^2 \theta \rangle$ . For ATR-FTIR, this is the only parameter obtained. Therefore, any orientation analysis must assume that all chemically identical groups at the interface adopt the same orientation (a “ $\delta$ -distribution”). In contrast, as discussed above, SFG can measure both  $\langle \cos \theta \rangle$  and  $\langle \cos^3 \theta \rangle$ . Thus, SFG can be used to deduce two different structural parameters; in a Gaussian distribution, for example, this would correspond to the average orientation and distribution width. More complex distributions require a combined approach, and higher-order vibrational spectroscopic techniques can measure more structural information.

For example, four-wave mixing (FWM) measures  $\langle \cos^2 \theta \rangle$  and  $\langle \cos^4 \theta \rangle$  parameters; such additional measurements are useful for characterizing complex distributions involving multiple distinct orientations. Unlike SFG (a three-photon process), FWM is a four-photon process. Energy-level diagrams for SFG and FWM are shown in Fig. 8.4 for comparison. A special case of FWM is coherent anti-Stokes Raman scattering (CARS, Fig. 8.4c), in which two of the input beams are the same frequency. CARS spectroscopy and imaging have been widely applied to study biological samples [92–94].

When the protein crystal structure is known, we can deduce the orientation of the entire molecule at the interface by calculating the combined hyperpolarizability for all  $\alpha$ -helical secondary structures in the protein. However, this requires the assumption that the structure at the interface is the same as the crystal structure. When the crystal structure is not known, or when structural changes in situ are suspected,

**Fig. 8.4** Energy-level diagrams for (a) SFG, (b) FWM, (c) CARS

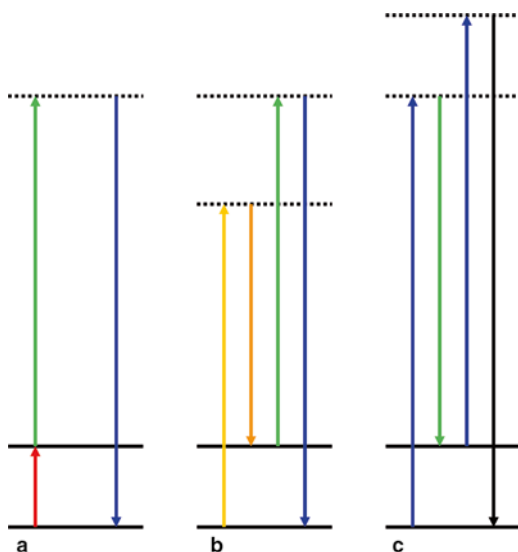


**Fig. 8.5** The model protein has three  $\alpha$ -helices and several  $\beta$ -sheets. If the orientations of such secondary structures can be deduced, the rough structure or conformation of the protein can be determined



measuring the unique orientations of individual secondary structure elements may help to understand the overall structure (Fig. 8.5). As discussed in Sect. 8.3.3.4.2, it is difficult to characterize multiple distinct orientations using ATR-FTIR alone; however, in combination with additional measurements from isotope labeling and other vibrational spectroscopies (such as SFG and FWM), more detailed orientation distributions can be measured as a guide to the overall orientation of helical segments of the protein.

Where the physical constraints of crystallization may not be expected to alter the native structure, the possibility of conformational changes (such as differences in the relative orientations of secondary structures upon binding) still exists. These changes may be difficult to observe through static techniques. Thus, if one collects enough measurements to characterize the orientations of multiple distinct helical segments individually, the in situ and time-resolved nature of SFG makes it possible to study protein flexibility in a native environment [80].

As SFG is extended to the study of larger and more complicated systems, tools for dealing with complicated structures become increasingly important. One approach is to calculate the hyperpolarizability of different domains and secondary structures of a large biomolecule as the sum of individual monomer hyperpolarizabilities based on *ab initio* calculations (taking into account perturbations or couplings); this idea is the basis for the freely available software NLOPredict, which uses values for a model amino acid [95–97]. As these calculations become more advanced, questions such as signal change due to flexibility or binding should become easier to address.

Because of the sensitivity of the amide I band to secondary structure and orientation, the experimental validation of empirical fitting procedures also becomes important for accurate orientation determination. By using a range of intermediate polarizations in which signals from two separate polarization combinations are observed (a technique known as *polarization mapping*), researchers are able to validate the empirically fit parameters and determine the relative phases of different vibrational modes, tasks that would be difficult to do using only the conventionally measured polarizations. Further, Wang et al. have shown that empirical fitting alone can produce misleading results and that the use of techniques such as polarization mapping can improve reliability [98].

In the following three sections, we shall present case studies demonstrating the value of SFG orientation measurements using amide I signals in a variety of different applications.

### Orientation of $\alpha$ -Helical Melittin Determined by Amide I Signals

Membrane-bound proteins and membrane-active peptides are important interfacial molecules of great interest, and SFG is well suited to their study in model lipid bilayers. (For more details on the model membrane, see Sect. 8.3.4.) SFG has recently been applied to study the effect of a variety of small, antimicrobial peptides in cell membranes [7]. The mechanism of activity for these peptides is of wide interest, and here the ability of SFG to determine complicated orientation distributions becomes valuable. Different models exist: It has been suggested that these peptides can either form a “carpet” parallel to the bilayer plane, or insert into the bilayer and form pores to disrupt cell membranes.

By combining ATR-FTIR with SFG, Chen et al. measured the orientation of the helical peptide melittin in a bilayer at the threshold concentration for antimicrobial activity; they found that two distinct orientations of the peptide were present simultaneously [42]. Using ATR-FTIR, only one parameter can be measured, namely, the intensity ratio of the s- and p-polarized ATR-FTIR absorbances. Thus, these results alone can yield only the average orientation. If every melittin molecule adopted the same orientation, ATR-FTIR would predict a tilt angle of  $54^\circ$  relative to the surface normal. However, the unique  $\langle \cos \theta \rangle$  and  $\langle \cos^3 \theta \rangle$  parameters measured by SFG were not consistent with either a  $\delta$ -distribution or a single Gaussian distribution (Fig. 8.6).

**Fig. 8.6**  $|\chi_{zzz}/\chi_{yyz}|$  ratio as a function of the  $\alpha$ -helix orientation angle, assuming a  $\delta$ -distribution or Gaussian distribution function. The shaded area represents the actual experimental result (Figures 8.6, 8.7 and 8.8 are reproduced with permission from Ref. [42]. © 2007, American Chemical Society)

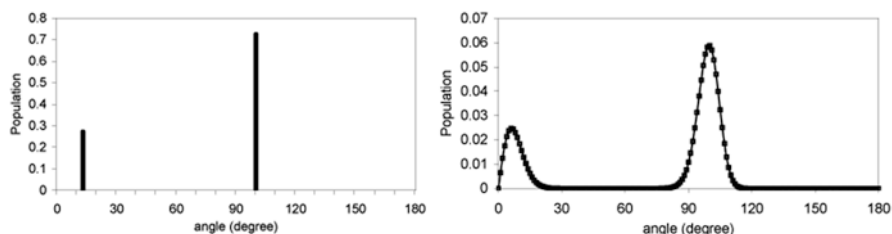
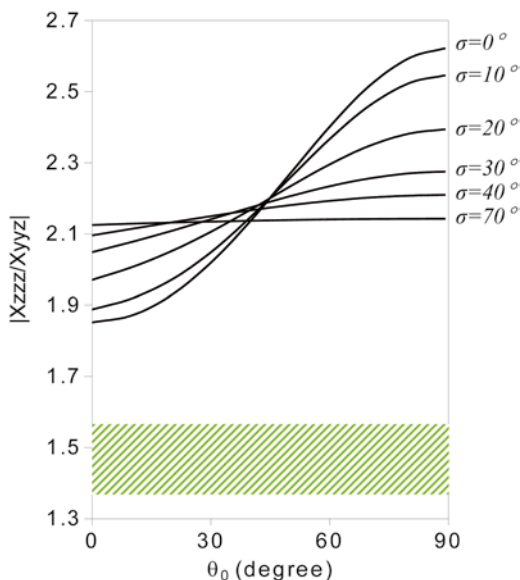


**Fig. 8.7** (a) Orientation distribution derived based on a dual  $\delta$ -distribution; (b) orientation distribution derived using the maximum-entropy function

Therefore, the orientation distribution must be more complicated. Under the assumption that two orientations of melittin existed simultaneously, combined SFG and ATR-FTIR results demonstrated that approximately 25 % of the melittin molecules lay down at a  $100^\circ$  angle, and the remainder stood up in the bilayer at a  $13^\circ$  angle (Fig. 8.7a). This more detailed picture resolves a conflict between previous ATR-FTIR measurements, which suggested that these peptides were either perpendicular *or* parallel to the membrane surface. In fact, *both* orientations are present, shown schematically in Fig. 8.8. To verify this, an additional method of data analysis was applied that did not require assuming the nature of the distribution to start.

For an unknown distribution, it has been shown that the maximum-entropy function provides a mathematical way to use multiple measurements to characterize the orientation while introducing the least bias. As shown in Fig. 8.7b, the resulting distribution was quite similar to what would be derived under the assumption of a

**Fig. 8.8** Schematic of two melittin orientations in the lipid bilayer

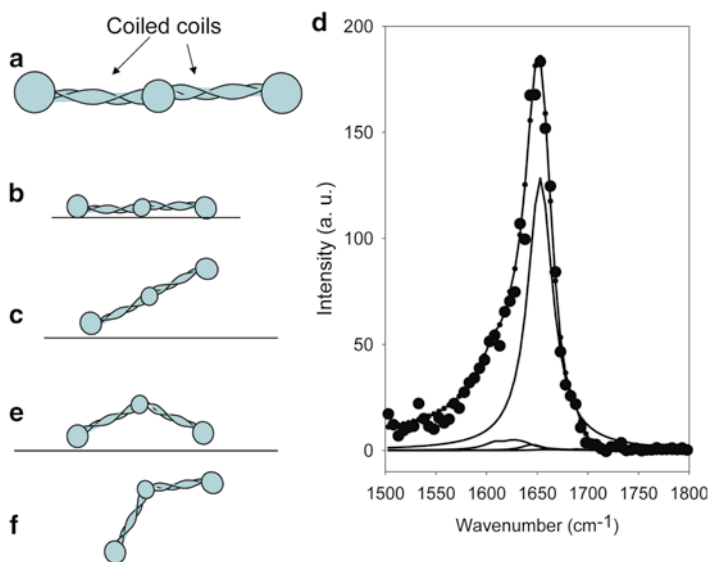
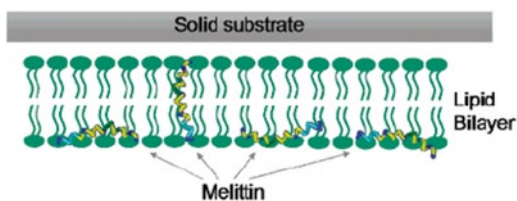


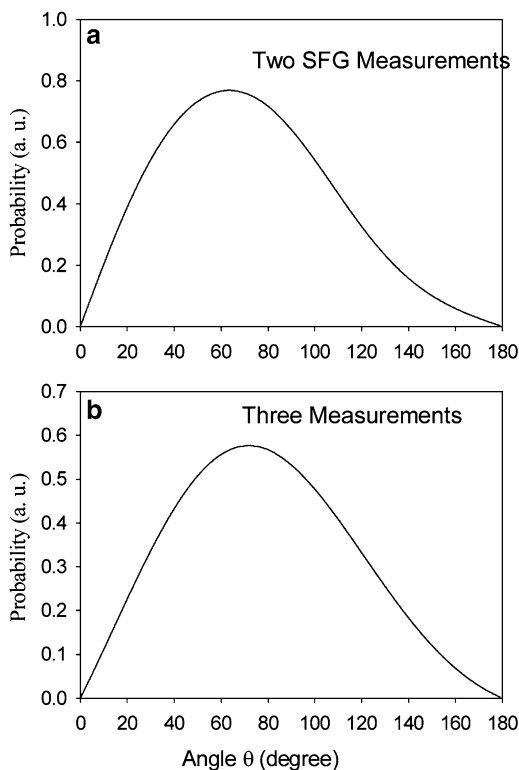
**Fig. 8.9** (a) Schematic of the fibrinogen native structure; (b), (c), (e), and (f): possible conformation of fibrinogen after adsorption to PS; (d) ssp SFG spectrum collected from fibrinogen molecules at the PS–solution interface (Adapted with permission from Ref. [47]. © 2008, American Chemical Society)

dual delta distribution. However, the maximum-entropy function requires no assumptions. This approach to data analysis will be particularly important when using SFG to characterize larger proteins with multiple distinct helical segments.

#### Orientation of $\alpha$ -Helical Coiled-Coils in Fibrinogen Determined by Amide I Signals

Fibrinogen is a blood protein that has been studied via a range of different techniques; it is well known that the surface conformation plays an important role in the formation of clots. A combination of vibrational spectroscopies was used to study the orientation distribution of two  $\alpha$ -helical coiled-coils of fibrinogen at the polystyrene (PS)–fibrinogen solution interface, Wang et al. found that adsorbed fibrinogen molecules adopt a bent structure at the interface [47].

**Fig. 8.10** Orientation distributions of fibrinogen coiled-coils deduced by (a) two and (b) three measurements (Reproduced with permission from Ref. [47]. © 2007, American Chemical Society)



Due to an approximate inversion symmetry in the native structure of fibrinogen (Fig. 8.9b, c), little signal would be expected if this was the adsorbed conformation. Experimentally, very strong SFG signals (Fig. 8.9d) were detected from  $\alpha$ -helical coiled-coils at the PS–fibrinogen solution interface, indicating that adsorbed fibrinogen molecules must adopt a bent structure instead (Fig. 8.9e, f).

In order to examine this bent structure in more detail, the orientation distribution of fibrinogen on PS was studied in two ways: first, by assuming a Gaussian distribution using SFG measurements alone (Fig. 8.10a), and then by using a combination of SFG and ATR-FTIR measurements to construct the orientation distribution using the maximum-entropy function (Fig. 8.10b), as outlined above. The two distributions were similar, showing that the Gaussian distribution is a good assumption; however, they were not identical, indicating that additional measurements would allow for a more accurate picture of the real distribution. Regardless, the distribution is quite broad, suggesting that adsorbed fibrinogen molecules can adopt a variety of orientations and conformations, possibly due to the nonuniform polymer surface. In contrast, melittin in bilayers adopted a narrow distribution due to the strong ordering of the lipid bilayer environment, which makes specific lipid–protein interactions more likely [42].

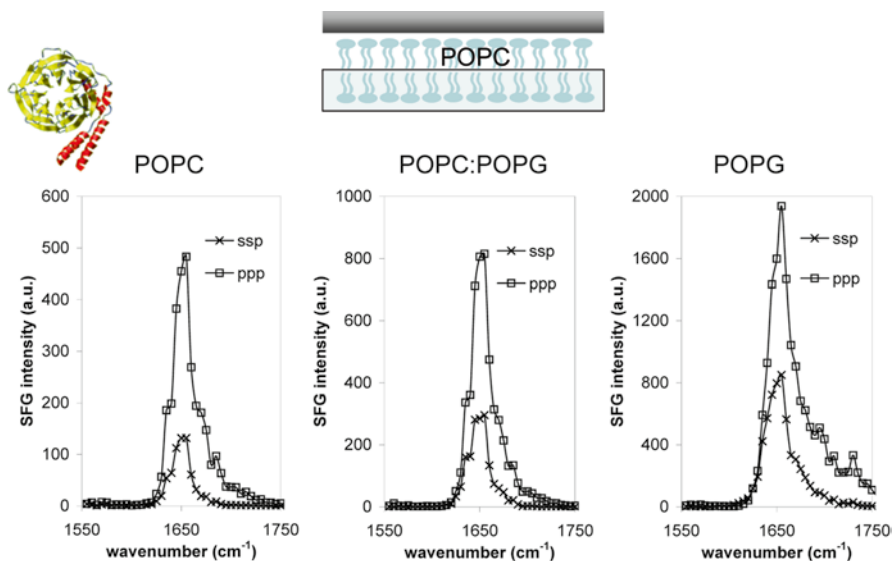


**Fig. 8.11** SFG spectra collected from G $\beta\gamma$  associated with different lipid bilayers: POPC:POPC; POPC:(POPC:POPG mixture); POPC:POPG. The weaker signal in each panel is collected using an ssp polarization combination; the stronger one is ppp. Intensity ratios of ssp and ppp SFG signals are varied in different lipid bilayers, indicating that G $\beta\gamma$  adopts different orientations. The orientation of G $\beta\gamma$  in the POPC:POPC bilayer is shown in the *upper left corner* (Figures 8.11, 8.12 and 8.13 reproduced with permission from Ref. [48]. © 2007, American Chemical Society)

### Orientation of G-Protein Deduced from SFG Amide I Signals of $\alpha$ -Helical Domains

As discussed above, the orientation of larger proteins may be determined by calculating the combined hyperpolarizability of all the helical segments in the molecule. In a study of the multihelix membrane signaling protein, G $\beta\gamma$ , Chen et al. used the orientation of  $\alpha$ -helical portions of the protein and the static crystal structure as a guide to the overall molecular orientation of the protein bound in a membrane; they demonstrated that the lipid composition can modulate that orientation (Fig. 8.11) [48]. This subunit of an important signaling protein is anchored to the bilayer via a geranylgeranyl group with a high membrane affinity. Significantly weaker signal intensities were observed in the absence of this group (Fig. 8.12): SFG experiments suggest that the geranylgeranyl group also anchors the protein in a specific orientation in preparation for binding (Fig. 8.13).

### $\beta$ -Sheets Yield Chiral Signals for Additional Measurements

Because  $\beta$ -sheets may be quasi-centrosymmetric, there was originally some question as to whether signals could be detected for this structure using SFG. In fact,

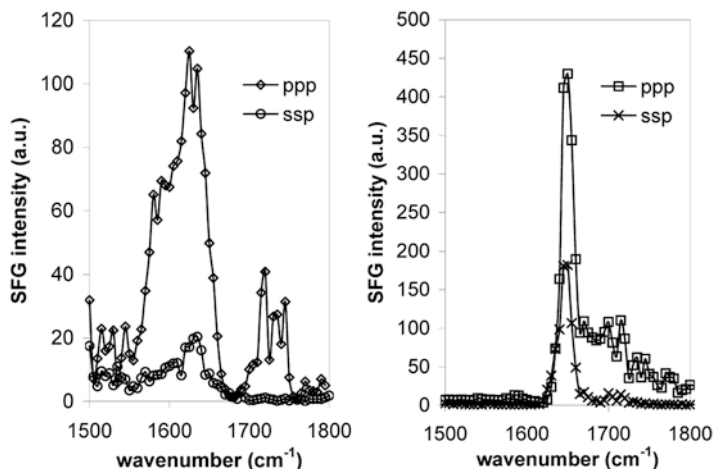


**Fig. 8.12** SFG ssp (weaker) and ppp (stronger) amide I spectra of interfacial  $G\beta\gamma$  adsorbed onto a POPG/POPG bilayer: (a) 5  $\mu\text{l}$  of 10 mg/ml geranylgeranylated  $G\beta\gamma$  was injected into the subphase, and stronger SFG signals indicative of an  $\alpha$ -helix structure were observed; (b) 25  $\mu\text{l}$  of 10 mg/ml of the soluble form of  $G\beta\gamma$  was brought into contact with the bilayer. Only relatively weak signals indicative of the  $\beta$ -sheet were observed

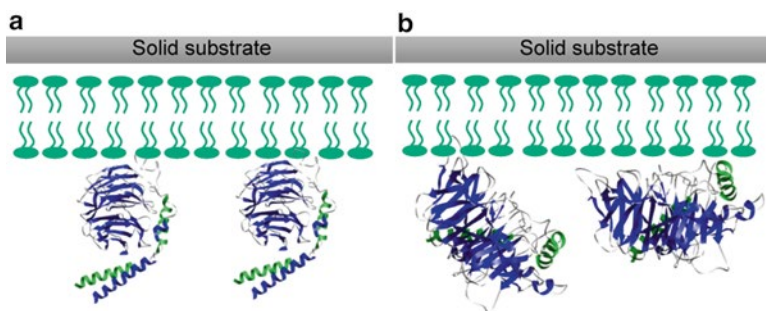


**Fig. 8.13** Schematics of  $G\beta\gamma$  adsorbed onto a POPG/POPG bilayer deduced from SFG spectra: (a) geranylgeranylated  $G\beta\gamma$ ; (b)  $G\beta\gamma$  with no geranylgeranyl group

Wang et al. have shown that  $\beta$ -sheets possess  $D_2$  symmetry; using a series of intermediate polarizations and careful fitting procedures, weak signals could be detected from a layer of adsorbed fibrinogen [49]. By using a small peptide (Tachyplesin I) with a greater fraction of  $\beta$ -sheet structure and high surface affinity, Wang's group could observe signals even without interference enhancement.

The symmetry of  $\beta$ -sheets allows for the detection of strong chiral signals that provide additional measurements [49]. This makes it possible to characterize both



tilt and twist angles at a complex interface (see Sect. 8.2.2.4, “Studying the Orientation of a  $\beta$ -sheet with SFG”). It has been shown that the chiral SFG signals observed originated with the layer of protein adsorbed on the surface, and not molecules in solution. Additional quantitative studies are expected as the study of  $\beta$ -sheets using SFG continues.

### **8.3.4 Planar-Supported Lipid Bilayers: A Model Membrane Environment**

#### **8.3.4.1 Introduction**

As outlined earlier, SFG provides powerful new tools for characterizing the structure of complicated proteins in the membrane environment; however, this same technique also makes it possible to understand changes in the lipid membrane itself. In particular, by taking advantage of isotope-labeled lipids, it is possible to monitor the orientation and ordering of lipid groups from both leaflets even as the protein interacts with the bilayer. This information is of particular importance to the study of interactions between antimicrobial peptides and cell membranes, for example, where changes in the bilayer structure have important consequences for understanding the mechanism, activity, and selectivity of antimicrobial peptides [1, 7].

#### **8.3.4.2 The Model System: Planar-Supported Lipid Bilayers (PSLB)**

The model membrane most commonly used in ATR-FTIR and SFG studies is the planar-supported lipid bilayer (PSLB) [99]. With the Langmuir–Blodgett and Langmuir–Schaefer techniques a single lipid bilayer is created on an optically transparent solid support. Much work has been done using SFG and a specially designed cell for temperature control to validate the model system as a useful mimic of the real lipid environment: Liu and Conboy have reported that these bilayer models show realistic behavior (such as phase-transition temperature) [100–102] when deposited on a thin optical substrate, providing evidence against the possibility of significant substrate effects. These experiments are very sensitive to molecular packing and ordering, including small changes in methyl and methylene group orientation for the lipid tails [20, 103].

#### **8.3.4.3 Asymmetric Bilayers Allow Study of Both Leaflets**

Using an asymmetric bilayer (such as with one leaflet deuterated and the other hydrogenated) enables time-dependent spectra to be examined for each individual

leaflet, yielding a detailed view of processes such as flip-flop [100] and membrane disruption by antimicrobial peptides [7].

Due to SFG's unique selection rules, changes in signal over time may be interpreted in light of bilayer disruption in each leaflet individually. By preparing a symmetric bilayer, for example, Chen et al. used time-dependent signals to study the kinetics of membrane disruption via small antimicrobial peptides and oligomers [104, 105]. If individually isotope-labeled leaflets are used instead (one hydrogenated and the other deuterated), it becomes possible to monitor changes in both leaflets at the same time [7, 100], including the orientation of methyl groups in the lipid tail [20, 103, 106–108]. Thus, in the case of a small antimicrobial oligomer, Chen et al. showed that the molecule acted as a “molecular knife” by disrupting primarily the outer leaflet of the bilayer and inserting at a certain critical concentration [104]. This concentration was similar to that observed as the minimum inhibitory concentration (MIC) in dye-leakage experiments using vesicles; however, SFG experiments provide a greater level of detail regarding the oligomer–bilayer interactions.

In addition to membrane bilayers, SFG has also been applied to the study of lipid or fatty acid mono- and multilayers [19, 54, 108–114]. From these studies, information on chain packing and conformation can be obtained.

### **8.3.5 Other Biomolecules: SFG Studies of Nucleic Acids**

SFG has recently been applied to the study of ordered DNA layers on solid surfaces, an area of potential interest in the development of high-throughput sensors and DNA “chips” for gene sequencing [115]. In addition to the conformational sensitivity of the technique, both single-stranded [116] and duplex [117] DNA oligonucleotides may be studied in terms of molecular chirality.

## **8.4 Future Directions, Summary, and Conclusions**

In the decade since SFG was first applied to biological molecules, a wide variety of increasingly complex systems have been studied (including proteins, peptides, and lipids). This trend is expected to continue, as improved methods of data analysis open the possibility of studying larger proteins adopting multiple distributions.

A number of advances in experimental technique are also possible. For example, doubly resonant SFG (DRSFG) has seen only limited application to biological systems as yet, but this technique promises very large improvements in sensitivity for very dilute samples. The theoretical foundation for double-resonance IR-UV(vis) SFG has been studied previously [57, 58]. Using DRSFG allows for more selective spectroscopic information and better assignment of the vibrational modes; in the future, DRSFG can be developed into a powerful technique to study biological molecules at interfaces.

SFG microscopes have also recently emerged [118–121]. Initial work has focused on the study of patterned self-assembled monolayers [122–124], demonstrating a spatial resolution of better than 3  $\mu\text{m}$ . We believe that SFG imaging will be valuable in biology for the study of questions such as the homogeneity of protein adsorption and how biomolecules respond to patterned surfaces.

Lastly (as discussed in Sect. 8.3.3.4.1), SFG can be combined with measurements from other techniques in order to characterize the orientation of more complicated molecules in more detail.

SFG has only recently been applied to the study of biological interfaces, yet the growth of the field has been extremely rapid. New advances in instrumentation design and reliability, as well as improved methods of data analysis, have opened the way for study of a wide range of biologically interesting samples. In many cases, these early studies are already giving way to more detailed explorations of the complex behavior of biomolecules at surfaces. The following areas are expected to see increased activity in the future:

- Membrane proteins are critically important, yet difficult to crystallize. It has been demonstrated that SFG, combined with other vibrational spectroscopic techniques, can detect these proteins in situ and provide sufficient measurements to characterize important structural details. Simultaneously, lipid signals can be studied to determine the effect of the protein on the membrane environment.
- Likewise, interactions between small peptides and cell membranes can be studied, with important consequences for drug design.
- Preliminary work has shown that SFG can also be used to probe protein–molecule interactions at the surface: Ligand binding is critical to drug design and also important for the development of biosensors.
- Interest in the functional behavior of DNA and RNA has grown in recent years. The binding of aptamers and “molecular beacons” are examples of sensing applications in which interfacial sensitivity will prove valuable.
- Lastly, work on biocompatibility and biofouling is expected to continue, as SFG provides an excellent and label-free probe for molecular ordering. By understanding the interactions that drive protein adsorption, researchers may develop better coatings and materials.

**Acknowledgments** We thank the Office of Naval Research (CN00014-02-1-0832), the National Science Foundation (CHE-0315857 and CHE-0449469), the Beckman Foundation, and the University of Michigan for their support.

## References

1. Zasloff M. Antimicrobial peptides of multicellular organisms. *Nature*. 2002;415:389–95.
2. Jiang Y, Lee A, Chen J, Ruta V, Cadene M, Chait BT, et al. X-ray structure of a voltage-dependent K<sup>+</sup> channel. *Nature*. 2003;423:33–41.
3. Horbett TA, Brash JL, editors. Proteins at interfaces II: fundamentals and applications, ACS symposium series. Washington, DC: American Chemical Society; 1995. p. 561.

4. Yebra DM, Kiil S, Dam-Johansen K. Antifouling technology—past, present and future steps towards efficient and environmentally friendly antifouling coatings. *Prog Org Coat.* 2004;50:75–104.
5. Gray JJ. The interaction of proteins with solid surfaces. *Curr Opin Struct Biol.* 2004; 14:110–5.
6. Nakanishi K, Sakiyama T, Imamura K. On the adsorption of proteins on solid surfaces, a common but very complicated phenomenon. *Biosci Bioeng.* 2001;91:233–44.
7. Chen X, Chen Z. SFG studies on interactions between antimicrobial peptides and supported lipid bilayers. *Biochim Biophys Acta.* 2006;1758:1257–73.
8. Wang J, Clarke ML, Chen X, Even MA, Johnson WC, Chen Z. *Surf Sci.* 2005;587:1–11.
9. Chen Z, Shen Y, Somorjai GA. Molecular studies on protein conformations at polymer/liquid interfaces using sum frequency generation vibrational spectroscopy. *Annu Rev Phys Chem.* 2002;53:437–65.
10. Bain CD. Sum-frequency vibrational spectroscopy of the solid/liquid interface. *J Chem Soc Faraday Trans.* 1995;91:1281–96.
11. Eisenthal KB. Liquid interfaces probed by second-harmonic and sum-frequency spectroscopy. *Chem Rev.* 1996;96:1343–60.
12. Richmond GL. Structure and bonding of molecules at aqueous surfaces. *Annu Rev Phys Chem.* 2001;52:357–89.
13. Shen YR, Ostroverkhov V. Sum-frequency vibrational spectroscopy on water interfaces: polar orientation of water molecules at interfaces. *Chem Rev.* 2006;106:1140–54.
14. Gopalakrishnan S, Liu D, Allen HC, Kuo M, Shultz MJ. Vibrational spectroscopic studies of aqueous interfaces: salts, acids, bases, and nanodrops. *Chem Rev.* 2006;106:1155–75.
15. Zhang D, Gutow JH, Eisenthal KB. Structural phase transitions of small molecules at air/water interfaces. *J Chem Soc Faraday Trans.* 1996;92:539–43.
16. Superfine R, Huang JY, Shen YR. Nonlinear optical studies of the pure liquid/vapor interface: vibrational spectra and polar ordering. *Phys Rev Lett.* 1991;66:1066–9.
17. Du Q, Superfine R, Freysz E, Shen YR. Vibrational spectroscopy of water at the vapor/water interface. *Phys Rev Lett.* 1993;15:2313–6.
18. Brown MG, Walker DS, Raymond EA, Richmond GL. Vibrational sum-frequency spectroscopy of alkane/water interfaces: experiment and theoretical simulation. *J Phys Chem B.* 2003;107:237–44.
19. Harper KL, Allen HC. Competition between DPPC and SDS at the air-aqueous interface. *Langmuir.* 2007;23:8925–31.
20. Conboy JC, Messmer MC, Richmond GL. Investigation of surfactant conformation and order at the liquid–liquid interface by total internal reflection sum-frequency vibrational spectroscopy. *J Phys Chem.* 1996;100:7617–22.
21. Baldelli S, Mailhot G, Ross P, Shen YR, Somorjai GA. Potential dependent orientation of acetonitrile on platinum (111) electrode surface studied by sum frequency generation. *J Phys Chem B.* 2001;105:654–62.
22. Lahann J, Mitragotri S, Tran T, Kaido H, Sundaram J, Choi IS, et al. A reversibly switching surface. *Science.* 2003;299:371–4.
23. Chou KC, Kim J, Baldelli S, Somorjai GA. Vibrational spectroscopy of carbon monoxide, acetonitrile, and phenylalanine adsorbed on liquid electrode interfaces by sum frequency generation. *J Electroanal Chem.* 2003;554–555:253–63.
24. Chen Z, Gracias DH, Somorjai GA. Sum frequency generation (SFG)–surface vibrational spectroscopy studies of buried interfaces: catalytic reaction intermediates on transition metal crystal surfaces at high reactant pressures; polymer surface structures at the solid–gas and solid–liquid interfaces. *Appl Phys B.* 1999;68:549–57.
25. Rupprechter G. A surface science approach to ambient pressure catalytic reactions. *Catal Today.* 2007;126:3–17.
26. Somorjai GA. New model catalysts (platinum nanoparticles) and new techniques (SFG and STM) for studies of reaction intermediates and surface restructuring at high pressures during catalytic reactions. *Appl Surf Sci.* 1997;121–122:1–19.

27. Belkin MA, Shen YR. Doubly resonant IR-UV sum-frequency vibrational spectroscopy on molecular chirality. *Phys Rev Lett.* 2003;91:213907.
28. Belkin MA, Kulakov TA, Ernst KH, Han SH, Shen YR. Resonant sum-frequency generation in chiral liquids. *Opt Mater.* 2003;21:1–5.
29. Ji N, Shen YR. A dynamic coupling model for sum frequency chiral response from liquids composed of molecules with a chiral side chain and an achiral chromophore. *J Am Chem Soc.* 2005;127:12933–42.
30. Briggman KA, Stephenson JC, Wallace WE, Richter LJ. Absolute molecular orientational distribution of the polystyrene surface. *J Phys Chem B.* 2001;105:2785–91.
31. Gautam KS, Schwab AD, Dhinojwala A, Zhang D, Dougal SM, Yeganeh MS. Molecular structure of polystyrene at air/polymer and solid/polymer interfaces. *Phys Rev Lett.* 2000;85:3854–7.
32. Shen YR. *Principles of nonlinear optics (Wiley series in pure and applied optics)*. New York: Wiley; 1984. p. 563.
33. Wang J, Even MA, Chen X, Schmaier AH, Waite JH, Chen Z. Detection of amide I signals of interfacial proteins in situ using SFG. *J Am Chem Soc.* 2003;125:9914–5.
34. Zhuang X, Miranda PB, Kim D, Shen YR. Mapping molecular orientation and conformation at interfaces by surface nonlinear optics. *Phys Rev B.* 1999;59:12632–40.
35. Wang J, Paszti Z, Even MA, Chen Z. Measuring polymer surface ordering differences in air and water by sum frequency generation vibrational spectroscopy. *J Am Chem Soc.* 2002;124:7016–23.
36. Lambert AG, Davies PB, Neivandt D. Implementing the theory of sum frequency generation vibrational spectroscopy: a tutorial review. *J Appl Spectrosc Rev.* 2005;40:103.
37. Hirose C, Akamatsu N, Domen K. Formulas for the analysis of the surface SFG spectrum and transformation coefficients of cartesian SFG tensor components. *Appl Spectrosc.* 1992;46:1051–72.
38. Moad AJ, Simpson GJ. A unified treatment of selection rules and symmetry relations for sum-frequency and second harmonic spectroscopies. *J Phys Chem B.* 2004;108:3548–62.
39. Lee S, Wang J, Krimm S, Chen Z. Irreducible representation and projection operator application to understanding nonlinear optical phenomena: hyper-Raman, sum frequency generation, and four-wave mixing spectroscopy. *J Phys Chem A.* 2006;110:7035–44.
40. Pauling L, Corey RB. Atomic coordinates and structure factors for two helical configurations of polypeptide chains. *Proc Natl Acad Sci U S A.* 1951;37:235–40.
41. Pauling L, Corey RB. Configurations of polypeptide chains with favored orientations around single bonds: two new pleated sheets. *Proc Natl Acad Sci U S A.* 1951;37:729–40.
42. Chen X, Wang J, Boughton AP, Kristalyn CB, Chen Z. Multiple orientation of melittin inside a single lipid bilayer determined by combined vibrational spectroscopic studies. *J Am Chem Soc.* 2007;129:1420–7.
43. Marsh D, Muller M, Schmitt F. Orientation of the infrared transition moments for an alpha-helix. *Biophys J.* 2000;78:2499–510.
44. Rintoul L, Carter EA, Stewart SD, Fredericks PM. Keratin orientation in wool and feathers by polarized Raman spectroscopy. *Biopolymers.* 2000;57:19–28.
45. Lee S, Krimm S. Ab initio-based vibrational analysis of alpha-poly(L-alanine). *Biopolymers.* 1998;46:283–317.
46. Lee S, Krimm S. Polarized Raman spectra of oriented films of alpha-helical poly(L-alanine) and its N-deuterated analogue. *J Raman Spectrosc.* 1998;29:73–80.
47. Wang J, Lee S, Chen Z. Quantifying the ordering of adsorbed proteins in situ. *J Phys Chem B.* 2008;112:2281–90.
48. Chen X, Boughton AP, Tesmer JGG, Chen Z. In situ investigation of heterotrimeric G protein  $\beta\gamma$  subunit binding and orientation on membrane bilayers. detection of chiral sum frequency generation vibrational spectra of proteins and peptides at interfaces in situ. *J Am Chem Soc.* 2007;129:12658–9.
49. Wang J, Chen X, Clarke ML, Chen Z. Detection of chiral sum frequency generation vibrational spectra of proteins and peptides at interfaces in situ. *Proc Natl Acad Sci U S A.* 2005;102:4978–83.

50. Chen X, Wang J, Sniadecki JJ, Even MA, Chen Z. Probing  $\alpha$ -helical and  $\beta$ -sheet structures of peptides at solid/liquid interfaces with SFG. *Langmuir*. 2005;21:2662–4.
51. Ong TH, Davies PB, Bain CD. Sum-frequency spectroscopy of monolayers of alkoxy-terminated alkanethiols in contact with liquids. *Langmuir*. 1993;9:1836–45.
52. Wang J, Chen C, Buck SM, Chen Z. Molecular chemical structure on poly(methyl methacrylate) (PMMA) surface studied by sum frequency generation (SFG) vibrational spectroscopy. *J Phys Chem B*. 2001;105:12118–25.
53. Esenturk O, Walker RA. Surface vibrational structure at alkane liquid/vapor interfaces. *J Chem Phys*. 2006;125:174701.
54. Holman J, Davies PB, Nishida T, Ye S, Neivandt DJ. Sum frequency generation from Langmuir-Blodgett multilayer films on metal and dielectric substrates. *J Phys Chem B*. 2005;109:18723–32.
55. Beattie DA, Haydock S, Bain CD. A comparative study of confined organic monolayers by Raman scattering and sum-frequency spectroscopy. *Vib Spectrosc*. 2000;24:109–23.
56. Huang JY, Shen YR. Theory of doubly resonant infrared-visible sum-frequency and difference-frequency generation from adsorbed molecules. *Phys Rev A*. 1994;49:3973–81.
57. Raschke MB, Hayashi M, Lin SH, Shen YR. Doubly-resonant sum-frequency generation spectroscopy for surface studies. *Chem Phys Lett*. 2002;359:367–72.
58. Hayashi M, Lin SH, Raschke MB, Shen YR. A molecular theory for doubly resonant IR–UV–vis sum-frequency generation. *J Phys Chem A*. 2002;106:2271–82.
59. Dreesen L, Humbert C, Sartenaer Y, Caudano Y, Volcke C, Mani AA, et al. Electronic and molecular properties of an adsorbed protein monolayer probed by two-color sum-frequency generation spectroscopy. *Langmuir*. 2004;20:7201–7.
60. Chen Z, Ward R, Tian Y, Malizia F, Gracias DH, Shen YR, et al. Interaction of fibrinogen with surfaces of end-group-modified polyurethanes: a surface-specific sum-frequency-generation vibrational spectroscopy study. *J Biomed Mater Res*. 2002;62:254–64.
61. Mermut O, Phillips DC, York RL, McCrea KR, Ward RS, Somorjai GA. In situ adsorption studies of a 14-amino acid leucine-lysine peptide onto hydrophobic polystyrene and hydrophilic silica surfaces using quartz crystal microbalance, atomic force microscopy, and sum frequency generation vibrational spectroscopy. *J Am Chem Soc*. 2006;128:3598–607.
62. Phillips DC, York RL, Mermut O, McCrea KR, Ward RS, Somorjai GA. Side chain, chain length, and sequence effects on amphiphilic peptide adsorption at hydrophobic and hydrophilic surfaces studied by sum-frequency generation vibrational spectroscopy and quartz crystal microbalance. *J Phys Chem C*. 2007;111:255–61.
63. Watry MR, Richmond GL. Orientation and conformation of amino acids in monolayers adsorbed at an oil/water interface as determined by vibrational sum-frequency spectroscopy. *J Phys Chem B*. 2002;106:12517–23.
64. Evans-Nguyen KM, Fuierer RR, Fitchett BD, Tolles LR, Conboy JC, Schoenfish MH. Changes in adsorbed fibrinogen upon conversion to fibrin. *Langmuir*. 2006;22:5115–21.
65. Kim J, Cremer PS. Elucidating changes in interfacial water structure upon protein adsorption. *Chemphyschem*. 2001;2:543–6.
66. Kim J, Kim G, Cremer PS. Investigations of water structure at the solid/liquid interface in the presence of supported lipid bilayers by vibrational sum frequency spectroscopy. *Langmuir*. 2001;17:7255–60.
67. Wang J, Buck SM, Even MA, Chen Z. Molecular responses of proteins at different interfacial environments detected by sum frequency generation vibrational spectroscopy. *J Am Chem Soc*. 2002;124:13302–5.
68. Wang J, Buck SM, Chen Z. Sum frequency generation vibrational spectroscopy studies on protein adsorption. *J Phys Chem B*. 2002;106:11666–72.
69. Kim J, Somorjai GA. Molecular packing of lysozyme, fibrinogen, and bovine serum albumin on hydrophilic and hydrophobic surfaces studied by infrared-visible sum frequency generation and fluorescence microscopy. *J Am Chem Soc*. 2003;125:3150–8.
70. Kim G, Gurau M, Kim J, Cremer PS. Investigations of lysozyme adsorption at the air/water and quartz/water interfaces by vibrational sum frequency spectroscopy. *Langmuir*. 2002;18:2807–11.

71. Jung SY, Lim SM, Albertorio F, Kim G, Gurau MC, Yang RD, et al. The Vroman effect: a molecular level description of fibrinogen displacement. *J Am Chem Soc.* 2003;125:12782–6.
72. Chen X, Sagle LB, Cremer PS. Urea orientation at protein surfaces. *J Am Chem Soc.* 2007;129:15104–5.
73. Dreesen L, Sartenaer Y, Humbert C, Mani AA, Méthivier C, Pradier C, et al. Probing ligand-protein recognition with sum-frequency generation spectroscopy: the avidin-biotin case. *Chemphyschem.* 2004;5:1719–25.
74. Dreesen L, Sartenaer Y, Humbert C, Mani AA, Lemaire JJ, Méthivier C, et al. Sum-frequency generation spectroscopy applied to model biosensors systems. *Thin Solid Films.* 2004;464–465:373–8.
75. Wang J, Buck SM, Chen Z. The effect of surface coverage on conformation changes of bovine serum albumin molecules at the air–solution interface detected by sum frequency generation vibrational spectroscopy. *Analyst.* 2003;128:773–8.
76. Kim J, Koffas TS, Lawrence CC, Somorjai GA. Surface structural characterization of protein- and polymer-modified polystyrene microspheres by infrared-visible sum frequency generation vibrational spectroscopy and scanning force microscopy. *Langmuir.* 2004;20:4640–6.
77. Arkin I. Isotope-edited IR, spectroscopy for the study of membrane proteins. *Curr Opin Chem Biol.* 2006;10:394–401.
78. Arkin IT, MacKenzie KR, Brunger AT. Site-directed dichroism as a method for obtaining rotational and orientational constraints for oriented polymers. *J Am Chem Soc.* 1997;119:8973–80.
79. Torres J, Adams PD, Arkin IT. Use of a new label,  $(^{13}\text{C})\text{C}=\text{C}(^{18}\text{O})$ , in the determination of a structural model of phospholamban in a lipid bilayer. Spatial restraints resolve the ambiguity arising from interpretations of mutagenesis data. *J Mol Biol.* 2000;300:677–85.
80. Wang J, Paszti Z, Clarke ML, Chen X, Chen Z. Deduction of structural information of interfacial proteins by combined vibrational spectroscopic methods. *J Phys Chem B.* 2007;111:6088–95.
81. Wang J, Clarke ML, Zhang Y, Chen X, Chen Z. Using isotope-labeled proteins and sum frequency generation vibrational spectroscopy to study protein adsorption. *Langmuir.* 2003;19:7862–6.
82. Clarke ML, Chen Z. Polymer surface reorientation after protein adsorption. *Langmuir.* 2006;22:8627–30.
83. Vroman L. Effect of adsorbed proteins on the wettability of hydrophilic and hydrophobic solids. *Nature.* 1962;196:476–7.
84. Pászti Z, Wang J, Clarke ML, Chen Z. Sum frequency generation vibrational spectroscopy studies of protein adsorption on oxide covered Ti surfaces. *J Phys Chem B.* 2004;108:7779–87.
85. Moore WH, Krimm S. Transition dipole coupling in Amide I modes of betapolypeptides. *Proc Natl Acad Sci U S A.* 1975;72:4933–5.
86. Shai Y. From innate immunity to de-novo designed antimicrobial peptides. *Curr Pharm Des.* 2002;8:715–25.
87. Huang HW. Action of antimicrobial peptides: two-state model. *Biochemistry.* 2000;39:8347–52.
88. Wang J, Paszti Z, Even MA, Chen Z. Interpretation of sum frequency generation vibrational spectra of interfacial proteins by the thin film model. *J Phys Chem B.* 2004;108:3625–32.
89. Knoesen A, Pakalnis S, Wang M, Wise WD, Lee N, Frank CW. Sum-frequency spectroscopy and imaging of aligned helical polypeptides. *IEEE J Sel Top Quant.* 2004;10:1154–63.
90. Clarke ML, Wang J, Chen Z. Conformational changes of fibrinogen after adsorption. *J Phys Chem B.* 2005;109:22027–35.
91. Chen X, Wang J, Paszti Z, Wang F, Schrauben JN, Tarabara VV, et al. Ordered adsorption of coagulation factor XII on negatively charged polymer surfaces probed by sum frequency generation vibrational spectroscopy. *Anal Bioanal Chem.* 2007;388:65–72.
92. Cheng J, Jia YK, Zheng G, Xie XS. Laser-scanning coherent anti-Stokes Raman scattering microscopy and applications to cell biology. *Biophys J.* 2002;83:502–9.
93. Cheng JX, Xie XS. Coherent anti-Stokes Raman scattering microscopy: instrumentation, theory, and applications. *J Phys Chem B.* 2004;108:827–40.

94. Volkmer A. Vibrational imaging and microspectroscopies based on coherent anti-Stokes Raman scattering microscopy. *J Phys D Appl Phys*. 2005;38:R59–81.
95. Moad AJ, Moad CW, Perry JM, Wampler RD, Goeken GS, Begue NJ, et al. NLOPredict: visualization and data analysis software for nonlinear optics. *J Comp Chem*. 2007;28:1996–2002.
96. Moad AJ, Simpson GJ. Self-consistent approach for simplifying the molecular interpretation of nonlinear optical and multiphoton phenomena. *J Phys Chem A*. 2005;109:1316–23.
97. Perry JM, Moad AJ, Begue NJ, Wampler RD, Simpson GJ. Electronic and vibrational second-order nonlinear optical properties of protein secondary structural motifs. *J Phys Chem B*. 2005;109:20009–26.
98. Wang J, Clarke ML, Chen Z. Polarization mapping: a method to improve sum frequency generation spectral analysis. *Anal Chem*. 2004;76:2159–67.
99. Tamm LK, McConnell HM. Supported phospholipid bilayers. *Biophys J*. 1985;47:105–13.
100. Liu J, Conboy JC. Direct measurement of the transbilayer movement of phospholipids by sum-frequency vibrational spectroscopy. *J Am Chem Soc*. 2004;126:8376–7.
101. Liu J, Conboy JC. Phase transition of a single lipid bilayer measured by sum-frequency vibrational spectroscopy. *J Am Chem Soc*. 2004;126:8894–5.
102. Liu J, Conboy J. 1,2-diacyl-phosphatidylcholine flip-flop measured directly by sum-frequency vibrational spectroscopy. *Biophys J*. 2005;89:2522–32.
103. Messmer MC, Conboy JC, Richmond GL. Observation of molecular ordering at the liquid-liquid interface by resonant sum frequency generation. *J Am Chem Soc*. 1995;117:8039–40.
104. Chen X, Tang H, Even MA, Wang J, Tew GN, Chen Z. Observing a molecular knife at work. *J Am Chem Soc*. 2006;128:2711–4.
105. Chen X, Wang J, Kristalyn CB, Chen Z. Real-time structural investigation of a lipid bilayer during its interaction with melittin using sum frequency generation vibrational spectroscopy. *Biophys J*. 2007;93:866–75.
106. Hirose C, Akamatsu N, Domen K. Formulas for the analysis of surface sum-frequency generation spectrum by CH stretching modes of methyl and methylene groups. *J Chem Phys*. 1992;96:997–1004.
107. Hirose C, Yamamoto H, Akamatsu N, Domen K. Orientation analysis by simulation of vibrational sum frequency generation spectrum: CH stretching bands of the methyl group. *J Phys Chem*. 1993;97:10064–9.
108. Ma G, Allen HC. DPPC Langmuir monolayer at the air-water interface: probing the tail and head groups by vibrational sum frequency generation spectroscopy. *Langmuir*. 2006;22:5341–9.
109. Voss LF, Hadad CM, Allen HC. Competition between atmospherically relevant fatty acid monolayers at the air/water interface. *J Phys Chem B*. 2006;110:19487–90.
110. Muller M, Schins JM, Roke S, Bonn M. In: Conchello J, Cogswell CJ, Wilson T, editors. Phase transitions in a lipid monolayer observed with vibrational sum-frequency generation. *SPIE Vol. 4964*, 2003. p. 90–97.
111. Ye S, Noda H, Morita S, Uosaki K, Osawa M. Surface molecular structures of Langmuir/Blodgett films of stearic acid on solid substrates studied by sum frequency generation spectroscopy. *Langmuir*. 2003;19:2238–42.
112. Ye S, Noda H, Nishida T, Morita S, Osawa M. Cd<sup>2+</sup>-induced interfacial structural changes of Langmuir–Blodgett films of stearic acid on solid substrates: a sum frequency generation study. *Langmuir*. 2004;20:357–65.
113. Roke S, Schins J, Miller M, Bonn M. Vibrational spectroscopic investigation of the phase diagram of a biomimetic lipid monolayer. *Phys Rev Lett*. 2003;90:128101.
114. Bonn M, Roke S, Berg O, Juurlink F, Stamouli A, Muller M. A molecular view of cholesterol-induced condensation in a lipid monolayer. *J Phys Chem B*. 2004;108:19083–5.
115. Ramsay G. DNA chips: state-of-the art. *Nat Biotechnol*. 1998;16:40–4.
116. Sartenaer Y, Tourillon G, Dreesen L, Lis D, Mani A, Thiry P, et al. Sum-frequency generation spectroscopy of DNA monolayers. *Biosens Bioelectron*. 2007;22:2179–83.
117. Stokes GY, Gibbs-Davis JM, Boman FC, Stepp BR, Condie AG, Nguyen ST, et al. Making “sense” of DNA. *J Am Chem Soc*. 2007;129:7492–3.



118. Florsheimer M, Brillert C, Fuchs H. Chemical imaging of interfaces by sum frequency microscopy. *Langmuir*. 1999;15:5437–9.
119. Shen Y, Swiatkiewicz J, Winiarz J, Markowicz P, Prasad PN. Second-harmonic and sum-frequency imaging of organic nanocrystals with photon scanning tunneling microscope. *Appl Phys Lett*. 2000;77:2946–8.
120. Humbert B, Grausem J, Burneau A, Spajer M, Tadjeddine A. Step towards sum frequency generation spectromicroscopy at a submicronic spatial resolution. *Appl Phys Lett*. 2001;78:135–7.
121. Schaller RD, Saykally RJ. Near-field infrared sum-frequency generation imaging of chemical vapor deposited zinc selenide. *Langmuir*. 2001;17:2055–8.
122. Hoffmann DMP, Kuhnke K, Kern K. Sum-frequency generation microscope for opaque and reflecting samples. *Rev Sci Instrum*. 2002;73:3221–6.
123. Kuhnke K, Hoffmann DMP, Wu XC, Bittner AM, Kern K. Chemical imaging of interfaces by sum-frequency generation microscopy: application to patterned self-assembled monolayers. *Appl Phys Lett*. 2003;83:3830–2.
124. Cimatu K, Baldelli S. Sum frequency generation microscopy of microcontact-printed mixed self-assembled monolayers. *J Phys Chem B*. 2006;110:1807–13.

# Chapter 9

## Near-Field Scanning Optical Microscopy: A New Tool for Exploring Structure and Function in Biology

Nicholas E. Dickenson, Olivia L. Mooren, Elizabeth S. Erickson,  
and Robert C. Dunn

**Abstract** Optical microscopy in the biological sciences has proven invaluable for understanding structure and dynamics in these complicated systems. It is a noninvasive tool that is amenable with fragile samples and is easily implemented under physiological conditions. It also benefits from a wide array of contrast mechanisms that can be exploited to gain detailed insight into sample properties. One limitation, however, concerns spatial resolution, which is limited to approximately half the excitation wavelength by the diffraction of light. Overcoming this limitation has motivated the development of near-field scanning optical microscopy (NSOM) or scanning near-field optical microscopy (SNOM). NSOM uses specially fabricated probes to deliver light down to the nanometric dimension, enabling optical microscopy with a spatial resolution of tens of nanometers. For the biological sciences, NSOM can simultaneously map sample fluorescence and topography with high spatial resolution and single-molecule detection limits. This makes NSOM a powerful new tool for understanding biological structure at the nanometric dimension.

### 9.1 Introduction

The ability to view and study biological structures directly on the spatial dimension on which they exist has proven invaluable for understanding structure function relationships. Historically, optical microscopy has proven particularly informative and throughout the years has steadily enhanced our understanding of tissue and cellular structure. Optical microscopy provides a relatively inexpensive, versatile platform for studying biological samples, with a wide array of complementary contrast

---

N.E. Dickenson • O.L. Mooren • E.S. Erickson • R.C. Dunn (✉)  
Department of Chemistry, Ralph N. Adams Institute for Bioanalytical Chemistry,  
The University of Kansas, 2030 Becker Drive, Lawrence, KS 66047, USA  
e-mail: [rdunn@ku.edu](mailto:rdunn@ku.edu)

mechanisms. For example, optical techniques can provide high time resolution, polarization and spectroscopic capabilities, high specificity, and single-molecule fluorescence-detection limits. Moreover, these can all be applied to living systems under biologically relevant conditions in a noninvasive manner.

One limitation of conventional optical microscopy, however, revolves around the maximal spatial resolution. When lenses are used to focus light, the maximal spatial resolution is limited by the diffraction of light and is generally restricted to half the excitation wavelength. When working in the visible part of the spectrum, therefore spatial resolution with aberration free optics is restricted to approximately 250–300 nm for conventional microscopy. Since many biologically interesting structures exist on smaller scales, other microscopy approaches have been developed.

Transmission electron microscopy (TEM) and scanning electron microscopy (SEM) have proven very powerful for understanding biological structures beyond the reach of optical techniques. These methods can resolve structures down to the nanometer scale and have been exploited to understand tissue architecture, membrane organization, and macromolecular structure, to name a few. These techniques have combined to provide a unique window into biological structures from which a wealth of functional data has been extracted. While these techniques offer vastly improved spatial resolution over optical microscopy, they do require extensive sample preparation and necessitate that the samples be in vacuum. These requirements can limit the applications and preclude the study of viable biological samples. With the development of scanning probe microscopy (SPM) techniques such as atomic force microscopy (AFM), however, achieving nanometric spatial resolution on viable biological tissues is now routine.

AFM uses a small stylus to interrogate sample surfaces and can be implemented on unfixed biological samples under buffered conditions. A number of AFM methods have been developed to probe various aspects of the sample surface, but, in general, topography information is the key parameter extracted from these measurements. These methods have nanometric spatial resolution, require very little sample preparation, and are, in general, minimally perturbative to the sample. However, since these measurements do rely mostly on topography, they lack the specificity inherent in immunofluorescence or in studies done with fluorescent proteins.

Optical microscopy, electron microscopy, and to a lesser extent scanning probe microscopy have proven important tools for probing biological structure and function. Near-field scanning optical microscopy (NSOM) is a technique that can complement these more established methods. In general, the goal behind the development of NSOM was to create a technique that combined the favorable aspects of the more established microscopies mentioned earlier. NSOM is a light-based microscopy that retains the specificity, spectral and polarization capabilities, and high time resolution inherent in optical microscopy. NSOM, however, circumvents the diffraction barrier that limits the spatial resolution in lens-based optical microscopy and thus provides a spatial resolution nearing that of electron microscopy and other scanning probe techniques.

Here we briefly review the basic concepts of NSOM, focusing on aperture-based methods. Following a brief overview of the technical aspects, several applications to biological samples will be discussed. These examples will help illustrate the capabilities of NSOM and also highlight some of the difficulties involved in probing biological systems with NSOM. These difficulties have largely limited NSOM applications to fixed biological systems. Finally, we will discuss progress in extending these measurements to viable samples, which has proven extremely difficult.

## 9.2 Near-Field Scanning Optical Microscopy (NSOM)

In conventional light microscopy, where a lens is used to focus light, spatial resolution is limited by diffraction from the limiting aperture in the optical path, which is usually determined by the diameter of the focusing element. Light passing through the focusing element interferes around the focal point, generating a diffraction pattern, the two-dimensional section of which in the focal plane leads to the well-known Airy disk pattern [1]. The size of the central spot in the Airy disk pattern dictates the maximal resolution achievable with the optical system. Assuming that collimated, coherent light is directed through an aberration-free microscope objective; then the spot size is given by

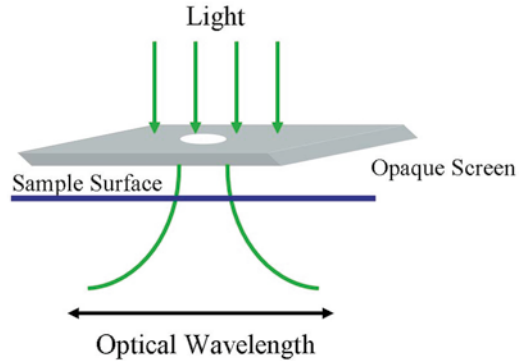
$$\text{spot size} = 0.77\lambda_{\text{vac}} / n \sin \theta \quad (9.1)$$

where  $\lambda_{\text{vac}}$  is the vacuum wavelength,  $n$  is the refractive index of the medium through which the light travels, and  $\theta$  is the half-angle through which the light is focused by the objective. The collection of terms in the denominator of Eq. (9.1) determines the minimal spot size and is collectively known as the numerical aperture (NA) of the objective [2].

While spot size can be directly quantified, resolution is a more subjective quantity and is usually discussed in terms of the Rayleigh criterion, which states that two features are resolvable if they are separated by a distance greater than or equal to that given by Eq. 9.1. With good signal-to-noise, finer separations can be resolved, while imperfections in the optics, poor signal-to-noise, or sample limitations tend to reduce the resolving power. Given these tradeoffs, the resolving power using conventional optics is approximately equal to  $\lambda/2$ . When one works in the visible region of the spectrum, therefore, spatial resolution is limited to approximately 250–300 nm [3, 4].

Near-field scanning optical microscopy (NSOM) is a scanning probe technique that enables optical measurements to be conducted with a spatial resolution beyond  $\lambda/2$ . This method evolved out of the explosion in scanning probe technologies such as atomic force microscopy (AFM). NSOM overcomes the diffraction limit by using light passing through a subwavelength-sized aperture to deliver light down to

**Fig. 9.1** Schematic representation of light passing through the subwavelength-diameter aperture of an opaque screen



the nanometric dimension [5, 6]. Light exiting the aperture of an NSOM probe will diffract out, as shown schematically in Fig. 9.1. By positioning the aperture near the sample surface, light exiting the aperture is forced to interact with the sample before diffracting out, and the spatial resolution is only limited by the size of the aperture and its proximity to the sample surface.

While the experimental details involved in implementing NSOM can be found elsewhere [5, 7, 8], we will briefly discuss aperture formation and implementing a feedback system for tip-sample distance control. These present the main obstacles that must be overcome for implementing NSOM measurements.

Several aperture-formation methods have been developed for NSOM, but those based on fiber optics have been the most widely adopted. In general, a single-mode optical fiber is heated and pulled to form a taper terminating at a small point that eventually forms the NSOM aperture [7]. A second method of forming NSOM probes uses chemical etching techniques to create the taper in the fiber. This method uses hydrofluoric acid (HF) as the etchant and usually employs some type of organic protection layer. The probe is dipped into the HF, and the meniscus formed by the HF and organic layer determines the overall shape and cone angle of the tip [9, 10]. While the pulling method generally provides a smoother taper in the probe, etching methods can create much smaller aspect ratio tapers, which have advantages for light throughput.

To confine the light within the tapered region, the sides of the probe are coated with a reflective metal coating. For the visible region of the spectrum, aluminum is the most reflective, with a skin depth of  $\sim 13$  nm at a wavelength of 500 nm. The high reflectivity enables confinement of light within the taper region of the probe with only 50–100 nm of aluminum [11]. Figure 9.2 shows magnified views of a typical fiber-optic NSOM probe. In the electron microscopy image shown in Fig. 9.2a, the granules from the aluminum coating are visible, as is the aperture at the very end of the probe where the light emerges. The aperture is more apparent in Fig. 9.2b, which shows the same probe after milling with a focused ion beam (FIB) instrument. In the optical image shown in Fig. 9.3, light emerging from the nanometric aperture of heated and pulled (a) and chemically etched (b) probes is visible.

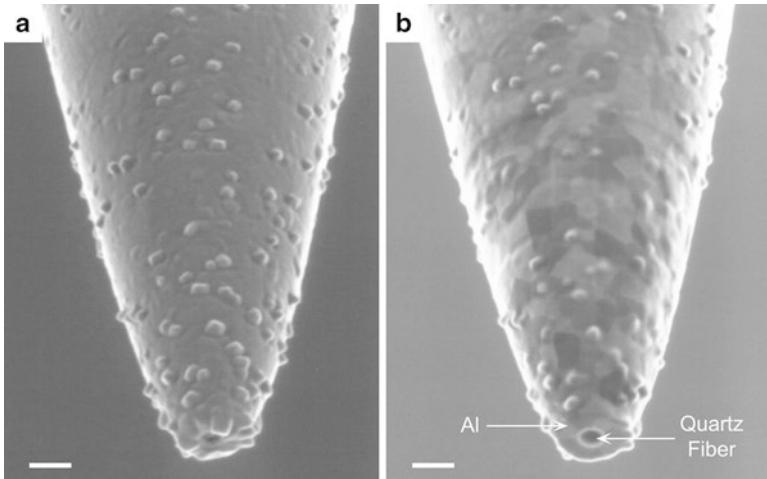


**Fig. 9.2** (a) Scanning electron micrograph of a tapered, single-mode, fiber-optic, near-field probe coated with aluminum to confine light. (b) The same probe after the end has been milled with the use of a focused ion beam (FIB) instrument. Scale bars are 150nm (Figure adapted from Ref. [12])

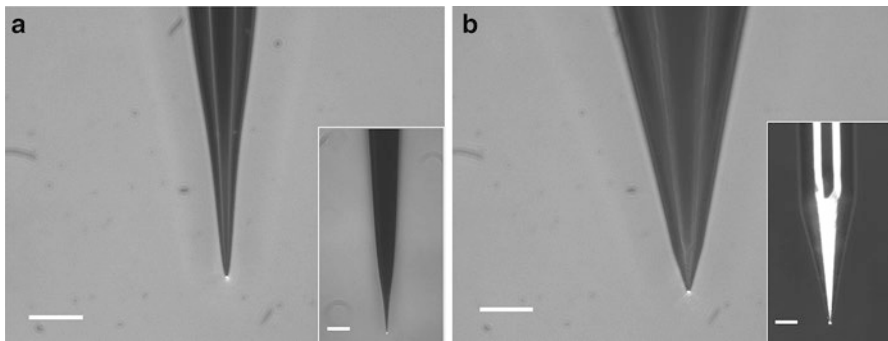
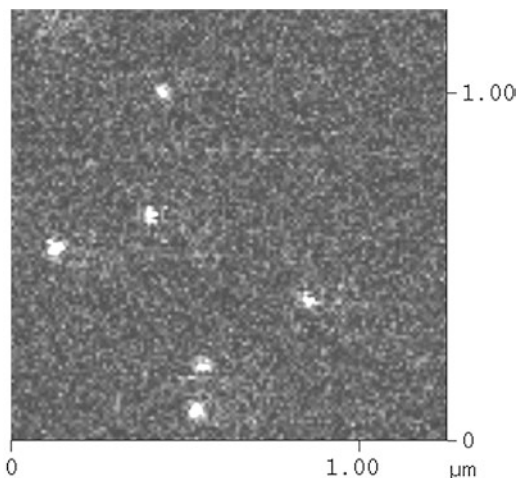


**Fig. 9.3** Magnified views of Al-coated NSOM probes manufactured by ( a) heating and pulling and (b) the Turner method of chemical etching. The scale bars represent 30 μm. Both probes exhibit single apertures at their apices, as indicated by the single spot of light exiting the probes. The overall geometries become apparent in the inserts, which are expanded views of the same probes (scale bars are 50 μm) (Figure adapted from Ref. [13])

Once the NSOM probe is formed, high-resolution NSOM measurements rely on the ability to position and maintain the probe within nanometers of the sample surface. A number of methods have been developed, including approaches based on shear-force feedback [14–16], tapping-mode [17, 18]—such as that developed for atomic force microscopy—and tuning-fork feedback [19]. All of these methods generally rely on oscillating the tip and monitoring changes in amplitude as the tip interacts with the surface. A feedback loop is implemented that moves the tip relative to the sample surface to keep the tip oscillation constant. All these methods

**Fig. 9.4** A  $1.25\text{-}\mu\text{m} \times 1.25\text{-}\mu\text{m}$  NSOM fluorescence image of single diI molecules entrapped within a DPPC monolayer. The full-width half-maximum of the intensity features is  $\sim 25$  nm, which reflects the size of the NSOM aperture used in the imaging (Figure adapted from Ref. [21])



enable nanometer control over the tip-sample gap and generate a force mapping of the sample topography, much like AFM. NSOM therefore provides simultaneous optical and topographical information about sample properties [20].

To illustrate the high spatial resolution and low detection limits of NSOM, Fig. 9.4 shows an NSOM fluorescence image of the dye molecule diI<sub>C</sub>(1,1'-dioctadecyl-3,3,3',3'-tetramethylindocarbocyanine perchlorate) doped into a DPPC ( $L\text{-}\alpha$ -dipalmitoylphosphatidylcholine) lipid monolayer. Each bright spot in this image represents the fluorescence from a single dye molecule in the lipid monolayer, which illustrates the single-molecule detection limits of NSOM. Since the dye molecule is much smaller than the NSOM aperture, the size of each fluorescence feature in Fig. 9.4 reveals the size of the NSOM aperture used to image the sample. The full-width half-maximum (FWHM) of the features is approximately 25 nm, which is roughly an order of magnitude better than the diffraction limit and illustrates the high spatial resolution possible with NSOM. For the biological sciences, this high resolution, along with the simultaneous force mapping of surface topography, provides a potentially powerful new tool. One concern, however, revolves around potential sample heating caused by the NSOM probe. As light is directed through the NSOM probe, heating occurs, which could potentially damage biological samples. Before discussing applications, therefore, we will briefly summarize light-induced heating of NSOM probes.

### 9.2.1 Sample Heating from NSOM probes

Sample heating from the NSOM probe has raised some concerns for biological applications. Metal-coated, fiber-optic NSOM probes increase in temperature as more light is coupled into the probe. As the diameter of the NSOM probe decreases in the taper region, eventually no propagating modes of the light are supported and

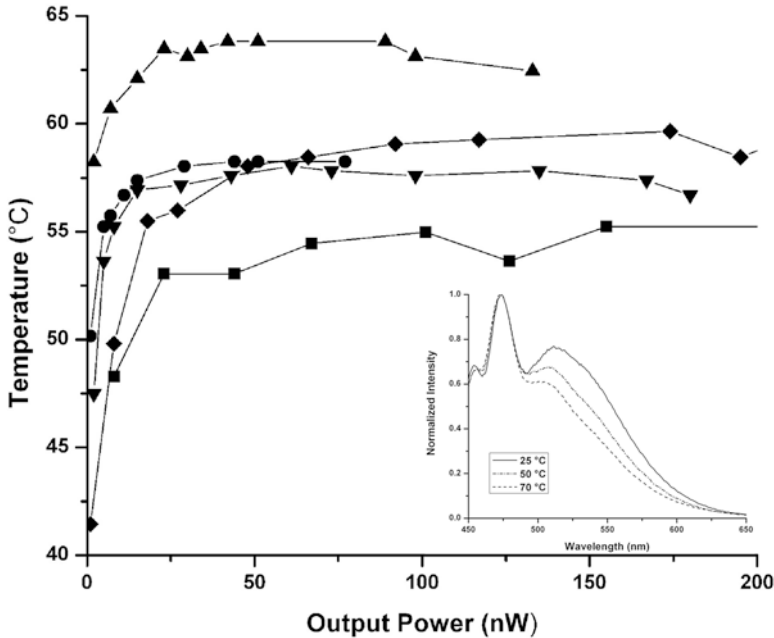


**Fig. 9.5** Plots of sample temperature as a function of output power for five representative NSOM probes fabricated using the pulling method. Each symbol corresponds to the heating curve of an individual NSOM probe. The insert shows the normalized temperature-dependent emission spectra for the thermochromic polymer, perylene and *N*-allyl-*N*-methylaniline, used to obtain sample heating data (Figure adapted from Ref. [21])

only highly decaying evanescent fields reach the aperture. This makes NSOM probes highly inefficient at delivering light [ 22, 23]. Typical NSOM probes have losses on the order of three orders of magnitude as the light travels toward the aperture. With tens to hundreds of microwatts coupled into the fiber optic, only tens to hundreds of nanowatts are delivered from the aperture, when measured in the far field. The remaining light is lost to reflection back up the fiber and to absorption losses into the metal coating surrounding the taper in the probe. The latter contributes to probe heating. Eventually, as more light is coupled into the NSOM probe, heating causes catastrophic probe failure where the aluminum coating forming the aperture is lost [3].

Measures of probe heating are complicated by the small size the NSOM aperture. Early studies used thermocouples positioned tens of microns from the tip aperture and found temperatures as high as 470 °C before eventual tip failure [ 24]. Studies attempting to measure temperatures directly at the NSOM aperture yielded results that ranged from less than 40 °C to 390 °C [25]. Recently, these measurements were extended using a thermochromic polymer to directly characterize the heating experienced by samples below an NSOM aperture [13, 21].

These studies used a polymer consisting of perylene and *N*-allyl-*N*-methylaniline (NA) that exhibits a “two-color” emission spectrum that changes with temperature.



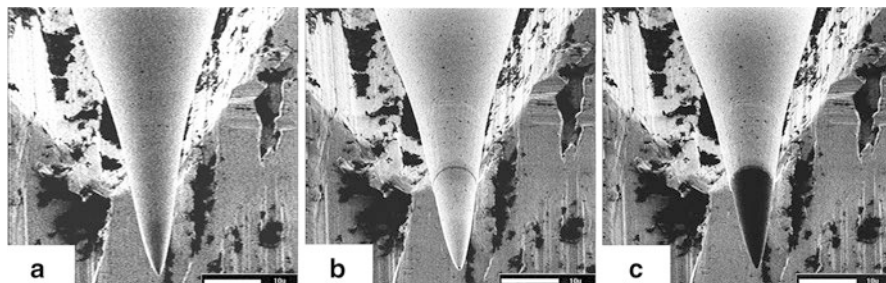


**Fig. 9.6** Sequence of electron micrographs of an Al-coated, fiber-optic NSOM probe taken as the laser power coupled into the probe was increased. **(a)** At low laser power, the aluminum coating on the tip remains intact. **(b)** As the power is increased, a ring-like fracture in the Al coating appears at a probe diameter of  $\sim 7\ \mu\text{m}$  and  $35\ \mu\text{m}$  from the apex. This results from the differential thermal expansion of the Al coating and the quartz fiber. **(c)** Finally, at higher powers, the complete failure of the probe is marked by the removal of the coating below the fracture, exposing the bare fiber beneath. Scale bars are each  $10\ \mu\text{m}$  (Figure adapted from Ref. [13])

The bulk emission spectrum consists of two peaks, located at  $\sim 475\text{nm}$  and  $\sim 510\text{nm}$ . Upon heating, the ratio between the 475-nm and 510-nm peaks increases (Fig. 9.5), which provides a marker of sample heating that is not sensitive to light intensity or sample concentration [26, 27]. As such, ratiometric measurements of the peak intensities enable precise characterization of probe heating directly below the NSOM aperture.

Sample heating as a function of output power from a sampling of NSOM probes is shown in Fig. 9.5. For all studies, the output of a 405-nm diode laser (Power Technology) was coupled into the NSOM probes. In general, all probes showed an initial rapid rise in sample heating that leveled out at elevated output power. At output powers of a few nanowatts, heating at the sample ranged from  $\sim 40\ ^\circ\text{C}$  to  $45\ ^\circ\text{C}$  and leveled to a maximum of approximately  $65\ ^\circ\text{C}$  at NSOM probe output powers ranging from 50 to  $100\ \text{nW}$  [21]. Slight variations in tip aperture size and taper geometry contribute to the range of heating results observed in Fig. 9.5. Interestingly, similar sample temperature profiles were measured with NSOM probes fabricated with the chemical etching technique [13]. Despite being much more efficient than probes fabricated using the heating method, sample heating with output power remains unchanged. In either case, the sample heating is modest, especially at low powers, and should not pose a major difficulty for biological applications. Moreover, the sample heating is expected to be lower under aqueous conditions, where heat can be more efficiently released into the surrounding media.

The leveling off in sample heating was ascribed to the heat-induced expansion of the NSOM probe, which increases the distance between the probe aperture and the sample surface. The large difference between the thermal expansion coefficients of the fiber optic and surrounding aluminum coating ( $\alpha_{\text{Al}} = 2.34 \times 10^{-5}\ ^\circ\text{C}^{-1}$  and  $\alpha_{\text{quartz}} = 0.5 \times 10^{-6}\ ^\circ\text{C}^{-1}$ ) leads to differential elongation in the probe as power is increased [28, 29]. This effectively increases the distance between the aperture and the sample as power is increased.

The large difference in thermal expansion coefficients for the fiber optic and surrounding metal coating of the NSOM probe also explains the catastrophic damage experienced at high powers. Figure 9.6 displays a series of high-resolution electron micrographs taken of the same NSOM probe as the input power was increased. At low powers, no damage is observed in the metal coating of the probe and the aperture at the end of the probe exposing the fiber dielectric appears dark (Fig. 9.6a). As power is increased in Fig. 9.6b, a dark ring representing a fracture in the aluminum coating is first observed approximately 35  $\mu\text{m}$  from the aperture. As power is further increased, this initial fracture eventually leads to the complete loss of aluminum from the region below the fracture, as seen in Fig. 9.6c. This loss of aluminum from around the taper region leads to the loss of the NSOM aperture and a dramatic increase in light throughput that is indicative of NSOM probe failure at high powers [13].

### 9.3 Biological Applications of NSOM

NSOM is generally used for studying surfaces and has been widely employed for studying biological films and membranes. For reviews see Dunn [5] and Edidin [8]. These studies have taken advantage of the simultaneously collected fluorescence and topography information with NSOM for characterizing the state of the membrane systems. Small domains in biological membranes have long been of interest; the high resolution of NSOM provides a tool that now allows these domains to be studied directly.

#### 9.3.1 Membranes

##### 9.3.1.1 Monolayers

The complex composition and structure of biological membranes have led to the development of methods for studying model membranes under more controlled conditions. The use of Langmuir–Blodgett films allows for the creation of monolayer or multilayer films, where temperature, composition, and phase can be precisely controlled. Langmuir–Blodgett films have therefore been widely adopted to study lipid phases and component distribution in models of natural membranes [30, 31].

The phases and component distribution in model membranes have been studied extensively with fluorescence microscopy. Many studies have shown that the inclusion of fluorescent lipid analogs, such as diIC<sub>18</sub>, into the lipid films will preferentially partition into the less-ordered regions of the film. For lipid monolayers transferred onto substrates in the liquid-expanded (LE)/liquid-condensed (LC) phase-coexistence region of the pressure isotherm, therefore, the condensed regions appear dark and the expanded regions appear bright in the fluorescence image. For example, Fig. 9.7a shows a fluorescence image of a DPPC lipid monolayer

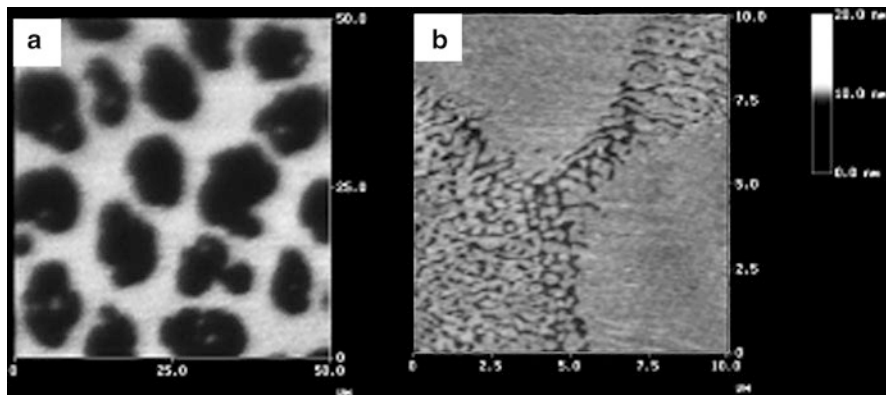


**Fig. 9.7** (a) Confocal fluorescence and (b) AFM images of a DPPC monolayer deposited at 9 mN/m onto cleaved mica using the Langmuir–Blodgett technique. At this surface pressure, the liquid-condensed (LC) and liquid-expanded (LE) phases of the monolayer coexist. (a) In the fluorescence image, bright regions incorporate a fluorescent lipid analog and mark the LE domains. The dark domains are the LC phase. (b) In AFM measurements, the LC domains appear higher than the surrounding LE/LC microdomains. Note that the appearance of microdomains within the expanded region of the AFM image is not resolved in the confocal image (Figure adapted from Hollars and Dunn [32])

doped with 0.25 mol% of diIC<sub>18</sub>, transferred onto a mica surface in the LE/LC phase-coexistence region. In the image, semicircular dark LC domains are surrounded by bright LE regions that contain the fluorescent lipid analog [32].

The phase structure in lipid monolayers can be studied with higher spatial resolution using techniques such as AFM. The small 0.5–0.8-nm height differences between the LE and LC phases in DPPC can be measured with AFM to map the phase partitioning with nanometric spatial resolution. Figure 9.7b shows an AFM image of a DPPC monolayer transferred under the same conditions as those shown in Fig. 9.7a. Semicircular domains of a higher topography mark the LC regions of the film. The lower-topography LE regions reveal a microstructure not resolved in the lower-resolution fluorescence image shown in Fig. 9.7a.

NSOM measurements offer the advantage of measuring both high-resolution fluorescence and topography simultaneously, which are particularly informative for studies of model membranes. Figure 9.8 shows the NSOM fluorescence (a) and topography (b) images of a DPPC monolayer doped with 0.25 mol% diIC<sub>18</sub>, transferred under the same conditions as the films shown in Figs. 9.7a, b. The higher spatial resolution in the fluorescence image reveals the microstructures in the LE regions not observed with far-field fluorescence measurements. These structures can be directly correlated with areas of lower topography seen in the NSOM topography image, confirming they arise from LE domains [32].

The high spatial resolution of NSOM fluorescence should be useful for understanding lipid rafts. Lipid rafts are small domains located within the cell membrane that are rich in cholesterol, glycolipids, and sphingolipids. These elusive structures

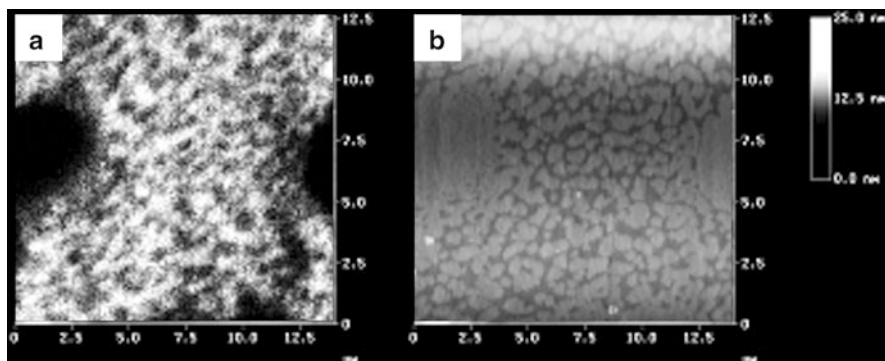


**Fig. 9.8** (a) High-resolution NSOM fluorescence image of the same DPPC monolayer depicted in Fig. 9.7. The bright domains reveal the LE-phase regions incorporating the dye, while the dark areas represent LC domains. (b) NSOM topography image collected simultaneously with the fluorescence shown in (a). The small LE/LC domains observed in the AFM image are visible in both the NSOM fluorescence and topography measurements (Figure adapted from Hollars and Dunn [32])

are thought to be organizing elements of the membrane used to modify the function of integral membrane components. Rafts were first classified as cellular membrane fractions that are resistant to cold, nonionic detergents such as Triton X-100. While there have been extensive biochemical studies of these detergent-resistant fractions, the believed small dimensions of rafts and their mobility within biological membranes have made them exceedingly difficult to study directly [33, 34].

Recently, the use of NSOM on model membranes has led to insights into the distribution and characteristics of submicron domains in lipid films. For example, Johnston and coworkers investigated the distribution of a commonly used lipid raft marker, ganglioside GM1, in a ternary lipid mixture [35]. For these studies, an LB monolayer composed of a 1:1:1 mol ratio mixture of DOPC, cholesterol, and sphingomyelin was prepared containing 1% GM1, a ganglioside that preferentially partitions into lipid rafts. A small amount of a fluorescently labeled lipid, Texas Red-DPPE, and 0.005% BODIPY GM1 provided two fluorophores that are both excited with 488-nm radiation. Figure 9.9a shows the NSOM fluorescence image of the monolayer following 488-nm excitation in which both labels are excited. Dark, semicircular domains are surrounded by bright LE regions in the NSOM fluorescence image. Of particular interest are the small, ~150-nm bright microdomains observed in the dark LC regions of the film. To understand the origin of these domains, the excitation wavelength was changed to 568 nm, which only excites the Texas Red-DPPE.

Figure 9.9b shows the same region of the membrane, with excitation wavelength at 568 nm. At this excitation energy, only the Texas Red-DPPE label is excited and the fluorescence reveals the phase separation in the monolayer. The bright microdomains previously seen in the LC regions are now absent, indicating that these

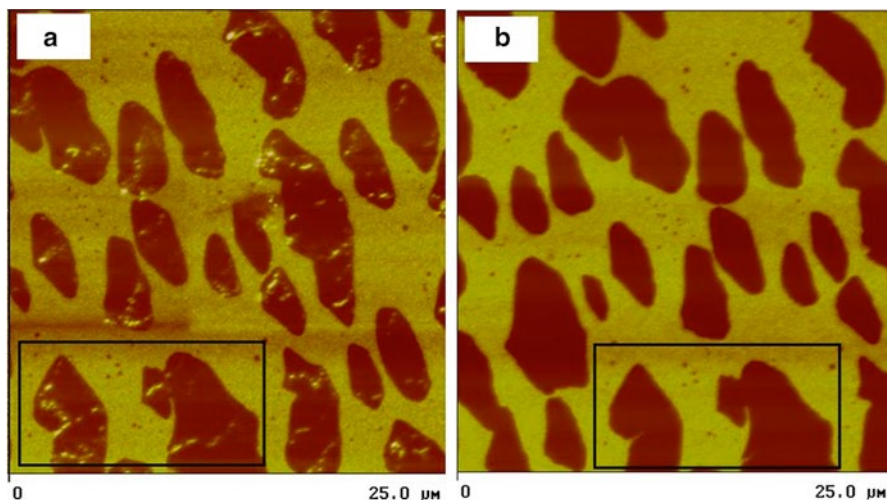


**Fig. 9.9** These are 25- $\mu\text{m} \times 25\text{-}\mu\text{m}$  NSOM fluorescence images of a 1:1:1 ternary mixture of sphingomyelin-cholesterol-DOPC monolayer transferred onto mica at 10 mN/m using the LB method. These films also contain 1% Texas Red-DPPE, 1 % ganglioside GM1, and 0.005% Bodipy-labeled GM1. Image (a) represents the fluorescence from both the GM1-Bodipy raft marker and the TR-DPPE. (b) The same area of the film but with only the TR-DPPE fluorophore excited. Similar areas of the two scans are outlined with boxes (Reprinted with permission from Burgos et al. 2003. Copyright 2003 The American Chemical Society [35])

domains contain the labeled GM1 raft marker. These domains are consistent with the formation of small raft domains, which agrees with dye-free AFM measurements showing similar small domains in the LC regions [36].

The high-resolution fluorescence and topography information from NSOM has also been exploited to help understand respiratory distress syndrome (RDS). RDS is associated with the lung surfactant, a monolayer of lipids and proteins that lines the lungs and reduces the surface tension to near zero. Prematurely born infants are often inflicted with RDS, which results from insufficiently developed lung surfactant. These infants have poor oxygen transport and labored breathing; left untreated, RDS can be fatal [37]. RDS can be treated through supplementing the deficient lung surfactant with artificial or natural lung surfactant mixtures. Survanta is one treatment for RDS that consists of bovine lung surfactant fortified with DPPC. NSOM has been used to help understand the phase structure and collapse of monolayers of Survanta [38].

For these studies, LB monolayers of Survanta doped with 0.08mol% of the fluorescent lipid analog diIC<sub>18</sub> were transferred onto a freshly cleaved mica surface at a series of surface pressures. At a surface pressure of 62 mN/m, just below the collapse pressure, confocal fluorescence imaging identifies buckling in the film. As shown in Fig. 9.10, the fluorescence image reveals a broad area where the phase structure overlaps, indicating buckling in the film.

**Fig. 9.10** A  $75\text{-}\mu\text{m} \times 100\text{-}\mu\text{m}$  confocal fluorescence image of a Survanta monolayer deposited onto mica with the LB technique. At a transfer pressure of  $62\text{ mN/m}$ , the film is near collapse and the overlapping phase structure in the fluorescence indicates the film has buckled. The scale bar is  $10\text{ }\mu\text{m}$  (Figure adapted from Ref. [38])

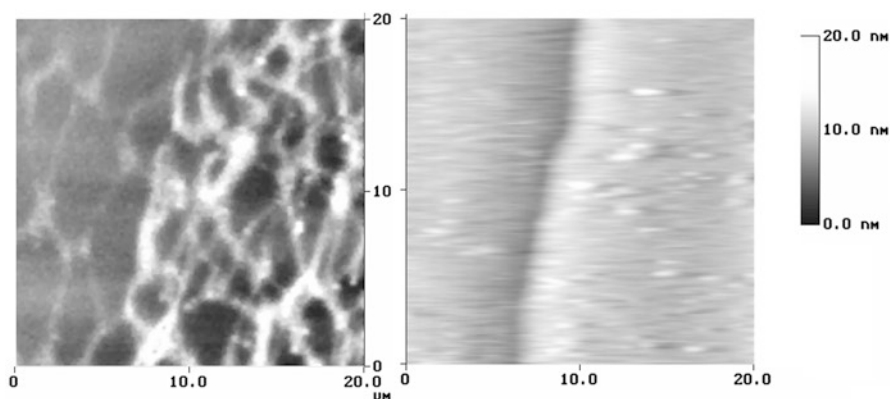
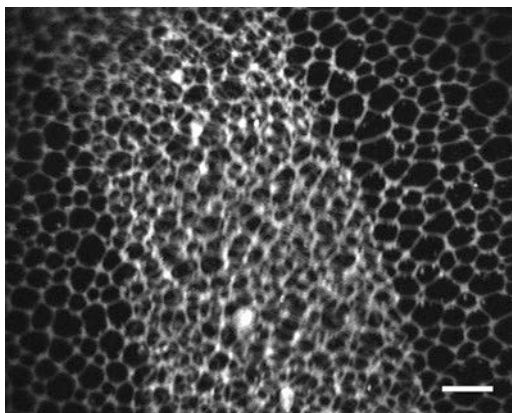


**Fig. 9.11** Two  $20\text{-}\mu\text{m} \times 20\text{-}\mu\text{m}$  simultaneously collected NSOM fluorescence (*left*) and topography (*right*) images of a fold in a Survanta film deposited by the LB technique at  $62\text{ mN/m}$ . Both images indicate a discontinuity in the monolayer consistent with the buckling suggested by far-field images (Figure adapted from Ref. [38])

Figure 9.11 shows NSOM fluorescence (left) and force (right) images of a Survanta monolayer transferred onto mica at the same surface pressure. The NSOM fluorescence image reveals a similar phase structure and overlapping structures indicative of buckling. Comparison of the NSOM fluorescence with the simultaneous force images confirms the formation of a multilayer region in the film as the membrane buckled and folded over itself. The simultaneously collected topography shows a ridge of approximately  $4\text{--}5\text{ nm}$  in the region of the fold, confirming that the membrane has partially folded over itself. This is consistent with the discontinuity in the phase information seen in the fluorescence image. Upon raising the surface pressure beyond the collapse pressure of the monolayer to  $65\text{ mN/m}$ , the monolayer no longer buckles but appears to break off from the rest of the membrane. The

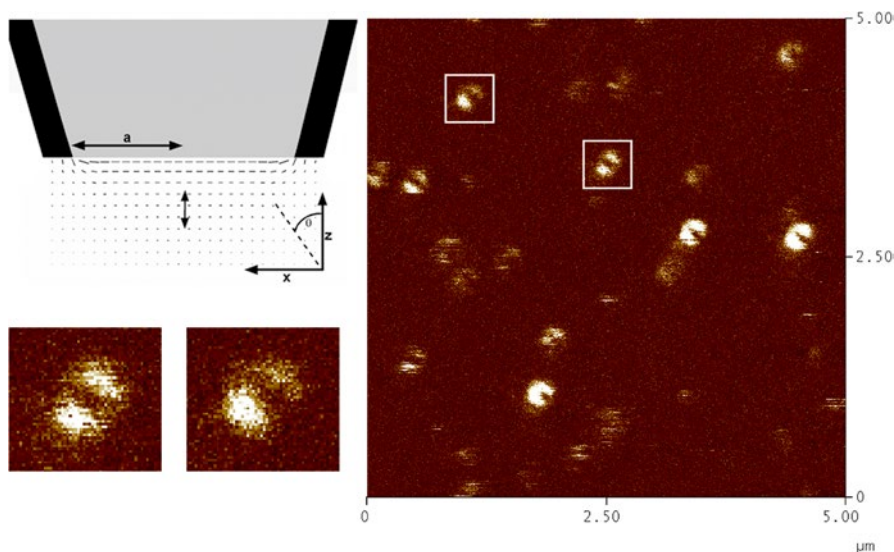


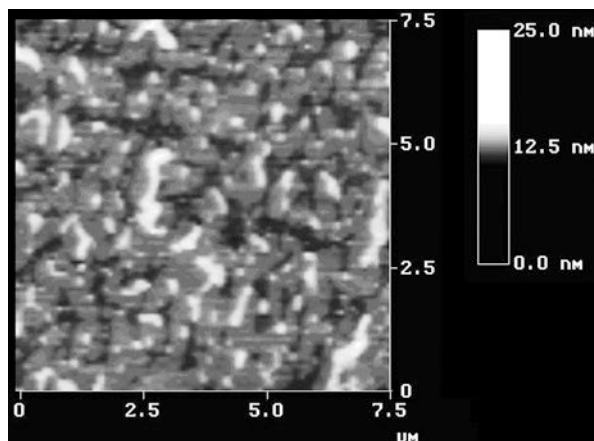
**Fig. 9.12** A schematic (*upper left*) of the electric fields near a metal-coated NSOM aperture as modeled by Bethe–Bouwkamp theory. The  $z$ -component in the electric field near the edge of the aperture can excite molecules with transition dipoles pointing at the probe. This leads to excitation when the molecule is located near the aperture edges and no excitation when centered below the aperture. The single-molecule fluorescence image reveals shapes indicative of molecules with this orientation (Figure adapted from Ref. [40])

NSOM data suggest that membrane buckling may be one mechanism by which LS is able to resist collapse at high pressures [38].

NSOM also has single-molecule fluorescence detection limits, which have been exploited to study the molecular-level structure in lipid monolayers. In 1994, Betzig and Chichester published a seminal NSOM paper that not only reported the single-molecule detection limits of NSOM, but also showed that the fields present at the NSOM aperture lead to patterns in the single-molecule fluorescence that reflect the three-dimensional orientation of the molecules [39]. Using carbocyanine dyes dispersed in a polymethyl-methacrylate (PMMA) matrix, they found a series of emission patterns that could be understood by modeling the fields at the NSOM aperture using Bethe–Bouwkamp theory [39]. The boundary condition between the metal coating and the dielectric fiber optic leads to a curvature in the fields at the NSOM aperture, as shown in Fig. 9.12. Molecules with transition dipoles vertically oriented will be excited when near the edge of the aperture, while those lying in the plane will be excited when centered under the aperture. This difference leads to patterns in the emission image, which can be analyzed to extract dye-orientation information.

These single-molecule emission patterns were used in single-molecule NSOM studies to probe the lipid membrane structure at the molecular level [40]. The goal was to analyze the single-molecule NSOM emission patterns from fluorescent lipid analogs doped into the lipid monolayer as probes of local structure. Figure 9.12

**Fig. 9.13** Atomic force micrograph of a  $7.5\text{-}\mu\text{m} \times 7.5\text{-}\mu\text{m}$  DPPC bilayer. Both layers were deposited at  $9\text{ mN/m}$  in the phase-coexistence region of the pressure isotherm. The second layer was transferred by the Langmuir–Schaefer method, creating the bilayer. The three quantized height levels in the bilayer differ by  $\sim 8\text{ \AA}$  as a result of the phase overlap in the two layers (Figure adapted from Hollars and Dunn [32])



shows an NSOM fluorescence image of a DPPC monolayer doped with the fluorescent lipid analog TRITC-DHPE. An analysis of the features found that the transition dipole moment of TRITC-DHPE was oriented approximately  $2^\circ$  from the normal and was not sensitive to changes in surface pressure from  $8.0$  to  $30.0\text{ mN/m}$ . This study found no evidence for TRITC-DHPE oriented parallel to the surface, but  $\sim 13\%$  of the observed signal was a result of analogs oriented at an angle of  $16^\circ$  or beyond from the normal.

In theory, these types of measurements can reveal the orientation of molecules embedded in a matrix and provide a molecular-level marker of orientation. However, other studies have found evidence of tip-induced changes in emission patterns that can influence extracted orientations [41, 42]. Further work understanding the magnitude of this effect is needed before confident orientations are extracted from single-molecule NSOM fluorescence measurements.

### 9.3.1.2 Bilayers and Multilayers

NSOM measurements have also proven useful for studies on multilayer membrane systems. The complexity of these systems quickly increases with the number of layers. For example, Fig. 9.13 shows an AFM image of a DPPC bilayer where each leaflet of the bilayer was transferred in the phase-coexistence region of the pressure isotherm. For these samples, the first layer was transferred onto mica using the LB technique and the second layer using the Langmuir–Schaefer approach. Three quantized height levels are observed in the AFM image of the bilayer [32]. These height changes correspond to the possible combinations of stacking between the LE and LC phases present in the individual leaflets of the bilayer. For example, the lowest topography features in the image correspond to the stacking of LE on LE, the next level corresponds to LE on LC or LC on LE, and, finally, the tallest structures



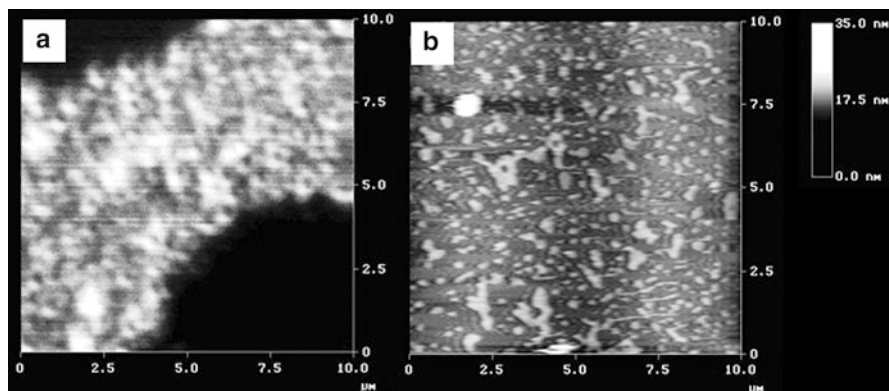


**Fig. 9.14** A 10- $\mu\text{m} \times 10\text{-}\mu\text{m}$  NSOM scan of the DPPC bilayer depicted in Fig. 9.12. The fluorescent diI lipid analog is included only in the bottom layer, while the upper layer is comprised of pure DPPC. The high-resolution fluorescence channel is shown in (a) and the simultaneously collected sample topography is depicted in (b) (Figure adapted from Hollars and Dunn 1998)

correspond to LC on LC. So while it is clear that phase structure is present in each leaflet of the bilayer, assigning this structure to each leaflet is not possible with AFM.

NSOM, however, can be used to study the microdomain structure present in each side of the bilayer by controlling which leaflet of the bilayer contains the fluorescent lipid analog. Figure 9.14 shows the NSOM fluorescence and topography of a DPPC bilayer similar to that shown in Fig. 9.13. In this bilayer, the lower leaflet was doped with the fluorescent lipid analog diIC<sub>18</sub>, which partitions into the LE phase. The fluorescence image shows a phase structure similar to that observed for DPPC monolayers, with dark LC regions surrounded by LE microdomains. Measurements with dye doped into the top layer reveal a similar structure. These measurements show that the phase structure is maintained in forming the bilayers and suggest that microdomains and lipid asymmetry can be probed with high resolution in these more complex systems [32].

In biological membranes, asymmetry is maintained across the bilayer and is critical for proper cellular function. Lipid and protein composition is different across the two leaflets of the plasma membrane of cells and loss of this asymmetry is a sign of apoptosis. Probing this asymmetry directly is difficult since the membrane thickness is only approximately 6 nm. Fluorescence resonance energy transfer (FRET), however, is a fluorescence technique that is sensitive to distances on this length scale and has been used extensively to probe membrane organization.

FRET takes advantage of Förster energy transfer between a donor and acceptor dye that are in close proximity to each other. Nonradiative energy transfer between dyes with the proper spectral properties is very sensitive to changes in the distance between the two dyes, making FRET a powerful tool for monitoring small displacements in biological systems [43, 44]. Several groups have combined the distance dependence of FRET with NSOM to create a new technique that has high lateral as

well as axial resolution, which should be capable of characterizing membrane asymmetry [45–47].

An initial demonstration of this technique utilized a tapered fiber optic that lacked the metal coating used in NSOM probes to confine the light within the probe. The end of the probe was instead coated using the LB technique with a DPPC monolayer doped with a rhodamine-labeled lipid [47]. The sample used in these studies consisted of a multilayer film consisting of a fluorescein-doped DPPC monolayer, three layers of arachidic acid that did not contain any dye, and finally another layer of dye-doped DPPC. A schematic of the experimental arrangement is shown in Fig. 9.15. For these studies, the fluorescein acted as the FRET donor dye and the rhodamine attached to the NSOM probe acted as the FRET acceptor.

Figure 9.15 shows the NSOM fluorescence images of the multilayer film following excitation of the donor at 458 nm. The two images shown represent the fluorescence from the donor (Fig. 9.15a) and acceptor (Fig. 9.15b). Comparing the two images illustrates the sectioning capabilities of combining FRET with NSOM. The features in the donor emission shown in Fig. 9.15a reveal the domains in both the top and bottom layers of the film that contain the donor dye though it is not possible from this image to assign from which layer the emission originates. The acceptor emission shown in Fig. 9.15b, however, arises from energy transfer from the excited donor in the sample to the tip-bound acceptor. As such, the energy-transfer efficiency from the top layer of the film is much higher than that from the bottom layer. In Fig. 9.15b, some domains become much weaker, indicating they reside in the bottom layer while other domains become brighter since they reside in the top layer, closer to the NSOM probe. The resolution of these domains also sharpens as expected since only dyes in closest approach contribute to the energy-transfer signal. As shown in Fig. 9.16, this study demonstrated that the FRET/NSOM technique can probe samples with a lateral resolution of  $\sim 140$  nm and  $z$ -sectioning capabilities of less than 8 nm.

Another advantage of combining FRET with NSOM is that the technique does not require the fiber-optic probes normally used in NSOM to deliver light. This was demonstrated where functionalized AFM probes were used in the FRET configuration to make high-resolution optical measurements. As before, an acceptor dye was attached to a silicon nitride AFM probe and the donor was distributed in the sample. Far-field excitation was used to excite the donor, and emission from the tip-bound acceptor was monitored to generate the high-resolution image. As before, high resolution is obtained because of the strong distance dependence of the energy-transfer mechanism [48].

In 2002, Shubeita and coworkers extended the FRET/NSOM technique [46]. In these studies, the acceptor dye was attached to an uncoated fiber-optic NSOM probe using a 30–100-nm optically transparent PMMA layer containing the dye. This creates a dye reservoir that extends the life of the measurement as mechanical wear depletes the acceptor from the probe. This creates a more robust system for sustained FRET/NSOM measurements.

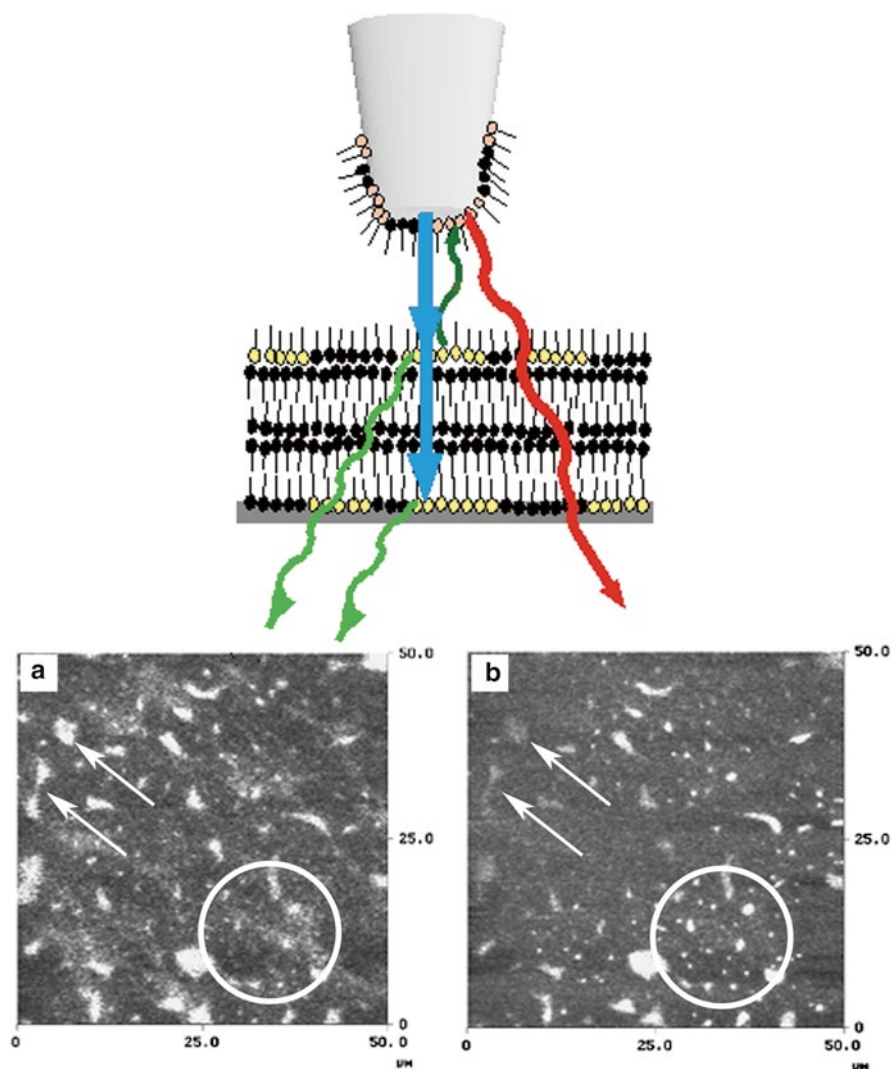


**Fig. 9.15** Schematic (*top*) of the experimental setup used in demonstrating the FRET/NSOM method. The fiber-optic probe is coated with a monolayer containing a FRET acceptor fluorophore. The sampled consisted of a multilayer film where only the top and bottom layers contained the donor dye. **(a)** This image shows the fluorescence from the donor dye in the sample. **(b)** Acceptor emission that arises from energy transfer from the excited donor dye in the sample to the tip-bound acceptor. Comparison of the two images taken in the same area show that some features in the FRET/NSOM image lose intensity, indicating they arise from domains in the bottom layer, while others becoming brighter and more resolved, indicating they are from the top layer (Figure adapted from Ref. [47])

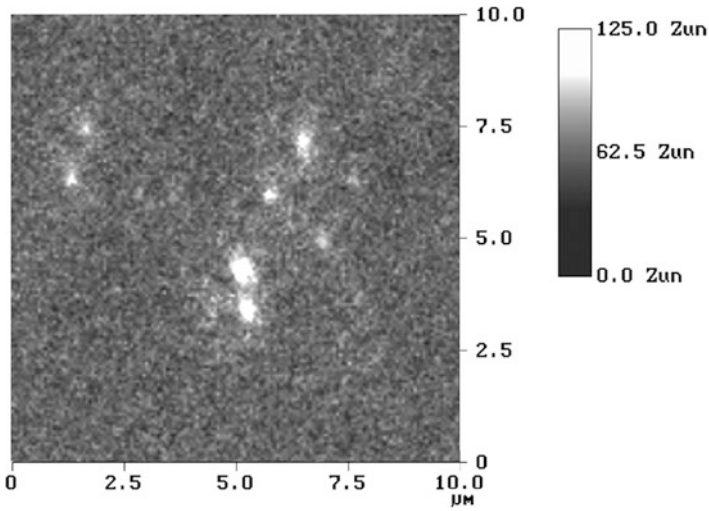


**Fig. 9.16** A 10- $\mu\text{m} \times 10\text{-}\mu\text{m}$  FRET/NSOM scan of the same membrane shown in Fig. 9.15. The tip-bound acceptor fluorescence was collected, while the excitation wavelength was resonant with the sample-bound donor fluorophore. The resulting fluorescence image reveals  $\sim 140\text{-nm}$  features (Figure adapted from Ref. [47])

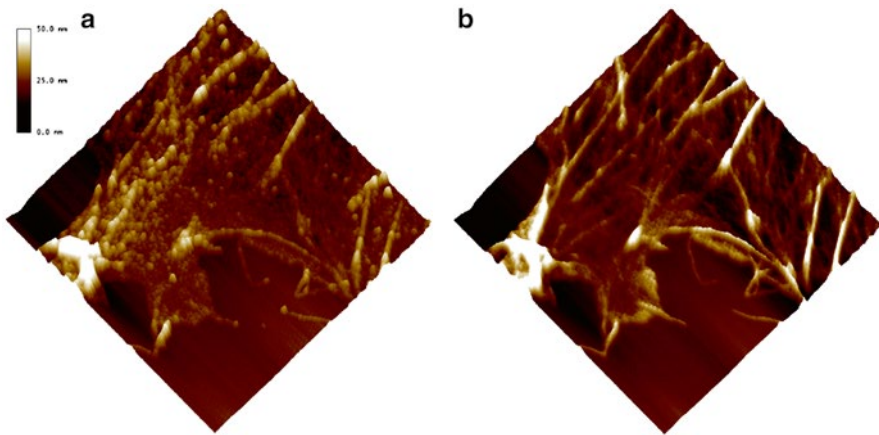


**Fig. 9.17** Two 20- $\mu\text{m} \times 20\text{-}\mu\text{m}$  NSOM fluorescence (a) and topography (b) images of a human arterial smooth muscle (HASM) cell in which the F-actin has been labeled with a fluorescent phalloidin conjugate

### 9.3.2 Cells

The extension of NSOM measurements into intact biological samples such as viable cells has been difficult. Working with fragile samples under buffered conditions presents several challenges for NSOM measurements that are proving very difficult

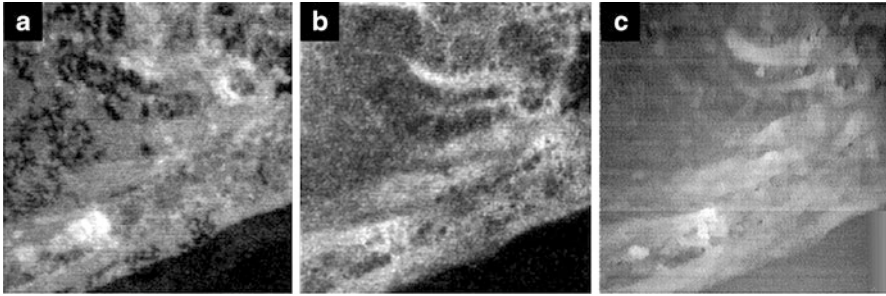


**Fig. 9.18** Near-field images of a fibroblast cell incorporating a fluorescently labeled phosphatidylcholine into the plasma membrane. The surface-presenting HLA class I proteins were also immunolabeled with a tetramethylrhodamine-conjugated antibody. The near-field fluorescence image (a) reveals the location and distribution of the fluorescent lipid analog, while (b) shows the antibody labeling of the HLA protein. (c) Simultaneously collected topography image of the cell (Reproduced with permission from Ref. [50]. Copyright 1998 The Biophysical Society)

to overcome. The limited success in this area will be discussed in the next section. Fixed biological tissues, however, are amenable with NSOM measurements both dry and under buffered conditions, opening vast new areas of research. For studies of fixed cells, the simultaneous collection of both high-resolution fluorescence and force information is particularly useful and informative. As an example, Fig. 9.17 shows the NSOM topography (a) and fluorescence (b) images of a fixed human arterial smooth muscle (HASM) cell in which the F-actin has been fluorescently labeled with phalloidin conjugated to the fluorescent alexa fluor 568 [49]. A strong correlation is observed between the F-actin fibers identified in both the fluorescence and force channels. The smallest fibers observed in the fluorescence have an FWHM of  $\sim 100$  nm, which reflects the size of the NSOM aperture used in the imaging. In addition, many of the fibers observed in the fluorescence image are not resolvable in the force image and would not be seen with techniques such as AFM.

Eddidin and coworkers exploited the high resolution of NSOM to probe lipid rafts in human fibroblast cells [50]. The fibroblasts were dual labeled with BODIPY phosphocholine (BODIPY-PC) and a monoclonal antibody specific for the HLA class I protein of the major histocompatibility complex (MHC). The latter was labeled with fluorescent tetramethylrhodamine. Figure 9.18a shows the high-resolution NSOM fluorescence image of the BODIPY-PC in the fibroblast membrane. Small,  $\sim 200$ -nm dark domains that exclude the fluorescent probe are visible in the upper left region of the cell. Interestingly, the NSOM fluorescence of the MHC shown in Fig. 9.18b reveals fluorescence from the areas seen in Fig. 9.18a to exclude the membrane probe. This supports the idea that small domains or rafts are supported in the membrane and used to organize membrane components. These measurements are also consistent with those done previously on model membrane systems [35]. The topography measurements shown in Fig. 9.18c reveal no significant correlation between the membrane topography and the location of the microdomains.

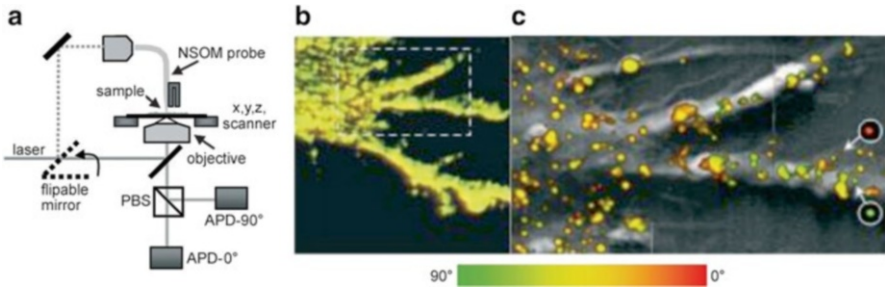


**Fig. 9.19** (a) Schematic of the experimental setup utilized for collection of confocal and NSOM images. (b) A 20- $\mu\text{m} \times 20\text{-}\mu\text{m}$  confocal fluorescence image of a dendritic cell with fluorescently immunolabeled DC-SIGN expressed on the membrane. (c) An overlay of simultaneously collected topography (*gray*) and NSOM fluorescence (*color*) of the region of the dendritic cell outlined in (b). The NSOM fluorescence has been color-coded according to emission polarization. Polarization at  $0^\circ$  is coded *red*, emission at  $90^\circ$  is *green*, and emission in between is coded as shown by the gradient scale

More recently, de Bakker and coworkers [51] investigated the distribution and molecular organization of DC-SIGN, a C-type lectin exposed on the surface of dendritic cells (DCs). Exposed clusters of DC-SIGN are responsible for the unique recognition of a variety of pathogens through binding to specific haptens. Though the role of these lectins is known, the mechanism through which they recognize specific pathogens is not well understood.

Figure 9.19a shows a schematic of the instrumental setup used to collect the confocal and NSOM data. Figure 9.19b shows a confocal fluorescence image of a fixed, dried DC in which the DC-SIGN lectins are labeled with monoclonal antibodies against the exposed epitopes of DC-SIGN. A Cy5 conjugated secondary antibody is used as the fluorescent marker of the antibody labeling. Figure 9.19c displays a 12- $\mu\text{m} \times 7\text{-}\mu\text{m}$  NSOM measurement from a section of the DC shown in Fig. 9.19b. The NSOM results are presented as an overlay of the fluorescence and topography information. Polarization information was also collected simultaneously onto two detectors and color-coded as a gradient scale where red represents a polarization of  $0^\circ$  and green represents  $90^\circ$  polarization.

The NSOM data reveal small clusters of DC-SIGN that are approximately 100 nm in diameter. The polarization data suggest that members of the clusters are randomly oriented although some single-molecule events resulted in pure polarization, as identified by the circles. Garcia-Parajo and coworkers were able to combine this information to determine DC-SIGN density through calibrated intensity measurements and also explore the molecular organization of several clusters through sequential NSOM imaging with single-molecule photobleaching. By utilizing a 2D Gaussian fit, the authors were able to determine the position of the fluorophores to within  $\sim 6$  nm. The image analysis of the high-resolution NSOM data revealed DC-SIGN cluster organization that is quite heterogeneous, a trait that may be key in the ability of immature dendritic cells to recognize a large variety of pathogens.

### 9.3.3 *Tip-Sample Interactions*

The previous examples on model membranes and fixed biological tissues help to illustrate the utility of NSOM in the biological sciences. The high-resolution fluorescence and topography information, single-molecule detection limits, along with the host of spectroscopic, time-resolved, and polarization capabilities offer a powerful set of tools. It should also be noted that since resolution does not depend on wavelength, as it does for far-field measurements, moving to longer wavelengths to avoid autofluorescence will not sacrifice resolution. However, extending NSOM measurements into unfixed biological tissues under buffered environments has proven extremely difficult.

One of the biggest obstacles for implementing NSOM measurements on fragile biological samples revolves around the forces generated in the feedback mechanism used to control the tip-sample gap. Because typical fiber-optic NSOM probes have large spring constants when compared with AFM probes, they have been less successful at imaging unfixed biological tissues under buffered conditions. While certain geometries have been shown capable of noninvasive imaging of unfixed samples, these often rely on complicated fabrication procedures that have reduced their utility. Future progress in this area will likely require a dramatic departure from current probe designs or feedback approaches.

Early NSOM approaches on fragile samples circumvented the force problem by scanning samples in constant height mode, with the tip feedback turned off. While some information can be gained from such studies, generally this is an unsatisfactory mode to collect NSOM images. A wealth of studies has shown that image contrast in NSOM can be strongly affected by changes in tip-sample gap [3–5]. Moreover, samples such as cultured cells can have large, micron-level height changes across the cell body. For high-resolution NSOM information, the probe must remain within nanometers of the sample surface during the measurements. Therefore, without an active feedback mechanism, resolution is not only lost but can change within an image, leading to difficulties in image interpretation.

While the problems associated with implementing a feedback scheme under aqueous environments were quickly solved using a number of approaches [52–55], reducing the forces involved has been more problematic. Attempts to reduce the forces have largely revolved around using a feedback signal not based on force, reducing the spring constant of the fiber-optic NSOM tip, or changing the probe itself.

A noncontact interferometric approach for controlling the NSOM tip-sample gap was shown to be gentle enough to image the air–liquid interface while in feedback [56]. This approach took advantage of the differences in path length for photons directly exiting the NSOM probe and those reflected off the sample surface as the probe approached the surface. Detecting the interferometric signal from the side resulted in oscillatory changes in the signal amplitude as the tip approached the sample [57]. The constructive and destructive interferences were observable when the probe was approximately one micron from the sample surface, providing a truly noncontact signal to implement a feedback scheme. While the technique was shown

to successfully provide feedback on dry samples in air or samples at the air–liquid interface, extending this arrangement into samples under aqueous conditions has proven difficult. The collection of the interferometric signal from the side is not easily implemented for samples under buffered conditions, and other collection geometries result in poor and unstable feedback signals.

Changing the spring constant of the fiber-optic NSOM probe and/or designing new probes with low spring constants are the most straightforward ways of circumventing the force problem. Chemically etching down the diameter of the fiber-optic NSOM probe with buffered HF leads to smaller spring constants [58]. However, when used either in the shear-force approach with linear probe geometries or in the tapping-mode arrangement with cantilevered NSOM probes, the smaller spring constant leads to a dramatic dampening of the oscillation under aqueous conditions. This reduces both the amplitude and stability of the feedback signal, which makes live cell imaging difficult.

The silicon nitride probes used in atomic force microscopy (AFM) have spring constants that are amenable with live cell imaging. This has led to various attempts to incorporate a near-field light source into these tips [3]. In one application, a solid immersion lens was incorporated with an AFM cantilever [59]. These probes were manufactured for solid-state applications, however, and were not meant to break the diffraction barrier or image biological samples. Thus, the spatial resolution was limited to approximately 250 nm, and the forces associated with these tips were not appropriate for imaging fragile samples.

More recent endeavors to couple AFM probes with NSOM applications have used focused ion beam (FIB) modification of conventional AFM probes [60–63]. In the most straightforward example, a small hole is drilled at the apex of the pyramid that acts as the AFM stylus. This hole acts as the aperture for light in NSOM applications. These probes have been used mostly in transmission measurements, from which it is difficult to extract reliable measures of spatial resolution due to the possible presence of tip-sample coupling artifacts. More reliable spatial information comes from NSOM fluorescence measurements. To date, fluorescence measurements taken with these probes have not reported subdiffraction limited spatial resolution; further experiments are needed to show that high resolution is possible with these probes.

In related studies [64], FIB modification of AFM probes has led to the development of hybrid probes that incorporate elements that act as NSOM light sources. In one example, an FIB was used to drill a 7- $\mu\text{m}$  hole in the end of a conventional AFM cantilever, and the pyramidal stylus normally used in AFM imaging was removed, as shown in Fig. 9.20. An 8- $\mu\text{m}$  high-index glass sphere was glued into the hole and further machined into a pyramid shape with the FIB. The sides were then coated with 50–100 nm of aluminum to confine the excitation light, and a small aperture was opened at the end the pyramid with the FIB. This process resulted in an AFM tip incorporating an element that acts as an NSOM light source.

A similar probe was fabricated using fiber-optic NSOM probes incorporated into silicon nitride AFM cantilevers [65]. Again with the use of FIB technology, a small hole is drilled into the end of an AFM probe. An aluminum-coated, fiber-optic



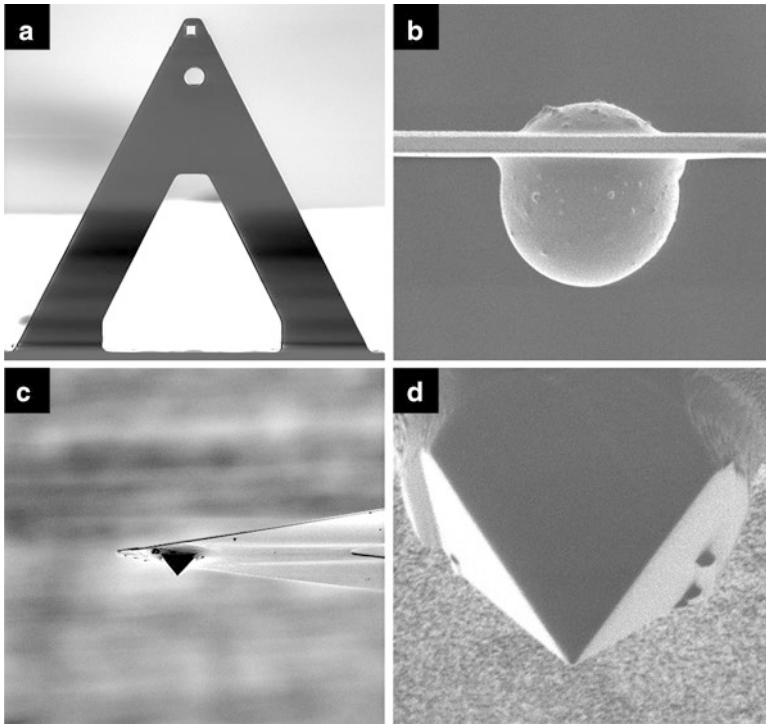


**Fig. 9.20** A series of images depicting the steps used in incorporating a high refractive index glass sphere into an AFM cantilever. A focused ion beam (FIB) instrument is used to carve a hole into the AFM cantilever, as shown in (a). An 8- $\mu\text{m}$  glass bead is then secured within the hole using UV-curable glue (b). The FIB is used to carefully carve the glass bead into a pyramid. The probe is then coated with a thin layer of aluminum to confine light. The completed probe is shown in (c) and a magnified view of the waveguide is shown in (d) (Figure adapted from Ref. [64])

NSOM probe is carefully lowered into the machined hole and glued into place. Once glued, the excess fiber is cut from the backside of the AFM tip with the FIB, as shown in Fig. 9.21. These tips have the advantage of using well-characterized fiber-optic NSOM probes to deliver the light combined with the low spring constants of commercial AFM cantilevers.

Figure 9.22 shows NSOM topography (a) and fluorescence (b) images taken with these probes on a sample containing small, fluorescent spheres embedded in a matrix. The fluorescence image reveals small, subdiffraction limited features that are not correlated with features in the topography image. This confirms the spatial resolution capabilities of these hybrid probes. Of more interest, however, are the NSOM fluorescence, force, and amplitude images shown in Fig. 9.23. These NSOM images were taken on a living HASM cell under buffered conditions. The adrenergic receptors were fluorescently labeled with prazosin BODIPY-FL, and repeated scans of the same cell found no evidence of damage caused by the NSOM/

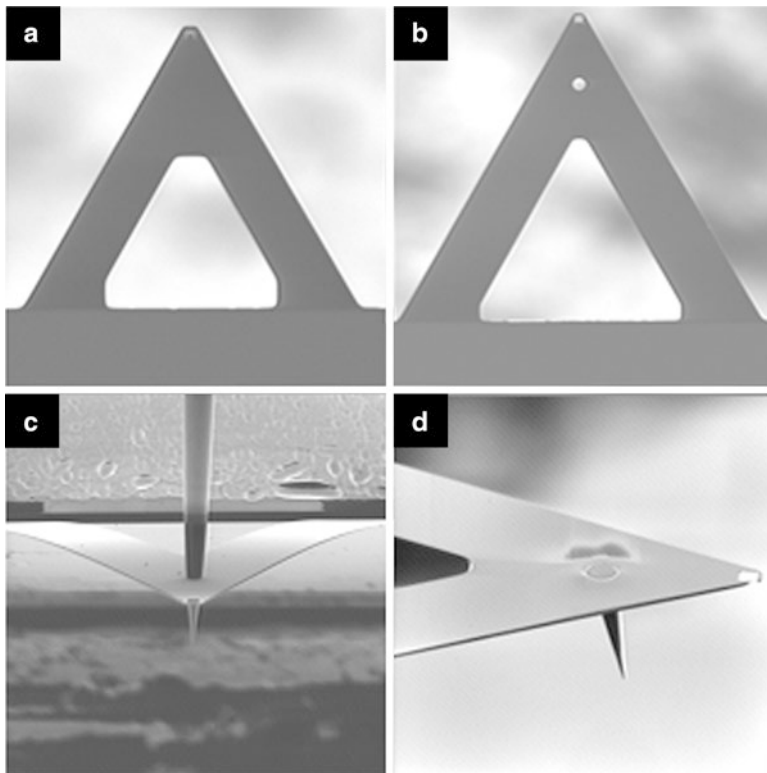


**Fig. 9.21** A series of images outlining the manufacture process for low-force NSOM probes. A commercial AFM cantilever ( **a** ) is placed inside a focused ion beam (FIB) instrument and a 7- $\mu\text{m}$ -diameter hole is carved into the cantilever as shown in ( **b** ). A fiber-optic NSOM probe is inserted into the hole ( **c** ) and secured with UV-curable glue. The fiber is then cut flush with the back of the cantilever ( **d** ) (Figure adapted from Ref. [65])

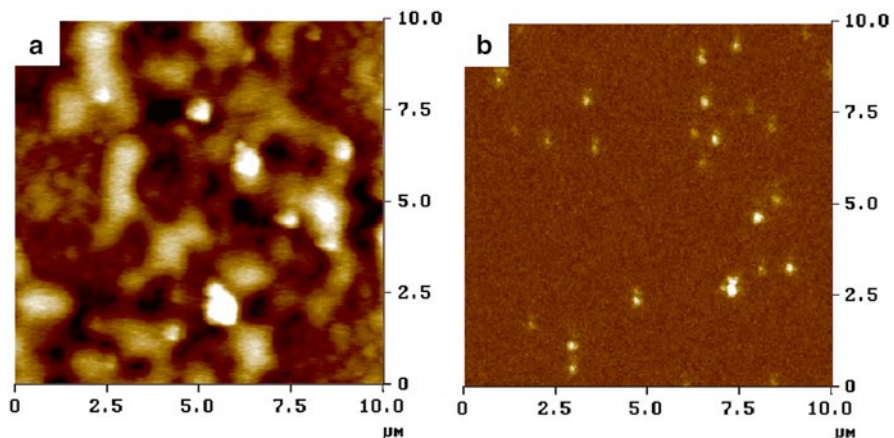


**Fig. 9.22** A 10- $\mu\text{m}$  $\times$ 10- $\mu\text{m}$  NSOM image taken using a hybrid AFM/NSOM probe like that shown in Fig. 9.20d. ( **a** ) and ( **b** ) display the simultaneously collected NSOM force and fluorescence images, respectively. The sample consisted of 50-nm fluorescent latex spheres embedded in a thin acetate matrix (Figure adapted from Ref. [65])

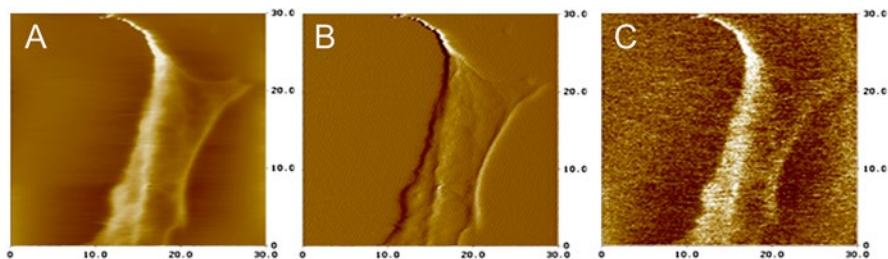


**Fig. 9.23** 30- $\mu\text{m}$   $\times$  30- $\mu\text{m}$  NSOM force (a), deflection (b), and fluorescence (c) images of a live human arterial smooth muscle cell. The hybrid probe shown in Fig. 9.20d was scanned in contact feedback mode under buffered conditions. The fluorescence image results from the labeling of adrenergic receptors with prazosin BODIPY-FL (Figure adapted from Ref. [65])

AFM hybrid probe. While these measurements illustrate that NSOM measurements on living cells are possible, the laborious nature of probe fabrication and the need for expensive FIB technology limit the applicability of this approach. Clearly, more developments are needed to make routine NSOM measurements of living tissues useful.

## 9.4 Summary

Progress in using NSOM to probe biological samples has been slowed by the technical difficulties involved, but NSOM now seems poised to take its place among other complementary techniques. The high-resolution fluorescence and force information seems particularly well suited for biological applications where both contrast mechanisms can add unique insights. Combined with the single-molecule detection limits and spectroscopic capabilities, this offers a powerful set of tools for the biological sciences.

**Acknowledgments** We gratefully acknowledge the support of NIH (GM65964) and the Madison and Lila Self Foundation. N.E.D. acknowledges the support from the NIH Dynamic Aspects of Chemical Biology training program (GM008545).

## References

1. Abbe E. Beitrage zur Theorie des Mikroskops und der Mikroskopischen wahrnehmung. Arch Mikrosk Anat. 1873;9:413–68.
2. Born M, Wolf E. Principles of optics. 7th ed. Cambridge, UK: Cambridge University Press; 1997.
3. Novotny L, Hecht B. Principles of nano-optics. 1st ed. New York: Cambridge University Press; 2006.

4. Pohl DW. Optics at the nanometre scale. *Philos Trans R Soc London Ser A Math Phys Eng Sci.* 2004;362:701–17.
5. Dunn RC. Near-field scanning optical microscopy. *Chem Rev.* 1999;99:2891–928.
6. Novotny L, Pohl DW, Hecht B. Scanning near-field optical probe with ultrasmall spot size. *Opt Lett.* 1995;20:970–2.
7. Betzig E, Trautman JK, Harris TD, Weiner JS, Kostelak RL. Breaking the diffraction barrier – optical microscopy on a nanometric scale. *Science.* 1991;251:1468–70.
8. Edidin M. Near-field scanning optical microscopy, a siren call to biology. *Traffic.* 2001;2: 797–803.
9. Hoffmann P, Dutoit B, Salathe R-P. Comparison of mechanically drawn and protection layer chemically etched optical fiber tips. *Ultramicroscopy.* 1995;61:165–70.
10. Turner DR. U.S. Patent No. 4,469,554. 1984
11. Hollars CW, Dunn RC. Evaluation of thermal evaporation conditions used in coating aluminum on near-field fiber-optic probes. *Rev Sci Instrum.* 1998;69:1747–52.
12. Mooren OL, Erickson ES, Dickenson NE, Dunn RC. Extending near-field scanning optical microscopy for biological studies. *JALA.* 2006;11:268–72.
13. Dickenson NE, Erickson ES, Mooren OL, Dunn RC. Characterization of power induced heating and damage in fiber optic probes for near-field scanning optical microscopy. *Rev Sci Instrum.* 2007;78:053712.
14. Betzig E, Finn PL, Weiner JS. Combined shear force and near-field scanning optical microscopy. *Appl Phys Lett.* 1992;60:2484–6.
15. Shalom S, Lieberman K, Lewis A, Cohen SR. A micropipette force probe suitable for near-field scanning optical microscopy. *Rev Sci Instrum.* 1992;63:4061–5.
16. Toledocrow R, Yang PC, Chen Y, Vaeziravani M. Near-field differential scanning optical microscope with atomic force regulation. *Appl Phys Lett.* 1992;60:2957–9.
17. Muramatsu H, Chiba N, Homma K, Nakajima K, Ataka T, Ohta S, Kusumi A, Fujihira M. Near-field optical microscopy in liquids. *Appl Phys Lett.* 1995;66:3245–7.
18. Talley CE, Cooksey GA, Dunn RC. High resolution fluorescence imaging with cantilevered near-field fiber optic probes. *Appl Phys Lett.* 1996;69:3809–11.
19. Naber A, Maas HJ, Razavi K, Fischer UC. Dynamic force distance control suited to various probes for scanning near-field optical microscopy. *Rev Sci Instrum.* 1999;70:3955–61.
20. Paesler MA, Moyer PJ. *Near-field optics: theory, instrumentation, and applications.* 1st ed. New York: John Wiley; 1996.
21. Erickson ES, Dunn RC. Sample heating in near-field scanning optical microscopy. *Appl Phys Lett.* 2005;87:201102.
22. Hecht B, Sick B, Wild UP, Deckert V, Zenobi R, Martin OJF, Pohl DW. Scanning near-field optical microscopy with aperture probes: fundamentals and applications. *J Chem Phys.* 2000; 112:7761–74.
23. Novotny L, Hafner C. Light propagation in a cylindrical waveguide with a complex, metallic, dielectric function. *Phys Rev E Stat Phys Plasmas.* 1994;50:4094–6.
24. Stahelin M, Bopp MA, Tarrach G, Meixner AJ, Zschokke-Granacher I. Temperature profile of fiber tips used in scanning near-field optical microscopy. *Appl Phys Lett.* 1996;68: 2603–5.
25. Rosa AHL, Yakobson BI, Hallen HD. Origins and effects of thermal processes on near-field optical probes. *Appl Phys Lett.* 1995;67:2597–9.
26. Latini G, Downes A, Fenwick O, Ambrosio A, Allegrini M, Daniel C, Silva C, Gucciardi PG, Patane S, Daik R, Feast WJ, Cacialli F. Optical probing of sample heating in scanning near-field experiments with apertured probes. *Appl Phys Lett.* 2005;86:011102–3.
27. Latini G, Downes A, Fenwick O, Ambrosio A, Allegrini M, Gucciardi PG, Patane S, Daniel C, Silva C, Daik R, Feast WJ, Cacialli F. Investigation of heating effects in near-field experiments with luminescent organic semiconductors. *Synth Met.* 2004;147:165–9.
28. Gucciardi PG, Colocci M, Labardi M, Allegrini M. Thermal-expansion effects in near-field optical microscopy fiber probes induced by laser light absorption. *Appl Phys Lett.* 1999;75: 3408–10.

29. Lienau C, Richter A, Elsaesser T. Light-induced expansion of fiber tips in near-field scanning optical microscopy. *Appl Phys Lett*. 1996;69:325–7.
30. McConnell HM. Structures and transitions in lipid monolayers at the air-water-interface. *Annu Rev Phys Chem*. 1991;42:171–95.
31. Mohwald H. Phospholipid and phospholipid-protein monolayers at the air/water interface. *Annu Rev Phys Chem*. 1990;41:441–76.
32. Hollars CW, Dunn RC. Submicron structure in L- $\alpha$ -dipalmitoylphosphatidylcholine monolayers and bilayers probed with confocal, atomic force, and near-field microscopy. *Biophys J*. 1998;75:342–53.
33. Edidin M. The state of lipid rafts: from model membranes to cells. *Annu Rev Biophys Biomol Struct*. 2003;32:257–83.
34. Simons K, Vaz WLC. Model systems, lipid rafts, and cell membranes. *Annu Rev Biophys Biomol Struct*. 2004;33:269–95.
35. Burgos P, Yuan CB, Viriot ML, Johnston LJ. Two-color near-field fluorescence microscopy studies of microdomains (“rafts”) in model membranes. *Langmuir*. 2003;19:8002–9.
36. Yuan C, Furlong J, Burgos P, Johnston LJ. The size of lipid rafts: an atomic force microscopy study of ganglioside GM1 domains in sphingomyelin/DOPC/cholesterol membranes. *Biophys J*. 2002;82:2526–35.
37. Schwartz RM, Luby NM, Scanlon JW, Kellogg RJ. Effect of surfactant on morbidity, mortality, and resource use in newborn-infants weighing 500 to 1500 g. *New Engl J Med*. 1994;330:1476–80.
38. Sibug-aga R, Dunn RC. High-resolution studies of lung surfactant collapse. *Photochem Photobiol*. 2004;80:471–6.
39. Betzig E, Chichester RJ. Single molecules observed by near-field scanning optical microscopy. *Science* 1993;262:1422–25.
40. Hollars CW, Dunn RC. Probing single molecule orientations in model lipid membranes with near-field scanning optical microscopy. *J Chem Phys*. 2000;112:7822–30.
41. Gersen H, Garcia-Parajo MF, Novotny L, Veerman JA, Kuipers L, van Hulst NF. Influencing the angular emission of a single molecule. *Phys Rev Lett*. 2000;85:5312–5.
42. Gersen H, Garcia-Parajo MF, Novotny L, Veerman JA, Kuipers L, Van Hulst NF. Near-field effects in single molecule emission. *J Microsc (Oxford)*. 2001;202:374–8.
43. Jares-Erijman EA, Jovin TM. FRET imaging. *Nat Biotechnol*. 2003;21:1387–95.
44. Selvin PR. The renaissance of fluorescence resonance energy transfer. *Nat Struct Biol*. 2000;7:730–4.
45. Sekatskii SK. Fluorescence resonance energy transfer scanning near-field optical microscopy. *Philos Trans R Soc London Ser A Math Phys Eng Sci*. 2004;362:901–9.
46. Shubeita GT, Sekatskii SK, Dietler G, Letokhov VS. Local fluorescent probes for the fluorescence resonance energy transfer scanning near-field optical microscopy. *Appl Phys Lett*. 2002;80:2625–7.
47. Vickery SA, Dunn RC. Scanning near-field fluorescence resonance energy transfer microscopy. *Biophys J*. 1999;76:1812–8.
48. Vickery SA, Dunn RC. Combining AFM and FRET for high resolution fluorescence microscopy. *J Microsc (Oxford)*. 2001;202:408–12.
49. Dickenson NE, Dunn RC. (Unpublished). Unpublished Data.
50. Hwang J, Gheber LA, Margolis L, Edidin M. Domains in cell plasma membranes investigated by near-field scanning optical microscopy. *Biophys J*. 1998;74:2184–90.
51. de Bakker BI, de Lange F, Cambi A, Korterik JP, van Dijk EM, van Hulst NF, Figdor CG, Garcia-Parajo MF. Nanoscale organization of the pathogen receptor DC-SIGN mapped by single-molecule high-resolution fluorescence microscopy. *Chemphyschem*. 2007;8:1473–80.
52. Burgos P, Lu Z, Ianoul A, Hnatovsky C, Viriot ML, Johnston LJ, Taylor RS. Near-field scanning optical microscopy probes: a comparison of pulled and double-etched bent NSOM probes for fluorescence imaging of biological samples. *J Microsc*. 2003;211:37–47.
53. Koopman M, de Bakker BI, Garcia-Parajo MF, van Hulst NF. Shear force imaging of soft samples in liquid using a diving bell concept. *Appl Phys Lett*. 2003;83:5083–5.

54. Oesterschulze E, Rudow O, Mihalcea C, Scholz W, Werner S. Cantilever probes for SNOM applications with single and double aperture tips. *Ultramicroscopy*. 1998;71:85–92.
55. Talley CE, Lee MA, Dunn RC. Single molecule detection and underwater fluorescence imaging with cantilevered near-field fiber optic probes. *Appl Phys Lett*. 1998;72:2954–6.
56. Shiku H, Dunn RC. Near-field scanning optical microscopy studies of L-ALPHA-DIPALMITOYL PHOSPHATIDYLCHOLINE monolayers at the air-liquid interface. *J Microsc (Oxford)*. 1999;194:461–6.
57. Shiku H, Krogmeier JR, Dunn RC. Noncontact near-field scanning optical microscopy imaging using an interferometric optical feedback mechanism. *Langmuir*. 1999;15:2162–8.
58. Lee MA, Talley CE, Vickery SA, Krogmeier JR, Hollars CW, Shiku H, Dunn RC. Progress toward imaging biological samples with NSOM. *Proc SPIE Intl Soc Opt Eng Scanning Force Microsc Biomed Appl*. 1999;3607:60–6.
59. Partovi A, Peale D, Wuttig M, Murray CA, Zydzik G, Hopkins L, Baldwin K, Hobson WS, Wynn J, Lopata J, Dhar L, Chichester R, Yeh JHJ. High-power laser light source for near-field optics and its application to high-density optical data storage. *Appl Phys Lett*. 1999;75:1515–7.
60. Dziomba T, Danzebrink KU, Lehrer C, Frey L, Sulzbach T, Ohlsson O. High-resolution constant-height imaging with apertured silicon cantilever probes. *J Microsc (Oxford)*. 2001;202:22–7.
61. Eckert R, Freyland JM, Gersen H, Heinzelmann H, Schurmann G, Noell W, Stauffer U, de Rooij NF. Near-field fluorescence imaging with 32 nm resolution based on microfabricated cantilevered probes. *Appl Phys Lett*. 2000;77:3695–7.
62. Lehrer C, Frey L, Petersen S, Sulzbach T, Ohlsson O, Dziomba T, Danzebrink HU, Ryssel H. Fabrication of silicon aperture probes for scanning near-field optical microscopy by focused ion beam nano machining. *Microelectron Eng*. 2001;57–8:721–8.
63. Radojewski J, Grabiec P. Combined SNOM/AFM microscopy with micromachined nanoapertures. *Mater Sci (Poland)*. 2003;21:321–32.
64. Krogmeier JR, Dunn RC. Focused ion beam modification of atomic force microscopy tips for near-field scanning optical microscopy. *Appl Phys Lett*. 2001;79:4494–6.
65. Kapkiai LK, Moore-Nichols D, Carnell J, Krogmeier JR, Dunn RC. Hybrid near-field scanning optical microscopy tips for live cell measurements. *Appl Phys Lett*. 2004;84:3750–2.

# Chapter 10

## Atomic Force Microscopy: Applications in the Field of Biology

J.K. Heinrich Hoerber

**Abstract** The invention of telescopes and microscopes about 400 years ago revolutionized our perception of the world, extending our sense of seeing. Extending it further and further has since been the driving force for major scientific developments. Local probe techniques extend our sense of touching into the micro- and nanoworld and in this way provide complementary new insight into these worlds we see with microscopic techniques. Furthermore, touching things is an essential prerequisite to manipulating things, and the ability to feel and manipulate single molecules and atoms for sure marks another of these revolutionizing steps in our relation to the world in which we live.

Local probes are small-sized objects, such as the very end of sharp tips, which interact with a sample, or better, the surface of a sample at selected positions. Proximity to or contact with the sample is required to have a high spatial resolution. This, in principle, is an old idea that appeared in the literature from time to time in context with bringing a source of electromagnetic radiation in close contact with a sample (Synge, *Philos Mag* 6:356, 1928; O'Keefe, *J Opt Soc* 46:359, 1956; Ash and Nicolls, *Nature* 237:510, 1972). It found no resonance and therefore was not pursued until the early 1980s. Nanoscale local probes require atomically stable tips and high-precision manipulation devices. The latter are based on mechanical deformations of spring-like structures by piezoelectric, electrostatic, or magnetic forces to ensure continuous and reproducible displacements with precision down to the picometer level. They also require very good vibration isolation. The resolution that can be achieved with local probes is given mainly by the effective probe size, its distance from the sample, and the distance dependence of the interaction between the probes and the sample measured. The last can be considered creating an effective aperture by selecting a small feature of the overall geometry of the probe tip, which then corresponds to the effective probe. One of the great advantages of local

---

J.K.H. Hoerber (✉)

HH Wills Physics Laboratory, University of Bristol, Tyndall Ave., Bristol BS8 1TL, UK  
e-mail: h.hoerber@bristol.ac.uk

probes is that they can work in any environment; this way, they provide the possibility to study live biological processes similar to optical microscopy, but at a resolution similar to electron microscopy (EM).

## 10.1 Introduction

The **atomic force microscope** (AFM) belongs to the large family of instruments called local or scanning probe microscopes. All of these instruments are based on the principle of measuring the interaction of a small tip structure with a sample surface at close distances. In the case of the first instrument of the family, the **scanning tunneling microscope** (STM), developed in the early 1980s by Binnig and Rohrer [4] at the IBM Research Laboratory in Zurich, the interacting tip is a single atom (see Fig. 10.1). This is possible because of the very short-range electronic interaction used with a decay length on the size of atoms. This interaction between the tip and surface, which allows electrons to cross a small gap before an electrical contact is made, is related to the quantum-mechanical process of electron tunneling reflected by the name. Such a tunneling current through a vacuum gap is in the range of pico- to nanoamps and drops by an order of magnitude if the distance changes from 0.4 to 0.5 nm. With atoms being the same size, it is possible that the main contribution to this tunneling current is related to the interaction of the foremost tip atom with a single atom at the surface closest to this tip atom. If the surface and the tip are moved with respect to one another at a constant average distance, the variations seen in the current reflect the topography of the surface with atomic resolution if the surface is homogeneous. In the case of different types of atoms present at the surface, the signal measured is a mixture of topography and differences between the atom species in their electronic interaction with the tip atom.

With this incredible resolution, the most important part of such a microscope is the mechanism that causes the tip to approach the surface and moves it across with the necessary precision and stability. The mechanism Binnig and Rohrer came up with is based on the piezoelectric effect discovered in 1880 by the brothers Pierre

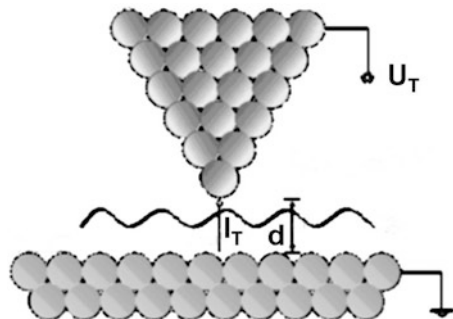


**Fig. 10.1** STM imaging with atomic resolution. The tip is scanned at a constant height over the surface, and the current measured between the tip and surface is modulated by the distribution of surface atoms



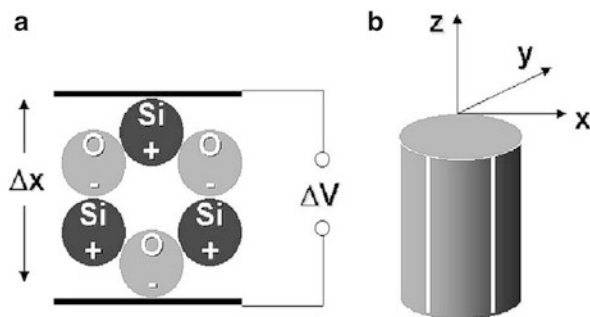


**Fig. 10.2** (a) An electric field applied across a quartz crystal interacts with the crystalline structure through its polarization, which affects the crystal structure and leads to a change in size. (b) The piezotube changes its length if a voltage difference between the inside electrode and all four outer electrodes is applied. The tube bends sideways if a voltage difference between the inside electrode and one segment of the outside electrodes is applied. In this way, a tip mounted in the direction of the  $z$ -coordinate can approach a surface very precisely and be scanned across with the same precision, which is mainly related to the stability of the voltage source used

and Jacques Curie. They noticed that mechanical stress affects the polarization of crystalline structures like quartz and that this can be used in reverse with an electric field applied across a quartz crystal to change its size. In the case of quartz, a very high electric field is necessary for only a small change in size. In the 1950s, ceramic materials such as perovskites were discovered, which change their size in the micrometer range with only a few hundred volts applied. Three stacks of ceramic discs were used in the first STMs to position the tip in all three dimensions with the necessary precision that allowed a precise approach of the tip to the surface and scanning it across. Meanwhile, more often a ceramic tube with an electrode on the inside and a segmented electrode on the outside is used, which allows tip movement in all three directions in a controlled way by applying a voltage between the inner electrode and all outside electrodes to approach and retract the tip and between the inner and individual outer electrodes to bend the tube sideways to do the scanning (Fig. 10.2).

To prevent the tip from crashing into the surface while scanning, due to roughness of the sample surface or when mechanical vibrations of the instruments occur, the electronics that controls the movement of the tip includes a “feedback loop” that limits the tip–surface interaction by moving the tip away from the surface if necessary to reduce the current below an upper limit. The feedback can keep the interaction constant during scanning if it is fast enough, which means the tip will follow the contour of a sample with homogeneous electronic properties. This imaging mode is called *constant current imaging*. The maximum speed of the feedback control, mainly determined by mechanical resonances, is the main limitation in scanning probe microscopy that determines how fast an image (picture) of an area with a certain size can be produced. Faster imaging can be done in so-called constant-height mode, but this is only possible on sample surfaces that are flat at the atomic scale to avoid the tip’s crashing into the sample at protrusions.

## 10.2 Atomic Force Microscopy

Due to the electronic interaction measured in the case of the STM, both the tip and the surface have to be conducting. This significantly limits the materials that can be investigated. In 1986, Binnig, together with Quate and Gerber, overcame this limitation with the invention of the next member of the probe microscope family, called the **atomic force microscope (AFM)** [5]. The idea that allows also the investigation of nonconducting materials was to use the “van der Waals” forces between atoms as a type of interaction present in all types of atoms. The corresponding interaction potential (Lennard–Jones potential) has a very weak attractive regime between 0.7 and .35 nm and becomes strongly repulsive with a  $1/r^{12}$  distance dependence below 0.35 nm. A microscope using these interactions between the tip and the surface atoms needs to detect forces in the nano- to pico-Newton range, thus asking for a very sensitive force-detection system. The most straightforward way to measure forces is by using a spring, which can be characterized by its spring constant connecting the spring extension (or bending in the case of a cantilever) and force by Hooke’s law:  $F = -k\Delta x$ . With such a linear force–distance relationship, a spring with a stiffness of 1 N/m needs a precision in the distance measurement in the nanometer range to achieve a force resolution in the nano-Newton range. The STM, invented just five years before by Binnig and collaborators, can easily measure distances with such a precision; therefore, it was the obvious choice to be used in the first AFM to detect the bending of a small cantilever with a tiny piece of diamond as a tip at the end. A schematic of the first AFM instrument is provided in Fig. 10.3.

Initially, there was doubt about whether the AFM could achieve a true atomic resolution and whether the van der Waals interaction of one tip atom with just one surface atom on crystalline surfaces is actually measured. Some researchers suggested that clusters of atoms on both sides interact with one another and that the structures seen are interference patterns created while scanning across the surface that have more or less a relationship to its atomic structure. It was much later that Giessibl could show that under certain conditions, even atomic substructures can be imaged with an AFM [7]. However, the normal case, especially on molecular

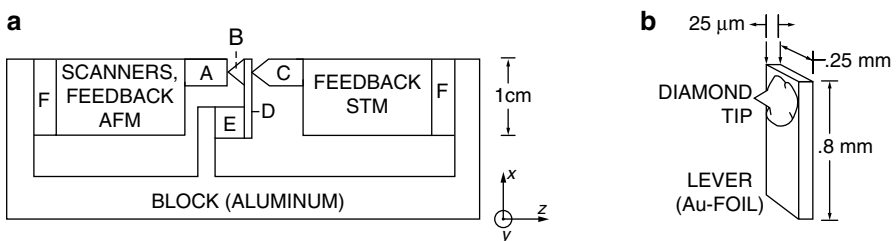


**Fig. 10.3** Schematic of the first AFM from the IBM patent application in 1986 (Adapted from Ref. [6]). In (a) the cantilever is not drawn to scale; the dimensions are shown in (b). A: sample, B: AFM diamond tip, C: STM tip, D: metal cantilever as sample for the STM detection, E: modulating piezo, F: viton vibration insulation

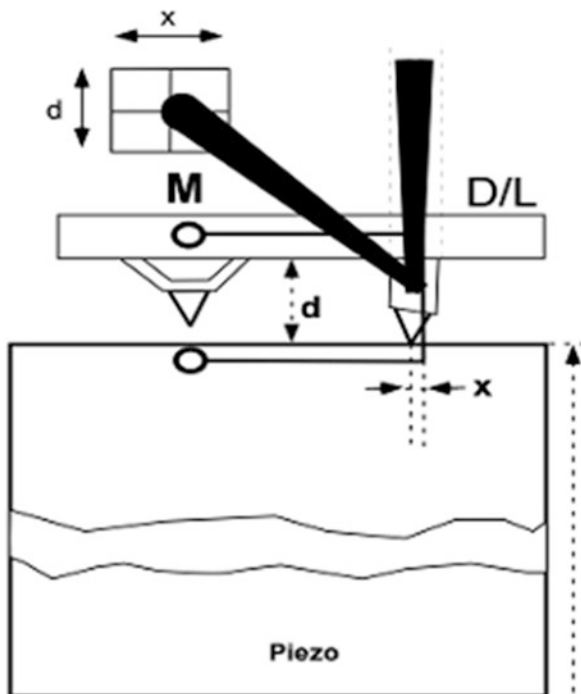


**Fig. 10.4** Optical detection scheme showing the laser beam deflected by the cantilever toward the quadrant photo detector

structures, turned out to be that more than one atom of the tip interacts due to various types of surface forces with a surface area of a corresponding size and in this way reduces the AFM resolution to the nanometer range.

An important development providing the basis for the successful use of the AFM in biology was the replacement of the STM detection with an optical detection scheme (Fig. 10.4), as this allowed measurements even in salt-containing solutions. In 1988, Meyer and Amer demonstrated that a reflected laser beam at the tip of a cantilever observed in some distance with a split photodiode can provide a sensitivity similar to that of the STM detection [8]. The standard detection scheme in most commercial AFMs is based meanwhile on a diode laser focused at the end of the cantilever directly above its tip. The bending of the cantilever changes the direction of the reflected laser beam and thus its position on the detector. The change in the intensity distribution between the two halves of the split diode leads to a change in the electric signals produced by both halves. If a sensitive amplifier is used to measure the signal difference between the two halves, it is possible to detect movements of the cantilever in the range below 1 nm, which, with a small cantilever spring constant of 0.01 N/m, leads to a force sensitivity in the range of 10 pN.

The cantilevers used are micro-machined from silicon or silicon nitride wafers with a length between 50 and 250  $\mu\text{m}$  and a thickness between 0.5 and 2  $\mu\text{m}$ , leading

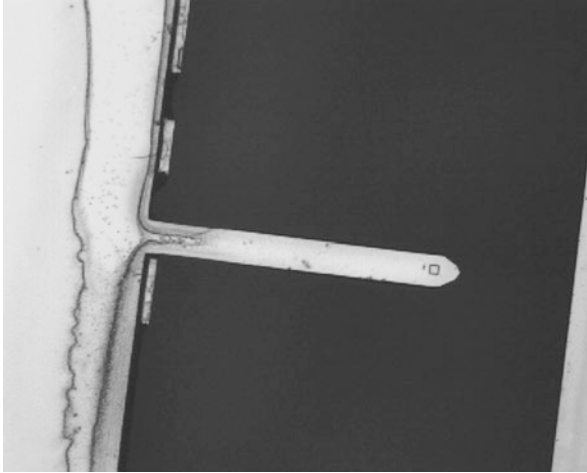


**Fig. 10.5** EM image of an AFM cantilever from below, with the tip visible at the end as a small 5- $\mu\text{m}$  square

to spring constants between 100 and 0.01 N/m (Fig. 10.5). The tips are made by different procedures and in some cases have a roof-shaped end due to the crystalline structure of the material used. In such a case, the resolution depends not only on the length of the ridge, but also on its tilt and the scanning direction with respect to the direction of the ridge. A so-called oxide-sharpening technique, which leads to final tip radii of only a few nanometers at a total tip length of 5–10  $\mu\text{m}$ , makes the smallest tip radii. The shape of cantilevers quite often is triangular, to provide a higher stability against lateral forces, which can become quite high due to friction effects while scanning the tip across a surface. These lateral or friction forces twist the cantilever sideward and lead to a movement of the laser beam on the detector perpendicular to the normal deflection, which can be measured by using a quadrant photodiode instead of a split one (Fig. 10.4).

With a device that can detect the bending of the cantilever, it becomes difficult to move the tip, which is usually done in an STM. Therefore, many AFMs have the sample mounted on the piezotube. As the sample normally has a larger mass than the cantilever, the system's resonance frequency decreases in such a setup, decreasing the scan speed. However, with a specially designed laser optic, the problem can be overcome and a scanning head can be made that can be placed over a fixed sample. Nevertheless, usual imaging speeds are in the range of minutes; the efforts to build fast-scanning AFMs are still ongoing, mainly based on reducing the cantilever size.

### **10.2.1 Application Modes**

As in the case of an STM, it is important to control the tip interaction while scanning with the AFM in order not to destroy the tip or sample due to surface roughness or

external vibrations. The electronic feedback in the case of an AFM tries to keep the force between the tip and the sample within limits. This way, if the reaction time of the feedback is fast compared to the scanning speed, the tip will follow the surface contour, applying the same force to the sample everywhere when working in the repulsive van der Waals regime. This mode is called *constant-force mode*. The feedback normally is created as fast as the system resonances allow when weighted linear, differential, and integral components of the signal are being used. Nevertheless, over slopes, the feedback with reasonable scan speeds always becomes too slow and characteristic image artifacts occur depending on whether the tip is not retracted or pushed down fast enough. For very flat samples, a *constant-height mode* is also possible, with forces between the tip and the sample changing during scanning, as higher sample structures will push up the cantilever tip in this case. The tip is kept in contact due to an average preadjusted loading force. In this mode, the cantilever's spring constant and the corresponding resonance frequency determine the reaction time and, therefore, the maximal scan speed:

$$F \sim \sqrt{\left(\frac{k}{m}\right)},$$

where  $F$  is the resonance frequency,  $k$  is the spring constant, and  $m$  is the mass of the cantilever.

If a tip with a certain interaction force is scanned over a sample, lateral forces act on the tip due to the friction between the tip and the sample. Measuring various lateral friction forces is a way to characterize inhomogeneous samples, where different components have different frictions. For such *friction-mode* measurements, the AFM has to be equipped with a quadrant photodiode instead of a split one, as mentioned earlier. If adjusted in the right way, the quadrant diode detects in one direction the normal bending of the cantilever and perpendicular its sideward twisting due to the lateral friction force. Friction and high forces on rough surfaces, together with a slow feedback, easily destroy soft samples, resulting very often in parts of the sample sticking to the tip. A way to reduce this risk is to use the AFM in a *dynamic mode*. In this mode, the cantilever is vibrating close to its natural resonance frequency driven by a small piezo mounted where the cantilever is fixed. With small oscillation amplitudes in the ångstrom range in the dynamic AFM mode, force gradients are measured, allowing measurements even in the narrow and shallow attractive range of the van der Waals forces.

Some instruments drive the cantilever oscillation with a magnetic coating above the tip, which allows for much better control of the tip motion in this dynamic mode, especially if the cantilever works in a fluid chamber. If a piezo is used, it has to be mounted outside the fluid chamber to avoid electrical shorting. In this case, the vibrating piezo excites acoustic waves, which drive the cantilever in a more indirect way that makes the control of the actual tip motion difficult.

Working in air under ambient conditions has a serious issue with water, as all materials have thin layers of water present on the outer surface, with the water thickness depending on the humidity, the temperature, as well as the actual material. During the approach of the cantilever tip to the surface, the water layer on the tip

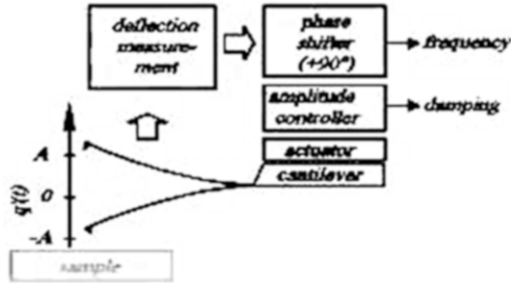


**Fig. 10.6** Principle of a dynamic AFM that uses an oscillating cantilever to measure tip interactions by amplitude and phase changes of the oscillation driven with a feedback using a phase-shifted signal to enhance the cantilever's quality factor, which is significantly reduced in liquid due to the viscosity

and that on the surface coalesce at one point during the approach and form a water meniscus. The forces generated by this meniscus are in the micro-Newton range; scanning this meniscus across a surface will wipe away everything that does not adhere well to the surface. With high enough amplitudes of the cantilever oscillations, in the so-called tapping mode, the water meniscus between the tip and the surface will break during each retraction cycle and no lateral forces of the meniscus will be produced.

In *dynamic mode*, the amplitude and phase changes of the vibrating cantilever reflect elastic and inelastic tip-sample interactions and can be used to characterize these material properties at the nanometer scale (Fig. 10.6). Images of inhomogeneous samples created using either the amplitude or the phase changes nicely depict distributions of different materials. Unfortunately, with the cantilever immersed into a liquid, the viscosity leads to a strong damping of the cantilever oscillations and a significant broadening of its resonance frequency curve, reducing the resolution in both the amplitude and the phase-shift signal. With a special type of feedback using a 90° phase-shifted input signal, it is possible to restore to some extent the so called quality factor of the cantilever, which was greatly reduced by the damping of the liquid.

### 10.2.2 Working in Liquid

The already-mentioned possibility to work with an AFM in liquid and especially in salt solutions extends the possibility of light microscopy to study the time course of processes from the micro- into the nanometer range. For biological applications, this opened a new era of studies on cellular structures and their dynamics. But as mentioned earlier, the cantilever motion in liquids is damped by the liquid's viscosity, and with the maximum speed the cantilever can be moved, the maximal imaging speed for high-resolution imaging is reduced. The viscous drag directly affects the mechanical properties of the cantilever immersed into a medium. How the

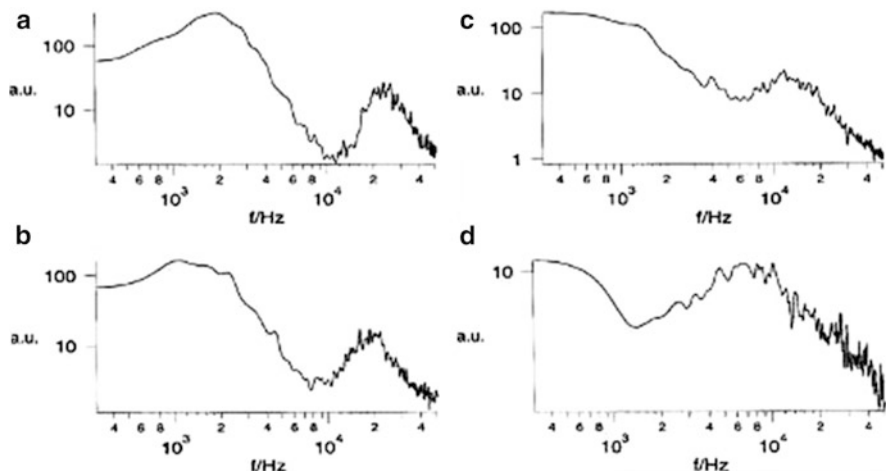


**Fig. 10.7** Changes to the frequency spectrum of a cantilever were measured while the ratio of the concentration of glycol to water is increased from 20 % (a) to 80 % (d) in 20 % increments

mechanical properties of a cantilever change with increasing viscosity is shown in Fig. 10.7, where the glycol concentration in water is increased systematically, leading to a significant increase in viscosity. The resonance curve is substantially broadened, and its maximum shifted from nearly 24 kHz at a 20 % glycol concentration down to 7 kHz at an 80 % concentration. These resonance curves were recorded as the difference between a cantilever moving in liquid driven by thermal fluctuations and the same cantilever in contact with the liquid chamber wall. This measuring protocol enables one to extract the instrument's mechanical and electrical noise (from the signal) to a level where the resonance curve excited by thermal fluctuations even in a very viscous medium can be measured.

The response of a mechanical cantilever to time-dependent external forces is described by a differential equation that characterizes the cantilever by its mass and its spring constant and the surrounding medium by its viscosity  $\eta$ , leading to a velocity-dependent damping  $\gamma$ :

$$F(t) = m d^2 z(t) / dt^2 + \gamma dz(t) / dt + kz(t),$$

$F$  = time-dependent driving force,

$m$  = moving mass,

$\gamma$  = velocity-dependent damping,

$k$  = spring constant.

With this equation, we can derive the maximum of the resonance curve of the cantilever as

$$f_{max} = \sqrt{\left( \frac{k}{m} - \frac{\gamma^2}{2m^2} \right)}.$$

**Fig. 10.8** Schematic of the different mass components necessary to describe the motion of a cantilever in a viscous medium

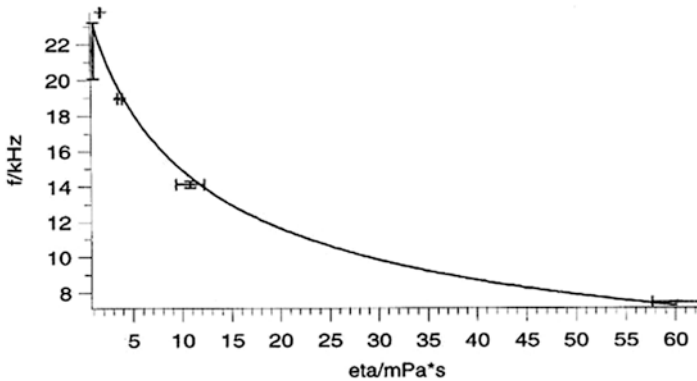
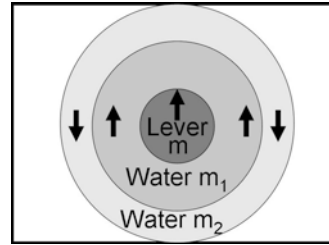


**Fig. 10.9** Fit to the maximum values of the resonance curves at different mixtures of water and glycol, which allows the values of  $m_1$  and  $m_2$  to be determined

To describe the way the resonance maximum changes with changing viscosity, as depicted in Fig. 10.8, the viscosity  $\eta$  and other parameters have to change to produce the monotonous decrease in the resonance frequency with increasing viscosity. There is no reason to assume that the spring constant of the cantilever may change, as it is only related to the material properties of the cantilever itself, which do not change. Another possibility is to assume that some mass of the medium is added to the cantilever mass. When a cantilever moves in a medium, some of the medium moves with the cantilever and some of the medium flows around these moving components to make way in front and to fill the space left behind.

Therefore, to account for the hydrodynamic effects, we need to add two additional components of mass into the equation (see Fig. 10.9):

$$F(t) = (m + m_1 + m_2) d^2 z(t) / dt^2 + g dz(t) / dt + Kz(t),$$

- $m$  = cantilever mass,
- $m_1$  = fluid mass moving with the cantilever,
- $m_2$  = fluid mass moving in the opposite direction.

With this equation, we can fit the observed changes of  $f_{max}$  and calculate the different mass components. Assuming that the shape of the cantilever is causing



only secondary effects, we can approximate the actual rectangular cantilever with a cylinder of the same mass and length, which allows us to solve the differential equation. The results show that in pure water twice the mass of the cantilever moves with the cantilever, and a little bit less than half the mass moves in the opposite direction. With an addition of 80 % glycol, and the corresponding high viscosity, 140 times the mass of the cantilever is moved together with it, but only 20 % more than in pure water is moving in the opposite direction. In the case of a cantilever with a diameter of 6  $\mu\text{m}$ , the layer of liquid moving with it changes from 2.4  $\mu\text{m}$  in pure water to 80  $\mu\text{m}$  if 80 % glycol is added. In the latter case with 80 % glycol, the layer thickness of the liquid moving against the cantilever is 200 nm, and in pure water it is 10 nm. This calculation shows that in water the hydrodynamic effects are limited to a range below 3  $\mu\text{m}$  around the cantilever. With an actual tip length of 5  $\mu\text{m}$  for most commercial cantilevers, this will not influence the sample interaction.

### 10.3 Applications in Biological Systems

Interactions of molecular structures are traditionally characterized by binding constants, on and off rates, and corresponding binding energies. The relevant energies for single binding events range from thermal energy up to some hundred times that of the thermal energy when covalent bonding is involved. Besides covalent bonds, hydrogen bonds, with energies between 4 and 16 kT, play an important role for macromolecular structures and their spatial organization. At interfaces of these structures, coulomb and dipole forces determine the interaction with the aqueous environment and thus between molecules. An important question for the biological function of these molecular interactions is their distance dependence in the actual environment. This question can be addressed using AFM force spectroscopy on the single-molecule level, giving a new, more physical view of the molecular interactions in terms of forces and their distance dependence.

An important aspect of measuring forces at the molecular level is the dependence of the force value on the timescale in which the force is applied. This connection can be understood by the deformation to the molecular interaction potentials caused by an applied force. This deformation leads to an effective lowering of the binding energy if the force tries to pull the molecular structures apart. Consider thermal fluctuations with a pulling force applied: It becomes more likely that the bond will break during a certain observation time. The off rate for the biotin–avidin binding, for instance, at room temperature is on the order of six months. If a small force of about 80 pN is applied, the lowering of the binding potential reduces the off rate to about 9 s. Doubling this force further decreases the lifetime of the binding by three orders of magnitude. Unfortunately, these experiments cannot be modeled with “molecular dynamic” computer simulations, as the timeframe of these simulations with the available computer power is limited to the pico- up to the nanosecond time range. Simulations of the rupture forces of biotin–avidin at this fast timescale lead to calculated forces of 600 pN. For AFM measurements completed at the time scale of 100 ms, the actual measured forces are 100–200 pN [9].

### 10.3.1 Intermolecular Forces

Protein adsorption is a very important topic for many biomedical and biotechnological applications. For instance, many chromatographic separations, such as hydrophobic, displacement, and ion-exchange chromatography, are based on differences in the binding affinities of proteins to surfaces. In addition, *in vitro* cell cultures require cell-surface adhesion, which is mediated by a sublayer of adsorbed proteins. The molecular basis of cell adhesion is, in general, an important process in tissue development, tissue engineering, and tissue tolerance to implants.

Protein adsorption to a surface is a net result of various complex interactions between and within all components, including the chemistry and topology of the solid surface, the protein itself, and the medium in which it takes place. The interaction forces involved include dipole and induced dipole moments, hydrogen bond formation, and electrostatic forces. All inter- and intramolecular forces contribute to a decrease in the Gibbs free energy during adsorption, defining the binding energy.

An important question for protein-adsorption processes is the reversibility of the adsorption process. One approach to this question is an analysis of the time course of adsorption. As the adsorption is a multiple-step process in most cases, this relates to the more specific question of until which step is the process reversible? The most common way to quantify adsorption is by using the adsorption isotherm, characterizing at a constant temperature the number of molecules adsorbed in relation to the steady-state concentration of the same molecules in the bulk solution. Adsorption isotherms provide a convenient method for determining whether or not an adsorption process is reversible. Reversibility is commonly observed with the adsorption of small molecules on solids, but only rarely in the case of more complex random coil polymers.

Proteins are polymers, but globular proteins do not have a random coil structure. The native state of these proteins in aqueous solution is highly ordered; most of the polypeptide backbone has little or no rotational freedom. Therefore, significant denaturing processes have to occur to form numerous contacts with any surface. Structural rearrangements may occur in a way that the internal stability of globular proteins prevents them from completely unfolding on a surface into a loose “loop and tail” type of structure. Thus, a subtle balance between intermolecular and intramolecular forces determines the number of protein-segment to surface contacts formed at steady state.

The thermodynamic description of the protein-adsorption process is based on the laws of irreversible thermodynamics [10]. The process is strongly time-dependent; some of the involved steps of molecular rearrangement are remarkably slow and probably lead to significant binding of proteins only on the timescale of seconds. With different timescales for the various interactions, the adsorption process can be divided into fast steps—which can be reversible—and slow steps, where protein structure rearrangements can occur controlled by the adhering surface and the rest of the environment. The latter processes are irreversible in most cases.

With the AFM, it is possible to measure the adhesion forces established by single proteins, such as protein A and tubulin molecules, within contact times of

milliseconds to seconds. Protein A and tubulin are both globular proteins and can be seen as examples of different types of protein binding. Protein A is often used to bind antibodies to solid substrates, and tubulin forms the filament structure of microtubules as part of the cell's cytoskeleton. The molecules can be attached to the cantilever tip and then brought into contact with different solid surfaces, which might be covered with layers of other molecular structures. To study implant compatibilities, bare metal surfaces such as gold or titanium are of interest. In addition, the optically transparent indium tin-oxide (ITO) is of relevance for the development of interfaces between biological molecules and electro-optic devices.

The procedure for measuring adhesion forces between proteins and surfaces using an AFM needs to define the approach speed, maximal applied force, contact time, retraction speed, retraction distance, and time away from the surface (see Fig. 10.10). With these parameters fixed, one can measure the interaction force by approaching gold, titanium, or ITO surfaces, for instance, with protein-coated tips. It turns out that for the first contact, there is a specific interaction characteristic for the different molecules and the different metals [11]. With the observed reproducibility of a certain value for an adhesion force within a series of measurements, it has to be assumed that in these experiments a well-defined interaction between a specific amino acid group located at the surface of the protein and the metal determines the first step of the adhesion process. The experiments performed by Eckert et al. [11] demonstrated that this technique, combined with an adequate preparation procedure, can be used to measure these first steps in the protein-adhesion process at the single-molecule level. Furthermore, these experiments demonstrated that the technique can be used to study the dependence of these interactions on the environment.

### 10.3.2 *Intramolecular Forces*

The modular structure of proteins in natural fibers and the cytoskeleton seems to be a general strategy for resistance against mechanical stress. One of the most abundant modular proteins in the cytoskeleton is spectrin. In erythrocytes, spectrin molecules are part of a two-dimensional network that provides the red blood cells with their special elastic features. The basic constituent of spectrin subunits is a structural repeat, which has 106 amino acids forming three antiparallel  $\alpha$ -helices with a left-handed coiled-coil structure. Helical linkers of 10–20 amino acids most likely connect the repeats. The mechanical properties of several modular proteins have been investigated by AFM so far. The first study was done on titin [12], which exhibits a  $\beta$ -sheet secondary structure. The experiments have demonstrated that the elongation events observed during stretching of single proteins may be attributed to the unfolding of individual domains; experiments with optical tweezers have corroborated these results [13, 14]. These studies suggest that single domains unfold one at a time in an all-or-none fashion when subjected to directional mechanical stress.

A major technological step forward in protein-folding studies with the AFM was the development of a double-tip detection system. The concept uses one tip that

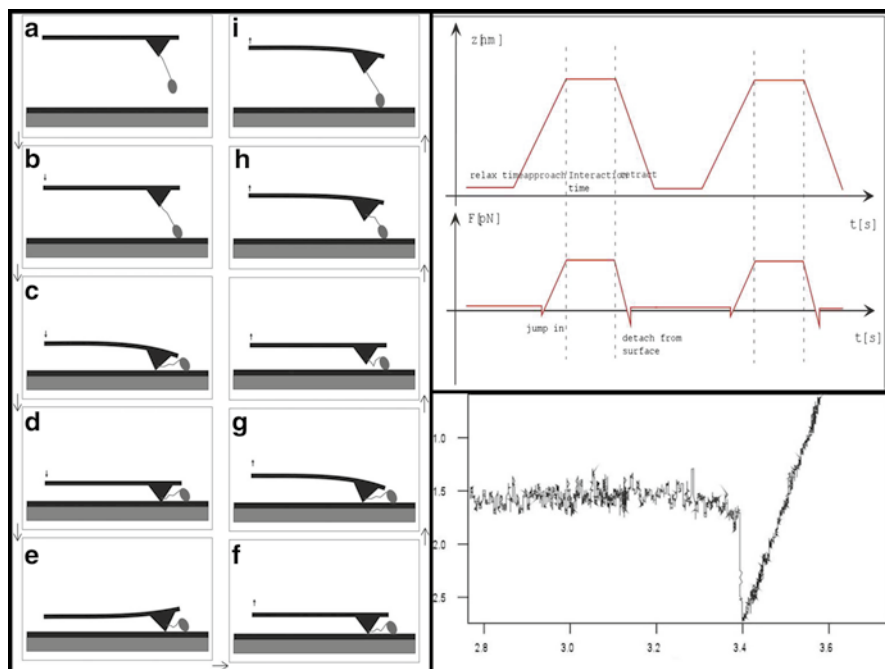


**Fig. 10.10** AFM approach and retraction scheme for molecular adhesion measurements. The image sequence to the *left* shows a cantilever-tip approach/retract cycle with a molecule linked to the tip by a molecular tether. The *top right image* depicts the changes during the cycle in the vertical position of the cantilever base; it is bending, which corresponds to the force acting on the cantilever tip. The *bottom right image* shows the movement of the cantilever tip during the approach. The *jump* indicates an adhesion force pulling the cantilever toward the surface due to attractive van der Waals forces. The following linear change corresponds to the cantilever response while pushed against the surface; its slope reflects the cantilever spring constant

stays in contact with the surface during the force and distance measurements, to stabilize the distance between the second force-measuring tip and the surface. This distance normally has drift speeds of several nanometers per second in AFM due to the long mechanical connection between the cantilever and the sample holder. The double-tip scheme (Fig. 10.11) allows long-term stabilization of this distance with a fraction-of-an-ångström precision over minutes and makes so-called force-clamp measurements over such timescales possible. With this technique, it became possible to perform unfolding and refolding experiments on extremely small protein structures such as spectrin, with only four repeats [15]. In these experiments (Fig. 10.12), the proteins were attached to clean, freshly prepared gold surfaces. While the clean tip of the second force-measuring cantilever approaches such a surface, a single molecule can become attached to its tip, and forces in the range of pico to nano-Newtons can be applied to the molecular structure. With forces of about 80 pN, the molecules are stretched at a speed of 3 nm/s to more than 10 times their folded length, reaching almost the total contour length. The force–extension

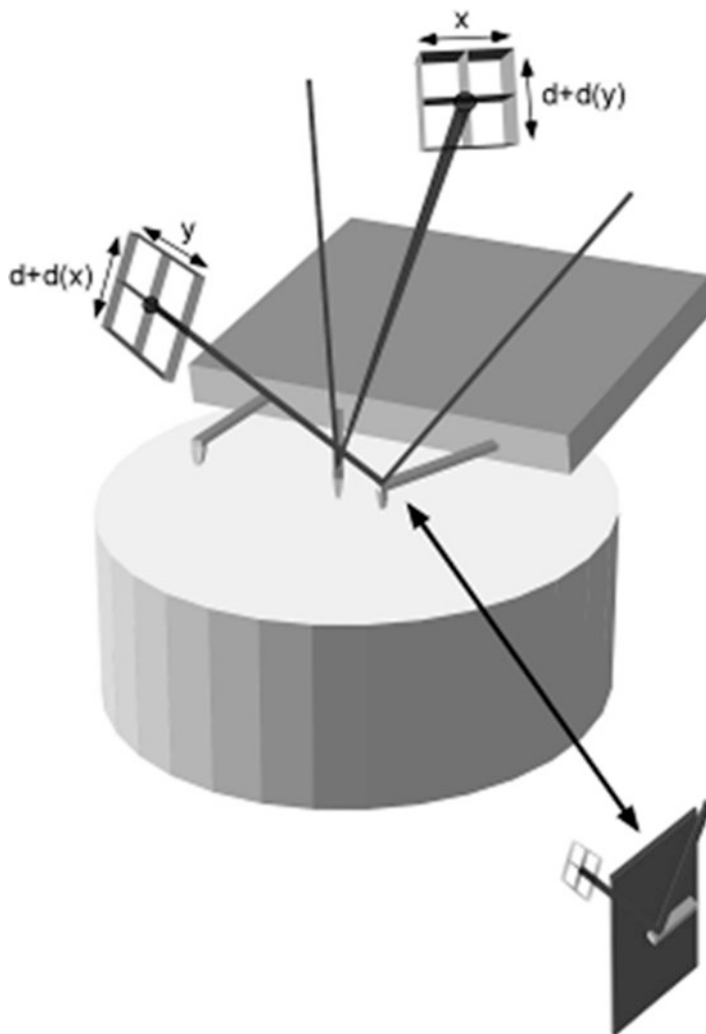


**Fig. 10.11** Schematic of double-cantilever AFM with one lever stabilizing the other cantilever's tip and surface distance, which allows it to be used exclusively measure forces

curves show characteristic sawtooth-like patterns. The reaction coordinate of unfolding is imposed by the direction of pulling, and unfolding events occurring in a single protein can be studied this way. Each peak in the bottom trace of Fig. 10.12 can be attributed to a breakage of a main stabilizing connection of a folded structure.

Recombinant DNA techniques were used in the experiments to construct chains of repeats from identical spectrin domains. The method extends the monomer (R16) at both ends, so that the polymeric protein product contains a 13-residue linker between the consecutive R16 units, with two cysteine residues at the C-terminal

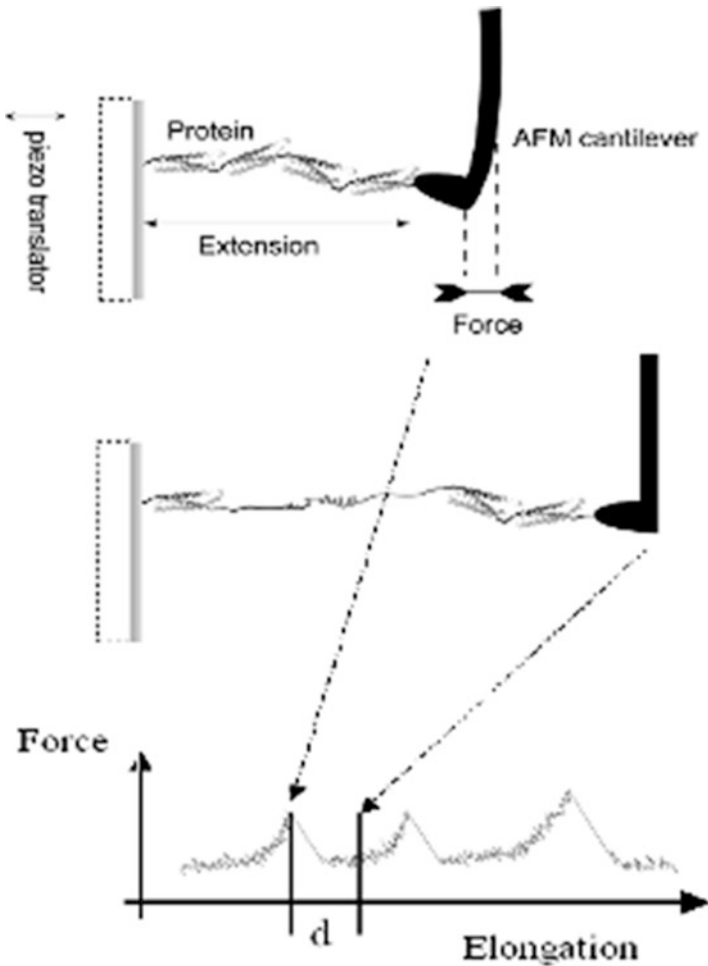
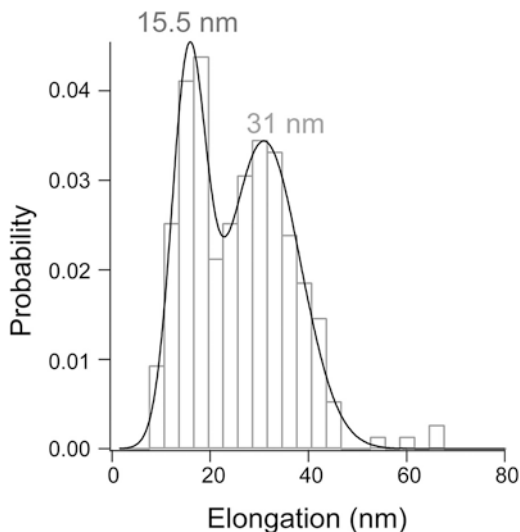


**Fig. 10.12** Stretching spectrin repeats between a gold surface and a cantilever tip

end. The force–extension relationship was measured on a four-repeat construct fixed to the gold surface with the cysteine residues introduced at the C-terminal end. In the sawtooth-like pattern of the force–extension curves (Fig. 10.12, bottom), each peak represents an unfolding event of one subunit. After each peak, the force drops back as additional length of the protein chain unfolds, is made available, and starts to extend. The maximal extension in these experiments is variable because the polymer is not always picked up at the end, and sometimes the tip can be attached to the surface at multiple locations. Nevertheless, the observed extensions never exceeded the contour length of four repeats.

The so-called worm-like chain (WLC) model describes the measured force–extension curves well. It predicts the isothermal restoring forces of a flexible

**Fig. 10.13** Distribution of elongation length observed by stretching the  $\alpha$ -helical spectrin with the AFM. The *left peak* relates to partial unfolding, as shown in Fig. 10.14, and the *right peak* relates to the total unfolding of the structure



polymer, acting as an entropic spring during extension. It also defines a persistence length to the polymer chain, which turns out to be 0.6 nm for the spectrin chain. Two consecutive force peaks are spaced by a distance that represents the gain in length produced by a single unfolding event. These distances were measured for several hundred unfolding events. The histogram (Fig. 10.13) of the measured distances reveals a length distribution with two statistically relevant peaks. When the histogram is fitted with two Gaussian distributions, the maxima are at 15.5 and 31 nm. The force distributions associated with the short and long elongation events can also clearly be separated. The mean force for the 15.5- and 31-nm elongation events are 60 and 80 pN, respectively, at a pulling speed of 3 nm/ms.

These experiments demonstrated for the first time at the single-protein level that  $\alpha$ -helical domains can unfold in several discrete steps in a much more complex way than previously suggested by molecular dynamic simulations. The appearance of different elongation events suggests that at least one intermediate state for the spectrin repeat exists between the folded state and the completely unfolded state (see Fig. 10.14). In thermodynamic studies, such an intermediate state has not been found. A statistical analysis of the AFM force curves shows that the short elongation events are half the length of the total unfolding length of one domain. The molecular pathway of unfolding of a spectrin domain can be simulated based on the AFM measurements and shows that the first steps involve a partial opening of the bundle and the loss of the secondary structure at the repeats connecting helices. The central part reorganizes around a hydrophobic core resembling a shorter version of the repeat structure.

Protein-folding and -unfolding pathways are very complex. However, by applying a force, the unfolding pathways can become very strongly restricted. The results with only two possible unfolding pathways can be explained along this line,

**Fig. 10.14** Normal spectrin repeat folding of the three  $\alpha$ -helices forming a slightly twisted “N” in space, with connection possibilities to other repeats at both ends. Below the stable intermediate structure is shown with the connecting  $\alpha$ -helices extended, but with the structure around the hydrophobic core still stable

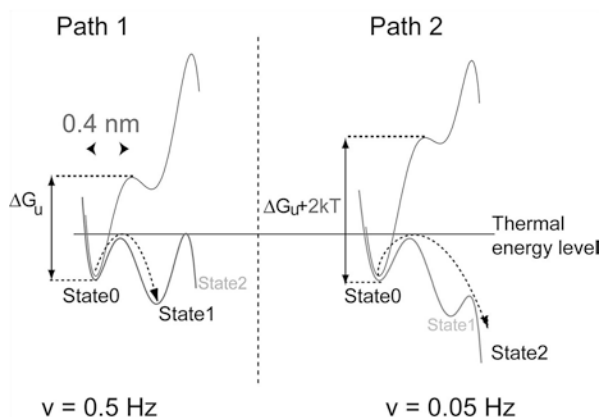
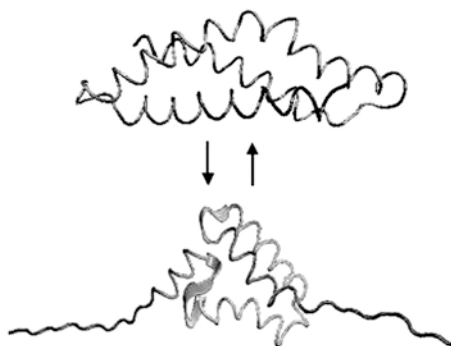


**Fig. 10.15** Energy scheme for the pathway leading to an intermediate state, and the energy scheme that shows how the process leads directly to the completely unfolded state when the force is applied faster and the energy landscape is further deformed

as outlined in Fig. 10.15. One leads directly from the folded to the unfolded state, the other first to an intermediate state. The intermediate state is conceptually available along both pathways, but each pathway by itself leads from the native folded state 0 either to the partially unfolded state 1 or to the completely unfolded state 2. The relative difference in the height of the free energy barrier along either of the two pathways determines whether state 1 or state 2 is attained. The advantage of such a modeling approach is that only one free parameter is needed for differentiating between the two pathways.

In the native folded state, the protein is in state 0 at the bottom of the potential well. The mechanical stress applied by the AFM tip not only decreases the barrier height for thermally activated unfolding but also reduces the options of the protein to follow either path 1 or 2 during unfolding (Fig. 10.15). A certain protein will follow only one path, leading to the observed bimodal probability distribution with 35 % and 65 % probability for path 1 and 2, respectively.



For such a simple model, a Monte Carlo simulation can be used to test the reaction kinetics simultaneously for the short and long elongation events, which means paths 1 and 2, respectively. The kinetics can be characterized by two parameters: the width of the first barrier, and an effective so-called attempt frequency related to the barrier height as an exponential multiplication factor normalized by the thermal energy. In such a simulation, there is no reason to assume a change in the width of the first barrier, but the attempt frequency should vary and needs to be adjusted to agree with the relative difference in barrier height. The force and elongation histograms obtained from 5,000 simulations reproduce the observed general features well, with a barrier width of 0.4 nm and a difference in the barrier height between both pathways of twice the thermal energy.

The experiments shed new light on the mechanical behavior of spectrin, which is an essential cytoskeletal protein with unique elastic properties. They demonstrated that the unfolding of spectrin repeats occurs in a stepwise fashion during stretching with stable intermediates. The stable stretched states under the applied forces show, on the one hand, that protein structures are determined by the environment and, on the other hand, how the elastic properties of spectrin come about. Actually, spectrin behaves within a certain force range as a quantized but perfectly elastic structure: Applied forces stretch the molecule to a defined length; after the forces are turned off, it goes back to the original state. These details about the unfolding of single domains revealed by precise AFM measurements show that force spectroscopy can be used to determine forces that stabilize protein structures and also to analyze the energy landscape and the transition probabilities between different conformational states.

### ***10.3.3 AFM and Optical Microscopy***

From the very beginning, the AFM was thought to be an ideal tool for biological research. Imaging living cells under physiological conditions and studying dynamic processes at the plasma membrane were envisioned although it was clear that such experiments are quite difficult, as the AFM cantilever is by far more rigid than cellular structures. Therefore, the way cells are supported becomes quite important. In addition, a parallel optical observation is necessary to control the cantilever-tip approach to distinct cellular features. In order to address these problems, the IBM Physics Group in Munich started the development of a special AFM built into an inverted optical microscope [16]. This instrument finally provided the first reproducible images of the outer membrane of a living cell held by a pipette in its normal growth medium. A conventional piezotube scanner moved this pipette. The detection system for the cantilever movement was, in principle, the normal optical-detection scheme, but a glass fiber was used as a light source very close to the cantilever to avoid optical distortions of the light while going through the water surface. This setup allowed a very fast scanning speed of up to a picture per second for imaging cells in constant-height mode. This is possible because the parts

moving in the liquid are very small and—quite different from the imaging of cells adsorbed to a microscope slide—no significant excitation of disturbing waves or convection in the liquid occurs. It is possible to keep the cell alive and well for days within such a liquid cell. This makes studies of live activities and kinematics possible in addition to the application of other cell physiology—measuring techniques. With this step in the development of scanning probe instruments, the capability of optical microscopy to investigate the dynamics of biological processes of cell membranes under physiological conditions was extended into the nanometer range. With imaging rates of up to one frame per second, structures as small as 10 nm could be resolved and their dynamics studied. This made it possible to visualize processes such as the binding of labeled antibodies, endo- and exocytosis, pore formation, and the dynamics of surface and membrane cytoskeletal structures in general.

With the cantilever's integrated tip, forces in the range from pico- to nano-Newtons are applied to the investigated cell; the mechanical properties of cell surface structures therefore dominate the imaging process. On the one hand, this fact mixes topographic and elastic properties of the sample in the images; on the other hand, it provides additional information about the underlying membrane's cytoskeleton and its dynamics in various situations during the life of a cell. To separate the elastic and topographic properties, we need further information. The additional information can be provided by using AFM modulation techniques. The pipette AFM concept is well suited for such modulation measurements, as the convection or excitation of waves in the solution caused by movement of the pipette is negligible and the modulation can be done very quickly. Nevertheless, for a thorough analysis of a cell wall elasticity map, we would have to record pixel by pixel a complete frequency spectrum of the cantilever response to derive image data in various frequency regimes. This would take too long for a highly dynamic system like a living cell; therefore, such analyses are restricted to certain small areas. Experiments performed on living cells with this setup showed in some cases a certain weak mechanical resonance in the regime of several kHz. In 2007, Cross and coworkers rediscovered this [17] and used it to characterize cancer cells. It might lead to new methods of medical diagnosis at the cellular level and to new techniques in drug development.

Figure 10.16 shows the schematic arrangement of the first AFM set up to study live cells. It was built on a highly stable sample holder stage within an inverted optical microscope. The sample area can be observed from below through a planar surface defined by a glass plate with a magnification of 600×–1200× and from above by a stereo microscope with a magnification of 40×–200×. The illumination is from the top through the less well-defined surface of the aqueous solution. In order not to block the illumination, the manipulator for the optical fiber and for the micropipette point toward the focal plane at a 45° angle. The lever is mounted in a fixed position within the liquid slightly above the glass plate tilted also by 45°. A single-mode optical fiber is used to avoid beam distortions at the water surface by bringing the end as close as possible to the lever within the liquid. To do so requires removing the last several millimeters of the fiber's protective jacket. The minimum distance is determined by the diameter of the fiber cladding and the

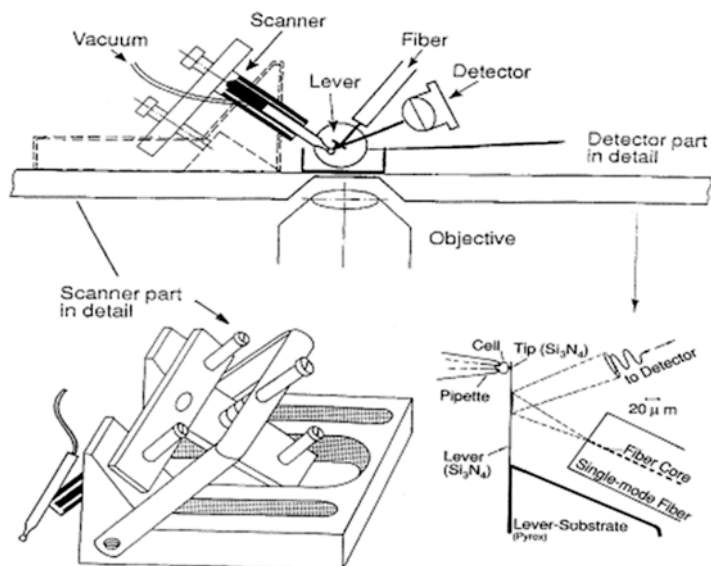


**Fig. 10.16** Schematic of the first AFM built in 1988 to image live cells under physiological conditions [16]

geometry of the lever. In the original experiments, fibers for 633-nm light with a nominal cladding diameter of 125  $\mu\text{m}$  and levers with a length of 200  $\mu\text{m}$  have been used. Holding the fiber at a 45° angle with respect to the lever means that the fiber core can be brought as close as 150  $\mu\text{m}$  to the lever. A 4- $\mu\text{m}$ -diameter core has a numerical aperture of 0.1, and the light emerging from the fiber therefore expands with an apex angle of 6°. For the geometry given above, the smallest spot size achievable is 50  $\mu\text{m}$ , approximately the size of the triangular region at the end of the cantilever. Due to the construction of the mechanical pieces holding the pipette and the fiber, the closest possible distance of the position-sensitive quadrant photodetector to the lever is about 2 cm. This implies a minimum spot size of 2.1 mm, within the 3-mm  $\times$  3-mm borders of the detector. Using a 2-mW HeNe laser under normal operational conditions produces a displacement sensitivity of better than 0.01 nm, with a signal-to-noise ratio of 10, which compares well with the sensitivity of other optical detection techniques. The advantage of this method is that there are no lenses and there is no air–liquid or air–solid interface for the incoming light beam to cross. Only the outgoing light crosses the water–air interface, as the detector cannot be immersed in the water, but this does not influence the information about the changes in the cantilever’s bending.

The pipette used for holding the cell in the setup was made from a 0.8-mm borosilicate glass capillary, which was pulled to about a 2–4- $\mu\text{m}$  opening in three pulling steps. It is mounted on the piezotube scanner and coupled to a fine and flexible Teflon tube, through which the pressure in the pipette can be adjusted by a piston or water pump. The pipette is fixed at an angle that allows imaging of the cell without

the danger of touching the pipette with the lever. All these components are located in a 50-ml container. The glass plate above the objective of the optical microscope forms the bottom of this container.

After several microliters of the cell suspension have been added, a single cell can be sucked onto the pipette and fixed there by maintaining low pressure in the pipette. Other cells are removed through the pumping system. The cell fixed at the pipette's end is placed close to the AFM lever by a rough approach with screws and finally positioned by the piezo scanner. When the cell is in close contact with the lever's tip, scanning of the capillary with the cell attached leads to position-dependent deflections of the lever. The levers used were micro-fabricated silicon nitride triangles with a length of 200  $\mu\text{m}$  and a spring constant of 0.12 N/m. The forces that can be applied with these levers and the sensitivity of the detection system can be as good as 0.1 nN.

With such forces acting on the plasma membrane of a cell, the stiffness of the structures dominates the images. Therefore, the scaffolds of the cortical layer of actin filaments and actin-binding proteins, which are cross-linked into a three-dimensional network and closely connected to the surface membrane, are prominent in the images. The relatively stable arrangements of the actin filaments are responsible for their relatively persistent structure. However, these surface actin filaments are not permanent. During phagocytosis or cell movement, rapid changes of their shape can be observed. These changes depend on the transient and regulated polymerization of cytoplasmic free actin or the depolarization during the breakdown of the actin filament complex. The timescale of cell surface changes on a larger scale observed with the AFM was about 1–2 h at room temperature. Except for small structures some 10 nm in size, everything is quite stable on this timescale. More and larger structures are rearranged within 10–15 min after these periods of stability.

In a series of experiments, Hörber and coworkers studied the membrane dynamics after infection of the cells with pox viruses [18]. The first effects were observed seconds to minutes after adding the virus solution to the chamber. After this time, the cell surface became smooth and so soft that the tip tended to penetrate the cell surface even with a loading force far below 1 nN. After a few minutes, the cells became rigid again; with stable imaging, the same structures as before became visible. During the first hour after infection, no significant variation in the membrane structures was observed. It is known that within 4–8 h, viruses are reproduced inside the cell and are passed through the cell membrane via exocytosis [19]. However, approximately 2.5 h after infection, with the AFM a series of processes started at the membrane. Single clear protrusions became visible, which were growing in size. The objects quickly disappeared and the original structure of the membrane was restored. Such processes sometimes occurred several times in the same area and lasted about 90 s for small protrusions of about 20 nm and up to 10 min for larger ones (up to 100 nm in size). Each process proceeded distinctly and apparently independently of the others, was never observed with uninfected cells, and was never observed before 2 h after infection.

The fact that the growing protrusions abruptly disappeared makes it likely that the exocytosis of particles related to the starting virus reproduction was observed,

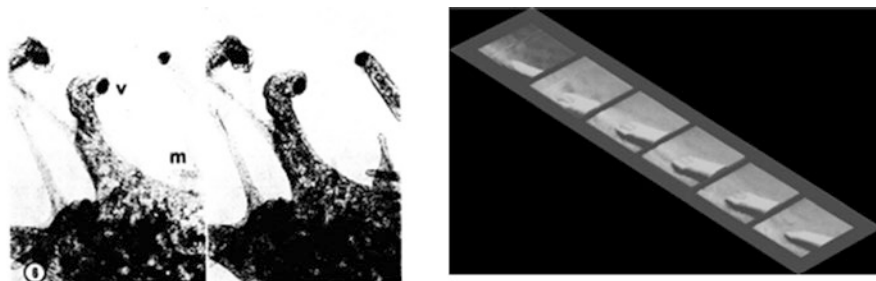


Fig. 10.17. Electron micrograph showing the structure of microvilli at the end of a whole BSC-1 cell

**Fig. 10.17** EM images of viral particles at the end of microvilli structures on the *left* taken from the publication by Stokes et al. (Adapted from Ref. [19]) compare well with processes observed by AFM [18] showing the process of microvillus development from the *lower right*, with the release of a particle at the end before the last image on the *upper left*

but not viruses. The first progeny viruses should appear 4–8 h after infection and are clearly bigger than the structures observed. Nevertheless, after 2–3 h, the early stage of virus reproduction is finished and the final virus assembly just begins. The observation of protrusions after this characteristic timespan supports the assumption that they are related to the exocytosis of protein agglomerates originating from the virus assembly.

Significantly more than 6 h after infection, even more dramatic changes at the cell membrane can be observed. Large protrusions, with cross sections of 200–300 nm, grow out of the membrane near deep folds. These events occur much less frequently than those observed after 2 h. These large protrusions also abruptly disappear, leaving behind small scars at the cell surface. Considering the timing and their size, it is very likely that these protrusions are now progeny viruses exiting the cell after the assembly is finished. With approximately 20–100 virus particles exiting an infected cell, and with roughly 1/40 of the cell surface accessible to the AFM tip, the observation of one or two of those events should be possible. In the experiments, the number of processes exhibiting the right size and timing observed varied between none and two. During the first experiment of 46 h of continuous observation of a single infected cell, such events were seen 19 and 35 h after infection. Stokes could show with electron microscopy that individual viruses sometimes exit the cell at the end of microvilli [19]. Such a process might have been observed in one case with the AFM when the cantilever tip was pushed up by the growing microvillus and the release of a hard structure with the right size for a viral particle was detected. The release of other hard structures of the right size occurred in flatter regions, but the number of microvilli observed always increased significantly after infection. The striking similarity between the EM and AFM images shown in Fig. 10.17 makes us believe that indeed the exocytosis of a progeny virus through the membrane of a living infected cell was observed and that the AFM can be used to study such processes.

These experiments make two advantages of the AFM obvious: First, it provides a resolution similar to that of the EM without the need for fixation and coating of the

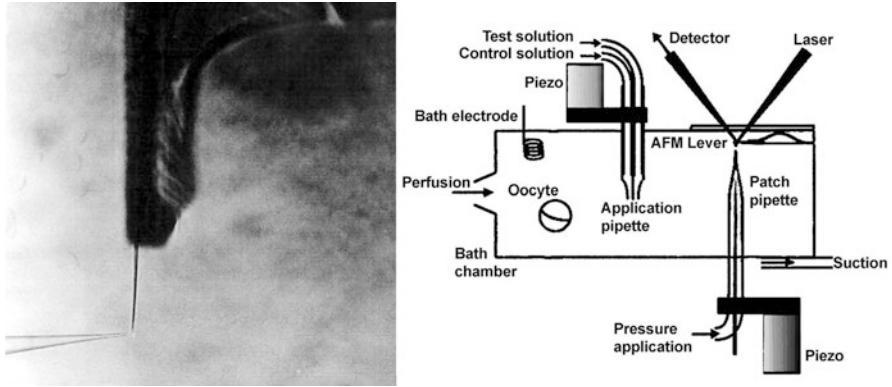


**Fig. 10.18** Schematic of the AFM/patch-clamp setup (*top*) with an image of the cantilever pipette approach controlled through an optical microscope (*left*)

sample; and, second, it can produce a movie of a biological process under natural conditions for the cells studied similar to what optical microscopy can provide at a lower resolution.

### 10.3.4 AFM Application in Electrophysiology

The method of fixing a cell to a pipette and scanning it across an AFM cantilever tip is flexible enough to allow the integration of and combination with well-established cell physiological techniques of manipulation and investigation of single cells. The structures observed with the AFM can be related to known features of membranes, but more important than just the imaging of structures with this technique is the possibility of observing their time evolution. In this way, the AFM can provide information that brings us closer to understanding not only the “being” of these structures, but also their “becoming.”

#### 10.3.4.1 Single Cells and Excised Membrane Patches

In principle, the AFM setup with the cell fixed on the end of a pipette allows simultaneous patch-clamp measurements for studying ion channels in the membrane of whole cells. Therefore, a logical step in the development of combinations of the AFM technique with established cell biological techniques was a combined patch-clamp /AFM setup that could be used to investigate excised membrane patches for single-ion-channel recording (see Fig. 10.18) [20]. In particular, the study of mechanosensitive ion channels in the membrane, which become activated by mechanical stress in the membrane, is an obvious application for a force-measuring device such

as an AFM. The importance of such ion channels is very obvious in our senses of touching and hearing. During the development that started in 1991, a new type of patch-clamp setup was developed that was much more stable to satisfy the needs of AFM applications. It was designed to accommodate the usual electrophysiological and optical components besides the AFM. The chamber—where a constant flow of buffer solution guarantees the right conditions for the experiments—consists of two optical transparent plastic plates, one at the top and one at the bottom, keeping the water inside just by its surface tension. In this way, this type of flow cell is accessible from two sides. The chamber is mounted on an *xyz*-stage together with the optical detection of the AFM lever movement and a double-barrel application pipette. The latter was integrated to use the setup also for standard patch-clamp measurements, with the application of chemicals and different kinds of ions at different concentrations to characterize the sample further. The patch-clamp pipette in this setup is again mounted on a piezotube scanner fixed within the field of view of an inverse optical microscope necessary to control the approach of the pipette to the cell and to the AFM cantilever tip. In patch-clamp experiments, small membrane pieces are excised from a cell inside the chamber, which can contain none, one, or a few of the ion channels to be studied. This allows the measurement of currents through a single ion channel that is only open on the timescale of micro- to milliseconds, resulting in currents in the picoampere range.

In such a setup, with a membrane patch at the end of the pipette, the AFM can image the tip of the pipette with the patch on top. Furthermore, changes in the patch according to the changing pressure in the patch pipette can be monitored, along with the reaction of the patch to the change of the electric potential across the membrane [20]. In the images, cytoskeleton structures are clearly seen excised together with the membrane. On these stabilizing structures of the membrane and on the rim of the pipette, resolutions down to 10–20 nm can be achieved, showing reproducible structures and changes that can be induced by the application of force.

Voltage-sensitive ion channels change shape in electrical fields, leading eventually to the opening of the ion-permeable pore. To investigate the size of this electromechanical transduction, the AFM setup was used in studies of cells from a cancer cell line (HEK 293) that were kept at a certain membrane potential (voltage-clamped) [21]. Cells transfected with *Shaker* K<sup>+</sup> ion channels were used as controls. In these control cells, movements of 0.5–5 nm normal to the plane of the membrane were measured, tracking a  $\pm 10$ -mV peak-to-peak AC carrier stimulus to frequencies above 1 kHz with a phase shift of 90–120°, as expected of a displacement current. The movement was outward with depolarization, and the amplitude of the movement only weakly influenced the holding potential. In contrast, cells transfected with a non-inactivating mutant of *Shaker* K<sup>+</sup> channels showed movements that were sensitive to the holding potential, decreasing with depolarization between –80 and 0 mV.

Further control experiments used open or sealed pipettes and cantilever placements just above the cells. The results suggested that the observed movement is produced by the cell membrane rather than by artificial movement of the patch pipette and/or acoustic or electrical interaction of the membrane and the AFM tip. The large amplitude of the movements and the fact that they also occurred in control

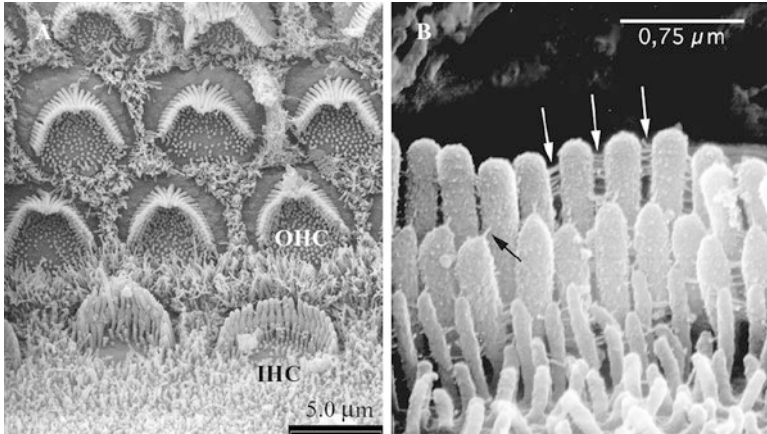


**Fig. 10.19** EM images of the mammalian hair cells of the inner ear with the V-shaped bundles of stereocilia. The *right image* shows a close-up where the lateral linkers between the stereocilia are marked by *arrows*

cells with a low density of voltage-sensitive ion channels imply the presence of multiple electromechanical motors. These experiments open up a route to exploit the voltage-dependent movements as a source of contrast for imaging membrane proteins with an AFM.

#### 10.3.4.2 Tissue Sections

Cochlear hair cells of the inner ear are responsible for the detection of sound (Fig. 10.19). They encode the magnitude and time course of an acoustic stimulus as an electric receptor potential, which is generated by a still-unknown interaction of cellular components. In the literature, different models for the mechano-electrical transduction of hair cells are discussed [22, 23]. All hypotheses have in common that a force applied to the so-called hair bundle—which are specialized stereocilia at the apical end of the cells—in the positive direction toward the tallest stereocilia opens transduction channels, whereas negative deflection closes them. For a better understanding of the transduction process, it is important to know what elements of the hair bundle contribute to the opening of transduction channels and to study their mechanical properties. The morphology of the hair cells is described precisely by scanning and transmission electron microscopy. Unfortunately, this method is restricted to fixed and dehydrated specimen. Therefore, the development of an AFM setup to enable studies of cochlear hair cells in physiological solution was thought to provide further information on the dynamic properties of the system.

To control the approach to the tissue section, the AFM was again built into a patch-clamp setup onto an upright differential interference contrast (DIC) light microscope [24]. A water-immersion objective was used to achieve a high



resolution of about 0.5  $\mu\text{m}$  even on organotypic cell cultures with a thickness of about 300  $\mu\text{m}$ . With this setup, it is possible to see ciliary bundles of inner and outer cochlear hair cells extracted from rats several days old and to approach these structures in a controlled way with the AFM cantilever tip. AFM images can be obtained by measuring the local force interaction between the AFM tip and the specimen surface while scanning the tip. The question of whether or not morphological artifacts occurred at the hair bundles during AFM investigation can be clarified by preparing the cell cultures for the electron microscope directly after the AFM measurements. Forces up to 1.5 nN applied in the direction of the stereocilia axis did not change the structure of the hair bundles. The resolution achieved with the AFM in this situation is high enough to image the tips of individual stereocilia and the typical shape of the ciliar bundle of inner and outer hair cells.

From AFM scan traces, the position of the individual stereocilium as well as its stiffness can be derived. The force interaction in the excitatory direction shows a stiffness increase with bending from  $0.73 \times 10^{-3}$  N/m, reaching a steady-state level at about  $2 \times 10^{-3}$  N/m. The mean stiffness value of stereocilia in the excitatory direction, calculated at the steady-state level, was determined to be  $(2.5 \pm 0.6) \times 10^{-3}$  N/m and  $(3.1 \pm 1.5) \times 10^{-3}$  N/m in the inhibitory direction. Taking into account the standard deviation of  $0.6 \times 10^{-3}$  N/m, the average force constant showed only a weak dependence on the position of the stereocilium in the excitatory direction. However, some stereocilia located at the center had an exceptionally high stiffness, and some located at the outer region revealed a very low stiffness. In the inhibitory direction, the mean stiffness in general is slightly higher, with a standard deviation 2.5 times above the excitatory direction. The higher stiffness might be explained by a direct contact between the taller and the adjacent shorter stereocilia, while in the excitatory direction, shorter stereocilia are pulled by elastic tip links. These links connect the rows of taller and shorter stereocilia [23]. The high standard deviation might be an effect of the variation in the spatial interaction between taller and shorter stereocilia. Depending on the angle between the scan direction and the direction defined by the centers of adjacent taller and shorter stereocilia, mechanical compliance can vary in a wide range. For the excitatory direction, two stiffness distributions are distinguishable. One group of values is located around  $2.2 \times 10^{-3}$  N/m, and a smaller one around  $3.1 \times 10^{-3}$  N/m, which corresponds to stereocilia located in the central region of the investigated hair bundles. Comparing the stiffness to the corresponding AFM images, one can find a correlation between the arrangement and stiffness of stereocilia. Those standing a little bit apart from their neighbors clearly show a higher stiffness, with a value of  $3.2 \times 10^{-3}$  N/m. A possible hypothesis may be that lateral links connecting these stereocilia with their direct neighbors are oriented in the direction of the exerted force. This will allow the transmission of additional force along these links to their neighbors.

The hypothesis above implies that all stereocilia standing closer display much less interaction with their neighbors mediated by side links. It can be directly tested by another AFM experiment. The force transmission between adjacent stereocilia in this experiment is examined by using a lock-in amplifier for detecting the transmitted forces stimulated by a glass fiber touching individual pairs of stereocilia.

AFM imaging again allows an exact localization of stereocilia and the stimulating glass fiber. The AFM force signal is detected by a lock-in amplifier in phase with the vertical oscillation of the AFM cantilever at 357 Hz. The lateral force transmitted by lateral links can be calculated from the output signal and related to the stereocilium's position. Only that half of the hair bundle can be taken into account, where the fiber is in contact with the directly stimulated stereocilium across its entire width but doesn't touch the nearest adjacent stereocilium at all. During the experiment, the arrangement of stereocilia and stimulating fibers was regularly controlled by AFM imaging. Force interaction between the stereocilia and the AFM tip leads to displacements of stereocilia from 0 nm to about 250 nm. Therefore, the relative displacement between the directly stimulated stereocilium and the stereocilium pushed by the AFM tip is expected to result in the continuous stretching of lateral links located in between. This allows detection of transmitted forces by lateral links for different states of stretching. For us to be able to compare the results more accurately, the forces have to be normalized with respect to the corresponding maximum force detected at the directly stimulated stereocilium. Normalized forces rapidly decrease from the directly stimulated to the first adjacent stereocilium. During the fiber tip's approach to the stereocilium, the relative position is detected, but not the preload force. Obviously, forces transmitted by lateral links rapidly decrease from a directly stimulated stereocilium to an adjacent stereocilium in the experiments done with rats at postnatal age day 4. This result supports the hypothesis of a weak interaction between stereocilia by lateral links.

In these experiments, the noise level made it difficult to distinguish between slight couplings by lateral links from mechanically independent stereocilia. Besides the modulation signal at 357 Hz, the same AFM curves of the identical outer hair cells contain information about the stiffness of stereocilia as described above. This information can be used to detect the mechanical effect of the touching glass fiber on the stiffness of adjacent stereocilia. If lateral links contribute to the stiffness measured at individual stereocilia, one would expect to see an increase in the stiffness of adjacent stereocilia compared to data shown for stereocilia investigated without the fiber attached. Stiffness data were derived only for the excitatory direction, where the AFM tip displaces the stereocilia toward the fiber tip. The results of these experiments show that not only does the stiffness of the directly touched stereocilium increase, but also the stiffness of the five stereocilia next to it increases. The mean stiffness in the excitatory direction turns out to be  $(4.8 \pm 1.8) \times 10^{-3}$  N/m, which is about 1.9 times higher than the mean stiffness of stereocilia not touched by the fiber.

In the experiments described, the AFM allows local stiffness measurements on the level of individual stereocilia. The results represent the local elastic properties of the directly touched stereocilium and its nearest neighbors. It can be seen that stiffness depends on the orientation of links with regard to the direction of the stimulus.

A stimulating fiber had only little mechanical effect on adjacent stereocilia if not in direct contact with the fiber. For a partial decoupling of the tectorial membrane from hair bundles of outer hair cells, it therefore can be assumed that only stereocilia still in contact with the tectorial membrane and their nearest neighbors are displaced by an incoming mechanical stimulus. Lateral links may not compensate for loss in contact with the tallest stereocilia of the outer hair cells. Decoupling of

the tectorial membrane following exposure to pure tones at high sound-pressure levels is supposed to protect hair cells and to avoid damage [25]. A strong interaction between the tectorial membrane and hair bundles of the outer hair cells seems to be essential for the efficacy of the cochlear amplifier and the transduction of sound into an electrical signal.

In the experiments described above, the AFM was used only to examine the elastic properties of stereocilia on hair cells, similar to all the micromechanical measurements that already have been performed on the entire stereocilia bundles of sensory hair cells using thin glass fibers directly attached to the bundle or by using fluid jets. The receptor potential or transduction current in these experiments was measured in response to the displacement of stereocilia. To study the kinetics of a single transduction channel over the whole range of its open probability requires a technique that allows stimulating a single stereocilium [26]. As shown in the previous section, the AFM is such a technique, allowing a force to be exerted very locally to an individual stereocilium. To patch the hair cells with a pipette necessitates removing the supporting cells with a cleaning pipette. After cleaning, a patch pipette filled with intracellular solution (concentrations in mM: KCl 135, MgCl<sub>2</sub> 3.5, CaCl<sub>2</sub> 0.1, EGTA 5, HEPES 5, ATP 2.5; at pH 7.4) can be attached to the lateral wall of the outermost row of outer hair cells. This so-called cell-attached configuration is the precursor of the whole-cell configuration where the microelectrode is in direct electrical contact with the inside of the cell. For low-noise measurements of single ion channels, the seal resistance should typically be in the range  $>1 \text{ G}\Omega$ . A pulse of suction applied to the pipette breaks the patch, creating a hole in the plasma membrane, and provides access to the cell interior. During recording, the electrical resistance between the inside of the pipette and the hair cell should be very small. Many voltage-activated K<sup>+</sup> ion channels are embedded in the lipid membrane of outer hair cells. The opening and closing of these channels increases the background noise level during transduction current measurements. The current response of outward-rectifying K<sup>+</sup> ion channels can be controlled by applying 10-mV voltage steps across the cell membrane (progressively increasing from  $-100$  to  $+40$  mV). The outward currents mainly correspond to potassium ion currents of voltage-gated K<sup>+</sup> channels. During transduction current measurements, the holding potential of the hair cell is set to  $-80$  mV, corresponding to the reversal potential of K<sup>+</sup> ion channels. After forming a seal, the AFM tip is moved to the top of the corresponding hair bundle under optical control. It then is used to successively displace each stereocilium within a hair bundle as described before, but in contrast to the force-transmission measurements, a sinusoidal voltage is now added to the normal AFM scan signal, modulating the AFM tip in horizontal directions with an amplitude of 190 nm at 98 Hz. In this way, the hair bundle is slightly displaced several times while interacting with the lateral side of the AFM tip. The tip is repeatedly scanning along the same line while approaching the hair bundle. As expected, an inward current cannot be detected until a stereocilium is displaced in the excitatory direction. In the experiments described above, a weak transmission of force from the directly stimulated stereocilium to adjacent stereocilia was detected, implying that only a few channels are opened. The results of the elasticity measurements are nicely complemented by the electrophysiological results of experiments where the tip of the AFM cantilever is repeatedly scanned across the same

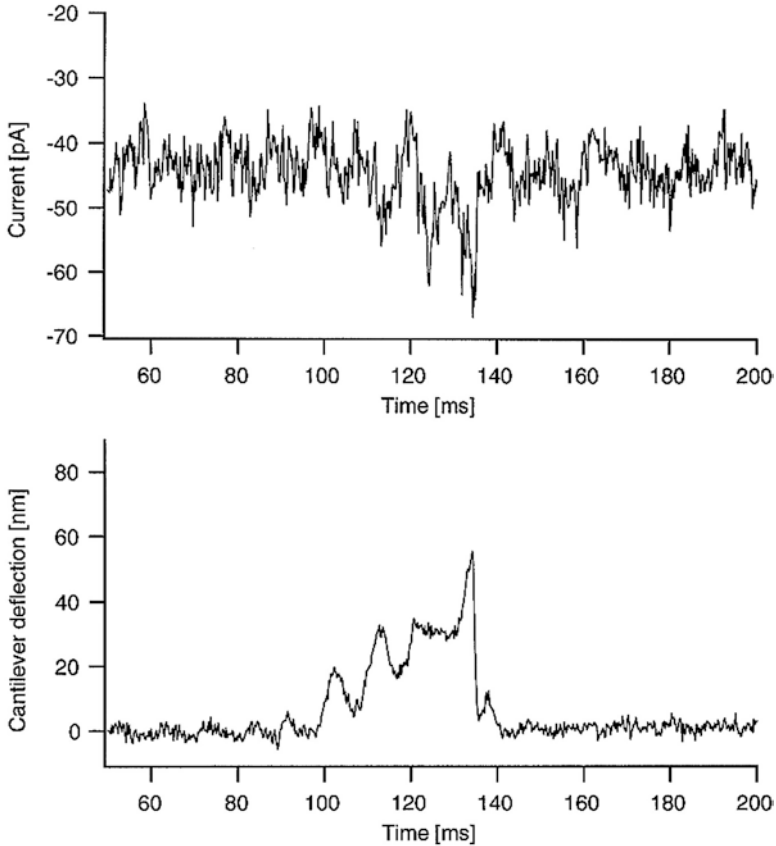


**Fig. 10.20** AFM force signal (*bottom*) and ion-current response (*top*) while stimulating a single stereocilium with the cantilever tip

stereocilium of an outer hair cell from the medial turn of a postnatal rat at day 3. With applied horizontal forces of up to 800 pN resulting in stereocilia displacements of about 350 nm in the excitatory direction and 250 nm in the inhibitory direction, the AFM tip opens up transduction channels in the excitatory direction for about 90–130 ms. The current amplitudes reflect the displacements and show for small forces the expected characteristics of single-channel currents. With these experiments, Langer and colleagues [26–34] demonstrated for the first time single-channel recording of mechanosensitive ion channels (Fig. 10.20).

## 10.4 Conclusion

Since its invention in 1986, the AFM was continuously developed to suit many different applications. In biological research, it provides high-resolution, three-dimensional imaging not only of single molecules and macromolecular assemblies, but also of

intact, living cells in physiological solutions and gives a detailed view of surface features of large biological structures such as grains and seeds. In addition to imaging, the AFM has the capability to simultaneously measure biophysical properties, such as the stiffness of molecular structures, but it also provides the means to analyze binding interactions down into the range of only a few pico-Newtons and to analyze the effect of the environment (pH, salt, temperature, etc.) on the interaction. The implications of this are far-reaching for many biomedical applications, including the development of new drugs, targeted drug delivery, biocompatible materials for implants, as well as *in vitro* and *in vivo* sensors, and in the agro-food area for quality control.

For the study of many biological samples, a parallel optical observation is essential to control the approach to the sample and to have available certain standard controls for the actual sample. However, an AFM built on top of an optical microscope loses part of its stability. A major technological breakthrough in this respect was the development of a multiple-detection scheme using two cantilevers in parallel to separate force and distance measurement. This development allows long-term stabilization of the distance between the cantilever tip and the surface with picometer precision, thereby enabling so-called force-clamp measurements. With such an approach, it is possible to perform unfolding and refolding experiments of even small protein structures, for instance. The details about the unfolding of single-protein domains revealed by precise AFM measurements have demonstrated that force spectroscopy can be used to determine the forces that stabilize protein structures and to analyze the energy landscape and the transition probabilities between different conformational states. In this way, the AFM can make essential contributions to the understanding of the connection between protein structure and function.

The AFM used as an imaging tool and as a force-measuring tool simultaneously allows the localization of molecular structures and the determination of their biophysical properties such as elasticity. Unfortunately, the AFMs that are currently available commercially are still quite large and bulky, expensive, and difficult to use, requiring a heavy vibration-stabilization platform. The future development of a mass-producible "micro-"AFM with a stability and price that enable field applications will extend the application range dramatically not only in biomedical and bioengineering laboratories, but also in many industrial areas, especially for quality control. Such a development will automatically include a much higher imaging speed, allowing the analysis of processes in the millisecond range. It will also eliminate many operational problems, which then can be fully managed by software developments.

The future AFM will be (1) compact, (2) rapid-scanning, (3) user-friendly, (4) mass-producible and, consequently, cheap.

## References

1. Syngé EH. A suggested method for extending microscopic resolution into the ultra-microscopic region. *Philos Mag.* 1928;6:356.
2. O'Keefe JA. Resolving power of visible light. *J Opt Soc.* 1956;46:359.

3. Ash EA, Nicolls G. Super-resolution aperture scanning microscope. *Nature*. 1972;237:510.
4. Binnig G, Rohrer H, Gerber C, Weibel E. Tunneling through a controllable vacuum gap. *Appl Phys Lett*. 1982;40:178.
5. Binnig G, Quate CF, Gerber C. Atomic force microscope. *Phys Rev Lett*. 1986;56:930.
6. Atomic force microscope and method for imaging surfaces with atomic resolution, issued to Gerd K. Binnig of IBM's Zurich Research Laboratory in 1988, U.S. Patent 4724318.
7. Giessibl FJ, Hembacher S, Bielefeldt H, Mannhardt J. Subatomic features on the silicon(111)-(7×7) surface observed by atomic force microscopy. *Science*. 2000;289(5478):422.
8. Meyer E, Amer NM. Novel optical approach to atomic force microscopy. *Appl Phys Lett*. 1988;53:2400.
9. Florin E-L, Moy VT, Gaub HE. Adhesion forces between individual ligand-receptor pairs. *Science*. 1994;264:415.
10. Haynes CA, Norde W. Globular proteins at solid-liquid interfaces. *Colloids Surf B Biointerfaces*. 1994;2:517–66.
11. Eckert R, Jeney S, Hörber JKH. Understanding intercellular interactions and cell adhesion: lessons from studies on protein-metal interactions. *Cell Biol Int*. 1998;21:707.
12. Rief M, Gautel M, Oesterhelt F, Fernandez JM, Gaub HE. Reversible Unfolding of Individual Titin Immunoglobulin Domains by AFM. *Science*. 1997;276:1109.
13. Kellermayer MSZ, Smith SB, Granzier HL, Bustamante C. Folding-unfolding transitions in single titin molecules characterized with force-measuring laser tweezers. *Science*. 1997;276:1112.
14. Tskhovrebova L, Trinick J, Sleep JA, Simmons RM. Elasticity and unfolding of single molecules of the giant muscle protein titin. *Nature*. 1997;387:308.
15. Altmann SM, Grunberg RG, Lenne PF, Ylanne J, Raae A, Herbert K, Saraste M, Nilges M, Hörber JKH. Pathways and intermediates in forced unfolding of spectrin repeats. *Structure*. 2002;10:1085–96.
16. Häberle W, Hörber JKH, Binnig G. Force microscopy on living cells. *J Vac Sci Technol*. 1991;B9:1210.
17. Cross SE, Yu-Sheng Jin, Jianyu Rao, Gimzewski JK. Nanomechanics of human metastatic cancer cells in clinical pleural effusions. *Nat Nanotechnol*. 2007;2:780–3.
18. Hörber JKH, Häberle W, Ohnesorge F, Binnig G, Liebich HG, Czerny CP, Mahnel H, Mayr A. Investigation of living cells in the nanometer regime with the scanning force microscope. *Scanning Microsc*. 1992;6:919.
19. Stokes GV. High-voltage electron microscope study of the release of vaccinia virus from whole cells. *J Virol*. 1976;18:636.
20. Hörber JKH, Mosbacher J, Häberle W, Ruppertsberg P, Sakmann B. A look at membrane patches with a scanning force microscope. *Biophys J*. 1995;68:1687.
21. Mosbacher J, Langer M, Hörber JKH, Sachs F. Voltage-dependent membrane displacements measured by atomic force microscopy. *J Gen Physiol*. 1998;111:65–74.
22. Corey DP, Hudspeth AJ. Analysis of the microphonic potential of the bullfrog's sacculus. *J Neurosci*. 1983;3:962.
23. Furness DN, Hackney CM, Benos DJ. The binding site on cochlear stereocilia for antisera raised against renal Na channels is blocked by amiloride and dihydrostreptomycin. *Hear Res*. 1996;93:136.
24. Langer MG, Öffner W, Wittmann H, Flösser H, Schaar H, Häberle W, Pralle A, Ruppertsberg JP, Hörber JKH. A scanning force microscope for simultaneous force and patch-clamp measurements on living cell tissues. *Rev Sci Instrum*. 1997;68:2583.
25. Adler HJ, Poje CP, Saunders JC. Recovery of auditory function and structure in the chick after two intense pure tone exposures. *Hear Res*. 1993;71:214.
26. Langer MG, Koitschev A, Haase H, Rexhausen U, Hörber JKH, Ruppertsberg JP. Mechanical stimulation of individual stereocilia of living cochlear hair cells by atomic force microscopy. *Ultramicroscopy*. 2000;82:269.

27. Goldsbury C, Scheuring S. *Curr Protoc Protein Sci.* 2002;17.7.1–17
28. Hörber JKH, Miles M. *Science.* 2003;302:1002–5.
29. Braga PC, Ricci D. *Atomic force microscopy: biomedical methods and applications.* Totowa: Humana Press; 2004.
30. Connell SDA, Smith DAM. *Mol Membr Biol.* 2006;23(1):17–28.
31. Forman JR, Clarke J. *Curr Opin Struct Biol.* 2007;17:58.
32. Yang H, Wang Y, Lai S, An H, Li Y, Chen F. *J Food Sci.* 2007;72(4):65–5.
33. Gonçalves RP, Buzhysnsky N, Scheuring S. *J Bioenerg Biomembr.* 2008;40:133–8.
34. Liu H, Fu S, Zhu JY, Li H, Zhan H. *Enzyme Microb Technol.* 2009;45:274–81.

# Chapter 11

## Multi-technique Characterization of DNA-Modified Surfaces for Biosensing and Diagnostic Applications

Chi-Ying Lee, Lara J. Gamble, Gregory M. Harbers, Ping Gong, David W. Grainger, and David G. Castner

**Abstract** Complementary surface analysis techniques—X-ray photoelectron spectroscopy (XPS), near-edge X-ray absorption fine structure (NEXAFS), time-of-flight secondary ion mass spectrometry (ToF-SIMS), and surface plasmon resonance (SPR)—were combined to characterize the structure and composition of DNA-modified surfaces. Both model systems [thiolated single-stranded DNA (ssDNA) on gold surfaces] and commercial systems (ssDNA spotted onto microarray slides) were investigated. Pure thiolated 20-mer ssDNA assembles onto gold, with the ssDNA binding spontaneously to the surface via the thiol groups and nitrogen atoms

---

C.-Y. Lee

National ESCA and Surface Analysis Center for Biomedical Problems,  
University of Washington, Box 351653, Seattle, WA 98195-1653, USA

Department of Chemical Engineering, University of Washington,  
Box 351653, Seattle, WA 98195-1653, USA

3M Health Care Business Group, Infection Prevention Division,  
3M China R&D Center, 222 Tian Lin Road, Shanghai 200233, China

L.J. Gamble

National ESCA and Surface Analysis Center for Biomedical Problems,  
University of Washington, Box 351653, Seattle, WA 98195-1653, USA

Department of Bioengineering, University of Washington,  
Box 351653, Seattle, WA 98195-1653, USA

G.M. Harbers

Replenish, Inc., 2645 Nina St., Pasadena, CA 91107, USA

Department of Pharmaceutics and Pharmaceutical Chemistry,  
University of Utah, Salt Lake City, UT 84112-5820, USA

P. Gong

Department of Pharmaceutics and Pharmaceutical Chemistry,  
University of Utah, Salt Lake City, UT 84112-5820, USA

Seventh Sense Biosystems, 286 Cardinal Medeiros Ave,  
Cambridge, MA 02141, USA



in the DNA bases, resulting in a monolayer with limited ssDNA chain order. XPS, NEXAFS, SPR, and radiotracer studies showed that when the pure ssDNA monolayers were exposed to short-chain functionalized alkyl thiol diluents [either 11-mercapto-1-undecanol (MCU) or oligo(ethylene glycol) (OEG)], the diluents initially displaced the weaker gold–nitrogen DNA interactions, reorienting the ssDNA chains to a more upright configuration. After longer exposures to diluent thiols, some ssDNA chains were displaced from the gold surface. The efficiency of the target hybridization to complementary DNA from solution depended on the structure and composition of the immobilized probe ssDNA surface. As the upright orientation of the ssDNA chains increased, the amount of hybridization increased. As ssDNA chains were displaced from the surface, the amount of hybridization decreased. Incorporating the diluent thiol eliminated the small amount of nonspecific binding from noncomplementary target DNA observed on the pure ssDNA monolayers. The DNA hybridization kinetics were significantly more rapid on the mixed ssDNA/MCU and ssDNA/OEG surfaces compared to the pure ssDNA surface. The OEG diluent was more effective than the MCU diluent at reducing nonspecific protein adsorption during DNA hybridization from blood serum. Nanoliter drops of amine-terminated ssDNA were robotically spotted onto a glass microscope slide with an amine-reactive microarray polymer coating; the resulting 150- $\mu\text{m}$  spots were imaged with XPS and ToF-SIMS. Imaging XPS provided single-spot phosphorous, nitrogen, sodium, and silicon elemental images. Small-spot XPS data were then used to quantify DNA hybridization efficiencies in each microspot as a function of the ssDNA concentration in the probe printing solution. The DNA microspots were also readily visualized in the negative ToF-SIMS images of key fragments from the DNA backbone (e.g.,  $\text{PO}_x$ ), DNA bases (A–H, T–H, G–H, C–H, etc.), and the substrate (e.g., Si). Principal component analysis (PCA) of the ToF-SIMS images was used to distinguish heterogeneities within the DNA microspots due to the variations in printing process and solution additives (salts, sodium dodecyl sulfate, etc.). The different types of data available from combining these complementary surface analytical methods provide new information essential

---

D.W. Grainger

Department of Bioengineering, University of Utah, Salt Lake City, UT 84112-5820, USA

Department of Pharmaceutics and Pharmaceutical Chemistry,  
University of Utah, Salt Lake City, UT 84112-5820, USA

D.G. Castner (✉)

National ESCA and Surface Analysis Center for Biomedical Problems,  
University of Washington, Box 351653, Seattle, WA 98195-1653, USA

Department of Bioengineering, University of Washington,  
Box 351653, Seattle, WA 98195-1653, USA

Department of Chemical Engineering, University of Washington,  
Box 351653, Seattle, WA 98195-1653, USA

e-mail: [castner@uw.edu](mailto:castner@uw.edu)

to understanding aspects of DNA on surfaces. Such information is important for designing and improving new technologies that employ nucleic acids on surfaces, including bioassays, diagnostics, molecular computing, self-assembling materials, and miniaturized separations.

## 11.1 Introduction

The current intensive interest in nucleic acids (e.g., DNA, RNA) on surfaces is driven both by the inherent interest in understanding the interfacial physics and chemistry of these molecules and by their importance for biosensing and advanced medical diagnostics. DNA's primary biological function involves information storage and transfer, imparted by its unique complementary recognition pairing between the base pairs adenine–thymine (A–T) and cytosine–guanine (C–G) (Fig. 11.1) as the foundation for genetic coding. The ability of a single-stranded DNA (ssDNA) molecule to “seek out” and complex or hybridize its complementary strand in a sample and the ease with which nucleic acids can be custom synthesized to comprise different lengths, sequences, and functional groups that allow attachment to various solid supports have led to the development of DNA-based detection systems, such as DNA microarrays [1–5] and biosensors [2, 6–8]. Microarrays, comprising thousands of hybridization reactions performed in parallel, are commonly used for genotyping and expression

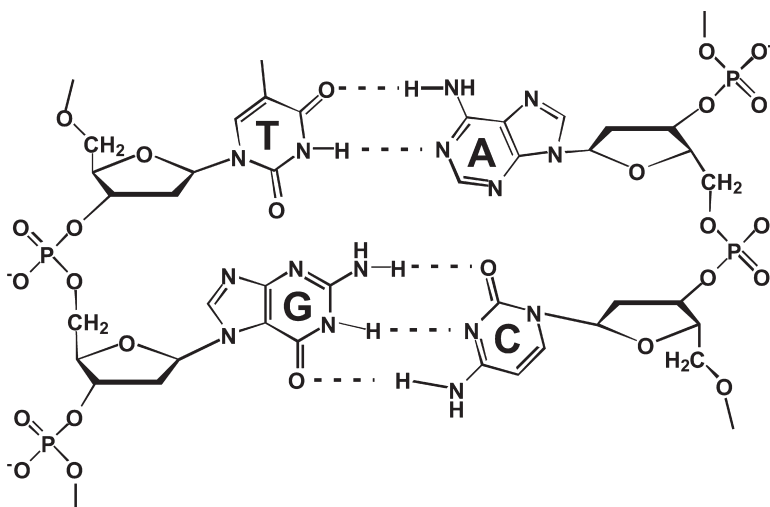


**Fig. 11.1** The DNA double-stranded helix recognition required for many DNA surface-capture assays. Each DNA molecular strand comprises a series of sugars, polyphosphate backbone, and attached purine or pyrimidine bases. Two complementary DNA strands complex into duplexes by specific Watson–Crick and/or Hooqsten hydrogen bonding between paired bases, adenine (A) with thymine (T), and guanine (G) with cytosine (C). Adenine and thymine interact with two hydrogen bonds per pairing, while guanine and cytosine interact with three hydrogen bonds per pairing

profiling. Several potential clinical applications have also begun to emerge as methods and capabilities for DNA microarrays and the data they generate improve. Biosensors tend to be dedicated to the detection of a small number of analyte sequences in a sample, with data acquisition often performed in real time. New biosensing technologies continue to be attractive, with perceived major impacts on the fields of medicine, forensics, environmental studies, and food safety.

Detection and sequence identification of DNA analyte molecules using DNA microarrays or biosensors rely on the fidelity of the hybridization of DNA *target* strands in solution samples to surface-immobilized complementary *probe* strands of known sequences. This bioassay seeks a specific response only for perfect matches between surface-bound ssDNA probes and complementary strands, with sensitive distinctions for one-base-pair mismatches. However, the nucleic acid hybridization behavior observed between complementary probe and target DNA molecules in bulk solution differs from identical hybridization at a solid–liquid interface. While factors that control hybridization between complementary DNA molecules in solution have been extensively investigated [9], fewer studies have focused on understanding differences in these interactions between surface-immobilized ssDNA probes and solution-phase targets, where molecular-level processes are more complex and interfacial behavior confounds the reaction. In surface hybridization, non-specific probe–surface interactions, electrostatic forces, and steric issues between adjacent immobilized DNA probes influence target hybridization and capture efficiency, kinetics, and capacity. For example, nucleotide primary amines on nonhybridized DNA segments can interact (e.g., covalently [10], or by acid–base adsorption) with the surface, becoming unavailable to hybridize with target DNA molecules. Thus, once an ssDNA probe is immobilized to a surface, several important parameters, including surface coverage (density) and orientation, must be determined to control target interactions. Since these properties determine the bioassay performance at several levels (e.g., molecular, macroscopic, signal generation, kinetic), the abilities to assess and control DNA molecular disposition at surfaces are critical for improving these formats. This need will undoubtedly push the limits of current surface analysis techniques to provide molecular specificity, extreme sensitivity, spatial information, and the ability to determine the chemistry and structure of the immobilized DNA molecules.

The need to design increasingly selective and sensitive DNA biosensors has stimulated a great deal of interest in understanding the basic physicochemical behavior of DNA molecules on various technological surfaces, including glass, silicon oxide, metal oxides, gold, and diamond-like carbon. Surface science has played a key role in furthering these studies. For example, X-ray photoelectron spectroscopy (XPS), time-of-flight secondary ion mass spectrometry (ToF-SIMS), near-edge X-ray absorption fine structure (NEXAFS), infrared spectroscopy (IR), and scanning probe microscopies (SPMs) represent often-employed surface analytical techniques for characterizing DNA-modified surfaces. While these techniques are powerful for investigating the DNA immobilization process, they generally encounter difficulties in monitoring surface-adsorption processes spatially, in real time and in liquid environments, which are critical aspects for studying DNA hybridization on surfaces.

Currently, in most commonly employed microarray systems, the detection and monitoring of DNA hybridization rely on the use of extrinsic fluorescent labeling of select DNA bases. Although fluorescence-based target detection has a number of attractive features (e.g., broad availability and ease of use), the complex reagent labeling processes present several problems (e.g., poor reproducibility, lack of absolute molecular detection) and are time-consuming [5]. Additionally, surface-derived fluorescence signal is subject to many measurement issues and sources of variation that preclude the accurate quantitation of analyte. Alternatively, label-free detection techniques, such as surface plasmon resonance (SPR) spectroscopy and SPR imaging [11–14], quartz crystal microbalance (QCM) [15, 16] and electrochemical DNA biosensors [8, 17], provide more direct methods of DNA assay while avoiding fluorescence metric issues. However, these techniques by themselves are not chemically selective methods and therefore must be used in combination with other analytical techniques, such as XPS, ToF-SIMS, NEXAFS, and IR, to provide accurate surface-sensitive information.

The aim of this chapter is to demonstrate the capabilities of several complementary surface analytical techniques, including XPS, ToF-SIMS, NEXAFS, and SPR, for investigating the surface and hybridization properties of immobilized ssDNA on microarray and biosensor surfaces. The information gained from these studies has helped provide a new understanding of ssDNA interfacial behavior by providing quantitative correlations between immobilized DNA surface properties (i.e., composition, density, and orientation) and the resultant hybridization efficiency from complex biological samples. The following sections summarize recent findings from ongoing experiments in our laboratories and present a description of ssDNA behavior on gold and commercial microarray surfaces provided by these various analytical techniques.

## **11.2 Assessing the Structure and Hybridization Properties of Mixed DNA/Alkylthiol Monolayers on Gold Using XPS, NEXAFS, and SPR**

The immobilization of ssDNA on a transducer surface is frequently the first step in DNA biosensor design. Several different strategies, including surface entrapment, physical adsorption, and chemical binding, are employed. Despite the large body of work recently devoted to this topic, the development of methods for surface-immobilizing ssDNA that preserve their original hybridization specificity with minimal nonspecific interactions remains elusive and hence is an important goal for improving the performance of DNA microarrays and biosensors. Thus, information about the structure and coverage of immobilized ssDNA and how these properties impact subsequent DNA target hybridization would be invaluable for optimizing the performance of DNA biosensors and other applications using surface-bound DNA oligomers.

The process of interfacial self-assembly and adlayer formation on surfaces provides a powerful tool to generate molecular films of biological molecules on several relevant substrates [18]. The convenience and flexibility of employing self-assembled monolayers (SAMs) and possibilities for controlling biomolecule density and surface orientation allow SAMs to play important roles in designing artificial biomolecular recognition devices. Chemisorbed adlayers of alkylthiols on gold [18] provide a high degree of control over surface chemical and physical properties, providing useful model systems for examining relationships between ssDNA surface composition and orientation, as well as subsequent hybridization behavior with solution-phase targets. Tarlov et al. [19] pioneered a technique for DNA immobilization that utilizes the sequential chemisorptive self-assembly of first a thiol-terminated single-stranded DNA (HS-ssDNA) monolayer onto gold surfaces, followed by exposure to a short hydroxyl-terminated alkylthiol surface diluent [e.g., mercaptohexanol (MCH)]. XPS [19, 20], neutron reflectivity [21], and SPR [22] have been used to study this mixed SAM system; the MCH has been shown to disrupt nonspecific interactions of DNA bases with the gold surface and enhance specific attachment through thiol–DNA chemistry. These studies have provided important quantitative information on possible ssDNA probe conformational changes in self-assembled mixed monolayers resulting from the MCH surface diluent. Immobilized ssDNA oligomers appear to behave differently when their packing density or other properties (e.g., DNA length) are varied in these films. To develop a deeper understanding of surface properties in these mixed DNA monolayers at the molecular level, the packing density and nonfouling properties of ssDNA were systematically changed by incorporating other alkylthiol diluents with different functional head groups [e.g., 11-mercapto-1-undecanol (MCU) and oligo(ethylene glycol) (OEG)] into ssDNA monolayers. These strategies for DNA immobilization onto gold surfaces are depicted schematically in Figs. 11.2a, b.

The effects of diluent backfilling time on the mixed adlayer composition, surface density, DNA orientation, and target hybridization efficiency of ssDNA oligomers were studied using complementary surface analytical techniques including XPS, NEXAFS, and SPR. XPS is used to quantify the composition of the DNA films. Polarization-dependent NEXAFS was used to probe the molecular orientation and ordering of surface-bound ssDNA molecules. SPR was used to measure the target DNA hybridization *in situ*.

XPS, also known as electron spectroscopy for chemical analysis (ESCA), is a quantitative surface analytical tool sensitive to the atomic composition of the outer 2–10 nm of a material (the XPS technique is discussed in more detail in Chap. 2 of this book). Compositional changes of mixed ssDNA/alkylthiol diluent monolayers on gold were followed as a function of the MCU or OEG diluent backfill time (0.5–18 h) starting from an initial ssDNA monolayer. Figure 11.3 shows XPS elemental compositions from pure ssDNA and mixed ssDNA/MCU monolayers. (Note: XPS analysis was also performed on the ssDNA/OEG monolayers [23]; data not shown.) For the surface chemistries used here, elements P and N are unique to DNA and are therefore good indicators of the relative amounts of ssDNA present on the surface under each condition. After short-term exposure of the DNA monolayer

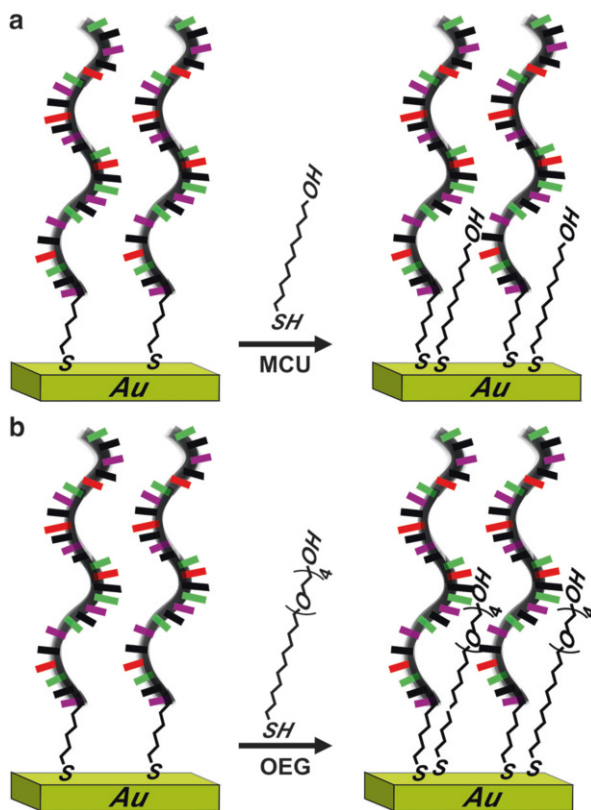


**Fig. 11.2** Scheme for thiolated, single-stranded DNA (HS-ssDNA) immobilization onto gold. Mixed ssDNA/mercapto-1-undecanol (MCU) (a) and ssDNA/oligo(ethylene glycol) (OEG) (b) monolayers of varying DNA surface coverage were assembled by a known, sequential two-step process onto gold surfaces. First, pure DNA monolayers were prepared by immersing freshly gold-coated substrates in HS-ssDNA solutions. After HS-ssDNA assembly, samples were rinsed thoroughly and then immersed in MCU or OEG diluent thiol solution for backfill times ranging from 30 min to 18 h. After the specified diluent thiol backfill time, samples were removed from the solutions, rinsed thoroughly, and stored under  $N_2$  until analysis

to the MCU diluent thiol (<1 h), the relative atomic percents of C and S increased, while the relative atomic percents of Au, P, N, and O all decreased (see Fig. 11.3). Increased C and S content is consistent with the presence of MCU, as the smaller MCU diluent thiols take up unoccupied gold sites surrounding the loosely packed DNA on the surface [19, 23, 24]. The corresponding Au signal decreased during this same short-term exposure of the DNA monolayer to MCU, consistent with this interpretation. MCU surface reactions could also displace other weaker, nonspecific interactions between nitrogen-containing DNA bases and gold, promoting single-point tethering of DNA oligomers on gold via thiolate bonds, with a greater tendency to orient away from the surface. NEXAFS data further support this contention.

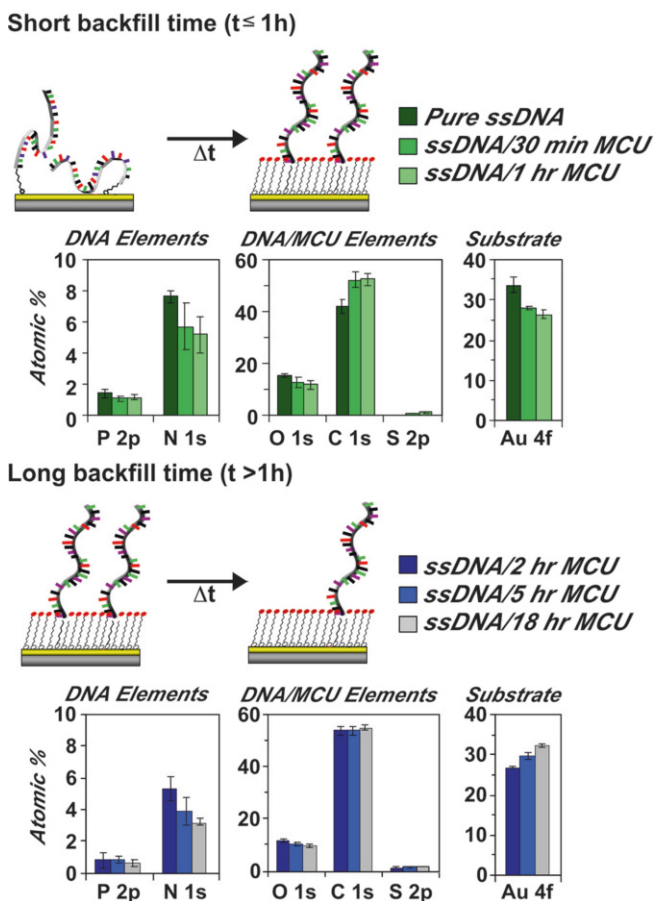
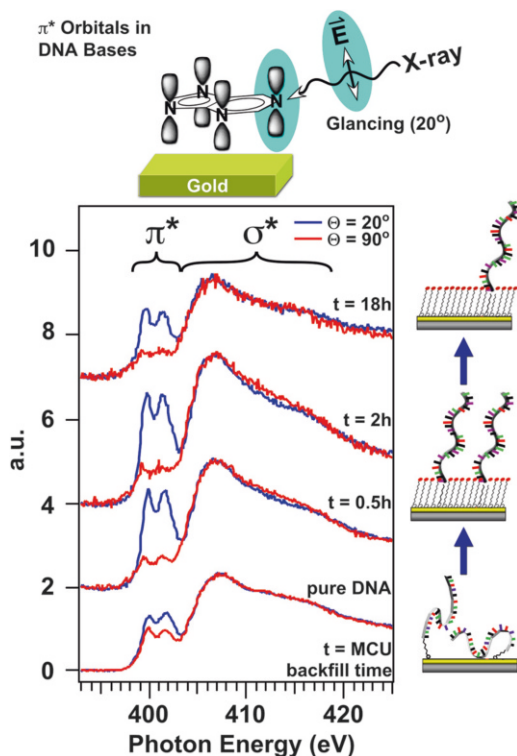


**Fig. 11.3** XPS compositional data for pure ssDNA and mixed ssDNA/MCU monolayers on gold as a function of MCU back-filling time. XPS results indicate that during short-term ( $\leq 1$  h, green bars, upper) MCU diluent thiol backfill, the MCU molecules incorporate into the unoccupied gold surface sites surrounding the loosely packed low-density thiolated-ssDNA. While the DNA displacement by MCU is initially slow, upon extended MCU backfill time ( $> 1$  h, blue bars, lower), the ssDNA surface coverage steadily decreases. This change is supported by the observed reduction in XPS P2p and N1s, and increase in S2p and Au4f signals at later times, reflecting thinner layers with higher density MCU sulfur and reduced DNA signals

XPS analysis of sequentially adsorbed ssDNA/MCU and ssDNA/OEG monolayers on gold indicated that both MCU and OEG molecules initially incorporate into the unoccupied surface sites surrounding the ssDNA [19, 23, 24]. While DNA displacement by the MCU and OEG diluents is initially slow, upon extended exposure or backfill time ( $> 1$  h), these diluents eventually also displace adsorbed ssDNA molecules from the gold surface. As seen in Fig. 11.3, the relative Au substrate atomic percent increased, while the relative atomic percent of P and N decreased further for the longer MCU exposure times. Thus, ssDNA surface coverage steadily decreased

**Fig. 11.4** Nitrogen K-edge NEXAFS spectra from pure ssDNA and mixed ssDNA/MCU monolayers on gold at normal ( $90^\circ$ ) and glancing ( $20^\circ$ ) incident X-ray angles ( $t$ =MCU backfill time in hours). The increase in the polarization dependence of nitrogen K-edge NEXAFS spectra indicates that DNA bases are oriented more parallel to the surface than bases in the pure ssDNA monolayer, and that ssDNA oligomers reorient on average toward a more upright orientation on the surface upon MCU addition (Adapted with permission from Ref. [24]. Copyright © 2006 American Chemical Society)



with longer MCU and OEG backfill times. These mixed DNA monolayers on gold displacement trends over time have been fully characterized in a companion work utilizing a  $^{32}\text{P}$  radiolabel assay [25]. The maximum probe coverage was observed to be  $4.4 (\pm 0.4) \times 10^{13}$  probes/ $\text{cm}^2$  for pure ssDNA adlayers without MCU backfill. With increasing MCU backfill time, the DNA surface coverage eventually reached a density of  $\sim 1.7 \times 10^{13}$  probes/ $\text{cm}^2$  after 18 h [23, 25, 26].

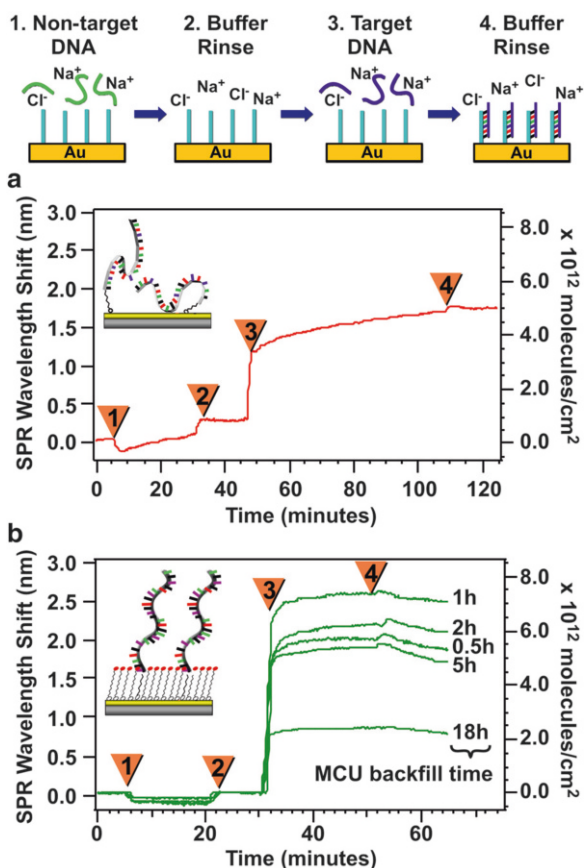
Polarization-dependent NEXAFS, also known as X-ray absorption near-edge structure (XANES) [27], was used to determine the orientation changes of these DNA monolayers as a function of diluent thiol exposure, co-adsorption, and DNA surface displacement. NEXAFS has been used to examine the surface molecular orientation and ordering for a variety of materials, including SAMs on gold [28] and polymers [29–32]. In previous DNA studies, NEXAFS has been used to characterize DNA nucleobases and nucleotides [33–37], as well as the orientation of poly-dA [37] and poly-dT [37, 38] DNA homo-oligomers on gold.

Figure 11.4 shows the nitrogen K-edge NEXAFS spectra from pure ssDNA and mixed ssDNA/MCU monolayers on gold at normal ( $90^\circ$ ) and glancing ( $20^\circ$ ) incident X-ray angles [24]. For the pure ssDNA monolayer, the intensity of the  $\pi^*$  peaks was slightly higher when the X-ray beam was at a glancing angle of incidence compared to that at normal incidence. Overlap of the  $\mathbf{E}$  vector of the polarized



X-ray source with the aromatic nitrogen bonds that cause the  $1s \rightarrow \pi^*$  transition at glancing incidence indicates that the DNA bases in a pure DNA film were, on average, oriented more parallel to the surface. Similar trends have previously been observed with surface-bound double-stranded DNA oligomers on gold [39]. This indicates that on average the ssDNA chains had a slightly perpendicular orientation to the substrate. It is believed that the electrostatic repulsive forces between the ssDNA chains may cause the chains to stand, on average, slightly upright on the surface although it is likely that overall they remain rather disordered. As the diluent molecules first incorporate into preadsorbed DNA monolayers (<1 h backfill time), DNA oligomers adopt a more upright orientation, due to MCU or OEG displacement of DNA nucleotide base amine groups from the gold interface [23, 24]. The ssDNA surface orientation (followed by monitoring the N  $1s \rightarrow \pi^*$  transition) reaches a maximum at ~0.5–1 h of MCU or OEG exposure, beyond which the ssDNA surface orientation decreases slightly due to DNA displacement. With less DNA on the surface, electrostatic repulsive interactions between ssDNA chains are less effective at holding the DNA molecules perpendicular to the surface, allowing more disorder among the immobilized DNA chains. Despite the reduction in the N  $1s$  nitrogen signal at longer diluent backfill times, NEXAFS polarization dependence at 18 h was still greater than that of the pure ssDNA surface, leading to the conclusion that the change in polarization dependence was due to relative orientation changes in the DNA layer [23, 24].

DNA hybridization on these mixed ssDNA/diluent thiol monolayers in purified target DNA samples as well as blood serum was measured by SPR [23, 25]. SPR is a surface-sensitive optical technique frequently used to detect binding of biological molecules such as DNA [26, 40–45] and proteins [46–51] onto chemically and biologically modified gold surfaces without the need for target labeling and complex sample preparation. For the pure ssDNA surface, SPR response to a noncomplementary ssDNA in buffer solution indicates a small amount of nonspecific ssDNA binding to the ssDNA surface (Fig. 11.5a). With complementary DNA target, a much higher SPR wavelength shift was observed, indicating the hybridization of surface-bound ssDNA probes with complementary ssDNA target. The SPR sensorgram also showed that target hybridization occurs slowly on the pure ssDNA surface, as the SPR curve for complementary ssDNA does not reach saturation even after 60 min of target incubation. In contrast, when MCU or OEG diluent was incorporated into the ssDNA monolayer before hybridization, the nonspecific binding of noncomplementary ssDNA to any of the mixed monolayer probe surfaces was not detected (Fig. 11.5b). This suggests that the alkylthiol diluents effectively block unoccupied surface sites to prevent nonspecific ssDNA surface binding, thereby increasing the hybridization selectivity to target. Furthermore, target hybridization to the mixed DNA/thiol diluent probe surfaces also reached saturation much more rapidly than to the pure DNA probe surface. The observed increase in hybridization kinetics as well as hybridization efficiency on surfaces with short-term exposure (30 min) to MCU or OEG (for which  $^{32}\text{P}$ -labeling results indicate DNA surface probe densities are comparable to the nonbackfilled pure DNA adlayer [25]) indicates that more than just the ssDNA surface density may be controlling the



**Fig. 11.5** Real-time SPR measurement of target DNA hybridization on (a) pure ssDNA and (b) mixed ssDNA/MCU adlayers from buffer (1 M NaCl-TE, pH 7.0) demonstrating the effects of MCU diluent backfill on DNA target hybridization. Kinetic sensorgram traces were characterized by the following common stepwise features: A measurement baseline was first established by running buffer over the probe surface. Then noncomplementary DNA (1  $\mu\text{M}$ ) in buffer was injected to test nonspecific target binding onto the probe surface (1). As the noncomplementary DNA adsorption approached saturation, the noncomplementary DNA solution was replaced with buffer to reestablish the baseline (2). Complementary DNA target (1  $\mu\text{M}$ ) was then injected to determine the amounts of hybridization (3). As the DNA hybridization approached saturation, the complementary DNA solution was replaced with buffer to rinse away loosely bound target DNA molecules from the probe surface (4). Data indicate that the target hybridization reaches a maximum at 1 h MCU backfill (surface density of  $3.55 \times 10^{13}$  molecules/cm<sup>2</sup>) (Adapted with permission from Ref. [25]. Copyright © 2006 American Chemical Society)

hybridization efficiency of surface-bound ssDNA. Orientation studies of ssDNA chains in identical adlayers using NEXAFS as described previously [23, 24] demonstrate that the initial MCU and OEG addition into the pure DNA adlayer displaces nonspecifically adsorbed DNA nucleobase amines from gold surface sites and reorients the probe DNA chains to a more upright configuration. With nucleobase amines

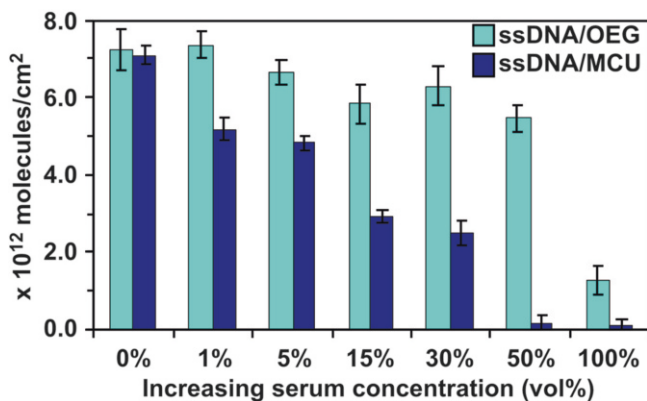


**Fig. 11.6** Amounts of DNA hybridization from various serum concentrations determined by SPR on ssDNA/MCU and ssDNA/OEG adlayers. For the ssDNA/MCU adlayer, the hybridization efficiency was significantly reduced (by roughly 50%) from 15% serum, and in 50% serum and higher concentrations, no hybridization was detected on the probe surface because of rapid, overwhelming amounts of nonspecific protein adsorption. OEG incorporation into the ssDNA adlayer significantly improved the surface resistance to both nonspecific protein and DNA adsorption, allowing the detection of small DNA target sequences from concentrated, complex biological mixtures

detached from the gold surface, probe DNA molecules are more likely single-point end-tethered and therefore more configurationally mobile than those in a pure DNA monolayer. This produces mixed DNA adlayers that are more accommodating for target DNA molecules to approach and to hybridize. SPR results indicate that the target hybridization signal reaches a maximum on surfaces following 1 h diluent backfill, after which the target hybridization signal decreases due to significant diluent thiol displacement of DNA probes from the adlayer surface [25].

In order for microarray technology to be widely adapted as a diagnostic tool and to perform reliably in field-based or direct sample-to-answer analyses, surface-capture nucleic acid biosensors will need to achieve improved target-detection limits and be able to capture target from complex milieu such as whole blood or other complex biological mixtures rather than depend on initially purified analytes free from assay-complicating proteins [52, 53]. Figure 11.6 demonstrates the effects of capturing target analyte from a model complex biological mixture. Although similar amounts of target capture were detected by SPR on both ssDNA/MCU and ssDNA/OEG adlayers from purified target DNA samples in buffer solution, the target hybridization efficiencies of these two probe surfaces differed significantly when performed in complex biological mixtures (e.g., serum) (Fig. 11.6). Although MCU addition into the ssDNA adlayer improved the surface hybridization by both orienting immobilized probe DNA (e.g., preventing ssDNA nonspecific interactions with the gold surface) and providing effective resistance to adsorption of noncomplementary DNA, these ssDNA/MCU surfaces were not sufficiently protein-resistant to perform measurements in complex milieu. Results of SPR-based DNA hybridization from various serum dilutions showed that both the DNA hybridization kinetics

and the capture efficiency were adversely affected by nonspecific protein adsorption, even at a minimum serum concentration of 1 v/v% when compared to target capture from pure buffer [25]. No target hybridization was detected on the ssDNA/MCU surfaces in SPR from serum concentrations above 30 %, indicating the substantial interference of nonspecific protein adsorption with specific DNA capture and hybridization. However, the target hybridization on ssDNA/OEG surfaces decreases only slightly (by roughly 20 %) as the serum concentration is increased to 50 %. In undiluted serum (100 %), the target hybridization on the probe surface was reduced by approximately 80 %, but still well above baseline noise, to  $1.3 \times 10^{12}$  molecules/cm<sup>2</sup>. Comparing these results to data for DNA hybridization on ssDNA/MCU-probe surfaces, Lee et al. found that OEG backfill significantly improves the selectivity of the DNA probe surface, allowing target detection directly from undiluted serum [23]. One conclusion is that an OEG diluent background is more effective at preventing nonspecific protein binding than the hydroxyl-terminated MCU alkylthiol diluent background, making it possible to detect a given target DNA strand within a solution containing a substantial protein background. Nevertheless, the differences between assay results from buffer versus those in complex media demonstrate the performance challenge for nucleic acid capture in the presence of substantial competing, nonspecific adsorption noise.

### 11.3 Surface Chemical State Image Analysis of DNA Microarrays Using XPS and ToF-SIMS

In addition to the immobilization chemistry used for attaching ssDNA probes to the solid supports, another important aspect of microarray fabrication is the physical deposition method used to create the DNA microspot patterns on the surface. Methods for fabricating micron-scale DNA patterns fall into two broad categories: (1) *in situ* synthesis, a base-by-base attachment to build up different DNA strands at different sites in the array; or (2) *ex situ* synthesis and the subsequent attachment of different complete strands at individual array sites [53]. For the former approach, Affymetrix has developed a photolithographic process to create DNA arrays using a series of exposures through masks to control the addition of bases to specific sites on the surface [54]. This method offers the advantage of having the oligonucleotide synthesized on the same support used for assay hybridization, obviating the need to remove the DNA strand from its synthetic support and reattach it to the microarray surface. However, *in situ* methods of DNA strand synthesis on the surface do not allow for independent confirmation of the fidelity of the probe synthesis, provide variation in probe density, or allow purification of the oligonucleotide after synthesis to eliminate incomplete strands or strands with excess bases, thereby reducing the overall array reliability. In addition, DNA probe lengths are limited practically to shorter oligomers (~25–50-mers).

In the second method, completely synthesized and prepurified DNA strands are attached to the array surface. Several factors must be considered in the production

of these microarrays using presynthesized oligonucleotides, including derivatization of the substrate with functional groups, derivatization of nucleic acid probes with complementary functional groups, delivery of minute volumes (e.g., nanoliters) of DNA solution to the surface using contact or noncontact printing techniques, and deactivation of remaining unreacted surface-bound functional groups after immobilization.

Micro-printing techniques are widely used for DNA microarray fabrication on commercial array slides containing hundreds to thousands of spotted micron-sized features. The printing process generally involves dispensing nanoliter drops of DNA print solutions onto solid reactive array surfaces using a robotic spotter interfaced with DNA probe source plates. The nanoliter drops of DNA solution evaporate within a few seconds of surface residence without reaching equilibrium in terms of DNA–surface interactions, covalent reactions on surfaces, or constant ionic strength. This rapid evaporative process produces distinct differences in immobilized DNA structure, density, and chemistry compared to bulk solution-coupling reactions between DNA and surfaces [55, 56]. The formation of dry DNA microspots with greater DNA density at the edges than in the middle (e.g., donut morphologies) is commonly observed, as drying or wetting print solution flows to spot edges upon rapid evaporation on micro-printed array surfaces [57]. When contact-based pin-printing methods are used, surface damage may also occur during the array printing process [1]. The resulting immobilized DNA density and distribution within individual microarray spots, completely distinct from that produced by bulk surface immobilization, have profound influences on the subsequent target-capture performance (see Sect. 11.2) [19, 26]. Spot-to-spot and intraspot variations in DNA surface density and distribution can therefore lead to inconsistent target capture, substantial spot–spot and assay–assay variability, inaccurate data quantification, and misleading results. Thus, the accurate quantitative analysis of printed DNA microarray diagnostics is possible only if controlled and reliable spot uniformity (i.e., spot density, intraspot DNA density control, spot size, and shape repeatability) is achieved.

XPS and ToF-SIMS each exhibit intrinsic strengths and weaknesses with respect to generating surface chemical state information at a high spatial resolution but used together provide a powerful complementary set of techniques. The quantitative nature of XPS combined with its 2–10-nm sampling depth makes it ideal for determining surface concentrations of biomolecules, including DNA [23, 24, 55, 58–61]. Innovations in X-ray focusing and lens/analyzer technology now permit XPS imaging at spatial resolutions lower than 10  $\mu\text{m}$  [62–65]. Although this spatial resolution remains orders of magnitude above that obtained with other microscopy techniques, imaging XPS has significant advantages in quantifying the sample surface composition. In contrast to imaging XPS, imaging ToF-SIMS is a more surface-sensitive technique (1–2-nm sampling depth), providing a significantly higher spatial resolution that allows a more detailed analysis of the compositional variability within a biomolecular pattern on solid substrates [66–68]. Previous studies have shown that static ToF-SIMS, in combination with multivariate analysis statistical methods such as principal component analysis (PCA), can provide the distribution of chemical species across a patterned surface at a submicrometer resolution [69, 70]. An example

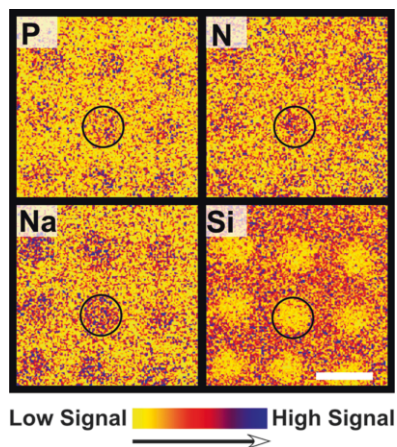


**Fig. 11.7** XPS elemental images ( $800\ \mu\text{m} \times 800\ \mu\text{m}$ ) of aminated DNA probes printed onto CodeLink microarray slides at  $40\text{-}\mu\text{M}$  DNA concentration. While phosphorus is unique to DNA, silicon is unique to the substrate. In combination, these elemental images enable unambiguous identification of the spatial distribution of DNA for the XPS region-of-interest (ROI) compositional analyses of the printed DNA microarray spots. The scale bar represents  $200\ \mu\text{m}$  (Reproduced with permission from Ref. [71]. Copyright © 2007 American Chemical Society)

of the value of the dual use of imaging XPS and imaging ToF-SIMS to determine the chemical composition, spatial distribution, and hybridization efficiency of amine-terminated ssDNA bound to commercial polyacrylamide-based microarray slides was published in 2007 [71].

Figure 11.7 shows XPS elemental images (P, N, Na, and Si) of noncontact printed DNA microarray spots ( $100\text{--}150\text{-}\mu\text{m}$  diameter) on CodeLink™ (GE Amersham microarray substrate) slides [55, 71]. Background-corrected P 2p images (Fig. 11.7) show a higher signal intensity in the immobilized DNA microspot regions. Although N, Na, and Si are present throughout the substrate surface, higher N 1s and Na 1s and lower Si 2p signal intensities were observed in the DNA microspots. Higher N and Na signal intensities correlate with nitrogen-containing DNA bases and sodium counterions associated with the DNA polyphosphate backbone. DNA coverage in printed regions attenuates the signal intensity from elements present in the underlying glass substrate (i.e., Si). Also, XPS imaging can distinguish between hybridized and unhybridized microspots on a commercial microarray slide without the use of radioactive or fluorescent labels. Figure 11.8 shows XPS overlay images displaying P, N, Na, and Si signal intensities from a hybridized (Fig. 11.8a) and an unhybridized (Fig. 11.8b) microarray slide. Prior to exposing the microarray slide to complementary target capture, similar XPS P 2p, N 1s, and Na 1s signal intensities were detected from all microspots, regardless of whether the microspots were printed utilizing complementary or noncomplementary probe sequences. After target hybridization, microspots with complementary probe sequences had higher XPS P 2p, N 1s, and Na 1s signal intensities compared to microspots with noncomplementary probe sequences, as expected [71].

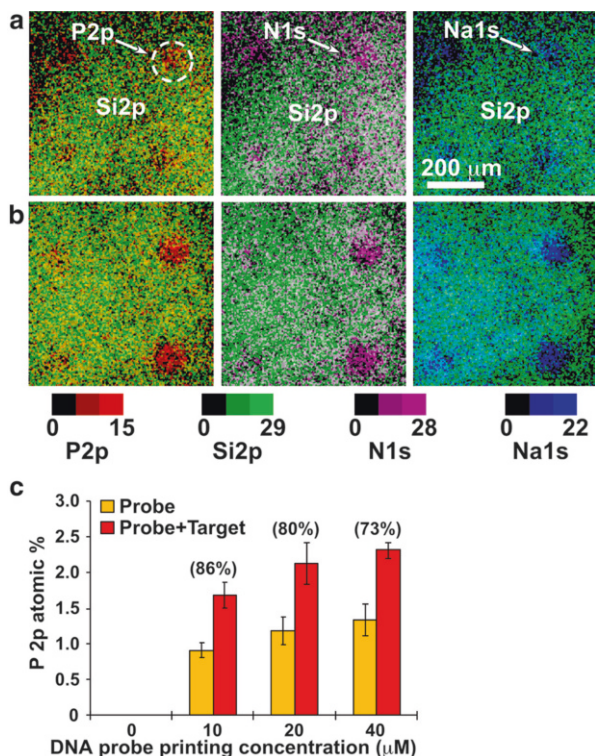


**Fig. 11.8** XPS overlay of phosphorous (P2p), nitrogen (N1s), and sodium (Na1s) with the substrate silicon (Si2p) signal intensity images ( $800 \mu\text{m} \times 800 \mu\text{m}$ ) from printed DNA probes on CodeLink™ polymer microarray slides before (a) and after (b) DNA target hybridization. Consistent with the target capture signal, the XPS P2p, N1s, and Na1s signal intensities from the hybridized regions are significantly higher than from the unhybridized regions. Amounts of DNA on CodeLink surfaces are proportional to the P2p atomic percent (at. %) (c). Microarrays were printed at three DNA probe concentrations (10, 20, and  $40 \mu\text{M}$ ). Target hybridization efficiencies for the microarray shown in parentheses above each concentration were derived as a percentage of probe molecules hybridized  $\{[(\text{P2p at. \% of hybridized spot}/\text{P2p at. \% of probe spot}) - 1] \times 100 \%\}$  (Reproduced with permission from Ref. [71]. Copyright © 2007 American Chemical Society)

Small-area region-of-interest (ROI) analyses were performed to obtain quantitative elemental composition information about individual DNA spots both before and after hybridization. The results from these ROI analyses were then used to determine target hybridization efficiencies for microarrays printed at various printed probe concentrations (e.g., 10, 20, and  $40 \mu\text{M}$ ). Microspots with hybridized complementary sequences show higher percentages of phosphorus (2.2 atomic percent, or at.%), nitrogen (13.1 at.%), and sodium (5.6 at.%) and lower substrate oxygen (23.0 at.%) and silicon (3.3 at.%) signals compared to microspots with unhybridized non-complementary probe spots (P=1.3, N=11.8, Na=3.1, O=25.7, and Si=5.4 at.%). Due to the substantial amounts of nitrogen (~8 at.%) in the unprinted CodeLink

acrylamide-based polymer layer [55], the phosphorus signal from the DNA backbone is the only unique characteristic element useful for quantifying relative amounts of surface-immobilized and hybridized DNA oligomers. The DNA surface coverage is proportional to the phosphorus atomic concentration, as has been shown previously for immobilized DNA on gold [25, 61] and polymer-modified silicon substrates [55, 58]. Figure 11.8c shows relative amounts of surface-immobilized probe and hybridized DNA obtained for each probe printing concentration from small-area XPS analysis [71]. Figure 11.8c shows the P 2p at.% from the DNA microspots' increases with increasing spotting-probe solution concentration. The target hybridization efficiencies shown in parentheses above each concentration in Fig. 11.8c were calculated from the XPS P 2p signal to determine the percentage of probe molecules hybridized  $\{[(\text{P 2p at.\% of hybridized spot}/\text{P 2p at.\% of probe spot}) - 1] \times 100\%$ . A hybridization efficiency of 86% was obtained for microspots printed at a probe concentration of 10  $\mu\text{M}$ . At higher probe printing concentrations (20 and 40  $\mu\text{M}$ ), slightly lower hybridization efficiencies (80% and 73%) were obtained [71]. A reduction in the hybridization efficiency at a higher probe coverage has been reported previously [25, 26, 55] and can be explained by steric and electrostatic crowding effects in closely packed DNA probes that hinder DNA target duplex formation on the microarray surface [72].

In addition to determining DNA microspot composition, knowing the distribution of immobilized DNA molecules within individual DNA microspots is desirable, as described above. Imaging ToF-SIMS is able to provide distinct analytical data on the lateral distribution of DNA within single-array microspots before and after target hybridization via detection of the characteristic DNA ion fragments (i.e., DNA bases and phosphate backbone) [59, 60, 73, 74]. Negative-ion ToF-SIMS ROI spectra from the DNA microspotted regions (Fig. 11.9b) show phosphate fragments from the DNA backbone ( $\text{PO}^-$ ,  $\text{PO}_2^-$ ,  $\text{PO}_3^-$ , and  $\text{H}_2\text{PO}_4^-$ ) at  $m/z$  47, 63, 79, and 97 [59, 60, 73, 74], as well as unique fragments from DNA bases such as adenine (Ade-H,  $m/z=134$ ), thymine (Thy-H,  $m/z=125$ ), guanine (Gua-H,  $m/z=150$ ), and cytosine (Cyt-H,  $m/z=110$ ) [59, 60]. These DNA-related peaks were absent in the negative-ion spectra from the unspotted substrate region (Fig. 11.9a), confirming their origin from surface-immobilized DNA molecules. Individual negative-ion ToF-SIMS images for selected masses show the distribution of printed DNA within an unhybridized microspot containing noncomplementary DNA probes (Fig. 11.10a) and a hybridized microspot containing complementary probes (Fig. 11.10b) from the microarray region printed with 40- $\mu\text{M}$  DNA solution [71]. A microarray spot diameter of approximately 150  $\mu\text{m}$  was determined from the ToF-SIMS  $\text{PO}_x^-$  images, which is comparable to that observed using fluorescence microscopy after printing (Fig. 11.10c). ToF-SIMS images of the Si<sup>-</sup> peak on the unhybridized microspots reveal a “donut” feature around the probe spot consistent with those seen in fluorescent images (Fig. 11.10c) (PCA analysis of these halos is presented later in the chapter). Also, consistent with XPS data, images for characteristic DNA fragments ( $m/z$  47, 63, 79, 97, 110, 125, 134, and 150) show higher signal intensities for the hybridized DNA microspot (Fig. 11.10b) [71].



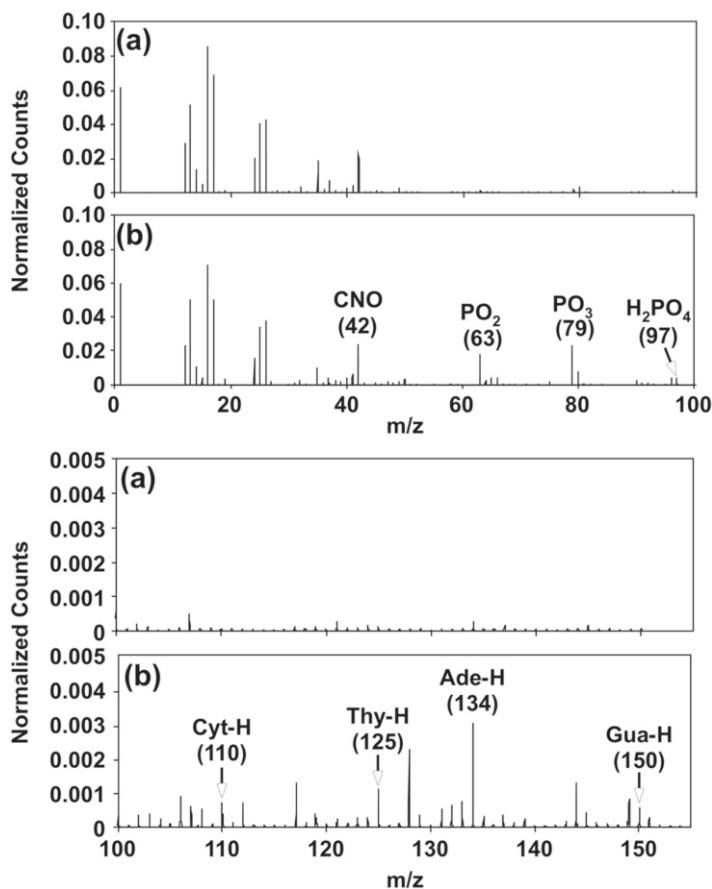


**Fig. 11.9** Negative-ion ToF-SIMS ROI spectra from the (a) substrate and the (b) DNA regions of the microarray surface. The DNA region shows characteristic nucleic acid peaks at  $m/z$  42 ( $\text{CNO}^-$ ), 63 ( $\text{PO}_2^-$ ), 79 ( $\text{PO}_3^-$ ), 97 ( $\text{H}_2\text{PO}_4^-$ ), 110 ( $\text{C}_4\text{H}_4\text{N}_3\text{O}^-$ , Cyt-H), 125 ( $\text{C}_5\text{H}_5\text{N}_2\text{O}_2^-$ , Thy-H), 134 ( $\text{C}_5\text{H}_4\text{N}_5^-$ , Ade-H), and 150 ( $\text{C}_5\text{H}_4\text{N}_5\text{O}^-$ , Gua-H) that were absent or present at much lower intensities in the background substrate region (Reproduced with permission from Ref. [71]. Copyright ©2007 American Chemical Society)

ToF-SIMS was also employed to identify the DNA hybridization signal by using a complementary target sequence in which 50% of the DNA bases were modified with one Br atom (Fig. 11.11a). Printed probe microarrays exposed to Br-modified DNA complementary targets produced strong Br signals from hybridized probe spots (Fig. 11.11c) compared to noncomplementary probes (Fig. 11.11b). ToF-SIMS' intrinsic high sensitivity in detecting brominated molecules, combined with its demonstrated submicron spatial resolution, opens new possibilities to exploit this analytical method to determine hybridization uniformity across single microarray spots.

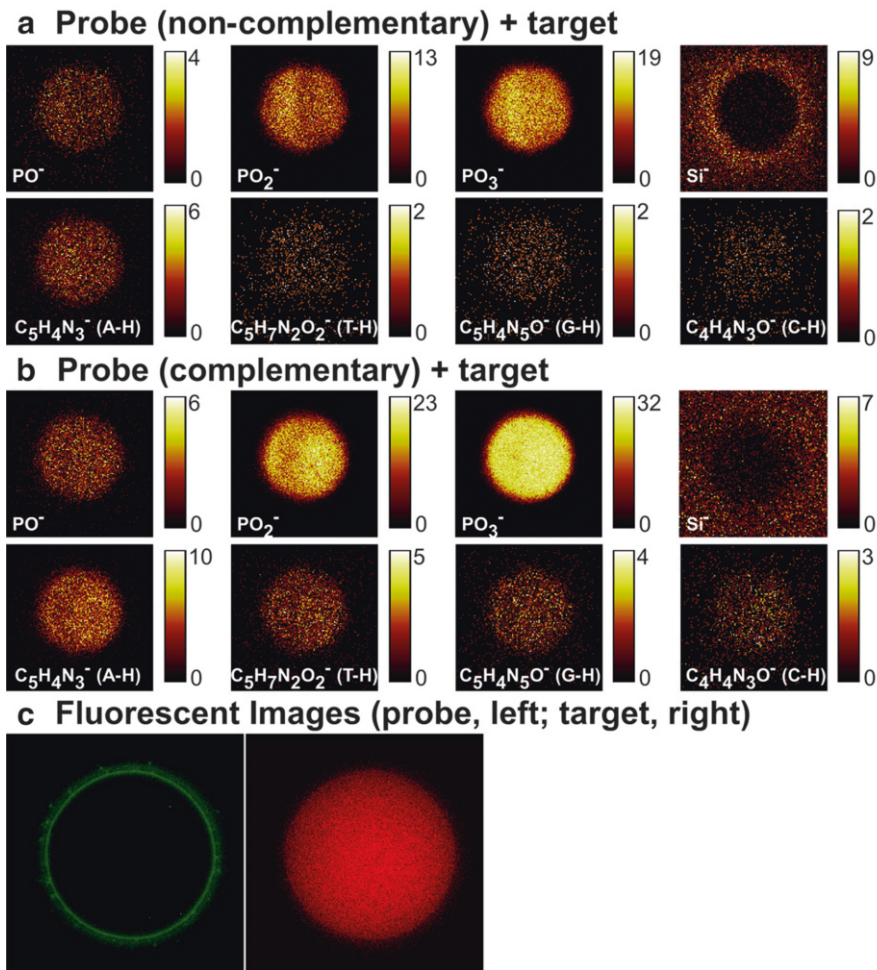


**Fig. 11.10** Representative negative-ion ToF-SIMS images showing the distribution of DNA and substrate fragments within a single (a) unhybridized and (b) hybridized microarray spot. The DNA fragments are localized to the noncontact printed regions but distributed inhomogeneously within the microspot. The Si image from the unhybridized probe spot (a) showed a “halo” feature around the spot. A brighter pixel intensity corresponds to higher DNA or substrate signals (counts per pixel). ToF-SIMS images are  $200\ \mu\text{m} \times 200\ \mu\text{m}$ . The fluorescent images of the printed probe (*left*) and hybridized target (*right*) were collected using a fluorescent microscope showing a “halo effect”; scale bar represents  $50\ \mu\text{m}$  (c) (Reproduced with permission from Ref. [71]. Copyright © 2007 American Chemical Society)

While specific peaks due to expected fragments can be readily identified in the SIMS spectra, such as the DNA molecular fragments identified above, the energetic SIMS process yields hundreds of peaks in the  $0\text{--}200\text{-}m/z$  range, making the interpretation of all peaks detected in a ToF-SIMS experiment difficult. To simplify data

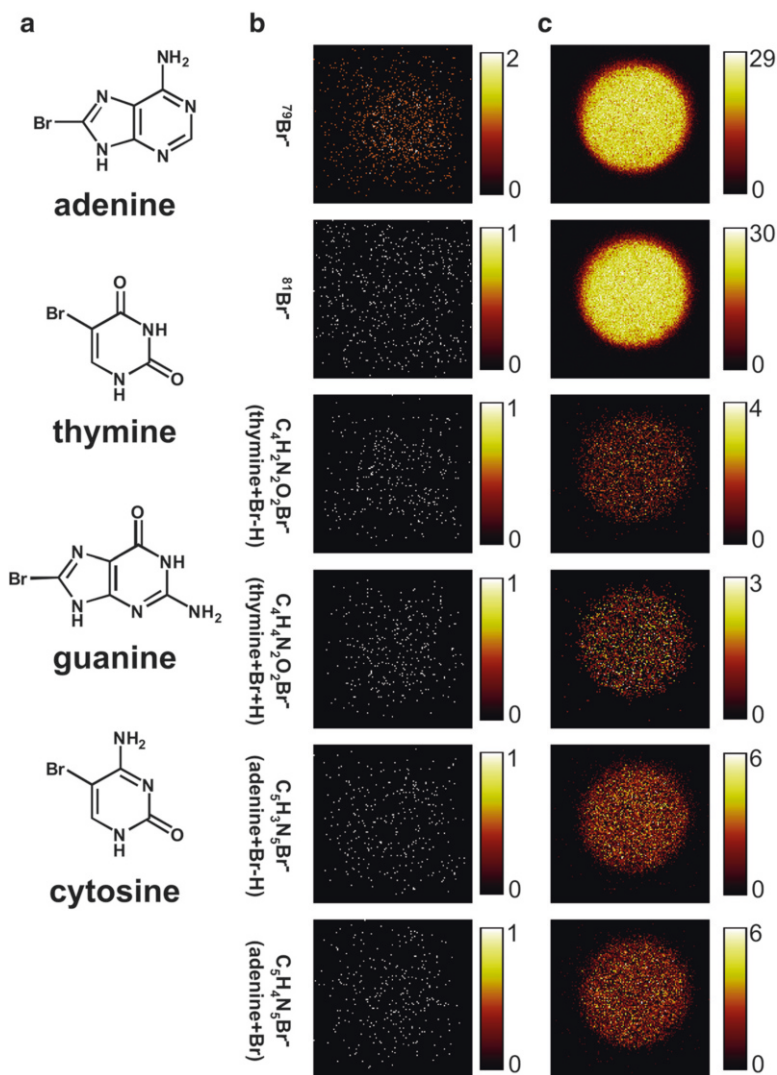


**Fig. 11.11** (a) Bromine modification of DNA target (50% brominated DNA bases comprise the DNA target sequence). Representative negative-ion ToF-SIMS images showing no Br fragments detected from the noncomplementary (unhybridized) microspots (b). Microarrays exposed to Br-modified DNA targets produce strong Br signals for complementary (hybridized) microspots after target hybridization (c). A brighter pixel intensity corresponds to higher DNA or substrate signals (counts per pixel). Images are  $200\ \mu\text{m} \times 200\ \mu\text{m}$  (Reproduced with permission from Ref. [71]. Copyright ©2007 American Chemical Society)

interpretation and identify image features related to other chemical species (e.g., salt ions and detergent molecules from the print buffer, organic species from the polymer layer, contaminants introduced by the printing process, etc.), the multivariate analysis technique of PCA was used for more detailed analyses of the



layer. PC 2 (Fig. 11.12b) shows image features that correspond to the salt ions, including  $\text{Cl}^-$ ,  $\text{NaOH}^-$ ,  $\text{CaO}^-$ , and so forth (bright regions), and SDS fragments (dark regions). PC 3 (Fig. 11.12c) captures the image feature that corresponds to the halo around the probe spot (dark regions). The PC 3 loadings plot (Fig. 11.12c) indicates that most major peaks with negative PC 3 loadings associated with the halo in the ToF-SIMS image are silicon- and sulfur-containing fragments possibly from the polymer-coated glass substrate exposed as a result of polymer-layer damage due to the microarray printing process or from silicon-containing contaminants wicking to the outside of the spot upon spotting. Studies are currently underway to examine DNA microspot heterogeneities in further detail.

## 11.4 Concluding Remarks

The work on immobilized DNA surface analysis presented in this chapter demonstrates the utility of XPS, ToF-SIMS, NEXAFS, and SPR for obtaining molecular-level information about the structure, coverage, and hybridization properties of immobilized ssDNA in model self-assembled monolayer systems as well as on commercial microarray substrates. Information gained from these studies has facilitated an improved understanding of ssDNA behavior on surfaces by providing quantitative correlations between immobilized DNA surface properties (i.e., density and orientation) and the resultant analyte's target hybridization efficiency from simple and complex biological samples. Such analyses are needed to understand the limitations of current DNA microarray assays and to design and engineer new DNA-based detection systems to meet biomedical and biosensing technological goals. Despite this substantial progress in quantifying several aspects of DNA on surfaces, new surface analytical method innovation is required to obtain even more challenging parameters relevant to DNA real-time assay. Detection limits, higher throughput, spatial information, and other surface properties could all be improved. Additionally, sum frequency generation spectroscopy (SFG) and multiplexed probe microscopy methods (SPM, AFM) that provide in situ information on DNA-surface and DNA-DNA interactions in wet aqueous conditions are likely to contribute in the near term to this suite of techniques. Optical waveguide methods interrogating DNA in complex milieu using creative probe designs will also contribute [75].

**Acknowledgments** We gratefully acknowledge support from NESAC/BIO (NIH grant no. EB-002027) and NIH grant no. EB-001473. NEXAFS studies were performed at the NSLS, Brookhaven National Laboratory, which is supported by the U.S. Department of Energy, Division of Materials Science and Division of Chemical Sciences. Dr. D. A. Fischer is thanked for his expert technical assistance with the NEXAFS experiments. Dr. D. Graham is thanked for assistance with PCA. We also thank Dr. S. Gollidge for expert technical assistance with the ToF-SIMS experiments performed at the Center for Advanced Materials Characterization in Oregon.

## References

1. Pirrung MC. How to make a DNA chip. *Angew Chem Int Edit.* 2002;41:1277–89.
2. Wang J. From DNA biosensors to gene chips. *Nucleic Acids Res.* 2000;28:3011–6.
3. Sanchez-Carbayo MS, Bornmann W, Cordon-Cardo C. DNA microchips: technical and practical considerations. *Curr Org Chem.* 2000;4:945–71.
4. Debouck C, Goodfellow PN. DNA microarrays in drug discovery and development. *Nat Genet.* 1999;21:48–50.
5. Churchill GA. Fundamentals of experimental design for cDNA microarrays. *Nat Genet.* 2002;32:490–5.
6. Yu DH, Blankert B, Vire JC, Kauffmann JM. Biosensors in drug discovery and drug analysis. *Anal Lett.* 2005;38:1687–701.
7. Zhai JH, Cui H, Yang RF. DNA based biosensors. *Biotechnol Adv.* 1997;15:43–58.
8. Rivas GA, Pedano ML, Ferreyra NF. Electrochemical biosensors for sequence-specific DNA detection. *Anal Lett.* 2005;38:2653–703.
9. Bloomfield VA, Crothers DM, Tinoco I. *Nucleic acids structures, properties, and functions.* Sausalito: University Science Books; 2000.
10. Huang E, Zhou FM, Deng L. Studies of surface coverage and orientation of DNA molecules immobilized onto preformed alkanethiol self-assembled monolayers. *Langmuir.* 2000;16:3272–80.
11. Wolf LK, Fullenkamp DE, Georgiadis RM. Quantitative angle-resolved SPR imaging of DNA-DNA and DNA-drug kinetics. *J Am Chem Soc.* 2005;127:17453–9.
12. Piliarik M, Vaisocherova H, Homola J. A new surface plasmon resonance sensor for high-throughput screening applications. *Biosens Bioelectron.* 2005;20:2104–10.
13. Shumaker-Parry JS, Aebersold R, Campbell CT. Parallel, quantitative measurement of protein binding to a 120-element double-stranded DNA array in real time using surface plasmon resonance microscopy. *Anal Chem.* 2004;76(7):2071–82.
14. Wark AW, Lee HJ, Corn RM. Long-range surface plasmon resonance imaging for bioaffinity sensors. *Anal Chem.* 2005;77:3904–7.
15. Lazerges M, Perrot H, Zeghib N, Antoine E, Compere C. In situ QCM DNA-biosensor probe modification. *Sens Actuator B-Chem.* 2006;120:329–37.
16. Su XD, Wu YJ, Knoll W. Comparison of surface plasmon resonance spectroscopy and quartz crystal microbalance techniques for studying DNA assembly and hybridization. *Biosens Bioelectron.* 2005;21:719–26.
17. He PA, Xu Y, Fang YZ. A review: electrochemical DNA biosensors for sequence recognition. *Anal Lett.* 2005;38:2597–623.
18. Love JC, Estroff LA, Kriebel JK, Nuzzo RG, Whitesides GM. Self-assembled monolayers of thiolates on metals as a form of nanotechnology. *Chem Rev.* 2005;105:1103–69.
19. Herne TM, Tarlov MJ. Characterization of DNA probes immobilized on gold surfaces. *J Am Chem Soc.* 1997;119:8916–20.
20. Moses S, Brewer SH, Lowe LB, Lappi SE, Gilvey LBG, Sauthier M, et al. Characterization of single- and double-stranded DNA on gold surfaces. *Langmuir.* 2004;20:11134–40.
21. Levicky R, Herne TM, Tarlov MJ, Satija SK. Using self-assembly to control the structure of DNA monolayers on gold: a neutron reflectivity study. *J Am Chem Soc.* 1998;120:9787–92.
22. Peterlinz KA, Georgiadis RM, Herne TM, Tarlov MJ. Observation of hybridization and dehybridization of thiol-tethered DNA using two-color surface plasmon resonance spectroscopy. *J Am Chem Soc.* 1997;119:3401–2.
23. Lee C-Y, Gamble LJ, Grainger DW, Castner DG. Mixed DNA/Oligo(ethylene glycol) functionalized gold surfaces improve DNA hybridization in complex media. *Biointerphases.* 2006;1:82–92.
24. Lee C-Y, Gong P, Harbers GM, Grainger DW, Castner DG, Gamble LJ. Surface coverage and structure of mixed DNA/alkylthiol monolayers on gold: characterization by XPS, NEXAFS, and fluorescence intensity measurements. *Anal Chem.* 2006;78:3316–25.

25. Gong P, Lee C-Y, Gamble LJ, Castner DG, Grainger DW. Hybridization behavior of mixed DNA/alkylthiol monolayers on gold: characterization by SPR and  $^{32}\text{P}$  radiometric assay. *Anal Chem*. 2006;78:3326–34.
26. Peterson AW, Heaton RJ, Georgiadis RM. The effect of surface probe density on DNA hybridization. *Nucleic Acids Res*. 2001;29:5163–8.
27. Stohr J. NEXAFS spectroscopy, vol. 25. New York: Springer; 1992.
28. Hahner G, Kinzler M, Thummler C, Woll C, Grunze M. Structure of self-organizing organic films – a near edge X-ray absorption fine-structure investigation of thiol layers adsorbed on gold. *J Vac Sci Technol A-Vac Surf Films*. 1992;10:2758–63.
29. Gamble LJ, Ravel B, Fischer DA, Castner DG. Surface structure and orientation of PTFE films determined by experimental and FEFF8-calculated NEXAFS spectra. *Langmuir*. 2002;18:2183–9.
30. Nagayama K, Sei M, Mitsumoto R, Ito E, Araki T, Ishii H, et al. Polarized NEXAFS studies on the mechanical rubbing effect of poly(tetrafluoroethylene) oligomer and its model compound. *J Electron Spectrosc Relat Phenom*. 1996;78:375–8.
31. Ziegler C, Schedelnieg T, Beams G, Clark DT, Salaneck WR, Sotobayashi H, et al. X-ray-absorption study of highly oriented poly(Tetrafluoroethylene) thin-films. *Langmuir*. 1994;10:4399–402.
32. Castner DG, Lewis KB, Fischer DA, Ratner BD, Gland JL. Determination of surface-structure and orientation of polymerized tetrafluoroethylene films by near-edge X-ray absorption fine-structure, X-ray photoelectron-spectroscopy, and static secondary ion mass-spectrometry. *Langmuir*. 1993;9:537–42.
33. Fujii K, Akamatsu K, Muramatsu Y, Yokoya A. X-ray absorption near edge structure of DNA bases around oxygen and nitrogen K-edge. *Nucl Instrum Methods Phys Res Sect B-Beam Interact Mater Atoms*. 2003;199:249–54.
34. Fujii K, Akamatsu K, Yokoya A. Near-edge X-ray absorption fine structure of DNA nucleobases thin film in the nitrogen and oxygen K-edge region. *J Phys Chem B*. 2004;108:8031–5.
35. Furukawa M, Fujisawa H, Katano S, Ogasawara H, Kim Y, Komeda T, et al. Geometrical characterization of pyrimidine base molecules adsorbed on Cu(110) surfaces: XPS and NEXAFS studies. *Surf Sci*. 2003;532:261–6.
36. Kirtley SM, Mullins OC, Chen J, Vanelp J, George SJ, Chen CT, et al. Nitrogen chemical-structure in DNA and related molecules by X-ray absorption-spectroscopy. *Biochim Et Biophys Acta*. 1992;1132:249–54.
37. Samuel NT, Lee C-YL, Gamble LJ, Fisher DA, Castner DG. NEXAFS characterization of DNA components and molecular-orientation of surface-bound DNA oligomers. *J Electron Spectrosc Relat Phenom*. 2006;152:134–42.
38. Petrovykh DY, Perez-Dieste V, Opdahl A, Kimura-Suda H, Sullivan JM, Tarlov MJ, et al. Nucleobase orientation and ordering in films of single-stranded DNA on gold. *J Am Chem Soc*. 2006;128:2–3.
39. Crain JN, Kirakosian A, Lin JL, Gu YD, Shah RR, Abbott NL, et al. Functionalization of silicon step arrays II: molecular orientation of alkanes and DNA. *J Appl Phys*. 2001;90:3291–5.
40. Brockman JM, Frutos AG, Corn RM. A multistep chemical modification procedure to create DNA arrays on gold surfaces for the study of protein-DNA interactions with surface plasmon resonance imaging. *J Am Chem Soc*. 1999;121:8044–51.
41. Nelson BP, Grimrud TE, Liles MR, Goodman RM, Corn RM. Surface plasmon resonance imaging measurements of DNA and RNA hybridization adsorption onto DNA microarrays. *Anal Chem*. 2001;73:1–7.
42. Smith EA, Wanat MJ, Cheng YF, Barreira SVP, Frutos AG, Corn RM. Formation, spectroscopic characterization, and application of sulfhydryl-terminated alkanethiol monolayers for the chemical attachment of DNA onto gold surfaces. *Langmuir*. 2001;17:2502–7.
43. Shumaker-Parry JS, Zareie MH, Aebersold R, Campbell CT. Microspotting streptavidin and double-stranded DNA Arrays on gold for high-throughput studies of protein-DNA interactions by surface plasmon resonance microscopy. *Anal Chem*. 2004;76(4):918–29.

44. Peterson AW, Heaton RJ, Georgiadis R. Kinetic control of hybridization in surface immobilized DNA monolayer films. *J Am Chem Soc.* 2000;122:7837–8.
45. Peterson AW, Wolf LK, Georgiadis RM. Hybridization of mismatched or partially matched DNA at surfaces. *J Am Chem Soc.* 2002;124:14601–7.
46. Xia N, Shumaker-Parry JS, Zareie MH, Campbell CT, Castner DG. A streptavidin linker layer that functions after drying. *Langmuir.* 2004;20:3710–6.
47. Green RJ, Frazier RA, Shakesheff KM, Davies MC, Roberts CJ, Tandler SJB. Surface plasmon resonance analysis of dynamic biological interactions with biomaterials. *Biomaterials.* 2000;21:1823–35.
48. Pavey KD, Olliff CJ. SPR analysis of the total reduction of protein adsorption to surfaces coated with mixtures of long- and short-chain polyethylene oxide block copolymers. *Biomaterials.* 1999;20:885–90.
49. Green RJ, Davies MC, Roberts CJ, Tandler SJB. Competitive protein adsorption as observed by surface plasmon resonance. *Biomaterials.* 1999;20:385–91.
50. Morgan H, Taylor DM. A surface-plasmon resonance immunosensor based on the streptavidin biotin complex. *Biosens Bioelectron.* 1992;7:405–10.
51. Daniels PB, Deacon JK, Eddowes MJ, Pedley DG. Surface-plasmon resonance applied to immunosensing. *Sensor Actuator.* 1988;15:11–8.
52. Gong P, Grainger DW. *Microarrays: methods and protocols.* 2nd ed. Totowa: Humana Press; 2007.
53. Grainger DW, Greef CA, Gong P, Lochhead MJ. *Microarrays: methods and protocols.* 2nd ed. Totowa: Humana Press; 2007.
54. Fodor SPA, Read JL, Pirrung MC, Stryer L, Lu AT, Solas D. Light-directed, spatially addressable parallel chemical synthesis. *Science.* 1991;251:767–73.
55. Gong P, Harbers GM, Grainger DW. Multi-technique comparison of immobilized and hybridized oligonucleotide surface density on commercial amine-reactive microarray slides. *Anal Chem.* 2006;78:2342–51.
56. Dufva M. Fabrication of high quality microarrays. *Biomol Eng.* 2005;22:173–84.
57. Ramakrishnan R, Dorris D, Lublinsky A, Nguyen A, Domanus M, Prokhorova A, et al. An assessment of Motorola CodeLink (TM) microarray performance for gene expression profiling applications. *Nucleic Acids Res.* 2002;30:e30.
58. Shen G, Anand MFG, Levicky R. X-ray photoelectron spectroscopy and infrared spectroscopy study of maleimide-activated supports for immobilization of oligodeoxyribonucleotides. *Nucleic Acids Res.* 2004;32:5973–80.
59. Lee CY, Canavan HE, Gamble LJ, Castner DG. Evidence of impurities in thiolated single-stranded DNA oligomers and their effect on DNA self-assembly on gold. *Langmuir.* 2005;21:5134–41.
60. May CJ, Canavan HE, Castner DG. Quantitative X-ray photoelectron spectroscopy and time-of-flight secondary ion mass spectrometry characterization of the components in DNA. *Anal Chem.* 2004;76:1114–22.
61. Petrovykh DY, Kimura-Suda H, Whitman LJ, Tarlov MJ. Quantitative analysis and characterization of DNA immobilized on gold. *J Am Chem Soc.* 2003;125:5219–26.
62. Walton J, Fairley N. Characterisation of the Kratos Axis Ultra with spherical mirror analyser for XPS imaging. *Surf Interface Anal.* 2006;38:1230–5.
63. Walton J, Fairley N. Transmission-function correction for XPS spectrum imaging. *Surf Interface Anal.* 2006;38:388–91.
64. Vohrer U, Blomfield C, Page S, Roberts A. Quantitative XPS imaging – new possibilities with the delay-line detector. *Appl Surf Sci.* 2005;252:61–5.
65. Walton J, Fairley N. Quantitative surface chemical-state microscopy by x-ray photoelectron spectroscopy. *Surf Interface Anal.* 2004;36:89–91.
66. Belu AM, Yang ZP, Aslami R, Chilkoti A. Enhanced TOF-SIMS imaging of a micropatterned protein by stable isotope protein labeling. *Anal Chem.* 2001;73:143–50.



67. Yang ZP, Belu AM, Liebmann-Vinson A, Sugg H, Chilkoti A. Molecular imaging of a micropatterned biological ligand on an activated polymer surface. *Langmuir*. 2000;16:7482–92.
68. Belu AM, Graham DJ, Castner DG. Time-of-flight secondary ion mass spectrometry: techniques and applications for the characterization of biomaterial surfaces. *Biomaterials*. 2003;24:3635–53.
69. Wagner MS, Graharn DJ, Castner DG. Simplifying the interpretation of ToF-SIMS spectra and images using careful application of multivariate analysis. *Appl Surf Sci*. 2006;252(19):6575–81.
70. Tyler BJ. Multivariate statistical image processing for molecular specific imaging in organic and bio-systems. *Appl Surf Sci*. 2006;252(19):6875–82.
71. Lee CY, Harbers GM, Grainger DW, Gamble LJ, Castner DG. Fluorescence, XPS, and TOF-SIMS surface chemical state image analysis of DNA microarrays. *J Am Chem Soc*. 2007;129:9429–38.
72. Heaton RJ, Peterson AW, Georgiadis RM. Electrostatic surface plasmon resonance: direct electric field-induced hybridization and denaturation in monolayer nucleic acid films and label-free discrimination of base mismatches. *Proc Natl Acad Sci U S A*. 2001;98:3701–4.
73. Hellweg S, Jacob A, Hoheisel JD, Grehl T, Arlinghaus HF. Mass spectrometric characterization of DNA microarrays as a function of primary ion species. *Appl Surf Sci*. 2006;252:6742–5.
74. Hashimoto H, Nakamura K, Takase H, Okamoto T, Yamamoto N. Quantitative TOF-SIMS imaging of DNA microarrays produced by bubble jet printing technique and the role of TOF-SIMS in life science industry. *Appl Surf Sci*. 2004;231–2:385–91.
75. Moiseev L, Unlu MS, Swan AK, Goldberg BB, Cantor CR. DNA conformation on surfaces measured by fluorescence self-interference. *Proc Natl Acad Sci U S A*. 2006;103:2623–8.

# Index

## A

- ADME. *See* Adsorption, distribution  
metabolism and excretion (ADME)
- Adsorption, distribution metabolism and excretion (ADME), 127–128
- ADXPS. *See* Angle-dependent XPS (ADXPS)
- AES. *See* Auger electron spectroscopy (AES)
- AFM. *See* Atomic force microscopy (AFM)
- Ahimou, F., 27
- Alpha( $\alpha$ )-helix  
melittin  
antimicrobial activity, 210  
fibrinogen coiled-coils, 212–213  
Gaussian distribution, 210–211  
G-protein, 214, 215  
maximum-entropy function, 211–212  
orientation distribution, 211  
orientation, 200–201
- Amer, N.M., 259
- Amide I protein signals  
advantages, 206–207  
detection, 207  
 $\alpha$ -helical melittin  
antimicrobial activity, 210  
fibrinogen coiled-coils, 212–213  
Gaussian distribution, 210–211  
G-protein, 214, 215  
maximum-entropy function, 211–212  
orientation distribution, 211
- measurements  
crystallization, 209  
FWM and CARS, 208, 209  
hyperpolarizability, 210  
polarization mapping, 210  
protein,  $\alpha$ -helices and  $\beta$ -sheets,  
208–209  
orientation and ordering, 207–208  
 $\beta$ -sheets yield chiral signals, 214–216
- Amide I vibrational mode, 197–198
- Angle-dependent XPS (ADXPS)  
and depth profiling, 11–12, 17, 31  
instruments, 12
- Aperture, NSOM  
aluminum coating, 231  
diffraction limit, 227  
fiber optics, 228  
light emerging, 228  
metal-coating, 238
- Appelhans, A.D., 72
- Application modes, AFM  
amplitude and phase changes,  
oscillation, 262  
cantilever oscillation, 261  
characteristic image artifacts, 261  
dynamic mode, 261  
electronic feedback, 261  
material properties, nanometer scale, 262  
surface roughness/external vibrations,  
260–261
- Arlinghaus, H.F., 53
- Artyushkova, K., 30
- Atomic force microscopy (AFM)  
application modes, 260–262  
and biological assays, 30  
biological systems (*see* Biological systems, AFM)  
biophysical properties, 285  
cellular structures and dynamics, 262  
commercial cantilevers, 265  
constant current imaging, 257  
depth calibration, 85, 86  
designed laser optic, 260

- Atomic force microscopy (AFM) (*cont.*)  
 and DPPC, 239  
 electronic interaction, 258  
 EM image, cantilever, 259–260  
 and FIB, 247  
 force-clamp measurements, 285  
 force-measuring tool, 285  
 frequency spectrum, cantilever, 263  
 high-resolution imaging, 262  
 hydrodynamic effects, 265  
 IBM patent application, 258  
 imaging tool, 285  
 LE/LC phases, 234, 240  
 local/scanning probe  
   microscopes, 256  
 mass components, 264  
 mechanical stress, 257  
 mechanical vibrations, 257  
 Ni/Cr layers, 79–80  
 optical detection scheme, 259  
 oxide-sharpening technique, 260  
 resonance curve, 263  
 silicon nitride, 241, 247  
 standard detection scheme, 259  
 STM imaging, 256  
 time-dependent external forces, 263  
 unbombarded sugar trehalose, 80–81
- Attenuated total reflectance Fourier transform  
 IR spectroscopy (ATR-FTIR)  
 amide I band, 206  
 $\alpha$ -helical melittin (*see* Alpha-helix)  
 PSLB, 216
- Auger electron spectroscopy (AES), 2
- B**
- Backscattered helium ions, 184, 185  
 Backscatter electrons, 172  
 Barber, M., 107  
 Beam–specimen interaction  
 beam penetration  
   “electron-greedy”, 180  
   energy transfer, 178  
   Monte Carlo modeling, 180–181  
   stopping power, 178–180  
 Monte Carlo computer simulations, 178  
 particles and detectors  
   backscattered helium, 184–185  
   cathodoluminescence (CL) effect, 186  
   detected photons, 185, 186  
   imaging modes, 188  
   mass spectrometry techniques, 187  
   MCP, 185, 186  
   myelin sheets, 187–188  
   secondary ions and neutrals, 187  
   SEs, 181–184  
   SIMS, 187  
   probe formation, 177–178  
   statistical methods, 178
- Benninghoven, A., 38  
 Berger, M.J., 179  
 Berman, E.S., 57, 60  
 Beta( $\beta$ )-sheet  
   chiral signals, 214–216  
   orientation, 201–202  
   peptide tachyplestin, 207
- Betzig, E., 238  
 Biesinger, M.C., 55–56  
 Binnig, G., 256, 258  
 Biointerface engineering, 29–30  
 Biological structures, NSOM  
   bilayers and multilayers  
     acceptor emission, 241, 242  
     AFM image, 239–241  
     cellular function, 240  
     donor fluorophore, 241, 243  
     DPPC, 239, 240  
     electric fields, 238, 240  
     fiber-optic probe, 242  
     FRET, 240–242  
     high-resolution fluorescence, 240  
     Langmuir–Blodgett (LB)  
       technique, 239  
     microdomain structures, 240  
     PMMA, 241  
     rhodamine, 241  
     single-molecule fluorescence image,  
       238, 240  
   biological films and membranes, 233  
   cells  
     confocal images, 245  
     DCs, 245  
     F-actin fibers, 244  
     fluorescence, 243, 244  
     HASM, 243, 244  
     HLA protein, 244  
     human fibroblast, 244  
     lectins, 245  
     MHC, 244  
     microdomains, 244  
     plasma membrane, 244  
     polarization, 245  
     topography, 243, 244  
     fluorescence, 233  
     monolayers (*see* Lipid monolayers)  
     tip–sample interactions (*see* Tip–sample  
       interactions)  
     topography, 233
- Biological systems  
 biotin–avidin, 265

- electrophysiology, 278–284
- intermolecular forces, 266–267
- intramolecular forces, 267–273
- MD computer simulations, 265
- molecular structures, 265
- and optical microscopy, 273–278
- Biomedical devices, 3
- Biomolecular analysis, ToF-SIMS.  
*See* Time-of-flight secondary ion mass spectrometry (ToF-SIMS)
- Biosensing, DNA-modified surfaces.  
*See* DNA-modified surfaces
- Boughton, A.P., 195–218
- Breitenstein, D., 37–63
- Briggs, D., 142, 157
- Brunelle, A., 56
- C**
- Cantilever
  - constant-height mode, 261
  - mass components, 264
  - mechanical properties, 262
  - optical detection scheme, 259
  - split photodiode, 259
  - tapping mode, 262
- Caprioli, R.M., 126
- Castaing, R., 105
- Castner, D.G., 21, 289–310
- Caudodorsal cell hormone (CDCH), 122
- Chemical composition
  - MIC, 29
  - SIMS imaging, 73
  - XPS, 27
- Cheng, J., 58
- Chen, Z., 195–218
- Chichester, R.J., 238
- Cluster ion source
  - beam characteristics, 46
  - chromatic aberration, 46
  - EI ion source, 44
  - G-SIMS, 167
  - ion-optical system, 45
  - LMIS, 43–44
  - separation and pulsing, 44–45
- Cluster SIMS. *See* Secondary ion mass spectrometry (SIMS)
- Collision cascades, 39–40
- Conboy, J.C., 216
- Constant force mode, 261
- Constant height mode
  - faster imaging, 257
  - imaging cells, 273
- Cross, S.E., 274
- Curie, J., 256–257
- Curie, P., 256–257
- D**
- Davies, J., 3
- DCA. *See* Dynamic contact angle (DCA)
- 3D chemical imaging. *See* Three-dimensional (3D) chemical imaging
- DCs. *See* Dendritic cells (DCs)
- de Bakker, B.I., 245
- Delcorte, A., 59, 60, 119
- Dendritic cells (DCs), 245
- Deoxyribonucleic acid (DNA)
  - elemental compositions, 24, 25
  - lipids, mucins and enzymes, 24–25
  - modified surfaces, biosensing (*see* DNA-modified surfaces)
- Depth profiling
  - and ADXPS, 11–12
  - chemical distribution, 17
  - coronene, C 1s spectra, 18
  - electron impact (EI) ion source, 54
  - measurements, 79
  - molecular, 81–84, 87, 91
  - sputtering, 48
  - ToF-SIMS, 38, 58
  - XPS, 19
- Dickenson, N.E., 225–250
- 3 Dimensional analysis
  - amino acids and phospholipids, 59
  - glutardialdehyde-fixed NRK cells, 49–50, 52, 59
  - organic samples, 62
- Dipalmitoylphosphatidylcholine (DPPC)
  - bilayer, AFM image, 239–240
  - high-resolution NSOM fluorescence, 234, 235
  - LE and LC phases, 234
  - monolayer, fluorescence, 233–234
  - RDS, 236
- DNA. *See* Deoxyribonucleic acid (DNA)
- DNA-modified surfaces
  - adenine–thymine (A–T) and cytosine–guanine (C–G), 291
  - hybridization, 293
  - microarrays, 291–292
  - structure and hybridization properties
    - hybridization, 300–301
    - immobilization, 294, 295
    - nitrogen K-edge NEXAFS spectra, 297
  - SAMs, 294

- DNA-modified surfaces (*cont.*)  
 SPR, 298, 299  
 ssDNA, 293, 298  
 XPS, 294, 296  
 X-ray absorption, 297  
 surface analytical techniques, 293  
 surface chemical state image analysis  
 categories, 301  
 fluorescence microscopy, 305, 307  
 hybridization efficiency, 305  
 image scores and loadings, 309–310  
 micro-printing techniques, 302  
 microspots, 304  
 negative-ion ToF-SIMS ROI spectra,  
 305, 306  
 XPS and ToF-SIMS, 302–303, 306, 308
- DPPC. *See* Dipalmitoylphosphatidylcholine  
 (DPPC)
- Drug metabolism  
 IMS protocols and instruments, 100  
 MRM-based imaging, 129  
 profile and ADME, 127–128  
 signal intensities, 128
- Duke, C.B., 2
- Dunn, R.C., 225–250
- Dynamic contact angle (DCA), 3
- E**
- Easton, C.D., 9–31
- Eckert, R., 267
- Edidin, M., 233, 244
- Electron impact (EI) ion source, 44
- Electron spectroscopy for chemical analysis  
 (ESCA), *See also* X-ray  
 photoelectron spectroscopy  
 (XPS), 10, 294
- Electrophysiology  
 single cells and excised membrane  
 patches  
 electromechanical motors, 279–280  
 optical transparent plastic plates, 279  
 single-ion-channel recording, 278  
 voltage-sensitive ion channels, 279  
 tissue sections  
 cochlear hair cells, inner ear, 280  
 DIC, 280  
 differential interference contrast  
 (DIC), 280  
 force interaction, 281  
 force transmission, 281  
 mechanically independent  
 stereocilia, 282  
 mechanical stimulus, 282  
 mechanosensitive ion channels, 284  
 micromechanical measurements, 283  
 sound-pressure level, 282–283  
 transduction current measurements, 283
- Electrospray-deposition (ESD) system, 121
- Elemental composition, 24, 25
- Erickson, E.S., 225–250
- Evans-Nguyen, K.M., 204
- F**
- Fairley, N., 30
- Fartmann, M., 57
- FIB. *See* Focused ion beam (FIB)
- Field ion microscope (FIM), 176
- Fluorescence  
 DNA hybridization, 293  
 microscopy, 305, 307  
 NSOM  
 confocal, 234, 236, 237  
 DCs, 245  
 F-actin fibers, 244  
 high spatial resolution, 234  
 images, 234, 240  
 lipid monolayer, 230  
 model membranes, 233  
 phalloidin, 244  
 tetramethylrhodamine, 244  
 radioactive, 303
- Fluorescence resonance energy transfer  
 (FRET), 240–242
- Focused ion beam (FIB), 247
- Formalin-fixed and paraffin-embedded (FFPE)  
 tissue, 113
- Fourier transform ion cyclotron resonance  
 (FT-ICR), 109, 111–112
- Fragmentation pathway  
 G-SIMS (*see* G-SIMS fragmentation  
 pathway mapping  
 (G-SIMS-FPM))  
 SMILES (*see* Simplified molecular input  
 line entry specification (SMILES))
- FRET. *See* Fluorescence resonance energy  
 transfer (FRET)
- Friction mode, 261
- FT-ICR. *See* Fourier transform ion cyclotron  
 resonance (FT-ICR)
- Full-width half-maximum (FWHM), 230
- FWHM. *See* Full-width half-maximum  
 (FWHM)
- G**
- Gamble, L.J., 289–310
- Garcia-Parajo, M.F., 245
- Gardella, J.A., 60

- Gas-phase basicity (GB), 105
- Gasteiger, J., 160
- Gentle secondary ion mass spectrometry (G-SIMS)
- bovine serum albumin, 154
  - cholesterol, caffeine and poly-L-lysine, 154, 155
  - drug-delivery systems and biomedical implants, 152
  - energy distribution, excited atoms, 145
  - fingerprint approach, 148
  - folic acid, molecular structure, 154, 155
  - fragmentation process, 143
  - G-SIMS-FPM (*see* G-SIMS fragmentation pathway mapping (G-SIMS-FPM))
  - hydrocarbon molecule, series  $C_nH_{2n}$ , 146
  - ion beam parameters, 150–151
  - Irganox 1010, 152, 153
  - low surface plasma temperature, 147
  - mass-scale calibration, 156
  - mass spectra, 142
  - molecular fragments, 146
  - multivariate methods, complementarity, 143
  - optimization, instrument parameters, 150
  - partition function relation, 146
  - 80:20 PLGA co-polymer, 153, 154
  - polycarbonate (PC) and Irganox 1010, 166–167
  - polycyclic aromatic hydrocarbon ions, 152
  - polymer industry, 142
  - polystyrene (PS) spectral intensities, 147–149
  - secondary ion formation, 153
  - spectra acquisition, 151–152
  - surface-energy distribution, 145
  - ToF systems, 154
- Giessibl, F.J., 258
- Gillen, G., 82
- Gilmore, I.S., 141–168
- Goetze, B., 171–192
- Gong, P., 289–310
- G proteins, 201, 214, 215
- Graham, D.J., 60
- Grainger, D.W., 289–310
- Green, F.M., 141–168
- G-SIMS. *See* Gentle secondary ion mass spectrometry (G-SIMS)
- G-SIMS fragmentation pathway mapping (G-SIMS-FPM)
- chemical permutations, 156
  - folic acid,  $g_{\max}$  values, 158, 159
  - and G-SIMS SMILES, 144
  - ion-trap systems, 157
  - 10-keV argon and cesium ions, 157, 158
  - low-energy collision, 156
  - mass scale and instrument optimization, 156
  - positive-and negative-ion data, 158
  - SIMS emission process, 157
  - surface plasma temperature, 157, 158
- G-SIMS imaging, 166–167
- Guerquin-Kern, J.-L., 38
- ## H
- Hagenhoff, B., 37–63
- Harbers, G.M., 289–310
- HASM. *See* Human arterial smooth muscle (HASM)
- Heeren, R.M.A., 99–133
- Helium ion microscope (HIM)
- Acidovorax, 172, 173
  - beam energies, 173
  - beam-specimen interaction, 178–188
  - detectable particles and detector, 174
  - imaging applications, biology, 192
  - inherent surface specificity, 172
  - ion source and ion column, 174
  - probe formation, 177–178
  - sample charging and preparation characteristics, 189
  - imaging biological specimens, 188
  - intercalated and principal cells, kidney, 191
  - rat kidney preparation, 191
  - ultrastructure, mouse tooth enamel, 189, 190
  - signal-to-noise ratio, 174, 175
  - source
    - electron and gallium ion beams., 176
    - nanometer-level precision, 177
    - ultrahigh-vacuum (UHV) vessel, 175, 176
- Hillenkamp, F., 103
- Hooke's law, 258
- Hörber, J.K.H., 255–285
- Human arterial smooth muscle (HASM), 243, 244
- ## I
- Identification and interpretation
- G-SIMS fragmentation pathways, 165–166
  - mass spectrum, 168
- Imaging
- chemical processes, 172
  - high-resolution imaging techniques, 172
  - high-resolution surface analysis, 172
  - HIM (*see* Helium ion microscope (HIM))
  - STEM, 172
  - surface specificity, 171

- Imaging (*cont.*)
- ToF-SIMS
    - applications, 58
    - epithelial cells, EthDI, 51, 54
    - LB films and SAM, 55–56
    - semiquantitative interpretation, 54
    - single cells, 57
    - tissue sections, 56–57
  - Imaging mass spectrometry (IMS)
    - applications, 109
    - biological surface analysis, 100–101
    - compositions and structures, surfaces, 100
    - description, 132–133
    - detection efficiencies, 109
    - FT-ICR, 111–112
    - IMMS, 112
    - instruments, 111–113
    - ion-optical microscope elements, 112
    - MALDI (*see* Matrix-assisted laser desorption/ionization (MALDI))
    - mass analyzer characteristics, 109
    - microprobe and microscope modes, 102, 103
    - molecular and spatial resolution, 99
    - molecular imaging technique, 99
    - proteins, lipids and carbohydrates, 120
    - publications, 100
    - silicon wafer masks, microstructures, 113
    - SIMS (*see* Secondary ion mass spectrometry (SIMS))
    - ToF, 110–111
  - Immobilized
    - DNA molecules, 292, 305
    - ssDNA probe, 292
  - IMMS. *See* Ion-mobility mass spectrometry (IMMS)
  - IMS. *See* Imaging mass spectrometry (IMS)
  - Interfaces, SFG
    - amide I protein signals (*see* Amide I protein signals)
    - CH and NH spectral signals
      - amino acids and peptides, 205
      - BSA, 204
      - hydrophobic groups, 204
      - pH values, 205
      - protein–protein interactions, 205
    - isotope labeling, 205–206
    - nucleic acids, 217
    - PSLB, 216–217
  - Intramolecular forces
    - double-cantilever AFM, 268–269
    - energy scheme, pathway, 272
    - force–extension relationship, spectrin, 269–270
    - Gaussian distributions, 271
    - $\alpha$ -helices, spectrin, 271, 272
    - isothermal restoring force, 270–271
    - modular structure, proteins, 267
    - protein-folding and-unfolding pathways, 267, 271
    - recombinant DNA techniques, 269
    - spectrin, mechanical behavior, 273
    - thermodynamic studies, 271
  - Ion-mobility mass spectrometry (IMMS), 112
  - Ion scattering spectroscopy (ISS), 2
  - Isotope labeling, 205–206
  - ISS. *See* Ion scattering spectroscopy (ISS)
- J**
- Joens, M.S., 192
- K**
- Karas, M., 103
  - Kozole, J., 71–97
  - Kulp, K.S., 60
- L**
- Langer, M.G., 284
  - Langmuir–Blodgett (LB) films
    - hydrogen atoms, 55
    - lipid mixtures, 55
    - Survanta monolayer, 236, 237
    - temperature, 56
  - Lee, C.-Y., 25, 289–310
  - LE/LC phases. *See* Liquid-expanded/condensed (LE/LC) phases
  - Leone, L., 27
  - Leufgen, K.M., 55
  - Levi-Setti, R., 57
  - Lewis, K.B., 12
  - Lipid imaging
    - single cells, 91–92
    - tissue imaging (*see* Tissue imaging)
  - Lipid monolayers
    - AFM, 233–235
    - buckling, 237
    - cellular membrane fractions, 235
    - confocal fluorescence, 233–234, 236, 237
    - DPPC lipid monolayer, 233–235
    - electric fields, 238
    - far-field images, 237
    - fluorescence image, 233, 236
    - GM1 rafts, 235–236
    - LB films, 233, 234, 236, 237
    - LE/LC, 233–235
    - lipid rafts, 234, 235

- microdomains, 234, 235
- PMMA, 238
- RDS, 236
- single-molecule fluorescence image, 238
- spatial resolution, 234
- sphingomyelin-cholesterol-DOPC, 235, 236
- topography, 234, 235, 237
- transition dipole moment, 239
- Lipidomics, 101, 113
- Lipids
  - enzymes, and DNA, 24–25
  - and mucins, 10
- Liquid-expanded/condensed (LE/LC) phases, 234, 240
- Liquid metal ion gun (LMIG), 72, 121
- Liquid metal ion source (LMIS)
  - advantages, 43
  - gold and bismuth sources, 43–44
  - needle, 43
  - parameters, 43
- Liu, J., 216
- Liu, Z.C., 25
- LMIG. *See* Liquid metal ion gun (LMIG)
- LMIS. *See* Liquid metal ion source (LMIS)
- Lou, L., 29
  
- M**
- Mahoney, C.M., 58
- Major histocompatibility complex (MHC), 244
- MALDI. *See* Matrix-assisted laser desorption/ionization (MALDI)
- Matrix-assisted laser desorption/ionization (MALDI)
  - carbohydrates and metabolites, plants, 129–130
  - cluster SIMS, 87
  - drug distribution and quantification, 127–129
  - element/metal detection, 131
  - HCCA classical vs. HCCA/ANI ionic matrix, 105, 107
  - image reconstructions, 105
  - imaging, lipids, 130, 131
  - ion-formation mechanisms, 104–105
  - ionic matrices, 105
  - laser irradiation, 104
  - laser performance and stability, 104
  - mass spectral analysis, 105
  - matrices and structures, 105, 106
  - microprobe mode, 103–104
  - microscope, 111–112
  - peptide and protein detection, 126
  - proteomics and clinical proteomics, 126–127
  - specific mass spectrometry imaging, 129, 130
  - system control, 104
  - thermodynamics, reaction, 105
- Matrix-enhanced SIMS (ME-SIMS)
  - dried droplet deposition, 116
  - glycerol matrices, 107
  - ionization enhancement, 118
  - lipids and peptides, 108–109
  - Lymnaea stagnalis* nervous tissue, 121, 123
  - vs. MALDI, 121, 122
  - matrices and applications, 115, 117
  - surface analysis, 121
- May, C.J., 53, 60
- McArthur, S.L., 9–31
- McLafferty, F.W., 40
- MCP detector. *See* Microchannel plate (MCP) detector
- MD simulations. *See* Molecular dynamics (MD) simulations
- Medium energy ion spectroscopy, 180
- Melittin
  - antimicrobial activity, 210
  - fibrinogen coiled-coils, 212–213
  - Gaussian distribution, 210–211
  - G-protein, 214, 215
  - maximum-entropy function, 211–212
  - orientation distribution, 211
- Metal-assisted SIMS (Meta-SIMS)
  - assistance, chemical modifications, 125
  - cellular localization, 121, 124
  - enhanced secondary ion signal, 107
  - gold islands, migration, 121–122
  - SSIMS, 108
  - surface analysis, 121
- Meyer, E., 259
- MHC. *See* Major histocompatibility complex (MHC)
- MIC. *See* Microbiological corrosion (MIC)
- Michel, R., 53
- Microarrays
  - and biosensor surfaces, 293
  - DNA hybridization, 293
  - micro-printing techniques, 302
- Microbiological corrosion (MIC), 29
- Microchannel plate (MCP) detector, 185, 186
- Milillo, T.M., 60
- Mishra, G., 9–31
- Molecular depth profiling
  - SIMS
    - advantages, cluster projectiles, 82
    - chemical damage, 81–82
    - C<sub>60</sub><sup>+</sup> primary ion fluence, PLA, 81, 82
    - description, 83–84



- Molecular depth profiling (*cont.*)  
 parameters, 83  
 polyatomic projectiles, 82  
 SF<sub>5</sub><sup>+</sup> primary ion fluence, 82, 83  
 variables, 84
- ToF-SIMS  
 EI ion source, 44  
 layered polymer system, 49, 51, 58  
 LB films, 58  
 primary ions, 48  
 sputter erosion, 48
- Molecular dynamics (MD) simulations  
 Ag solid crystal, 15-keV Ga, 73, 74  
 Au atoms, 76  
 C atom, 15-keV C<sub>60</sub>, 73–74  
 5-keV Au<sub>3</sub> and 5-keV C<sub>60</sub>, 75–76  
 physical damage, 79
- Molecular structure  
 G-SIMS (*see* Gentle secondary ion mass spectrometry (G-SIMS))  
 SMILES (*see* Simplified molecular input line entry specification (SMILES))
- Molecular weight  
 biochemical properties, 120  
 secondary-ion images, polymer, 110
- Monroe, E.B., 56–57
- Mooren, O.L., 225–250
- Multiple reaction monitoring (MRM)-based imaging, 129
- Multi-technique, DNA-modified surfaces.  
*See* DNA-modified surfaces
- Multivariate statistical analysis, 302
- N**
- Near-field scanning optical microscopy (NSOM)  
 and AFM, 226  
 Airy disk pattern, 227  
 aperture, 228  
 biological applications (*see* Biological structures, NSOM)  
 chemical etching, 228, 229  
 and DPPC, 230  
 fiber optics, 228  
 and FIB instrument, 228, 229  
 fluorescence, 230  
 and FWHM, 230  
 hydrofluoric acid (HF), 228  
 light passing, 227, 228  
 numerical aperture, 227  
 optical measurements, 227  
 probes, sample heating, 230–233  
 and SEM, 228, 229  
 shear-force feedback, 229  
 spatial resolution, 226, 227  
 SPM and TEM, 226  
 tissue and cellular structure, 225
- Nonspecific binding, 298, 301
- Notte, J., 171–192
- Nucleic acids  
 biosensors, 300  
 hybridization, 292  
 probes, 302
- Nygren, H., 56
- O**
- Obst, M., 172
- Odom, R.W., 107–108
- Ogaki, R., 152
- Operational modes, ToF-SIMS  
 data collection, 49  
 depth profiling, 58  
 3 dimensional analysis, 49–50, 52, 58–59  
 imaging  
 applications, 58  
 epithelial cells, EthDI, 51, 54  
 LB films and SAM, 55–56  
 semiquantitative interpretation, 54  
 single cells, 57  
 tissue sections, 56–57  
 intensity, sputtering, 49, 51  
 mass-spectrometric techniques, 49, 50  
 spectrometry  
 DNA oligomers, 53  
 DPPC, 50, 53  
 enzyme activity, 54  
 proteins, 53
- Optical microscopy *See also* Near-field scanning optical microscopy (NSOM)  
 biological process, 276–277  
 cell membrane, exocytosis, 276  
 cell physiology-measuring techniques, 274  
 cell suspension, 276  
 conventional piezotube scanner, 273  
 exocytosis, progeny virus, 277  
 live cells, physiological conditions, 274, 275  
 membrane dynamics, 276  
 modulation measurements, 274  
 phagocytosis/cell movement, 276  
 piezotube scanner, 275  
 position-sensitive quadrant photodetector, 275  
 virus reproduction, 276–277
- Optical waveguide lightmode spectroscopy (OWLS), 9

- Orientation analysis, SFG  
  CH groups  
    advantage, 198  
    fitted signal intensity, 199  
    methyl groups, 199–200  
    protein secondary structures, 200  
   $\alpha$ -helix, 200–201  
   $\beta$ -sheet, 201–202  
OWLS. *See* Optical waveguide lightmode spectroscopy (OWLS)
- P**  
Pacholski, M.L., 37–38  
Paynter, R.W., 11, 17, 21  
PCA. *See* Principal component analysis (PCA)  
Physiological conditions, AFM. *See* Optical microscopy  
Planar-supported lipid bilayer (PSLB)  
  advantage, isotope-labeled lipids, 216  
  asymmetric bilayers, 216–217  
  Langmuir–Blodgett and Langmuir–Schaefer techniques, 216  
PMMA. *See* Polymethyl-methacrylate (PMMA)  
Polyatomic ion source, 38, 72  
Polymethyl-methacrylate (PMMA), 241  
Principal component analysis (PCA)  
  DNA microspot, 309  
  ToF-SIMS negative-ion image, 309  
Probes  
  DNA/thiol diluent, 298  
  hybridization, 301  
  NSOM, sample heating  
    catastrophic damage, 232, 233  
    chemical etching technique, 232  
    electron micrographs, 232, 233  
    emission spectrum, 231–232  
    fiber optics, 231  
    laser power, 232, 233  
    *N*-allyl-*N*-methylaniline, 231, 232  
    output power, 232  
    perylene, 231, 232  
    power technology, 232  
    thermal expansion, 232, 233  
    thermochromic polymer, 231, 232  
  nucleic acid, 302  
  ssDNA, 292  
Proteins and peptides  
  amide I protein signals (*see* Amide I protein signals)  
  high-resolution XPS C 1s spectrum, 21, 23  
  surface nitrogen, 21, 22  
  XPS, 21
- Proteomics  
  MALDI mass-spectrometric imaging, 127  
  microspot deposition, matrix, 126  
  microspotted matrix depositio, 126  
  spraying system, 126  
PSLB. *See* Planar-supported lipid bilayer (PSLB)
- Q**  
Quantitative analysis, XPS, 13, 30  
Quartz crystal microbalance (QCM), 9, 76–77
- R**  
Radial distribution chamber (RDC), 14, 15  
Ratner, B.D., 11, 12, 17, 21  
Respiratory distress syndrome (RDS), 236  
Richter, K., 56  
Rohrer, H., 256  
Rutherford backscatter spectroscopy, 180, 184  
Rutherford, E., 180, 184
- S**  
SAMs. *See* Self-assembled monolayers (SAMs)  
Scanning electron microscopy (SEM)  
  charging effects, 172  
  granules, aluminum coating, 228, 229  
  high gas pressures, 188  
  high-resolution imaging instrument, 172  
  imaging biological specimens, 188  
  sample preparation protocols, 191  
  SEs, 181, 182  
Scanning near-field optical microscopy (SNOM), 5  
Scanning probe microscopy (SPM)  
  biological structure and function, 226  
  constant current imaging, 257  
  spatial resolution, 226  
Scanning transmission electron microscope (STEM), 172  
Schnieders, A., 37–63  
Schultz, J.A., 130  
Schwieters, J., 110  
Seah, M.P., 141–168  
Secondary electrons (SEs)  
  characteristic bright-edge effect, 182, 184  
  collagen fibers, 182  
  Everhart–Thornley detector, 182, 183  
  helium-induced, 182  
  image formation, 181  
  type-one secondary electrons (SE1), 182

- Secondary ion mass spectrometry (SIMS)  
 Au<sub>3</sub><sup>+</sup>/Bi<sub>3</sub><sup>+</sup> and C<sub>60</sub><sup>+</sup> projectiles, 86–87  
 biological tissue (*see* Tissue imaging)  
 chemical sensitivity, 4  
 cluster ion sources, 72  
 description, 72–73  
 3D image, depth calibration, 85–86  
 2D image, pixel size, 84–85  
 energetic (keV) atomic projectiles, 72  
 enhancement, molecular ion yield, 106–107  
 gas-phase ion sources, 72  
 high-spatial-resolution analytical  
 microscopy, 105  
 ion optics, 105  
 MALDI, 87  
 matrix-enhanced, 107–108  
 MD simulations (*see* Molecular dynamics  
 (MD) simulations)  
 metal-assisted, characteristics, 108–109  
 molecular depth profiling, 81–84  
 physical damage  
 ion beam, 79  
 nickel/chromium (Ni/Cr) layers, 79–80  
 sugar trehalose, AFM, 80–81  
 surface sensitivity, 79  
 postionization, 96  
 sample preparation, 95–96  
 single cells (*see* Single-cell imaging)  
 surface analysis and imaging, 106  
 surface metallization and matrix  
 deposition, 119–120  
 ToF analyzer, 105  
 ToF-SIMS (*see* Time-of-flight secondary  
 ion mass spectrometry (ToF-SIMS))  
 yield enhancement  
 Langmuir–Blodgett techniques, 77  
 neutrals, 77  
 organic materials, 77  
 PS-200 and Gramicidin D, 77–78  
 QCM, 15-keV C<sub>60</sub>, 76–77
- Self-assembled monolayers (SAMs), 55,  
 294, 297
- SEM. *See* Scanning electron microscopy  
 (SEM)
- SERS. *See* Surface-enhanced Raman  
 scattering (SERS)
- SFG vibrational spectroscopy. *See* Sum  
 frequency generation (SFG)  
 vibrational spectroscopy
- Shubeita, G.T., 241
- Sigmund, P., 39
- Signor, L., 128
- Simplified molecular input line entry  
 specification (SMILES)  
 archetypal molecular entities, 165  
 ASCII text string, 161  
 Daylight Chemical Information Systems, 161  
 DENDRAL project, 160  
 description, 161  
 folic acid text, 162  
 fragmentation mass and level, folic acid, 163  
 informatics, 161  
 mass-based tree structure, 163  
 mass spectra prediction, 160  
 secondary ion intensities, 164  
 SIMS library spectra, 164  
 simulated fragmentation pathways, 161–162  
 syntax and grammar, 161  
 valine and tyrosine, 164
- SIMS. *See* Secondary ion mass spectrometry  
 (SIMS)
- Simulated spectra  
 fragmentation library, 168  
 SMILES fragmentation pathway, 164
- Single-cell imaging  
 fusion pores, 91  
 peptides and lipids  
 biological applications, 125  
 cellular localization, MetA-SIMS,  
 121, 124  
 direct molecular imaging, *Lymnaea  
 stagnalis* nervous tissue, 121, 123  
 gold deposition, 124  
 lateral resolution analyte diffusion,  
 121–122  
 MALDI stigmatic imaging, rat brain  
 tissue, 125  
 ME-SIMS vs. MALDI, 121, 122  
 surface-enhanced SIMS, 121  
 surface metallization, 121  
*Tetrahymena*, 93–94  
*Xenopus laevis* oocyte, 94–95
- Single molecule detection  
 lipid monolayer, 230, 238  
 polarization, 245
- Single-stranded DNA (ssDNA).  
*see* DNA-modified surfaces
- Sjövall, P., 57
- Slodzian, G., 105
- Small spot spectroscopy, 19–20
- Smentkowski, V.S., 1–5, 60
- SMILES. *See* Simplified molecular input line  
 entry specification (SMILES)
- SNOM. *See* Scanning near-field optical  
 microscopy (SNOM)
- Somorjai, G.A., 204
- Sostarecz, A.G., 55, 58
- SPM. *See* Scanning probe microscopy (SPM)

- SPR. *See* Surface plasmon resonance (SPR)
- SSIMS. *See* Static secondary ion mass spectrometry (SSIMS)
- Static secondary ion mass spectrometry (SSIMS)
- bovine serum albumin samples, 154
  - degraded fragment products, 156
  - dominant intensity ions, 148
  - polyamino acid poly-L-lysine, 154
  - polystyrene (PS), 148, 149
- Stauber, J., 99–133
- Stephens, W.E., 110
- Stokes, G.V., 277
- Stylus, 226, 247
- Sum frequency generation (SFG) vibrational spectroscopy
- amide I protein signals (*see* Amide I protein signals)
  - blood coagulation, 195
  - description, 217–218
  - experimental procedures
    - components, 202–203
    - DR-SFG signal intensity, 203–204
    - instruments, 202
    - “near” total internal reflection, 203
    - surface sensitivity, 203
  - interfaces, biological molecules (*see* Interfaces, SFG)
  - lipid membranes, 196
  - nonlinear optical process
    - ATR-FTIR probes, 197
    - CH stretching modes, 198
    - materials, 196–197
    - SERS, 198
    - vibrational modes, FTIR, 197
  - orientation analysis (*see* Orientation analysis, SFG)
  - surface-sensitive in situ probes, 196
- Surface analysis instrumentation
- applications, 2
  - biological sample analysis, 2, 3
  - instruments and data analysis protocol, 5
  - sample preparation methods, 5
- Surface-enhanced Raman scattering (SERS), 198
- Surface metallization (MetA-SIMS), 108–109
- Surface plasmon resonance (SPR)
- DNA hybridization, 294
  - measurement, 298, 299
  - and spectroscopy, 293
- Surface roughness, 260–261
- T**
- Tachyplesin I, 215
- Tandem mass spectrometry (MS), 128, 132
- Tapping mode, 262
- Tarlov, M.J., 294
- TEM. *See* Transmission electron microscopy (TEM)
- Thompson, C.E., 60
- Thompson, M.W., 39
- Three-dimensional (3D) chemical imaging
- depth calibration, 85–86
  - Xenopus laevis* oocyte cell, 94–95
- Time-of-flight secondary ion mass spectrometry (ToF-SIMS)
- charge compensation, 47–48
  - data quality
    - secondary ionization probability, 59–60
    - statistical evaluation, 60–61
  - depth profiling, 48
  - description, 38
  - development, 37–38
  - DNA hybridization, 306
  - formation
    - cluster primary ions, 41–42
    - collision cascades, 39–40
  - GCIB sources, 62
  - G-SIMS-FPM, 156, 157
  - ion detection, 47
  - life science applications, 63
  - operational modes (*see* Operational modes, ToF-SIMS)
  - primary ions (*see* Cluster ion source)
  - pumping rate, vacuum system, 61
  - quantification, 61–62
  - separation process, 46–47
  - and XPS, 293, 302
- Tip-sample interactions
- AFM, 247–249
  - biological tissues, 246
  - FIB, 247–249
  - fiber-optic, 246
  - fragile samples, 246
  - HASM cell, 248, 250
  - hybrid probe, 248, 250
  - interferometric signal, 246
  - model membranes, 246
  - noninvasive imaging, 246, 247
  - refractive index, 248
  - silicon nitride probes, 247
  - thin acetate matrix, 248, 249
  - topography, 248
- Tissue analysis
- components, 25
  - hard tissue, 28–29
  - microbial cells, 27, 28
  - UHV technique, 27–28

- Tissue imaging  
 cellular membranes, 88  
 human atherosclerotic plaque, 91  
 in vivo analysis, 88  
 mouse brain  
   anatomic structures, 88–89  
   lipid heterogeneity, 89, 90  
   phosphocholine and cholesterol, 90  
   raclopride drug, 90–91
- Tissue surfaces  
 biodistribution and metabolism, 132  
 enhanced-surface IMS techniques, 132, 133  
 MALDI (*see* Matrix-assisted laser desorption/ionization (MALDI))  
 metallization and matrix-deposition, 119–120  
 SIMS (*see* Secondary ion mass spectrometry (SIMS))  
 spatial resolution, 132  
 surface modifications  
   matrix deposition, 115–118  
   metal deposition, 118–119  
   organic solvent treatment, 115  
 tissue collection  
   biological samples, 114–115  
   fast frozen, 114  
   frozen and FFPE, 113, 114  
   trypsin digestion, 132
- ToF-SIMS. *See* Time-of-flight secondary ion mass spectrometry (ToF-SIMS)
- Topography  
 immunofluorescence, 226  
 microdomains, 244  
 semicircular domains, 234
- Transmission electron microscopy (TEM), 172, 226
- Tunneling  
 quantum-mechanical process, 256  
 vacuum gap, 256
- Turecek, F., 40
- Tyler, B.J., 60
- U**
- Ultrahigh-vacuum (UHV), 10, 13, 14, 28
- Urbassek, H.M., 40
- V**
- Vaidyanathan, S., 57, 59
- Van der Waals force, 258, 261
- Vickerman, J.C., 142, 157
- Vroman, L., 206
- W**
- Wagner, M.S., 21, 53
- Walton, J., 30
- Wang, J., 207, 210, 212, 215
- Weininger D., 161
- Winograd, N., 37–38, 58, 71–97
- Woods, A.S., 130
- Worm-like chain (WLC) mode, 270
- Wucher, A., 42, 85
- Wu, K.J., 107–108
- X**
- XPS. *See* X-ray photoelectron spectroscopy (XPS)
- X-ray photoelectron spectroscopy (XPS)  
 and ADXPS, 11–12  
 analytical techniques, 293  
 biointerface engineering, 29–30  
 biomolecules  
   lipids, mucins, enzymes and DNA, 24–26  
   proteins and peptides, 21–24  
 elements, 10–11  
 and ESCA, 10  
 freeze hydration, 12  
 imaging and mapping, 13  
 instrumentation  
   charge neutralization, 15–17  
   depth profiling, 17–19  
   imaging and mapping, 20–21  
   organic and biological systems, 13  
   RDC, 14, 15  
   small spot spectroscopy, 19–20  
 QCM and AFM, 9  
 SPR and OWLS, 9  
 surface sensitivity, 11  
 and tissue analysis (*see* Tissue analysis)  
 and ToF-SIMS, 302  
 and UHV, 10
- Z**
- Zeitvogel, F., 172